Bangladesh's "queen of cholera" campaigns for vaccines p. 572

Language-like patterns in whale song pp. 581 & 649

Calculating genetic risks for kidney disease p. 625

Science

$15
7 FEBRUARY 2025
SPECIAL ISSUE
science.org
AAAS

POLAR WORLD

Fundación BBVA

18th Edition
BBVA Foundation Frontiers of Knowledge Awards

With the collaboration of
CSIC
Consejo Superior de Investigaciones Científicas

The **BBVA Foundation Frontiers of Knowledge Awards** recognize and reward world-class research and artistic creation, prizing contributions of singular impact for their originality and significance. The name of the scheme is intended to denote not only research work that substantially enlarges the scope of our current knowledge – pushing forward the frontiers of the known world – but also the meeting and overlap of different disciplinary areas and the emergence of new fields.

The Frontiers of Knowledge Awards honor fundamental disciplinary or interdisciplinary advances across a broad expanse of the knowledge map of the 21st century.

The BBVA Foundation is assisted in the award process by the **Spanish National Research Council (CSIC)**.

Categories

1/ **Basic Sciences (Physics, Chemistry, Mathematics)**
2/ **Biology and Biomedicine**
3/ **Information and Communication Technologies**
4/ **Climate Change and Environmental Science**
5/ **Economics, Finance and Management**
6/ **Humanities**
7/ **Social Sciences**
8/ **Music and Opera**

Nomination

Nominations are invited from scientific or artistic societies and organizations, public or private R&D centers, university and hospital departments, schools of music, orchestras, and organizations working on or around the issue of climate change, as well as other institutions specified in the call conditions.

Entry submission

The nomination period concludes at **16:00 GMT on June 30, 2025**.

www.frontiersofknowledgeawards-fbbva.es

Fundación BBVA
Plaza de San Nicolás, 4 · 48005 Bilbao
Paseo de Recoletos, 10 · 28001 Madrid
awards-info@fbbva.es

CONTENTS

7 FEBRUARY 2025 • VOLUME 387 • ISSUE 6734

SPECIAL SECTION

THE POLAR WORLD

INTRODUCTION

NEWS

POLICY FORUM

REVIEWS

ON THE COVER

Climate change in the polar regions of our warming world is threatening to transform many of its features, such as this icy tableau in the Fish Islands off the coast of the Antarctic Peninsula. There is still much to learn about these places before we know better what those changes may be. See the special section beginning on page 588. *Photo: Pete McBride*

SEE ALSO BOOKS p. 584; RESEARCH ARTICLE BY FICHTNER *ET AL.* 10.1126/SCIENCE.ADP8094

PHOTO: PETE MCBRIDE

NEWS

IN BRIEF

IN DEPTH

FEATURES

INSIGHTS

PERSPECTIVES

Left to right: Marianne Bronner, Elham Azizi, Guosong Hong, and Maayan Levy

Navigating to the forefront of innovation: A celebration of immigrant scientists

Scientific progress in the United States is inextricably linked to the lives and stories of immigrants. Their efforts have improved lives worldwide and established this country as a beacon of scientific discovery. Immigrants represent 28% of the American recipients of Nobel Prizes awarded in physics, chemistry, and medicine between 1901 and 2024.

The Vilcek Foundation was established in 2000 to recognize and celebrate immigrant contributions to culture and society in the United States, with a focus on biomedical science and the arts and humanities. In 2025, the foundation awards a total of $250,000 in prizes to immigrant scientists, honoring foreign-born professionals at the forefront of research in immunotherapy, brain imaging, metabolite-based therapy, and human development. Marianne Bronner receives the $100,000 Vilcek Prize in Biomedical Science; Elham Azizi, Guosong Hong, and Maayan Levy each receive a $50,000 Vilcek Prize for Creative Promise.

Marianne Bronner

California Institute of Technology

Marianne Bronner was 4 years old when her family fled communist Hungary. Her early enthusiasm for physics transformed into a fascination with developmental biology, particularly the functions of neural crest stem cells (NCSCs). This group of transient, migratory cells found early in vertebrate development differentiate into a wide variety of cell types in the body and may have potential in regenerative therapies. Bronner's career-long examination of NCSCs has led to the identification of the mechanisms that drive genetic regulation of cell migration and differentiation, and furthered scientists' understanding of NCSC involvement in congenital disorders, cancer metastasis, and heart regeneration. She receives the Vilcek Prize for advancing science's understanding of how NSCSs contribute to the development of the nervous system, heart, and skeleton.

A pioneer in her field, Bronner prioritizes helping mentees develop their strengths and navigate careers. "I've never taken for granted the access to opportunities in a free country that helped me realize my dream of being a scientist."

Elham Azizi

Columbia University

Elham Azizi embodies the concept of a multidisciplinary approach to difficult problems. The Iranian-born computational biologist leverages an innate curiosity and background in genomics and bioengineering to reveal insights into cancer progression and persistence. She receives a Vilcek Prize for Creative Promise in recognition of ongoing efforts to enlist machine learning and artificial intelligence to unmask how the immune system interacts with complex diseases.

Azizi's efforts capitalize on tools offering an unprecedented opportunity to model a patient's unique immunological fingerprint and disease phenotype. "The ultimate goal is to translate strategies for targeting cancer and other diseases into effective, personalized immunotherapies for patients."

Guosong Hong

Stanford University

Born to working-class parents in China, Guosong Hong's fascination with the physical and chemical properties of matter was ignited by a children's book of chemistry experiments. Now a materials scientist at Stanford University, his research has accelerated breakthroughs in biological imaging and neuromodulation. Hong receives the Vilcek Prize for Creative Promise in recognition of his development of noninvasive methods to visualize complex physiological processes in real time.

Hong's work to optimize deep-tissue and brain imaging promises to allow glimpses of previously invisible biological processes. "The culture of academic freedom in this country has guided my career," he says. "Collaborations with brilliant colleagues continue to motivate new discoveries."

Maayan Levy

Stanford University

Immunologist and microbiologist Maayan Levy receives the Vilcek Prize for Creative Promise in recognition of her work on the efficacy of metabolites for the prevention and treatment of cancer, chronic inflammation, and other diseases.

Growing up in Israel, Levy witnessed firsthand how immigration can affect integration and equality; she carries this core experience in her practice, and advocates for minority students in the sciences. She is also a passionate supporter of women in STEM, especially those with children. As a principal investigator and mother, Levy appreciates the demands and rewards of each role and advocates for colleagues balancing parenthood and careers in science. "Creating an environment that minimizes compromises between being a scientist and mother encourages people to excel at both."

Scan to learn more:

Sponsored by

VILCEK FOUNDATION

PHOTOS: COURTESY OF VILCEK FOUNDATION

BOOKS *ET AL.*

LETTERS

RESEARCH

IN BRIEF

RESEARCH ARTICLES

Malaria

Evolution

DEPARTMENTS

PHOTO: PAUL STAROSTA/GETTY IMAGES

SCIENCE (ISSN 0036-8075) is published weekly on Friday, except last week in December, by the American Association for the Advancement of Science, 1200 New York Avenue, NW, Washington, DC 20005. Periodicals mail postage (publication No. 484460) paid at Washington, DC, and additional mailing offices. Domestic individual membership, including subscription (12 months): $165 ($74 allocated to subscription). Domestic institutional subscription (51 issues): $2865; Foreign postage extra: Air assist delivery: $135. First class, airmail, student, and emeritus rates on request. Canadian rates with GST available upon request, GST #125488122. Publications Mail Agreement Number 1069624. **Printed in the U.S.A.**

Change of address: Allow 4 weeks, giving old and new addresses and 8-digit account number. **Postmaster:** Send change of address to AAAS, P.O. Box 96178, Washington, DC 20090–6178. **Single-copy sales:** $15 each plus shipping and handling available from backissues.science.org; bulk rate on request. **Authorization to reproduce** material for internal or personal use under circumstances not falling within the fair use provisions of the Copyright Act can be obtained through the Copyright Clearance Center (CCC), www.copyright.com. The identification code for *Science* is 0036-8075. *Science* is indexed in the *Reader's Guide to Periodical Literature* and in several specialized indexes.

EDITORIAL

Keeping our eye on the ball

Willie E. May is the vice president of research and economic development at Morgan State University, Baltimore, MD, USA, and is the immediate past president of the American Association for the Advancement of Science, Washington, DC, USA. willie.may@morgan.edu

Unnerving. Concerning. Alarming. This is how many in the research community are describing the first weeks of the Trump administration.

The flurry of White House executive orders included withdrawals from the Paris Climate Agreement and the World Health Organization, limiting America's seat at the global scientific community table. Other edicts, striving to roll back decades of anti-discrimination and immigration policies, could make it more difficult to recruit and keep top science and technology talent. The temporary freeze on hiring, meetings, and communications across federal agencies such as the US National Science Foundation and the US Department of Health and Human Services, including the US Food and Drug Administration, the US Centers for Disease Control and Prevention, and National Institutes of Health, has created uncertainty and put public health and research in limbo.

Although these orders raise concerns, it is too early to know how they might be clarified, modified, implemented, or even rescinded. In particular, the scientific community should not allow these signals to distract it from fostering a resilient science and technology enterprise over the long term.

Jarring as it may be, this transition of government is an opportunity to reflect on the responsibilities of scientists and engineers to advocate for thoughtful investments in science that meet the challenges facing global society. These times should inspire a renewed determination to strengthen and safeguard research. This requires the scientific community to meet the future with measured optimism.

> "These times should inspire... determination to strengthen and safeguard research."

In the US, science has flourished under investments in fundamental research and cooperation between government, industry, academia, and philanthropy. For many Americans, these investments have provided quality education, expanded job opportunities, and ensured healthier lives. But the strategies that supported science in the 20th century need to keep up with the accelerated pace of technological change and threats to the well-being of society and the planet in the coming years.

As part of the commitment of the American Association for the Advancement of Science (AAAS, the publisher of *Science*) to accelerate a new era of investment, there will be a sneak peek of a Vision for American Science & Technology (VAST) at the AAAS Annual Meeting this month in Boston, Massachusetts. With the guidance of a task force (of which I am a member) representing 70 leaders in industry, government, and academia, VAST will unveil recommendations to reshape research and development strategies to promote investment and cross-sector collaborations in materials science, quantum computing, artificial intelligence, biotechnology, energy, and other areas essential to economic development and national security.

VAST recognizes the benefits that US-educated international scientists bring to the United States. But investments in the scientific enterprise will wither unless more Americans are empowered to enter science, technology, engineering, mathematics and medicine (STEMM). In my roles at AAAS and academia, I am committed to ensuring that societal and scientific challenges are met by problem solvers from a broad range of backgrounds, experiences, and geographies, who are prepared to make a difference.

Even as the legal landscape evolves, AAAS remains steadfast in its determination to develop this essential workforce. As the backbone organization of the STEMM Opportunity Alliance, AAAS and 260 partner organizations are following a road map for adding 20 million new STEMM workers to fortify the US economy by 2050.

This moment of transition in the United States is also a reminder for scientists to engage policy-makers and reach out to communities in the spirit of cooperation and service. In a Pew Research Center survey released late last year, only 45% of Americans said that scientists are good communicators, whereas 65% believe scientists are focused on solving real-world problems. The scientific community must take this feedback seriously if it is to bolster public trust and establish stronger mutual respect.

Athletes are often told to "keep their eyes on the ball." The future of science requires the scientific community to follow this same advice by providing thoughtful investments, a strong and adaptable workforce, and dedication to scientific responsibility. The primary job at this moment is to stay focused on the work that advances these goals.

–Willie E. May

10.1126/science.adw4149

A world less safe and secure

On 20 January, President Trump announced the withdrawal of the United States from the World Health Organization (WHO). President Trump shares many of the same concerns about WHO as previous administrations, including improved transparency, financial oversight, and accountability. He also believes that China has exerted undue influence on WHO—a charge that WHO adamantly denies. But the US cannot influence WHO if it is not at the table. WHO will remain at the center of global health governance, but this withdrawal will limit US leadership to protect public health and challenge WHO coordination in facing global challenges.

The US was central to the creation of WHO and has been its most influential member for over 75 years. US leadership has been foundational to WHO's achievements, from the eradication of smallpox and ongoing polio eradication initiative to its health-for-all strategy. As WHO's largest state funder, the US provides 22% of WHO's assessed contributions, alongside funds earmarked to US priorities, including HIV/AIDS and health emergencies.

> **"The US will be on the outside looking in… "**

Yet, when the US joined WHO in 1948, a joint resolution of Congress gave it the "right to withdraw from the Organization on a 1-year notice." Withdrawing from WHO now will forfeit US voting power and political leadership at the World Health Assembly, the WHO decision-making body, severely reducing its ability to set the world's health agenda, defend fundamental US interests, and advance crucial WHO reforms. The US will be on the outside looking in while the most consequential decisions are taken, including the adoption of a new Pandemic Agreement and the election of the next director-general in 2027. As global norms are set and scientific standards issued, the absence of the US will undermine scientific research, health security, and foreign policy.

The US benefits from WHO collaborations to advance scientific research. Seventy-one WHO Collaborating Centers are based in the US, including 18 at the Centers for Disease Control and Prevention. Withdrawing from WHO will limit domestic public health agencies and the US pharmaceutical industry, which rely on access to disease surveillance, pathogen samples, and genomic data through a vast network of WHO laboratories and other partners. As the US faces a major H5N1 influenza outbreak in livestock, US scientists would have reduced access to WHO's Global Influenza Surveillance and Response System to develop lifesaving countermeasures against H5N1 and ensure seasonal influenza vaccines.

WHO membership provides extensive networks to support US health security, safeguarding American lives and economic growth. WHO's Global Outbreak Alert and Response Network provides real-time data on novel outbreaks needed for early detection and response. The US has long looked to WHO to strengthen alliances and advance its national interests. If the US becomes the only major country outside WHO, allies would view America as an unreliable partner. It would feed a subversive narrative that the US is not a genuine partner with the Global South and weaken US diplomacy throughout the world.

Absent US funding and leadership, WHO could be severely weakened, making every country less healthy and safe. The agency's budget gap will be roughly $3.3 billion, with no state likely to compensate for that funding gap. Loss of US support will diminish WHO's ability to identify, report, and respond to public health emergencies. Much of WHO's work is unseen but critically important, including technical assistance, standard setting, and advocacy for evidence-based policies.

Within the World Health Assembly, new power structures and alliances will emerge that may shift key WHO policies important to the US in preparing for future pandemics, including the 2024 amendments to the International Health Regulations and a new Pandemic Agreement. Advancing US health priorities outside of WHO cannot compensate for being at the table in the world's premier health agency.

WHO without US leadership may give rise to a new global health order, where the loss of WHO authority will push other nations toward bilateral initiatives that advance national geopolitical priorities. This fractured global health ecosystem will undermine international cooperation and global solidarity necessary to respond to health threats that transcend national boundaries. It will also make it far more difficult to ensure equitable access to lifesaving medical resources—an important lesson from the COVID-19 pandemic. Without US leadership, this new multipolar governance landscape will reshape the very meaning of global health, challenging a divided world as it faces future health challenges.

–Lawrence O. Gostin and Benjamin Mason Meier

Lawrence O. Gostin is Distinguished University Professor at Georgetown University, co–faculty director of the O'Neill Institute for National and Global Health Law, and director of the World Health Organization Collaborating Center on National and Global Health Law, Washington, DC, USA. gostin@georgetown.edu

Benjamin Mason Meier is a professor of Global Health Policy at the University of North Carolina at Chapel Hill, Chapel Hill, NC, USA and a senior scholar at the O'Neill Institute for National and Global Health Law, Washington, DC, USA. bmeier@unc.edu

Science AAAS

Editor-in-Chief Holden Thorp, hthorp@aaas.org

Executive Editor Valda Vinson

Editor, Research Jake S. Yeston **Editor, Insights** Lisa D. Chong **Deputy Executive Editor** Lauren Kmec

DEPUTY EDITORS Stella M. Hurtley (UK), Phillip D. Szuromi, Sacha Vignieri **SR. EDITORS** Caroline Ash (UK), Michael A. Funk, Angela Hessler, Di Jiang, Priscilla N. Kelly, Marc S. Lavine (Canada), Sarah Lempriere (UK), Mattia Maroso, Yevgeniya Nusinovich, Ian S. Osborne (UK), L. Bryan Ray, H. Jesse Smith, Keith T. Smith (UK), Jelena Stajic, Peter Stern (UK), Yury V. Suleymanov, Valerie B. Thompson, Brad Wible **ASSOCIATE EDITORS** Jack Huang, Sumin Jin, Bianca Lopez, Sarah Ross (UK), Madeleine Seale (UK), Corinne Simonti, Ekeoma Uzogara **SENIOR LETTERS EDITOR** Jennifer Sills **NEWSLETTER EDITOR** Christie Wilcox **RESEARCH & DATA ANALYST** Jessica L. Slater **LEAD CONTENT PRODUCTION EDITORS** Chris Filiatreau, Harry Jach **SR. CONTENT PRODUCTION EDITOR** Amelia Beyna **CONTENT PRODUCTION EDITORS** Anne Abraham, Robert French, Julia Haber-Katris, Nida Masiulis, Abigail Shashikanth, Suzanne M. White **SR. EDITORIAL MANAGERS** Carolyn Kyle, Beverly Shields **SR. PROGRAM ASSOCIATE** Maryrose Madrid **EDITORIAL ASSOCIATES** Aneera Dobbins, Joi S. Granger, Lisa Johnson, Anita Wynn **SR. EDITORIAL COORDINATORS** Jeffrey Hearn, Alexander Kief, Ronmel Navas, Jerry Richardson, Isabel Schnaidt, Alice Whaley (UK), Brian White **EDITORIAL COORDINATORS** Clair Goodhead (UK), Kat Kirkman, Samantha Price **ADMINISTRATIVE COORDINATOR** Karalee P. Rogers **ASI DIRECTOR, OPERATIONS** Janet Clements (UK) **ASI OFFICE MANAGER** Victoria Smith **ASI SR. OFFICE ADMINISTRATORS** Dawn Titheridge (UK), Jessica Waldock (UK) **COMMUNICATIONS DIRECTOR** Meagan Phelan **DEPUTY DIRECTOR** Matthew Wright **SENIOR WRITERS** Walter Beckwith, Joseph Cariz **WRITERS** Abigail Eisenstadt, Mahathi Ramaswamy **SENIOR COMMUNICATIONS ASSOCIATES** Zachary Graber, Sarah Woods **COMMUNICATIONS ASSOCIATES** Kiara Brooks, Haley Riley, Mackenzie Williams

News Editor Tim Appenzeller

NEWS MANAGING EDITOR John Travis **INTERNATIONAL EDITOR** David Malakoff **DEPUTY NEWS EDITORS** Rachel Bernstein, Shraddha Chakradhar, Elizabeth Culotta, Martin Enserink, David Grimm, Eric Hand, Kelly Servick, Matt Warren (Europe) **SR. CORRESPONDENTS** Daniel Clery (UK), Jon Cohen, Jeffrey Mervis, Elizabeth Pennisi **ASSOCIATE EDITORS** Jeffrey Brainard, Michael Price **NEWS REPORTERS** Adrian Cho, Jennifer Couzin-Frankel, Phie Jacobs, Jocelyn Kaiser, Rodrigo Pérez Ortega (Mexico City), Robert F. Service, Erik Stokstad, Paul Voosen, Meredith Wadman **CONTRIBUTING CORRESPONDENTS** Vaishnavi Chandrashekhar, Dan Charles, Warren Cornwall, Andrew Curry (Berlin), Ann Gibbons, Sam Kean, Eli Kintisch, Kai Kupferschmidt (Berlin), Andrew Lawler, Mitch Leslie, Virginia Morell, Dennis Normile (Tokyo), Cathleen O'Grady, Elisabeth Pain (Careers), Charles Piller, Richard Stone (Senior Asia Correspondent), Gretchen Vogel (Berlin), Lizzie Wade (Mexico City) **CAREERS** Katie Langin (Associate Editor) **INTERNS** Hannah Richter **COPY EDITORS** Julia Cole (Senior Copy Editor), Hannah Knighton, Cyra Master (Copy Chief) **ADMINISTRATIVE SUPPORT** Meagan Weiland

Creative Director Beth Rakouskas

DESIGN MANAGING EDITOR Chrystal Smith **GRAPHICS MANAGING EDITOR** Chris Bickel **PHOTOGRAPHY MANAGING EDITOR** Emily Petersen **MULTIMEDIA MANAGING PRODUCER** Kevin McLean **DIGITAL DIRECTOR** Kara Estelle-Powers **DESIGN EDITOR** Marcy Atarod **DESIGNER** Noelle Jessup **SENIOR SCIENTIFIC ILLUSTRATOR** Noelle Burgess **SCIENTIFIC ILLUSTRATORS** Austin Fisher, Kellie Holoski, Ashley Mastin **SENIOR GRAPHICS EDITOR** Monica Hersher **GRAPHICS EDITOR** Veronica Penney **SENIOR GRAPHICS SPECIALISTS** Holly Bishop, Nathalie Cary **SENIOR PHOTO EDITOR** Charles Borst **PHOTO EDITOR** Elizabeth Billman **SENIOR PODCAST PRODUCER** Sarah Crespi **SENIOR VIDEO PRODUCER** Meagan Cantwell **SOCIAL MEDIA STRATEGIST** Jessica Hubbard **SOCIAL MEDIA PRODUCER** Sabrina Jenkins **WEB DESIGNER** Jennie Pajerowski

Chief Executive Officer and Executive Publisher Sudip Parikh

Publisher, Science Family of Journals Bill Moran

DIRECTOR, BUSINESS SYSTEMS AND FINANCIAL ANALYSIS Randy Yi **DIRECTOR, BUSINESS OPERATIONS & ANALYSIS** Eric Knott **MANAGER, BUSINESS OPERATIONS** Jessica Tierney **MANAGER, BUSINESS ANALYSIS** Cory Lipman **BUSINESS ANALYSTS** Kurt Ennis, Maggie Clark, Isacco Fusi **BUSINESS OPERATIONS ADMINISTRATOR** Taylor Fisher **DIGITAL SPECIALIST** Marissa Zuckerman **SENIOR PRODUCTION MANAGER** Jason Hillman **SENIOR MANAGER, PUBLISHING AND CONTENT SYSTEMS** Marcus Spiegler **CONTENT OPERATIONS MANAGER** Rebecca Doshi **SENIOR CONTENT & PUBLISHING SYSTEMS SPECIALIST** Jacob Hedrick **SENIOR PRODUCTION SPECIALIST** Kristin Wowk **PRODUCTION SPECIALISTS** Kelsey Cartelli, Audrey Diggs **DIGITAL PRODUCTION MANAGER** Lisa Stanford **ADVERTISING PRODUCTION OPERATIONS MANAGER** Deborah Tompkins **DESIGNER, CUSTOM PUBLISHING** Jeremy Huntsinger **SR. TRAFFIC ASSOCIATE** Christine Hall **SPECIAL PROJECTS ASSOCIATE** Shantel Agnew

MARKETING DIRECTOR Sharice Collins **ASSOCIATE DIRECTOR, BUSINESS DEVELOPMENT** Justin Sawyers **GLOBAL MARKETING MANAGER** Allison Pritchard **ASSOCIATE DIRECTOR, MARKETING SYSTEMS & STRATEGY** Aimee Aponte **JOURNALS MARKETING MANAGER** Shawana Arnold **MARKETING ASSOCIATES** Ashley Hylton, Lorena Chirinos Rodriguez, Jenna Voris **SENIOR DESIGNER** Kim Huynh

DIRECTOR AND SENIOR EDITOR, CUSTOM PUBLISHING Erika Gebel Berg

DIRECTOR, PRODUCT & PUBLISHING DEVELOPMENT Chris Reid **DIRECTOR, PRODUCT MANAGEMENT** Kris Bishop **PRODUCT DEVELOPMENT MANAGER** Scott Chernoff **PUBLISHING PLATFORM MANAGER** Jessica Loayza **SR. PRODUCT ASSOCIATE** Robert Koepke **PRODUCT ASSOCIATES** Caroline Breul, Anne Mason

ASSOCIATE DIRECTOR, INSTITUTIONAL LICENSING MARKETING Kess Knight **BUSINESS DEVELOPMENT MANAGER** Rasmus Andersen **ASSOCIATE DIRECTOR, INSTITUTIONAL LICENSING SALES** Ryan Rexroth **INSTITUTIONAL LICENSING MANAGER** Nazim Mohammedi, Claudia Paulsen-Young **SENIOR MANAGER, INSTITUTIONAL LICENSING OPERATIONS** Judy Lillibridge **MANAGER, RENEWAL & RETENTION** Lana Guz **SYSTEMS & OPERATIONS ANALYST** Ben Teincuff **FULFILLMENT ANALYST** Aminta Reyes

ASSOCIATE DIRECTOR, US ADVERTISING Stephanie O'Connor **US MID WEST, MID ATLANTIC AND SOUTH EAST SALES** Chris Hoag **US WEST COAST SALES** Lynne Stickrod **ASSOCIATE DIRECTOR, INTERNATIONAL** Roger Goncalves **SALES REP, ROW** Sarah Lelarge **SALES ADMIN ASSISTANT, ROW** Victoria Glasbey **DIRECTOR OF GLOBAL COLLABORATION AND ACADEMIC PUBLISHING RELATIONS, ASIA** Xiaoying Chu **ASSOCIATE DIRECTOR, INTERNATIONAL COLLABORATION** Grace Yao **SALES MANAGER** Danny Zhao **MARKETING MANAGER** Kilo Lan **ASCA CORPORATION, JAPAN** Rie Rambelli (Tokyo), Miyuki Tani (Osaka)

DIRECTOR, COPYRIGHT, LICENSING AND SPECIAL PROJECTS Emilie David **RIGHTS AND PERMISSIONS ASSOCIATE** Elizabeth Sandler **LICENSING ASSOCIATE** Virginia Warren **RIGHTS AND LICENSING COORDINATOR** Dana James **CONTRACT SUPPORT SPECIALIST** Michael Wheeler

---

EDITORIAL
science_editors@aaas.org

NEWS
science_news@aaas.org

INFORMATION FOR AUTHORS
science.org/authors/science-information-authors

REPRINTS AND PERMISSIONS
science.org/help/reprints-and-permissions

MULTIMEDIA CONTACTS
SciencePodcast@aaas.org
ScienceVideo@aaas.org

MEDIA CONTACTS
scipak@aaas.org

PRODUCT ADVERTISING & CUSTOM PUBLISHING
advertising.science.org/products-services
science_advertising@aaas.org

CLASSIFIED ADVERTISING
advertising.science.org/science-careers
advertise@sciencecareers.org

JOB POSTING CUSTOMER SERVICE
employers.sciencecareers.org
support@sciencecareers.org

MEMBERSHIP AND INDIVIDUAL SUBSCRIPTIONS
science.org/subscriptions

MEMBER BENEFITS
aaas.org/membership/benefits

INSTITUTIONAL SALES AND SITE LICENSES
science.org/librarian


Share

NEWS

“It’s stunning to me. Why are they capitulating in advance?”

University of North Carolina at Chapel Hill biologist Mark Peifer, in *STAT*, about the American Society for Microbiology’s removal of projects from its website. The group said it was reviewing those related to President Donald Trump’s executive orders restricting federally funded research on diversity and other topics.

IN BRIEF

Edited by **Jeffrey Brainard**

INFECTIOUS DISEASES

New Ebola vaccine tested in Uganda outbreak

Researchers in Uganda launched the first trial of a new candidate vaccine against the Sudan ebolavirus on 3 February, just 4 days after the country announced a new outbreak of the deadly pathogen. Merck developed the vaccine (pictured above) but ultimately donated it to the nonprofit IAVI. Data from a study in healthy volunteers presented at a 2024 meeting showed the vaccine is safe and triggers an immune response. The trial, led by the World Health Organization and Makerere University, will use an unusual ring vaccination design, in which vaccines are given to contacts of known patients as well as contacts’ contacts. (The same setup helped demonstrate efficacy of Merck’s vaccine for the better known Zaire ebolavirus during a large 2014–16 outbreak in West Africa.) Uganda announced on 30 January that a nurse in Kampala had died of Sudan Ebola, which kills between 41% and 70% of those infected, marking the country’s sixth Ebola outbreak since 2000. As *Science* went to press, health workers had found 45 of the nurse’s contacts but reported no new cases.

A slightly menacing asteroid

SPACE DEFENSE | Astronomers recently identified an asteroid they calculated has a 1.5% chance of striking Earth in December 2032 and is large enough to cause “severe” blast damage up to 50 kilometers from the impact site. The object, dubbed 2024 YR4, measures between 40 and 90 meters in diameter and was observed in late December 2024 by a telescope in Chile operated by the University of Hawaii. NASA ranks it as a three on the Torino scale—which ranges from zero, or no risk of collision, to 10, certain collision—making it the second highest ranked asteroid after one named Apophis, which was spotted in 2004 and reached a rating of four before further tracking brought it back to zero. Additional observations of 2024 YR4 will help researchers refine the asteroid’s orbit and its chance of impact.

Nonopioid pain drug approved

BIOMEDICINE | A long-awaited nonopioid pain drug won approval last week from the U.S. Food and Drug Administration to treat moderate to severe short-term pain, such as from tissue injury after surgery or trauma. Suzetrigine, an oral drug marketed by Vertex Pharmaceuticals as Journavx, is the first of a new class of pain treatments to reach the market. They are designed to

PHOTO: WORLD HEALTH ORGANIZATION

avoid risks—including slowed breathing and the potential for addiction—that come with opioid drugs like oxycodone. Rather than targeting opioid receptors in the brain, suzetrigine works by blocking a sodium channel called Nav1.8 on pain-sensing nerves. It outperformed a placebo in its two pivotal trials, in people with acute pain after surgeries to remove bunions and excess abdominal fat. Many hope suzetrigine will also prove effective against harder to manage chronic pain conditions. But a phase 2 study of people suffering from one such ailment, the nerve condition lumbosacral radiculopathy, found that levels of pain reduction from the drug and a placebo were statistically similar. The company said it plans to proceed with a phase 3 trial involving chronic pain "pending discussions with regulators."

Research monkeys die in accident

ANIMAL WELFARE | Twenty-two monkeys died of carbon monoxide poisoning in November 2024 at a facility operated by one of the largest suppliers of the animals for U.S. research, a regulator said this week, marking another in a series of problems reported there. The dead were among 54 cynomolgus macaques housed in an enclosure at Alpha Genesis's facility in Yemassee, South Carolina, which holds a total of 6000 monkeys. The 54 were apparently exposed to the gas from a malfunctioning heater, the U.S. Department of Agriculture says in a report, which cited the company for a "critical" violation of the Animal Welfare Act, the most serious category. Two weeks earlier, 43 monkeys escaped the facility, as had dozens more in earlier incidents stretching back to 2014. Alpha Genesis received more than $19 million in contract payments from the U.S. National Institutes of Health in 2024.

China builds laser fusion lab

ENERGY | China appears to be constructing a massive laser fusion research facility in southwestern Sichuan province, according to expert analysis of satellite photos. The complex, which has a target chamber at the center of laser bays, could be used for research on both nuclear weapons and clean energy, according to specialists quoted by Reuters last week. They estimate the device's experiment bay is larger than that of the National Ignition Facility in California, which currently hosts the world's most energetic laser. In what is called inertial confinement fusion, intense lasers heat and compress a small fuel pellet containing isotopes of hydrogen until pairs of nuclei fuse into helium nuclei and release energy. Such facilities can also study nuclear weapon physics without a test explosion, which is prohibited by the Comprehensive Nuclear-Test-Ban Treaty. Reuters reported that officials in China did not respond to requests for comment.

A worker last month took radiation readings at the Chornobyl Nuclear Power Plant in Ukraine.

PHOTO: JUSTIN YAU/SIPA VIA AP IMAGES

SECURITY

Trump freeze stops nonproliferation projects

President Donald Trump's administration's freeze on U.S. foreign aid has ground to a halt hundreds of nonproliferation and research-security programs in many countries. Among the casualties are efforts to secure dangerous pathogens in labs, train biologists to disrupt a bioweapon attack, strengthen controls on the export of sensitive technologies, and prevent rogue nations from evading international sanctions. "We're really cutting off a lot of information that's crucial for us to understand what's going on in the world, and that's dangerous," says Shawn Baker-Garcia, CEO of Coalescion, a nonprofit that carries out nonproliferation work. In Ukraine, for example, the suspensions include projects to restore a science lab near the defunct Chornobyl Nuclear Power Plant that Russian troops vandalized in 2022 and install new radiation monitoring equipment at radioactive-waste storage sites nearby. Nonproliferation specialists are hoping a review, led by U.S. Secretary of State Marco Rubio, will validate their programs as vital to U.S. interests and allow them to continue (see related story, p. 564).

Divisive U.K. autism study halted

GENETICS | Organizers have shelved a controversial U.K. project that planned to scan the DNA of 10,000 autistic people to learn more about the condition and health problems that accompany it. The Spectrum 10K study, launched by University of Cambridge scientists in 2021, received endorsements from celebrities and attracted thousands of volunteers. But it also triggered a public backlash, with some in the autistic community voicing fears that researchers sought to develop a prenatal test for autism, raising the specter of eugenics. Others demanded more transparency about how data would be used. The project was paused within 1 month of its launch and became beset by delays before its organizers last week announced they were pulling the plug. They said that since the study's inception, teams around the world have collected health and genetic data about autistic people that U.K. researchers can access, avoiding the need to collect new data.

Ex-NOAA director chosen again

ENVIRONMENT | President Donald Trump this week nominated meteorologist Neil Jacobs to lead the U.S. National Oceanic and Atmospheric Administration (NOAA). During Trump's first term, Jacobs led NOAA's satellite and weather prediction divisions and served as acting administrator from 2019 to 2021. He has since remained active in efforts to improve weather forecasting. His nomination will likely face scrutiny because of his role during "SharpieGate" in 2019, when Jacobs collaborated with Department of Commerce operatives to issue a statement reprimanding an office of the National Weather Service. That office had countered Trump's inaccurate statement that Hurricane Dorian could strike Alabama.

U.S. science agencies are struggling to conform to orders from President Donald Trump.

PHOTO: PETE MAROVICH/*THE NEW YORK TIMES* VIA REDUX

U.S. SCIENCE POLICY

Trump orders cause chaos at science agencies

Wild week of canceled meetings, program changes, and data purges creates high anxiety

By **Jeffrey Mervis**

It was one of those head-snapping, blink-and-you'll-miss-it weeks in Washington, D.C. Many U.S. science agencies abruptly abandoned normal operations last week to focus on a slew of executive orders from President Donald Trump targeting what he calls "woke gender ideology;" diversity, equity, and inclusion (DEI); foreign aid; the "green new deal;" and support for "nongovernmental organizations that undermine the national interest." Those orders, which began to flow just hours after Trump's 20 January inauguration, led agencies to temporarily suspend new awards, review existing grants, block grantee access to funds already allocated, and halt meetings of grant-review panels. They also removed calls for proposals in specific areas, websites, and access to public databases that deal with now off-limits topics. Adding to the chaos: a 27 January White House memo intended to freeze huge chunks of federal spending deemed to violate the executive orders.

The torrent of activity left many researchers bewildered—and fearful of what might come next.

As *Science* went to press, a few agencies had backed off some of their initial steps. The National Science Foundation (NSF), which had blocked grantee access to its cash management system, lifted the hold on 2 February. The National Institutes of Health (NIH), which hadn't frozen grants but canceled key funding meetings, expected to resume at least some meetings of committees that review proposals. And two federal judges, ruling on different lawsuits, blocked implementation of the memo that froze funding, which the White House soon withdrew.

Yet many scientists remain in limbo at thousands of academic institutions and nongovernmental agencies that rely on federal research grants. And some lawmakers, especially Democrats, are complaining vociferously that agency attempts to comply with Trump's executive orders violate laws that govern many science agencies. The laws "are not optional, and they cannot be unilaterally wished away by executive order," Representative Zoe Lofgren (CA), the senior Democrat on the House of Representatives science committee, warned in a 2 February letter to the heads of five major research agencies, urging them to fight back.

Such warnings suggest turmoil is far from over. Here's a review of what's happened so far.

WORK AND FUNDING PAUSES

The 27 January White House memo triggered a frenzy among institutions and organizations, which receive most federal research grants and funnel the money to investigators. Some took the unilateral, preemptive step of telling scientists to suspend travel or purchases connected with those grants, in some cases causing immediate hardship. NSF's payment freeze led some of the postdocs it funds to complain on social media they were unable to pay rent and other bills.

Some agencies reversed course, however, after a federal judge issued a temporary restraining order blocking the memo's implementation on 31 January. This week, a second judge extended a similar order blocking the White House memo.

Although the spending memo has been rescinded, the executive orders governing how it would have been applied remain in force. For some agencies, that has meant stopping work already underway or telling scientists that efforts focused on DEI and accessibility (DEIA) are no longer valued.

On 23 January, for example, NASA told all grantees and contractors to "immediately … cease and desist all DEIA activities." One early casualty was a program pairing NASA mission scientists with college students from underrepresented groups, including training those scientists to be better mentors.

On 27 January, the Department of Energy (DOE) issued similar guidance, and the next day its $8 billion Office of Science withdrew a requirement that researchers include a plan for Promoting Inclusive and Equitable Research (PIER) in every research proposal. DOE told reviewers judging proposals already in the pipeline to ignore any PIER plans, saying they wouldn't affect what DOE decided to fund.

One academic physicist who requested anonymity to protect relations with DOE characterizes the change as a return to business as usual, noting that DOE didn't provide additional funds to support PIER activities. The Office of Science "didn't get into DEI with exuberance, and it didn't get out of DEI with exuberance," the physicist quips.

EXISTING GRANTS VETTED

NIH says the agency is not reviewing awarded grants—although they are vetting language in some announcements that invite scientists to submit proposals on a particular topic. So far, NSF appears to be the only agency to have created a system for deciding whether an already awarded grant violates the executive order.

NSF officials declined to comment on the intricate, multistep process, which began last week. But people with direct knowledge say it started with NSF senior managers selecting 10,000 grants, from a pool of roughly 50,000 active awards, for review. They then enlisted staff to vet the awards using a list of key words that included "diversity," "inclusion," "women," and "race." To be sure, a sizable share of those words refers to scientific designations, such as plant diversity, that have nothing to do with DEIA; those awards were dropped from the review.

Some 1200 grants, however, contained two or more potential red flags, the sources said. Most were in NSF's education directorate, one of the agency's eight major granting units. Those grants were then subjected to closer scrutiny, with an eye toward identifying those openly designed to broaden the pool of NSF investigators but outside the typical definition of a DEIA project. Among others, grants awarded under NSF's 44-year-old program to support scientists in rural states that historically get little NSF funding appear to be getting a close look.

The winnowing process is expected to yield a small number of projects that will need to be modified so the investigators can continue the work without violating the executive order. But it's not clear how many projects will be affected.

"The goal is to try and make sure that every [active] award is fully funded," says one NSF staffer who requested anonymity for fear of retribution. "After all, they were chosen for both scientific merit and broader impacts," a reference to the two criteria that NSF uses in making every award.

> **"Our country is hobbling ourselves by canceling these programs."**
>
> **Needhi Bhalla**
> University of California, Santa Cruz

NEW AWARDS PAUSED

NSF stopped posting notices of new awards the day after Trump took office, apparently preparing for the review of its existing grants. As *Science* went to press, that pause was still in place, but several NSF sources said they expected it to be lifted this week once the vetting ended.

At NIH, applications for grant renewals or new proposals face scrutiny. If they involve DEIA, NIH sources say, they will be declined, or investigators will have to remove that component before the proposal is considered.

DATABASES REMOVED

A 29 January memo from the Office of Personnel Management gave agencies 2 days to pull down websites and end projects that "inculcate or promote gender ideology." At the Centers for Disease Control and Prevention (CDC), that purge swept up multiple web pages involving race or containing the term LGBTQ (for lesbian, gay, bisexual, transgender, and queer). Many pages that went dark provided access to CDC data, such as the results of a widely used survey of youth risk behaviors and the agency's social vulnerability index, which uses metrics such as poverty to rank communities' vulnerability to natural disasters. Scientists and advocacy groups rushed to download data before the deadline.

"I knew it was going to be bad, but I didn't know it was going to be this bad," says Angela Rasmussen, a virologist at the University of Saskatchewan who says she spent half a night trying to download data on influenza surveillance. "It's like a data apocalypse."

SOLICITATIONS WITHDRAWN

NIH staff have pulled down descriptions of initiatives offering funding of efforts to improve DEIA and have revised requests for proposals that violate the orders. For example, the web pages for Maximizing Opportunities for Scientific and Academic Independent Careers, a program that helps postdocs from diverse backgrounds transition to independent research, have disappeared.

The program announcement for NIH's main science, technology, engineering, and math education program, the NIH Science Education Partnership Award, has also vanished. Several training grant solicitations have been altered so that they now appear to have expired.

"Our country is hobbling ourselves by canceling these programs," says cell biologist Needhi Bhalla of the University of California, Santa Cruz. These undergraduates, graduate students, and postdocs "bring important, unique, and novel insights and breadth to solving challenging, scientific problems," she adds.

NIH is also revising study descriptions for clinical trials and other studies seeking to recruit diverse cohorts. The changes are intended to make clear that the goal is not to give preference to a minority group, but to ensure that research focuses on all populations afflicted with a disease. But scientists within and outside NIH worry those steps may not be enough to satisfy political appointees at the Department of Health and Human Services, NIH's parent agency.

NSF, too, has taken down online program announcements, including both ongoing solicitations and new calls for proposals to advance work in a specific or field topic. These actions, in some cases erasing any record of the announcement, differ from NSF's standard practice of retiring, or archiving, a solicitation because it is outdated or NSF decided to reallocate the funds.

Much remains uncertain, as agencies wait for additional guidance from the White House on how to implement Trump's executive orders. They will then tell grantees what to do to adhere to the terms of their awards. The stakes are high for science. NSF, for one, has already reminded institutions they risk losing their grants if they are not in compliance. ■

With reporting by Adrian Cho, Jocelyn Kaiser, Paul Voosen, and Meredith Wadman.

GEOLOGY

After abuse, Inuit group closes off ancient rock belt

The nearly 4-billion-year-old rocks offer a look into Earth's earliest years

By **Rachel Berkowitz**

For nearly 2 decades, geologist Jonathan O'Neil of the University of Ottawa has sampled and studied what he believes are the oldest rocks on the planet, in the northernmost reaches of Canada's Quebec province. Estimated to be about 3.8 billion years old—and perhaps much older—the rocks lie on tribal Inukjuak lands near Hudson Bay, and O'Neil relied on support from the Inuit locals to study them. But following several incidents of abuse by a few other scientists, the tribe has said "no more" to all samplers.

"Other geologists who came to do research took large amounts of rock and scarred and damaged the land," explains Tommy Palliser, a member of the Inuit community and president of the Pituvik Landholding Corporation (PLC), which manages the land for the tribe. Excavations at the outcrops exposed near the shore of the Hudson Bay have left the land with "jagged edges" and looking "not pristine," he says. Moreover, another board member of PLC found rock collected from the site for sale on the internet for upward of $10,000. "We were pretty disgusted with this," Palliser says. As a result, the Pituvik decided last year to close the area to extractions entirely.

O'Neil understands the Pituvik's decision, noting that in 2017 he saw evidence of sampling that was "not very considerate … almost unethical" and a traditional inukshuk stone structure, used as a navigational marker by the Inuit, that had been vandalized. But he and others mourn what may be lost to science. Geologists are frustrated by the vanishingly small amounts of material that have survived since Earth's formation 4.56 billion years ago, says Aaron Cavosie, a geologist at Curtin University who studies ancient minerals. For now, the Acasta Gneiss in northwestern Canada holds the age record at 4.03 billion years old, based on easy-to-date zircon crystals embedded in its grains.

But the Hudson Bay rocks, part of the Nuvvuagittuq Greenstone Belt, are not far behind. Gold-standard dating techniques on zircon-rich samples from the Nuvvuagittuq have repeatedly confirmed a 2002 date of at least 3.75 billion years old. And based on an unusual isotope signature in their composition, O'Neil believes the rocks at Nuvvuagittuq are older. He says he has the material

The layered rocks (bottom) of the Nuvvuagittuq Greenstone Belt (top) may preserve traces of early life and primordial magnetic fields that scientists hoped to study.

PHOTOS: (TOP TO BOTTOM) JONATHAN O'NEIL; DAVID HUTT/ALAMY

needed to make that argument, but also that he hoped to revisit specific areas to study early traces of life such as microscopic structures and mineralized chemical byproducts, which he will now not be able to do.

Other scientists were also drawn to the unusual formations. PLC handled permits and arranged logistics in the 521-square-kilometer region surrounding the community of Inukjuak. Inuit leaders guided permitted scientists, who collected anywhere from a single grapefruit-size sample to several hundred kilograms of rocks. "Sometimes I would bring people myself, by canoe," Palliser says. He recalls the beauty of the rocks, which Pituvik Elders describe as *Qupuartuuq*: rock with different shades of colors. "When you look at it, you can really see the swirls of blacks and whites and grays," Palliser says.

But in 2016, he recalls, a group branding itself as "museum curators" brought excavating equipment to Inukjuak, ferrying it to the site in a large boat. "When we realized they were taking such large amounts of rock we were astonished," he says. PLC limited samples eventually down to softball size before the COVID-19 pandemic shut down the site. But when site visits resumed and when Palliser and others saw some of the extractors trying to profit off these rocks "without our knowledge and consent," they'd had enough. The Pituvik pulled the plug.

Losing access will deprive scientists of the chance to study some of Earth's earliest years. Claire Nichols, a geologist at the University of Oxford who studies early Earth's magnetic field, found records of ancient magnetism in Greenland rocks that were part of an ancient ocean's crust. "We were excited to see if the same was true for Nuvvuagittuq," she says, given it was also part of an ancient ocean. Her request to visit the rock belt last year and collect samples was denied, but she understands why. "There have been many issues with bad sampling practice" in her field of paleomagnetism, she says.

The incident may have a silver lining. PLC is now collaborating with scientists to fund and set up a provincial park that would protect the Nuvvuagittuq rocks. "There would be no more taking of material. You come and see firsthand the geology and the rocks themselves," Palliser says. The Inuit community would remain stewards of the land, and that's as it should be, O'Neil says. "For most people this may be a remote area in the Canadian North, but this is home for the Inuit people and has been for hundreds of years." ■

Rachel Berkowitz is a freelance journalist based in Eastsound, Washington, and Burnaby, Canada.

PHOTO: CORE CONSTRUCTION

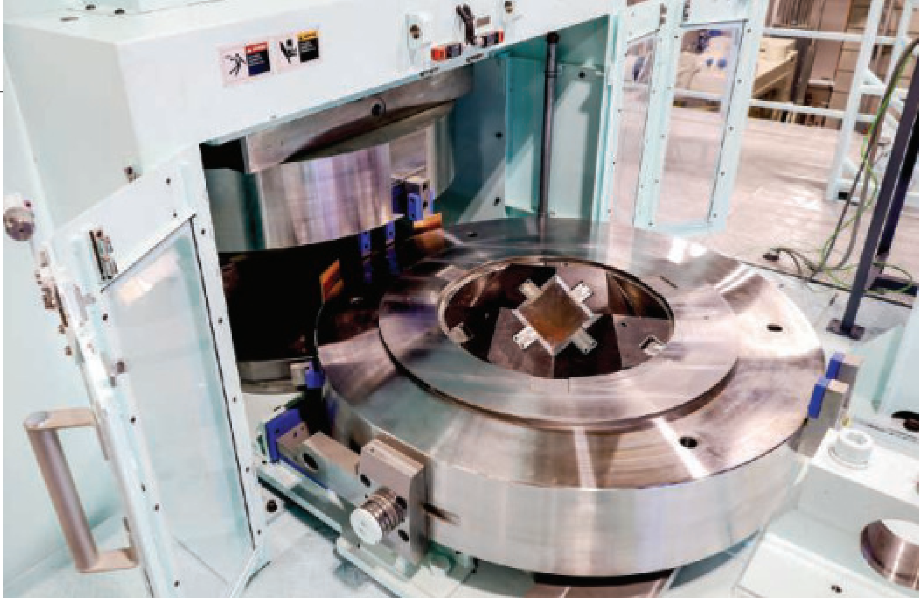

A massive press at Arizona State University will subject rocks to deep-Earth pressures and temperatures.

EARTH SCIENCE

New complexity emerges in Earth's 'boring' middle region

Planetary CT scans and lab experiments reveal layering and intricate flows in the mantle

By **Paul Voosen**

Earth's middle depths are dull, or so geophysicists thought. The crust is fractured and convulsed by plate tectonics; in the core, churning liquid iron generates the planet's magnetic field. In between is the mantle, 2900 kilometers of hot, pressurized rock, convecting feebly like a superslow lava lamp. Studies of earthquake waves that probe the middle mantle showed little structure other than plumes of hot rock rising all the way through its thickness and the remnants of surface plates, called slabs, that have slid from the surface to its depths.

New work is changing that picture. A mysterious new mantle layer has emerged, and the mantle's flow patterns appear more complex than was thought. They are hectic, variable, jumbled, with some reaching the mantle's surface and some stalling below, rather like the erratic churning in a pot of potatoes that has just reached a boil. For a long time, much of the mantle was thought "boring," says Dan Shim, a mineralogist at Arizona State University (ASU). "But now we're starting to see some complexity there."

Geophysicists use the shifting speeds of earthquake waves as they pass through the mantle to create a sort of planetary CT scan, a coarse reconstruction of Earth's interior. A decade ago, a breakthrough paper in *Nature* made a definitive case that plumes of superhot rock can rise all the way from the mantle's base to the crust, fueling hot spots such as Hawaii. But that paper, and others since, also revealed a puzzle: Although some hot spots made it all the way through, many plumes—along with sinking slabs—also stalled and flattened at various points. "It all started by observing these flat slabs and flat plumes," says Claudia Adam, a geophysicist at Kansas State University.

One sticking point appeared at a depth of 660 kilometers. It made geophysical sense: Seismic waves uniformly change speed at this depth, where ringwoodite, a form of olivine—the upper mantle's predominant mineral—breaks down under immense pressure into two other minerals. But researchers were puzzled by another stagnation, seen at a depth of 1000 kilometers, where there is no known transition in mantle minerals and no detected change in the speed of earthquakes.

In work presented late last year at an American Geophysical Union meeting, however, geophysicist Keely O'Farrell at the University of Kentucky and Yuping Wang, a former graduate student, glimpsed a change in mantle properties at 1050 kilometers' depth. The change marks the start of what they've dubbed the middle mantle transition zone (MMTZ).

The duo began with three distinct pictures of the mantle, built with different seismic techniques. They let a machine learning algorithm search broadly through each method's data set for depths where seismic waves changed in behavior. This unbiased hunt turned up the well-known discontinuities, but also something fresh: the MMTZ. "We're confident it's there and it's something we should explore," O'Farrell says.

The new evidence builds on earlier hints. A decade ago, there were some seismic signs, published in *Science*, suggesting the mantle grew more viscous below 1000 kilometers. In 2023, a paper in *Nature Communications* reported a speed change at that depth under the Pacific Ocean. And that same year, a *Nature* paper suggested an increase in the grain size of the dominant minerals at that depth might explain the seismic changes. Meanwhile, differences between the isotopic ratios of noble gases emitted at hot spots, which vent the deep mantle, and at midocean ridges, which tap shallower depths, also suggest something is inhibiting mantle convection in this depth, adds Rita Parai, a geochemist at Washington University in St. Louis. "The vibes are right."

> **"It all started by observing these flat slabs and flat plumes."**
>
> **Claudia Adam**
> Kansas State University

While geophysicists begin to explore this mysterious new layer, mineralogists are upending understanding of the more familiar transition, at 660 kilometers. For many decades, geophysicists thought it had a uniform depth. But improved seismic evidence has shown that, puzzlingly, when a mantle plume or slab hits this boundary, it shifts up or down by 20 kilometers.

Three recent experimental studies, including one published last week in *Nature Communications*, have squeezed mantle minerals to enormous pressures to re-create the phase transitions—changes in minerals' crystal structure—that take place around this depth. The studies show that depending on the temperature of the material, the depths and pressures of the transitions can vary far more than once thought, explaining why the seismic boundary shifts up or down. And because a phase change alters the density of the rock, these variations also change its buoyancy. "They're nonlinear," says Junjie Dong, a mineral physicist at the California Institute of Technology who led the *Nature Communications* study. That means the intrinsic heat of a descending continent or rising mantle plume could starkly alter whether it stagnates at this layer.

The first of the three studies, published in *Nature* in 2022, looked at why the so-called 660 boundary sometimes gets pushed downward where descending slabs hit it. The researchers squeezed and heated minerals to mantlelike conditions in massive multi-anvil presses in Germany and Japan while monitoring their composition with x-rays. They found that at the colder temperatures seen in old slabs, such as one descending under Japan, the biggest factor affecting their density is a phase change in akimotoite, a rare silicate mineral, not ringwoodite. That akimotoite transition takes place at slightly greater depths, depressing the boundary.

A second study from many of the same researchers, published in *Nature Geoscience* in 2023, looked at another phase change, in which garnet breaks down into bridgmanite and corundum, the second hardest mineral after diamond. They found that the pressure needed varied widely with temperature, meaning this phase change could simultaneously help stall subducting slabs and accelerate hot mantle plumes, says Takayuki Ishii, a mineral physicist at Okayama University who led the work. "Such a polarity change in one transition had never been discovered before," he says.

In the most recent study, Dong and co-authors returned to the classic ringwoodite transition. At the time of their experiment, the United States lacked an appropriate multi-anvil press. Instead they relied on a less capable press that could not quite match mantle conditions, then used machine learning to combine their results with previously published data. They charted how ringwoodite altered at different temperatures and pressures, finding evidence that its phase transition wouldn't do much to impede subducting slabs—more evidence that akimotoite instead is the dominant player, Shim says.

Enlisting artificial intelligence to combine experimental data from different methods leaves some wary, including Shim. The next step, in his view, is to study all of the transitions around the 660 layer together in one experiment. A new $14 million multi-anvil press should make that possible in a few months when the Facility for Open Research in a Compressed Environment (FORCE), backed by the National Science Foundation, opens to U.S. scientists at ASU. "We're looking forward to having that capability and approaching this problem," Shim says.

O'Farrell is hopeful that FORCE will also be able to simulate conditions at the 1000-kilometer boundary she has glimpsed. "We're going to make a list: 'Can you squeeze all these things for us?'" ■

INFECTIOUS DISEASES

Indonesia's new capital poses public health risks

Scientists worry about potential rise in malaria and insect-borne viral diseases

By **Dyna Rochmyaningsih**

One of the biggest infrastructure projects in Southeast Asia is unfolding at the edge of the rainforest on eastern Borneo: the construction of a new Indonesian capital. Ibu Kota Nusantara (IKN), as it's called, will replace Jakarta, which is overcrowded and sinking at an alarming rate, making it increasingly flood-prone. Already, some 17,000 hectares of pulpwood plantations and mangroves have been cleared, and buildings are rising. The first occupants are expected to arrive in a few years.

They may, however, be moving into harm's way. The province of East Kalimantan, where IKN is located, is a hot spot for vector-borne diseases such as malaria. It may also host a relatively rare form of malaria caused by the parasite *Plasmodium knowlesi*. As deadly as the better known *P. falciparium*, it thrives in degraded forest areas and is on the rise in Southeast Asia. Without more research and control measures, moving at least 1 million people from malaria-free Jakarta to the new capital "will be naïve," says epidemiologist Henry Surendra of Monash University, Indonesia, the first author on a December 2024 commentary in *Nature Communications* about IKN's public health risks.

IKN is the legacy of former President Joko Widodo, who wanted a new capital at the center of the giant archipelago to help develop the eastern part of the country and offset the dominance of Jakarta and the rest of Java. "We need equitable development that is not Java-centric," Widodo said. But critics say he appears to have picked the location because a business tycoon who has long supported Widodo's political career owns land concessions in the area. And the project has been surrounded by controversy from the start.

Ibu Kota Nusantara, billed as a "smart forest city," has been surrounded by controversy from the start.

In 2022, the Indonesian parliament approved the plan in less than 2 months, with little public consultation. There's not much democratic oversight of the powerful agency managing planning and construction, which some say has appropriated Indigenous lands on dubious legal grounds. "So many processes were circumvented," says Deden Rukmana, a professor of city planning and urban design at the University of Texas at Arlington. Environmentalists question promises about the sustainability of the "smart forest city," as Widodo has called it, and have asked for environmental impact assessments. "We are really demanding transparency," says Anggi Prayoga of Forest Watch Indonesia.

The risk of malaria and other infectious diseases is a newer concern. Although 85% of Indonesia's population lives in malaria-free zones—and the government hopes to eliminate the disease by 2030—the country still has more than 400,000 cases a year. Most are in Indonesian New Guinea, but East Kalimantan is another endemic zone, with less than one-quarter of the population of Indonesian Borneo but about 85% of its malaria cases. More than half of those are in Penajam Paser Utara, one of the two districts IKN will straddle.

A 2020 assessment of IKN by the National Planning and Development Agency highlighted the risks, citing data including the abundance of disease-carrying mosquitoes. At least two construction workers caught malaria in 2022 while at the site, according to the Ministry of Health. Last year, 54 cases were reported there, but the ministry claimed the patients were infected elsewhere. Although the construction authority has taken some control measures, such as handing out mosquito nets to workers, it's not well-equipped for the job, says Mirza Buana, a legal scholar at Lambung Mangkurat University in Central Kalimantan: "It has all the authorities but no capabilities." The agency has shifted most of the tasks—such as vector control and screening workers entering or leaving IKN—to district health officials, who have struggled to keep up.

Surendra is particularly worried about the potential spread of *P. knowlesi*, a parasite first discovered in the 1930s. It emerged as a public health threat in the early 2000s, in areas in the Malaysian part of Borneo where forests were cleared for oil palm plantations. It has since been identified in many Southeast Asian countries.

P. knowlesi primarily infects long-tailed macaques, highly adaptable monkeys that thrive at the forest edge, and is spread by forest-dwelling *Anopheles* mosquitoes that occasionally bite humans as well. People working in or near the forest, including hunters and loggers, are at the highest risk. Because it has an animal reservoir, the disease is impossible to eliminate completely. Mosquitoes don't transmit *P. knowlesi* between people—or very poorly—but some scientists worry that could change.

Studies have confirmed that several *Anopheles* species that transmit *P. knowlesi* live in East Kalimantan, and one lab-confirmed infection has occurred in IKN. But Surendra says others may have gone undetected because of the lack of molecular testing. The disease may also have been misdiagnosed, says Ibrahim Said, a biologist at the State Institute for Islamic Studies, because under a microscope, *P. knowlesi* can resemble *P. falciparium* and *P. malariae*, yet another malaria parasite found in Indonesia.

By creating puddles and other standing water reservoirs, massive construction could also lead to a surge of *Aedes* mosquitoes, which can transmit a host of diseases, including dengue—of which IKN had 650 cases last year—Zika, and chikungunya. "We don't have data on most of those diseases now," Surendra says, "but absence does not mean nonexistence." His team is planning to collect blood samples from people in IKN and surrounding areas, looking for antibodies that could signal a past infection.

In their commentary, Surendra and his colleagues argue for more research to assess the risks, especially of *P. knowlesi*, and for strengthening environmental monitoring and disease surveillance. Surendra sees opportunity in the relocation as well. It may force Indonesia to take malaria elimination more seriously, he says, and help alleviate long-neglected health disparities between western and eastern Indonesia. Rukmana adds that building a megacity in malaria-prone areas "is very possible," with careful planning. Without it, "the public will become the victim." ■

A risky relocation

East Kalimantan province, the home of Indonesia's new capital, is a malaria hot spot. Scientists worry in particular about *Plasmodium knowlesi*, a malaria parasite that's already on the rise in the Malaysian part of Borneo.

Dyna Rochmyaningsih is a journalist based in South Sumatra, Indonesia.

CREDITS: (PHOTO) WILLY KURNIAWAN/REUTERS VIA REDUX; (GRAPHIC) V. PENNEY AND K. FRANKLIN/*SCIENCE*

BIOMEDICINE

A new 'mini-CRISPR' flexes its editing power in monkey muscles

The downsized DNA-slicing machinery may reach more tissues to take aim at more diseases

By **Jennifer Couzin-Frankel**

In the years since the gene-editing tool CRISPR burst onto the scene, it's run into a big limitation: The classic CRISPR system is too unwieldy to get into many of the body's tissues and do its slicing and dicing. Now, researchers from a company co-founded by Jennifer Doudna of the University of California, Berkeley, who won the 2020 Nobel Prize for helping develop CRISPR, are reporting what they hope will be a significant step forward. In a preprint posted last week, the researchers describe a "mini-CRISPR" that they successfully shipped into muscle cells in mice and monkeys, where it efficiently edited a gene linked to neuromuscular disorders.

What's reported is "truly impressive," says Nic Bengtsson, who studies gene editing in neuromuscular diseases at the University of Washington and wasn't involved in the work. The mini–gene editor, carried into cells by a virus commonly used in gene therapy, looks promising as a kind of "off-the-shelf system, ready to use" for a variety of conditions, he says. Still, he cautions, questions and hurdles remain before the strategy can be tested in people.

CRISPR, which originally evolved in bacteria as part of their immune system, is akin to a set of molecular scissors that cleaves DNA at precise locations, allowing it to excise a problem portion of a gene, with help from a strand of RNA that guides it to its target. In December 2023, U.S. regulators approved the first CRISPR-based therapy, to treat sickle cell disease. That treatment involves extracting a patient's blood stem cells and using CRISPR to fix them before reinfusing them into the body.

Clinical trials are ongoing for treatments that deliver CRISPR's editing machinery directly into the bloodstream, where it has successfully edited genes in liver cells. But that approach, which packaged CRISPR proteins into fat particles, hasn't yet worked in other tissues because few lipid particles reach them. Researchers instead would like to employ the well-studied adeno-associated virus, or AAV, often used for delivery of gene therapy, to ferry DNA encoding CRISPR. Doing so is challenging, however, in part because the CRISPR's components are bulky—in particular the enzyme Cas9 that cuts DNA, which typically includes more than 1300 amino acids. That's too much DNA to squeeze into a single AAV, so researchers have instead tried delivering CRISPR and its guide RNA using two or more AAVs. But so far, it hasn't worked very well.

Multiple research teams have been working to craft miniaturized CRISPR systems that are still effective at editing but can be packed into just one AAV vector. Among these is the team at Mammoth Biosciences—which may have hit on success. Its scientists began by sifting through genetic sequence data from all sorts of CRISPR varieties that turn up in microbes. They put an initial 176 candidates through "a barrage of tests," and found "that needle in the haystack," says Lucas Harrington, the company's chief scientific officer and co-founder and a former student of Doudna's. Called NanoCas, it has 425 amino acids, making it about one-third the length of Cas9. Harrington and his colleagues engineered it so it could effectively slice mammalian DNA.

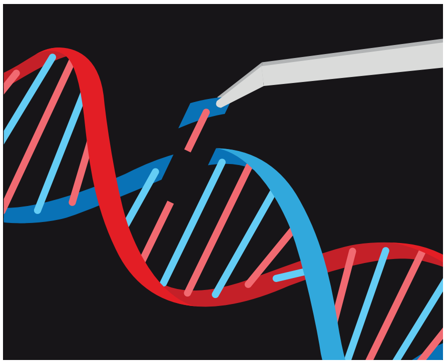

ILLUSTRATION: TRAFFIC ANALYZER/GETTY IMAGES

That slimdown allowed the DNA for the editing system to fit inside a single AAV vector. The group showed NanoCas could edit DNA in various mammalian cells in the lab, then moved into mice. When they used it to shut off a cholesterol gene called PCSK9 in the liver, NanoCas successfully edited about 60% of cells, a performance at least as good as Cas9.

Then they turned to a tougher target for traditional CRISPR: muscle. In mice, they tested whether NanoCas could slice a mutation out of a gene called dystrophin, which encodes a key scaffolding protein in muscle cells. In people with Duchenne muscular dystrophy, a devastating muscle wasting disease that typically surfaces in early childhood, that mutation renders them unable to make any or enough functional protein. Although treatments can slow the disease's progression, there is no cure.

In mice with a human version of the mutated dystrophin gene, the NanoCas strategy seemed to work well, editing 10% to 40% of the cells across a range of muscle types, including heart and calf muscle. (These engineered mice don't get sick like people with the mutation, so the team couldn't assess potential effects on Duchenne symptoms.)

Finally, a big test came in three healthy macaque monkeys. The researchers injected an AAV carrying DNA for the CRISPR-containing viral vector and its guide RNA into the animals' bloodstreams. They monitored liver function, as liver damage can be a risk of AAV therapy; that and other health measures stayed in normal range, they found. Depending on muscle type, NanoCas edited the dystrophin gene in up to 30% of the monkeys' skeletal muscle cells; the number was somewhat lower in heart muscle, about 15%.

Those levels are "certainly in a range you would expect to be clinically meaningful," says Terence Flotte, a gene therapist and dean of the University of Massachusetts T.H. Chan School of Medicine.

But he and others note it's early days. There's no information yet on whether the strategy can help a sick animal get better. AAV also comes with risks, including immune reactions and potential "off-target" effects, in which healthy DNA is modified by accident. "Their preliminary data is encouraging," but "limited," says Mark Kay, a gene therapist at Stanford University. Still, he's heartened by how easily this miniature CRISPR can slip into an AAV vector, which opens up a raft of new tissue targets, including for Duchenne.

Harrington acknowledges the challenges, including concerns about AAVs, but is hopeful about what's to come. "The fact that we can now very efficiently edit with a single AAV" makes delivering CRISPR into the body and editing previously inaccessible tissues "not just theoretical," he says. Harrington says Mammoth will continue to work on Duchenne and send its NanoCas system after targets relevant to other muscle disorders as well as brain diseases. "We are really trying to think, 'What can we do as quickly as possible?'" ■


2024 Winner
Laura Seeholzer, Ph.D.
University of California San Francisco,
School of Medicine, USA

For research on airway neuroendocrine cells responding to external threats

eppendorf
& Science
PRIZE FOR
NEURO
BIOLOGY

Application Deadline
June 15, 2025

Call for Entries 2025

Eppendorf & Science Prize for Neurobiology
The annual Eppendorf & Science Prize for Neurobiology is an international prize which honors young scientists for outstanding neurobiological research based on methods of molecular, cellular, systems, or organismic biology. If you are 35 years of age or younger and doing great research, now is the time to submit an entry for this prize.
It's easy to apply! Write a 1,000-word essay and tell the world about your work.

eppendorf.com/prize

As the winner, you could be next to receive
> Prize money of US$25,000
> Publication of your work in *Science*
> Full support to attend the Prize Ceremony held in conjunction with the Annual Meeting of the Society for Neuroscience in the USA
> 10-year AAAS membership and online subscription to *Science*
> Complimentary products worth US$1,000 from Eppendorf
> An invitation to visit Eppendorf in Hamburg, Germany

eppendorf
Science
AAAS

AAAS® and Science® are registered trademarks of the American Association for the Advancement of Science, USA. Eppendorf® and the Eppendorf Brand Design are registered trademarks of Eppendorf SE, Germany. All rights reserved, including graphics and images. Copyright © 2025 by Eppendorf SE. Photography: Brian Carey, figMedia

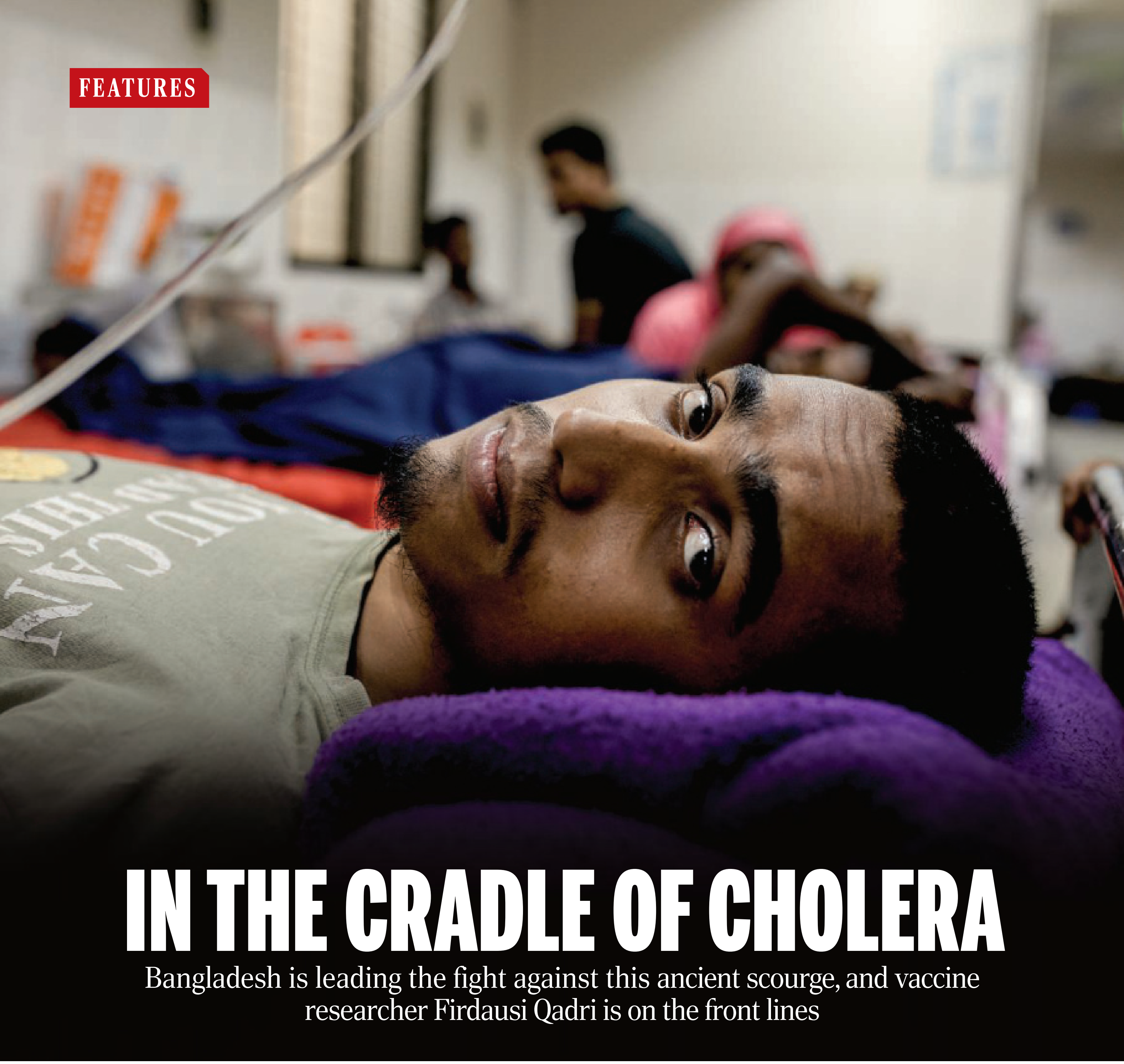

IN THE CRADLE OF CHOLERA

Bangladesh is leading the fight against this ancient scourge, and vaccine researcher Firdausi Qadri is on the front lines

By **Martin Enserink**, *in Dhaka, Bangladesh*

Photography by **Anik Rahman**

Mohammad Abu Raihan Shanto had suffered from uncontrollable diarrhea for 3 days, until he became so weak he couldn't walk and relatives took him to a hospital. Now, the 19-year-old madrassa student was hooked up to an intravenous drip to rehydrate his body, and he felt slightly better, although he was still weak and his eyes looked hollow. "I thought I was going to die," Shanto said through an interpreter as his mother and a younger brother looked on.

Shanto's hospital bed, like those of scores of other patients in the large hospital hall, had no sheets but a plastic cover, and a hole in the middle with a blue bucket underneath. That allowed patients to empty their bowels without getting up. ("He is having a discharge right now as we talk," the interpreter helpfully said as Shanto briefly closed his eyes.) About 10 meters away, a man sitting on his bed vomited loudly.

They had come to the right place: a hospital in central Dhaka operated by the International Centre for Diarrhoeal Disease Research, Bangladesh (ICDDR,B). It is known internationally as a crown jewel of South Asian science and locally as the best place to go if you have severe diarrhea caused by cholera or one of the many other intestinal bacteria flourishing in Bangla-

This story was supported by the Pulitzer Center.

Mohammad Abu Raihan Shanto was treated for severe diarrhea and dehydration in Dhaka, Bangladesh, last summer.

desh. (Rather than use the tortuous acronym, ICDDR,B's website suggests to visitors: "Just ask your driver for the cholera hospital.") Untreated cholera can kill within hours through catastrophic dehydration, but here treatment—primarily rehydration—is free, and most patients are discharged within 24 hours.

The center is also the domain of Firdausi Qadri, "the queen of cholera," as Philippe Barboza of the World Health Organization (WHO) calls her. Qadri, who heads ICDDR,B's Mucosal Immunology and Vaccinology Unit, housed five stories above the hospital, has spent her career studying a range of enteric diseases, but most of her work has been on cholera, and it has given her near-legendary status. Qadri is "a scientific giant," Swedish vaccine researcher Jan Holmgren wrote in 2021. A "godmother" to the field, says Julia Lynch, who heads the cholera program at the International Vaccine Institute (IVI) in Seoul, South Korea, which has close ties with ICDDR,B. "She's phenomenal," Lynch says. "An amazing, compassionate, hardworking person who's also a terrific scientist."

Much of Qadri's work has focused on demonstrating the benefits of a generation of simple, cheap oral cholera vaccines and advocating for their use. The rollout of these vaccines, first developed by Holmgren at the University of Gothenburg more than 4 decades ago, has been agonizingly slow, in part because there's no money in making vaccines for diseases of the poor, but also because many in the public health community were skeptical. After all, vaccines do little to address cholera's root cause: the lack of clean water and sanitation that help *Vibrio cholerae* thrive.

It wasn't until about a decade ago that countries began to use vaccination more widely, in part thanks to Qadri's advocacy. "She has been a leader on oral cholera vaccines for a very long time, and has just carried out a whole series of studies that demonstrate how you can do it," says David Sack, a veteran cholera scientist at the Johns Hopkins Bloomberg School of Public Health.

But as the teeming hospital ward at ICDDR,B showed, oral vaccines have not eliminated cholera—not by a long shot. An international stockpile that distributes the vaccines to poor countries with support from Gavi, the Vaccine Alliance has too few doses to meet the global demand. The Bangladeshi government, struggling with many other urgent health problems, is not investing in vaccination. Complicating matters, the vaccine offers protection for just a couple of years. Progress in providing clean drinking water and sanitation has been slow as well, both in Bangladesh and other cholera-prone countries.

As a result, several plans to dramatically curtail cholera, both globally and in Bangladesh, are off track. In 2022, Dhaka saw its worst outbreak in more than 25 years; the ICDDR,B hospital treated more than 42,000 patients in a 41-day period. Outbreaks have surged globally in the past 2.5 years as well, driven in part by conflict and climate change. "It's frustrating," Qadri says.


Firdausi Qadri, the "godmother" of the cholera field, in a Dhaka neighborhood where she runs many studies.

When *Science* visited in June 2024, the hospital had just dealt with another big influx of patients, peaking at more than 1300 a day. Many had cholera, although few were actually tested, as the treatment for severe diarrhea is similar regardless of the cause. Staff had erected two air-conditioned tents in a parking lot to receive patients. More patients were parked in hallways and corridors. (You'd expect the place to smell horrible, but it didn't: Cleaning crews frequently replaced the buckets and mopped the tiled floors.)

The institute now faces another, urgent problem: Last week, it said it had laid off more than 1000 employees across 10 projects and studies in response to a 3-month "freeze" in U.S. foreign assistance, which helps support it. Qadri declined to comment on the move, and an ICDDR,B spokesperson would not say whether her research would be affected. He said, "We hope to resume our activities soon."

Over lunch last summer, Qadri said she remained an optimist, confident cholera can be vanquished—and that science can help solve other public health problems in her tumultuous country, which saw its authoritarian government overthrown in a surprise revolution last year. At age 73, Qadri works six long days a week at ICDDR,B and at a private institute she co-founded a decade ago to address neglected health needs and train young scientists. "I want to do so much," Qadri said before she got up for her next meeting. "Do you think I'm a madwoman?"

IT'S NO COINCIDENCE that "the mecca of cholera research," as Holmgren calls it, is in Bangladesh. Bacteria emerging from the brackish water of the Ganges River delta are believed to be the origin of six of the seven cholera pandemics that have washed over the globe the past 200 years, killing tens of millions of people, stoking fear and panic, and inspiring novels and movies. (The third pandemic, from 1846 to 1860, struck London, where physician John Snow famously showed cholera was carried not by bad air, but by contaminated water. The seventh began in 1961 and is ongoing.)

ICDDR,B was established as the Cholera Research Laboratory in 1960 by the Southeast Asia Treaty Organization, a U.S.-backed group aimed at stopping the rise of communism. During its first 60 years, the lab was led by foreign scientists, who helped bring in collaborations, expertise, and funding. (The center's hallways are lined with photos of famous visitors, including Hillary Clinton and Melinda French Gates.) In 2021, nutrition scientist Tahmeed Ahmed became the first Bangladeshi to head the center.

In the 1960s, ICDDR,B played a pivotal role in the development and testing of oral rehydration solution, a cheap, simple mix of glucose and salts that can be dissolved in water and given to diarrhea patients to replace lost fluids and prevent dehydration. "Bangladesh's gift to the world," as Ahmed called it, became a first-line treatment globally, saving millions of lives. The institute has since expanded into malaria and other mosquito-borne diseases, HIV/AIDS, malnutrition, child and maternal health, and other medical challenges facing Bangladesh. But it also helps prevent diseases that cross borders, says U.S. cholera scientist John Clemens, who headed ICDDR,B from 2013 to 2021. He predicts halting financial support "will be very expensive for the U.S. in the long run."

Qadri was born in Dhaka when Bangladesh was still a province of Pakistan. Her parents divorced when she was young, and she was mostly raised by her grandparents. Her grandmother insisted she pursue a good education, which was unusual at the time in Bangladesh's Muslim-majority society. "Girls have to have their own profession, their own education, and their own earning power," Qadri says her grandmother told her. Qadri's older sister, who became a physician, urged her to study "something more modern, more trendy, like molecular biology, microbiology, or biochemistry," Qadri says. "No need for another doctor in the family."

Her studies at Dhaka University, where she got a master's degree in molecular biology, were interrupted for 9 months by the brutal war that led to Bangladesh's independence in 1971. Hundreds of thousands, perhaps millions, were killed by the Pakistani military and affiliated militias, including many students and academics. Qadri's family came out unscathed, but "when it was over we didn't know whether to smile or cry because so many people we knew were dead." She says the episode strengthened her love of country.

In 1977, Qadri moved to the United Kingdom with her husband, also a scientist, to do a Ph.D. in biochemistry and immunology at the University of Liverpool. She loved life there—the colonial era had instilled a deep appreciation of England in her family, she says—but the couple returned to Bangladesh in 1980 to help rebuild the destitute country. In 1986, she joined ICDDR,B as a postdoc. Since then, she's worked on many intestinal pathogens common in Bangladesh, including *Shigella*, *Escherichia coli*, and rotavirus, but her main focus has been cholera.

A long, winding journey

Oral cholera vaccines first proved their mettle almost 4 decades ago, but their development and introduction has been a long, slow process. Today, as outbreaks are raging in dozens of countries, there is a huge shortage of doses.

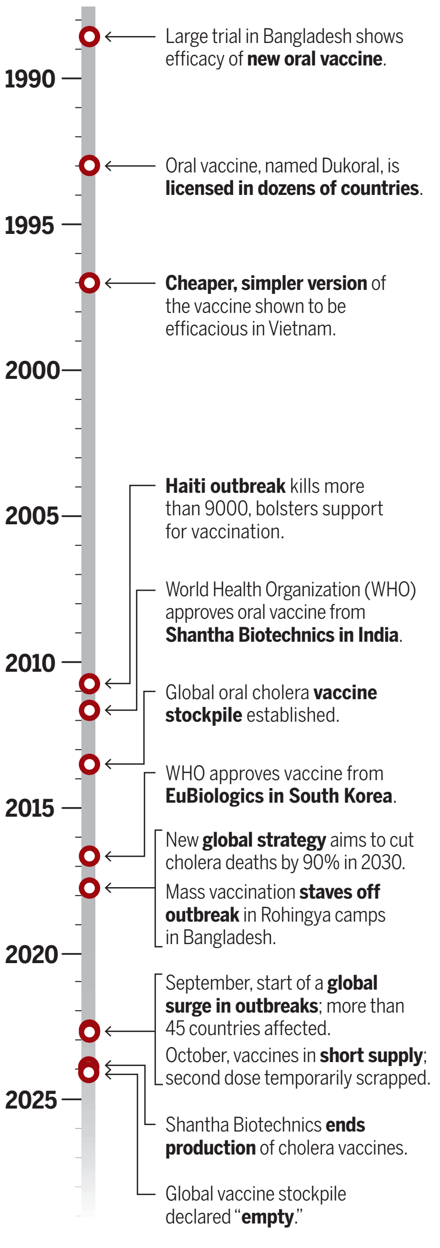

Large trial in Bangladesh shows efficacy of **new oral vaccine**.

Oral vaccine, named Dukoral, is **licensed in dozens of countries**.

Cheaper, simpler version of the vaccine shown to be efficacious in Vietnam.

Haiti outbreak kills more than 9000, bolsters support for vaccination.

World Health Organization (WHO) approves oral vaccine from **Shantha Biotechnics in India**.

Global oral cholera **vaccine stockpile** established.

WHO approves vaccine from **EuBiologics in South Korea**.

New **global strategy** aims to cut cholera deaths by 90% in 2030.

Mass vaccination **staves off outbreak** in Rohingya camps in Bangladesh.

September, start of a **global surge in outbreaks**; more than 45 countries affected.

October, vaccines in **short supply**; second dose temporarily scrapped.

Shantha Biotechnics **ends production** of cholera vaccines.

Global vaccine stockpile declared "**empty**."

GRAPHIC: N. CARY/*SCIENCE*

ON A WARM TUESDAY MORNING, Qadri showed *Science* around a slum in Mirpur, a neighborhood in northern Dhaka, with a few younger scientists and assistants in tow.

The streets were lined with gray concrete apartment blocks. Inside, families of five or more lived in a single room, their possessions stacked against the walls, a big TV screen hanging over the bed. Qadri stopped occasionally to make small talk with residents, inquire about their children's health, or ask to see their vaccination cards.

The neighborhood is one of ICDDR,B's main research sites. Qadri led a study here in more than a quarter-million people, published in 2015, to show that mass cholera vaccination among the urban poor is feasible. Today, one study is testing the duration of the vaccine's protection in children. There are also trials of new vaccines against typhoid and *Shigella*, and one to explore whether vaccinations against cholera, typhoid, measles, and rubella can be combined.

It's not hard to see why pathogens that travel the fecal-oral route could thrive in the neighborhood. Most households have running water, disinfected at the source with chlorine, but the supply is uneven. Occasionally, water pressure drops, allowing dirty water to leak into the neighborhood's pipes and tubes. Multiple households can share a single kitchen and a single foul-smelling toilet, meaning anybody infected with cholera can easily expose many others.

Providing clean drinking water, sanitation, and hygiene—WASH in cholera jargon—is the best way to prevent the disease. "It's why you don't have cholera in London and New York anymore," Qadri says. It's also a very tall order for a poor, extremely densely populated country. Bangladesh, less than one-third the size of Spain, has more than 170 million inhabitants, more than 20 million of them in greater Dhaka.

Scientists have long tried to tame cholera with vaccines instead. The 20th century brought injected vaccines made of whole, killed *V. cholerae* cells. But they sometimes had severe side effects, and the injections could hurt, recalls Qadri, who got them as a child: "It was so painful that we would hide under the bed." Worse, large-scale trials in the 1960s showed these vaccines provided poor protection: 50% at most, for just a few months, and only in adults. WHO stopped recommending them in the 1970s.

At his lab in Sweden, Holmgren pioneered a new strategy: an oral vaccine that would elicit so-called mucosal immunity in the lining of the gut, blocking the bacterium where it attacks. His vaccine also contained whole killed *V. cholerae* cells, but they were combined with the so-called B-subunit, a part of the microbe's toxin protein, and given orally rather than injected. A 1985 study in Bangladesh led by Clemens showed two doses offered about 85% protection during the first 2 years.

The vaccine, named Dukoral, was licensed

A slum in Dhaka, the Bangladeshi capital. A lack of clean drinking water, sanitation, and hygiene creates conditions in which *Vibrio cholerae* can thrive.

PHOTO: ANIK RAHMAN

in many countries in the early 1990s and is produced today by Valneva, a France-based company. But it has always remained a "traveler's vaccine" used by people from developed countries. "It was just too complex and too expensive to work in mass vaccination campaigns," Lynch says. The stomach's acids break down the B-subunit, so recipients need to take the vaccine with 150 milliliters of a fizzy buffer solution, which makes shipping and distributing it pricey and cumbersome.

But the toxin subunit was not essential. Holmgren helped transfer the technology to Vietnamese researchers, who dropped the subunit and tested a vaccine made of only killed cells—but still taken orally. Trials published in 1997 showed two doses provided about 66% protection. A team led by Clemens, who led IVI between 1999 and 2011, further refined the vaccine and then transferred the technology to Shantha Biotechnics in India, which agreed to produce it cheaply for use in developing countries. For their work on the vaccine, Holmgren and Clemens won several prestigious awards, including the Albert B. Sabin Gold Medal.

Within WHO and elsewhere in the global health community, however, some saw oral vaccines as a technological fix and a distraction from WASH measures—which prevent many other waterborne diseases—and from early detection and proper treatment. "There were always discussions between the WASH people and the vaccine people," Qadri says.

Vaccination remained rare, and Qadri's frustration grew. Sometimes she could hear patients retching and vomiting in the hospital from her office, she says, "and I was very disappointed. I felt my work didn't have any meaning." To expand vaccine use, she helped organize a 2007 meeting in Dhaka that brought together governments, global health agencies, and vaccinemakers. She also won support from the Bill & Melinda Gates Foundation for the feasibility study in Mirpur.

A turning point came in October 2010, when cholera broke out in Haiti, 10 months after an earthquake that killed 200,000 people. Hundreds of thousands got sick and more than 8000 died in the first year. The tragedy drove home that working on WASH was all well and good, Holmgren says, but vaccines could save lives in the meantime. "It was absolutely decisive," he says. (That the outbreak originated in a camp for U.N. peacekeepers may have helped sway opinions within WHO, itself a U.N. organization.)

In 2013, a consortium of global health organizations set up a cholera vaccine stockpile that allowed countries suffering from a cholera outbreak to apply for an emergency shipment. Initially, the stockpile contained only Shantha's vaccine, but in 2016 it added a second, very similar vaccine produced by South Korea–based EuBiologics with help from IVI.

In 2017, a humanitarian crisis in Bangladesh showed just how powerful the vaccine stash could be. Genocidal violence against the Rohingya, a Muslim minority in Myanmar, led an estimated 700,000 people to flee across the border, into the southern tip of Bangladesh. The Bangladeshi government and international organizations scrambled to provide safety and shelter in massive camps near the city of Cox's Bazar. "It was such a sad sight," says Qadri, who flew to the area within weeks after the influx and has since visited dozens of times. "There were people sitting everywhere, in the rain and mud, with such a vacant look on their face."

Bangladesh has made impressive economic strides in the past 25 years, but almost one-fifth of its 173 million people still live below the poverty line, many in Dhaka's slums.

It was also a cholera epidemic waiting to happen. "My heart told me we had to do something quickly," Qadri says. With help from ICDDR,B, the Bangladeshi government submitted a request for 900,000 doses to the stockpile in late September 2017. It was approved within 24 hours, and in November more than 200 vaccination teams swarmed out across the camps. The outbreak didn't happen. Since then, there have been eight additional vaccination rounds in the camps, whose population has swollen to well over 1 million.

Optimism rose about the potential of the oral vaccines. In 2017, a broad coalition of agencies and groups called the Global Task Force on Cholera Control published a plan for a 90% reduction in cholera deaths by 2030 that relied on improving WASH and early outbreak detection but also called for "large-scale" use of vaccines. "As many as 20 countries could eliminate the disease as a threat to public health by 2030," the plan said. Hot spots such as Bangladesh, which occasionally seed outbreaks elsewhere, would get special attention. ("There is no controlling cholera without controlling cholera in Bangladesh," Clemens says.) The country's own National Cholera Control Plan for 2019-2030, which Qadri helped write, set a similar 90% reduction target for the country, by 2030.

In 2018, Gavi's Board approved a proposal to make vaccines from the stockpile available not just for "reactive" campaigns—in response to outbreaks or humanitarian crises—but also for "preventive" campaigns in places like Bangladesh where the disease strikes every year. To be eligible for support, countries would have to strengthen surveillance, identify areas of intense transmission, and submit a detailed multiyear plan.

Bangladesh—and Qadri—embraced the idea. The country wrote an application for 100 million doses of vaccine, which a Gavi review panel approved in November 2023 and is currently being finalized.

BUT THINGS HAVEN'T GONE according to plan. Cholera cases did decline globally for a few years after the 2017 road map, but the COVID-19 pandemic wiped out part of those gains. Then came the massive outbreak in Bangladesh in 2022, and others in war-torn countries such as Sudan, Syria, and the Democratic Republic of the Congo. Climate change, and the extreme weather it favors, made things worse. Droughts, which can lead people to resort to unclean water, triggered outbreaks in Zambia and Zimbabwe; floods, which can destroy infrastructure and contaminate drinking water, did so in Kenya.

The stockpile hasn't kept up. In 2022, French pharma giant Sanofi, the parent company of Shantha, ended the production of cholera vaccines, despite protests from WHO. (Critics suspect Sanofi didn't deem the vaccines profitable enough; a company spokesperson says Sanofi only produced 10% of doses globally anyway and supply from other producers was set to grow.)

That has left EuBiologics as the only supplier, and it only produced about 50 million doses last year, far short of the demand. Allocating doses has become "like Sophie's choice," says Barboza, WHO's representative on the international group managing the stockpile. In late 2022, the panel decided to temporarily switch to a one-dose regimen, which a 2016 trial by Qadri in Bangladesh had suggested offered reasonable protection, although not in children under age 5.

Bangladesh has an alternative source of vaccine, at least on paper: IVI has also transferred its vaccine technology to Incepta Pharmaceuticals, which has a big, state-of-the-art production facility in Dhaka's outskirts. But the government, which is facing many other health challenges, hasn't deemed cholera urgent enough to buy from Incepta. The company can't supply the global stockpile either, because WHO has not yet approved its version of the vaccine. "We are completely locked," says Abdul Muktadir, Incepta's frustrated CEO. "We can't sell anything."

Things are now beginning to look up. EuBiologics recently increased its manufacturing capacity and may produce more than 70 million doses this year, and the stockpile is back up to 5 million doses, seen as the minimum needed to address emergencies. "We're in a much better place than we were a year ago," says Gavi cholera expert Allyson Russell. Two other companies,

PHOTO: ANIK RAHMAN

Sathi Akhter (center) came to ICDDR,B last summer because her 6-year-old son (right) had severe diarrhea.

PHOTO: ANIK RAHMAN

in South Africa and India, are expected to bring similar vaccines to the market in 2026, which should further ease shortages. Still, when Bangladesh might get its 100 million doses is unclear. "It's sad when you have a way to prevent disease and you can't use it," Qadri says.

BANGLADESH IS AT A MAJOR CROSSROADS. In August 2024, student protests toppled the country's autocratic government, which had tried to suppress them with deadly violence. Now, 84-year-old Muhammad Yunus, a microfinance pioneer and Nobel Peace Prize winner, is leading an interim government and heading the effort, along with students, to write a new constitution. Recent reports have documented the disappearance of thousands of political opponents and widespread corruption under Sheikh Hasina, the ousted prime minister.

Last summer Qadri spoke warmly of Hasina, calling her a "humanitarian," in part because of her support for Qadri's work. Qadri later told *Science* she didn't know much about what went on in Hasina's government. "I'm not a political person," she said. "There are young people now taking over. I'm waiting to see what will happen."

She did take heart from the progress Bangladesh has made. Its economy has grown at more than 6% annually for many years, in part thanks to a burgeoning garment industry that has provided millions with a living wage and made women more independent. In other positive signs, the birth rate has plummeted, from 3.6 children per woman in 1995 to below two, and the share of people living below the national poverty line has dropped steeply.

"It's sad when you have a way to prevent disease and you can't use it."

Firdausi Qadri, ICDDR,B

Qadri hopes the new government will devote more resources to science. ICDDR,B enjoys support from many foreign sources—"Without the Gates foundation, I would be nothing," Qadri says—but the country's own expenditure on R&D is just above 0.3% of gross domestic product, among the lowest in the world. In the meantime, Qadri has set up her own initiative—"my gift to the country," as she calls it. Using money from her awards, including €500,000 from a prestigious French prize in 2012, she and her husband in 2014 launched the Institute for Developing Science and Health initiatives (IDESHI). "I wanted to create something different, something new," she says—a place for training young scientists whose culture she could shape herself. Today IDESHI employs more than 60 people working on a broad range of neglected health issues in Bangladesh. For example, a Gates-supported project aims to increase awareness of cervical cancer and encourage vaccination against the human papillomavirus (HPV), which causes it. It's a delicate task, because HPV is transmitted sexually. "In our culture we do not talk about sex," Qadri says.

Another project aims to prevent thalassemia, a blood disorder caused by a recessive gene that many people unknowingly carry. Marriages between cousins, common in Bangladesh, increase the risk. The project is encouraging people to get tested and, if they have the gene, avoid marrying another carrier. "A woman often hesitates to express that she is a carrier," says Kasrina Azad, the medical officer leading the project. "In our culture, it's like she has bad blood or something. So she faces a lot of stigma."

More than half of the staff at IDESHI are women, and Qadri herself has undoubtedly "blazed a trail" in Bangladesh, Lynch says. "I've seen her interact with government officials, and everyone is just like, 'Oh, you don't mess with her,'" she says. "She's so respected, they listen to what she has to say."

On 11 January, Qadri headed back to the Rohingya camps, where workers were about to launch another round of cholera vaccinations, in response to a worrisome rise in cases. The battle against Bangladesh's ancient scourge was continuing—and Qadri would never give up her role in it, she said: "Do I look like I can retire?" ■

INSIGHTS

The mantis shrimp has strong dactyl clubs that can withstand high-velocity impacts by filtering stress waves.

PERSPECTIVES

PHOTO: PAUL STAROSTA/GETTY IMAGES

MATERIALS SCIENCE

Naturally twisted to sieve stress

Mantis shrimp display phononic behavior similar to that of artificial metamaterials

By **Pablo D. Zavattieri**

Architected metamaterials—artificial structures with unusual properties that arise from tailored geometry—can guide deformation and energy flow in desirable ways. A subset of metamaterials called phononic bandgap materials can reflect, scatter, or absorb energy by manipulating the way mechanical waves interact with the periodic structures of the material. Waves within a specific frequency range cannot travel through such a material, creating a phononic bandgap. This effect is useful for technologies such as acoustic imaging, acoustic cloaking, shock proofing, and energy harvesting. Architected metamaterials are artificially made; does a similar phenomenon exist in nature? On page 659 of this issue, Alderete *et al.* (*1*) report that a mantis shrimp's dactyl club has phononic bandgaps in which stress waves of specific frequency ranges are filtered. This demonstrates that natural materials can exhibit phononic behavior that is observed in artificial metamaterials, opening the possibility for designing bioinspired and biohybrid phononic bandgap materials.

Natural phononic bandgap material

Dactyl clubs of a mantis shrimp consist of multiple layers of helicoidal fibers that make up a Bouligand structure. The periodic architecture creates a phononic bandgap in which stress waves within a specific frequency range cannot travel through the material. This gives the clubs unusual impact resistance.

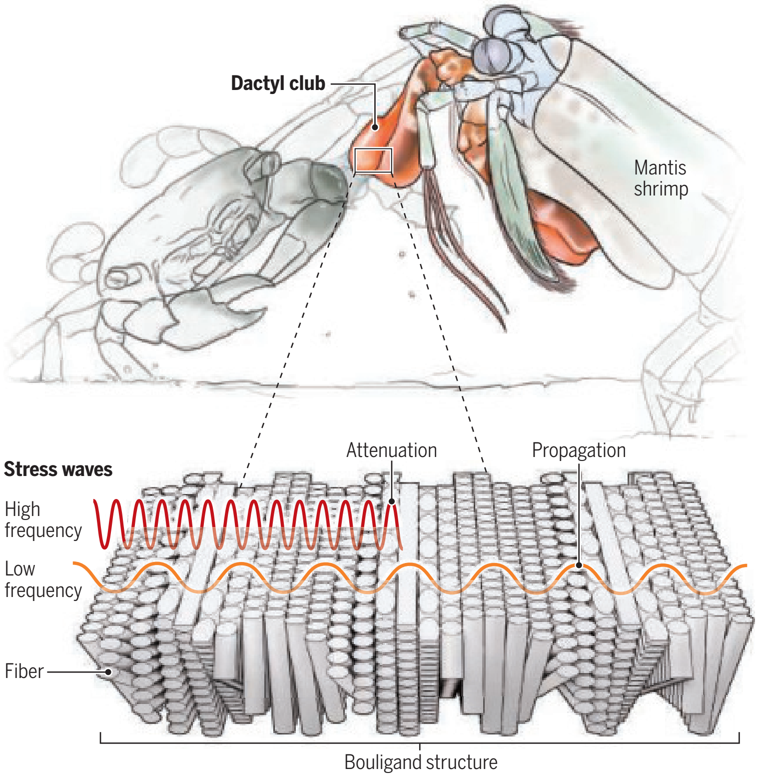

Nature has long used sophisticated strategies to manipulate mechanical waves for survival. For example, moth wings are covered by tiny modified hairs (scales) that resonate in the same frequency. These natural acoustic resonators provide camouflage against echolocating predatory bats (*2*). Mosquito antennae have lightweight, vibrating hairlike structures with a tapered geometry, which allow them to detect specific acoustic cues for mating and foraging (*3*). In addition to acoustic wave control, nature can offer solutions for structural challenges through mechanisms that control stress waves. The mantis shrimp is known for its strong dactyl clubs with extraordinary impact resistance and durability. This marine crustacean can crack open hard shells by delivering high-velocity impacts with this appendage without incurring damage to its own body (*4*). The unusual toughness of the club stems from a hierarchical Bouligand structure that consists of multiple layers of helicoidal fibers and mineralized chitin. This periodic structure delocalizes stress waves and controls nucleation, propagation, and the coalescence of cracks. The layers promote local hardening behavior, damage distribution, and energy dissipation to provide pseudoplasticity and ductility to an otherwise brittle dactyl club (*5*–*7*).

The phononic behavior is similar to the interplay of constructive and destructive interference of capillary waves, which are seen as ripples on the surface of water, or acoustic waves from vibrations of a violin string. Previous theory hypothesized that the mantis shrimp uses the phononic mechanism to filter stress waves for impact resistance (*8*), and experimentally validating this hypothesis has been challenging for the past decade. Alderete *et al.* demonstrate phononic shielding behavior of a mantis shrimp's dactyl club through rigorous experiments. The authors show that enhanced impact resistance is the result of filtering stress waves—a property previously attributed solely to synthetic phononic crystals. The periodic, helicoidal structure of Bouligand architecture selectively attenuates a range of stress wave frequencies generated upon high-intensity impacts (see the figure). This filtering effect reduces localized stress concentrations and distributes the applied mechanical energy more uniformly. Thus, the outer layers of the dactyl club act as damage-resistant shields for the inner layers.

Alderete *et al.* performed time-resolved laser ultrasonic experiments and observed key phononic behaviors in the dactyl club, such as Bloch harmonics, dispersive surface modes, flat dispersion bands, and Bragg scattering-driven bandgaps, which are often present in synthetic phononic crystals. The club exhibited Bragg bandgaps in the megahertz range, where waves of specific frequencies dissipate because of destructive interference caused by multiple wave reflections from the periodic structure. The authors also noted flat dispersion bands (constant frequency regardless of momentum), which indicated localization and trapping of stress waves within a material. These observations suggest that a mantis shrimp shields itself from high-frequency shocks by sophisticated phononic mechanisms. The experimental demonstration of energy dissipation and localization in a naturally occurring hierarchical structure could bring a new perspective into the design of phononic bandgap materials.

Beyond the study of Alderete *et al.*, challenges remain in scaling natural materials for industrial applications. Translating the Bouligand structure of a mantis shrimp into a functional phononic bandgap material requires selecting a combination of materials with mechanical anisotropy and stiffness that resemble those of the shrimp. Additionally, wave dispersion characteristics—that is, a relationship between propagation speed and frequency of a wave—are dictated by both the architecture and properties of constituents. These are crucial for designing architected composites with desired stress wave filtering (*9*).

The interplay between structural hierarchy and wave properties also prompts consideration of whether phononic bandgaps exist in similar structural motifs of different species. For example, the helicoidal structures in beetle wings (*10*, *11*) have good strength and are fracture resistant. The discovery of other natural phononic structures and understanding their limitations could unlock new designs with capabilities beyond existing impact-resistance materials and energy dissipation systems. ■

Lyles School of Civil and Construction Engineering, Purdue University, West Lafayette, IN, USA. Email: zavattie@purdue.edu

GRAPHIC: N. BURGESS/*SCIENCE*

REFERENCES AND NOTES

1. N. A. Alderete *et al.*, *Science* **387**, 659 (2025).
2. T. R. Neil, Z. Shen, D. Robert, B. W. Drinkwater, M. W. Holderied, *Proc. Natl. Acad. Sci. U.S.A.* **117**, 31134 (2020).
3. A. A. Trikanad, P. S. Dasika, H. Pantoja-Sánchez, X. E. Bernal, P. D. Zavattieri, *Acta Biomater.* **192**, 165 (2025).
4. J. C. Weaver *et al.*, *Science* **336**, 1275 (2012).
5. L. K. Grunenfelder *et al.*, *Acta Biomater.* **10**, 3997 (2014).
6. N. Suksangpanya, N. A. Yaraghi, D. Kisailus, P. Zavattieri, *J. Mech. Behav. Biomed. Mater.* **76**, 38 (2017).
7. A. Garnica *et al.*, *Extreme Mech. Lett.* **71**, 102190 (2024).
8. N. Guarín-Zapata, J. Gómez, N. Yaraghi, D. Kisailus, P. D. Zavattieri, *Acta Biomater.* **23**, 11 (2015).
9. N. Guarín-Zapata, J. Gómez, D. Kisailus, P. D. Zavattieri, *J. Mech. Phys. Solids* **131**, 344 (2019).
10. M. Asgari, N. A. Alderete, Z. Lin, R. Benavides, H. D. Espinosa, *Acta Biomater.* **122**, 236 (2021).
11. A. Zaheri *et al.*, *Adv. Funct. Mater.* **28**, 1803073 (2018).

10.1126/science.adv3100

SYNTHETIC BIOLOGY

Relating DNA sequence, organization, and function

Cross-species mosaic genomes provide insight into synthetic chromosome design

By **Geoffrey Fudenberg**[1] *and* **Vijay Ramani**[2, 3]

As molecular geneticist François Jacob wrote, living organisms reflect "the very nature of a historical process full of contingency" (*1*). Evolutionary contingency constrains relationships between genome sequence, organization, and function. However, technologies for engineering ever-larger stretches of DNA now enable synthetic regulatory reconstitution experiments (*2*–*4*) in which foreign DNA, freed from historical contingency, can be placed directly into a host cell. Such "in hostia" reconstitutions complement classic in vitro approaches for determining the rules of genomic regulation. Notably, in hostia reconstitutions assess the regulatory "ground state" of a host cellular environment—that is, the propensity for inserted DNA to be active or silent. On page 627 of this issue, Meneu *et al.* (*5*) describe what happens when bacterial DNA is introduced into yeast cell nuclei as synthetic chromosomes. The spontaneous formation of active or inactive chromatin, dependent on sequence composition of the exogenous chromosomes, has implications for synthetic chromosome design.

Meneu *et al.* chose chromosomes from the bacteria *Mycoplasma mycoides* or from *Mycoplasma pneumoniae* to artificially introduce into the budding yeast *Saccharomyces cerevisiae*. During the interphase stage of the cell cycle, the *M. pneumoniae* chromosome was transcriptionally active and organized similarly to the host genome. By contrast, the *M. mycoides* chromosome was relatively silent, displaying little transcription, and adopted a compacted three-dimensional (3D) organization, which the authors called "unconventional." The divergent organization of the *M. mycoides* chromosome appears to relate to its much lower content of the nucleotides guanine and cytosine as compared to that of *M. pneumoniae* or the host yeast genome sequences (24% versus ~40%). Notably, DNA sequences from *M. mycoides* assumed this unconventional organization even when reconstituted as mosaic chimeric chromosomes, interspersed with the sequence of a yeast chromosome. Because this silent state had not been previously characterized for foreign DNA reconstituted in yeast host cells, the observations of Meneu *et al.* raise broader evolutionary questions about the regulatory function of chromatin in Eukarya. Although chromatin is often studied for its ability to promote transcriptional activation, chromatin also serves essential repressive functions (*6*). These functions include both conditional gene repression and silencing parasitic genomic elements. Given the ancient origins of parasitic genomic elements in eukaryotic genomes, the capacity of host chromatin to "frustrate" parasitic element expression is likely ancestral. Budding yeast such as *S. cerevisiae* lost or only sparingly use many of the ancestral silencing mechanisms for parasitic elements, such as histone methylation, RNA splicing, and RNA-dependent silencing. Meneu *et al.* may have uncovered an alternative mechanism whereby the *S. cerevisiae* genome silences—or at the very least ignores—certain foreign genetic material but not others. Understanding the rules by which organisms compute self versus nonself remains an exciting future prospect.

> **"...the observations of Meneu *et al.* raise broader evolutionary questions about the regulatory function of chromatin in Eukarya."**

During the mitotic phase of the cell cycle, the synthetic *M. mycoides* chromosome appeared compacted similarly to the host genome by the mechanism of DNA loop extrusion, a process whereby molecular motors actively organize the genome in 3D. Yet, the synthetic *M. mycoides* chromosome lacked the mitotic signature of well-positioned loops between sites of convergent transcription observed across yeast chromosomes and the synthetic *M. pneumoniae* chromosome. Sites of convergent transcription are also enriched for contacts between sister chromatids in mitosis (*7*) and positioned loops in meiosis (*8, 9*) in which homologous chromosome pairing and recombination occur. The observations of Meneu *et al.* thus raise the question of whether sister chromatid alignment, homologous recombination, and DNA repair are compromised for the *M. mycoides* chromosome. In the future, synthetic chromosomes could provide a platform to dissect the interplay of loop extrusion and DNA repair (*10*).

Moving forward, it will be instructive to compare findings from in hostia approaches with those obtained through in vitro reconstitution. "Bottom-up" in vitro experiments can recapitulate increasingly complex features of chromosome organization at ever-larger scales. Testing whether purified protein complexes are sufficient to determine genome organization and function in vitro is especially valuable when complexes can compensate for one another, such as the chromatin remodeling complexes BAF (Brahma associated factor) and the larger TIP60 (including lysine acetyltransferase 5, KAT5) (*11*). For *S. cerevisiae* components and DNA sequences, in vitro reconstitution has been used to assess chromatin states (*12*) and 3D organization of the genome (*13*). Recent work extended this analysis to the single-fiber level for chromatin reconstituted in vitro using mammalian DNA sequences (*14*), including in the context of chromatin condensation (*15*). By combining results from in hostia experiments across a broad panel of evolutionarily distinct organisms with precise in vitro reconstitutions, studies can further clarify both necessary and sufficient factors to explain rules of genome regulation across the kingdom of life. ■

---

[1] Department of Quantitative and Computational Biology, University of Southern California, Los Angeles, CA, USA. [2] Department of Biochemistry and Biophysics, University of California San Francisco, San Francisco, CA, USA. [3] Gladstone Institute for Data Science and Biotechnology, San Francisco, CA, USA. Email: fudenber@usc.edu

REFERENCES AND NOTES

1. F. Jacob, *Science* **196**, 1161 (1977).
2. S. Pinglay *et al.*, *Science* **377**, eabk2820 (2022).
3. R. Brosh et al., *Mol. Cell* **83**, 1140 (2023).
4. R. Ordoñez *et al.*, *Mol. Cell* **84**, 1842 (2024).
5. L. Meneu *et al.*, *Science* **387**, eadm9466 (2025).
6. D. H. Madhani, *Cell* **155,** 744 (2013).
7. M. E. Oomen, A. K. Hedger, J. K. Watts, J. Dekker, *Nat. Methods* **17**, 1002 (2020).
8. S. A. Schalbetter, G. Fudenberg, J. Baxter, K. S. Pollard, M. J. Neale, *Nat. Commun.* **10,** 4795 (2019).
9. H. Muller *et al.*, *Mol. Syst. Biol.* **14**, e8293 (2018).
10. A. Dumont *et al.*, *Mol. Cell* **84**, 3237 (2024).
11. B. J. E. Martin *et al.*, *Cell* **186**, 5290 (2023).
12. N. Krietenstein *et al.*, *Cell* **167**, 709 (2016).
13. E. Oberbeckmann, K. Quililan, P. Cramer, A. M. Oudelaar, *Nat. Genet.* **56**, 483 (2024).
14. N. J. Abdulhay *et al.*, *Nat. Struct. Mol. Biol.* **30**, 1571 (2023).
15. C. Moore *et al.*, *bioRxiv* 2024.09.10.611504 (2024).

10.1126/science.adv1576

EVOLUTION

Convergent evolution in whale and human vocal cultures

The complex songs of humpback whales conform to fundamental laws of language

By **Andrew Whiten**[1] and **Mason Youngblood**[2]

Culture pervades the lives of numerous animal species, in a great diversity of forms (*1*), but the songs of the humpback whale are among animal culture's most extraordinary manifestations. Sung only by males, the songs penetrate the ocean for many miles and are suspected to attract females for mating through their musical complexity. Year by year, the songs may become more complex and perhaps more alluring to females. However, in the southwestern Pacific, a totally new song emerges every few years that is adopted across the ocean (*2*). The rapidity with which new songs and variations are copied demonstrates that they are culturally transmitted, but the evolutionary forces that shape the complex song structures over time have remained mysterious. On page 649 of this issue, Arnon *et al.* (*3*) report that fundamental laws identified in quantitative linguistics and in the culturally evolved learnability of human languages apply to whale song.

Just as human vocalizations are structured by a hierarchy of phonemes, words, phrases, sentences, and narratives, so, too, are the songs of humpback whales. They display a similar complex hierarchical structure in which sound "units" are strung together to make stereotyped "phrases," repeated in turn to shape "themes" that are organized into elaborate songs that last as long as 30 min. In the 1930s and '40s, the linguist George Zipf identified striking quantitative patterns that appear to be universal in the world's languages (*4*). Zipf's rank-frequency law asserts that the frequencies of the specific units, such as words, that make up a language are highly skewed, following a power-law distribution. Thus, in any particular language, the most common word (in English, it is "the") occurs twice as often as the next most common ("of"), three times as often as the third ("and"), and so on. How one might discover whether such phenomena occur in whale songs is not immediately obvious. To humans, the units of language to be considered, such as words, are obvious because they are known and spoken. But to the human ear, a whale song is perceived as just a stream of sounds. However, human infants must learn to distinguish language units within the stream of sounds in continuous spoken language. Much is known about how infants use various acoustic cues to segment speech, such as changes in pitch, loudness, and pauses (*5*). After the development of ingenious algorithms inspired by this understanding and tested in segmenting human speech (*6*), Arnon *et al.* applied essentially the same approach to a substantial corpus of humpback whale song recordings collected over 8 years.

When Arnon *et al.* plotted the frequency of humpback whale subsequences against their rank (similar to "the" = 1, "of" = 2, and so on in English) on a logarithmic scale, the data followed a straight line, diagnostic of Zipf's rank-frequency law. Based on comparisons with other empirical work in linguistics, the authors made two intriguing inferences about what this striking whale-human commonality may mean. Children tasked with segmenting artificial linguistic units showed that this behavior is facilitated by Zipfian frequency distributions (*7*). That this law also characterizes humpback whale song likely indicates that the hierarchical structure of song facilitates cultural learning in whales, too (see the figure). Also, because the repeated transmission of artificial languages in human microsociety experiments, in which communication among a small group of people in a controlled setting is observed over time, can shape the evolution of Zipfian dis-

---

[1] School of Psychology and Neuroscience, University of St Andrews, St Andrews, UK. [2] Institute for Advanced Computational Science, Stony Brook University, Stony Brook, NY, USA. Email: aw2@st-andrews.ac.uk

Hierarchical structure in humpback whale song and human language

Humpback whale songs display complex hierarchical structure and may take more than 30 min to sing. These songs are composed of multiple themes, themes are composed of phrases, and phrases are composed of sound units, analogous to the hierarchical structuring of human speech and song. Recordings rendered here are from (*14, 15*).

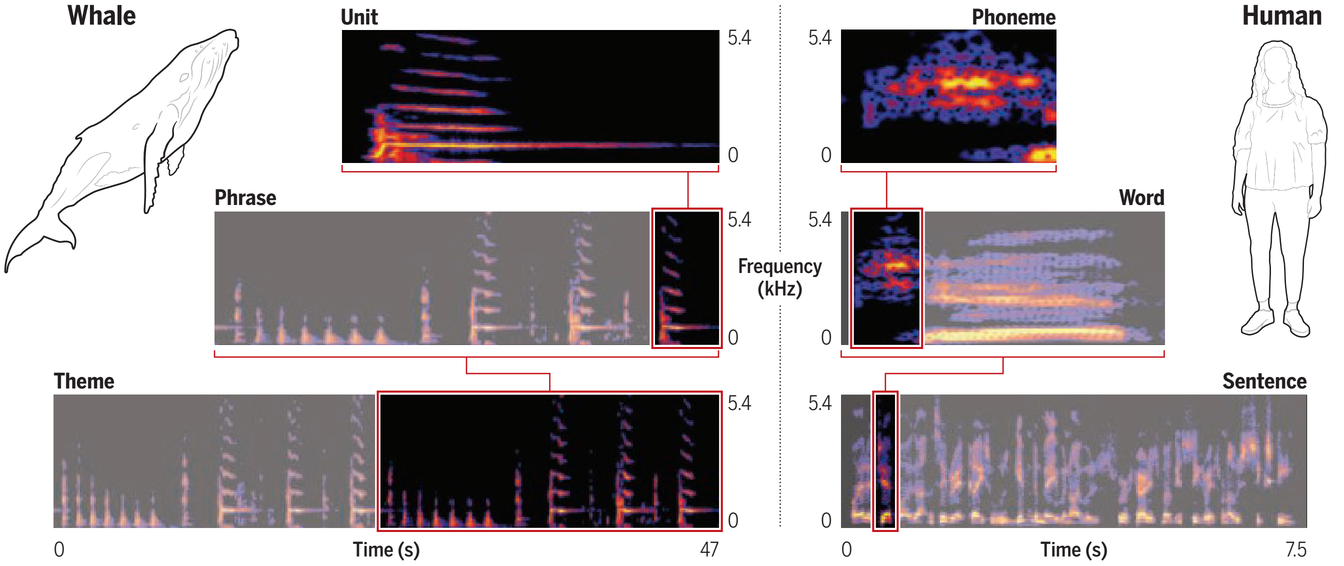

CREDITS: (GRAPHIC) A. FISHER/*SCIENCE*; (DATA) E. C. GARLAND *ET AL.* (*14*); F. SEIFART *ET AL.* (*15*)

The complexity of humpback whale songs is suspected to attract females for mating.

PHOTO: D. PARER AND E. PARER-COOK/MINDEN PICTURES

tributions (*6*), it is plausible that Zipfian distributions are the products of long periods of cultural evolution of vocal repertoires in humpback whales.

Zipf also elaborated a second law in linguistics, which asserts that the most common items in a language will be the shortest (*4*). Arnon *et al.* show that Zipf's law of abbreviation also holds for the subsequences detected in whale songs. These findings build on previous work on Zipf's laws in humpback whale song (*8*, *9*), demonstrating that similar Zipfian patterns exist at multiple hierarchical levels in humpback whale song, as they do in human language.

Zipf's rank-frequency law is arguably the most mysterious of the high-profile linguistic laws, so a note of caution about the tantalizing inferences of Arnon *et al.* regarding its importance in humpback whale song is warranted. Learnability with respect to complex vocal sequences is just one of several potential hypotheses to explain the phenomenon (*10*). Power-law distributions have been reported in a variety of contexts, including gene expression and city sizes, and may emerge through a diversity of processes. Indeed, the ubiquity of power laws has led some linguists to argue that they might be statistical artifacts. However, given that Zipfian distributions can enhance learnability in humans and that they can result from iterative selection as communicative cultures are repeatedly transmitted, learnability may well be the most parsimonious explanation for their presence in other forms of learned communication systems, with humpback whale song arguably providing the most compelling case to date.

Over the past decade, researchers have increasingly identified parallels between properties of animal communication and aspects of human language. The vocal repertoires that distinguish different clans of sperm whales, for example, have been argued to represent symbolic markers of clan membership because they appear to be most different between clans that overlap the most in their spatial distribution (*11*). Thus, clans with the most spatial overlap are the most distinctive in their identity codas. Zipf's laws and their variations, together with other linguistic principles such as Menzerath's law (the longer a unit, such as a word, the shorter its constituent elements, such as phonemes), have now been reported in a wide array of animals, including whales, primates (*12*), and birds (*13*). From what is known, humpback whale song and bird song exhibit patterns that follow these laws and principles without conveying the semantic meanings that human languages do. To this extent, we should perhaps be comparing whale songs to human music. What these important parallels highlight is that communication systems in distantly related species may nevertheless converge toward similar structures, especially those that are complex, culturally learned, and effective. ■

REFERENCES AND NOTES

1. A. Whiten, *Science* **372**, eabe6514 (2021).
2. J. A. Allen, E. C. Garland, R. A. Dunlop, M. J. Noad, *Proc. R. Soc. London Ser. B* **285**, 2 (2018).
3. I. Arnon *et al.*, *Science* **387**, 649 (2025).
4. G. K. Zipf, *Human Behavior and the Principle of Least Effort: An Introduction to Human Ecology* (Addison-Wesley, 1949).
5. B. Pelucchi, J. F. Hay, J. R. Saffran, *Cognition* **113**, 244 (2009).
6. I. Arnon, S. Kirby, *Sci. Rep.* **14**, 5255 (2024).
7. O. Lavi-Rotbain, I. Arnon, *Cognition* **223**, 105038 (2022).
8. J. A. Allen, E. C. Garland, R. A. Dunlop, M. J. Noad, *Proc. R. Soc. London Ser. B* **286**, 20192014 (2019).
9. T. S. Kang, thesis, Durham University (2021).
10. S. T. Piantadosi, *Psychon. Bull. Rev.* **21**, 1112 (2014).
11. H. Whitehead, *R. Soc. Open Sci.* **11**, 231353 (2024).
12. M. L. Gustison, S. Semple, R. Ferrer-I-Cancho, T. J. Bergman, *Proc. Natl. Acad. Sci. U.S.A.* **113**, E2750 (2016).
13. M. Youngblood, *Proc. R. Soc. London Ser. B* **291**, 20240250 (2024).
14. E. C. Garland *et al.*, *J. Acoust. Soc. Am.* **142**, 460 (2017).
15. F. Seifart, L. Paschen, M. Stave, Language Documentation Reference Corpus (DoReCo), version 93 1.2 (2022).

10.1126/science.adv2318

MALARIA

Not just monkey business

Functional genomics in malaria unlocks comparative biology across the family tree

By **Robert W. Moon**[1] *and* **Ellen S. C. Bushell**[2,3]

In 2023, there were more than 263 million malaria cases and 597,000 related deaths worldwide, according to the World Health Organization (WHO). Given that nearly half the world's population is at risk for malaria—and notwithstanding the rollout of new vaccines offering some protection to the most vulnerable—understanding the biology of these pathogens is crucial for addressing this public health problem. On pages 628 and 629 of this issue, Oberstaller *et al.* (*1*) and Elsworth *et al.* (*2*), respectively, report the application of transposon mutagenesis screens to the monkey malaria parasite *Plasmodium knowlesi* to determine which of the ~5000 genes in its genome are essential for replication in the host's blood. These studies mark a milestone in comparative biology across malaria parasite species. Conserved essential genes constitute potential targets for drugs or vaccines against all species, whereas uniquely essential genes reflect the divergent biology and evolution of these pathogens.

Human malaria is caused by a range of species within the *Plasmodium* genus and is transmitted by mosquitoes. *Plasmodium falciparum* causes most malaria deaths and infections, whereas *Plasmodium vivax* infection is widespread and associated with relapsing disease. *P. knowlesi*, which naturally infects macaques, has emerged as a substantial cause of human infections across Southeast Asia. Zoonotic malaria poses a notable challenge because established methods for malaria control focus on treating cases and killing mosquitoes within the home. With zoonotic malaria, macaques

---

[1]Department of Infection Biology, Faculty of Infectious and Tropical Diseases, London School of Hygiene and Tropical Medicine, London, UK. [2]Department of Molecular Biology, Umeå University, Umeå, Sweden. [3]The Laboratory for Molecular Infection Medicine Sweden, Umeå University, Umeå, Sweden. Email: rob.moon@lshtm.ac.uk; ellen.bushell@umu.se

act as an untouchable reservoir of parasites, so infections can arise when a mosquito bites a human after feeding on an infected macaque. Monkey malaria has a key political dimension too—Malaysia's century-long malaria control program eliminated all "human" malaria parasites in 2018, yet zoonotic malaria has so far stood in the way of its WHO malaria elimination certification.

Among the human-restricted species, only *P. falciparum* blood stages can be cultured in vitro, which is a prerequisite for screening drugs, testing vaccines, and studying gene function. Because *P. falciparum* occupies an evolutionarily divergent clade compared with all other human-infective species, there is a paucity of tools to study the biology of *P. vivax*. Phylogenetically nestled among the non–*P. falciparum* human malaria parasites, and a close cousin of *P. vivax*, *P. knowlesi* fills this gap. *P. knowlesi* has a distinguished history as a laboratory model that has enabled the discovery of classic malaria biology, such as antigenic variation (*3*). The development of strains that can be grown in vitro with human red blood cells has relieved dependence on nonhuman primate materials, and transfection efficiencies (delivering foreign DNA into cells) have improved substantially (*4*–*6*). This has accelerated the use of *P. knowlesi* to study parasite biology and as an in vitro surrogate for *P. vivax* vaccine development (*7*, *8*). The ability to switch between two different host cells (monkey and human) in vitro also makes *P. knowlesi* a powerful system for studying determinants of host cell tropism. Notably, the studies by Elsworth *et al.* and Oberstaller *et al.* were conducted in macaque and human erythrocytes, respectively, with the prospect of identifying genes required for infection of each host.

> **"Conserved essential genes constitute potential targets for drugs or vaccines against all species…"**

Despite a growing interest in *P. knowlesi* biology and its use as a model system, there are few functional genomics datasets available. Determining gene function at scale is challenging in *Plasmodium*. The pathways for RNA interference (a gene-silencing mechanism) and nonhomologous end-joining (a DNA repair mechanism) are missing, which means that RNA interference approaches and classical CRISPR genome editing–based screens to determine gene function are not possible in *Plasmodium*. Instead, gene disruption is achieved by homologous recombination, in which nucleotide sequences are exchanged between two molecules of DNA. This approach is inefficient and difficult with respect to cloning gene-targeting vectors carrying DNA rich in adenine (A) and thymine (T)—nucleotides that are abundant in *Plasmodium* genomes.

In the more genetically tractable murine model parasite *Plasmodium berghei*, these challenges have been overcome, facilitating the development of a genome-scale barcoded library of gene-targeting vectors that, on insertion into the parasite genome, generate mutants lacking specific genes. Although these screens identify gene essentiality with high confidence, the genome coverage (>60%) is restricted by vector availability (*9*). By contrast, transposon-mediated mutagenesis used by Oberstaller *et al.* and Elsworth *et al.* is not limited by the low efficacy of homologous recombination or the availability of gene-specific targeting vectors. The piggyBac transposition approach is governed by the expression of an exogenous enzyme that facilitates transposon insertion into specific sites (TTAA) across the genome. Gene essentiality is determined on the basis of the lack of insertions in any given gene. It thereby turns the challenge of working with AT-rich *Plasmodium* genomes into a strength and enables genome-scale genetic screens in *P. falciparum* (*10*). Transfection efficiencies are much higher in *P. knowlesi* than in *P. falciparum*, and thus transposon insertion coverage is greatly increased in the studies of Elsworth *et al.* and Oberstaller *et al.* This increases the confidence with which genes can be designated as essential and allows this to be determined at the level of functional domains within genes.

Notably, the availability of datasets for multiple *Plasmodium* species permits comparison of gene essentiality across species. The genetic screens querying blood-stage essentiality in *P. knowesi*, *P. falciparum* (*10*), and *P. berghei* (*9*) identify a markedly high degree of gene essentiality compared with that in free-living unicellular eukaryotes. By comparison of genes with orthologs in all three species, Oberstaller *et al.* and Elsworth *et al.* identified core essential genes shared across *Plasmodium*. These represent metabolic and housekeeping processes as well as those related to the apicoplast, the apicomplexan relic chloroplast organelle. Both studies also identified genes that are differentially essential or dispensable to the two human-infective parasites. By showing that ornithine aminotransferase and glutamate dehydrogenase 3—which supply metabolic intermediates to the tricarboxylic acid (TCA) cycle—are essential only in *P. knowlesi*, Elsworth *et al.* reveal that, in contrast to *P. falciparum*, blood stages of *P. knowlesi* and *P. vivax* are far more dependent on the TCA cycle. Conversely, Oberstaller *et al.* demonstrate that the nucleoside transporter 1, which is essential for scavenging host purines in *P. falciparum*, is dispensable in *P. knowlesi*. Because purine levels differ between human and macaque erythrocytes, this could relate to *P. knowlesi* adaptation to distinct hosts.

Comparisons of gene essentiality between *P. falciparum*, *P. berghei*, and the related single-celled parasite *Toxoplasma gondii* have revealed a strong conservation of essential genes within the Apicomplexa phylum (*10*). The development of new genetic tools for the parasite *Cryptosporidium* (*11*) will enable further comparisons across the phylum and will provide information about the shared evolutionary path of apicomplexan parasites as well as their adaptation to infect and interact with a diverse range of host cells.

Current analyses of *P. knowlesi* and *P. falciparum* focus on the parasite blood stages that can be cultivated in vitro. Future studies should aim to translate these to the transmission (*12*) and liver stages (*13*), as achieved for *P. berghei*. Although current *P. knowlesi* laboratory strains transmit poorly, overcoming these challenges will enable genus-level comparison of how gene essentiality profiles are redefined as the parasite navigates its complex life cycle. Although *P. knowlesi* shares much of its biology with *P. vivax*, it does not cause disease relapse through formation of hypnozoites, a dormant stage in the liver. Development of the *Plasmodium cynomolgi* model (*14*), which forms latent hypnozoites, should be informative. Similarly, understanding how gene essentiality changes in response to drugs or altering experimental conditions can provide vital leads to understanding how parasites respond to their environment (*15*). ■

REFERENCES AND NOTES

1. J. Oberstaller *et al.*, *Science* **387**, eadq7347 (2025).
2. B. Elsworth *et al.*, *Science* **387**, eadq6241 (2025).
3. K. N. Brown, I. N. Brown, *Nature* **208**, 1286 (1965).
4. C. H. M. Kocken *et al.*, *Infect. Immun.* **70**, 655 (2002).
5. C. Lim *et al.*, *Nat. Commun.* **4**, 1638 (2013).
6. R. W. Moon *et al.*, *Proc. Natl. Acad. Sci. U.S.A.* **110**, 531 (2013).
7. F. Mohring *et al.*, *eLife* **8**, e45829 (2019).
8. T. A. Rawlinson *et al.*, *Nat. Microbiol.* **4**, 1497 (2019).
9. E. Bushell *et al.*, *Cell* **170**, 260 (2017).
10. M. Zhang *et al.*, *Science* **360**, eaap7847 (2018).
11. L. C. Watson *et al.*, bioRxiv 10.1101/2024.11.22.624643 (2024).
12. C. Sayers *et al.*, *Cell Syst.* **15**, 1075 (2024).
13. R. R. Stanway *et al.*, *Cell* **179**, 1112 (2019).
14. A. C. Y. Chua *et al.*, *Nat. Commun.* **10**, 3635 (2019).
15. M. Zhang *et al.*, *Nat. Commun.* **12**, 4563 (2021).

10.1126/science.adv2328

Earth's polar regions affect and are affected by humanity's collective actions.

PHOTO: MICHAEL GREENFELDER/ALAMY STOCK PHOTO

POLAR SCIENCE

Probing the planet's poles

A paleontologist explores our intertwined fate with Earth's most remote regions

By **Sarah Boon**

Paleontologist Neil Shubin's *Ends of the Earth* offers readers a comprehensive overview of the geology, oceanography, glaciology, geopolitics, and climatology of the planet's polar regions: Antarctica and the Arctic. Shubin writes clearly and understandably about various complex topics, incorporating stories about his own fieldwork experiences in these places and arguing that polar science offers a "lens to see the natural world and the extraordinary ways we have come to know it."

Shubin explains how climate cycles have influenced global-scale glaciation patterns, describing the "Snowball Earth" hypothesis, which posits that Earth was covered in ice at least two times in the past: once 710 million years ago and a second time 660 million years ago, with each period lasting ~10 million years. After each freezing period, the theory goes, Earth's temperature rose quickly, and the ice melted completely.

The impacts of these climatic changes are reflected in the movement of various *Homo* species across Europe, Asia, the Middle East, and Africa. Shubin describes recent research that shows that their travels were affected by habitat, glacial, and climate changes caused by predictable shifts in Earth's orbit around the Sun.

Shubin notes that the story of the poles has largely been told by men who were explorers first and scientists second. To rectify this, he highlights the work of three trailblazing women researchers in polar geology: Margaret Bradshaw, one of the first women to lead field teams in Antarctica; Maureen Raymo, who studies terrestrial weathering and the carbon cycle; and Mary Dawson, a paleontologist who discovered that the Arctic was warm 50 million years ago and animals could travel between continents.

Shubin takes a deep time view of Earth's history, but he also understands the importance of studying current conditions in the polar regions. His book includes an interview with Eric Rignot, a researcher at NASA's Jet Propulsion Laboratory, who describes using satellite imagery to identify changes in the extent of the Antarctic Ice Sheet and to capture the collapse of the Larsen Ice Shelves A and B.

Polar glacier changes have also been observed on the seafloor, both through traditional methods such as sediment cores and by means of newer tools such as remotely operated vehicles (ROVs). Atlantic sediment cores contain layers of rock shaped by glaciers, suggesting that the North American ice sheets calved and drifted east, dropping their load of subglacial rocks along the way. ROVs have also revealed that Antarctic glaciers bob up and down with the tide. Shubin describes why these changes are important: When floating Antarctic glaciers melt owing to their proximity to warmer ocean water, this removes the buffer that prevents inland glaciers from flowing out to sea and drawing large amounts of ice from the interior of the Antarctic Ice Cap along with them.

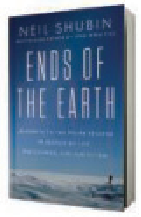

Ends of the Earth: Journeys to the Polar Regions in Search of Life, the Cosmos, and Our Future
Neil Shubin
Dutton, 2025. 288 pp.

International agreements keep the Antarctic free from development, dividing it into sectors in which each invested country does research. The geopolitics of the Arctic are more complicated. Shubin delves into the Canadian government's relocation of Québecois Inuit to barren lands farther north—an act critics argue was simply to establish the country's presence in the region, with no consideration for the people involved. Although countries that border the Arctic Ocean have ratified the United Nations Convention on the Law of the Sea, there remain arguments about what parts of the seabed belong to whom, especially with regard to mineral resources.

While these regions may seem remote from civilization, Shubin lays bare the cascading impacts of changes at the poles on other parts of the globe. These include an increased release of greenhouse gases from melting permafrost, accelerated global warming as the ice cover declines and surface reflectivity is reduced, changes to animal populations that are not adapted to warmer Arctic temperatures, and even the reemergence of once-frozen diseases, such as anthrax. One of the most important impacts is on the Atlantic Meridional Overturning Circulation (AMOC), an ocean current that brings warm water to the north Atlantic and keeps Europe "warm" relative to other locations at the same latitude. A collapse of the AMOC, which some experts argue is already occurring, could bring colder weather to these countries.

"Having led my own expeditions to polar regions for several decades, the work has become a part of me," writes Shubin. "But the converse is also true: our lives become part of the landscape itself." Following this line of reasoning, it is important to remember that our lives in nonpolar regions affect what happens at the poles. ■

10.1126/science.adu5421

The reviewer is a freelance writer and editor from Vancouver Island, Canada, and the author of the forthcoming book *Meltdown: The Making and Breaking of a Field Scientist* (Univ. of Alberta Press, 2025). Email: snowhydro1@gmail.com

PUBLIC HEALTH

The future of measles

A pediatrician confronts the disease's persistence in a world where eradication is possible

Booster Shots: The Urgent Lessons of Measles and the Uncertain Future of Children's Health
Adam Ratner
Avery, 2025. 288 pp.

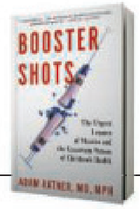

By **Arthur Caplan**

When I was a little boy of 6, I contracted polio in one of the last large outbreaks in the United States. My horrified parents observed the paralysis that emerged in my neck and legs and brought me to Boston Children's Hospital, where, ironically, an earlier breakthrough had been achieved that resulted in me being one of the last Americans to be sickened by the disease. It was here, in 1949, that microbiologist John Enders and physicians Thomas Weller and Frederick Robbins discovered a method for culturing poliovirus in human tissue samples. Jonas Salk's injectable polio vaccine became publicly available 6 years later, just as I fell ill, and—together with Albert Sabin's subsequent oral vaccine—led to the near eradication of polio globally. I mention all this because in his important and accessible (albeit often depressing) new book, *Booster Shots*, pediatrician Adam Ratner contrasts the almost complete eradication of polio with humanity's utter failure to eradicate measles.

The measles vaccine is safe and effective, yet the disease resists elimination.

PHOTO: COURTNEY PERRY/*THE WASHINGTON POST* VIA GETTY IMAGES

The two diseases once appeared to be on the same trajectory. Indeed, as he had done with polio, John Enders, together with physician Thomas Peebles, isolated the measles virus in human tissue in 1954. A vaccine was licensed by 1963. Why then did the two diseases diverge? Our failure to send measles into the history books has not been due to a lack of knowledge but, as Ratner engagingly recounts, a failure to take the requisite political steps to prevent and eradicate it (not to mention numerous other infectious diseases).

Measles has long been understood as a highly contagious disease with a predictable incubation period and variable outcomes related to malnutrition, congested living arrangements, travel, and age. All this is well known thanks to the work of the 19th-century physician Peter Ludvig Panum, who was sent from Copenhagen to manage a deadly measles epidemic in the remote Faroe Islands in 1846. What he discovered affected not only the understanding of measles but also the entire foundation of medicine.

The then prevailing theory of disease causation invoked "miasma"—bad quality air. Panum was something of a skeptic. He took advantage of the remoteness of the Faroes and the isolation of its villages to trace the start of a novel outbreak and its subsequent spread, firmly establishing the contagion theory of disease (later confirmed by Louis Pasteur and Robert Koch as "germ theory").

Returning to the present day, by the year 2000, vaccination had eliminated measles in the United States. As of December 2024, however, 283 measles cases had been reported in 30 US states and the District of Columbia, with >80% of those cases occurring in unvaccinated individuals or those whose vaccination status was unknown (*1*).

Ratner sees many causes for the failure to eradicate measles. Some are familiar: a world indifferent to the plight of the poor; a failure to grapple with the threat endemic measles poses when travel is easy; an inability to respond rapidly when outbreaks occur, especially during wars; and the lack of a serious, well-funded, coordinated international effort, as had been mounted with polio.

The poor of the world cannot get vaccines. The rich can, but for those with resources, other factors can discourage measles vaccination. A fear that the vaccine may cause autism—a false claim perpetuated again and again by fraudsters and quacks—is to blame, along with the relaxation of school mandates; the latter is driven by antigovernment sentiments that prioritize personal freedom over the duty to protect the vulnerable. Ratner notes that it does not take too many hesitant and refusing parents to get a fulminating outbreak underway, as the virus is highly infectious, and vaccines are not 100% protective.

Nonetheless, Ratner remains a self-proclaimed optimist about eradicating measles. It is, for one, very cost-effective. Ratner suggests $58 saved for every dollar spent. He also notes that "the goal itself is worthy…eradication will save children's lives—millions of them."

I agree, but unlike Ratner, I am not optimistic. Before we can make headway on this goal, attitudes about our duties to the global poor must change. Add a growing, dangerous adulation of unbridled free choice, and vaccines are undeniably in trouble. Those touting liberty will not be swayed by efforts at correcting misinformation. They are not anti-vaccination out of ignorance. Rather, they are devotees of a highly dubious ethic that worships individual autonomy over community responsibility.

The worst enemy of measles is, Ratner capably shows, a vaccine. But the worst enemies of the measles vaccine are those unconcerned about the fate of others. ■

The reviewer is at the Division of Medical Ethics, NYU Grossman School of Medicine, New York, NY, USA. Email: arthur.caplan@nyumc.org

REFERENCES AND NOTES

1. National Foundation for Infectious Diseases, Infectious Diseases: Measles; https://www.nfid.org/infectious-disease/measles/.

10.1126/science.adu8834

The palm cockatoo (*Probosciger aterrimus*) is one of many vulnerable species in Australia.

PHOTO: D. PARER AND E. PARER-COOK/MINDEN PICTURES

Edited by **Jennifer Sills**

Addressing Australia's biodiversity crisis

As Australia's 2025 federal election approaches, political parties and candidates must demonstrate increased commitment to addressing climate change and biodiversity loss. Without urgent action, species (*1*) and ecosystems (*2*) already under severe pressure will continue to decline and collapse, and global biodiversity targets, such as establishing a trend of recovery by 2030 (*3*), will be nearly impossible to achieve. Australia must become a conservation leader by protecting and repairing its extraordinary and largely endemic biodiversity.

More than 2000 species and over 100 ecological communities are threatened with extinction in Australia (*4*), and the list continues to grow rapidly. Koalas were listed as endangered in 2022 under national environmental law (*5*), and the Great Barrier Reef is deteriorating through repeated bleaching events (*6*). Yet funding for conservation in Australia is insufficient and well below levels of other nations with similar socioeconomic characteristics and capacity, such as the United States (*7*).

Australia's primary environmental law, the Environment Protection and Biodiversity Conservation Act, has failed to enable the federal government to effectively protect the environment and cannot adequately address current and future environmental challenges (*8*). The current federal government promised to reform the law to remedy these shortfalls, but the process has stalled (*9*).

In the meantime, Australia's government is hoping to greatly improve conservation outcomes by creating a "nature repair market" (*10*). This initiative would reward individuals and corporations for investing in nature restoration projects. Conservation investment from industry is welcome, but this market may not fill the void in government funding. Moreover, a market mechanism may be less efficient than direct investment from government (*11*). Either way, the market's credibility will be undermined if the downward trend of Australia's biodiversity continues due to ineffective environmental laws.

The next Australian government must prioritize conservation by fast-tracking environmental law reform and strengthening enforcement. Development proposal assessments should explicitly consider emissions as "climate triggers" and either rule out proposals deemed too severe or require developers to meaningfully mitigate the impacts of projects. Only urgent action to address climate change can prevent long-term and widespread environmental damage. An annual investment of AUS $7.3 billion per year (*12*), about 0.3% of gross national product, for 30 years would support substantial progress toward protecting and recovering Australia's environments and species (*8*). Australia's next administration must commit to this investment to help meet national and global environmental and conservation goals.

Euan G. Ritchie[1*] **and Dale G. Nimmo**[2]
[1]School of Life and Environmental Sciences, Deakin University, Burwood, VIC, Australia.
[2]Gulbali Institute, School of Agricultural, Environmental and Veterinary Sciences, Charles Sturt University, Thurgoona, NSW, Australia.
*Corresponding author.
Email: e.ritchie@deakin.edu.au

REFERENCES AND NOTES

1. S. Legge *et al.*, *Science* **381**, 622 (2023).
2. D. M. Bergstrom *et al.*, *Glob. Chang. Biol.* **27**, 1692 (2021).
3. Nature Positive; https://www.naturepositive.org/.
4. Australian Government, "Species profile and threats database" (2025); http://www.environment.gov.au/cgi-bin/sprat/public/sprat.pl; To find the number of threatened species and communities: Under "Other EPBC Act Lists," click "Threatened Fauna" (666 species in total, minus 75 Extinct, Extinct in the Wild, and Conservation Dependent species), "Threatened Flora" (1472 species in total, minus 35 Extinct species), and "Ecological Communities" (107 total), for a total of 2135 species and ecological communities.
5. Australian Government, "Koala listing under national environmental law" (2023).
6. B. Nogrady, "Australia's Great Barrier Reef is 'transforming' because of repeated coral bleaching," *Nature* News, 19 April 2024.
7. B. A. Wintle, *Conserv. Lett.* **12**, e12682 (2019).
8. Australian Government, "Second independent review of the EPBC Act" (2021).
9. M. Tsikas/AAP, "Australia's long-sought stronger environmental laws just got indefinitely deferred. It's back to business as usual," *The Conversation*, 17 April 2024.
10. Australian Government, "Nature repair market" (2023).
11. K. Kedward *et al.*, *SSRN* 10.2139/ssrn.4306836 (2022).
12. Wentworth Group of Concerned Scientists, "Blueprint to repair Australia's landscapes" (2024).

10.1126/science.adt6042

Australia's inadequate marine protection

In October 2024, the Australian government announced the expansion of the Heard and McDonald Islands Marine Park Reserve and claimed that 52% of Australian waters are now protected, making the nation the "global leader in marine conservation" (*1*). That announcement disregards evidence that Australia's Marine Protected Area (MPA) network has consistently failed to protect important areas of biodiversity (*2*–*6*). Australia must substantially improve its MPA network before claiming conservation success.

Although, as the government claimed, MPAs cover 52% of Australia's waters, MPA status does not guarantee protection. In 30% of the nation's waters, MPA network status does not prohibit threats to biodiversity such as mining, mining exploration, and commercial fishing (*5*). The other 22% of Australia's MPA-designated waters are safeguarded by MPAs that do not permit extractive activities (*7*), but about

66% of those waters are located in four of Australia's offshore territories, two of which are unoccupied by humans. Although these MPAs are among the biggest globally (*8*), they are in areas largely free from direct human threats. Only about 8% of Australia's MPAs are zoned and located in a way that mitigates human impacts and delivers conservation benefits (*9*, *10*).

The expansion of the Heard and McDonald Islands MPA exemplifies Australia's quantity-over-quality approach (*1*). Most of the new, fully protected areas are too deep to support commercial fisheries and therefore face no direct threats (*11*). As a result, protecting them arguably offers little conservation benefit. Meanwhile, key conservation features such as undersea canyons, seamounts, and fish spawning grounds remain unprotected and vulnerable (*11*).

By claiming global leadership while ignoring evidence-based best practices to safeguard its marine life, Australia is making a mockery of the Kunming-Montreal Global Biodiversity Framework's bold ambitions (*12*), especially Target 3, which calls for protection of 30% of oceans in areas of biodiversity importance and representation. To meet this goal, Australia must focus on features of high ecological importance where threats can be meaningfully abated through formal marine protection. Prioritizing and fully protecting such areas will enable the country to balance extractive marine activities with biodiversity conservation needs.

Madeline Davey* and James E. M. Watson
School of the Environment, University of Queensland, Brisbane, QLD, Australia.
*Corresponding author.
Email: madeline.davey@uq.edu.au

REFERENCES AND NOTES

1. T. Plibersek, Media release: "Australia now protects more ocean than any other country on earth" (Minister's Office, 2024); https://minister.dcceew.gov.au/plibersek/media-releases/australia-now-protects-more-ocean-any-other-country-earth .
2. E. P. Pike *et al.*, *Conserv. Lett.* **17**, e13020 (2024).
3. B. Cockerell *et al.*, *Biol. Conserv.* **252**, 108813 (2020).
4. C. R. Margules, R. L. Pressey, *Nature* **405**, 243 (2000).
5. R. Devillers *et al.*, *Aquat. Conserv. Mar. Freshw. Ecosyst.* **30**, 1758 (2020).
6. C. M. Roberts *et al.*, *Ecol. Applic.* **13**, 215 (2003).
7. J. Day *et al.*, *Guidelines for Applying the IUCN Protected Area Management Categories to Marine Protected Areas* (IUCN, 2012).
8. Marine Conservation Institute, The Marine Protection Atlas; https://mpatlas.org/large-mpas/
9. J. Lubchenco, K. Grorud-Colvert, *Science* **350**, 382 (2015).
10. E. Sala, S. Giakoumi, *ICES J Mar. Sci.* **75**, 1166 (2018).
11. A. J. Constable, I. D. Cresswell, N. J. Bax, K. Reid, "Understanding the marine ecosystems surrounding Heard Island and McDonald Islands (HIMI) and their conservation status" (Australian Marine Conservation Society, 2024); https://www.marineconservation.org.au/wp-content/uploads/2024/07/HIMI_Report_FINAL.pdf.
12. Convention on Biological Diversity, "Kunming-Montreal global biodiversity framework" (UN Environment Programme Montreal, 2022).

COMPETING INTERESTS

M.D. was a paid consultant for the creation of maps for visualizations in the Constable *et al.* 2024 report for the Heard and McDonald Islands conservation values assessment.

10.1126/science.adt7848

Generative AI exacerbates the climate crisis

The economic benefits of generative artificial intelligence (AI) could reach US$7.9 trillion annually (*1*). The emergence of groundbreaking generative AI tools has spurred development (*2*). However, the explosion of generative AI is exacerbating the global climate crisis. The scientific community, industry, and policy-makers must urgently address its effects.

ChatGPT, a natural language processing tool released by OpenAI in 2022 (*3*), has sparked a global wave of large language models, driving a surge in demand for intelligent computing power. Concurrently, climate challenges continue unabated. The combined electricity consumption of the AI and cryptocurrency industries reached 460 terawatt-hours (TWh) in 2022, accounting for about 2% of the global total energy consumption. Consumption is projected to reach 1000 TWh by 2026 (*4*). In 2024, increased energy consumption by data centers drove a surge in carbon emissions (*5*). As the generative AI industry expands, its electricity consumption is expected to grow rapidly (*5*).

The energy consumption of generative AI stems from the huge computational power required during model training and the resources expended in responding to user queries (*6*). ChatGPT will likely consume more than half a million kilowatt-hours of electricity daily to handle about 200 million user requests (*7*). The latest model, OpenAI o1, incurs even greater carbon emissions when tackling complex reasoning tasks (*8*). High-performance hardware, such as graphics and tensor processing units, requires additional electricity to power cooling systems and consume substantial amounts of water (*9*).

Principles such as the Montreal Declaration for a Responsible Development of Artificial Intelligence (*10*) have been widely accepted in pursuit of sustainable generative AI. Since 2023, internet technology companies around the world have invested heavily in purchasing clean energy (*11*). However, greenhouse gas emissions have still risen substantially because of the surge in generative AI research and development (*4*).

Researchers must explore methods to reduce generative AI's energy consumption. For example, measuring AI's total footprint on the environment throughout its life cycle can pinpoint opportunities to reduce its negative effects. Transferring knowledge from a complex model to a simpler, smaller, and more efficient model can reduce computational costs while maintaining model performance. Transforming high-dimensional data into low-dimensional data while maintaining important information can help simplify the data, reduce computational costs, and improve model performance (*6*). In addition, enterprises need to publicly disclose the actual energy consumption of their generative AI projects. Nations should regulate generative AI technologies and refine sustainable generative AI regulations. Strengthening regional communication will facilitate the creation of international standards and norms as well as knowledge sharing and innovation (*12*). Countries should also bolster support for renewable energy sources and raise public awareness of generative AI's environmental impact through education and advocacy.

Qiong Chen[1], Jinghui Wang[2], Jialun Lin[1]*
[1]School of Biomedical Information and Engineering, Hainan Medical University (Hainan Academy of Medical Sciences), Haikou, China.
[2]Modern Education Technology Center, Hainan Medical University (Hainan Academy of Medical Sciences), Haikou, China.
*Corresponding author. Email: linjl@hainmc.edu.cn

REFERENCES AND NOTES

1. "The economic potential of generative AI: The next productivity frontier" (McKinsey & Company, 2023); https://www.mckinsey.com/capabilities/mckinsey-digital/our-insights/the-economic-potential-of-generative-ai-the-next-productivity-frontier#introduction.
2. "Generative AI: Steam engine of the fourth industrial revolution?" (World Economic Forum, 2024); https://www.weforum.org/events/world-economic-forum-annual-meeting-2024/sessions/industry-applications-of-generative-ai/.
3. "Introducing ChatGPT" (OpenAI, 2022); https://openai.com/index/chatgpt/.
4. "Electricity 2024: Analysis and forecast to 2026" (International Energy Agency, 2024); https://www.iea.org/reports/electricity-2024.
5. "Powering the AI revolution" (Morgan Stanley, 2024); https://www.morganstanley.com/ideas/ai-energy-demand-infrastructure.
6. J. An, W. Ding, C. Lin, *Nature* **615**, 586 (2023).
7. A. de Vries, *Joule* **7**, 2191 (2023).
8. M. Zeitlin, "What does OpenAI's new breakthrough mean for energy consumption?" (HEATMAP, 2024); https://heatmap.news/technology/openai-o1-energy.
9. Z. Wang, "How AI consumes water: The unspoken environmental footprint" (Deepgram, 2024); https://deepgram.com/learn/how-ai-consumes-water.
10. "Montreal Declaration for a responsible development of artificial intelligence" (Université de Montréal, 2018); https://www.montrealdeclaration-responsibleai.com.
11. K. Harrison, "Amazon is top green energy buyer in a market dominated by US" (BloombergNEF, 2024); https://about.bnef.com/blog/amazon-is-top-green-energy-buyer-in-a-market-dominated-by-us/.
12. R. Raper *et al.*, *Sustainability* **14**, 4019 (2022).

10.1126/science.adt5536

EXTREME CONDITIONS

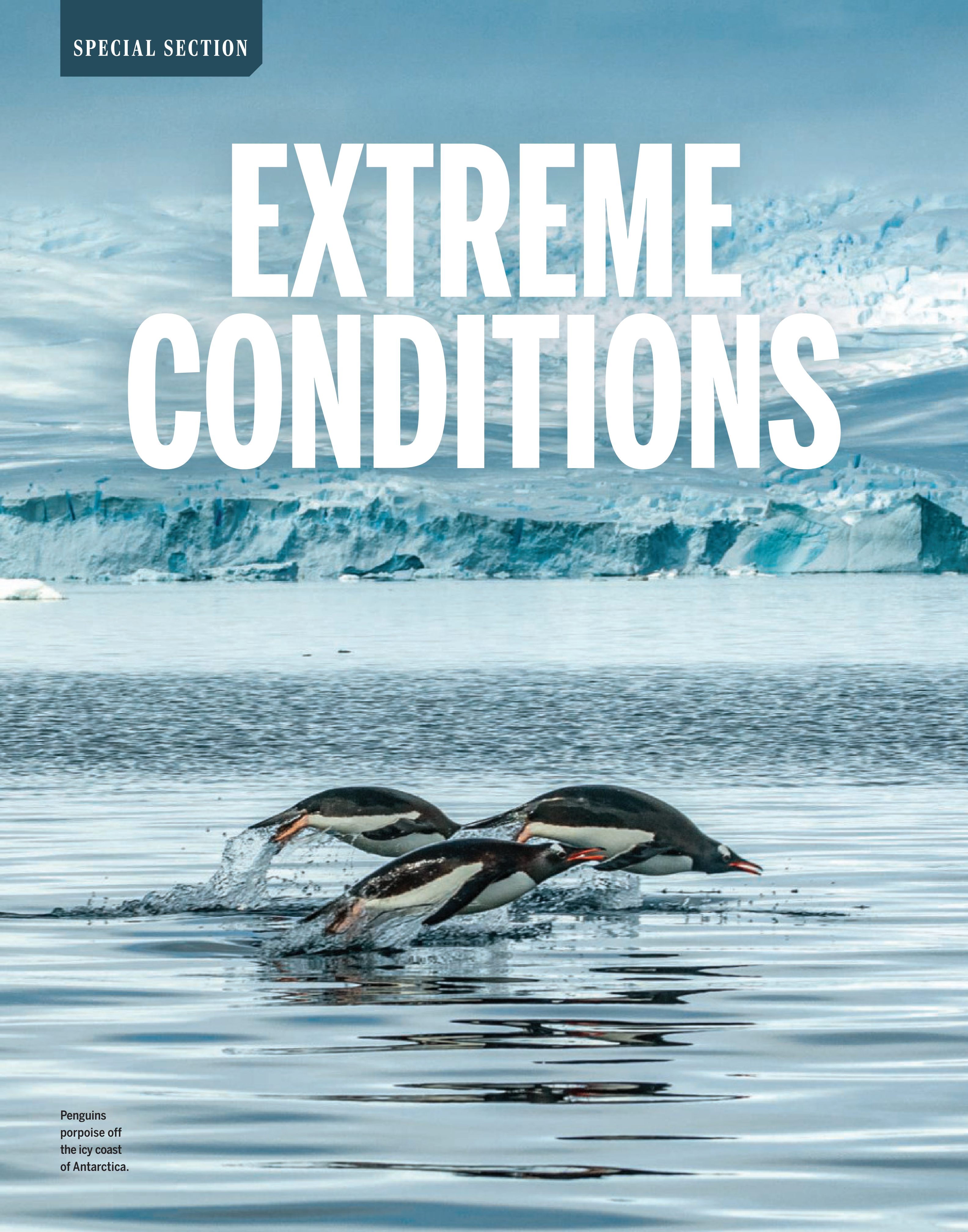

Penguins porpoise off the icy coast of Antarctica.

PHOTO: PETE MCBRIDE

By **Jesse Smith**, **Bianca Lopez**, *and* **Brad Wible**

Nowhere in the world is climate change having greater impacts on the environment than at the poles. Still, despite our understanding of the broad effects that global warming is driving there, our knowledge of the details of this process is full of holes. To describe what the polar regions will look like and to guide future research into those places, in this Special Issue we present three Reviews and a Policy Forum that discuss the most important recognized knowledge gaps regarding how the Antarctic Ice Sheet is losing mass; the state of Antarctica's terrestrial biodiversity and how it is responding to climate change; what the landscape of the Arctic will resemble if national commitments to slow global warming by reducing greenhouse gas emissions are met; and how we can help ensure that research about the Arctic addresses the needs of the nearly 4 million people that live there and promotes international scientific cooperation despite existing geopolitical divisions. Given the disproportionate influence of the polar regions on Earth properties such as sea level, albedo, and greenhouse gas emissions from thawing permafrost, climate warming at high latitudes and its implications are critical to understand. Thus, it is incumbent on us to learn all that we can about how we are affecting the poles, what can be done to mitigate the harmful changes we are causing there, and how we might manage the changes that are occurring. Addressing these issues now, in the first year of what the United Nations has declared the "Decade of Action for Cryospheric Sciences," is both fitting and important for the health of the whole planet.

10.1126/science.adw2518

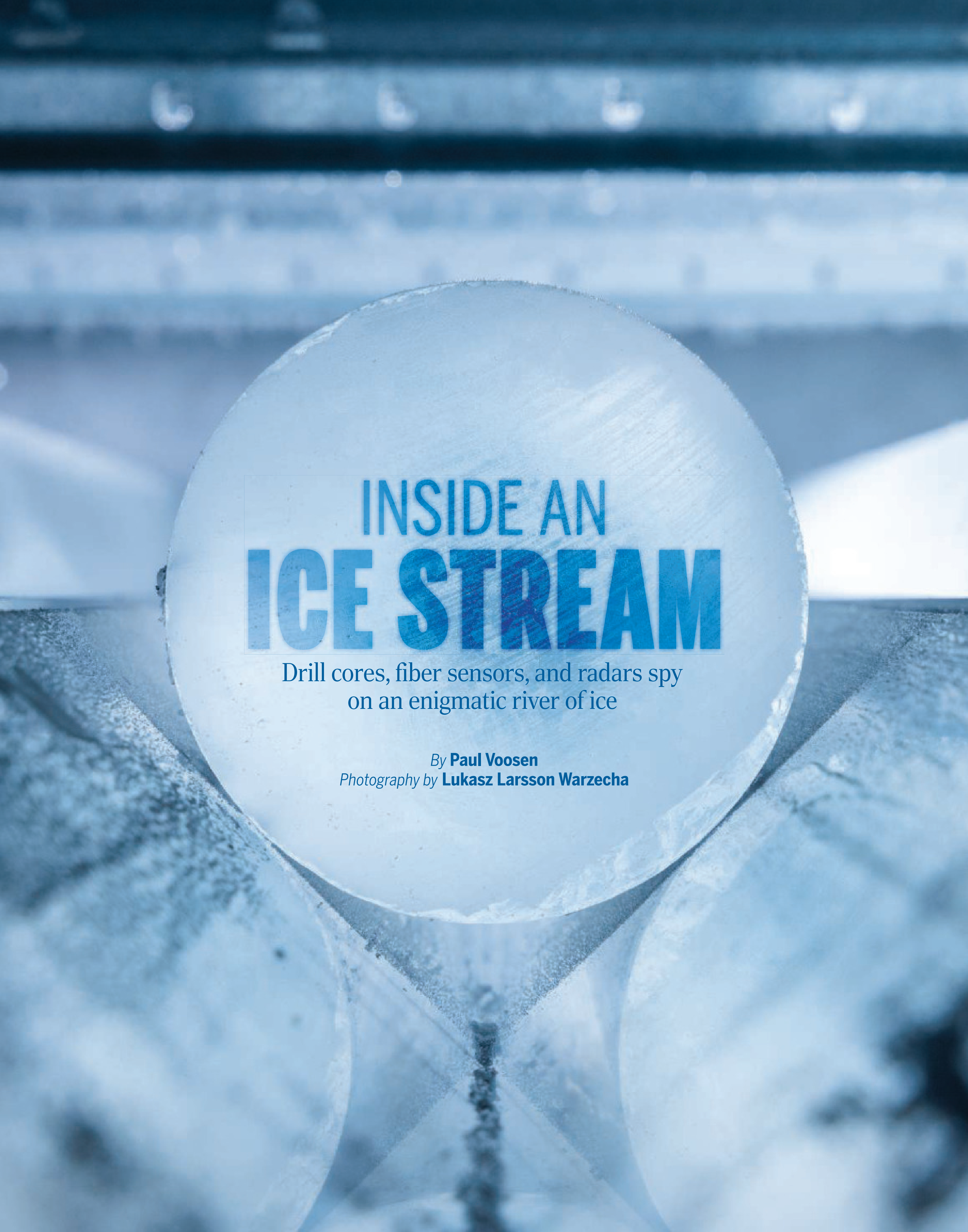

INSIDE AN ICE STREAM

Drill cores, fiber sensors, and radars spy on an enigmatic river of ice

By **Paul Voosen**
Photography by **Lukasz Larsson Warzecha**

Ice cores from 2300 meters' depth await processing (left) at the East Greenland Ice-core Project, a Danish-led drilling project in northeastern Greenland. The work took place in trenches dug in the snow and then covered with inflatable roofs (above).

Wherever the ice sheet that covers Greenland finds an outlet to the coast, it is sliding seaward, and far faster than it used to. Inland the motion slows—except in northeastern Greenland. There, three neighboring outlet glaciers are fed by a narrow channel of fast-moving ice that reaches 700 kilometers into the interior. On color-coded maps of ice velocity, the channel looks like a dagger aimed at the ice sheet's heart. Called the Northeast Greenland Ice Stream (NEGIS), it accounts for some 12% of the ice sheet's mass loss. Its rapid flow—more than 50 meters a year—is a mystery, says Dorthe Dahl-Jensen, a glaciologist at the University of Copenhagen (KU). "We really have a very, very basic understanding."

Ten years ago, Dahl-Jensen and others set out to solve that mystery by drilling right through the ice stream. The East Greenland Ice-core Project (EastGRIP), which ended last year, lost 2 years to the COVID-19 pandemic before it reached bottom at a depth of 2670 meters. But it is already yielding transformative results—including a worrying discovery that the bottom of the ice stream is not frozen to bedrock, as previously thought. Instead, from top to bottom, the ice moves as a block toward the ocean. "The whole block of ice is sliding on water and mud," Dahl-Jensen says. That raises fears that the stream could accelerate as the climate continues to warm.

The Greenland Ice Sheet has now lost mass every year since 1996. Last year's loss was the lowest in a decade—but the ice sheet still shed 80 gigatons of water, according to the Geological Survey of Denmark and Greenland, which is the equivalent of about 2.5 million liters, or an Olympic swimming pool, every second. Melt from Greenland accounts for more than one-quarter of the current rate of global sea level rise, which has surged to more than 4 millimeters a year. Some 7 meters of potential rise are locked up in Greenland ice.

Evidence from other ice cores suggests the ice sheet is vulnerable. Grit found at the bottom of the Camp Century core in northwestern Greenland showed the site was ice free during an interglacial period some 400,000 years ago, and that the ice sheet as a whole lost 1 kilometer in thickness, says Paul Bierman, a geochemist at the University of Vermont. "There's now compelling evidence that Greenland's ice sheet has melted substantially if not completely when temperatures were similar to today," Bierman says.

Yet projecting the future of Greenland's ice loss this century and beyond remains a huge challenge. Ice streams are the primary reason why, says Sune Olander Rasmussen, a KU climate scientist who worked on EastGRIP. There are two main ways Greenland sheds ice. First, there's direct melting from warmer air and waters—a gradual process, though still hugely hazardous. U.N. projections that Greenland will contribute no

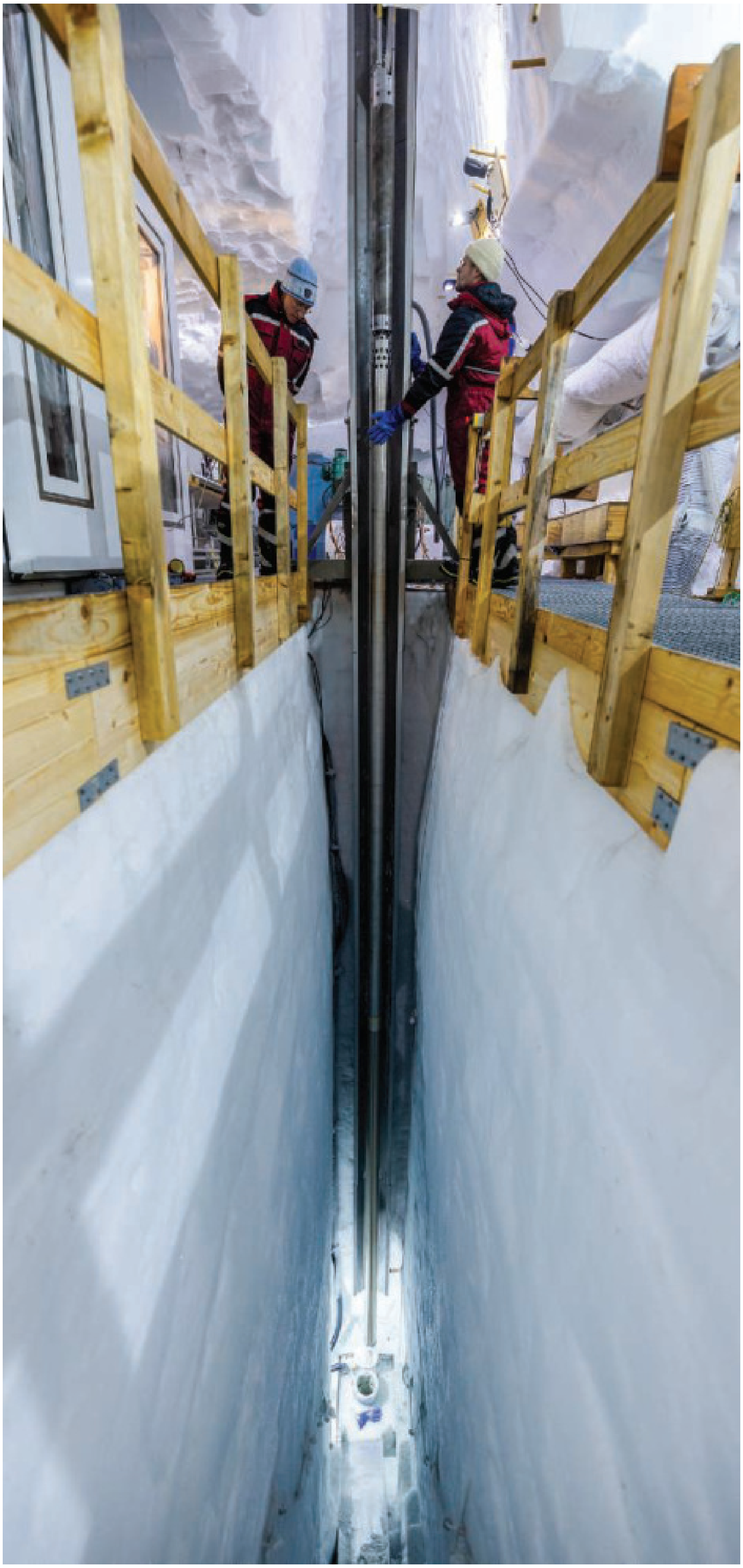

Workers at EastGRIP lower a drill rig into a borehole (above). Between drilling runs, lead scientist Dorthe Dahl-Jensen (right, in blue parka) and her team deployed a borehole logger to detect shifts in the hole's shape, which reveal variations in the ice's speed.

PHOTOS: LUKASZ LARSSON WARZECHA


FREIHEIT

A geodesic dome, bathed in midnight sunlight, served as EastGRIP's kitchen, mess hall, office area, and air control tower. Its cozy comforts boosted morale in the frigid, isolated conditions—as did impromptu volleyball games.

PHOTOS: LUKASZ LARSSON WARZECHA

more than 18 centimeters of sea level rise by century's end are based primarily on direct melting.

Then there are the ice streams and all the iceberg-calving coastal glaciers. "What we're really worried about is how fast ice is exported into the ocean," Rasmussen says. This second process is far less predictable. That's why it was so important to study it at EastGRIP.

THE DANES ARE FAMED for drilling ice cores in Greenland, an effort they have pursued for decades. The main goal of earlier projects was to extract a record of abrupt climate change from ancient air frozen into the ice. EastGRIP was the first core drilled to understand how an ice stream moves. "Normally we'd avoid this at all costs," Rasmussen says. "Glaciologists want very little flow"—it can distort the annual layering that allows the cores to be dated.

Drilling began in 2016. The site looked like the rest of the ice sheet—flat, white, windswept. But Dahl-Jensen and her team had long since figured out how to create *hygge*, or Danish coziness, in bleak spots. Researchers and staff slept in heated tents, and a two-story black geodesic dome was the heart of the camp, home to a full kitchen, dining area, and work spaces. The drilling happened in caves created by digging trenches, then inflating massive balloons inside to form snow-covered roofs. Researchers rotated through second jobs—cleaner, cook's assistant, water supply manager—so the team as a whole could focus on science. "The whole world ceases up there," says Tyler Jones, a paleoclimatologist at the University of Colorado Boulder. "It's a very freeing place to be."

No amount of *hygge* can ease working outside at nearly 3000 meters' altitude and temperatures between –20°C and –30°C. "You can't eat enough to replenish your energy reserves," says Andreas Fichtner, a seismologist at ETH Zürich. Still, the location lured visitors, among them a team led by Daniela Jansen, a geophysicist at the Alfred Wegener Institute (AWI). For 3 weeks in 2018, they flew AWI's Polar 6 research plane low over the ice, using its ice-penetrating radar to examine its structure, including internal folds that record the history of the stream.

What the researchers found and reported last year in *Nature Communications* was a surprise: NEGIS has only existed for the past 2000 years—not since the last ice age, as commonly believed. It seems the streaming locations on an ice sheet "can jump around," Jansen says. If so, adds Dave Roberts, a glacial geologist at Durham University, "that fundamentally shifts our understanding of how ice streams switch on and off."

Although studying climate wasn't the project's primary goal, researchers took the opportunity to probe the mysterious spurts of abrupt warming that punctuated the ice ages. Known as Dansgaard-Oeschger (D-O) events, each one raised air temperatures over Greenland by more than 15°C for a few decades. To trace how the Greenland climate changed season by season during the

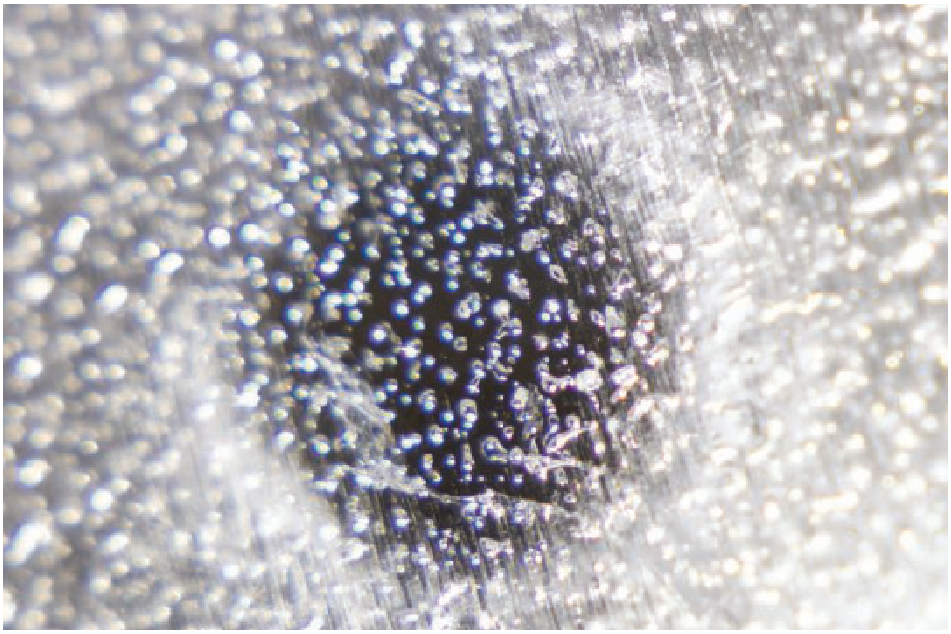

D-O events, Jones and his colleagues melted samples of core and analyzed the gases released using laser spectroscopy techniques first pioneered in Antarctica. They wanted to measure shifting ratios of hydrogen and oxygen, which provide a fine-scale record of ancient temperature.

In a preprint, Jones and his colleagues report that the variability of Greenland's weather declined for centuries before many of the warming events. They suggest a possible explanation: The stable weather resulted from a retreat of seasonal sea ice over the North Atlantic Ocean. The ice retreat also allowed the ocean to release more heat to the air, setting the stage for a decades-long warming spike. "It's a massive reorganization of the climate system," Jones says.

BY 2019, after 4 years of drilling, the borehole was 2.1 kilometers deep, about four-fifths of the way to the bottom. Then came the COVID-19 pandemic. When the researchers returned to the camp in 2022, they found it buried under meters of new snow and ice. "The structures on the surface drowned," Dahl-Jensen says; the ceilings of the snow caves collapsed. It took half the season to dig out the site with chainsaws. "I think we moved 16 tons of ice blocks," she says.

For the last month of the 2022 season, Fichtner joined the camp. He's a pioneer in a technique that turns fiber optic cables into dense arrays of seismometers by detecting the minuscule stretching caused by passing seismic waves. He mostly worked on the ice surface, but on the last day of the season, after drilling had stopped, Dahl-Jensen allowed him to unspool his fiber cable down the borehole itself.

It was a perilous experiment—if the cable broke under its own weight, it could jam the borehole and end the project. To lessen the tension, Fichtner rested the cable on the borehole's slightly inclined side. Then, by setting off explosions at the surface and picking up seismic waves racing through the ice, he hoped to capture the ice stream's structure in fine detail.

But it was what the team saw between the blasts that shocked Fichtner. Researchers thought massive ice sheets, unlike noisy, cracking glaciers, flow silently, like viscous fluids. But rather than absolute quiet,

PHOTOS: LUKASZ LARSSON WARZECHA

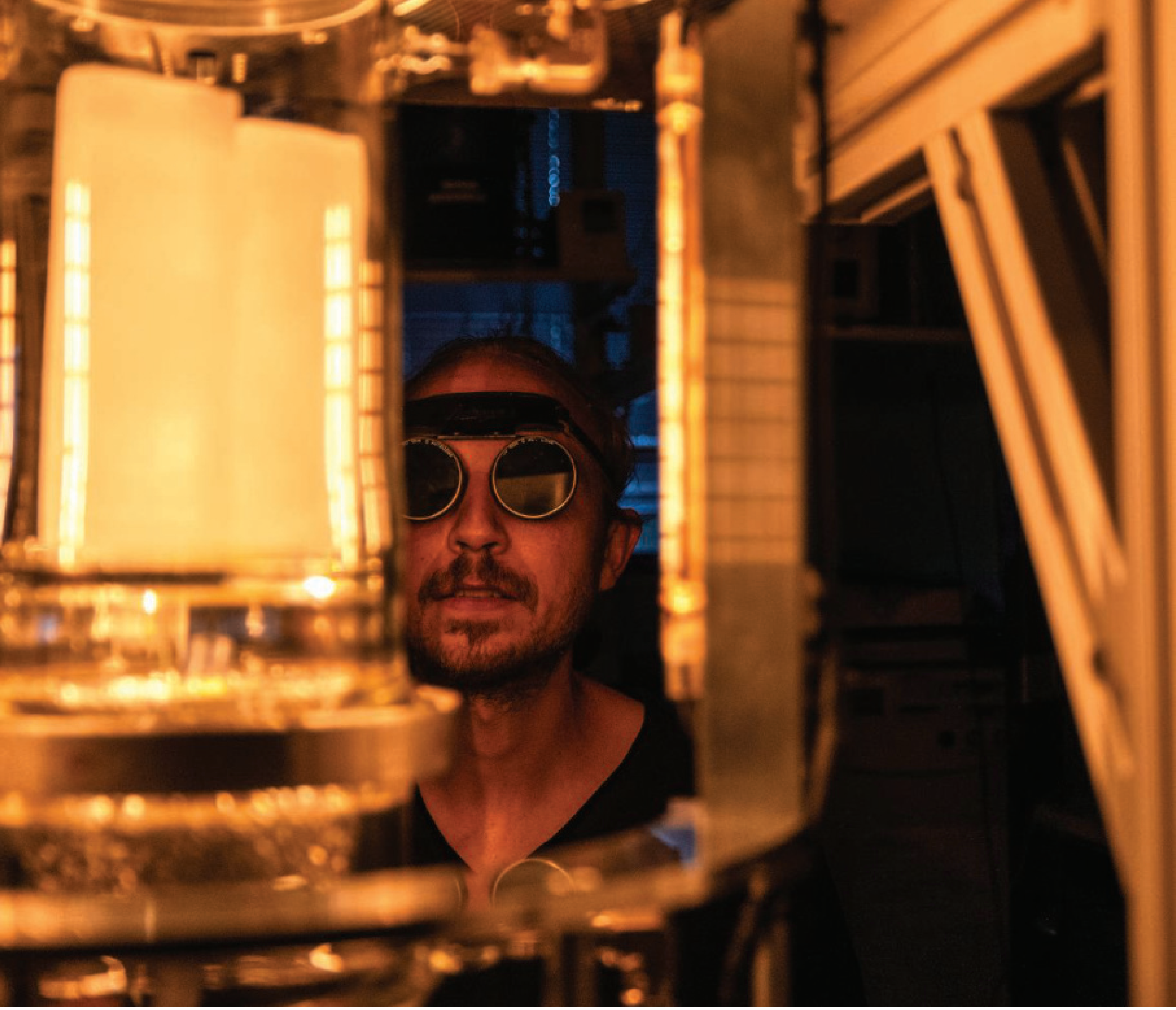

At the University of Copenhagen, researchers use a diamond saw to cut samples of ice for further analysis (top left). Air bubbles trapped in the core (bottom left) can be extracted (above) to reveal the composition of the ancient atmosphere.

Fichtner's cable picked up two cascades of minute ice quakes. Their magnitude suggests they emanate from centimeter-scale, faultlike features found in many ice cores, Fichtner and his team report in a paper online this week in *Science*. If such quakes turn out to be widespread, the sudden lurches they signal could help explain why ice streams move faster than modelers can simulate. "It's a plausible missing link," Fichtner says.

The next year, in 2023, drilling finished in dramatic fashion, with a struggle to recover the end of the core. It turned out the drill head had hit mud and grit at the bottom of the hole and gotten stuck. That discovery made sense given what Dahl-Jensen's team was learning from instruments lowered into the borehole to track the speed of ice at different depths.

Open any textbook, Dahl-Jensen says, and it will tell you the bottom fifth of an ice stream is a shearing zone, where the ice slows and finally adheres to the bedrock. That's not what the borehole loggers said. "We were expecting to get into this shear, but we never did," she says. The bottom of the ice was moving just as fast as the top, because it was sliding on mud. If the finding holds up, and turns out to be true of other ice streams, it would suggest the streams are pushing more ice into the ocean than previously believed, Dahl-Jensen says—and that the flow could readily speed up.

Even though the EastGRIP team packed up camp last summer, the borehole will remain accessible for decades, enabling researchers to keep monitoring ice movement. Given the new evidence of the ice stream's changeability—and vulnerability—the borehole will be a critical sentinel, Roberts says: "We could be right on the cusp of this threshold where we start to see accelerated retreat." ■

Lukasz Larsson Warzecha is a Sweden-based photographer and cinematographer who specializes in environmental and scientific documentary journalism.

SCIENCE DIPLOMACY

Arctic research cooperation in a turbulent world

Rapid Arctic change requires multifaceted approaches with Arctic peoples at the forefront

By **Jennifer Spence, John Holdren, Fran Ulmer**

The Arctic sits at the leading edge of some of the most pressing problems the world faces today—coping with the growing and socioeconomically uneven impacts of climate change; finding an appropriate balance between economic development and conservation; and coordinating governance across local, regional, and international boundaries—all made more challenging by increasing populism and distrust of government, renewed great-power competition, rising geopolitical tensions, and fears about the stability of the rules-based international order. In the Arctic, as in the rest of the world, these issues are complex, interconnected, and compounding each other. In what follows, we elaborate on three central issues: current scientific understanding of the regional and global impacts of Arctic climate change, ensuring that Arctic research addresses the needs of Arctic peoples and communities, and the importance of sustaining Arctic cooperation in challenging geopolitical times.

Because temperatures in the Arctic are increasing approximately three times faster than the global average (*1*), the interacting impacts in this region are, in a way, advance notice of what awaits the rest of the world as global temperatures continue to rise. But there are more immediate reasons that what happens in the Arctic should be of interest to the wider world. Rapid climate change in the Far North is responsible for ever-larger wildfires that are sending smoke into midlatitudes (*2*); it is contributing to the increased frequency and magnitude of extreme weather events across the Northern Hemisphere (*3*); and it is adding to sea-level rise around the world (*1*). Furthermore, climate change in the Arctic is a driver of international tension and conflict over terms of access to Arctic Ocean resources and the management of the sea routes that are opening up as sea ice shrinks, which could add to an already vexing geopolitical landscape (*4*).

More positive reasons for global interest in the Arctic also exist. These include the global recognition and respect for the region's Indigenous peoples, distinctive wildlife, and fragile lands and waters; the role the Far North needs to play as a leader in climate adaptation strategies; and the Arctic's history of developing innovative governance mechanisms that prioritize the engagement of Indigenous peoples and other Arctic residents (*1*, *4*–*6*). Notable as well has been the region's history of leveraging research and science diplomacy, through institutions such as the Arctic Council and the Agreement to Prevent Unregulated High Seas Fisheries in the Central Arctic Ocean, to support sustainable development, resource management, and environmental protection across borders.

REGIONAL AND GLOBAL IMPACTS

Rapid warming in the Arctic is compounding challenges that face communities, Indigenous peoples, and economic development in the region, even as it propagates substantial impacts globally. The reasons for the Arctic's rapid pace of warming are well understood scientifically, making clear that the region will continue to be at the leading edge of global climate change (*7*). Improved and expanded monitoring and research over the past 10 to 15 years has increased understanding of how Arctic warming affects northern environmental conditions and processes, the impacts of climate change on Arctic peoples and ecosystems, and how Arctic conditions affect the rest of the world. Here are a few examples.

Loss of sea ice

Since the start of adequate satellite measurements in 1979, the late summer coverage of sea ice in the Arctic Ocean has declined by almost 50% and its volume by about 75% (*1*). That has brought some potential benefits (although some may see in these considerable risks): new northern navigation routes, increased access to seabed resources, and perhaps expanded commercial fishing. But it also has brought serious environmental challenges: more marine pollution, soot, and marine-mammal impacts from increased ship traffic; the ongoing and expected effects of sea-ice decline on seals, walruses, and polar bears that are central to the subsistence and cultures of Indigenous communities; and the effects of the retreat of sea ice from the shoreline on storm waves, coastal erosion, and the very viability of coastal communities. The effect of sea-ice decline on the pole-to-equator temperature difference is combining with other climate-linked changes in the Far North and beyond to alter atmospheric circulation patterns and ocean currents across the Northern Hemisphere, with widespread impacts on weather extremes and marine biota (*3*, *7*).

Loss of land ice

Arctic glaciers other than those emanating from the Greenland Ice Sheet have lost about 180 billion tonnes of ice per year in the 21st century, accelerating river-bank erosion, increasing river turbidity, reducing salinity in the Arctic Ocean, and contributing to global sea-level rise (*7*). The average loss from the Greenland Ice sheet in this period has been in the same range—even larger than that from Antarctica (*1*). The Antarctic Ice Sheet is far larger but until now has been losing ice more slowly.

Permafrost thaw

Impacts of permafrost thaw across the Arctic and sub-Arctic are many (*1*, *6*). The resulting ground subsidence can tilt and rupture buildings, roads, and village walkways over tundra as well as infrastructure for water, sanitation, and energy. Thawing also compounds the effects of sea-ice retreat on coastal erosion. Likewise dismaying, permafrost thaw is releasing mercury and toxic wastes and could well be releasing long-dormant pathogens—all formerly stored safely in frozen ground. It has become clear that release of carbon dioxide and methane from thawing permafrost could become large enough in coming decades to reduce meaningfully the so-called "carbon budget"—the remaining headroom for direct human emissions of CO_2 worldwide that is consistent with staying below a global-average temperature increase of 2°C (*8*). This amounts to a threat to increase all of the adverse impacts of climate change worldwide.

Wildfires

Much better understood now than 20 years ago are the climate-linked factors that have been increasing the area burned by wildfires across the Arctic and sub-Arctic. The best linear fit to the most recent data for the permafrost regions of Alaska and Canada combined shows a roughly fourfold increase in average annual area burned between 1960 and 2023 (*1*). It is projected that the area burned could

---

John F. Kennedy School of Government, Harvard University, Cambridge, MA, USA. Email: jennifer_spence@hks.harvard.edu

double again in the next 25 years. Trends in Russia appear similar. Regional effects of these wildfires include destruction of timber, wildlife habitat, and infrastructure; accelerated permafrost thaw; and immense quantities of toxic smoke afflicting local populations. Impacts beyond the region include propagation of smoke into the midlatitudes and release of large amounts of stored carbon, contributing to the pace of climate change globally (*1*, *8*).

MEET THE NEEDS OF ARCTIC PEOPLES AND COMMUNITIES

Much is known about rapid climate change in the Arctic and how it affects the region and the world, but more research is essential to more confidently predict the evolution of climate-linked stresses along various trajectories of global temperature increase and thus to be able to craft appropriate mitigation and adaptation strategies. This work must link studies of the Arctic climate itself with other research in both natural and social science that addresses all the ways altered climates affect ecosystems and social systems. Researchers increasingly recognize the interlinkages of climate change, biodiversity loss, and pollution (the Triple Planetary Crisis) and the importance of addressing together all the stressors that are affecting Arctic communities.

The Arctic is home to close to 4 million people, including Indigenous peoples with ancient cultures and traditions that are intimately connected to the lands, waters, and animals of the region (*4*). For them, climate change is not an abstract challenge in the future but a force that is affecting their lives today: exacerbating the challenges of water and food insecurity, economic instability, housing shortages, failing infrastructure, and potential relocation. Thus it is essential that Arctic research be shaped by the needs of the region's peoples and communities. Dedicated attention and resources need to be assigned to supporting Arctic communities to be resilient in this period of transformation and change (*1*). For example, as the world seeks to transition to a low-carbon future, how can it be ensured that the approaches used to access rare earth minerals or place new wind farms in the Arctic are done in collaboration with the communities that will be affected?

Fundamental to Arctic research is not only what is studied but also how research is done and who is both involved with and driving the research agenda. In 2022, the Inuit Circumpolar Council released a protocol for equitable and ethical engagement with Inuit (*9*). This along with similar statements made by other Arctic Indigenous peoples provide a clear framework for researchers and decision-makers doing work in the region. The coproduction of knowledge with Arctic Indigenous peoples is an important tenet that has been included in a growing number of recent research initiatives. Many funding bodies that support Arctic research now include evaluation criteria related to Indigenous engagement and/or prioritize projects that include Indigenous partners. The Fourth International Conference on Arctic Research Planning (ICARP IV) process 2022–2026 has taken steps to include Arctic Indigenous peoples in every aspect and stage of its work, including a Research Priority Team dedicated to coproduction and Indigenous-led methodologies (*10*). This is not to suggest that Arctic institutions have figured out how to effectively do community-driven and coproduced research; rather, it emphasizes that many in the research community are working with Arctic communities to actively grapple with how to do this well.

The village Saatut is in Greenland's Uummannaq Fjord system.

PHOTO: REDA/GETTY IMAGES

Effective, relevant, and timely research requires cooperation across disciplines and knowledge systems. There are many Arctic institutions that have dedicated substantial effort to understanding the limitations of Western science and to incorporate methods that produce holistic, place-based research and knowledge that meets the needs of Arctic peoples (*1*, *6*). Innovative approaches to research cooperation in the Arctic could be useful in other regions, providing new solutions for the world's most pressing challenges. For example, as the frequency, severity, and extent of wildland fires grow in the Arctic, Gwich'in Council International has been leading efforts to revitalize community fire management practices. These practices not only demonstrate the intimate knowledge that the Gwich'in hold of their homelands but also introduce solutions that serve the health of the people and the lands on which they depend (*11*).

COOPERATION IN A DIVIDED WORLD

Although there are those who champion the idea of an international treaty to govern the Arctic, similar to Antarctica, this approach is not supported by the eight states that hold sovereignty in the region [United States, Canada, Kingdom of Denmark (Greenland), Iceland, Norway, Sweden, Finland, and Russia]. The Arctic states point to the United Nations Convention on the Law of the Sea (UNCLOS) as the legal instrument that gives them primary authority and responsibility to govern the region and dismiss any suggestion that other legal mechanisms are needed or desired (*4*). According to UNCLOS guidelines, a vast majority of the Arctic Ocean falls within the maritime jurisdictions claimed by the Arctic coastal states. In fact, countries seeking observer status in the Arctic Council, the region's primary intergovernmental forum, are required to acknowledge Arctic states' sovereignty in the Arctic and the existing legal framework that apply to the Arctic Ocean and "provides a solid foundation for the responsible management of this ocean" [(*12*), p. 14].

The idea of the Arctic as a geographical unit for governance is relatively new. It was not until the Cold War was coming to an end that Arctic agreements and institutions were developed that enabled Russia and the West to build relationships and establish governance mechanisms around the shared priorities of scientific collaboration, sustainable development, and environmental protection. Multilateral agreements and institutions such as the Agreement on the Conservation of Polar Bears (1973), the International Arctic Science Committee (1990), the International Arctic Social Sciences Association (1990), the Barents Euro-Arctic Council (1993), and the Arctic Council (1996) are classic examples of peace-building through science diplomacy. The creation of these institutions was driven by scientific concerns and questions but also served a broader purpose of opening channels of communication, building trust, and defining which states had the authority and legitimacy to make decisions within the Arctic region.

For the next 25 years, a multitude of international institutions and convening events focusing on the Arctic evolved and expanded, putting scientific cooperation at the heart of the region's multilateral governance. Examples include the University of the Arctic (2001), the Fourth International Polar Year (2007–2008), Arctic Science Ministerial events (2016, 2018, and 2021), and the Multidisciplinary drifting Observatory for the Study of Arctic Climate (MOSAiC) Expedition (2019–2020). These events and institutions fostered relationships and shared objectives that enabled important agreements such as the adoption of the Agreement to Prevent Unregulated High Seas Fisheries in the Central Arctic Ocean (2021). Through this agreement, Arctic coastal states invited other states with distant water fishing capacity (China, Japan, South Korea, and the European Union) to join them in establishing the first legally binding, multilateral agreement to take a precautionary approach to protect an area from commercial fishing before fishing had begun (*13*). Signatories agreed to refrain from any commercial fishing in the Central Arctic Ocean and to undertake joint science to better understand the ecosystem.

In parallel with the science diplomacy agenda of Arctic nations, the Indigenous peoples of the region have worked for decades to create a place for themselves within many of these multilateral institutions. Their presence at these tables is recognized as an innovative feature of Arctic governance that keeps local and regional priorities on the agenda and elevates Indigenous Knowledge and perspectives. Their participation has also shaped the values and norms of many of these institutions and the culture of Arctic research cooperation and diplomacy more broadly (*1*, *6*, *7*).

In 2022, however, Russia's full-scale invasion of Ukraine had immediate spillover effects on Arctic collaboration. Not only were formal diplomatic ties in the region frozen, but Western states also halted funding for research projects that included Russian institutions or experts (a measure not imposed during the Cold War). Nearly 3 years on, diplomatic ties between Russia and the seven other Arctic states remain severely damaged, but some avenues for research cooperation have slowly resumed through the working groups of the Arctic Council (*14*) and a limited number of other multilateral and bilateral institutions.

Unquestionably, there are risks and complications associated with resuming some research cooperation with Russia. But the compelling need to share time-sensitive observations and research across borders cannot be ignored, given the pace of change and the demand for information to support decisions. The Arctic is one bioregion with some regional variations but functionally interconnected. It is not possible to understand Arctic change by focusing on one country or just one community. That is why it has been so important to share information and collaborate on research and resource management across national borders (*15*). Russia's importance to all of this can hardly be overstated, given the substantial portion of the region that falls within its jurisdiction.

These are still early days in these renewed research cooperation efforts. The relationships that are being sustained or reestablished are still fragile, and their effectiveness is uncertain. But the pressing need for continued research cooperation in the Arctic combined with the existing mechanisms that can facilitate this work may position researchers and diplomats working in this region as leaders in shaping a new era of science diplomacy. Although we believe that the Arctic is an important and appropriate location for science diplomacy to be advanced, it is critical that policy-makers and experts reflect on what research cooperation should look like in this new context and what role science diplomacy can and should play. With this in mind, we offer two observations that can inform how research cooperation advances in the Arctic and how the Arctic might be a model for other regions.

First, it is important to remember that the Arctic has benefitted for decades from recognizing that effective governance is about more than governments. Although government-to-government relations are currently limited, the network of institutions and individuals doing work in the Arctic remains vital. Arctic Indigenous peoples organizations, universities, foundations, businesses, and nongovernmental organizations have played important roles in advancing cross-border research cooperation and sustaining people-to-people relationships. Their efforts will be even more critical moving forward, and it is important to find ways to support these efforts. For example, the ICARP IV process 2022–2026 and the International Polar Year 2032–33, provide important and timely opportunities to convene and mobilize diverse actors to advance strategic Arctic research priorities for the region and the globe.

Second, Arctic research cooperation is critical for global scientific understanding, and global action is needed to respond to the challenges facing the Arctic. This means that irrespective of geopolitical tensions, Arctic research cooperation is best served by continuing to include experts from outside the region. Germany, the United Kingdom, China, and India, as examples, have all demonstrated an interest in and a willingness to commit expertise and resources to Arctic research cooperation. Although there are risks and sensitivities around inviting actors from outside the region, existing Arctic institutions such as the Arctic Council and the International Arctic Science Committee provide long established mechanisms to include these experts. At the same time, non-Arctic actors need to recognize the distinct culture and values of Arctic research. They need to seek to understand and respect the high importance placed on Indigenous Knowledge and conduct research that meets the needs of Arctic communities. This means being transparent about research plans and projects and sharing relevant data and analyses.

Close to 30 years of solid Arctic research cooperation has created a strong foundation for people-to-people relationships and multilateral governance mechanisms that can still be leveraged. An opportunity exists for the Arctic to serve as a model for how to sustain research cooperation on issues of common concern during difficult and uncertain times, but success will require investments in the next generation of Arctic policy-makers and researchers and a commitment to the institutions that support Arctic research cooperation and diplomacy. ■

REFERENCES AND NOTES

1. T. A. Moon, M. L. Druckenmiller, R. L. Thoman, Eds., *Arctic report card 2024* (National Oceanographic and Atmospheric Administration, 2024).
2. M. E. Maldarelli *et al.*, *JAMA Netw. Open* **7**, e2450759 (2024).
3. J. Meng, J. Fan, U. S. Bhatt, J. Kurths, *Nat. Commun.* **14**, 6574 (2023).
4. Pervaze A. Sheikh *et al.*, Changes in the Arctic: Background and Issues for Congress, report R41153, Congressional Research Service, 30 July 2024.
5. J. Biden, *Tribal consultation and strengthening nation-to-nation relationships* (The White House, 2021).
6. D. Cambou, T. Koivurova, *Routledge Handbook of Indigenous Peoples in the Arctic* (Routledge, 2021), pp. 320–324.
7. R. Hugonnet *et al.*, *Nature* **592**, 726 (2021).
8. S. M. Natali *et al.*, *Proc. Natl. Acad. Sci. U.S.A.* **118**, e2100163118 (2021).
9. Inuit Circumpolar Council (ICC), *Circumpolar Inuit Protocols for Equitable and Ethical Engagement* (ICC, 2022).
10. International Arctic Science Committee (IASC), *Fourth International Conference on Arctic Research Planning* (IASC, 2024).
11. E. Alexandar, *The Circle* **3**, 12 (2021).
12. Arctic Council, Arctic Council Rules of Procedure (Arctic Council, 2013).
13. C. Calderwood, F. A. Ulmer, *Polar Rec.* **59**, e1 (2023).
14. Arctic Council, *Arctic Council Advances Resumption of Project-level Work* (Arctic Council, 2024).
15. *Nature* **607**, 422 (2022).

10.1126/science.adr7939

REVIEW

Antarctica in 2025: Drivers of deep uncertainty in projected ice loss

Helen Amanda Fricker[1]*, Benjamin K. Galton-Fenzi[2,3,4], Catherine Colello Walker[5], Bryony Isabella Diana Freer[1], Laurie Padman[6], Robert DeConto[7]

Antarctica is a vital component of Earth's climate system, influencing global sea level, ocean circulation, and planetary albedo. Major knowledge gaps in critical processes—spanning the atmosphere, ocean, ice sheets, underlying beds, ice shelves, and sea ice—create uncertainties in future projections, hindering climate adaptation and risk assessments of ice intervention strategies. Antarctica's ice sheet could contribute 28 centimeters to sea level by 2100, and potentially more if we surpass warming thresholds that trigger instabilities and rapid retreat. We review recent advances in understanding the changing stability of the ice sheet margins and identify key processes that require further research. Progress requires high-resolution satellite data, targeted field campaigns, improved modeling, and refined theory. Increased investment and interdisciplinary collaboration are essential to uncovering Antarctica's hidden processes and reducing uncertainties in future projections.

The Antarctic Ice Sheet (AIS) is Earth's largest freshwater reservoir, storing enough ice to add 58 m to global sea level if it all melted, with ~5.3 m from the West Antarctic Ice Sheet (WAIS) and the rest from the East Antarctic Ice Sheet (EAIS) (*1*). Other land ice reservoirs are the Greenland Ice Sheet (GrIS; 7.4 m) and glaciers and ice caps (GIC; 0.5 m). During the 20th century, global sea level rise (SLR) was dominated by ocean thermal expansion and GIC melt (*2*); however, over the past two decades, accelerated mass loss from GrIS and WAIS has made land ice (including GIC) the largest contribution [(*2*, *3*); Fig. 1A]. Between 1979 and 1989, the total AIS contribution was just 0.11 mm per year (*4*). In the early 1990s, AIS SLR contribution started to accelerate, reaching 0.19 mm per year for the period 1992 to 1996 and 0.32 mm per year for 2017 to 2020 (*3*). Models often do not capture the trends, leading to large differences between simulated and observed ice sheet changes. Projections initialized in 2016 indicate that most simulations produce a growing ice sheet over the ~5-year overlap period with observations, and this growth persists for several decades before eventual retreat occurs (Fig. 1B). This leads to diverging outcomes over time and greater uncertainty in long-term projections (*5*). Future AIS mass is so poorly known that the IPCC considers it "deeply uncertain" (*6*). The AIS could raise sea levels by 28 cm by 2100, equaling the contribution due to thermal expansion, and up to 6.9 m by 2300 under high emissions [(*6*); Fig. 1B], with uneven impacts globally (*7*). Flood risks are compounded by increased storminess from climate change, leading to the need for more complex adaptation strategies (*8*).

WAIS and EAIS have been identified as being vulnerable to crossing tipping points where abrupt, irrecoverable change occurs if a threshold in global average temperature is exceeded (*9*). The temperature threshold for WAIS is estimated at >1.5°C above preindustrial levels, which could occur by 2030 (*10*). Owing to its size, thickness, and location, EAIS is thought to be less sensitive, with a threshold of 4°C, based on response to past climate perturbations [(*11*); Fig. 2A]. These thresholds may be conservative, given that they are inferred from paleo warming rates that are much lower than those of today (*12*) and given the uncertainty in how globally averaged warming manifests in Antarctica. Projections of ice sheet tipping points are sensitive to where the models start from (initial conditions), the geometry of ice and the underlying bed, climate forcing, representation of the processes that control the change (*6*, *13*, *14*), and model numerics. Small variations in these inputs can lead to large differences in projected SLR. Determining the exact timing and magnitude at which tipping points are reached remains a huge challenge; therefore, AIS projections diverge widely in both the onset and magnitude of mass loss (*8*, *15*).

Uncertainty in future AIS mass loss stems from a limited understanding of physical processes that act at dynamic ice margins, which are missing or crudely represented in models (Fig. 2B), combined with uncertain future changes in climate forcing (*14*, *16*, *17*). These processes are undersampled because they occur on spatial and temporal scales and in locations beyond our present observational capabilities (see the scales of change in Fig. 2B) and involve complex feedbacks between the AIS, ice shelves, sea ice, seabed, ocean, and atmosphere (*2*, *18*), with insufficient observations (*19*, *20*). As more data

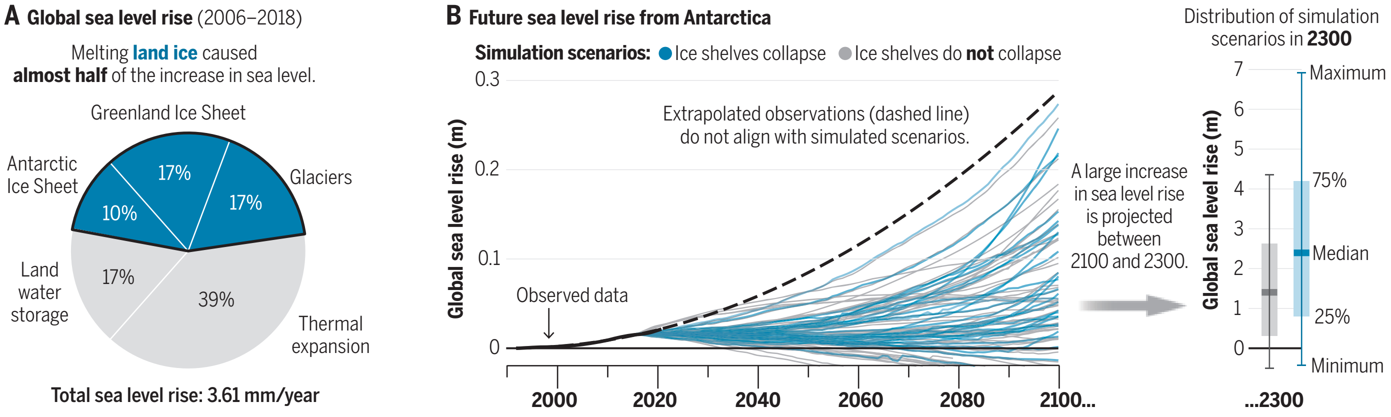

Fig. 1. Antarctica as a dynamic freshwater reservoir. (**A**) AIS contribution to global SLR for 2006–2018 compared with contributions from other sources (*2*). (**B**) Observed AIS contribution to SLR for 1992–2020 (*201*) and projected future contribution to 2100 and 2300 (*5*), amid deep uncertainty (*6*).

CREDIT: ADAPTED BY M. HERSHER/*SCIENCE*

---

[1]Scripps Polar Center, IGPP, Scripps Institution of Oceanography, University of California, San Diego, La Jolla, CA, USA. [2]Australian Antarctic Division, Kingston, TAS, Australia. [3]Australian Antarctic Program Partnership (AAPP), Institute for Marine and Antarctic Studies, University of Tasmania, Hobart, TAS, Australia. [4]Australian Centre for Excellence in Antarctic Science (ACEAS), University of Tasmania, Hobart, TAS, Australia. [5]Department of Applied Ocean Physics and Engineering, Woods Hole Oceanographic Institution, Woods Hole, MA, USA. [6]Earth and Space Research, Corvallis, OR, USA. [7]Department of Earth, Geographic, and Climate Sciences, University of Massachusetts Amherst, Amherst, MA, USA.
*Corresponding author. Email: hafricker@ucsd.edu

are acquired at finer scales through new satellite missions and fieldwork, we are learning more about these processes, moving us closer to being able to represent them in models. In this Review, we summarize key pieces of the Antarctic system and the advances in our understanding of relevant processes, instabilities, and feedbacks since 2020, the epoch of the latest IPCC report (*21*). We highlight opportunities for impactful future research as we approach the Fifth International Polar Year (Box 1).

Pieces of the Antarctic system

Antarctica functions like a millennial-scale freshwater conveyor belt, accumulating snowfall that compacts into ice and returning melted freshwater to the ocean. At the same time, the AIS acts as a heat sink, slowing changes in the global heat content of Earth's atmosphere and oceans (*22*). Snowfall and ice accumulate gradually across the continent, with the total surface mass balance reaching ~2300 billion tonnes (or gigatonnes; Gt) per year (*23*). Being thicker in the interior, ice flows under the influence of gravity to the margins, where it forms floating ice shelves (Fig. 2B). Ice is then lost by iceberg calving and ocean-driven basal melting (Fig. 3), which pumps freshwater into the Southern Ocean either locally via meltwater plumes or away from the continent as icebergs melt. In steady state, the gains are balanced by losses at the margins. How climate warming will affect future snow accumulation is uncertain; however, there is a general consensus that losses around the edge of the continent will increase (*5*). Future AIS mass loss is contingent on how climate forcings evolve and how this triggers key processes around the margin.

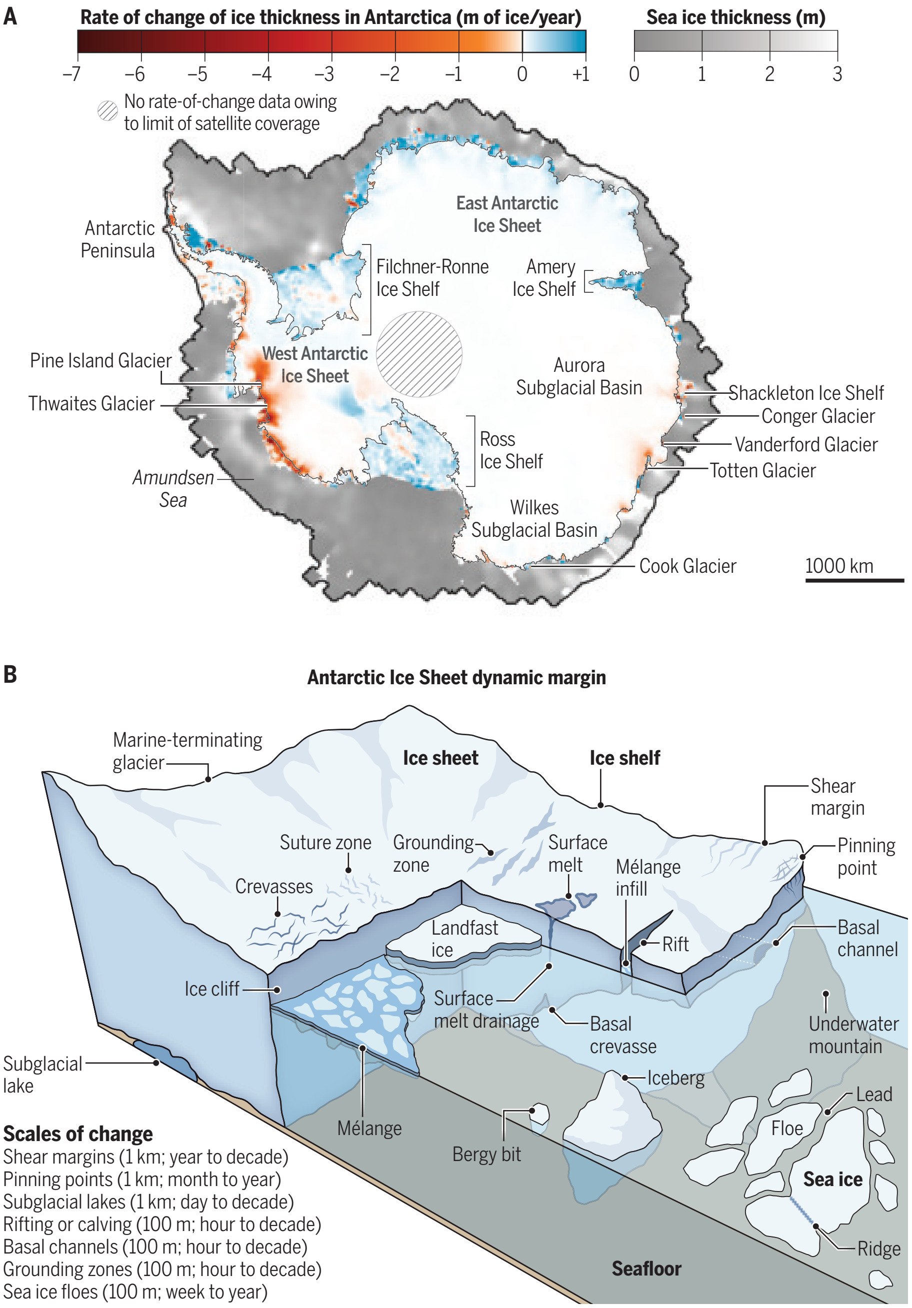

Fig. 2. Antarctica's land ice and sea ice. (**A**) AIS thickness changes for 2003–2019 from Ice Cloud and land Elevation Satellite (ICESat) and ICESat-2 satellite laser altimetry (*48*) as well as sea ice thickness for January 2020 from ICESat-2 (*111*) [from (*203*)]. [Credit: Modified from (*48*), (*202*), and (*111*) CC BY 4.0] (**B**) Features associated with processes acting in AIS's dynamic ice margins on a range of spatial and temporal scales (table at bottom left).

CREDIT: ADAPTED BY A. FISHER AND M. HERSHER/*SCIENCE*

Antarctica's subglacial system is a basal lubricant

The speed of AIS ice flow is influenced by basal conditions that determine how easily ice slides over the bed owing to the presence of liquid water and bed deformability. Fastest ice flow tends to occur where pressurized water is present at the base (*24*). Subglacial water is generated as ice melts from frictional heat caused by the glacier flow, geothermal heat flux, and pressure melting (*25*). Basal meltwater production rates are low (millimeters per year) but, over the vast AIS, the volume is substantial [59 Gt per year; (*26*)]. The AIS subglacial system is largely insulated from climate; by contrast, in Greenland the surface meltwater can reach the bed to drive a seasonal ice flow cycle (*27*). Observations of seasonal signals have only recently emerged on the Antarctic Peninsula, which are primarily attributed to seasonal modulation of ice-ocean-atmosphere interactions, with particular sensitivity to glacier terminus change, ocean temperatures, and surface water availability that may penetrate to the bed (*28*, *29*). Elsewhere, AIS surface melt is mostly confined to ice shelves (*30*, *31*), but if it were to migrate above the grounding line (GL; Fig. 3) and then reach the bed, some AIS outlets could evolve toward more seasonally varying flow speeds and accelerated ice loss [for example, see (*32*)].

Subglacial hydrology is rarely observed, and so it is either crudely represented in or missing from models [for example, see (*33*)]. Our observational capability was transformed in the mid-2000s by the realization that fluctuations in local surface elevation are signatures of subglacial hydrology (*34*, *35*), with satellite laser altimetry tallying >140 interconnected subglacial lakes that are continuously filling and draining (*36*). Localized ice flow acceleration has been observed during periods of subglacial lake drainage (*37*–*39*), but the impact on wider ice sheet dynamics remains poorly sampled (*40*). Subglacial water follows the hydropotential,

Box 1. Bridging the gaps in SLR projections.

The wide range of present Antarctic SLR projections is too broad for policy-makers to use effectively. Improving these projections requires a better understanding of mass balance processes, especially those occurring on short spatial (~100 m to ~1 km) and temporal (daily to seasonal) scales, which are presently underrepresented in models because observations have been insufficient in space and time.

Main knowledge gaps

To reduce uncertainties in Antarctic mass loss and better inform policy decisions and adaptation strategies, we must advance knowledge of the following:

- Subglacial hydrology, basal processes, and internal ice deformation and structure
- Ice sheet geometry and the potential for MISI
- GZ state and variability and the role of buttressing
- Sub–ice shelf cavity melting, ocean circulation, and ice-ocean interactions
- Fracturing and calving dynamics and the potential for MICI
- Feedbacks between the ice sheet, sea ice, and other parts of the climate system
- Interactions between global climate and regional climate at the ice sheet margin, including accumulation and surface warming

These knowledge gaps require mapping of the seabed and bedrock underlying the ice sheet, determination of the properties under the grounded ice and floating ice shelves, enhanced simulation and modeling, and stronger interdisciplinary and multinational research to investigate feedbacks.

Essential actions

- Advance understanding of processes by monitoring relevant variables across a range of space and time scales with airborne and satellite missions that ensure continuity and innovation through high-resolution, frequent sampling: Key future missions include the NASA–ISRO Synthetic Aperture Radar (NISAR) mission (ice velocity and deformation), the European Space Agency's Copernicus Polar Ice and Snow Topography Altimeter (CRISTAL) mission (surface elevation), and the proposed Earth Dynamics Geodetic Explorer (EDGE) mission (surface elevation)
- Perform targeted field observations for evaluation and calibration of remote-sensing techniques and to develop field-based understanding of processes
- Expand field observations beyond WAIS, particularly to at-risk EAIS outlet glaciers and ice shelves
- Develop high-fidelity simulations that exploit progress in closing the main knowledge gaps and the reproduction of observed changes for future projections with substantially reduced uncertainties, for example, Ice Sheet Modeling Intercomparison for the seventh IPCC Ice Sheet Model Intercomparison Project for Coupled Model Intercomparison Project–Phase 7 (ISMIP7)
- Educate and inspire the next generation of Antarctic ice sheet researchers
- Provide actionable projections with well-constrained uncertainties that inform policy decisions and adaptation strategies

Funding and advocacy

Strong advocacy for Antarctic research is crucial to secure sustained funding and refine projections, which are essential for guiding climate policies and global adaptation strategies. This requires enhanced coordination among scientific, governmental, public, and private stakeholders, as well as increased international collaboration [e.g., coordinated through the Climate and Cryosphere (CLiC) project and the Scientific Committee on Antarctic Research's INStabilities & Thresholds in ANTarctica (SCAR INSTANT) research program].

and, in some regions, subtle thickness changes may divert water from one drainage basin to another (*41*). Evidence of a deep groundwater network beneath a WAIS ice stream (*42*) indicates another source for subglacial water. It has been hypothesized that this groundwater interaction may be crucial on decadal timescales (*43*). Identifying the sources, thickness, and pressure of subglacial water beneath the ice sheet will be critical for understanding its present and future controls on ice dynamics (*44*, *45*).

Antarctica's ice shelves are buttressing dams

Most AIS outlet glaciers presently terminate in ice shelves. Ice shelf contact with pinning points (where the ice base touches seabed highs) and lateral shear margins (where ice is in contact with rock or slow-moving ice) leads to buttressing of upstream ice (*46*). Each basin experiences drivers of change on different timescales (Fig. 3), giving each ice shelf a unique ratio of mass loss processes. If mass losses exceed gains, then the ice shelf thins and/or the GL retreats, resulting in reduced basal friction, less drag at pinning points and sidewalls, and less buttressing (*46*, *47*). As a result, more ice discharges to the ocean, increasing SLR. Regions where the grounded AIS is losing the most mass are those where ice shelves are thinning (*48*). Hence, although the net loss of grounded ice determines SLR, understanding the role of floating ice is crucial to predict change.

Ice shelf thinning can trigger faster ice flow hundreds of kilometers away (*46*, *49*) and can be especially impactful if it occurs upstream of a stable "safety zone" (*47*) or causes the ice to detach from pinning points (*50*, *51*). Buttressing can be lost through thinning, unpinning, and complete ice shelf disintegration, a phenomenon that involves a series of interconnected processes such as enhanced calving (*52*, *53*), increased basal melting leading to ice shelf thinning (*54*, *55*), and, as observed on the Antarctic Peninsula, "hydrofracture" that results from excessive surface melt [(*56*); Fig. 3A].

Antarctica's sub-ice cavities are the hidden link to the ocean

Sub-ice cavities host a distinctive ocean environment where externally driven circulation of heat and salt couples with buoyant glacial meltwater generated by basal melting. Key factors that influence basal melt rates include ice depth and basal slope as well as seabed geometry (*57*, *58*). Ice shelves are often classified as cold or warm cavity, with distinct modes of melting and circulation (Fig. 3B). In reality, multiple modes and combinations of oceanic conditions can influence a single ice shelf at different times and locations (*57*, *59*). In warm cavities such as in the Amundsen Sea, Circumpolar Deep Water can exceed the local freezing point temperature by 2°C (*60*, *61*), with models suggesting that it would take 3 years to travel to the GL (*62*), where it drives melt rates of 10 to 100 m per year (*63*). In cold cavities, such as the Amery Ice Shelf, melt rates near the deep GL (Fig. 3B) are highest because the in situ freezing point temperature decreases with pressure (*64*). The resulting cold Ice Shelf Water can refreeze as marine ice at shallow ice drafts, redistributing ice (*57*, *59*, *63*) and stabilizing ice shelves (*65*). In both cavity types, rapid melting can occur at the ice fronts because of more energetic oceanic conditions as well as warmer upper-ocean waters in summer (*66*, *67*).

Future changes in Southern Ocean temperature, circulation, and sea ice conditions could shift the distribution of basal melting and refreezing (*68*). The complex interplay between buoyant intrusions of subglacial meltwater (*69*), ice-base geometry (*58*), and turbulent processes near the ice-ocean boundary leads to the emergence of several other melting and freezing regimes that are understudied (*59*, *70*). Substantially improved knowledge of the ice shelf cavity environment, including bed geometry, ocean

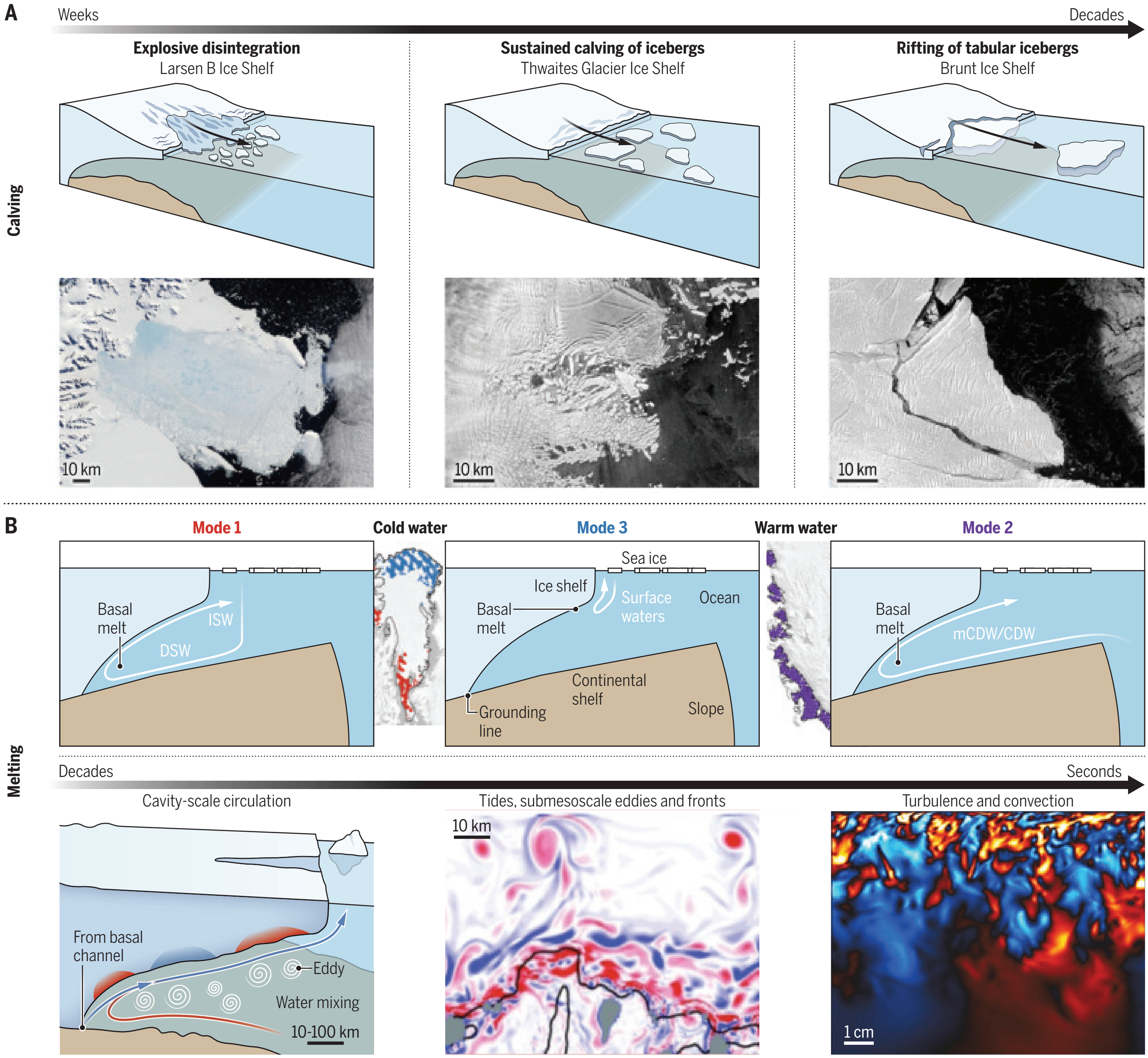

Fig. 3. Antarctica's mass loss processes and their spatial and temporal scales. (**A**) Calving is an irregular process where ice breaks off from outlet glaciers and ice shelves, ranging from large tabular icebergs calved every few decades, to more frequent smaller icebergs, to complete disintegration (*130*). [Credit: Modified from (*130*)] (**B**) Basal melting is a continuous process driven largely by cavity-scale circulation controlled by the cavity geometry (including the ice draft and slope, and the seabed shape) and by long-term changes in ocean conditions seaward of the ice front; mesoscale processes (such as eddies, fronts, and tides) that control how the ocean heat enters the cavity; and smaller-scale processes (such as turbulence and convection) (*57*, *59*). [Credit: Modified from (*59*) (bottom left), (*204*) CC BY 3.0 (bottom middle), and (*59*) (bottom right)] CDW, Circumpolar Deep Water; DSW, Dense Shelf Water; mCDW, modified Circumpolar Deep Water.

circulation, and mass loss processes, is needed to reduce uncertainties in projections of ice shelf mass loss (see Box 1).

Antarctica's grounding zones are complex intertidal estuaries

Antarctic ice first meets the sub–ice shelf cavity at the GL, which can migrate with ocean tides to create a grounding zone (GZ; Fig. 4), where the ice transitions from being always grounded to always floating. Ice flowing across the GL typically thins rapidly, as a result of stretching as basal friction is removed and high basal melt rates (*63*). Underwater surveys have revealed that basal melt close to the GL varies down to submeter scales as a result of local variations in basal ice topography (*61*). Autonomous phase-sensitive radio echo sounding (ApRES) instruments have revolutionized the measurement of basal melt rates; however, these techniques are difficult to apply in flexure zones, regions of crevassing, or where firn compaction rates and vertical shear profiles are difficult to determine (*71*–*73*). ApRES-derived estimates of melt rates can be combined with estimates from satellite-derived ice thickness changes (*63*); however, these are undersampled in the GZ owing to complex surface topography

CREDIT: ADAPTED BY A. FISHER/SCIENCE

and the breakdown of hydrostatic equilibrium (*74*), creating an observation gap in regions where melt rates are the highest.

Recent studies have shown that seawater intrusions driven by ocean tides can penetrate the GZ (Fig. 4), causing variations in basal melt on short timescales (*75*). Satellite-based radar interferometry (*76–78*) and laser altimetry observations (*79*) with high spatial resolution and frequent temporal sampling reveal that the GL can migrate up to 15 km between low and high tide, pumping relatively warm, salty ocean water further beneath the ice sheet every few hours (*80*). Significant long-term GL retreat and acceleration in Amundsen Sea glaciers has been attributed to vigorous ice-ocean interactions in their GZs (*75*, *81*).

Evidence is also emerging of a link between subglacial hydrology and ice shelf basal melting (Fig. 4). Injection of freshwater across the GZ into the ice cavity can enhance melting that reduces ice shelf buttressing, which has been proposed as an important mechanism for some EAIS glaciers (*69*, *82*). Models suggest that under high greenhouse gas emissions, this effect can increase the SLR contribution of a drainage basin by up to 30% (*83*). Focused discharge of subglacial freshwater across the GL can drive the development of large basal channels that mechanically weaken the ice shelf (*75*). Some studies have observed tens of kilometers of migration of seawater underneath the ice sheet, along estuaries formed by subglacial hydrology in the GZ, where water can be trapped for weeks before draining (*77*, *80*). Some models predict that the density difference between fresh subglacial discharge and salty ocean water can form a "salt wedge" that permits the diffusion of seawater up to several kilometers upstream of the GZ (*84*, *85*). This layered seawater intrusion theory—distinct from, yet potentially occurring alongside, the tidal intrusion mechanism—remains unobserved in Antarctica with present observational capabilities. Such irregular, widespread interactions between ice and seawater in the GZ could be impactful on AIS evolution (*85–87*), potentially doubling future SLR contributions (*88*); there is also a suggestion that this may introduce new tipping-point behaviors (*89*, *90*). Explicit representations of these GZ melt processes are missing from most ice sheet models (*80*).

Another GZ interaction involves sediment transfer from the ice sheet to the ocean, which can influence the stability of the GZ (*91*, *92*) (Fig. 4). Depositional features can also give insights into present and past ice dynamics; for example, more than 75 "GZ wedges" have been identified on the Antarctic seafloor, which form as sediment is delivered to the GZ during periods where the ice margin remains stable for a long time (*93*). GZ wedges, which are typically <15 km long and 15 to 100 m thick, can act as topographic pinning points that can stabilize the GL, with evidence that they halted WAIS retreat for hundreds to thousands of years during the last deglaciation (*94*). Smaller amplitude, regularly spaced corrugation ridges observed offshore of Thwaites Glacier and Larsen Inlet are thought to record sequential low-tide seafloor sediment imprints that may provide evidence of rapid GL retreat of hundreds of meters per day during the last deglaciation (*95*, *96*). Similar features in Pine Island Bay have been interpreted as the imprint of icebergs dragging on the seafloor at tidal frequencies (*97*). Although there are few direct observations, understanding feedbacks between ice dynamics and sediment redistribution in GZs is essential for interpreting their past stability and projecting future ice sheet retreat.

Antarctica's sea ice regulates global climate and ice sheet change

Antarctica's surrounding sea ice (Fig. 2A) covers an area of ~18.5 × 10^6 km^2 (~6% of the global ocean) at its winter maximum (September) and shrinks to nearly 16% of that in summer (*98*). Sea ice is a dynamic, seasonally varying component of the Antarctic environment, exerting a strong influence on the ocean and climate (*17*). Sea ice increases Earth's albedo, reflecting incoming solar radiation, and helps to regulate global temperature (*99*). The seasonal formation and melt of sea ice modifies ocean salinity and temperature, altering stratification and circulation patterns that govern the distribution of heat along the continental shelf, shaped by regional weather patterns and climate feedbacks (*100*). These processes determine where and how relatively warm waters can melt ice shelves, which can influence ice shelf stability and future sea level rise [for example, see (*101*, *102*)]. In turn, changes in ice shelf melting can affect sea ice, generating complex climate feedbacks (*103*). Sea ice also plays a crucial role in marine ecosystem activity (*104*).

A significant and unpredicted decline in Antarctic sea ice extent began in 2016, with partial recovery in 2019 to 2020 followed by consecutive years of near-historic lows (*105*), leading to increased coastal exposure to open water (*106*). The lowest annual sea ice extent was 1.79 × 10^6 km^2 in February 2023, which is ~10% less than the 2022 record low that marked the first time annual minimum extent dropped below 2 × 10^6 km^2 (*107*). The ongoing decline signals a major shift in Southern Ocean conditions (*105*), which has implications for sea ice and its influence on the AIS, the broader climate system (*108*, *109*) and ecosystems (*110*). Sea ice thickness—a key factor for ice strength, landfast ice formation, and summer survival—is challenging to measure in Antarctica because of thick snow cover, flooding, and difficulty in resolving leads to provide relative freeboard assessments (*111*). Accurately mapping sea ice freeboard and structure at scales that capture most sea ice floes (Fig. 2B) is essential for providing the detailed data needed to improve models of sea ice evolution (*112*) and explain why change has occurred.

Instabilities and feedbacks of the Antarctic system

Geometric instabilities at dynamic ice margins

Simple relationships predict the potential for two geometry-based high-end retreat scenarios, which are considered to be possible AIS instabilities: the marine ice sheet instability (MISI) and the marine ice cliff instability (MICI). MISI is based on the understanding that because seaward ice flux increases with ice thickness, GLs located on retrograde bed slopes are inherently unstable (*113*, *114*). In such locations, the weakening or loss of ice shelf buttressing can trigger a self-sustaining drawdown at the ice margins: Initial thinning causes the GL to retreat into deeper water, where a higher strain rate increases mass loss from the ice sheet, leading to further retreat and thinning. Although some studies suggest that MISI is underway in WAIS (*81*, *115*), others suggest that present-day GL retreat is driven by external climate forcing alone (*116*), though continued warming may eventually lead to MISI onset (*117*). Some EAIS outlets are also potentially vulnerable to MISI (*118*, *119*). MICI is predicated on simple force balance arguments that suggest that the stable height to which a marine-terminating ice cliff (Fig. 2B) can grow is limited by ice strength to ~100 m (*120*). If triggered, unstable cliff failure can repeatedly expose thicker ice upstream, driving rapid ice loss at the margin (*121*). As proposed, MICI could contribute multimeter SLR on century timescales (*2*).

MICI remains controversial and has not been directly observed in Antarctica, although observations of speed-up and enhanced calving at thick marine-terminating glaciers after ice shelf loss have been noted at Crane Glacier on the Antarctic Peninsula (*122*) and in Greenland (*123*). Paleo records of iceberg plow ridges in Pine Island Bay (*124*), previously attributed to grounding of floating ice during breakup (*97*), have been cited as indirect evidence for MICI. By contrast, a statistical analysis of modeling uncertainties (*125*) concluded that MICI is not required to reproduce sea level estimates in the geologic past. Process-based modeling suggests that slow ice shelf loss can mitigate MICI, but outcomes vary widely depending on assumptions of ice properties and ice strength (*126*). Other models suggest that speed-up and dynamic thinning of unbuttressed ice fronts can suppress ice cliff calving in the absence of ice shelves (*127*, *128*). An incomplete understanding of the material properties (strength) of glacial ice and the processes involved in triggering and amplifying ice shelf loss, calving, and cliff retreat (*129*, *130*) continues to make the role of MICI in retreat scenarios difficult to parameterize and quantify (*131*, *132*). Given the potential for MICI (and fracture and calving processes in general) to contribute to future ice loss, rifting and calving at thick ice margins should be further evaluated through observations at spatial and temporal scales relevant to processes involved in ice shelf, glacier, and ice front stability. Further research on the initiation and propagation of fracturing, the

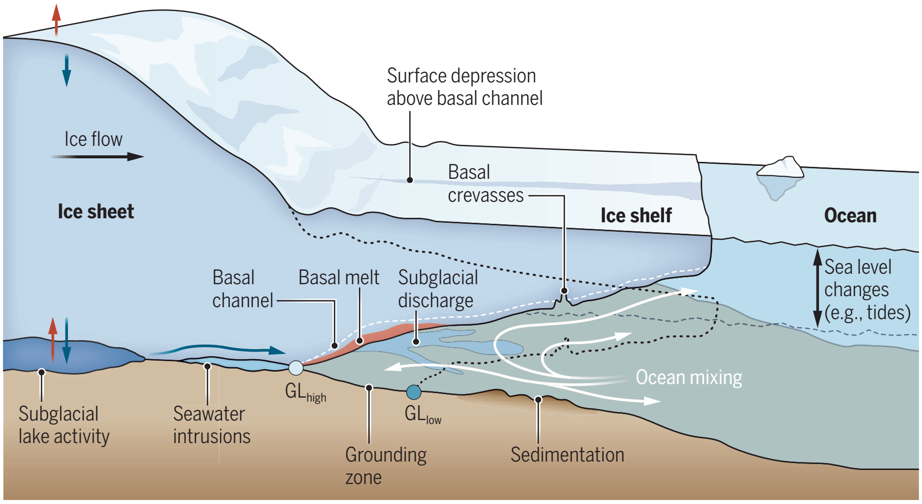

Fig. 4. Antarctica's grounding zones. Changes in ocean sea level, including from tides, can move the GL by up to several kilometers across the GZ (from $\mathrm{GL_{low}}$ to $\mathrm{GL_{high}}$). Processes acting in and around the GZ—driven by interactions between ice, bedrock, sediment, subglacial hydrology, and the ocean—can vary on short spatial and temporal scales. Tides can pump relatively warm seawater kilometers inland, enhancing basal melting in and upstream of the GZ. Subglacial water flux from the ice sheet bed to the ocean across the GL can also enhance basal melting in the GZ, which can lead to the development of basal channels that are visible in satellite altimetry as surface depressions. Sediment flux into the sub–ice shelf cavity can increase GL stability. All of these interactions can influence long-term ice dynamics. Figure is not to scale.

CREDIT: ADAPTED BY A. FISHER/SCIENCE

role of GL location and floating versus grounded ice, upstream ice thickness gradients, surface melt, bedrock shape, and flow velocities is needed.

Feedbacks at dynamic ice sheet margins

Processes at AIS dynamic margins are interconnected and can compound. For example, ice front retreat due to increased iceberg calving can increase ocean heat supply to the deep GL (*133*, *134*). Enhanced basal melting leads to ice shelf thinning and the incision of basal channels (*135*), leaving ice shelves more susceptible to hydrofracture (*136*). Processes acting in certain locations, such as basal melting or rifting along shear margins or pinning points, can have a disproportionate impact, triggering rapid ice shelf retreat and flow acceleration (*137*, *138*). This can potentially lead to more crevassing, rifting, and ice front retreat. Such feedbacks have been implicated in the ongoing retreat and acceleration of Pine Island Glacier (*53*, *139*).

Not all feedbacks at ice sheet margins are positive. For example, ice sheet models accounting for glacial-isostatic adjustment, including the gravitational, rotational, and deformational response of a viscoelastic Earth to changing ice loads (*140*), demonstrate that bedrock uplift and a local sea level drop in the vicinity of retreating GZs can slow retreat. The effect is strongest in West Antarctica, where the mantle has relatively low viscosity (*141*), allowing for faster uplift rates. This negative feedback could slow both MISI- and MICI-driven retreat, although it will weaken as the pace of AIS ice loss increases.

Feedbacks between coastal processes and the AIS

The configuration of the coastal icescape (sea ice, fast ice, and icebergs) affects mass-loss processes (Fig. 3) through modification of ocean properties (*142*). Sea ice may enhance buttressing (*106*, *143*), mitigate the impacts of swells (*144*, *145*) and tsunamis (*146*, *147*) on ice fracture, and reduce frontal melting and small-scale calving (*148*, *149*). This role is amplified when thick landfast sea ice forms, anchored by complex coastlines and grounded icebergs (*150*), which affects polynya activity, associated abyssal ventilation, and the properties of water masses entering the cavity (*151*). Large calving events can greatly reduce polynya activity and the production of dense water that ventilates the abyssal global oceans (*152*). Poorly constrained calving models, limited water depth data, and complex sea ice physics hinder projections of changes in the coastal icescape.

AIS response to large-scale climate variability

Climate variability modes like the Southern Annular Mode and El Niño–Southern Oscillation influence ocean properties on the continental shelf (*153*), sea ice extent (*154*), and ice sheet/shelf surface mass accumulation (*155*), affecting the changing mass balance of WAIS ice shelves (*156*) and the grounded AIS (*157*). Modeling studies project that some cold-cavity ice shelves could transition to warm cavities by 2100 (*158*, *159*), caused in part by feedbacks as initial inflows of warm ocean waters drive melting that intensifies the cavity overturning circulation, continuing to draw in warmer water. However, these transitions may be delayed because an initial response to climate warming can involve a weakened sub-ice circulation and lowered basal melt rates (*160*).

Keeping track of the pieces of the Antarctic system

Antarctica's size and remoteness mean that changes on a continental scale can be tracked only by satellite. Three complementary techniques track grounded AIS mass: gravimetry; mass fluxes from ice flow rates, ice thickness, and climate models; and elevation changes combined with a firn density model. These techniques can then be combined (*3*). The net AIS mass budget is shaped by snow accumulation and seaward ice flow, influenced by complex interactions among the atmosphere, ocean, and ice (*48*), which occur on multiple scales. Therefore, comprehensive monitoring should span broad spatial and temporal scales, resolving features such as outlet glaciers (*28*, *161*) and ice shelves (*63*) while also capturing seasonal to annual changes. Only three studies have provided a comprehensive assessment of grounded and floating ice using the same data over the same time period (*48*, *162*, *163*) (Fig. 2A). Observations at higher spatial and temporal resolution can inform about processes not yet captured in models.

Broad-scale monitoring

Between 1992 and 2020, AIS experienced an overall net mass loss of grounded ice (*3*), dominated by trends in WAIS (82 ± 9 Gt per year) and the Antarctic Peninsula (13 ± 5 Gt per year). Most WAIS changes occur in the Amundsen Sea basins, where glaciers have accelerated because of reduced ice shelf buttressing and GL retreat (*46*, *48*, *54*). EAIS is near steady state or in slightly positive balance because losses from increased ocean-driven melt are offset by gains from increased inland snowfall, which is attributed to a warming and more moisture-laden atmosphere (*3*, *48*). Between 2003 and 2018, mass gains were concentrated in Queen Maud Land, whereas mass loss occurred in several MISI-susceptible ice outlets draining the Aurora and Wilkes subglacial basins (*48*), accompanied by GL retreat (*164*). Flow rates have increased in numerous EAIS outlets on both grounded ice [e.g., Cook Glacier (*165*) and Vanderford Glacier (*166*)] and floating ice [e.g., ice shelves of Scott Glacier (*167*), Totten Glacier (*168*), and Denman Glacier (*169*)].

Snow accumulation across AIS increased significantly between 2019 and 2023 (*170*). In WAIS, much of the mass gain was due to short-period extreme events, such as atmospheric rivers (ARs) (*170*–*172*). In 2019 to 2020 alone, this reduced WAIS's SLR contribution by 60 ± 16 Gt per year (*170*). Record mass gains occurred in 2022 (*173*), primarily because of an increase in precipitation events over EAIS, including ARs. In March 2022, a powerful 3-day AR delivered an estimated

306 Gt of precipitation (*174*), accounting for 32% of the total AIS precipitation for that month, and up to 90% in some parts of EAIS, particularly Wilkes Land. AR intensity may be linked to interannual climate modes, but both the intensity and frequency of extreme precipitation events are expected to rise as the climate warms throughout the 21st century (*172*). An open question is whether increased snowfall in the AIS interior will be sufficient to offset increased melting and calving at the margins.

Process-based understanding

Recent satellite data show changes on process-relevant spatial and temporal scales. In WAIS, Pine Island Glacier Ice Shelf transitioned in 2015 from a previously quasi-stable cycle of advance and retreat at its calving front to a calving regime characterized by more frequent calving of tabular icebergs (Fig. 3B) and calving front retreat (*175*) (Fig. 3B). Portions of the Thwaites ice tongue underwent an abrupt change from a previously intact ice shelf into fragmented remnants (*176*, *177*). Studies of ice shelf rifts have suggested that their activity may relate to internal formation mechanics (*178*) and glaciological stresses as well as to atmospheric and oceanic forcings, for example, winds (*179*), sea surface slope or wave swell (*180*, *181*) and tsunamis (*147*), ocean circulation (*61*), and strength of intrarift mélange (*182*). Observations of ice shelves with short calving cycles (Fig. 3A) have shown that ocean and atmospheric forcings can lead to ungrounding from pinning points, driving increased calving rates, for example, at Pine Island Glacier around 2006 (*133*), Thwaites Glacier (*183*), and Thwaites Eastern Ice Shelf (*177*, *184*). At Thwaites, the evolving interaction with a pinning point after the loss of Thwaites Western Ice Tongue in 2008 likely triggered shearing and fracture propagation related to enhanced weakening (*137*, *178*, *185*), with another ungrounding anticipated within the next decade (*50*).

In East Antarctica, there have been many signs of change, for example, recent terminus change after sea ice breakout (*186*) and GL retreat (*166*, *187*), but the first observed ice shelf disappearance was Conger-Glenzer in 2022 (*55*), after decades of retreat that began in the late 1990s when small calving events isolated it from Shackleton Ice Shelf. This was followed by phases of retreat, relative stability, and ultimate rapid disintegration driven by long-term thinning, reduced buttressing effect, and ungrounding from a pinning point. The evolution of the Shackleton-Denman system itself involved structural changes in the floating shear margins, rift propagation, and small-scale calving (*167*), possibly aided by seawater infiltration in some regions adjacent to Shackleton Ice Shelf (*164*, *188*) that may affect ice rheology (*189*). These could all be early signs of EAIS responding to warming.

Antarctica as a target for "ice intervention" to mitigate sea level rise

Intervention to slow ice loss has recently been suggested (*190*, *191*), with two primary strategies. Underwater curtains would divert warm water from reaching the ice outlets and redirect colder water toward them instead, potentially slowing ice melt and GZ retreat (*192*). Whether this will actually slow overall AIS mass loss is uncertain (*193*); it might simply reroute warm water to other ice shelves (*194*). Drilling and drying strategies aim to stabilize glaciers by increasing basal friction of sliding ice streams by drilling deep holes and removing lubricating water from the subglacial drainage system. This idea is based on observations of natural processes at Kamb Ice Stream. However, most outlets differ markedly from Kamb, and the actual impact on glacier sliding is expected to be highly dependent on poorly mapped and modeled bed and basal conditions. Because subglacial water is constantly replenished and may be connected to underlying groundwater (*42*), any impact would be short-term, and any efforts would need to be sustained.

Geoengineering in Antarctica faces immense challenges owing to its vast scale, technical and logistical difficulties, harsh polar conditions, and environmental concerns, including impacts on marine life and the risk of contaminating subglacial areas (*195*). Perhaps the greatest risk, however, lies in unintended consequences from our limited understanding of how ice sheets respond to climate and human activities. With the guiding principle of "first, do no harm," it is crucial that we prioritize improving our knowledge. This will help us better assess our options for the future and make informed decisions about what actions we can responsibly take. Effective methods will necessitate substantial, long-term investments in research, infrastructure, and ongoing monitoring—resources that would be more wisely allocated to addressing the fundamental deep uncertainties instead (*195*).

Commitment to change

The AIS is expected to continue losing ice in response to the heat already absorbed by the climate system (*196*). To date, only a small fraction of this global heat imbalance has contributed to AIS melting (*22*, *163*). Increased melt rates for WAIS may be committed for the next century (*197*). The pace and extent of AIS evolution are uncertain (*198*, *199*), influenced by the instabilities and feedbacks discussed here, and other processes that remain underobserved, or unknown altogether. Projected rapid ice loss would partially offset global warming (*200*) by converting the heat into ice melt but would still cause SLR and alter ocean circulation as a result of the cooling and freshening of the oceans.

Uncertainty remains over how much Antarctica will warm within the Paris Agreement's 1.5°C target, owing to climate model uncertainties and potential polar amplification, which could cause Antarctica to warm sooner and exceed the global average. Even without the expected amplified warming, a global target of 1.5°C may not prevent the AIS from crossing tipping points within decades (*9*). The response timescale of the AIS is deeply uncertain, but its future contribution to SLR (Fig. 1B) could substantially exceed the IPCC medium-confidence projections within the next decades to century (*2*, *5*).

Summary and outlook

Antarctica stores a vast amount of freshwater, and its future evolution is the largest cause of uncertainty in SLR projections. Most of this uncertainty stems from insufficient understanding of key processes that affect the marginal ice shelves that buttress the ice sheet and the response of grounded ice when ice shelves are lost. Present observations are insufficient, in both space and time, to constrain the mechanisms responsible for abrupt mass loss, leaving them only crudely represented or missing entirely from ice sheet models. The impact of seasonal to decadal variations in climate forcing is also uncertain. Constraining the uncertainty in AIS evolution requires radically improved understanding of its mass-loss processes. Adequate sampling and tracking of changes can only be achieved through cooperative, new, and sustained observations from satellites and in situ observations (both on ice and in the surrounding ocean), combined with high-fidelity modeling to investigate key processes related to ice-ocean interactions, surface melting, and fracture of ice (Box 1).

Sir Douglas Mawson's words about his 1914 Antarctic expedition, "We had come to probe its mystery, we had hoped to reduce it to terms of science, but there was always the 'indefinable' which held aloof, yet riveted our souls," remain relevant in 2025. Our comprehension may always be incomplete, leaving open the likelihood that Antarctica's complexities surpass our capacity for complete understanding. However, societies need to understand Antarctica to be able to adapt in response to its changes. Yet despite this dire need and deep uncertainty, the pace of progress remains too slow, underscoring the need for a fundamental shift in our approach to polar science as we begin to identify and understand the once-indefinable unknowns. As we approach the Fifth International Polar Year (2031–2033), present limitations in observations and models highlight that polar science remains underequipped to fully address the complexities of Antarctica's system. We are at a time when a substantial increase in resourcing is needed to provide transformative advancements in research tools, data collection, and modeling capabilities, which are essential to unravel the key processes that shape the evolution of Earth's largest freshwater reservoir and to finally answer the critical questions: How much and how fast?

REFERENCES AND NOTES

1. M. Morlighem *et al.*, *Nat. Geosci.* **13**, 132–137 (2020).
2. B. Fox-Kemper *et al.*, in *Climate Change 2021: The Physical Science Basis. Contribution of Working Group I to the Sixth*

Assessment Report of the Intergovernmental Panel on Climate Change, V. Masson-Delmotte *et al*., Eds. (Cambridge Univ. Press, 2021), pp. 1211–1362.

3. I. N. Otosaka *et al*., *Earth Syst. Sci. Data* **15**, 1597–1616 (2023).
4. E. Rignot *et al*., *Proc. Natl. Acad. Sci. U.S.A.* **116**, 1095–1103 (2019).
5. M. Oppenheimer *et al*., in *The Ocean and Cryosphere in a Changing Climate: Special Report of the Intergovernmental Panel on Climate Change*, H.-O. Pörtner *et al*., Eds. (Cambridge Univ. Press, 2019), pp. 321–445.
6. H. Seroussi *et al*., *Earths Futur.* **12**, e2024EF004561 (2024).
7. S. Sadai, R. A. Spector, R. DeConto, N. Gomez, *Earths Futur.* **10**, e2022EF002940 (2022).
8. B. K. Galton-Fenzi *et al*., in *Antarctica and Planet Earth*, M. Meredith, J. Melbourne-Thomas, M. Raphael, A. Naveira Garabato, Eds. (Taylor and Francis Group, 2024), chap. 7.
9. D. I. Armstrong McKay *et al*., *Science* **377**, eabn7950 (2022).
10. N. S. Diffenbaugh, E. A. Barnes, *Proc. Natl. Acad. Sci. U.S.A.* **120**, e2207183120 (2023).
11. C. R. Stokes *et al*., *Nature* **608**, 275–286 (2022).
12. J. E. Tierney *et al*., *Science* **370**, eaay3701 (2020).
13. A. A. Robel, H. Seroussi, G. H. Roe, *Proc. Natl. Acad. Sci. U.S.A.* **116**, 14887–14892 (2019).
14. D. Li, R. M. DeConto, D. Pollard, *Sci. Adv.* **9**, eadd7082 (2023).
15. F. Pattyn, M. Morlighem, *Science* **367**, 1331–1335 (2020).
16. C.-Y. Tsai, C. E. Forest, D. Pollard, *Clim. Dyn.* **55**, 1875–1892 (2020).
17. L. G. Bennetts *et al*., *Rev. Geophys.* **62**, e2022RG000781 (2024).
18. R. S. W. van de Wal *et al*., *Earths Future* **10**, EF002751 (2022).
19. O. Gagliardini, G. Durand, T. Zwinger, R. C. A. Hindmarsh, E. Le Meur, *Geophys. Res. Lett.* **37**, L14501 (2010).
20. J. L. Bamber, M. Oppenheimer, R. E. Kopp, W. P. Aspinall, R. M. Cooke, *Earths Future* **10**, EF002772 (2022).
21. Intergovernmental Panel on Climate Change (IPCC), *Climate Change 2023: Synthesis Report. Contribution of Working Groups I, II and III to the Sixth Assessment Report of the Intergovernmental Panel on Climate Change*, Core Writing Team, H. Lee, J. Romero, Eds. (IPCC, 2023).
22. K. von Schuckmann *et al*., *Earth Syst. Sci. Data* **15**, 1675–1709 (2023).
23. R. Mottram *et al*., *Cryosphere* **15**, 3751–3784 (2021).
24. C. R. Stokes, *Earth Surf. Process. Landf.* **43**, 85–123 (2018).
25. C. Dow, N. Ross, H. Jeofry, K. Siu, M. Siegert, *Nat. Geosci.* **15**, 892–898 (2022).
26. F. Pattyn, *Earth Planet. Sci. Lett.* **295**, 451–461 (2010).
27. H. J. Zwally *et al*., *Science* **297**, 218–222 (2002).
28. K. Boxall, F. D. W. Christie, I. C. Willis, J. Wuite, T. Nagler, *Cryosphere* **16**, 3907–3932 (2022).
29. B. J. Wallis, A. E. Hogg, J. M. Van Wessem, B. J. Davison, M. R. Van Den Broeke, *Nat. Geosci.* **16**, 231–237 (2023).
30. L. D. Trusel *et al*., *Nat. Geosci.* **8**, 927–932 (2015).
31. R. L. Dell, I. C. Willis, N. S. Arnold, A. F. Banwell, S. De Roda Husman, *Nat. Geosci.* **17**, 624–630 (2024).
32. G. A. Jones *et al*., *Geophys. Res. Lett.* **50**, e2023GL103673 (2023).
33. S. Sun *et al*., *J. Glaciol.* **66**, 891–904 (2020).
34. D. J. Wingham, M. J. Siegert, A. Shepherd, A. S. Muir, *Nature* **440**, 1033–1036 (2006).
35. H. A. Fricker, T. Scambos, R. Bindschadler, L. Padman, *Science* **315**, 1544–1548 (2007).
36. S. J. Livingstone *et al*., *Nat. Rev. Earth Environ.* **3**, 106–124 (2022).
37. L. A. Stearns, B. E. Smith, G. S. Hamilton, *Nat. Geosci.* **1**, 827–831 (2008).
38. T. A. Scambos, E. Berthier, C. A. Shuman, *Ann. Glaciol.* **52**, 74–82 (2011).
39. M. R. Siegfried, H. A. Fricker, S. P. Carter, S. Tulaczyk, *Geophys. Res. Lett.* **43**, 2640–2648 (2016).
40. B. I. D. Freer *et al*., *J. Geophys. Res. Earth Surf.* **129**, e2024JF007724 (2024).
41. F. S. McCormack *et al*., *Cryosphere* **17**, 4549–4569 (2023).
42. C. D. Gustafson *et al*., *Science* **376**, 640–644 (2022).
43. A. A. Robel, S. J. Sim, C. Meyer, M. R. Siegfried, C. D. Gustafson, *Sci. Adv.* **9**, eadh3693 (2023).
44. E. Kazmierczak, S. Sun, V. Coulon, F. Pattyn, *Cryosphere* **16**, 4537–4552 (2022).
45. E. Kazmierczak, T. Gregov, V. Coulon, F. Pattyn, *Cryosphere* **18**, 5887–5911 (2024).
46. G. H. Gudmundsson, F. S. Paolo, S. Adusumilli, H. A. Fricker, *Geophys. Res. Lett.* **46**, 13903–13909 (2019).
47. J. J. Fürst *et al*., *Nat. Clim. Chang.* **6**, 479–482 (2016).
48. B. Smith *et al*., *Science* **368**, 1239–1242 (2020).
49. R. Reese, G. H. Gudmundsson, A. Levermann, R. Winkelmann, *Nat. Clim. Chang.* **8**, 53–57 (2018).
50. C. T. Wild *et al*., *Cryosphere* **16**, 397–417 (2022).
51. B. W. J. Miles, R. G. Bingham, *Nature* **626**, 785–791 (2024).
52. M. Braun, A. Humbert, A. Moll, *Cryosphere* **3**, 41–56 (2009).
53. S. Lhermitte *et al*., *Proc. Natl. Acad. Sci. U.S.A.* **117**, 24735–24741 (2020).
54. F. S. Paolo, H. A. Fricker, L. Padman, *Science* **348**, 327–331 (2015).
55. C. C. Walker *et al*., *Nat. Geosci.* **17**, 1240–1248 (2024).
56. T. Scambos, C. Hulbe, M. Fahnestock, in *Antarctic Peninsula Climate Variability: Historical and Paleoenvironmental Perspectives*, E. Domack *et al*., Eds., Antarctic Research Series, vol. 79 (American Geophysical Union, 2003), pp. 79–92.
57. M. S. Dinniman *et al*., *Oceanography* **29**, 144–153 (2016).
58. I. Vaňková *et al*., *Geophys. Res. Lett.* **50**, e2023GL102960 (2023).
59. M. G. Rosevear, B. Gayen, C. A. Vreugdenhil, B. K. Galton-Fenzi, *Annu. Rev. Mar. Sci.* **16**, 1–30 (2024).
60. A. K. Wåhlin *et al*., *Sci. Adv.* **7**, eabd7254 (2021).
61. B. E. Schmidt *et al*., *Nature* **614**, 471–478 (2023).
62. A. Dinh, E. Rignot, M. Mazloff, I. Fenty, *Geophys. Res. Lett.* **51**, e2024GL110078 (2024).
63. S. Adusumilli, H. A. Fricker, B. Medley, L. Padman, M. R. Siegfried, *Nat. Geosci.* **13**, 616–620 (2020).
64. B. K. Galton-Fenzi, J. R. Hunter, R. Coleman, S. J. Marsland, R. C. Warner, *J. Geophys. Res.* **117**, 2012JC008214 (2012).
65. B. Kulessa, D. Jansen, A. J. Luckman, E. C. King, P. R. Sammonds, *Nat. Commun.* **5**, 3707 (2014).
66. K. Lindbäck *et al*., *Cryosphere* **13**, 2579–2595 (2019).
67. C. L. Stewart, P. Christoffersen, K. W. Nicholls, M. J. M. Williams, J. A. Dowdeswell, *Nat. Geosci.* **12**, 435–440 (2019).
68. K. A. Naughten *et al*., *J. Clim.* **31**, 5243–5261 (2018).
69. D. E. Gwyther, C. F. Dow, S. Jendersie, N. Gourmelen, B. K. Galton-Fenzi, *Geophys. Res. Lett.* **50**, e2023GL103765 (2023).
70. A. Wåhlin *et al*., *Sci. Adv.* **10**, eadn9188 (2024).
71. K. W. Nicholls *et al*., *J. Glaciol.* **61**, 1079–1087 (2015).
72. I. Vaňková, K. W. Nicholls, H. F. J. Corr, K. Makinson, P. V. Brennan, *J. Geophys. Res. Earth Surf.* **125**, e2019JF005280 (2020).
73. S. Cook, K. W. Nicholls, I. Vaňková, S. S. Thompson, B. K. Galton-Fenzi, *Ann. Glaciol.* **63**, 27–32 (2022).
74. A. M. Chartrand, I. M. Howat, *J. Glaciol.* **69**, 1663–1676 (2023).
75. P. Milillo *et al*., *Nat. Geosci.* **15**, 48–53 (2022).
76. P. Milillo *et al*., *Sci. Adv.* **5**, eaau3433 (2019).
77. H. Chen, E. Rignot, B. Scheuchl, S. Ehrenfeucht, *Geophys. Res. Lett.* **50**, e2022GL102430 (2023).
78. E. Rignot *et al*., *Proc. Natl. Acad. Sci. U.S.A.* **121**, e2404766121 (2024).
79. B. I. D. Freer, O. J. Marsh, A. E. Hogg, H. A. Fricker, L. Padman, *Cryosphere* **17**, 4079–4101 (2023).
80. E. Rignot, *Nat. Clim. Chang.* **13**, 1010–1013 (2023).
81. E. Rignot, J. Mouginot, M. Morlighem, H. Seroussi, B. Scheuchl, *Geophys. Res. Lett.* **41**, 3502–3509 (2014).
82. T. Pelle, J. S. Greenbaum, C. F. Dow, A. Jenkins, M. Morlighem, *Sci. Adv.* **9**, eadi9014 (2023).
83. T. Pelle, J. S. Greenbaum, S. Ehrenfeucht, C. F. Dow, F. S. McCormack, *J. Geophys. Res. Earth Surf.* **129**, e2023JF007513 (2024).
84. E. A. Wilson, A. J. Wells, I. J. Hewitt, C. Cenedese, *J. Fluid Mech.* **895**, A20 (2020).
85. A. A. Robel, E. Wilson, H. Seroussi, *Cryosphere* **16**, 451–469 (2022).
86. B. R. Parizek *et al*., *J. Geophys. Res. Earth Surf.* **118**, 638–655 (2013).
87. R. T. Walker *et al*., *Earth Planet. Sci. Lett.* **361**, 422–428 (2013).
88. H. Seroussi, M. Morlighem, *Cryosphere* **12**, 3085–3096 (2018).
89. A. T. Bradley, I. J. Hewitt, *Nat. Geosci.* **17**, 631–637 (2024).
90. Y. Wang *et al*., *Cryosphere* **18**, 5117–5137 (2024).
91. K. Christianson *et al*., *Geophys. Res. Lett.* **40**, 5406–5411 (2013).
92. L. M. Simkins, S. L. Greenwood, J. B. Anderson, *Cryosphere* **12**, 2707–2726 (2018).
93. C. L. Batchelor, J. A. Dowdeswell, *Mar. Geol.* **363**, 65–92 (2015).
94. R. B. Alley, S. Anandakrishnan, T. K. Dupont, B. R. Parizek, D. Pollard, *Science* **315**, 1838–1841 (2007).
95. A. G. C. Graham *et al*., *Nat. Geosci.* **15**, 706–713 (2022).
96. C. L. Batchelor *et al*., *Nature* **617**, 105–110 (2023).
97. M. Jakobsson *et al*., *Geology* **39**, 691–694 (2011).
98. C. L. Parkinson, D. J. Cavalieri, *Cryosphere* **6**, 871–880 (2012).
99. D. K. Perovich *et al*., *Geophys. Res. Lett.* **34**, 2007GL031480 (2007).
100. S. E. Stammerjohn, D. G. Martinson, R. C. Smith, X. Yuan, D. Rind, *J. Geophys. Res. Oceans* **113**, C03S90 (2008).
101. C. A. Greene, D. A. Young, D. E. Gwyther, B. K. Galton-Fenzi, D. D. Blankenship, *Cryosphere* **12**, 2869–2882 (2018).
102. M. Haigh, P. R. Holland, *Geophys. Res. Lett.* **51**, e2024GL108406 (2024).
103. A. Silvano *et al*., *Sci. Adv.* **4**, eaap9467 (2018).
104. N. S. Steiner *et al*., *Elementa* **9**, 00007 (2021).
105. A. Purich, E. W. Doddridge, *Commun. Earth Environ.* **4**, 314 (2023).
106. P. A. Reid, R. A. Massom, *Nat. Commun.* **13**, 1164 (2022).
107. E. Gilbert, C. Holmes, *Weather* **79**, 46–51 (2024).
108. S. Aoki *et al*., *Commun. Earth Environ.* **3**, 142 (2022).
109. A. Duspayev, M. G. Flanner, A. Riihelä, *Geophys. Res. Lett.* **51**, e2024GL109608 (2024).
110. O. Schofield *et al*., *Trends Ecol. Evol.* **39**, 1141–1153 (2024).
111. S. Kacimi, R. Kwok, *Cryosphere* **14**, 4453–4474 (2020).
112. M. Ionita, *Front. Earth Sci.* **12**, 1333706 (2024).
113. J. Weertman, *J. Glaciol.* **13**, 3–11 (1974).
114. C. Schoof, *J. Fluid Mech.* **573**, 27–55 (2007).
115. I. Joughin, B. E. Smith, B. Medley, *Science* **344**, 735–738 (2014).
116. E. A. Hill *et al*., *Cryosphere* **17**, 3739–3759 (2023).
117. R. Reese *et al*., *Cryosphere* **17**, 3761–3783 (2023).
118. M. Mengel, A. Levermann, *Nat. Clim. Chang.* **4**, 451–455 (2014).
119. T. Pelle, M. Morlighem, F. S. McCormack, *Geophys. Res. Lett.* **47**, e2019GL086821 (2020).
120. J. N. Bassis, C. C. Walker, *Proc. R Soc. A* **468**, 913–931 (2011).
121. R. M. DeConto, D. Pollard, *Nature* **531**, 591–597 (2016).
122. C. Needell, N. Holschuh, *Geophys. Res. Lett.* **50**, e2022GL102400 (2023).
123. I. Joughin, D. E. Shean, B. E. Smith, D. Floricioiu, *Cryosphere* **14**, 211–227 (2020).
124. M. G. Wise, J. A. Dowdeswell, M. Jakobsson, R. D. Larter, *Nature* **550**, 506–510 (2017).
125. T. L. Edwards *et al*., *Nature* **566**, 58–64 (2019).
126. F. Clerc, B. Minchew, M. Behn, *Geophys. Res. Lett.* **46**, 12108–12116 (2019).
127. J. N. Bassis, B. Berg, A. J. Crawford, D. I. Benn, *Science* **372**, 1342–1344 (2021).
128. M. Morlighem *et al*., *Sci. Adv.* **10**, eado7794 (2024).
129. R. B. Alley *et al*., *Annu. Rev. Earth Planet. Sci.* **51**, 189–215 (2023).
130. J. N. Bassis *et al*., *Annu. Rev. Earth Planet. Sci.* **52**, 221–247 (2024).
131. B. R. Parizek *et al*., *Geology* **47**, 449–452 (2019).
132. A. J. Crawford *et al*., *Nat. Commun.* **12**, 2701 (2021).
133. A. T. Bradley, D. T. Bett, P. Dutrieux, J. De Rydt, P. R. Holland, *J. Geophys. Res. Oceans* **127**, e2022JC018621 (2022).
134. M. Poinelli, Y. Nakayama, E. Larour, M. Vizcaino, R. Riva, *Geophys. Res. Lett.* **50**, e2023GL104588 (2023).
135. K. E. Alley, T. A. Scambos, R. B. Alley, *Ann. Glaciol.* **63**, 18–22 (2022).
136. C.-Y. Lai *et al*., *Nature* **584**, 574–578 (2020).
137. J. A. MacGregor, G. A. Catania, M. S. Markowski, A. G. Andrews, *J. Glaciol.* **58**, 458–466 (2012).
138. S. Wang *et al*., *J. Geophys. Res. Earth Surf.* **127**, e2021JF006346 (2022).
139. I. Joughin, D. Shapero, B. Smith, P. Dutrieux, M. Barham, *Sci. Adv.* **7**, eabg3080 (2021).
140. N. Gomez *et al*., *Sci. Adv.* **10**, eadn1470 (2024).
141. V. R. Barletta *et al*., *Science* **360**, 1335–1339 (2018).
142. P. St-Laurent, S. E. Stammerjohn, T. Maksym, *J. Geophys. Res. Oceans* **129**, e2023JC020467 (2024).
143. T. Surawy-Stepney *et al*., *Cryosphere* **18**, 977–993 (2024).
144. R. A. Massom *et al*., *Nature* **558**, 383–389 (2018).
145. N. J. Teder, L. G. Bennetts, P. A. Reid, R. A. Massom, *Environ. Res. Lett.* **17**, 045026 (2022).
146. K. Brunt, E. Okal, D. MacAyeal, *J. Glaciol.* **57**, 785–788 (2011).
147. C. C. Walker, J. N. Bassis, H. A. Fricker, R. J. Czerwinski, *J. Geophys. Res. Earth Surf.* **118**, 2354–2364 (2013).
148. M. K. Becker *et al*., *Geophys. Res. Lett.* **48**, e2020GL091207 (2021).
149. C. A. Greene, A. S. Gardner, N.-J. Schlegel, A. D. Fraser, *Nature* **609**, 948–953 (2022).
150. A. D. Fraser *et al*., *Rev. Geophys.* **61**, e2022RG000770 (2023).
151. G. Van Achter *et al*., *Ocean Model.* **169**, 101920 (2022).
152. E. A. Cougnon *et al*., *Geophys. Res. Lett.* **44**, 11519–11527 (2017).
153. M. F. Huguenin, R. M. Holmes, P. Spence, M. H. England, *Geophys. Res. Lett.* **51**, e2023GL104518 (2024).
154. R. J. Matear, T. J. O'Kane, J. S. Risbey, M. Chamberlain, *Nat. Commun.* **6**, 8656 (2015).
155. J. M. A. Macha *et al*., *Geophys. Res. Lett.* **51**, e2024GL109423 (2024).
156. F. S. Paolo *et al*., *Nat. Geosci.* **11**, 121–126 (2018).
157. M. A. King, P. Christoffersen, *Geophys. Res. Lett.* **51**, e2024GL108844 (2024).
158. H. H. Hellmer, F. Kauker, R. Timmermann, T. Hattermann, *J. Clim.* **30**, 4337–4350 (2017).
159. J. Jin, A. J. Payne, C. Y. S. Bull, EGUsphere egusphere-2024-1287 [Preprint] (2024); https://doi.org/10.5194/egusphere-2024-1287.
160. K. A. Naughten *et al*., *Nat. Commun.* **12**, 1991 (2021).
161. B. J. Wallis *et al*., *Nat. Commun.* **14**, 7535 (2023).
162. A. Shepherd, H. A. Fricker, S. L. Farrell, *Nature* **558**, 223–232 (2018).
163. T. Slater *et al*., *Cryosphere* **15**, 233–246 (2021).
164. V. Brancato *et al*., *Geophys. Res. Lett.* **47**, e2019GL086291 (2020).
165. B. W. J. Miles, C. R. Stokes, S. S. R. Jamieson, *Cryosphere* **12**, 3123–3136 (2018).
166. H. J. Picton, C. R. Stokes, S. S. R. Jamieson, D. Floricioiu, L. Krieger, *Cryosphere* **17**, 3593–3616 (2023).
167. S. S. Thompson *et al*., *Cryosphere* **17**, 157–174 (2023).
168. R. Li *et al*., *Nat. Commun.* **14**, 4061 (2023).
169. B. W. J. Miles *et al*., *Cryosphere* **15**, 663–676 (2021).
170. B. J. Davison *et al*., *Nat. Commun.* **14**, 1479 (2023).
171. S. Adusumilli, M. A. Fish, H. A. Fricker, B. Medley, *Geophys. Res. Lett.* **48**, e2020GL091076 (2021).
172. L. Barthélemy, F. Codron, V. Favier, J. Wille, Authorea 171387374.47240076/v1 [Preprint] (2024); https://doi.org/10.22541/au.171387374.47240076/v1.
173. S. Adusumilli, H. A. Fricker, A. S. Gardner, in *State of the Climate in 2022: Antarctica and the Southern Ocean*, K. R. Clem, M. N. Raphael, Eds. (American Meteorological Society, 2023).
174. J. D. Wille *et al*., *J. Clim.* **37**, 757–778 (2024).
175. S. Jeong, I. M. Howat, J. N. Bassis, *Geophys. Res. Lett.* **43**, 11,720–11,725 (2016).

176. B. W. J. Miles *et al*., *J. Glaciol.* **66**, 485–495 (2020).
177. K. E. Alley *et al*., *Cryosphere* **15**, 5187–5203 (2021).
178. J. N. Bassis, H. A. Fricker, R. Coleman, J. B. Minster, *J. Glaciol.* **54**, 17–27 (2008).
179. C. C. Walker, J. N. Bassis, H. A. Fricker, R. J. Czerwinski, *J. Glaciol.* **61**, 243–252 (2015).
180. B. P. Lipovsky, *J. Geophys. Res. Oceans* **123**, 4014–4033 (2018).
181. D. Francis, K. S. Mattingly, S. Lhermitte, M. Temimi, P. Heil, *Cryosphere* **15**, 2147–2165 (2021).
182. E. Larour, E. Rignot, M. Poinelli, B. Scheuchl, *Proc. Natl. Acad. Sci. U.S.A.* **118**, e2105080118 (2021).
183. H. Seroussi *et al*., *Geophys. Res. Lett.* **44**, 6191–6199 (2017).
184. D. I. Benn *et al*., *Cryosphere* **16**, 2545–2564 (2022).
185. E. Rignot, *Philos. Trans. R. Soc. Ser. A* **364**, 1637–1655 (2006).
186. B. W. J. Miles, C. R. Stokes, S. S. R. Jamieson, *Sci. Adv.* **2**, e1501350 (2016).
187. T. Li, G. J. Dawson, S. J. Chuter, J. L. Bamber, *Cryosphere* **17**, 1003–1022 (2023).
188. N. Ribeiro *et al*., *J. Geophys. Res. Oceans* **128**, e2023JC019882 (2023).
189. S. Cook, B. K. Galton-Fenzi, S. R. M. Ligtenberg, R. Coleman, *Cryosphere* **12**, 3853–3859 (2018).
190. R. Minunno, N. Andersson, G. M. Morrison, *Earth Sci. Rev.* **241**, 104431 (2023).
191. D. R. Macayeal, K. Mankoff, B. Minchew, J. Moore, M. Wolovick, Glacial climate intervention: A research vision, Version 2, U.S. Antarctic Program Data Center (USAP-DC) (2024); https://doi.org/10.15784/601797.
192. B. Keefer, M. Wolovick, J. C. Moore, *PNAS Nexus* **2**, pgad053 (2023).
193. A. Alevropoulos-Borrill, N. R. Golledge, S. L. Cornford, D. P. Lowry, M. Krapp, *Commun. Earth Environ.* **5**, 150 (2024).
194. Ö. Gürses, V. Kolatschek, Q. Wang, C. B. Rodehacke, *Cryosphere* **13**, 2317–2324 (2019).
195. M. Siegert *et al*., ResearchGate 10.13140/RG.2.2.13179.94246 [Preprint] (2024); https://doi.org/10.13140/RG.2.2.13179.94246.
196. A. K. Klose, V. Coulon, F. Pattyn, R. Winkelmann, *Cryosphere* **18**, 4463–4492 (2024).
197. K. A. Naughten, P. R. Holland, J. De Rydt, *Nat. Clim. Chang.* **13**, 1222–1228 (2023).
198. J. Garbe, T. Albrecht, A. Levermann, J. F. Donges, R. Winkelmann, *Nature* **585**, 538–544 (2020).
199. D. Li, R. M. DeConto, D. Pollard, Y. Hu, *Nat. Commun.* **15**, 5178 (2024).
200. S. Sadai, A. Condron, R. DeConto, D. Pollard, *Sci. Adv.* **6**, eaaz1169 (2020).
201. A. Shepherd *et al*., Antarctic and Greenland Ice Sheet mass balance 1992-2020 for IPCC AR6, Version 1.0, UK Polar Data Centre, Natural Environment Research Council, UK Research and Innovation (2021); https://doi.org/10.5285/77B64C55-7166-4A06-9DEF-2E400398E452.
202. L. A. Magruder *et al*., *Nat. Rev. Earth Environ.* **5**, 120–136 (2024).
203. J. Kingslake, J. C. Ely, I. Das, R. E. Bell, *Nature* **544**, 349–352 (2017).
204. T. Hattermann, L. H. Smedsrud, O. A. Nøst, J. M. Lilly, B. K. Galton-Fenzi, *Ocean Model.* **82**, 28–44 (2014).

ACKNOWLEDGMENTS

We thank the World Climate Research Programme Climate and Cryosphere Project (CliC) for coordinating this special issue, the EDGE Science Team for inspiration, and two reviewers whose comments substantially improved this paper. **Funding:** This work was funded by Eric and Wendy Schmidt (H.A.F.), NASA Cryospheric Sciences grant 80NSSC23K0934 (H.A.F.), the Australian Government by the Antarctic Science Collaboration Initiative Program (ASCI000002) (B.K.G.-F.), the Australian Research Council Special Research Initiative, the Australian Centre for Excellence in Antarctic Science (SR200100008), NASA Cryospheric Sciences grant 80NSSC22K0380 (C.C.W.), NASA Physical Oceanography grant 80NSSC23K0356 (C.C.W.), the Natural Environment Research Council (NERC) Satellite Data in Environmental Science (SENSE) Centre for Doctoral Training (NE/T00939X/1) (B.I.D.F.), a Schmidt AI Postdoctoral Fellowship (B.I.D.F.), NASA Cryospheric Sciences grants 80NSSC21K0911 and 80NSSC24K1029 (L.P.), the National Science Foundation (2213875 and 2035080) (R.D.), and NASA Cryospheric Sciences grant 80NSSC22K1707 (R.D.). **Competing interests:** The authors declare that they have no competing interests.

Submitted 19 October 2024; accepted 3 January 2025
10.1126/science.adt9619

REVIEW

Advances and shortfalls in knowledge of Antarctic terrestrial and freshwater biodiversity

L. R. Pertierra[1,2,3,4]*, P. Convey[3,5,6], A. Barbosa[7]†, E. M. Biersma[8], D. Cowan[9], J. A. F. Diniz-Filho[10,11], A. de los Ríos[12], P. Escribano-Álvarez[1], C. I. Fraser[13], D. Fontaneto[14,15], M. Greve[2], H. J. Griffiths[5], M. Harris[2], K. A. Hughes[5], H. J. Lynch[16], R. J. Ladle[11,17], X. P. Liu[13], P. C. le Roux[2], R. Majewska[18,19], M. A. Molina-Montenegro[20], L. S. Peck[5], A. Quesada[21], C. Ronquillo[4], Y. Ropert-Coudert[22], L. G. Sancho[23], A. Terauds[24,25], G. Varliero[9,26], J. A. Vianna[3,27,28], A. Wilmotte[29], S. L. Chown[30], M. Á. Olalla-Tárraga[1], J. Hortal[4,11]

Antarctica harbors many distinctive features of life, yet much about the diversity and functioning of Antarctica's life remains unknown. Evolutionary histories and functional ecology are well understood only for vertebrates, whereas research on invertebrates is largely limited to species descriptions and some studies on environmental tolerances. Knowledge on Antarctic vegetation cover showcases the challenges of characterizing population trends for most groups. Recent community-level microbial studies have provided insights into the functioning of life at its limits. Overall, biotic interactions remain largely unknown across all groups, restricted to basic information on trophic level placement. Insufficient knowledge of many groups limits the understanding of ecological processes on the continent. Remedies for the current situation rely on identifying the caveats of each ecological discipline and finding targeted solutions. Such precise delimitation of knowledge gaps will enable a more aware, representative, and strategic systematic conservation planning of Antarctica.

Antarctica, one of Earth's last great wildernesses, harbors singular and underappreciated biodiversity (*1*). In just two centuries of exploration, research on Antarctic ecosystems has generated critical insights into the evolution and functioning of biodiversity at the cold, nutrient-deficient, and dry limits to life on Earth (*2*, *3*). Antarctic ecosystems provide vital services (*4*), including modulating global oceanic and atmospheric systems, and the continent is a bellwether of the planet's climate state, given its rapid transformation and its global connections and impacts (*5*).

Antarctic terrestrial biodiversity faces considerable threats from global environmental change and human pressures, including wildlife disturbance and invasive alien species (*6*, *7*). Its isolation, extreme conditions, and comparatively low disturbance levels (*1*) make Antarctica a key sentinel for global change (*4*). In recent decades, extensive international research cooperation has led to breakthroughs in understanding of Antarctic biodiversity, overturning previous paradigms of evolutionary patterns and processes across biological scales (*8*, *9*). The coexistence of several national biological research programs studying the relatively low diversity of the continent make the inventory of Antarctic organisms more complete than in many other regions (Fig. 1). Despite such considerable funding, scientific progress has been uneven, with research biased toward mainstream fields of study, focusing on the most accessible or charismatic species (*10*). Substantial knowledge gaps remain, particularly with regard to complex functions and remote and cryptic ecosystems and species (*11*). Early syntheses of available knowledge of Antarctic biodiversity have, however, largely

---

[1]Departamento de Biología, Geología, Física y Química Inorgánica, Universidad Rey Juan Carlos, Mostoles, Spain. [2]Department of Plant and Soil Sciences, University of Pretoria, Pretoria, South Africa. [3]Millennium Institute of Biodiversity of Antarctic and sub-Antarctic Ecosystems (BASE), Santiago, Chile. [4]Department of Biogeography and Global Change, Museo Nacional de Ciencias Naturales (MNCN-CSIC), Madrid, Spain. [5]British Antarctic Survey, Cambridge, UK. [6]Department of Zoology, University of Johannesburg, Johannesburg, South Africa. [7]Departamento de Ecología Evolutiva, Museo Nacional de Ciencias Naturales, MNCN-CSIC, Madrid, Spain. [8]Natural History Museum of Denmark, University of Copenhagen, Copenhagen, Denmark. [9]Centre for Microbial Ecology and Genomics, Department of Biochemistry, Genetics and Microbiology, University of Pretoria, Pretoria, South Africa. [10]Departamento de Ecologia, Instituto de Ciências Biológicas, Universidade Federal de Goiás, Goiânia, Brazil. [11]National Institute for Science and Technology in Ecology, Evolution, and Biodiversity Conservation (INCT EECBio), Universidade Federal de Goiás, Goiânia, Brazil. [12]Departamento de Biogeoquimica y Ecologia Microbiana, Museo Nacional de Ciencias Naturales, MNCN-CSIC, Madrid, Spain. [13]Department of Marine Science, University of Otago, Dunedin, New Zealand. [14]Natural Research Council, Water Research Institute (CNR-IRSA), Verbania, Italy. [15]National Biodiversity Future Center (NBFC), Palermo, Italy. [16]Department of Ecology and Evolution, Stony Brook University, Stony Brook, New York, USA. [17]Institute of Biological and Health Sciences, Federal University of Alagoas, Maceió, Brazil. [18]Faculty of Biosciences and Aquaculture, Nord University, Bodø, Norway. [19]Unit for Environmental Sciences and Management, North-West University, Potchefstroom, South Africa. [20]Instituto de Ciencias Biológicas, Universidad de Talca, Talca, Chile. [21]Departamento de Biologia, Universidad Autónoma de Madrid, Cantoblanco, Spain. [22]Centre d'Etudes Biologiques de Chizé, La Rochelle Université, Villiers-en-Bois, France. [23]Departamento de Biologia Vegetal II, Universidad Complutense de Madrid, Madrid, Spain. [24]Australian Antarctic Division, Department of Climate Change, Energy, the Environment and Water, Kingston, TAS, Australia. [25]Securing Antarctica's Environmental Future, Queensland University of Technology, Brisbane, QLD, Australia. [26]Rhizosphere Processes Group, Swiss Federal Research Institute WSL, Birmensdorf, Switzerland. [27]Faculty of Biological Sciences, Pontificia Universidad Católica de Chile, Santiago, Chile. [28]Millennium Institute Center for Genome Regulation, Santiago, Chile. [29]Bios Research Unit, University of Liège, Liège, Belgium. [30]Securing Antarctica's Environmental Future, Monash University, Melbourne, VIC, Australia.
***Corresponding author. Email: luis.rpertierra@mncn.csic.es**
†Deceased.

overlooked the substantial biases resulting from shortcomings in understanding the continent's ecological dynamics (*12*), critically limiting the development of effective conservation efforts (*13*). This underscores the need for a more informed account of recent advances, gaps, and biases in biodiversity knowledge to guide future research and conservation investments (*14*). In this analytical review, we provide a comprehensive assessment of the state of knowledge of all terrestrial biodiversity in Antarctica [see materials and methods (*15*) and supporting data files (*16*)]. We compiled all records on Antarctic species identities into TerrANTALife, a database covering all terrestrial and freshwater eukaryotic species and amplicon sequence variants of prokaryotes (*9*, *17*) of the continent. Data coverage was evaluated through discovery rates and spatial distribution of survey completeness for spatiotemporal occurrence data and using major global repositories (*18*–*22*) for mapping out coverage of other aspects of biodiversity (Fig. 2). We classify knowledge limitations (hereafter, "shortfalls") into basic areas of ecological and evolutionary research (*14*): (i) species inventory; (ii) evolution of Antarctic life; species' (iii) spatial and (iv) temporal dynamics; trait-based (v) environmental tolerances and (vi) ecosystem functions; and (vii) biotic interactions. We assess the severity of these knowledge shortfalls relative to the scientific and conservation value of the missing information. Policies that account for uncertainty and knowledge gaps are better suited to advance scientific research and conservation practice under the Antarctic Treaty System (*13*, *23*). Lastly, the current state of ecological knowledge was assessed by a panel of Antarctic biodiversity experts through an IDEA (investigate, discuss, estimate, and aggregate) elicitation process (*24*) (Fig. 3).

Advances in describing Antarctic biodiversity and evolution

About 2100 terrestrial eukaryotic species have been identified from Antarctica, including nearly 1000 fungi (half of them lichen-forming), >400 animals, 300 plants, and >400 SAR/protists (such as stramenopiles, alveolates, rizarians, and other unrelated unicellular organisms including amoebae) (*17*). For most groups, more than half of the known Antarctic species have been discovered in the past 50 years (Fig. 1), partly driven by the growth in Antarctic research after the International Geophysical Year (1957–1958) and the International Polar Year (2007–2008) scientific campaigns. Many endemic species, especially prokaryotes, remain undiscovered (*25*). Limited species descriptions for all major groups and underexplored regions reveal considerable potential for further discoveries (Fig. 1). Comprehensive inventories are essential for effective area protection and threat assessment (*13*, *26*) and, indirectly, for safeguarding future bioprospecting potential.

Knowledge of animal diversity varies widely (*27*), from comprehensive vertebrate inventories to moderately complete checklists for invertebrates such as microarthropods, other soil and freshwater microinvertebrates, and ecto- and endoparasites (Fig. 1). Knowledge of ancestry and phylogenetic relationships is, however, limited to a few species, mostly of megafauna

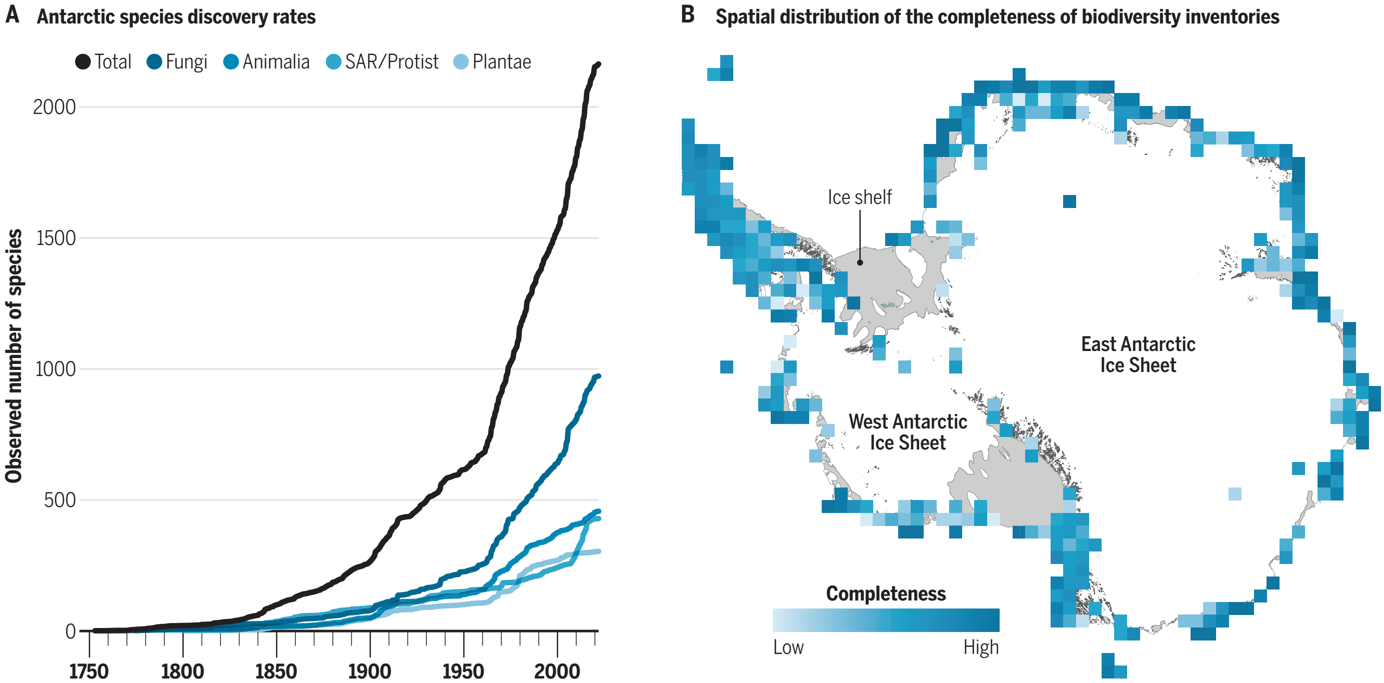

Fig. 1. Spatial and temporal process of inventory of the terrestrial Antarctic biota. (**A**) Historical discovery rates of species that are present in terrestrial and freshwater ecosystems of Antarctica. Curves indicate the total number of species inventoried through time for the four eukaryotic kingdoms (sensu lato): Animalia, Fungi, Plantae, and SAR/protist (including stramenopiles, alveolates, rizarians, and other unrelated unicellulars such amoaebas). The curated list of 2193 known eukaryotic species analyzed here (*15*, *16*) was compiled in (*17*). For all these species, the year of first discovery and description in Antarctica, together with the first description worldwide (for species present on other continents), were taken from global metarepositories (*18*, *26*). (**B**) Survey completeness indicates how well the local species composition is characterized by the available occurrence data [supporting files 3 and 4 (*16*)]. It is calculated as the slope of the relationship between survey effort—measured as number of occurrence records—and the number of new species added to the local inventory. High completeness indicates slope values close to 0 (i.e., no new species are recorded with extra surveys), whereas progressively lower completeness values indicate progressively higher current rates of addition of new species to the local inventory with new surveys. Completeness was calculated with *KnowBR* (*53*) for local inventories at a grid size of 50 km by 50 km, randomizing the order of entrance of new records in each cell to account for temporal unevenness in survey effort. Occurrence records for all the Antarctic eukaryotic terrestrial species were retrieved first from the GBIF repository. This dataset was complemented with Wauchope *et al.*'s (*26*) compilation of additional records from scientific literature and technical reports such as protected area management plans, which is available at the Australian Antarctic Data Centre (*121*).

CREDIT: ADAPTED BY V. PENNEY/*SCIENCE*

(Figs. 2 and 3). Expanding molecular studies to microarthropods and other microinvertebrates has revealed previously unknown species and inferred species-level divergences in mites (*28*), springtails (*29*), tardigrades (*30*), nematodes (*31*), and rotifers (*32*), although species counts remain uncertain for parasites, gastrotrichs, and flatworms. With a limited fossil record, diversification patterns can be alternatively inferred from population genetics and time-calibrated phylogenies on the basis of non-Antarctic lineages (*33*, *34*). Although marine vertebrates breeding on land are relatively well studied, there are major gaps in knowledge about their speciation (*35*) and hybridization (*36*) processes.

Knowledge of floral diversity is generally adequate for the two native vascular plant species (Antarctic hair grass, *Deschampsia antarctica*, and Antarctic pearlwort, *Colobanthus quitensis*) and the greater diversity of bryophytes and lichen-forming fungi (Fig. 2 and fig. S1). In contrast, knowledge of free-living microalgal and fungal groups is poorer, with further taxonomic progress expected from molecular analyses. Molecular and phylogeographic tools have clarified relationships among plant populations and some dispersal dynamics. Although the phylogeography of some Antarctic plants has been assessed phylogenetically in depth (*37*), most Antarctic flora has yet to be studied with molecular methods. Similarly, comprehensive phylogenetic and phylogeographic studies are limited to a few lichen genera [e.g., (*38*, *39*)].

Antarctic microorganisms are, in general, poorly known across all groups, from algae and other protists to fungi to bacteria, archaea, and viruses (Fig. 3). Nevertheless, increased surveys coupled with molecular techniques have uncovered a rich cryptic diversity often hiding in plain sight (*40*). Knowledge of the molecular diversity of snow algae (*41*) and freshwater algae is limited, although a diatom compendium is now available (*42*). Comprehensive surveys of autotrophic microorganisms are restricted to a few regions of terrestrial Antarctica, such as the McMurdo Dry Valleys, with estimates suggesting that more than half of the species remain undescribed [e.g., Cyanophyta (*43*)]. In contrast, heterotrophic protists are better known, although total species numbers are uncertain (*44*). Considerable information gaps remain for other unicellular Eukaryota, such as yeasts (*45*). Broad characterizations of microbial metacommunities in regions such as Victoria Land (*46*) have identified >80,000 bacterial amplicon sequence variants for the continent (*17*). Although inventorying microbial diversity in subglacial and endoglacial environments and the atmosphere entails specific technological challenges, there have been many notable discoveries of life surviving at extreme habitats in recent years (*47*–*49*). Finally, knowledge of virus diversity remains extremely poor, albeit a few highly localized surveys in freshwater and soil systems have identified at least 10,000 genotypes across virus families [e.g., (*50*, *51*)]. Thus, viruses represent the last frontier of Antarctic diversity.

CREDIT: ADAPTED BY A. MASTIN AND N. CARY/*SCIENCE*

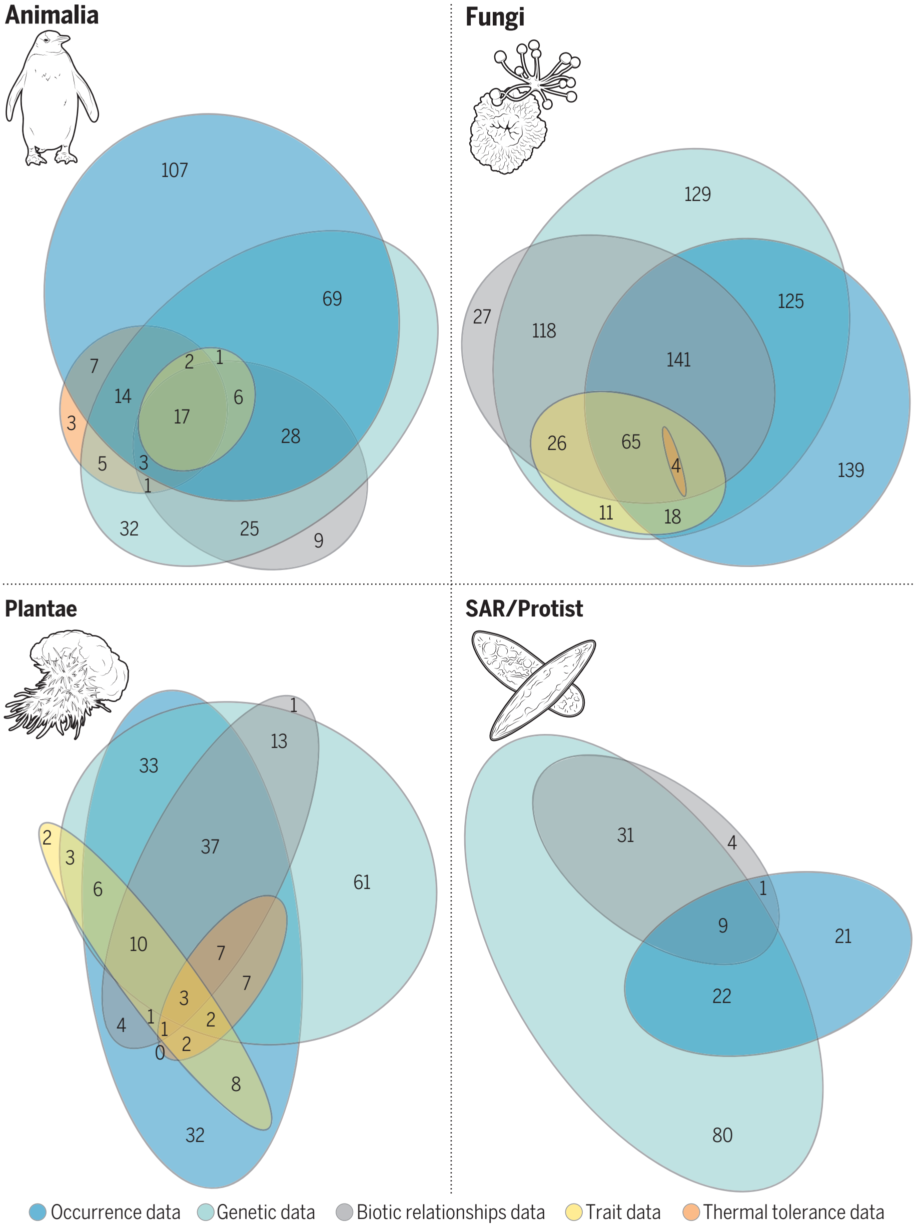

Fig. 2. Cross-availability of data on different ecological and evolutionary aspects per species for all Antarctic eukaryotes. Venn diagrams depicting cross-availability of ecological and evolutionary data for all Antarctic species within each of the four eukaryote kingdoms, measured as counts of species with data entries in centralized metarepositories representative of five disciplines (*15*, *16*). The disciplines represented and their indicators are: (i) geographic distribution knowledge, georeferenced GBIF occurrence records (*18*); (ii) evolutionary knowledge, genome sequences deposited in GenBank (*19*); (iii) functional traits knowledge, measured trait info availability in either EltonTraits (*122*) for fauna or Plant Traits Database (TRY) (*21*) for flora; (iv) abiotic tolerance knowledge, profiling of thermal limits gathered in the Globtherm dataset (*22*), expanded with Antarctic literature; and (v) biotic relationships knowledge, between-species interactions listed in the Global Biotic Interactions (GloBI) database (*20*).

Advances in mapping the spatiotemporal dynamics of Antarctic biota

Surveys of terrestrial biodiversity in Antarctica have been uneven in both space and time (*52*). Inference methods accounting for survey effort (*53*) show that biodiversity inventories remain poor for many areas (Fig. 1B). Georeferenced species occurrence records on the Global Biodiversity Information Facility (GBIF) metarepository vary widely between taxonomic groups (Fig. 2 and fig. S2). Nonetheless, GBIF mobilizes occurrence records for many species that are little known in most other respects (*18*). Relatedly, species distributions modeling has been widely used to assess the risk of invasive species expansion [e.g., (*54*)] but has seldom been applied to native species distributions, in contrast to the Southern Ocean marine biota.

Repeated surveys and monitoring programs are absent for most groups and regions. Long-term fauna and vegetation trend data exist for very few locations (Argentine Islands, Signy Island, Bailey Peninsula, and Cape Hallett), where surveys have been sporadically repeated over the course of 30 to 60 years without any planned program [e.g., (*55*, *56*)]. Experts identified substantial gaps in knowledge of population trends across almost all major Antarctic biodiversity groups (Fig. 3). However, decade-long multitaxa monitoring stations recently set up in areas such as the Victoria Land Dry Valleys are starting to offer insights into local ecosystem dynamics (*57*). Expanding this approach is promising but faces the critical challenge of a lack of long-term funding for maintaining such monitoring stations.

Large vertebrates illustrate the value of long-term research. Dynamic population trend studies across species ranges have been consolidated for many breeding vertebrates, such as in the Mapping Application for Penguin Populations and Projected Dynamics series (*58*). These data reveal increasing abundance of some penguin species (e.g., *Pygoscelis papua*) and declines in others (*P. antarctica*). Satellite imagery and repeated surveys of breeding colonies enable comprehensive mapping of seabird or seal species [e.g., (*59*)]. For several seals, penguins, and other seabirds, robust data exist on population ecology aspects such as predator-prey dynamics (*60*) or breeding phenology (*61*).

In contrast, knowledge of spatiotemporal patterns of Antarctic invertebrates ranges from moderate to poor (Fig. 3). Biogeographic studies remain scarce but with some notorious exceptions establishing regional population ancestry and paleobiogeographic inferences in groups such as Collembola (*62*) with even some species-specific, large-scale studies (*29*). Nematodes lack even preliminary species inventories for the continent, hampering phylogeographic analyses [but see (*31*)]. Studies of invertebrate population dynamics are largely restricted to describing life cycles and biodemographic rates [e.g., in tardigrades (*63*) and nematodes (*64*)]. Interannual abundance and population trends of native soil microarthropods remain poorly studied, with very few studies on temporal population dynamics (*56*).

Data mobilization is high for the Antarctic flora (Fig. 2), albeit knowledge about spatiotemporal patterns of plants and fungi is moderate (Fig. 3). Detailed ground surveys have enabled assessment of population trends for vascular plants and some mosses in maritime Antarctica, including the rapid expansion of vascular plants in Signy Island during the past decade, linked to regional warming (*65*). The non-native grass *Poa annua*, introduced to Thomas Point, King George Island, in the 1980s, has spread widely and with increasing speed since, with a resilient soil seedbank that has hampered eradication (*66*). Remote systems such as drones and satellite imagery are advancing vegetation mapping on the continent (*67*). Rapid shifts in moss and lichen populations have been detected but are generally monitored, with notable exceptions, only for a few groups and locations, such as East Antarctica (*68*). Albeit restricted, studies of lichen community dynamics show that this group may be particularly sensitive to climate change (*69*), and surveys in remote regions such as Shackleton Glacier (~87°S) offer future opportunities for range-shift monitoring (*70*, *71*).

Knowledge on microbiome spatiotemporal patterns lags behind that of flora and fauna (Fig. 3). Nonetheless, remote sensing mapping of the total extent of green snow algae in the Antarctic Peninsula offers a promising way forward (*72*). Moreover, biogeographic regionalizations of diatoms and cyanobacteria indicate high endemism and well-defined bioregions within Antarctica (*42*, *73*). Some local-scale studies of biological soil crusts provide estimates of algal growth, which may serve as proxies for the terrestrial Cyanophyta biomass (*74*). Techniques such as environmental DNA metabarcoding are rapidly advancing the understandig of soil microbial diversity spatiotemporal variations, offering novel insights on the structure and temporal trends of microorganism comunities across environmental gradients (*75*).

Advances in characterizing functional traits and abiotic tolerances

All Antarctic taxa face severe knowledge gaps with regard to functional traits, their variability, and, above all, their ecological significance in extreme environments (Figs. 2 and 3 and fig. S3). Basic knowledge about the functional strategies and trait-function relationships of Antarctic primary producers is still required to understand their adaptations, and the lack of systematic trait inventories prevents comparison with organisms from other regions. The apparently high number of Antarctic species with substantial functional trait data is misleading, as it is limited to certain characteristics of a few plant and animal groups (Fig. 3). Most studies of environmental tolerances have focused on responses to low temperatures, regional climate change, and ozone layer depletion (*7*). Without accurate information on species across space and time, which is lacking for many groups (Fig. 3), it is impossible to understand how traits such as temperature tolerance vary within communities among seasons and geographic locations. These knowledge gaps hinder conservation, as traits can predict species' responses to environmental change, and inform bioprospecting, for example, by identifying previously unknown molecules of pharmacological importance.

The most detailed functional trait information available is for breeding vertebrates, particularly about the physiology, reproduction, and foraging strategies of penguins and seals (*76*, *77*). However, ethical constraints make characterizing abiotic stress tolerances in vertebrates challenging, thus requiring researchers to rely on correlative niche modeling and adaptive genomic studies to infer their responses to environmental change (*78*).

Virtually no trait information is available for many invertebrate groups, with the notable exceptions of cold and desiccation tolerance strategies studied for a handful of model arthropods such as the mite *Alaskozetes antarcticus*, the springtail *Cryptopygus antarcticus*, and the dipterans *Belgica antarctica* and *Parochlus steinenii* (*79*, *80*). In nonarthropod microinvertebrates, functional studies also focus on abiotic stress tolerance, including cold and desiccation tolerance, as well as other edaphic factors such as salinity [e.g., nematodes (*81*), tardigrades (*82*), and rotifers (*83*)]. Although functional ecology studies are limited to a small fraction of the microinvertebrate species living in species-rich regions such as the Antarctic Peninsula, they cover a high proportion of those residing in species-poor areas such as the Dry Valleys. Thus, advancing functional knowledge requires prioritizing underrepresented guilds in species-rich regions.

Various studies have examined the responses to extreme conditions of the two native vascular plants of the maritime Antarctic, including photoprotection, photosynthetic activity, desiccation, cold tolerance, and fitness [e.g., (*84*, *85*)], although adaptations to low temperature, desiccation, and radiation stress remain poorly understood. For the more diverse bryophytes, trait coverage is generally poorer than for other aspects of biodiversity (Fig. 3). Case studies in the maritime Antarctic are limited to a few bryophyte species and locations, focusing on climate warming responses [e.g., (*86*)]. In contrast, the few bryophyte species present in continental Antarctica have been studied relatively extensively [e.g., (*87*)].

The assessment of functional knowledge by experts was higher for lichens than other groups (Fig. 3), with many studies focusing on growth (*69*) and metabolic activity (*88*). Research in maritime and continental Antarctica has addressed the influence of abiotic factors including temperature, light, and water availability on lichen photosynthesis and growth (*89*, *90*). Strong links between lichen diversity, annual growth, average temperature, and precipitation have also been demonstrated across the continent (*91*).

Studies on microorganisms have been mostly limited to snow algal growth and tolerances and baseline knowledge on freezing and radiation resistance [e.g. (*92*)]. Genomic, metagenomic, and proteomic research on Antarctic prokaryotes is already yielding insights into functional

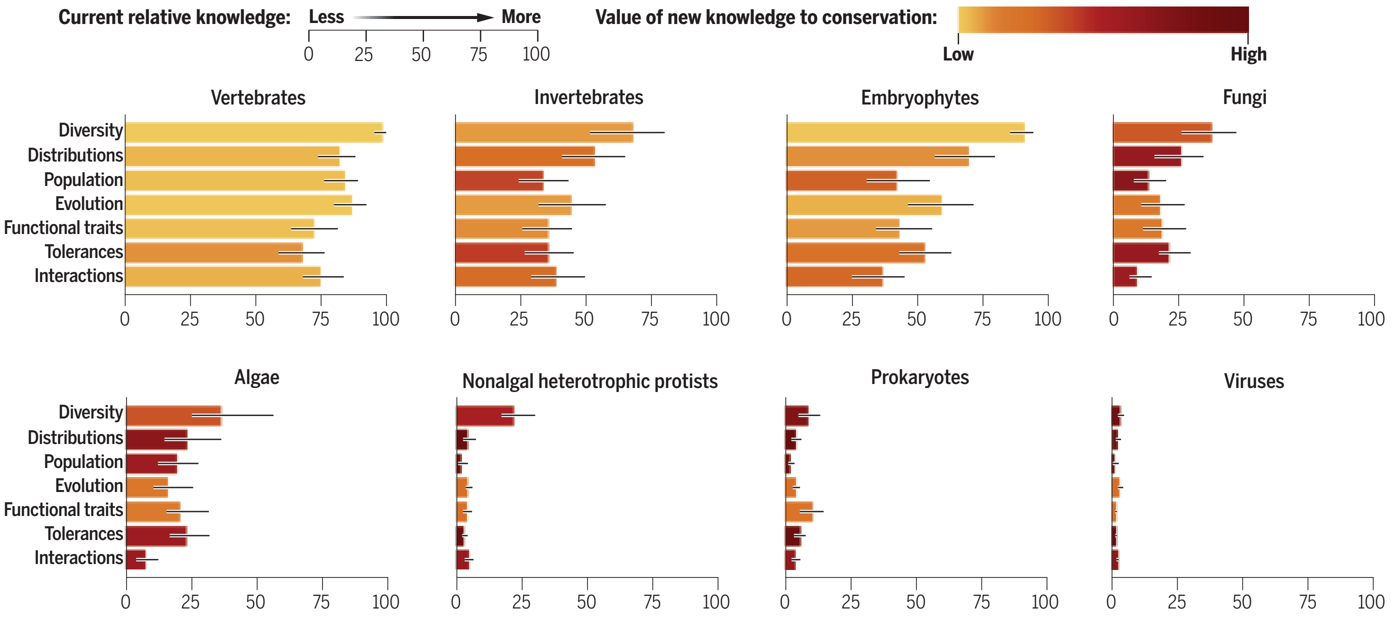

Fig. 3. Assessment of biodiversity knowledge gaps and implications for applied conservation practice through an expert elicitation. The 29 participant experts were consulted to evaluate Antarctic science progression around the seven main biodiversity knowledge shortfalls: species diversity ("Diversity"), geographic distributions ("Distributions"), population dynamics ("Population"), evolutionary relationships ("Evolution"), functional traits ("Functional traits"), abiotic tolerances ("Tolerances"), and biotic relationships ("Interactions") (*14*). Scores indicate the joint knowledge progression perceived by the experts toward having a baseline knowledge in each discipline about eight eukaryotic and prokaryotic groups present in the terrestrial Antarctic (*15*, *16*). The *x* axes indicate the scoring provided by the experts. Scores close to 0 indicate large knowledge gaps, and scores close to 100 indicate extensive coverage. The "best estimate" (i.e., the prevailing view) is shown together with uncertainty levels (constructed from minimum and maximum perceived estimates and confidence levels) using the IDEA elicitation formula (*24*). Note that "algae" includes both cyanophyta, green algae, and diatoms, as they are typically studied together. Bars are colored by the shortfall filling importance for conservation identified by experts. This importance was calculated as the integration of the depth of the knowledge gap set by Antarctic biodiversity experts and the joint general value for conservation practices (set as climate change action, biosecurity, pollution control, living resources management, and area protection) set by five experts in biodiversity knowledge shortfalls science. Red indicates high filling importance, and yellow indicates comparatively low importance.

CREDIT: ADAPTED BY V. PENNEY/*SCIENCE*

traits at the community level (*93*), although in situ functional assay data are scarce. For instance, recent soil habitability studies have identified the functional attributes of microbial communities driven by abiotic gradients (*75*, *94*), but metatranscriptomic studies documenting gene expression at the community level are severely hampered by the low mRNA extraction yields resulting from the low biomass and low transcription rates in many Antarctic habitats, particularly soils. Some community-level functional data exist on carbon fixation, respiration rates, nitrogen cycling, and trace gas (CO_2, H_2O) assimilation (*93*–*95*), yet microbial community responses to abiotic conditions remain poorly understood. Recent in situ and ex situ studies have explored the effects of radiation, temperature, nutrient supplementation, and/or soil wetting [e.g., (*96*)], but largely focusing on microbial community composition rather than on its functionality. Although the abiotic and, to a lesser extent, biotic drivers behind the response of microbial community structure to environmental gradients are beginning to be disentangled (*97*, *98*), their influence on ecosystem functioning over space and time is still unresolved.

Advances in understanding species interactions and ecological networks

The role of biotic interactions in structuring Antarctic terrestrial ecosystems remains largely unexplored. Competitive interactions have been classically considered to play a minor role in Antarctica compared with other regions owing to the reduced biodiversity and extreme abiotic pressures (*99*). Growing evidence of such interactions, albeit still limited, is now emerging at all levels (*11*, *100*). Although there is a basic understanding of which are the primary producers, grazers, predators, parasites, and detritivores in terrestrial food webs (*101*), interactions are seldom quantified, and the original expectations of progress (*102*) have only materialized for a few systems (*103*). Indeed, databases hold virtually no records of ecological interactions even for goups with data about other aspects of biodiversity (Figs. 2 and 3 and fig. S4), despite the critical importance of this knowledge for biosecurity and living resources management, which requires understanding the resilience of ecological networks to disturbances.

Complex hypotheses about interactions have only been assessed in the best-studied animal groups, such as coastal macrofauna (seals and seabirds) (*104*). Trophic interactions between different elements of the terrestrial food web can, however, be informed by stable isotope studies [e.g., (*105*)], although few such studies are yet available [but see (*106*)]. Lists of ectoparasites, epibionts, and endoparasites of Antarctic vertebrates have recently been published (*107*), and a recent study describes forms of neutral commensalism of tardigrades associated with seabird nests (*108*).

Several studies have assessed potential competition and facilitation among native and non-native vascular plants (*109*), but little attention has been given to bryophytes and lichens, which are the primary components of Antarctic vegetation. Although competition for space would appear to be the most important biotic interaction affecting these groups, its impact on the composition and structure of their communities in Antarctica has not been studied in depth. Symbiotic relationships, such as between lichen photobionts and mycobionts, have been more widely explored [e.g., (*110*)], and the symbiont forms of rhizobacteria, fungal endophytes of plants, have received increasing attention (*111*). Plant competition and succession under climate change is also emerging as a growing field that requires long-term in situ monitoring and/or ex situ experimentation (*109*).

The analysis of interspecific microbial interactions remains a more complex challenge, but the study of carbon pathways (*11*) and the use of quorum-sensing techniques (*112*) offer additional insights into the characterization of trophic connectivities in polar ecosystems. Nonetheless, interactions between primary producers (phototrophic and chemoautotrophic taxa), heterotrophic prokaryotes, and microscopic eukaryotes are very poorly understood [but see (*113*)], perhaps with the exception of the recently characterized soil food webs of the McMurdo Dry Valleys (*114*). Virus and bacteriophage activity remains largely unexplored, although metabarcoding and metagenomics are starting to clarify their influence on Antarctic host species and communities (*51*, *115*). Knowledge of species interactions is entirely lacking for SAR/protist species (Fig. 3).

Future directions for Antarctic biodiversity science and identifiable priority gains of knowledge for conservation practice

Systematic knowledge acquisition in Antarctica that maximizes the value of information for understanding and preserving its biodiversity requires four consecutive steps: (i) completing biodiversity inventories; (ii) obtaining robust spatial and temporal data coverage; (iii) collecting the information required to address the remaining knowledge shortfalls; and (iv) managing and mobilizing data into centralized information repositories that allow biodiversity trends to be assessed.

Representative biodiversity inventories

Many species remain to be discovered or (re) described, including differentiating cryptic taxa. The increasing application of molecular biology approaches is enhancing the identification of species and cryptic speciation events, leading to rapid increases in knowledge of microbial diversity. The main challenges remaining in the description of Antarctic terrestrial and freshwater diversity arise primarily from survey limitations and the paucity of experienced taxonomists. Two main steps are required to overcome these challenges: training of specialists and increasing application of evolutionary and environmental omics approaches [such as recent work on soil biodiversity detection (*116*)]. Environmental DNA surveying requires not only systematic implementation but also the availability of both voucher specimens with precise taxonomic identifications and more comprehensive and quality-controlled sequence databases and biological sample repositories (*9*).

Increasing spatiotemporal coverage

Biodiversity science relies on the availability of representative collections. A systematic monitoring favors a better understanding of global change dynamics and conservation practice. Many ice-free locations and inland waters in Antarctica have not been surveyed or resurveyed since the early 20th century or the initiation of substantive scientific research activities in the 1950s (*25*). Thus, virtually no recent spatial data are available to fill knowledge gaps in areas including environmental tolerance breadth, patterns of functional traits, and forms of biological interactions for most of the continent. Improved characterization of species' distributions requires spatially targeted broad field surveys to reduce spatial biases in remote areas such as the Prince Charles Mountains or the Queen Maud Mountains (*71*, *116*) together with development of remote sensing imagery and analyses (*25*).

Data upscaling and standarization

Environmental vulnerability studies have informed policy-making discussions about the protection of, for example, the emperor penguin as an Antarctic Specially Protected Species (*117*) but are still lacking for terrestrial biota. Overall, current gaps in knowledge about species interactions make it very difficult to understand the cascading effects of global change beyond the impacts on each species considered in isolation (*7*). Interdisciplinary studies that evaluate relationships between groups through, for instance, genomic, fatty acid, and/or isotope-based analyses of food webs, are required. Disentangling biotic interactions will also require promotion of interdisciplinary integrative research that examines functional relationships between groups, such as the diversity and influence of viruses in Antarctic host species and communities (*115*). Baseline descriptions of species co-occurrence should be augmented by manipulative field experiments or, alternatively, growth chamber experiments that realistically mimic Antarctic field conditions [e.g., (*118*)]. Because of microorganisms' complexity and plasticity, standardized collection remains both a challenge and a necessary step in the characterization of functional aspects. Standardized protocols are required to ensure that future studies of the responses of different groups to global change are comparable.

Data mobilization, centralization, and reanalysis

A critical component of knowledge acquisition is data mobilization and centralization, that is, data retrieval from bibliographic sources, institutional repositories, and/or private databases and harmonization into open repositories with transparent data audit and consolidation (*18*). Data mobilization, centralization, and reanalysis ultimately make important contributions to providing policy-makers with the critical summaries of biodiversity and ecosystem functioning trends required for supporting their strategic conservation planning efforts. Notably, recent calls have raised the need to integrate existing Antarctic biological data from decentralized sources (*119*). The complementary adoption and expansion of monitoring "model bio-sentinel" organisms and "priority areas" can help identify rapid changes (*120*), alleviating current knowledge gaps. In this work, we have identified species and groups of organisms that have data across multiple aspects of biodiversity (Fig. 3). Further assessment of the representativeness of these organisms would eludicate how well they provide baseline systems of reference and would contribute to priorizing additional target groups or species. In this context, combining (i) works increasing data completeness for particular species with (ii) in-depth case studies would provide basic, yet representative, understanding of their responses to global change, helping to maximize conservation gains under limited funding. An assessment of priority knowledge gains, as conducted here, can set the basis for developing strategic programs to fill critical knowledge gaps. However, the full "value of information" that balances the scientific, economic, and societal costs and gains of priorizing research to improve completeness across key aspects of biodiversity remains to be ascertained for Antarctica (*12*).

Conclusions

Recent scientific advances have shed new light on the functioning of Antarctic ecosystems. Major gaps in knowledge of Antarctic biodiversity still hamper our understanding of the functioning of its ecosystems, limiting the effectiveness of conservation policies and actions. This continent-wide review of biodiversity knowledge shortfalls provides a basis for future integrative analyses of research needs and ways to inform conservation requirements in a changing environment, not only for Antarctica but also as a model approach for scaling up shortfall assessments from a single taxonomic group to whole biomes that can be applied to other regions. To address the here-described shortfalls, future research planning should establish targeted international collaborative programs focused on addressing these key questions. Despite more than a century of Antarctic research and exploration under an umbrella of international scientific cooperation, there is still much to learn about the ecology and biogeography of this enigmatic continent. Moreover, the pervasive impacts of contemporary human-induced environmental change urgently require these knowledge gaps to be filled to better safeguard the continent's singular biodiversity and the ecosystem services it provides.

REFERENCES AND NOTES

1. R. I. Leihy *et al.*, *Nature* **583**, 567–571 (2020).
2. N. B. Dragone *et al.*, *J. Geophys. Res. Biogeosci.* **126**, e2020JG006052 (2021).
3. J. Goordial *et al.*, *ISME J.* **10**, 1613–1624 (2016).
4. L. R. Pertierra *et al.*, *Ecosyst. Serv.* **49**, 101299 (2021).
5. J. L. Bamber, M. Oppenheimer, R. E. Kopp, W. P. Aspinall, R. M. Cooke, *Proc. Natl. Acad. Sci. U.S.A.* **116**, 11195–11200 (2019).

6. S. L. Chown, C. M. Brooks, *Annu. Rev. Environ. Resour.* **44**, 1–30 (2019).
7. P. Convey, L. S. Peck, *Sci. Adv.* **5**, eaaz0888 (2019).
8. P. Convey *et al*., *Biol. Rev. Camb. Philos. Soc.* **83**, 103–117 (2008).
9. G. Varliero *et al*., *Microbiome* **12**, 9 (2024).
10. M. C. Kennicutt II *et al*., *One Earth* **1**, 95–113 (2019).
11. P. Almela, D. Velázquez, E. Rico, A. Justel, A. Quesada, *Front. Microbiol.* **10**, 628 (2019).
12. J. R. Lee *et al*., *PLOS Biol.* **20**, e3001921 (2022).
13. L. M. Phillips, R. I. Leihy, S. L. Chown, *Conserv. Biol.* **36**, e13885 (2022).
14. J. Hortal *et al*., *Annu. Rev. Ecol. Evol. Syst.* **46**, 523–549 (2015).
15. Materials, methods, and supplementary figures are available as supplementary materials.
16. L. R. Pertierra *et al*., Supplementary Files to: Advances and shortfalls in the knowledge of Antarctic terrestrial biodiversity [Data set]. In Science, version 2, Zenodo (2024); https://doi.org/10.5281/zenodo.13988131.
17. L. R. Pertierra *et al*., *Biodivers. Data J.* **12**, e106199 (2024).
18. J. M. Heberling, J. T. Miller, D. Noesgaard, S. B. Weingart, D. Schigel, *Proc. Natl. Acad. Sci. U.S.A.* **118**, e2018093118 (2021).
19. M. Leray, N. Knowlton, S.-L. Ho, B. N. Nguyen, R. J. Machida, *Proc. Natl. Acad. Sci. U.S.A.* **116**, 22651–22656 (2019).
20. J. H. Poelen, J. D. Simons, C. J. Mungall, *Ecol. Inform.* **24**, 148–159 (2014).
21. J. Kattge *et al*., *Glob. Change Biol.* **26**, 119–188 (2020).
22. J. M. Bennett *et al*., *Sci. Data* **5**, 180022 (2018).
23. J. D. Shaw, A. Terauds, M. J. Riddle, H. P. Possingham, S. L. Chown, *PLOS Biol.* **12**, e1001888 (2014).
24. V. Hemming, M. A. Burgman, A. M. Hanea, M. F. McBride, B. C. Wintle, *Methods Ecol. Evol.* **9**, 169–180 (2018).
25. I. Hawes *et al*., *Antarct. Sci.* **35**, 64–88 (2023).
26. H. S. Wauchope, J. D. Shaw, A. Terauds, *Nat. Commun.* **10**, 946 (2019).
27. X. P. Liu, G. A. Duffy, W. S. Pearman, L. R. Pertierra, C. I. Fraser, *Ecography* **2022**, e06312 (2022).
28. G. E. Collins *et al*., *Genes* **14**, 606 (2023).
29. A. Carapelli, C. Leo, F. Frati, *Antarct. Sci.* **29**, 311–323 (2017).
30. A. Velasco-Castrillón *et al*., *Invertebr. Syst.* **29**, 578–590 (2015).
31. A. Velasco-Castrillón, M. I. Stevens, *Soil Biol. Biochem.* **70**, 272–284 (2014).
32. A. Velasco-Castrillón, T. J. Page, J. A. E. Gibson, M. I. Stevens, *Biodiversity* **15**, 130–142 (2014).
33. G. E. Collins *et al*., *Proc. Natl. Acad. Sci. U.S.A.* **117**, 22293–22302 (2020).
34. P. Convey, E. M. Biersma, A. Casanova-Katny, C. S. Maturana, in *Past Antarctica: Paleoclimatology and Climate Change*, M. Oliva, J. Ruiz-Fernández, Eds. (Academic Press, 2020), pp. 181–200.
35. J. A. Vianna *et al*., *Proc. Natl. Acad. Sci. U.S.A.* **117**, 22303–22310 (2020).
36. R. M. Brown, N. M. S. M. Techow, A. G. Wood, R. A. Phillips, *PLOS ONE* **10**, e0121688 (2015).
37. E. M. Biersma *et al*., *J. Biogeogr.* **47**, 1663–1673 (2020).
38. E. Lagostina, F. Dal Grande, S. Ott, C. Printzen, *Appl. Plant Sci.* **5**, 1700054 (2017).
39. I. Garrido-Benavent, S. Pérez-Ortega, A. de Los Ríos, H. Mayrhofer, F. Fernández-Mendoza, *Mol. Phylogenet. Evol.* **155**, 107020 (2021).
40. I. Garrido-Benavent *et al*., *Front. Microbiol.* **11**, 126 (2020).
41. M. P. Davey *et al*., *New Phytol.* **222**, 1242–1255 (2019).
42. E. Verleyen *et al*., *Ecography* **44**, 548–560 (2021).
43. J. C. Nabout, B. da Silva Rocha, F. M. Carneiro, C. L. Sant'Anna, *Biodivers. Conserv.* **22**, 2907–2918 (2013).
44. A. R. Thompson, *Polar Biol.* **44**, 1467–1484 (2021).
45. R. L. Farrell *et al*., *Polar Biol.* **34**, 1669–1677 (2011).
46. A. Sakaeva *et al*., *Polar Biol.* **39**, 2441–2456 (2016).
47. D. A. Pearce *et al*., *Front. Microbiol.* **7**, 16 (2016).
48. B. C. Christner *et al*., *Nature* **512**, 310–313 (2014).
49. M. Guglielmin *et al*., *Sci. Rep.* **13**, 177 (2023).
50. A. López-Bueno *et al*., *Science* **326**, 858–861 (2009).
51. O. Zablocki *et al*., *Appl. Environ. Microbiol.* **80**, 6888–6897 (2014).
52. P. Convey *et al*., *Ecol. Monogr.* **84**, 203–244 (2014).
53. J. M. Lobo *et al*., *Ecol. Indic.* **91**, 241–248 (2018).
54. G. A. Duffy *et al*., *Divers. Distrib.* **23**, 982–996 (2017).
55. C. Colesie, C. V. Walshaw, L. G. Sancho, M. P. Davey, A. Gray, *Wiley Interdiscip. Rev. Clim. Change* **14**, e810 (2023).
56. G. W. Yeates, M. B. Scott, S. L. Chown, B. J. Sinclair, *Pedobiologia* **52**, 375–386 (2009).
57. W. S. Andriuzzi, B. J. Adams, J. E. Barrett, R. A. Virginia, D. H. Wall, *Ecology* **99**, 312–321 (2018).
58. G. R. W. Humphries *et al*., *Polar Rec. (Gr. Brit.)* **53**, 160–166 (2017).
59. M. LaRue *et al*., *Sci. Adv.* **7**, eabh3674 (2021).
60. W. Z. Trivelpiece *et al*., *Proc. Natl. Acad. Sci. U.S.A.* **108**, 7625–7628 (2011).
61. M. B. Schrimpf, C. Che-Castaldo, H. J. Lynch, *Polar Biol.* **43**, 111–122 (2020).
62. A. Carapelli, P. Convey, F. Frati, G. Spinsanti, P. P. Fanciulli, *Biol. J. Linn. Soc. Lond.* **120**, 788–803 (2017).
63. T. Altiero, I. Giovannini, R. Guidetti, L. Rebecchi, *Hydrobiologia* **761**, 277–291 (2015).
64. C. M. de Tomasel, B. J. Adams, F. G. Tomasel, D. H. Wall, *J. Nematol.* **45**, 39–42 (2013).
65. N. Cannone, F. Malfasi, S. E. Favero-Longo, P. Convey, M. Guglielmin, *Curr. Biol.* **32**, 1599–1606.e2 (2022).
66. H. Galera *et al*., *Glob. Ecol. Conserv.* **19**, e00679 (2019).
67. C. V. Walshaw *et al*., *Nat. Geosci.* **17**, 755–762 (2024).
68. S. A. Robinson *et al*., *Nat. Clim. Chang.* **8**, 879–884 (2018).
69. L. G. Sancho *et al*., *Sci. Rep.* **7**, 5689 (2017).
70. R. D. Seppelt *et al*., *Antarct. Sci.* **22**, 691–702 (2010).
71. T. G. A. Green, L. G. Sancho, R. Türk, R. D. Seppelt, I. D. Hogg, *Polar Biol.* **34**, 1211–1220 (2011).
72. A. Gray *et al*., *Nat. Commun.* **11**, 2527 (2020).
73. B. Durieu *et al*., *Ecography* **2005**, e07489 (2025).
74. E. Pushkareva *et al*., *Syst. Appl. Microbiol.* **41**, 363–373 (2018).
75. N. B. Dragone *et al*., *mSystems* **7**, e01330-21 (2022).
76. L. Amo, M. Rodríguez-Gironés, A. Barbosa, *Mar. Ecol. Prog. Ser.* **474**, 277–285 (2013).
77. K. Heerah *et al*., *Deep Sea Res. Part II Top. Stud. Oceanogr.* **88-89**, 23–33 (2013).
78. M. A. Cimino, H. J. Lynch, V. S. Saba, M. J. Oliver, *Sci. Rep.* **6**, 28785 (2016).
79. M. J. Everatt, P. Convey, M. R. Worland, J. S. Bale, S. A. L. Hayward, *J. Therm. Biol.* **38**, 264–271 (2013).
80. T. Contador *et al*., *Sci. Rep.* **10**, 9087 (2020).
81. M. A. Poage, J. E. Barrett, R. A. Virginia, D. H. Wall, *Arct. Antarct. Alp. Res.* **40**, 119–128 (2008).
82. I. Giovannini, T. Altiero, R. Guidetti, L. Rebecchi, *J. Exp. Biol.* **221**, jeb160622 (2018).
83. B. Hespeels *et al*., *BMC Biol.* **21**, 72 (2023).
84. H. Köhler, R. A. Contreras, M. Pizarro, R. Cortés-Antíquera, G. E. Zúñiga, *Front. Plant Sci.* **8**, 921 (2017).
85. L. A. Cavieres *et al*., *Plant Ecol.* **217**, 343–358 (2016).
86. A. V. Perera-Castro *et al*., *Front. Plant Sci.* **11**, 1178 (2020).
87. L. J. Clarke, S. A. Robinson, *New Phytol.* **179**, 776–783 (2008).
88. J. Raggio, T. G. A. Green, L. G. Sancho, *Polar Biol.* **39**, 113–122 (2016).
89. B. Schroeter, T. G. A. Green, A. Pintado, R. Türk, L. G. Sancho, *Antarct. Sci.* **29**, 517–530 (2017).
90. C. Colesie, T. G. A. Green, J. Raggio, B. Büdel, *Arct. Antarct. Alp. Res.* **48**, 449–460 (2016).
91. L. G. Sancho, A. Pintado, *Polar Biol.* **27**, 312–319 (2004).
92. S. K. Schmidt, L. Vimercati, *J. Microbiol.* **57**, 243–251 (2019).
93. M. Ortiz *et al*., *Proc. Natl. Acad. Sci. U.S.A.* **118**, e2025322118 (2021).
94. N. Fierer *et al*., *Proc. Natl. Acad. Sci. U.S.A.* **109**, 21390–21395 (2012).
95. M. Ji *et al*., *Nature* **552**, 400–403 (2017).
96. H. N. Buelow *et al*., *Front. Microbiol.* **7**, 1040 (2016).
97. E. M. Adriaenssens *et al*., *Microbiome* **5**, 83 (2017).
98. E. M. Bottos *et al*., *FEMS Microbiol. Ecol.* **96**, fiaa042 (2020).
99. I. D. Hogg *et al*., *Soil Biol. Biochem.* **38**, 3035–3040 (2006).
100. T. Caruso *et al*., *Commun. Biol.* **2**, 63 (2019).
101. D. N. Thomas *et al*., *The Biology of Polar Regions* (Oxford Univ. Press, ed. 2, 2008).
102. W. Block, in *Antarctic Nutrient Cycles and Food Webs*, W. R. Siegfried, P. R. Condy, R. M. Laws, Eds. (Springer Berlin Heidelberg, 1985), pp. 614–619.
103. X. Xue, A. R. Thompson, B. J. Adams, *Appl. Soil Ecol.* **193**, 105110 (2024).
104. E. P. Pickett *et al*., *Ecol. Evol.* **8**, 9764–9778 (2018).
105. S. Bokhorst, P. Convey, R. Aerts, *Curr. Biol.* **29**, 1721–1727.e3 (2019).
106. E. A. Shaw *et al*., *Polar Biol.* **41**, 1013–1018 (2018).
107. R. E. T. Vanstreels, R. L. Palma, S. V. Mironov, *Int. J. Parasitol. Parasites Wildl.* **12**, 275–290 (2020).
108. Ł. Kaczmarek *et al*., *Polar Biol.* **41**, 283–301 (2018).
109. M. A. Molina-Montenegro, D. M. Bergstrom, K. J. Chwedorzewska, P. Convey, S. L. Chown, *NeoBiota* **51**, 19–40 (2019).
110. H. T. Lumbsch, N. Wirtz, *Lichenologist* **43**, 553–559 (2011).
111. J. Gallardo-Cerda *et al*., *Polar Biol.* **41**, 1973–1982 (2018).
112. W. S. See-Too *et al*., *Sci. Rep.* **7**, 42968 (2017).
113. K. C. Lee *et al*., *Front. Microbiol.* **9**, 2619 (2018).
114. A. R. Thompson, A. J. Roth-Monzón, Z. T. Aanderud, B. J. Adams, *Microorganisms* **9**, 1555 (2021).
115. M. Wille *et al*., *ISME J.* **14**, 1768–1782 (2020).
116. P. Czechowski, M. de Lange, M. Knapp, A. Terauds, M. I. Stevens, *Front. Ecol. Environ.* **20**, 550–557 (2022).
117. F. Abadi, C. Barbraud, O. Gimenez, *Glob. Change Biol.* **23**, 1353–1359 (2017).
118. S. Bokhorst, P. Convey, R. van Logtestijn, R. Aerts, *Glob. Change Biol.* **28**, 816–828 (2022).
119. K. M. O'Brien *et al*., *Proc. Natl. Acad. Sci. U.S.A.* **119**, e2212800119 (2022).
120. J. Handley *et al*., *Front. Mar. Sci.* **7**, 602972 (2021).
121. A. Terauds *et al*., The Biodiversity of Ice-free Antarctica Database, Ver. 5, Australian Antarctic Data Centre (2024); http://dx.doi.org/doi:10.4225/15/59100ba9157f7.
122. H. Wilman *et al*., *Ecology* **95**, 2027 (2014).

ACKNOWLEDGMENTS

This work is dedicated to the memory of Andrés Barbosa, who sadly passed away in 2023. His large contributions to polar research extend to this work, as he died while we were preparing the second version of this manuscript. He will be sorely missed. We kindly thank two anonymous reviewers for their valuable suggestions. We also thank O. Lopez Hilzinger for graphic design assistance. **Funding:** Research was funded with Spanish "ANTECO" (CGL2017-89820-P) and EU-Biodiversa "ASICS" projects (Spanish PCI2020-120690-2 and South African NRF). L.R.P. was also partly supported with a Spanish Juan de la Cierva Fellowship (IJC-2016-30503) and a Chilean BASE contract, ANID – Programa Iniciativa Milenio – ICN2021_002 – BASE. P.C. and H.J.G. are supported by NERC core funding to the British Antarctic Survey's "Biodiversity, Evolution and Adaptation" Team. Conceptual and methodological work on biodiversity shortfalls by J.H., J.A.F.D.-F., and R.J.L. has been supported by project NICED (grant PID2022-140985NB-C21, funded by Spanish MCIN/AEI/10.13039/501100011033/FEDER, EU), an International Cooperation Project funded by the Brazilian National Council for Scientific and Technological Development (CNPq 441125/2023-9 and 201048/2024-8), and by the National Institute for Science and Technology (INCT) in Ecology, Evolution, and Biodiversity Conservation (CNPq 465610/2014-5 and FAPEG 201810267000023). L.G.S. and A.d.I.R. were supported by PID2019-105469RB-C21/C22 (MICINN, AEI). J.A.V. was supported by FONDECYT 1210568, ICN2021_044 (CRG). This is also a contribution to Securing Antarctica's Environmental Future (SAEF), an Australian Research Council Special Research Initiative. In-kind funding supported C.I.F.'s time involvement through the following government-funded grants: Antarctic Science Platform (ANTA-1801), Rutherford Discovery Fellowship (RDF-UOO1803), and Marsden Fund (MFP-20-UOO-173). D.F. was funded by Italian National Antarctic Research Program (PNRA) projects 2013/AZ1.13 and PNRA16_00120-A1 (TNB-CODE) and Italian National Biodiversity Future Center (NBFC) award CN_00000033. Funding sources to E.M.B. were NERC-CONICYT (NE/P003079/1) and Carlsberg Foundation (CF18-0267). A.Q. was funded by the Spanish projects CTM2011-28736 and CTM 2016-79741R. Finally, this paper contributes to the Scientific Committee on Antarctic Research (SCAR) Scientific Research Programme "Integrated Science to Inform Antarctic and Southern Ocean Conservation" (Ant-ICON). **Competing interests:** S.L.C. was president of the Scientific Committee on Antarctic Research (SCAR) from 2016 to 2021 and immediate past president until 2022. He is now a lifetime honorary member of SCAR. The authors declare that they have no other competing interests. **Data and materials availability:** Materials and methods and supplementary figures are available in the supplementary materials. All supporting data and code needed to evaluate the conclusions in the paper have been deposited in Zenodo (*16*). The Antarctic biodiversity checklists generated for this work are available in (*17*).

SUPPLEMENTARY MATERIALS

science.org/doi/10.1126/science.adk2118
Materials and Methods
Figs. S1 to S4

Submitted 8 August 2023; accepted 8 January 2025
10.1126/science.adk2118

REVIEW

Disappearing landscapes: The Arctic at +2.7°C global warming

Julienne C. Stroeve[1,2]*†, Dirk Notz[3]†, Jackie Dawson[4], Edward A. G. Schuur[5], Dorthe Dahl-Jensen[1,6], Céline Giesse[3]

Under current nationally determined contributions (NDCs) to mitigate greenhouse gas emissions, global warming is projected to reach 2.7°C above preindustrial levels. In this review, we show that at such a level of warming, the Arctic would be transformed beyond contemporary recognition: Virtually every day of the year would have air temperatures higher than preindustrial extremes, the Arctic Ocean would be essentially ice free for several months in summer, the area of Greenland that reaches melting temperatures for at least a month would roughly quadruple, and the area of permafrost would be roughly half of what it was in preindustrial times. These geophysical changes go along with widespread ecosystem disruptions and infrastructure damage, which, as we show here, could be substantially reduced by increased efforts to limit global warming.

In 2024, Earth's annual average near-surface air temperature exceeded 1.5°C above preindustrial levels for the first time in modern history (*1*). This warming was accompanied by numerous and often devastating weather extremes worldwide, providing a glimpse into our near-future world when average global warming levels will continue to exceed the aspirational +1.5°C temperature target of the Paris Agreement. How far temperatures will rise above this target depends on future human greenhouse gas emissions and the response of the global carbon cycle. The former largely relies on the nationally determined contributions (NDCs) that nations commit to and achieve. Current country-level pledges to reduce carbon emissions under the Paris Agreement are projected to result in global temperatures rising to 2.7°C (in a range of 2.5° to 3°C) above preindustrial levels by 2100 (*2*), well above the 2°C threshold long considered to define dangerous climate change.

Human-induced climate change is affecting every region across the globe (*3*), with the Arctic being among the most impacted. This extraordinary part of our planet, which has fascinated us with its remoteness, wildlife, culture, and beautiful landscapes for generations, is the fastest-warming region on Earth, currently warming nearly four times as much as the global average (*4*). The loss of sea ice is key in this warming, such that regions like the Barents Sea, which has largely lost its winter ice cover, has warmed seven times more than the global average (*4*), whereas warming over the Greenland ice sheet is more modest at 1.6 times the average (*5*). If global temperatures reach 2.7°C above preindustrial levels, the Arctic, representing the Circumpolar North (*6*), will be transformed beyond contemporary recognition. This transformation is due not only to the magnitude of warming but also to the current pace of change, which is unprecedented compared with the changes seen over the past several thousand years (*7*). These changes will generate widespread and cascading risks, challenging the adaptability of ecosystems and human societies both within and beyond the Arctic region.

To explore the consequences of the current insufficient action to limit global warming to "well below 2°C" and to visualize how fundamentally this will alter our current way of life, we examined how the Arctic would differ at +2.7°C compared with +1.5°C and preindustrial temperature levels. We focused on existing studies that show broad qualitative agreement. In doing so, we took the Intergovernmental Panel on Climate Change (IPCC) Sixth Assessment report (AR6) as a starting point and updated their knowledge and understanding of changes in three major elements of the Arctic cryosphere (sea ice, the Greenland ice sheet, and permafrost) and how these changes are cascading to create impacts and risks for Arctic ecosystems, economies, and cultures.

The Arctic under the Paris Agreement: Impacts at 1.5°C of global warming

To understand how the Arctic will be altered under 1.5°C of global warming, we first examined air temperature because its increase drives many of the changes discussed here. In a world that is 1.5°C warmer, Arctic air temperatures will exceed levels that were considered extremely warm under preindustrial conditions on more than 80% of all days of the year (Fig. 1). This shift is consistent across seasons, with preindustrial extremes particularly exceeded in autumn owing to delayed sea-ice formation. In winter, previous cold extremes will no longer occur, and the coldest daily winter temperatures will be as warm or warmer than the previously warmest temperatures on those days.

In addition to changes within individual seasons, the amplitude of the seasonal cycle is decreasing. Observational records and climate model simulations show that Arctic warming is three times higher in winter than in summer (*8*, *9*). This results in a reduction of the seasonal cycle amplitude by about 2°C per degree of global warming and substantial warming of winter cold extremes (*9*).

Enhanced Arctic warming is accompanied by considerable reductions in the sea-ice cover throughout the year, which are most pronounced in September (Fig. 2A). During preindustrial times and until the end of the 20th century, the Arctic Ocean featured a stable perennial ice cover, after which large reductions started to emerge (*10*). In 2012, the minimum sea-ice extent (SIE, defined as all areas with at least 15% sea-ice concentration) fell below 4 million km^2 for the first time in modern history, a decrease of 50% compared with the 1979 to 1997 average. At 1.5°C of global warming, pan-Arctic summer sea ice is expected to hover around this low level, yet there remains a possibility of an occasional ice-free September (SIE < 1 million km^2) between 2030 and 2050, regardless of which shared socioeconomic pathway (SSP) emission scenario is followed (*11*, *12*). Predicting the exact timing of

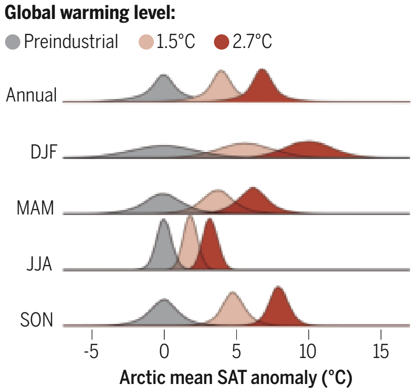

Fig. 1. Changes in the distribution of daily Arctic surface air temperature with global warming. Probability distributions of anomalies in daily Arctic mean surface air temperature (SAT) relative to preindustrial levels (gray) at 1.5°C (orange) and 2.7°C (red) global warming for the annual mean and for the individual seasons winter [December-January-February (DJF)], spring [March-April-May (MAM)], summer [June-July-August (JJA)], and fall [September-October-November (SON)]. Data are based on simulations from the Max Planck Institute Earth System Model version 1.2, low resolution (MPI-ESM1.2-LR) large ensemble (details provided in supplementary materials).

---

[1] Centre for Earth Observation Science (CEOS), Clayton H. Riddell Faculty of Environment, Earth and Resources, University of Manitoba, Winnipeg, MB, Canada. [2] National Snow and Ice Data Center (NSIDC), Cooperative Institute for Research in Environmental Sciences (CIRES), University of Colorado, Boulder, CO, USA. [3] Institute of Oceanography, Center for Earth System Research and Sustainability (CEN), University of Hamburg, Hamburg, Germany. [4] Geography, Environment and Geomatics, University of Ottawa, Ottawa, ON, Canada. [5] Center for Ecosystem Science and Society (ECOSS), Northern Arizona University, Flagstaff, AZ, USA. [6] Niels Bohr Institute, University of Copenhagen, Copenhagen, Denmark.
***Corresponding author. Email: Julienne.Stroeve@umanitoba.ca**
†These authors contributed equally to this work.

an ice-free year, or of regionally ice-free conditions, such as the record long open water season within the Northwest Passage (NWP) in 2024, is challenging because of internal variability, which dominates sea-ice fluctuations on subdecadal timescales (*13*). However, new estimates suggest that the daily SIE could drop below 1 million km^2 before 2030 (*14*). Such internal variability also explains why no new pan-Arctic sea-ice record minima has occurred since 2012: A persistent Arctic dipole pattern with its impacts on ocean heat transport into the Arctic and freshwater transport into the Canadian Arctic from Siberian rivers contributed to stabilizing the ice cover at about half its preindustrial extent over the past decade (*15*). On longer timescales, the amount of sea-ice loss and the rise in global mean temperature will nevertheless remain linearly related to the amount of anthropogenic greenhouse gas emissions (*16*, *17*). Thus, Arctic sea ice will continue to decrease on decadal timescales with continuing net greenhouse gas emissions.

Like the quick, large-scale response of the sea-ice area, the surface melt area of the Greenland ice sheet expands strongly with rising temperatures (Fig. 2B). At +1.5°C of global warming, the area that undergoes more than a month of melting conditions more than doubles compared with that occurring during preindustrial conditions. By contrast, changes in the total mass balance of the Greenland ice sheet unfold on much longer timescales. Assessments of current mass balance changes relative to preindustrial conditions are limited by the short-term observational record, and future assessments are challenged by model limitations as well as short- and long-term climate variability (*5*). However, observations have revealed that throughout most of the 20th century, the Greenland ice sheet was relatively stable, with its annual mass gain from snowfall roughly balanced by mass loss from iceberg calving and meltwater runoff. Today, at global warming levels around 1.5°C, Greenland is losing mass at a high rate, a shift which started in the 1980s (*18*) and accelerated in the first two decades of the 21st century, with Greenland annually losing 270 gigatons (Gt) of ice—six times the rate observed in the 1980s. The amount of ice that is currently lost from Greenland every year would be enough to cover an area the size of Manhattan Island with ice about 3 km in thickness. This loss contributes approximately 0.75 mm per year to sea level rise (SLR), accounting for about 20% of the observed rise (*19*, *20*).

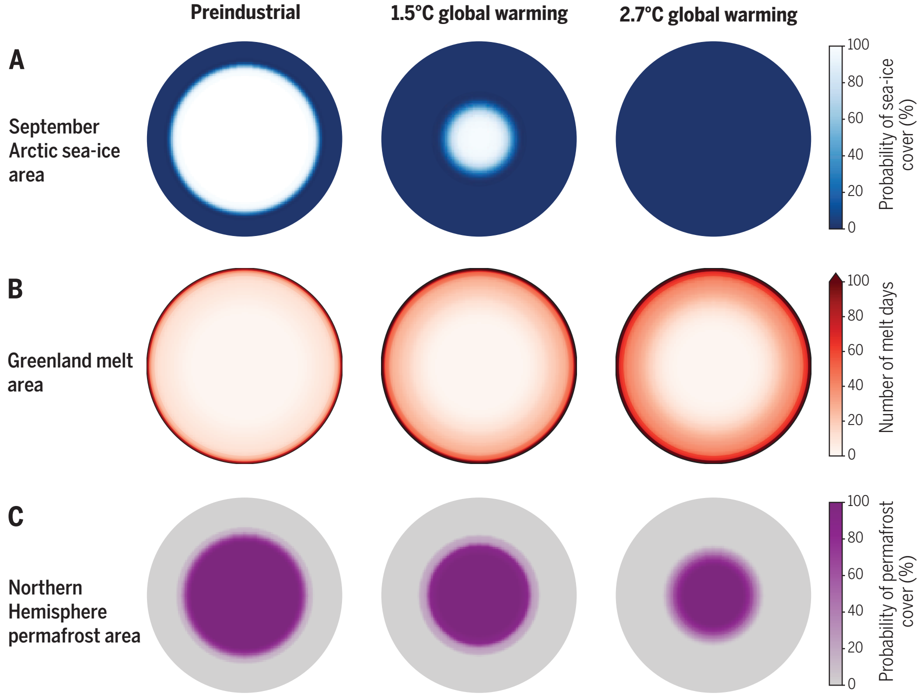

Fig. 2. Areal changes in Arctic sea ice, Greenland melt area, and Northern Hemisphere permafrost for preindustrial levels and for 1.5°C and 2.7°C global warming. (**A**) Area of the Arctic Ocean (blue) overlaid with Arctic sea-ice area in September (white). The white-to-blue colors indicate the probability of sea-ice coverage in a single year at the respective warming level, based on the interannual variability of bias-corrected sea-ice area from the MPI-ESM1.2-LR large ensemble. (**B**) Area of Greenland overlaid with the area that experiences a given number of melt days per year. Melt days are calculated as the average number of days per year with a daily mean surface air temperature >0°C in the ACCESS-ESM1.5 model. (**C**) Land area north of 45°N (gray) overlaid with the area of Northern Hemisphere underlain by permafrost (purple). The purple-to-gray colors indicate the probability of near-surface permafrost coverage at the respective warming level, based on the model uncertainty of 13 selected CMIP6 models (details provided in supplementary materials).

Although surface melting dominates Greenland's current mass loss (*21*), a recent study indicates that total mass loss has been underestimated because the retreat of marine-terminating glacier fronts had not been accounted for (*22*). This glacier retreat contributed an extra 1140 Gt of mass loss from 1985 to 2022, in addition to the 5390 Gt estimated from 1992 to 2020 by the Ice Sheet Mass Balance Intercomparison Exercise (IMBIE) (*17*). Although this additional mass loss from the floating parts of marine-terminating glaciers does not contribute to sea level rise because the ice has already been in the ocean, these recent findings confirm that ice retreat has far outpaced ice growth in recent decades. Moreover, retreat of the glacier fronts can trigger increased ice discharge further upstream, such that marine terminating glaciers will continue to play a key role in mass loss from Greenland (*23*).

The response time of permafrost (perennially frozen ground) falls between that of sea-ice and ice-sheet mass loss. Permafrost underlies approximately 15 million km^2 of the northern high latitudes, an area roughly the size of North America (*24*) and can be hundreds of meters thick in the coldest regions. It is the surface permafrost (0- to 3-m ground depth) that is the quickest to respond to warming and has the most influence on ecosystems and people (*6*). The entire northern permafrost region is known to contain from 1440 to 1600 Gt of organic carbon, with an additional poorly quantified estimate of 1000 Gt in deeper deposits and subsea permafrost (*25*, *26*). This amounts to two to three times the carbon currently in the atmosphere, which is why the release of even just a small fraction of this large frozen carbon pool could substantially increase the atmospheric concentration of carbon dioxide and methane, thus accelerating the rate of climate change.

At 1.5°C global warming, model simulations suggest a reduction of surface permafrost area of about 25% relative to preindustrial conditions (Fig. 2C). Consistent with these simulations, the observational record shows clearly that permafrost landscapes have started to undergo widespread changes: The temperature of deeper permafrost (measured at 15- to 25-m depth by a network of boreholes) reaches record-high levels year after year, with the measured temperatures in 2023 being the highest on record (*27*). Absolute temperature changes are greatest in the coldest permafrost further north, whereas lower temperature increases to the south represent energy diverted into melting ice within permafrost ground. Surface permafrost degradation as a result of melting ice, observed in the form of abrupt thaw and changes in the depth of the surface-active layer that thaws in summer, is also widespread, although the extent and driving processes of these changes vary regionally and temporally (*28*–*30*).

Some ecosystems around the permafrost region have already started to transition into net carbon emission sources (*31*, *32*), and ecosystem tipping points have been crossed at current warming levels (*33*). At the same time, some nonpermafrost ecosystems in the region have remained net carbon sinks because of Arctic greening (*34*). Accumulating evidence at the regional scale from ground-based and aircraft-based measurements suggests that entire regions have become net carbon sources to the atmosphere (*35*, *36*). These assessments, however, still differ from large-scale Earth system models (*37*) and atmospheric greenhouse gas concentration inversion models (*38*). The Arctic, acting as a regional-scale net carbon source to the atmosphere, is an unequivocal threshold for the permafrost carbon feedback to climate change. At the same time, weakening of the long-term carbon sink—even if it hasn't fully transitioned into a source—as observed today and faster than models have predicted, already accelerates climate change (*26*).

With the current level of global warming of around 1.5°C, the Arctic is already markedly different from its preindustrial state. Even if we were to stabilize future temperatures immediately at 1.5°C, the Arctic cryosphere will continue to shrink across a wide range of temporal and spatial scales.

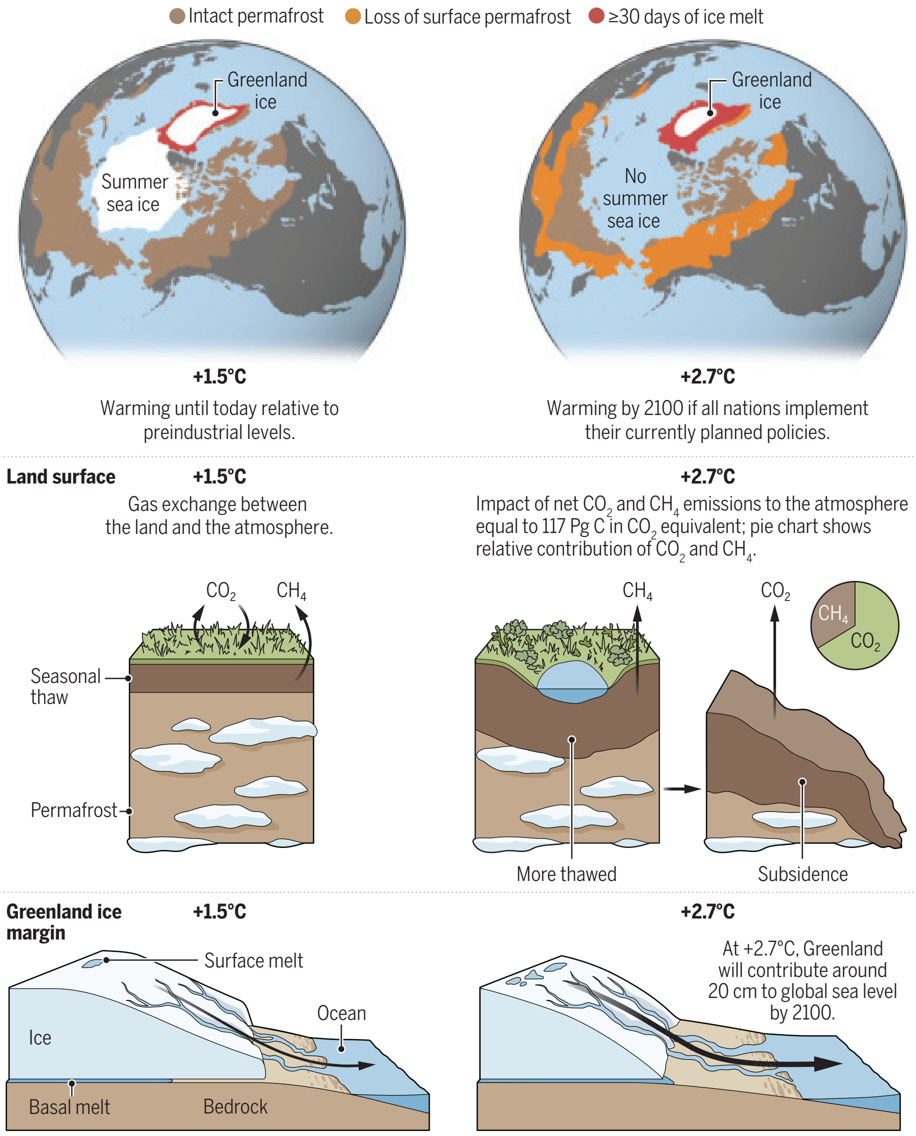

+1.5°C

Warming until today relative to preindustrial levels.

+2.7°C

Warming by 2100 if all nations implement their currently planned policies.

Land surface **+1.5°C**

Gas exchange between the land and the atmosphere.

+2.7°C

Impact of net CO_2 and CH_4 emissions to the atmosphere equal to 117 Pg C in CO_2 equivalent; pie chart shows relative contribution of CO_2 and CH_4.

Greenland ice margin **+1.5°C**

+2.7°C

At +2.7°C, Greenland will contribute around 20 cm to global sea level by 2100.

Fig. 3. Today's Arctic approaching 1.5°C and the future Arctic under 2.7°C of global warming. Shown are the changes in September sea-ice area, changes in the Greenland melt area exceeding 30 days, and changes in areas overlaid by at least 3 m of permafrost (top). Additional greenhouse gas emissions from permafrost degradation (middle) are shown at 2.7°C (units of Pg C in CO_2 equivalent, with pie chart illustrating proportional impact of methane and carbon dioxide) together with expected sea level rise contribution from Greenland (bottom).

ADAPTED BY K. HOLOSKI/*SCIENCE* FROM VICTOR O. LESHYK

The Arctic under the current level of NDCs: Impacts at 2.7°C of global warming

If global warming reaches 2.7°C by the end of this century, impacts on the Arctic will far exceed those observed today: Virtually every day of the year will have Arctic air temperatures exceeding preindustrial temperature extremes, with, for example, the expected average warming in winter exceeding 10°C (Fig. 1). At such warming levels, the Arctic Ocean will have lost its perennial sea-ice cover in all years (Figs. 2A and 3)—a change unprecedented in human history. The ice-free state in summer will extend over several months and will occur in every year (*39*). The last time the Arctic Ocean was ice free for extended periods of time was the Last Interglacial at around 130,000 years ago (*40*). In winter, the sea-ice cover will be much thinner than today and will often no longer extend to the coasts because of the shorter sea-ice growth season and the high amount of winter warming.

Melting in Greenland will be substantially enhanced at 2.7°C because the area of the ice sheet that experiences more than a month of surface temperatures >0°C roughly quadruples compared with preindustrial conditions (Figs. 2B and 3). The lowered albedo further enhances surface-meltwater runoff (*41*); this runoff is anticipated to be a primary factor in the increasing mass loss from Greenland in a warming climate, leading to an accelerating rise in global sea levels by several centimeters over the coming decades (*42*). The contribution of Greenland ice loss to global sea level rise at 2.7°C might additionally increase through the partial loss of outlet glaciers in North Greenland, where the upstream basins contain enough ice to raise global sea levels by 2.1 m. The long-term stability of these outlet glaciers is currently unclear, yet they already experienced large-scale mass losses between 2000 and 2020 due to increased basal melting from warmer ocean temperatures (*43*). Given the large number of governing positive and negative feedbacks and our limited ability to faithfully simulate their interactions, the uncertainty of quantitative estimates of Greenland's absolute contribution to global sea level rise over time at 2.7°C remains large (*5*). A recent estimate has Greenland contributing 20 ± 0.9 cm (*44*) over the next 80 years.

Whether the long-term mass loss from Greenland will eventually become irreversible—and the time frame needed to reach this condition—remain uncertain: Model simulations ignoring elevation-related feedbacks indicate that the surface mass balance of the Greenland ice sheet could become negative at 2.7°C, which implies irreversible ice loss at this warming level (*45*). Other studies suggest that the ice loss could become irreversible at a threshold of between 1.7° and 2.3°C of global warming (*46*, *47*) or at cumulative emissions of 1000 to 1500 Gt C (*48*).

Others suggest there is no discrete warming or CO_2 threshold but rather a range of steady-state ice sheet masses for different temperature increases (*49*).

Despite these uncertainties, with increasing warming, Greenland mass loss will accelerate, and a new equilibrium will be reached only after increasing amounts of net mass loss. Geological data propose that 400,000 years ago during the interglacial period stage 11, when global warming was likely still <2.7°C, Greenland might have lost 20% of its ice, raising the global sea level by several meters (*50*, *51*). This amount of ice loss will unfold over centuries or even millennia, with the potential rebuilding of ice mass in a cooler climate taking even longer. Therefore, if we lose substantial parts of the Greenland ice sheet at 2.7°C of global warming, we might consider that ice to be gone forever on any reasonable human timescale.

Lastly, at 2.7°C of global warming, surface permafrost area is expected to decrease substantially. CMIP6 (Coupled Model Intercomparison Project Phase 6) models project a loss of around 8 million km^2 (or about 50% of preindustrial area) based on no permafrost remaining in the top 0 to 3 m (Figs. 2C and 3; see materials and methods for details). In the remaining permafrost regions, active-layer depths will increase (*52*), which, even in the coldest locations, will lead to surface subsidence and abrupt thaw in areas that contain excess ice (*6*, *53*). Although increases in Arctic temperatures are one of the primary drivers of permafrost thaw, changes in the frequency of extreme rain events and wildfire pose additional disturbances that can accelerate permafrost degradation. As a result, changes in permafrost are likely to be experienced as punctuated disturbances tied to extreme events occurring regionally, such as heat waves and extreme precipitation, rather than as gradual change.

The thawing of permafrost under 2.7°C of global warming could contribute an additional 117 Gt C (in CO_2 equivalent) in the form of carbon dioxide and methane released to the atmosphere by 2100 (Fig. 3), with both gases playing an equally important role in the climate feedback (*26*). This amount of carbon is on the same order of what may be released by a large industrialized nation over the same time frame, contributing an additional 10 to 15% carbon emissions to those from human sources. On a global scale, this release of carbon dioxide and methane will reduce the remaining carbon budget for reaching any given global warming target (*54*). For example, the remaining carbon budget for a global warming level of 1.5°C was estimated by IPCC AR6 to be about 140 Gt C beyond 2020; top-down emergent constraints suggest a remaining budget since 2020 of 186 ± 116 Gt C (*55*).

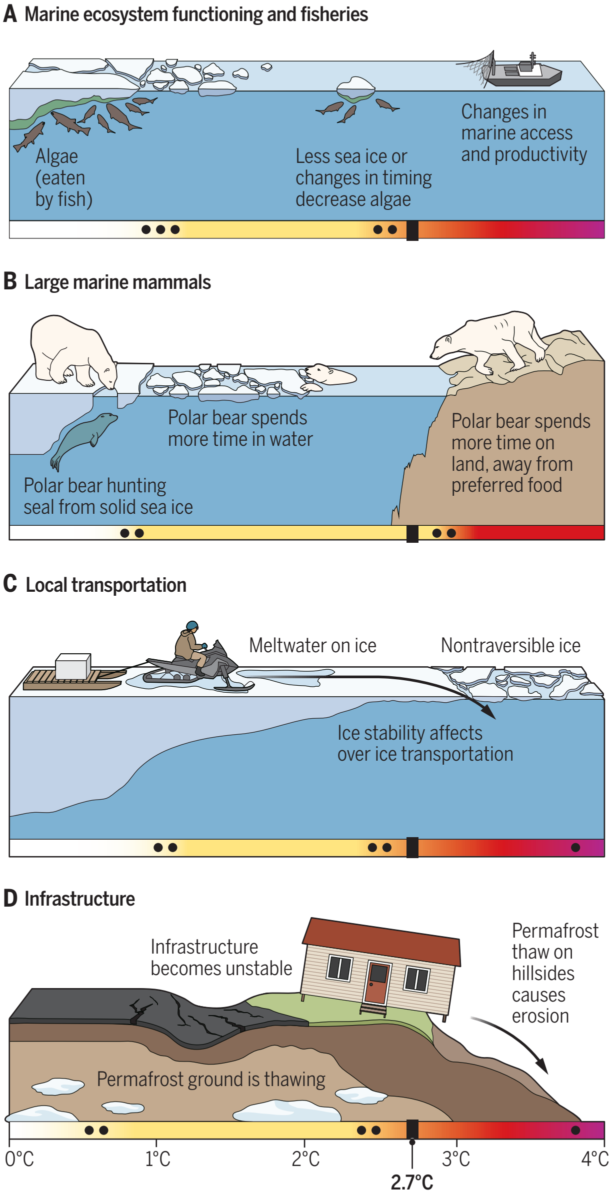

Fig. 4. Schematic of burning ember diagrams as a function of global warming levels. Impacts of global warming on (**A**) marine ecosystem functioning and fisheries, (**B**) large marine mammals, (**C**) local transportation, and (**D**) infrastructure. Colors indicate risk level as a function of global warming: white, undetectable; yellow, moderate; red, high; purple, very high. Black bar indicates 2.7°C. Confidence in assessment of risk transitions by warming levels is indicated by the number of dots shown, from three (high) to one (low). No dots indicate confidence could not be assessed or a risk transition threshold was not met.

ADAPTED BY K. HOLOSKI/*SCIENCE* FROM VICTOR O. LESHYK

Cascading risks to ecosystems and society at 2.7°C of global warming

As these findings show, at 2.7°C, the Arctic climate system transformation will be so extensive that the Arctic will no longer resemble the one we know today, with far-reaching consequences. Already at the current level of global warming, climate-related hazards and impacts are widespread and will become more frequent and intense as global warming continues (*56*). With direct and attributable changes being amplified in the Arctic, their knock-on effects will create cascading risks across all sectors of society, extending across local to international borders.

At 2.7°C, some of the most severe cascading concerns arising from the loss of sea ice, permafrost thaw, and Greenland mass loss, include risks to (i) marine ecosystems and fisheries, (ii) large marine mammals and seabirds, (iii) local transportation and shipping, and (iv) infrastructure. Using a standardized and transparent method established and refined over the past three IPCC assessment cycles, we present here a series of adapted burning ember diagrams that visualize risk thresholds as a function of global mean temperature increase. We highlight Arctic systems that are projected to pose particularly high levels of risk at 2.7°C, defined through both expert assessments and current literature and in consideration of the probability of severe and widespread impacts, the presence of critical irreversibility, and adaptation limits (*57*) (Fig. 4).

Marine ecosystems and fisheries

Loss of sea ice will severely impact marine ecosystems and marine life that have evolved and adapted to the natural low-light and cold-ocean conditions (Fig. 4A). Key ecosystem components such as ice algae, phytoplankton, zooplankton, and cold water corals have varied tolerance levels to expected warming, acidification, deoxygenation, and particulate organic carbon flux. The impacts of these ecosystem components will have implications for subsistence-based and large-scale commercial fisheries by 2.7°C, because fish stocks are expected to contract poleward and toward geopolitical and national boundaries (Fig. 4A). This will affect transboundary stocks, increase conflict in fisheries management, and alter distances to major distribution ports. Reductions in fish productivity, yields, and biomass also pose risks to regional and global food and nutritional security, especially among local Indigenous peoples already experiencing food and nutritional scarcity (*58*).

Large marine mammals and seabirds

A new analysis based on CMIP6 models projects that the southern Hudson Bay polar bear population will be the first population of bears likely to disappear between 1.5° and 2°C of global warming (*59*). By 2.7°C, the western Hudson Bay population will likely also face extinction (*59*), while polar bears in other Arctic regions will start to experience fasting periods similar to those currently seen in Hudson Bay (Fig. 4B). Other Arctic marine mammals, such as Beluga whales and ice-dependent seals, will face moderate risk at 2.7°C warming, with potential irreversible impacts related to shifts in their range and prey, as well as increased pup mortality rates (*60*). New studies show that Arctic seabirds are particularly vulnerable at 2.7°C (*61*, *62*) because of their low temperature–mediated plasticity in reproductive timing and vulnerability to mismatches in prey abundance.

Local transportation and maritime shipping

New studies show that local travel by road, over sea ice, and along land trails will create increased safety risks well before 2.7°C (*63*) (Fig. 4C). Risk of injury or mortality is already increasing on ice roads and along sea-ice trails as a result of river and sea-ice variability and diminishing reliability of Indigenous knowledge. Search and rescue needs and costs will increase, and changes in landfast sea ice will limit safe subsistence hunting among Indigenous peoples and increase food insecurity (*58*). Simultaneously, prolonged ice-free conditions will facilitate longer open water season lengths and expanded routing options for domestic resupply, fisheries, tourism, and international trade (*64*–*66*). However, increasingly mobile sea ice and extreme weather events will increase navigational risks. The northern sea route along the coast of Russia will be ice free earlier and for longer than other routes [including the NWP and transpolar route (TPR) via the central Arctic Ocean], yet pressure will increase on the NWP and TPR, considering ongoing geopolitical tensions with Russia. Increased shipping activity will further increase underwater noise (*67*), ship strikes (*68*), and pollution (*69*) that exacerbate habitat disruption, breeding challenges, and feeding stress for marine species. Moreover, these impacts can extend through the food web, affecting the displacement, ecosystem stability, and population viability that further jeopardizes the food security of Indigenous communities (*70*, *71*).

Infrastructure

Thawing surface permafrost as a climate hazard has a direct influence on ecosystems and people (*6*) (Fig. 4D). When the top layer thaws, the melting ground ice results in ground subsidence as earth materials collapse into the volume previously occupied by ice. Ground-ice loss can also lead to abrupt thawing, triggering rapid geomorphic changes in permafrost terrain beyond what would be expected from gradual temperature changes alone (*26*). In the Arctic, a large fraction of the industrial and economic development in the region is built upon permafrost, including its use for the storage of industrial waste. A recent estimate suggests that most of these contaminated sites will be impacted by permafrost degradation by the end of the century (*72*), releasing contaminants into the food web. Although changes to permafrost unfold over years and decades, they are characterized by regional-scale responses of the landscapes that often appear catastrophic to residents and the global society. As such, permafrost thaw poses a direct threat to Arctic ecosystems and human health (*72*), as well as causing extensive damage to infrastructure and triggering coastal erosion, threatening the sustainable development of Arctic communities (*73*).

Lastly, sea level rise increases the risks of coastal erosion and flooding, loss of ecosystems, and saltwater intrusion into freshwater resources (*74*). SLR combined with sea-ice loss leads to large expanses of open water (fetch) that facilitate larger waves, leading to greater risks of coastal erosion and cascading implications for built infrastructure and coastal communities within the Arctic region (*75*). Given the large range of uncertainty in sea level rise projections, coastal communities are being forced to develop resilience plans for an uncertain future.

Compounding effects

Many of the direct and cascading impacts (observed) and risks (projected) arising from global warming can be compounded and accentuated by additional factors, including geopolitics, international tensions (war), fluctuating commodity prices, global trade policies, global demand and/or supply of precious minerals and other natural resources, supply chain disruptions, and pandemics, among many other socioeconomic or political influences (*57*, *76*). These compounding factors can sometimes occur rapidly, and at other times they can slowly influence climate-related risk levels and our ability to mitigate and adapt to climate-related changes; therefore they warrant careful consideration in any assessment. Recent Arctic examples include the diminishment of the ecosystem monitoring network that resulted from the loss of scientific collaboration in response to the Russian invasion of Ukraine (*77*); the full carbon flux monitoring network, including sites within the Russian Federation, contains 50% more information than a network without those sites. This loss can be partially compensated by building new infrastructure in places such as North America, but doing so comes at a cost and cannot recover all the data and knowledge that is missing in the face of diminished science cooperation (*78*). Further, in response to Russia's invasion of Ukraine, NATO is increasing its military readiness in the Arctic, which could lead to further militarization of the region and thus increased human presence that impacts how the natural environment is managed. The conflict has also led to higher energy prices and increased pressure on the exploitation of Arctic natural resources: For example, in 2023 the Biden administration approved a large oil-drilling project in the National Petroleum Reserve-Alaska; although new offshore-drilling leases are "temporarily" suspended, this moratorium could be reversed at any time.

An uncertain future

Anthropogenic activities, particularly fossil-fuel combustion, have increased the concentration of greenhouse gases in our planet's atmosphere to levels that are the highest in the history of humankind. This increase underscores humanity's dominating influence on the climate system, affecting all climate components from the depths of the ocean to the top of the atmosphere, and from the tropics to the polar regions.

To illustrate the scale of these impacts in the Arctic, we focused this review on projected conditions at two specific warming levels: +1.5°C and +2.7°C. However, we note that a future warming of +2.7°C should not be considered as a worst-case scenario. Rather, it represents the warming level that our planet would reach if all nations fulfill their promises of reducing greenhouse gas emissions as given in the NDCs. Should these promises not be kept, global warming could well exceed +2.7°C. By contrast, with increased efforts, a maximum warming level well below +2.7°C is still in reach.

To prevent further degradation and meet the needs of present and future generations will require bold, collaborative, and immediate action worldwide. This involves substantial investments in sustainable consumption and production, natural resource management, poverty eradication, green energy transitions, and the promotion of environmental and social sustainability. Reducing human carbon emissions through climate mitigation will help dampen changes in the Arctic and lessen global impacts. Additionally, there is an urgent need to invest in local and regional adaptation strategies to address the inevitable impacts and cascading risks of sea-ice loss, permafrost degradation, and rising sea levels, and these efforts must include the voices of the Indigenous people that call the Arctic home (*79*). Indigenous people in the Arctic have long understood the interconnectedness between their cultures, livelihoods, and the environment. As the Arctic transforms, they are increasingly advocating for policy changes that not only address the immediate environmental threats they face but also ensure that their rights, sovereignty, and traditional knowledge are respected as part of all climate solutions (*79*, *80*).

Given the Arctic's relative underdevelopment compared with other regions in the Northern Hemisphere, there is an opportunity to implement best practices and lessons learned, including the need for Indigenous codevelopment to foster a self-determined, sustainable, and innovative green economy (*81*, *82*). Transitioning energy use and production, enhancing maritime infrastructure, and aligning closely with the United Nations' Sustainable Development Goals are vital steps.

Although humanity has adapted to a wide range of climate conditions, continued warming and associated extreme heat, extreme weather events, and sea level rise could render parts of the world uninhabitable. In the Arctic, the global warming level decides the fate of entire landscapes: As remote and hostile as they might appear to any visitor, these distinctive landscapes are among the most vulnerable of our planet and are home to Indigenous peoples who hold knowledge and wisdom that cannot be forgotten or ignored. The future of the Arctic truly lies in our hands.

REFERENCES AND NOTES

1. Copernicus Climate Change Service, "The year 2024 set to end up as the warmest on record," (2024); https://climate.copernicus.eu/year-2024-set-end-warmest-record.
2. J. Rogelj *et al*., *Science* **380**, 1014–1016 (2023).
3. IPCC, in *Climate Change 2021: The Physical Science Basis*, V. Masson-Delmotte *et al.*, Eds. (Cambridge Univ. Press, 2021), pp. 3–32.
4. M. Rantanen *et al*., *Commun. Earth Environ.* **3**, 168 (2022).
5. E. Hanna *et al*., *Nat. Rev. Earth Environ.* **5**, 193–210 (2024).
6. M. Meredith *et al*., in *IPCC Special Report on the Ocean and Cryosphere in a Changing Climate*, H.-O. Pörtner *et al.*, Eds. (Cambridge Univ. Press, 2019), pp. 203–320.
7. M. B. Osman *et al*., *Nature* **599**, 239–244 (2021).
8. R. Bintanja, E. C. van der Linden, *Sci. Rep.* **3**, 1556 (2013).
9. C. Giesse, D. Notz, J. Baehr, *Earth's Futur.* **12**, e2024EF004961 (2024).
10. J. Stroeve, D. Notz, *Environ. Res. Lett.* **13**, 103001 (2018).
11. A. Jahn, M. Holland, J. Kay, *Nat. Rev. Earth Environ.* **5**, 164–176 (2024).
12. D. Notz, SIMIP Community, *Geophys. Res. Lett.* **47**, e2019GL086749 (2020).
13. N. C. Swart, J. Fyfe, E. Hawkins, J. Kay, A. Jahn, *Nat. Clim. Chang.* **5**, 86–89 (2015).
14. C. Heuzé, A. Jahn, *Nat. Commun.* **15**, 10101 (2024).
15. I. V. Polyakov *et al*., *Science* **381**, 972–979 (2023).
16. D. Notz, J. Stroeve, *Science* **354**, 747–750 (2016).
17. B. Fox-Kemper *et al*., in *Climate Change 2021: The Physical Science Basis*, V. Masson-Delmotte *et al.*, Eds. (Cambridge Univ. Press, 2021), pp.1211–1362.
18. J. Mouginot *et al*., *Proc. Natl. Acad. Sci. U.S.A.* **116**, 9239–9244 (2019).
19. R. Rietbroek, S.-E. Brunnabend, J. Kusche, J. Schröter, C. Dahle, *Proc. Natl. Acad. Sci. U.S.A.* **113**, 1504–1509 (2016).
20. S. B. Simonsen, V. R. Barletta, W. T. Colgan, L. S. Sørensen, *Geophys. Res. Lett.* **48**, e2020GL091216 (2021).
21. J. Box *et al*., *Nat. Clim. Chang.* **12**, 808–813 (2022).
22. C. A. Greene, A. S. Gardner, M. Wood, J. K. Cuzzone, *Nature* **625**, 523–528 (2024).
24. J. Obu, *J. Geophys. Res. Earth Surf.* **126**, e2021JF006123 (2021).
23. Y. Choi, M. Morlighem, E. Rignot, M. Wood, *Commun. Earth Environ.* **2**, 26 (2021).
25. U. Mishra *et al*., *Sci. Adv.* **7**, eaaz5236 (2021).
26. E. A. Schuur *et al*., *Annu. Rev. Environ. Resour.* **47**, 343–371 (2022).
27. M. L. Druckenmiller *et al*., *Bull. Am. Meteorol. Soc.* **105**, S277–S330 (2024).
28. K. Nyland *et al*., *Polar Geogr.* **44**, 167–185 (2021).
29. J. M. Young *et al*., *Geophys. Res. Lett.* **49**, e2022GL100559 (2022).
30. L. Farquharson, V. E. Romanovsky, A. Kholodov, D. Nicolsky, *Nat. Geosci.* **15**, 475–481 (2022).
31. E. A. Schuur *et al*., *J. Geophys. Res. Biogeosci.* **126**, e2020JG006044 (2021).
32. E. S. Euskirchen *et al*., *Glob. Change Biol.* **30**, e17139 (2024).
33. E. A. G. Schuur *et al*., *Philos. Trans. R. Soc. Lond. Ser. A* **381**, 20220201 (2023).
34. C. R. See *et al*., *Nat. Clim. Chang.* **14**, 853–862 (2024).
35. R. Commane *et al*., *Proc. Natl. Acad. Sci. U.S.A.* **114**, 5361–5366 (2017).
36. A.-M. Virkkala *et al*., *Nat. Clim. Chang.* **2025** (2025).
37. A. D. McGuire *et al*., *Proc. Natl. Acad. Sci. U.S.A.* **115**, 3882–3887 (2018).
38. L. Bruhwiler, F. Parmentier, P. Crill, M. Leonard, P. Palmer, *Curr. Clim. Change Rep.* **7**, 14–34 (2021).
39. D. Notz, J. Stroeve, *Curr. Clim. Change Rep.* **4**, 407–416 (2018).
40. F. Vermassen *et al*., *Nat. Geosci.* **16**, 723–729 (2023).
41. M. Zeitz, R. Reese, J. Beckmann, U. Krebs-Kanzow, R. Winkelmann, *Cryosphere* **15**, 5739–5764 (2021).
42. H. Goelzer *et al*., *Cryosphere* **14**, 3071–3096 (2020).
43. R. Millan *et al*., *Nat. Commun.* **14**, 6914 (2023).
44. J. Y. Park *et al*., *Nat. Commun.* **14**, 636 (2023).
45. B. Noël, L. van Kampenhout, J. Lenaerts, W. van de Berg, M. van den Broeke, *Geophys. Res. Lett.* **48**, e2020GL090471 (2021).
46. N. Bochow *et al*., *Nature* **622**, 528–536 (2023).
47. F. Pattyn *et al*., *Nat. Clim. Chang.* **8**, 1053–1061 (2018).
48. D. Höning, M. Willeit, A. Ganopolski, *Environ. Res. Lett.* **19**, 024038 (2024).
49. J. Gregory, S. George, R. Smith, *Cryosphere* **14**, 4299–4322 (2020).
50. A. A. Cluett, E. K. Thomas, *Proc. Natl. Acad. Sci. U.S.A.* **118**, e2022916118 (2021).
51. A. J. Christ *et al*., *Science* **381**, 330–335 (2023).
52. X. Peng *et al*., *Earths Futur.* **11**, e2023EF003573 (2023).
53. L. M. Farquharson *et al*., *Geophys. Res. Lett.* **46**, 6681–6689 (2019).
54. S. M. Natali *et al*., *Proc. Natl. Acad. Sci. U.S.A.* **118**, e2100163118 (2021).
55. P. M. Cox *et al*., *Nat. Commun.* **15**, 1885 (2024).
56. S. I. Seneviratne *et al*., in *Climate Change 2021: The Physical Science Basis*, V. Masson-Delmotte *et al.*, Eds. (Cambridge Univ. Press, 2021), pp. 1513–1766.
57. A. Constable *et al*., in *Climate Change 2022: Impacts, Adaptation and Vulnerability*, H.-O. Pörtner *et al.*, Eds. (Cambridge Univ. Press, 2022), pp. 2319–2368.
58. G. A. Gibson *et al*., *Earth Sci. Syst. Soc.* **4**, 10082 (2024).
59. J. Stroeve *et al*., *Commun. Earth Environ.* **5**, 296 (2024).
60. L. Boveng, H. Ziel, B. McClintock, M. Cameron, *Deep Sea Res. Part II Top. Stud. Oceanogr.* **181-182**, 104904 (2020).
61. C. Sauser *et al*., *Front. Ecol. Evol.* **11**, 1107992 (2023).
62. J. M. Morten *et al*., *Glob. Change Biol.* **29**, 5596–5614 (2023).
63. H. E. Greaves *et al*., *Environ. Res. Lett.* **18**, 025006 (2023).
64. L. Mudryk *et al*., *Nat. Clim. Chang.* **11**, 673–679 (2021).
65. M. M. Bennett, S. R. Stephenson, K. Yang, M. T. Bravo, B. De Jonghe, *Mar. Policy* **121**, 104178 (2020).
66. H. P. Huntington *et al*., *Transp. Res. Part D Transp. Environ.* **118**, 103731 (2023).
67. M. Ladegaard *et al*., *Sci. Rep.* **11**, 23360 (2021).
68. D. D. W. Hauser, K. L. Laidre, H. L. Stern, *Proc. Natl. Acad. Sci. U.S.A.* **115**, 7617–7622 (2018).
69. C. Pertoldi, C. Sonne, R. Dietz, N. M. Schmidt, V. Loeschcke, *J. Zool.* **279**, 321–328 (2009).
70. E. K. Galappaththi, J. D. Ford, E. M. Bennett, F. Berkes, *J. Environ. Manage.* **250**, 109534 (2019).
71. K. K. Holsman *et al*., *Nat. Commun.* **11**, 4579 (2020).
72. M. Langer *et al*., *Nat. Commun.* **14**, 1721 (2023).
73. J. Hjort *et al*., *Nat. Rev. Earth Environ.* **3**, 24–38 (2022).
74. S. Cooley *et al*., in *Climate Change 2022: Impacts, Adaptation and Vulnerability*, H.-O. Pörtner *et al.*, Eds. (Cambridge Univ. Press, 2022), pp. 379–550.
75. D. Nielsen *et al*., *Nat. Clim. Chang.* **12**, 263–270 (2022).
76. H. P. Huntington *et al*., *Ambio* **51**, 298–306 (2022).
77. E. López-Blanco *et al*., *Nat. Clim. Chang.* **14**, 152–155 (2024).
78. E. Schuur, M. Pallandt, M. Göckede, *Nat. Clim. Chang.* **14**, 410–411 (2024).
79. Inuit Circumpolar Council, On thin ice: Inuit Climate Leadership for the World-UNFCCC COP 28 Position Paper (2023); https://www.inuitcircumpolar.com/news/on-thin-ice-inuit-climate-leadership-for-the-world-unfccc-cop-28-position-paper/.
80. S. Watt-Cloutier, *The Right to Be Cold* (Univ. of Minnesota Press, 2018).
81. R. Hill, F. J. Walsh, J. Davies, A. Sparrow, M. Mooney, *Glob. Environ. Change* **65**, 102161 (2020).
82. M. Jorgensen, *Rebuilding Native Nations: Strategies for Governance and Development* (Univ. of Arizona Press, 2007).
83. N. J. Steinert, M. V. Debolskiy, E. Burke, F. García-Pereira, H. Lee, Dataset: Evaluating permafrost definitions for global permafrost area estimates in CMIP6 climate models (2023); https://zenodo.org/doi/10.5281/zenodo.10103000.

ACKNOWLEDGMENTS

We thank the World Climate Research Programme Climate and Cryosphere (CliC) Project for coordinating this special issue. We thank V. Leyshk for providing artwork for Figs. 3 and 4. We thank the World Climate Research Programme, which, through its Working Group on Coupled Modelling, coordinated and promoted CMIP6. We thank the climate modeling groups for producing and making available their model output, the Earth System Grid Federation (ESGF) for archiving the data and providing access, and the multiple funding agencies who support CMIP6 and ESGF. **Funding:** J.C.S. was funded under the Canada 150 Research Chairs Program, C150 grant 50296. Additional funding was provided by Horizon 2020 CRiceS grant 101003826. D.N. acknowledges funding from the Deutsche Forschungsgemeinschaft under Germany's Excellence Strategy (EXC 2037; CLICCS – Climate, Climatic Change, and Society; project no. 390683824). J.D. was funded under the Canada Research Chairs Program. C.G. acknowledges funding from the German Environment Agency (UBA) with funds provided by the Federal Ministry for the Environment, Nature Conservation, Nuclear Safety and Consumer Protection (BMUV; grant 3722 18 302 1). D.D-J. was funded under the Canada Excellence Research Program grant CERC-2018-00002 and the ERC Synergy Program Green2Ice. E.A.G.S. was funded by NSF Arctic System Science Research Networking Activities grant 1931333 and by the Minderoo Foundation. The data analysis for this study was performed with computing resources from the German Climate Computing Center (Deutsches Klimarechenzentrum, DKRZ). **Author contributions:** Project administration and supervision: J.C.S.. Writing (original draft and reviewing) and conceptualization: J.C.S., D.N., J.D., T.S., and D.D-J. Visualization: C.G. and T.S. **Competing interests:** The authors declare that they have no competing interests. **Data and materials availability:** All data used for this study are publicly available. The CMIP6 data can be accessed from the ESGF at https://esgf-metagrid.cloud.dkrz.de/search/cmip6-dkrz/. The precalculated permafrost area of CMIP6 models was retrieved from Zenodo (*83*). The code to generate Figs. 1 and 2 is available at https://gitlab.rrz.uni-hamburg.de/bax2799/arctic-gwl-analyses.

SUPPLEMENTARY MATERIALS

science.org/doi/10.1126/science.ads1549
Materials and Methods
References (*84*–*88*)

Submitted 26 August 2024; accepted 6 January 2025
10.1126/science.ads1549

RESEARCH

IN *SCIENCE* JOURNALS

Edited by **Michael Funk**

TOPOLOGICAL OPTICS

Viewing topology in higher dimensions

The symmetry and topology of physical systems are closely related to the symmetries governing the topological properties. Quasicrystals are ordered systems but have no translation or rotational symmetries. Theoretical work has shown that quasicrystals can be understood as the projection of a higher-dimensional crystal onto a lower-dimensional space. Tsesses *et al*. developed a plasmonic-based system in which to study the implications of that projection for topological invariants. When going into four-dimensional space and projecting it down into two dimensions, the complex dynamics of light waves on the plasmonic quasicrystal exhibited motions of four-dimensional topological charge vectors and associated topological charge conservation laws. This approach allows the study of topological systems in higher dimensions. — Ian S. Osborne

Science p. 644, 10.1126/science.adt2495

Artistic depiction of a four-dimensional regular lattice that forms a quasicrystalline pattern with fivefold symmetry when projected in two dimensions.

PLANT SCIENCE

Hydropatterning of maize roots

In a heterogeneous soil landscape, plant root systems must locate water. Scharwies *et al*. found that some maize varieties produce lateral roots at locations where water is limited, whereas others more efficiently direct growth toward water. Uncovering the genetic basis for this trait variance, the authors found that auxin, ethylene, and an arabinogalactan protein work together to encourage lateral root development where water is present while suppressing lateral roots from forming on drier parts of the root. Variation in genes underlying these components leads to variation in root hydropatterning, potentially affecting the success of some maize varieties in drier environments. —Madeleine Seale

Science p. 666, 10.1126/science.ads5999

EVOLUTION

Untangling the giant Y in a plant

The Y chromosome is notorious for its degeneration in XY species; however, giant Y chromosomes have been noted in several species. Moraga *et al*. and Akagi *et al*. sequenced the genomes of the plant *Silene latifolia* and several relatives to gain insight into the evolution of dioecy in this species and the features of their approximately 500-megabase Y chromosome. Both groups found that there has been degeneration of ancestral genes and large expansions of transposable elements on both the X and Y chromosomes. They also identified several candidate sex-determining genes. These studies reveal the evolutionary dynamics of the first flowering plant in which sex chromosomes were observed. —Corinne Simonti

Science p. 630, 10.1126/ science.adj7430, p. 637, 10.1126/ science.adk9074

SPECTROSCOPY

Squeezing more out of spectroscopy

Optical-frequency combs and dual-comb spectroscopy have already been shown to enable high-resolution spectroscopy. Herman *et al*. have now taken dual-comb spectroscopy to the quantum regime, demonstrating the metrological advantage of using quantum mechanically squeezed light in optical-frequency combs. Dual-frequency comb spectroscopy using squeezed light enhances the sensitivity of molecular detection, in this case for hydrogen sulfide, with the quantum noise reduction leading to a twofold quantum speedup in the determination of gas concentration. This approach will motivate further development using squeezed states for frequency comb metrology, high-resolution spectroscopy, and sensing applications. —Ian S. Osborne

Science p. 653, 10.1126/science.ads6292

IMAGE: TIM DAVIS

NEUROSCIENCE

Flexibility by suppressing instinct

It has been proposed that one of the many functions of the sensory cortex is to modify the vigor of instinctive responses by modulation of subcortical circuits. Mederos *et al*. uncovered a subcortical synaptic plasticity mechanism for learning to suppress instinctive defensive behavior. The critical pathway was the projection from higher-order visual areas posterolateral of the primary visual cortex (area V1) to the ventral lateral geniculate nucleus (vLGN), which modulated instinctive fear responses based on experience. After learning, this pathway was no longer needed. This learning-induced plasticity involved endocannabinoid-mediated long-term suppression of inhibitory synapses onto vLGN neurons activated by posterolateral higher-order visual areas, which decreased presynaptic release probability. —Peter Stern

Science p. 682, 10.1126/science.adr2247

METABOLISM

Role of blood vessels in diabetes

Insulin resistance, often induced by obesity, is the underlying abnormality for type 2 diabetes. Most studies looking at mechanisms for obesity and insulin resistance have examined cells known to play key roles in metabolism, such as those in the liver, skeletal muscle, and adipose tissue. Cho *et al*. shifted their focus to the vasculature, more specifically, endothelial insulin signaling. The authors discovered that adrenomedullin, a peptide hormone that increases in concentration in the setting of obesity, inhibits insulin signaling in the endothelium of both humans and mice. In addition to examining the underlying mechanism, the authors showed in mouse models that an adrenomedullin receptor antagonist has beneficial effects on insulin sensitivity, suggesting a potential direction for future therapeutic approaches. —Yevgeniya Nusinovich

Science p. 674, 10.1126/science.adr4731

GPCR SIGNALING

Mutual GPCR–G protein regulation

Ghrelin is a peptide hormone that acts on its G protein–coupled receptor (GPCR) to stimulate appetite. Signal transduction by GPCRs requires the activation of intracellular heterotrimeric G proteins in a process involving transient conformational changes in both the receptor and the $G\alpha$ subunit. Mannes *et al*. developed synthetic peptides that mimicked the stabilizing effect of $G\alpha_q$ on the active conformation of the ghrelin receptor. Biochemical assays using these peptidomimetics demonstrated that G protein coupling allosterically increased the receptor's affinity for ghrelin, and that G protein activation occurred through a series of distinct interactions with the receptor. —Annalisa M. VanHook

Sci. Signal. (2025) 10.1126/scisignal.ado7692

IMMUNOTHERAPY

Fine-tuning of trogocytosis

T cells can exchange certain membrane-bound proteins in a carefully controlled process called trogocytosis, but the mechanisms that fine-tune T cell trogocytosis remain to be determined. Using human and murine chimeric antigen receptor (CAR) T cells, Barbera *et al*. found that T cells actively transferred CARs through trogocytosis, which allowed recipient T cells to acquire antitumor immunity. Trogocytosis was mediated by the transmembrane domains of membrane-bound proteins, which influenced the way that proteins were anchored to the plasma membrane. —Hannah M. Isles

Sci. Immunol. (2025); 10.1126/sciimmunol.ado2054

IN OTHER JOURNALS

Edited by **Corinne Simonti** *and* **Jesse Smith**

REGENERATION

Not so different after all

Several species of spiny mice (*Acomys dimidiatus, A. kempi,* and *A. percivali*) have long been of interest because of their tissue regeneration capabilities. These mice also show traits not seen in other mice, such as having pups born with fur and open eyes. In this study, Riddell *et al.* examined the regenerative abilities of several species of mice and two outgroups. They found that one mouse species demonstrated similar regenerative capabilities to the *Acomys* species, the closely related *Lophuromys zena*. This species does not share *Acomys* species' other nontraditional traits, but these results hint that enhanced regeneration may be found across the broader clade, suggesting potential targets for future study. —Corinne Simonti

Proc. Natl. Acad. Sci. U.S.A. (2024) 10.1073/pnas.2420726122

The regenerative properties shown by the eastern spiny mouse (*Acomys dimidiatus*) may be more broadly shared across the clade.

PHOTO: GERARD LACZ/SCIENCESOURCE

INFERTILITY

Taking up the cause(s) of infertility

Infertility is a common multifactorial disorder that affects a sizeable percentage of couples worldwide, and up to one-third of affected patients have no known explanation for their diagnosis. Previous genetic studies of female infertility have identified some common mutations that may be involved. Ruotsalainen *et al*. analyzed tens of thousands of female patients with infertility

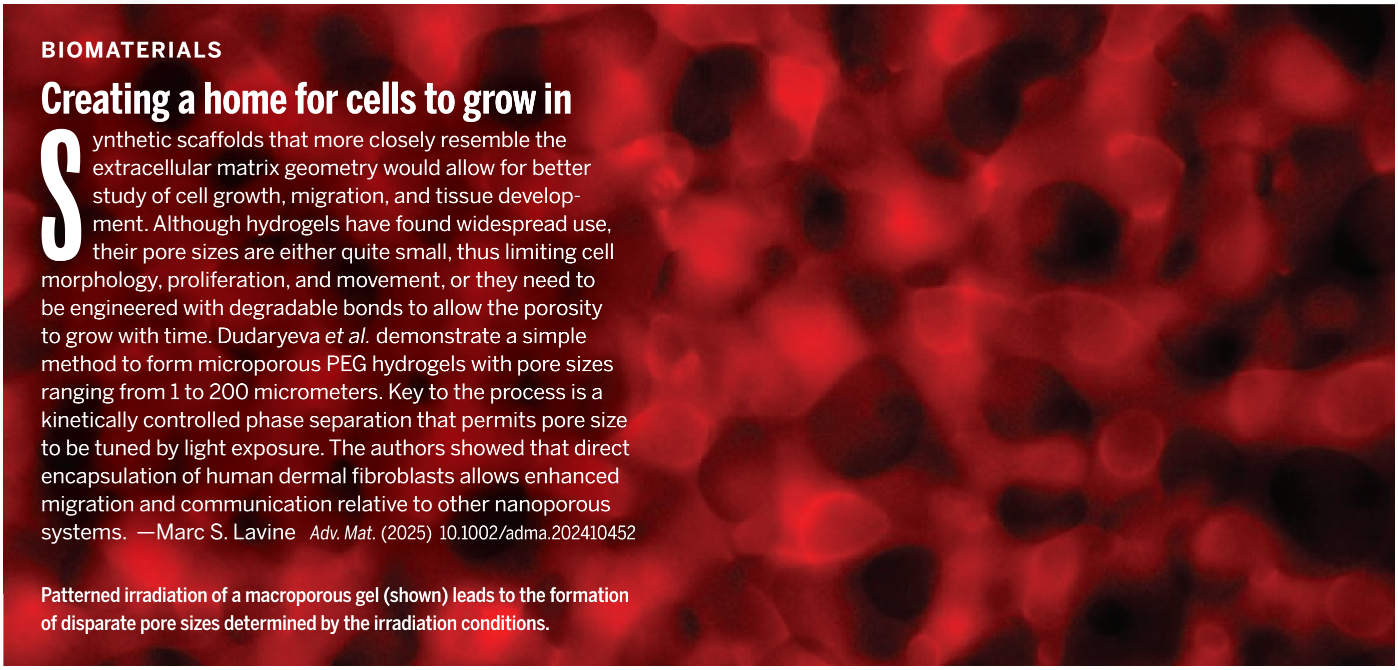

BIOMATERIALS

Creating a home for cells to grow in

Synthetic scaffolds that more closely resemble the extracellular matrix geometry would allow for better study of cell growth, migration, and tissue development. Although hydrogels have found widespread use, their pore sizes are either quite small, thus limiting cell morphology, proliferation, and movement, or they need to be engineered with degradable bonds to allow the porosity to grow with time. Dudaryeva *et al.* demonstrate a simple method to form microporous PEG hydrogels with pore sizes ranging from 1 to 200 micrometers. Key to the process is a kinetically controlled phase separation that permits pore size to be tuned by light exposure. The authors showed that direct encapsulation of human dermal fibroblasts allows enhanced migration and communication relative to other nanoporous systems. —Marc S. Lavine *Adv. Mat.* (2025) 10.1002/adma.202410452

Patterned irradiation of a macroporous gel (shown) leads to the formation of disparate pore sizes determined by the irradiation conditions.

and controls from the FinnGen database, which provides a large and well-curated dataset in a relatively homogeneous population. This enabled the authors to identify rarer but clinically relevant genes that had not been previously linked to female infertility in human patients. —Yevgeniya Nusinovich

Am. J. Hum. Genet. (2024) 10.1016/j.ajhg.2024.10.018

NEUROSCIENCE

Aging of the brain and heart

Aging significantly affects both brain and heart health and is associated with an increased risk of various neurodegenerative and cardiovascular conditions. The brain and heart are linked through extensive biophysiological pathways. Amirmoezzi *et al.* studied a cohort of middle-aged and older individuals to estimate the biological age of the brain and heart using both whole-brain and network-specific approaches. Brain age was estimated using magnetic resonance imaging (MRI)–derived morphology and connectivity features, and heart age was estimated from cardiac MRI, carotid ultrasound, and pulse-wave analysis. Cardiovascular aging, specifically the decline in functional capacity and physiological changes, was associated with the aging of distinct brain networks and subcortical regions. —Peter Stern

J. Neurosci. (2024) 10.1523/JNEUROSCI.1440-24.2024

PARENTING

Parents favor agreeable kids

Although most parents are unwilling to admit that they have a "favorite child," their children often sense that one sibling is favored. Perceived parental favoritism has been linked to developmental consequences, including children's mental health, self-worth, academic achievement, child-parent relationship quality, and emotional stability. Jensen and Jorgensen-Wells conducted a meta-analysis of 30 published journal articles involving nearly 20,000 participants to identify predictors of favoritism. They found that parents slightly favored daughters and easier-to-parent children (i.e., those who were agreeable and responsible). Younger siblings were slightly favored, and older siblings were given more autonomy. Because intentional or unintentional favoritism can affect children's well-being and lifelong relationships, early intervention may mitigate damaging family dynamics. —Ekeoma Uzogara

Psychol. Bull. (2025) 10.1037/bul0000458

2D MATERIALS

Making a single-crystal layer large

Scaling up the production of two-dimensional (2D) transition metal dichalcogenides for industrial applications is hindered by high defect density and low uniformity. Traditional crystal growth techniques such as the Czochralski method are often not suitable for 2D materials because of their high melting points and difficulty in controlling the thickness of the deposited layers. Jiang *et al.* report growth of a centimeter-scale single-crystal molybdenum disulfide (MoS_2) using a liquid-to-solid crystallization mechanism that is similar to the Czochralski method. The authors used a low-melting-point precursor and chemical processes to increase the nucleation barrier while reducing the diffusion barrier. The MoS_2 layers thus produced were transferred to silicon wafers for fabrication of field effect transistors with high yields and minimal performance variation. —Sumin Jin

Nat. Mater. (2025) 10.1038/s41563-024-02069-7

INORGANIC CHEMISTRY

Boron in its element

Most boron compounds engage all three of their available valence electrons in bonding. Kennedy *et al.* now report the synthesis, isolation, and crystal structure of a compound in which a single boron center remains in its elemental zeroth oxidation state while exclusively accepting dative bonds from two cyclic alkyl(amino) carbenes. The orange-brown compound was paramagnetic and oxygen sensitive but otherwise stable up to 170°C. It accepted an electron to form a red-pink lithium boride that was also structurally characterized, and it could contrariwise be oxidized to a purple cyanoborylene. —Jake S. Yeston

J. Am. Chem. Soc. (2025) 10.1021/jacs.4c14915

IMAGE: O. DUDARYEVA *ET AL.*, *ADV. MAT.* (2025) 10.1002/ADMA.202410452

RESEARCH ARTICLE SUMMARY

NEPHROLOGY

Kidney multiome-based genetic scorecard reveals convergent coding and regulatory variants

Hongbo Liu*, Amin Abedini, Eunji Ha, Ziyuan Ma, Xin Sheng, Bernhard Dumoulin, Chengxiang Qiu, Tamas Aranyi, Shen Li, Nicole Dittrich, Hua-Chang Chen, Ran Tao, Der-Cherng Tarng, Feng-Jen Hsieh, Shih-Ann Chen, Shun-Fa Yang, Mei-Yueh Lee, Pui-Yan Kwok, Jer-Yuarn Wu, Chien-Hsiun Chen, Atlas Khan, Nita A. Limdi, Wei-Qi Wei, Theresa L. Walunas, Elizabeth W. Karlson, Eimear E. Kenny, Yuan Luo, Leah Kottyan, John J. Connolly, Gail P. Jarvik, Chunhua Weng, Ning Shang, Joanne B. Cole, Josep M. Mercader, Ravi Mandla, Timothy D. Majarian, Jose C. Florez, Mary E. Haas, Luca A. Lotta, Regeneron Genetics Center, GHS-RGC DiscovEHR Collaboration, Theodore G. Drivas, Penn Medicine BioBank, Ha My T. Vy, Girish N. Nadkarni, Laura K. Wiley, Melissa P. Wilson, Christopher R. Gignoux, Humaira Rasheed, Laurent F. Thomas, Bjørn Olav Åsvold, Ben M. Brumpton, Stein I. Hallan, Kristian Hveem, Jie Zheng, Jacklyn N. Hellwege, Matthew Zawistowski, Sebastian Zöllner, Nora Franceschini, Hailong Hu, Jianfu Zhou, Krzysztof Kiryluk, Marylyn D. Ritchie, Matthew Palmer, Todd L. Edwards, Benjamin F. Voight, Adriana M. Hung, Katalin Susztak*

INTRODUCTION: More than 800 million people worldwide suffer from kidney disease, with nearly 1 million dying annually from renal failure. Kidney function is highly heritable, predominantly influenced by common genetic variants. Genome-wide association studies (GWASs) map associations between these variants and disease, yet more than 90% of GWAS-identified variants reside in noncoding genome regions. This presents notable challenges in pinpointing their target genes and regulatory functions, a dilemma known as the "variant-to-gene" or "variant-to-function" problem.

RATIONALE: In the past decade, various tools have been developed to connect genetic variants to disease development. These include mapping the association of variants with quantitative traits, such as gene expression (eQTL; QTL, quantitative trait loci), chromatin accessibility (acQTL), and DNA methylation (meQTL). Allele-specific analysis offers valuable insights for fine-mapping these elusive causal regulatory variants. Single-cell multimodal methodologies have further enabled analysis at the single-cell level. This study aimed to define the genetic architecture of glomerular filtration rate (GFR) and use complementary omics datasets and tools to nominate regulatory variants, genes, and cell types involved in kidney function regulation.

RESULTS: We conducted a multiancestry GWAS for kidney function, measured by the estimated GFR based on serum creatinine (eGFRcrea), involving 2.2 million individuals. Our analysis identified 1026 (97 previously unknown) independent loci. By mapping kidney function–associated common DNA variants across European-, East Asian–, and African-ancestry populations, we observed an attenuation of newly identified signals in European populations and highlighted the value of population diversity for further discoveries.

Additionally, we analyzed genotype effects on allele-specific gene expression and regulatory circuitries in more than 700 kidneys and 237,000 cells. We developed a statistical approach named Open4Gene, which identified 1351 target genes of genetic variants located within open chromatin regions.

Furthermore, we introduced the "Kidney Disease Genetic Scorecard" concept, which integrates 32 types of data to support genetic information and nominate causal genetic variants and genes for kidney disease. The Kidney Disease Genetic Scorecard prioritized 24,437 regulatory variants targeting 1060 genes. We also observed convergence of coding and regulatory variations in specific genes, identifying 1363 coding variants disrupting 782 genes, with 601 genes also targeted by regulatory variants. Notably, 124 genes were identified as amenable to targeting by FDA-approved drugs, presenting opportunities for drug repurposing and therapeutic development.

CONCLUSION: We provide a genetic blueprint for kidney function, enabling genetics-based prognostication and drug discovery. This study presents a large-scale analysis of the genetic architecture of human kidney function, utilizing various omics datasets to offer biological insights. Emphasizing the convergence of coding and regulatory variants on key disease genes, we introduce the concept of a Kidney Disease Genetic Scorecard for disease diagnostics and therapeutic development. ■

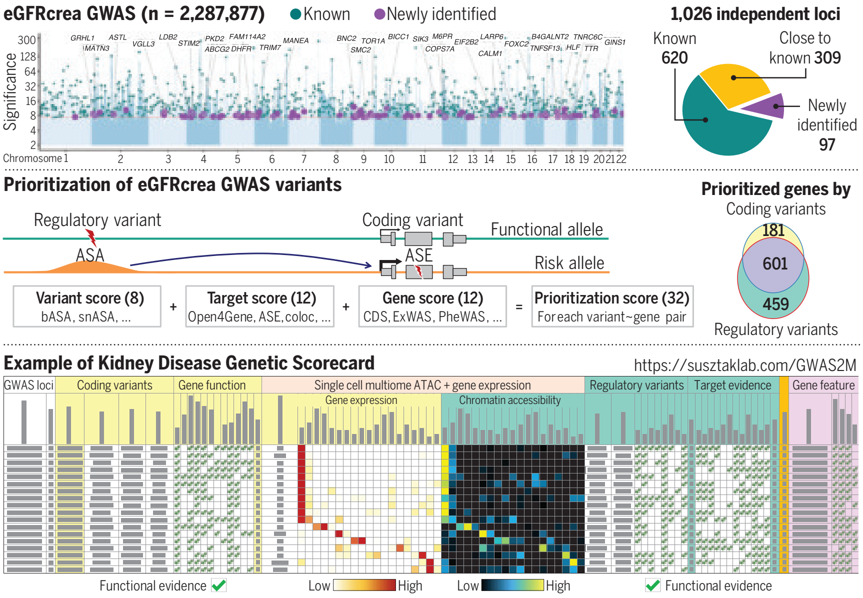

Kidney Disease Genetic Scorecard uncovers the genetic architecture of kidney function and putative target genes. We conducted a multiancestry GWAS in 2.2 million individuals and identified 1026 (97 previously unknown) independent loci. Integrating 32 types of genetic information, we present the Kidney Disease Genetic Scorecard for prioritizing potentially causal genes, cell types, and druggable targets for kidney disease. ASA, allele-specific accessibility; ASE, allele-specific expression; bASA, bulk assay for transposase-accessible chromatin (ATAC)–based allele-specific accessibility; snASA, single-nuclear ATAC-based allele-specific chromatin accessibility; coloc, colocalization; CDS, coding sequence; ExWAS, exome-wide association study; PheWAS, phenome-wide association study.

The list of authors and their affiliations is available in the full article online.

*Corresponding author. Email: Hongbo Liu (hongbo_liu@urmc.rochester.edu); Katalin Susztak (ksusztak@pennmedicine.upenn.edu)

Cite this article as H. Liu *et al.*, *Science* **387**, eadp4753 (2025). DOI: 10.1126/science.adp4753

READ THE FULL ARTICLE AT
https://doi.org/10.1126/science.adp4753

RESEARCH ARTICLE SUMMARY

IMMUNOMETABOLISM

Nutrient-driven histone code determines exhausted $CD8^+$ T cell fates

Shixin Ma, Michael S. Dahabieh, Thomas H. Mann, Steven Zhao, Bryan McDonald, Won-Suk Song, H. Kay Chung, Yagmur Farsakoglu, Lizmarie Garcia-Rivera, Filipe Araujo Hoffmann, Shihao Xu, Victor Y. Du, Dan Chen, Jesse Furgiuele, Michael A. LaPorta, Emily Jacobs, Lisa M. DeCamp, Brandon M. Oswald, Ryan D. Sheldon, Abigail E. Ellis, Longwei Liu, Peixiang He, Yingxiao Wang, Cholsoon Jang, Russell G. Jones, Susan M. Kaech*

INTRODUCTION: Effector $CD8^+$ T cells (TEFF), also known as "killer" T cells, can gradually lose their cytotoxicity and become dysfunctional or exhausted (TEX) in the face of chronic infections and cancer, compromising protective immunity and weakening the therapeutic effects of immune checkpoint blockade (ICB) and chimeric antigen receptor (CAR) T cell therapy. TEX cell development is governed by multiple epigenetic and metabolic changes, making it critical to understand how these processes are linked. Fundamental questions include whether $CD8^+$ T cells prefer specific nutrients as they differentiate, and how the metabolism of specific types of nutrients influences epigenetic modifications and gene expression, leading to TEX differentiation. Central to these questions is whether changes in histone modifications, such as acetylation, are regulated by the total intracellular pools of metabolites produced by key nutrients [e.g., acetyl–coenzyme A (CoA)] or by local pools produced at specific loci via nuclear-localized metabolic enzymes. This raises the possibility that epigenetic remodeling can be selectively tuned at specific loci by nutrient types and the enzymes that metabolize them, offering opportunities for metabolic programming of cellular differentiation states and functions. In this study, we found that shifts in nutrient preferences and metabolism drive TEX cell differentiation by directing local acetyl-CoA production at specific gene loci, leading to epigenetic remodeling and T cell dysfunction.

RATIONALE: Histone acetylation relies on the availability of metabolite acetyl-CoA. Acetyl-CoA synthetase 2 (ACSS2) and ATP-citrate lyase (ACLY) are two key acetyl-CoA synthetases that generate acetyl-CoA from acetate and citrate, respectively. We found that ACSS2 and ACLY are differentially expressed in TEFF cells and TEX cells. This differential expression pattern led us to hypothesize that these enzymes could directly link nutrient-specific acetyl-CoA production to distinct epigenetic states during TEX cell differentiation, allowing us to address the question of whether there is a "metabolic code" that instructs the histone code.

RESULTS: We showed that ACSS2 and ACLY are differentially expressed in TEFF and TEX cells in both mice (in tumors and during chronic viral infection) and humans (in tumors). This distinct expression pattern was driven by chronic T cell receptor signaling. Our data further revealed that as TEX cells differentiate, they shift their nutrient preference from acetate to citrate for acetyl-CoA production by down-regulating ACSS2 while maintaining ACLY activity. Mechanistically, ACSS2 and ACLY form distinct functionally independent complexes with histone acetyltransferases EP300 and KAT2A, respectively, within the nucleus. These ACSS2-EP300 and ACLY-KAT2A complexes translate distinct nutrient signals into compartmentalized, locally sourced acetyl-CoA pools. Specifically, the ACSS2-EP300 complex drove histone acetylation and gene expression at effector and memory gene loci, whereas the ACLY-KAT2A complex promoted histone acetylation and gene expression at TEX-related gene loci, ultimately determining $CD8^+$ T cell fates. Nuclear overexpression of ACSS2 or inhibition of ACLY prevented TEX cell differentiation and synergized with ICB to enhance antitumor T cell responses. Notably, ACLY depletion in human CAR T cells also enhanced antitumor immunity.

CONCLUSION: These findings offer new insights into nutrient-driven histone codes in T cell differentiation, providing potential targets for cancer therapy. Our results identify new strategies to metabolically optimize antitumor T cells by enhancing nuclear-localized ACSS2 or inhibiting ACLY, the latter being actively explored in oncology to inhibit tumor growth. Although this study primarily focuses on $CD8^+$ TEX cell differentiation, it reveals a broader paradigm for how nutrient preference in cells can control locus-specific epigenetic reprogramming and cellular differentiation. ■

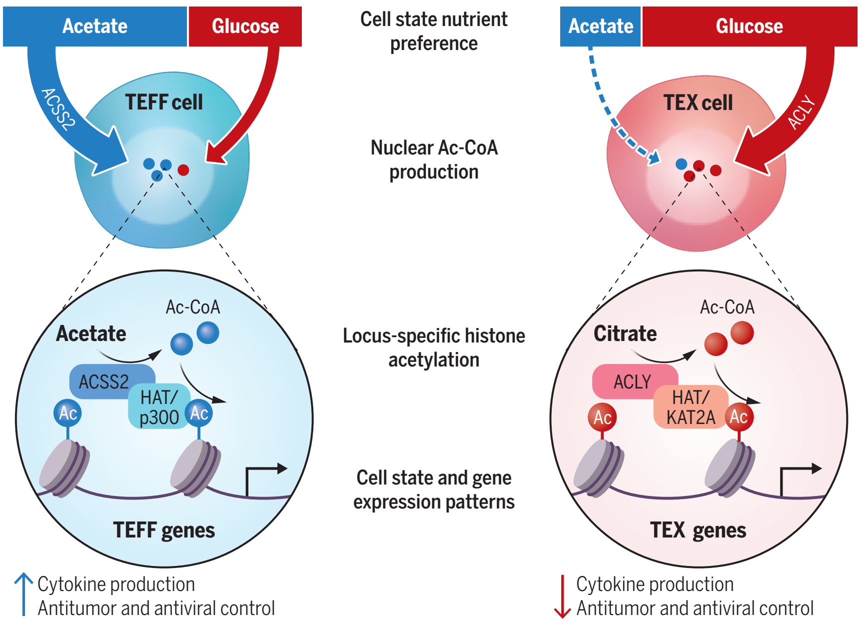

Distinct nutrient utilization through ACLY and ACSS2 drives locus-specific histone acetylation and CD8 T cell fate decisions. Selective acetate and glucose utilization by TEFF and TEX cells through ACSS2 and ACLY (top). ACSS2 collaborates with the histone acetyltransferase (HAT) p300, whereas ACLY interacts with the HAT KAT2A to drive locus-specific histone acetylation and T cell differentiation (bottom).

The list of author affiliations is available in the full article online.
*Corresponding author. Email: skaech@salk.edu
Cite this article as S. Ma *et al*., *Science* 387, eadj3020 (2025). DOI: 10.1126/science.adj3020

READ THE FULL ARTICLE AT
https://doi.org/10.1126/science.adj3020

RESEARCH ARTICLE SUMMARY

EPIGENETICS

Sequence-dependent activity and compartmentalization of foreign DNA in a eukaryotic nucleus

Léa Meneu†, Christophe Chapard†, Jacques Serizay†*, Alex Westbrook, Etienne Routhier, Myriam Ruault, Manon Perrot, Alexandros Minakakis, Fabien Girard, Amaury Bignaud, Antoine Even, Géraldine Gourgues, Domenico Libri, Carole Lartigue, Aurèle Piazza, Agnès Thierry, Angela Taddei, Frédéric Beckouët, Julien Mozziconacci*, Romain Koszul*

INTRODUCTION: The composition of genomic sequences, such as GC content, nucleotide motifs, and repeats, varies from one species to another and within the same genome. Composition correlates with gene transcriptional activity and chromosome organization, and all genome sequences have coevolved with the chromatin-associated complexes they encode to precisely regulate these two features. However, when foreign DNA—including exogenous mobile elements and natural or artificial genes—invades or integrates a host nucleus, it encounters regulatory mechanisms and rules under which it has not evolved. How host cells process and eventually adopt these unfamiliar exogenous sequences remains largely unexplored.

RATIONALE: We investigated chromatin assembly on foreign DNA sequences by integrating two types of DNA into *Saccharomyces cerevisiae*: megabase-long bacterial chromosomes and shorter eukaryotic sequences. We profiled chromatin composition, activity, and folding in these foreign DNA sequences and investigated the molecular mechanisms governing their adaptation to the host environment. Finally, we used machine learning models to identify sequence features that influence chromatin formation and activity on these integrated DNA molecules.

RESULTS: We found that bacterial DNA sequences form chromatin and are covered by nucleosomes, but that their transcriptional activity depends on sequence composition. Exogenous sequences with a GC content mirroring the host sequence become actively transcribed and intermingle with transcriptionally active yeast chromosomes in the nuclear space. Transcription of these sequences follows the original bacterial gene orientation, suggesting an intrinsic directional bias that may facilitate their adaptation to the host environment. By contrast, AT-rich chromosomes adopt an inactive chromatin state characterized by longer nucleosome spacing and a globular tridimensional shape segregated from yeast chromosomes. These two chromatin states spontaneously emerged, partitioning the hybrid genome into spatially distinct nuclear compartments that mirror the euchromatin-heterochromatin compartmentalization of metazoans. Transcriptional inactivation and compartmentalization occur independently of both canonical H3K9me3 mediated heterochromatin—absent in *S. cerevisiae*—and of yeast SIR-mediated heterochromatin. Compartmentalization disappears when transcription is reduced, suggesting that this phenomenon may involve mechanical constraints or biochemical changes in the environment of active genes. During mitosis, compartmentalization is lost as chromatin is compacted by cohesin-mediated loops, paralleling the transient compartment disruption observed in metazoans at this stage.

Deep learning models trained only on yeast chromosomes accurately predict chromatin composition and activity on foreign DNA based on the DNA sequence alone. This implies that the behavior of any DNA in a host cell follows deterministic sequence-based rules, which could help to predict the behavior of exogenous DNA not only during natural gene transfer events but also in synthetic genome engineering projects.

CONCLUSION: The spontaneous formation of transcriptionally active and inactive chromatin compartments in a eukaryotic genome lacking such structures provides insights into their emergence during evolution. When foreign DNA sequences are integrated into the yeast genome, their underlying sequence composition determines their chromatin state and ability to recruit the host transcriptional machinery. These predictable sequence-specific properties highlight the fundamental links between DNA sequence composition, chromatin organization, and nuclear architecture. Such sequence-dependent features could have contributed to the emergence of bipartite compartmentalization of genomes during evolution, either by sequestering inactive genetic material or by facilitating the functional integration of active sequences, thus potentially creating reservoirs of genetic novelty. ■

The list of authors and their affiliations is available in the full article online.
*Corresponding author. Email: romain.koszul@pasteur.fr (R.K.); julien.mozziconacci@mnhn.fr (J.M.); jacques.serizay@pasteur.fr (J.S.)
Cite this article as L. Meneu *et al*., *Science* **387**, eadm9466 (2025). DOI: 10.1126/science.adm9466

READ THE FULL ARTICLE AT
https://doi.org/10.1126/science.adm9466

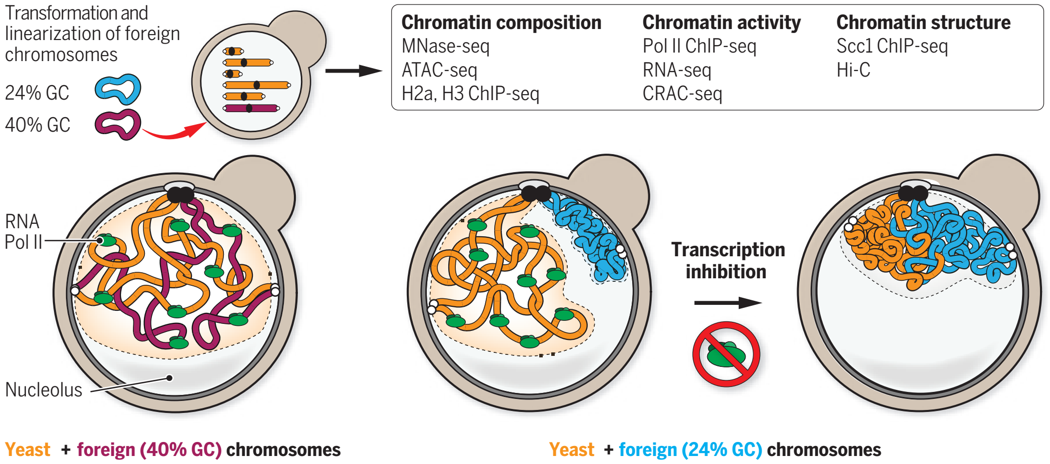

Different fates of foreign chromosomes in a yeast nucleus. Bacterial or eukaryotic chromosomes with a GC content similar to yeast sequences (in purple) become actively transcribed and intermingle with host chromosomes. By contrast, foreign chromosomes with a lower GC (in blue) form a distinct, transcriptionally silent globular compartment within the nucleus. This segregation requires active transcription but is independent of canonical heterochromatin formation.

RESEARCH ARTICLE SUMMARY

MALARIA

Supersaturation mutagenesis reveals adaptive rewiring of essential genes among malaria parasites

Jenna Oberstaller*†, Shulin Xu†, Deboki Naskar†, Min Zhang, Chengqi Wang, Justin Gibbons, Camilla Valente Pires, Matthew Mayho, Thomas D. Otto, Julian C. Rayner*, John H. Adams*

INTRODUCTION: Malaria parasites are highly divergent from model eukaryotes. Their distinctive biology means that many large-scale genome engineering methods that have been used effectively in model organisms, such as RNA interference or guide RNA–based CRISPR/Cas9 screening, are not applicable. As a result, there have been few systematic studies of gene function. The relatively poor level of functional annotation in *Plasmodium* genomes is a major barrier for the much-needed rational development of new antimalarial drugs and vaccines.

RATIONALE: *Plasmodium knowlesi* is a zoonotic pathogen that is part of a large, understudied group of *Plasmodium* subgenus parasites that includes *Plasmodium vivax*, the dominant cause of malaria in South America and much of Asia. When cultured in human red blood cells, *P. knowlesi* has a rapid growth rate and high transfection efficiency, making it an ideal model system for large-scale experimental genetic studies. We used the *piggyBac* transposon mutagenesis system to generate high-density maps of gene essentiality in *P. knowlesi* parasites, providing the first large genetic screen in the *Plasmodium* subgenus representative of all other non-*falciparum* human-infecting species.

RESULTS: We generated and mapped >175,000 transposon insertions in the *P. knowlesi* genome, which is substantially more than our previous ~38,000 insertion study of *P. falciparum*. This “supersaturation” level of mutagenesis, with an average transposon insertion frequency of every 138 base pairs, allowed us to score essentiality for 98% of genes. Further, the extraordinary density of mutations also allowed us to identify protected “void” regions within some genes, where insertions were not tolerated and which frequently contained predicted functional domains. This domain-level resolution of essentiality provides a completely new level of *Plasmodium* genome annotation.

CONCLUSION: We compared our data with previously published genome-scale genetic studies of *P. falciparum* and the rodent malaria model *Plasmodium berghei*. Although the essentiality or redundancy of genes was conserved across all three species for the majority of genes for which data were available, a large number of genes are differentially essential, revealing species-specific adaptations. Our results indicate that *Plasmodium* essential gene evolution was conditionally linked to adaptive rewiring of metabolic networks for different hosts and their intracellular microenvironments, and that *P. knowlesi* in particular has a high level of metabolic plasticity that evidence suggests extends to other *vivax*-clade malaria parasites. These data provide new evolutionary insights into both distinct human-infective malaria parasite clades, which will inform multispecies target identification and intervention strategies. ■

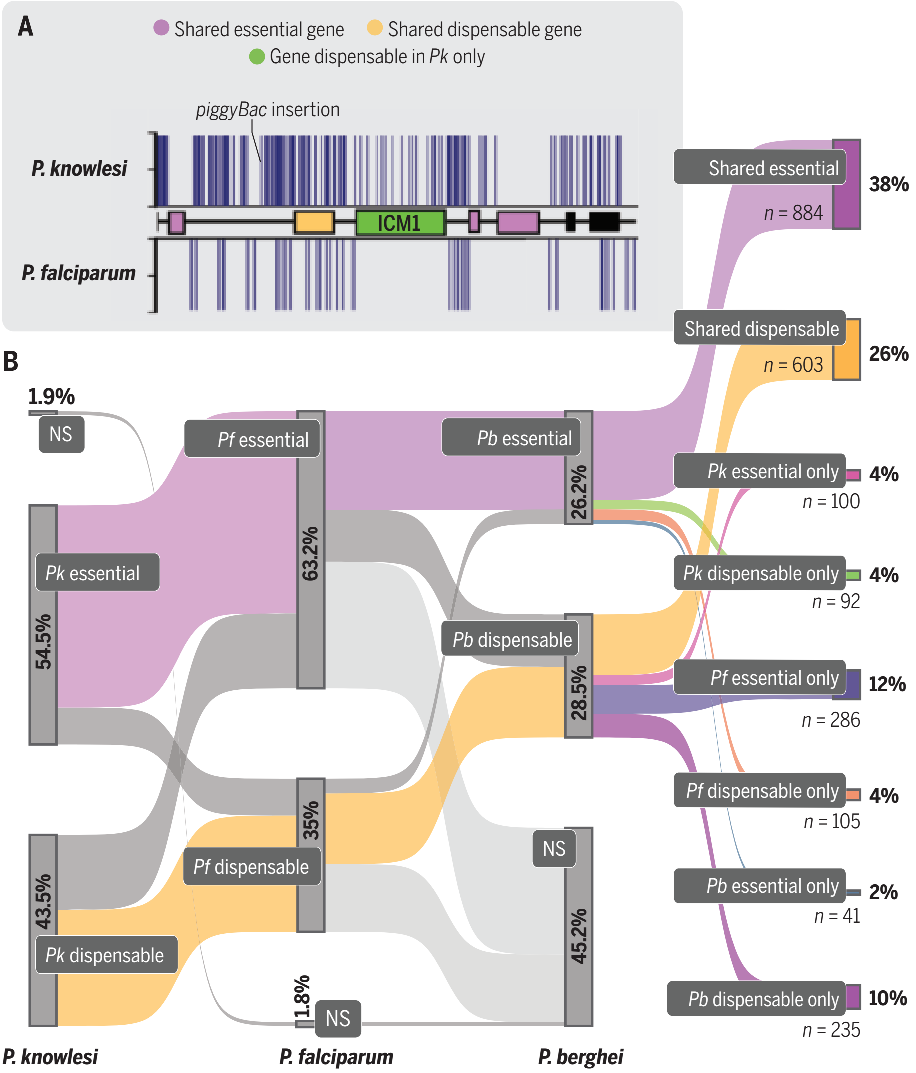

Supersaturation *P. knowlesi* mutagenesis identifies genes essential for blood-stage survival, revealing critical similarities and differences between both human malaria parasite lineages. (**A**) High-resolution map of a syntenic region between *P. knowlesi* and *P. falciparum* chromosomes centered on ICM1, a gene that is essential in *P. falciparum* and tolerates no insertions disrupting the coding DNA sequence but is dispensable in *P. knowlesi*. (**B**) Shared genes switch essentiality between malaria parasites, indicating species-specific adaptations.

The list of author affiliations is available in the full article online.
*Corresponding author. Email: ja2@usf.edu (J.H.A.); jobersta@usf.edu (J.O.); jcr1003@cam.ac.uk (J.C.R.)
†These authors contributed equally to this work.

Cite this article as J. Oberstaller *et al.*, *Science* **387**, eadq7347 (2025). DOI: 10.1126/science.adq7347

READ THE FULL ARTICLE AT
https://doi.org/10.1126/science.adq7347

RESEARCH ARTICLE SUMMARY

MALARIA

The essential genome of *Plasmodium knowlesi* reveals determinants of antimalarial susceptibility

Brendan Elsworth†, Sida Ye†, Sheena Dass†, Jacob A. Tennessen, Qudseen Sultana, Basil T. Thommen, Aditya S. Paul, Usheer Kanjee, Christof Grüring, Marcelo U. Ferreira, Marc-Jan Gubbels, Kourosh Zarringhalam*, Manoj T. Duraisingh*

INTRODUCTION: Approximately 249 million cases of malaria, caused by infection with *Plasmodium* species parasites, result in about 608,000 deaths annually. Measures to combat the parasites that cause malaria have become compromised because of reliance on a small arsenal of drugs and emerging drug resistance. Moreover, zoonotic cases of malaria are increasing in prevalence in Southeast Asia, caused by infection with *Plasmodium knowlesi* and *Plasmodium cynomolgi*. These parasites are evolutionarily closely related to *Plasmodium vivax* and serve as powerful in vitro models because *P. vivax* cannot be cultured in vitro.

RATIONALE: The genomes of each *Plasmodium* spp. reveal conservation but also substantial differences. Although functional genetic studies in *Plasmodium* spp. parasites have provided information on the essentiality and function of genes throughout the *Plasmodium* life cycle, the lack of high-confidence genome-wide essentiality data limits the ability to prioritize targets for vaccines and therapeutics, particularly for parasites in the *P. vivax* clade, which includes *P. knowlesi*. In this study, we harnessed the development of high-efficiency molecular genetics in *P. knowlesi* to elicit genome-wide piggyBac transposon mutagenesis and provide the most complete determination of gene essentiality for the blood-stage infection in any *Plasmodium* spp. with the resolution to define truncatable genes.

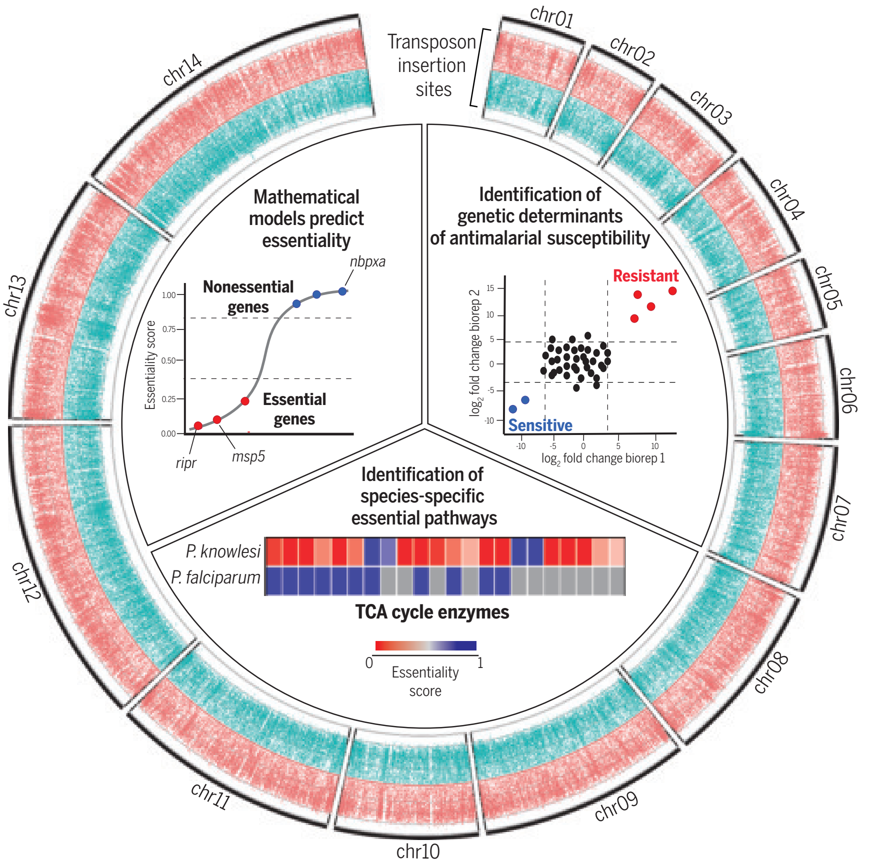

A high-resolution transposon mutagenesis screen in *P. knowlesi* informs antimalarial discovery and reveals drug resistance determinants. A near-saturation piggyBac transposon screen in *P. knowlesi* and improved models for calling gene essentiality provide a high-confidence genome-wide map of gene essentiality, allowing for comparative essentiality studies, prioritization of drug and vaccine targets, and identification of genes that alter antimalarial susceptibility. chr, chromosome.

RESULTS: We observed 1,456,750 independent transposon insertions, ~38-fold more than was previously achieved in the *Plasmodium falciparum* piggyBac screen. A mathematical simulation was used to determine that we have achieved a 3.6-fold higher number of insertions than the required level of insertions to reach gene-level saturation. Overall, 2037 genes (38.68%) with at least one TTAA site (that serve as targeting sites for the piggyBac transposon) were classified as essential, 2124 (40.34%) were classified as dispensable, and 1105 (20.98%) were indeterminate. The number of essential genes is similar to previous observations in apicomplexans but is higher than in many free-living organisms, which reflects the highly specialized parasitic lifestyle of *Plasmodium* spp. that relies heavily on host metabolism. We further identified 126 genes whose disruption results in reduced fitness, 122 genes that can tolerate 5′ or 3′ truncation, and 53 essential long noncoding RNAs (lncRNAs). We found that the essentiality of the druggable genome is broadly conserved between *Plasmodium* spp.; however, we identified the *P. falciparum* drug target bifunctional farnesyl/geranylgeranyl diphosphate synthase (FPP/GGPPS) as dispensable in *P. knowlesi*. Notably, *P. knowlesi* showed a greater reliance on the tricarboxylic acid (TCA) cycle genes, and both *P. knowlesi* and *P. vivax*—in contrast to *P. falciparum*—are inhibited by the aconitase inhibitor sodium fluoroacetate. Perturbation analyses with the frontline antimalarial artemisinin revealed modulators that both increase and decrease susceptibility.

CONCLUSION: The essentiality of the *P. knowlesi* genome will be a useful tool for antimalarial drug and vaccine target prioritization and for comparative essentiality studies across apicomplexan parasites and eukaryotes. To make the data readily accessible to the community, we provide a web-based app that can be used interactively to examine gene essentiality scores (https://umbibio.math.umb.edu/PkEssenDB/); the data are also available through VEuPathDB. ■

The list of author affiliations is available in the full article online.
*Corresponding author. Email: kourosh.zarringhalam@umb.edu (K.Z.); mduraisi@hsph.harvard.edu (M.T.D.)
†These authors contributed equally to this work.
Cite this article as B. Elsworth *et al.*, *Science* 387, eadq6241 (2025). DOI: 10.1126/science.adq6241

S READ THE FULL ARTICLE AT
https://doi.org/10.1126/science.adq6241

RESEARCH ARTICLES

EVOLUTION

The *Silene latifolia* genome and its giant Y chromosome

Carol Moraga[1,2,3]†, Catarina Branco[1,4,5,6]†, Quentin Rougemont[7]†, Pavel Jedlička[8], Eddy Mendoza-Galindo[9], Paris Veltsos[10], Melissa Hanique[11], Ricardo C. Rodríguez de la Vega[7], Eric Tannier[1,12], Xiaodong Liu[13], Claire Lemaitre[14], Peter D. Fields[15], Corinne Cruaud[16], Karine Labadie[16], Caroline Belser[16], Jerome Briolay[17], Sylvain Santoni[18], Radim Cegan[8], Raquel Linheiro[1,4,5,6], Gabriele Adam[11], Adil El Filali[1], Vinciane Mossion[19], Adnane Boualem[11], Raquel Tavares[4,5,6], Amine Chebbi[20], Richard Cordaux[21], Cécile Fruchard[1], Djivan Prentout[22], Amandine Velt[23], Bruno Spataro[1], Stephane Delmotte[1], Laura Weingartner[24], Helena Toegelová[25], Zuzana Tulpová[25], Petr Cápal[25], Hana Šimková[25], Helena Štorchová[26], Manuela Krüger[26], Oushadee A. J. Abeyawardana[26], Douglas R. Taylor[27], Matthew S. Olson[28], Daniel B. Sloan[15], Sophie Karrenberg[29], Lynda F. Delph[30], Deborah Charlesworth[31], Aline Muyle[1,9], Tatiana Giraud[7], Abdelhafid Bendahmane[11], Alex Di Genova[2,3,32], Mohammed-Amin Madoui[15,33], Roman Hobza[8], Gabriel A. B. Marais[1,4,5,6,34]*

In many species with sex chromosomes, the Y is a tiny chromosome. However, the dioecious plant *Silene latifolia* has a giant ~550-megabase Y chromosome, which has remained unsequenced so far. We used a long- and short-read hybrid approach to obtain a high-quality male genome. Comparative analysis of the sex chromosomes with their homologs in outgroups showed that the Y is highly rearranged and degenerated. Recombination suppression between X and Y extended in several steps and triggered a massive accumulation of repeats on the Y as well as in the nonrecombining pericentromeric region of the X, leading to giant sex chromosomes. Using sex phenotype mutants, we identified candidate sex-determining genes on the Y in locations consistent with their favoring recombination suppression events 11 and 5 million years ago.

Among the multiple paths that the evolution of sex chromosomes can take, some have led to giant Y chromosomes (*1*, *2*). Giant Y chromosomes may result from massive accumulation of repeats, including transposable elements (TEs), but their structure, precise role in sex determination, and evolution remain poorly understood (*3*–*6*). Giant Y chromosomes were first identified in plant species with separate sexes (dioecious plants) (*3*) and also exist in animals (*4*). In the past decade, great advances have been made in studying sex chromosomes using genomics and bioinformatics (*5*, *6*), but no giant plant Y chromosome has yet been assembled.

Silene latifolia (Caryophyllaceae) is a dioecious plant described in the 18th century and studied by many, including Darwin (*7*). Its XY sex-determination system was discovered 100 years ago (*8*). The Y is ~550 Mb, the X is ~400 Mb, and the total haploid genome size is ~2.7 Gb (*9*). Genetic maps show that the X and the Y are largely nonrecombining and share only a single pseudoautosomal region (PAR) (*10*). Recombination has been suppressed progressively, forming groups of X-Y gene pairs with differing synonymous divergence levels, called evolutionary strata (*11*–*13*). The repeat richness (*14*) and size of the *S. latifolia* Y have, however, prevented its assembly so far. Mutants with deletions on the Y chromosome and altered sex phenotypes indicate the presence of three sex-determining regions (*15*, *16*). A candidate gene (*Clavata3*) in one of the regions involved in female sterility has recently been proposed (*17*, *18*), but the other sex-determining genes remain unknown.

To study the repeat-rich Y chromosome, we used Oxford Nanopore Technologies (ONT) sequencing and generated a new marker-dense genetic map to obtain a chromosome-scale *S. latifolia* genome assembly. We also used high-quality genome assemblies of closely related nondioecious *Silene* species as outgroups to make inferences about the evolution of the *S. latifolia* sex chromosomes. We compared the epigenetics (DNA methylation and small RNAs) of the X and the Y. To identify individual candidate sex-determining genes, we sequenced mutants with Y deletions for three sex phenotypes [hermaphrodites and asexuals with early or intermediate or with late abnormalities in anther development, described in (*16*)], and generated expression data at two critical stages in male and female flower development.

The structure and gene content of the sex chromosomes

To assemble the complex *S. latifolia* genome, we used the sequencing, assembly and annotation strategy detailed in the supplementary text, section S1; Table 1; tables S1 to S4; and figs. S1 to S5 (*19*). Our assemblies of the X and the Y chromosomes are high quality. In systems in which the X and Y are differentiated by many single-nucleotide polymorphisms (SNPs) and insertions-deletions (indels), female/male read-depth ratios using stringent mapping parameters are expected to be ~1, ~2, and ~0 for

---

[1] Laboratoire Biométrie et Biologie Evolutive (LBBE), CNRS/Université Claude Bernard Lyon 1, Villeurbanne, France. [2] Instituto de Ciencias de la Ingeniería, Universidad de O'Higgins, Rancagua, Chile. [3] Centro UOH de Bioingenieria (CUBI), Universidad de O'Higgins, Rancagua, Chile. [4] CIBIO, Centro de Investigação em Biodiversidade e Recursos Genéticos, InBIO, Laboratório Associado, Campus de Vairão, Universidade do Porto, Vairão, Portugal. [5] Departamento de Biologia, Faculdade de Ciências, Universidade do Porto, Porto, Portugal. [6] BIOPOLIS Program in Genomics, Biodiversity and Land Planning, CIBIO, Campus de Vairão, Vairão, Portugal. [7] Université Paris-Saclay, CNRS, AgroParisTech, Laboratoire Ecologie Systématique et Evolution, UMR 8079, Bâtiment 680, Gif-sur-Yvette, France. [8] Department of Plant Developmental Genetics, Institute of Biophysics of the Czech Academy of Sciences, Brno, Czech Republic. [9] Centre d'Ecologie Fonctionnelle et Evolutive (CEFE), University of Montpellier, CNRS, EPHE, IRD, Montpellier, France. [10] Ecology, Evolution and Genetics Research Group, Biology Department, Vrije Universiteit Brussel, Brussels, Belgium. [11] Institute of Plant Sciences Paris-Saclay (IPS2), Université Paris-Saclay, CNRS, INRAE, Université d'Évry, Gif-sur-Yvette, France. [12] Inria Lyon Research Center, Villeurbanne, France. [13] Department of Biology, University of Copenhagen, Copenhagen, Denmark. [14] Institut de Recherche en Informatique et Systèmes Aléatoires (IRISA), Université de Rennes, Inria, CNRS, Rennes, France. [15] Department of Biology, Colorado State University, Fort Collins, CO, USA. [16] Genoscope, Institut François Jacob, CEA, CNRS, Université d'Évry, Université Paris-Saclay, Évry, France. [17] Développement de Techniques et Analyse Moléculaire de la Biodiversité (DTAMB), Université Claude Bernard Lyon 1, Campus de la Doua, Villeurbanne, France. [18] Genomic Platform, Amélioration Génétique et Adaptation des Plantes Méditerranéennes et Tropicales (AGAP), Université de Montpellier, CIRAD, INRAE, Montpellier, France. [19] Department of Ecology and Genetics, Division of Plant Ecology and Evolution, Uppsala University, Uppsala, Sweden. [20] Efor, Grosspeter Tower (Spaces), Basel, Switzerland. [21] Évolution Génomes Comportement Écologie, Université Paris-Saclay, CNRS, IRD, Gif-sur-Yvette, France. [22] Department of Biological Sciences, Columbia University, New York, NY, USA. [23] Santé de la Vigne et Qualité du Vin (SVQV), INRAE, Colmar, France. [24] University of Louisville School of Medicine, Undergraduate Medical Education, Louisville, KY, USA. [25] Institute of Experimental Botany of the Czech Academy of Sciences, Olomouc, Czech Republic. [26] Plant Reproduction Laboratory, Institute of Experimental Botany, Czech Academy of Sciences, Prague, Czech Republic. [27] Department of Biology, University of Virginia, Charlottesville, VA, USA. [28] Department of Biological Sciences, Texas Tech University, Lubbock, TX, USA. [29] Department of Ecology and Genetics, Division of Plant Ecology and Evolution, Uppsala University, Uppsala, Sweden. [30] Department of Biology, Indiana University, Bloomington, IN, USA. [31] Institute of Ecology and Evolution, School of Biological Sciences, University of Edinburgh, Ashworth Laboratories, Edinburgh, UK. [32] Center for Mathematical Modeling, UMI-CNRS 2807, Santiago, Chile. [33] Service d'Etude des Prions et des Infections Atypiques (SEPIA), Institut François Jacob, Commissariat à l'Energie Atomique et aux Energies Alternatives (CEA), Université Paris Saclay, Fontenay-aux-Roses, France. [34] GreenUPorto–Sustainable Agrifood Production Research Centre, Departamento de Biologia, Faculdade de Ciências, Universidade do Porto, Vairão, Portugal.

***Corresponding author. Email: gabriel.marais@cnrs.fr**

†These authors contributed equally to this work.

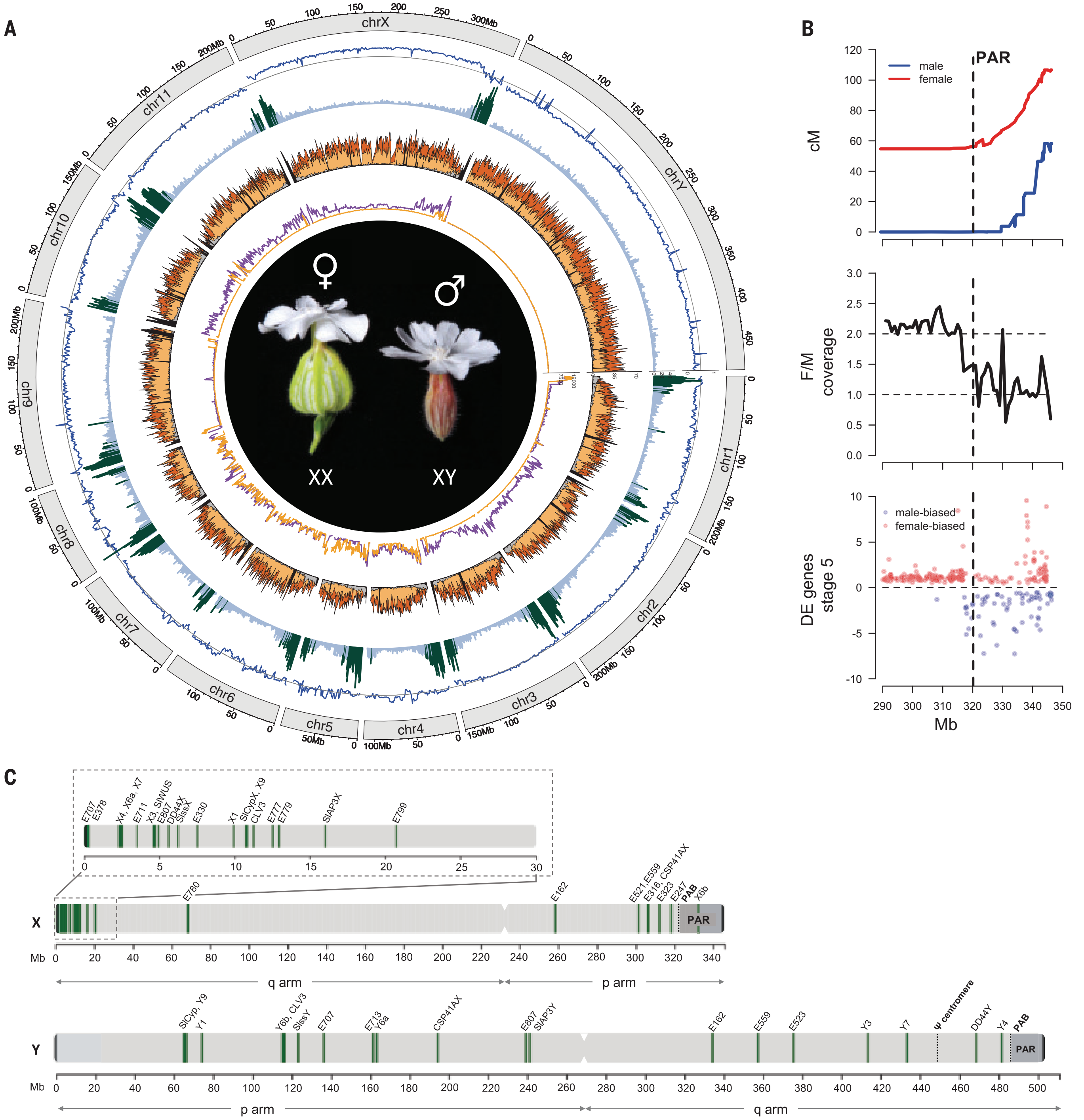

Fig. 1. Assembly of the *S. latifolia* male genome. (**A**) Circos plot of the *S. latifolia* male genome. Circles from the outside to the inside correspond to the following: (i) Coverage ratio (female/male). (ii) Gene density, where regions with high densities (exceeding average density plus 1 standard deviation) are highlighted in dark green. (iii) Density of repeat families; subtelomere- and centromere-associated satellite elements (black) and LTR elements—Ty3/Gypsy (orange), Ty1/Copia (yellow), LINE (violet), and Helitron (gray). (iv) SNP density in the male (orange) and female (purple), consistent with the sequenced male being highly homozygous (although some chromosomes show heterozygosity) and with male and female being full siblings. chr, chromosome. (**B**) Zoom-in on the X chromosome, showing recombination in males (blue) and females (red) defining the pseudoautosomal boundary at position 321 Mb on the X chromosome (top). The boundary was confirmed by other features, such as the female/male (F/M) sequence coverage ratio (middle) and a change in significant differential expression (DE) between male and female flowers (stage 5) (bottom); the full analysis of differential gene expression is shown in fig. S18. All panels have data summarized in 1-Mb windows. (**C**) Structure of the sex chromosomes, p and q arms, centromeres, and the PAR and pseudoautosomal boundary (PAB) are depicted. The sex-linked genes characterized in previous work are also shown. A zoom-in on the q arm of the X is showing a number of those genes. [Photo credits: Paris Veltsos and Lynda Delph]

the autosomes, X chromosome, and Y chromosome, respectively, as observed in our data (Fig. 1A). A smaller set of experimentally validated sex-linked genes compiled previously (*20*, *21*) also mapped as expected to their previously assigned X or Y positions (Fig. 1C). The X chromosome sequence obtained is 346 Mb, with a distribution of genes and repeats (in particular centromere- and subtelomere-associated repeats) as expected for a metacentric chromosome (Fig. 1A). Sex-specific recombination data, the female/male read coverage ratio, and differential expression identified the PAR (Fig. 1, B and C). This PAR is a small, gene-rich region of 25 Mb with 1286 genes (51 genes per megabase versus the X-chromosomal mean of 10 genes per megabase). Our X assembly is very similar to that of a recently published *S. latifolia* female genome (*13*) (fig. S6). The Y chromosome assembly is 485 Mb long, excluding the PAR. Y-specific centromeric repeats locate the centromere and a remnant of a former centromere [called a pseudocentromere (*22*)] at the expected locations (Fig. 1A). The Y assembly roughly agrees with the deletion-based map of the Y chromosome (*16*) given the uncertainties in the map (fig. S3).

Evolution of the sex chromosomes

The high-quality assembly of the X and Y chromosomes illuminates the evolution of recombination suppression between the sex chromosomes of *S. latifolia*. We detected three evolutionary strata and extensive rearrangements on the sex chromosomes, especially the Y. To analyze rearrangements and estimate synonymous site divergence (d_S) between the X and Y copies, we used gametologs (X-Y gene pairs) that also have 1:1 orthologs in the two nondioecious outgroup species, *Silene conica* and *Silene vulgaris*. A change-point analysis of these X-Y d_S values of 401 gametolog pairs, based on the gene rank in the X chromosome assembly, divided the nonrecombining region into four adjoining X chromosome sectors with different means (Fig. 2, A to C, and fig. S7A) and defined three evolutionary strata—S1, S2 and S3—based on the different d_S levels (Fig. 2, A to C). A larger set of 598 gametologs (X-Y gene pairs without requiring orthologs in the outgroups) gave similar results (fig. S7B). Strata S1 and S2 are in good agreement with previously defined strata (fig. S7, C and D); S3 has not been detected before. It splits the oldest stratum, S1, in two, owing to a lower mean X-Y d_S compared with its two flanking regions, S1a and S1bc (Fig. 2C and fig. S7D; S1b and S1c are associated with two different inversions). Strata S3 and S2 have similar mean X-Y d_S, but S3 has much higher X-Y synteny compared with S2, and the two strata were formed differently. Strata S1 and S3 are small regions, both located within the first 27 Mb of the X chromosome q arm. Stratum S2, on the other hand, is very large and includes most of the X chromosome, including the pericentromeric regions on both arms. Using a molecular clock approach, we estimate that strata S2 and S3 both evolved most recently—5.4 [95% confidence interval (4.4, 6.5)] and 4.4 (3.3, 5.5) million years ago (Ma), respectively—whereas stratum S1 arose 11.8 (10.6, 13.1) Ma, which is inferred to be when the *S. latifolia* sex chromosomes originated (*23*).

Table 1. Statistics for the male genome and sex chromosomes of *S. latifolia*. All metrics were calculated for the total genome assembly as well as specifically for the sex chromosomes. Contigs were obtained using N1 (a single N opens a gap). MITE, miniature inverted-repeat transposable element; LINE, long interspersed nuclear element.

Genome metrics	Whole genome	X chromosome	Y chromosome
Total assembled size (bp)	2,716,527,704	346,484,273	486,334,681
Number of contigs	1545	59	37
N50 (bp)	18,434,108	29,020,133	36,745,246
N90 (bp)	6,521,844	11,745,531	27,237,198
Number of scaffolds	912	21	11
N50 (bp)	200,709,446	50,520,191	59,479,783
N90 (bp)	141,278,959	21,428,974	44,285,091
Largest length size (bp)	237,716,014	133,616,578	135,552,442
Gaps (%)	1.44	6.56	0.59
Anchored of the total sequences (anchoring rate)	2,575,517,323 (94.8%)		
Annotated protein-coding genes	35,436	3520	2301
Mean gene length (bp)	4155	4332	4045
BUSCO score of annotated protein-coding genes from all scaffolds*	C: 92.5% [S: 78.1%, D: 14.4%], F: 0.7%, M: 6.8%, *n*: 425		
Identified repeats	79.20%	77.75%	81.24%
Annotated repeats	61.18%	58%	65%
LTR retrotransposons	54.42%	52.7%	60.55%
DNA transposons	4.11%	3.11%	3.22%
MITE	0.14%	0.098%	0.068%
LINE	0.48%	0.37%	0.55%
Satellite repeats	2.04%	2.014%	1.18%

*C, complete; S, single copy; D, duplicated; F, fragmented; M, missing; *n*, total number of BUSCO genes.

Gene order comparisons between *S. latifolia* and two nondioecious close relatives, *S. conica* and *S. vulgaris* used as outgroups, revealed large syntenic blocks with some rearrangements (fig. S8). The *S. latifolia* Y chromosome is most rearranged compared with the X or the homologous chromosomal blocks in either outgroup, with the notable exception of the S3 stratum, which includes 4 Mb of X-Y synteny (Fig. 2A and figs. S8 and S9). The *S. latifolia* X shows homology with chromosome 5 of *S. conica*, and smaller parts of chromosomes 1, 2, and 6, and with four *S. vulgaris* scaffolds (1, 3, 6, and 16) (Fig. 2A and fig. S8). Reconstruction of the rearrangements between the X, the Y, and the homologous chromosomal blocks in the outgroups (figs. S9 and S10) suggests that stratum S1 may have evolved by two inversions early in the evolution of the sex chromosomes, one on the X encompassing S1a to S1b and one on the Y including S1c.

Stratum S3 is the only region of extended synteny between the X and Y chromosomes. Together with its slightly lower d_S mean compared with that of the other strata, this suggests that S3 is the most recent stratum that we could detect (Fig. 2, fig. S7D, and fig. S9). Comparisons between *S. latifolia* X and the homologous chromosomal blocks in the outgroups suggest that S3 genes were ancestrally located among S1 genes (fig. S9). We therefore propose that S3 (initially within the X region that evolved to become the S1 stratum) was lost from the Y and later regained by a recent duplicative translocation from the X, resetting the X-Y d_S to zero about 4.4 Ma. Stratum S2 is more rearranged than S3, consistent with being older than S3, and probably arose through a different mechanism. Reconstruction of the rearrangements between the X, the Y, and the outgroups (fig. S11) indicates that S2 could not have formed by a single rearrangement. We found several inversions, some of them pericentric, as previously suggested (*16*, *22*). Many may have occurred after recombination stopped, possibly mediated by the high abundance of repeats.

Our repeat analysis revealed very high TE densities—mainly the long terminal repeat (LTR) retrotransposons *Copia* and *Gypsy*—on the Y but also, to a lesser extent, on the X compared with the autosomes (Table 1, table S4, and Fig. 1). The two *S. latifolia* sex chromosomes are 4 to 5.5 times as large as the *S. conica* chromosome 5, whereas there is only a twofold increase for the *S. latifolia* autosomes compared with their *S. conica* homologs. In eukaryotes, the

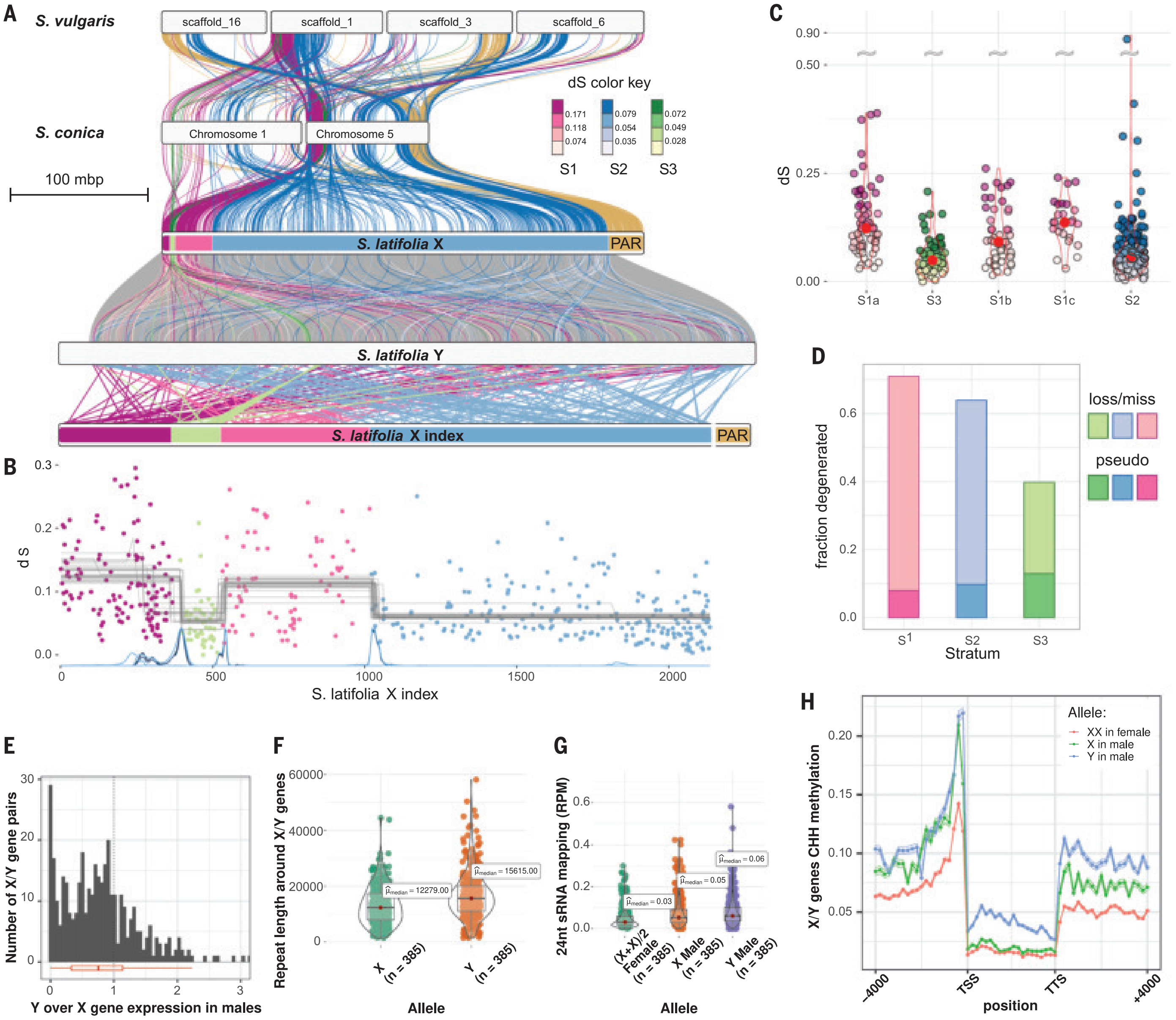

Fig. 2. The evolution of the *S. latifolia* sex chromosomes. (**A**) Syntenic relationships between *S. latifolia* gametologs and autosomal genes in *S. conica* and *S. vulgaris*. Links between homologous chromosomal blocks in the outgroups and *S. latifolia* X are colored by evolutionary strata. Links between *S. latifolia* X and Y are colored by synonymous divergence bins (inset). Synteny between *S. latifolia* Y coordinates and *S. latifolia* X gene rank is shown at the bottom. The *S. latifolia* X chromosome tracks are colored by median synonymous divergence of the strata. The PAR region on *S. latifolia* Y, not shown, is placed to the right of the chromosome track. (**B**) Change-point analysis of d_S along the X chromosome using 401 one-to-one gametologs with d_S values < 0.3. The *x* axis shows gene ranking on the X. Lines at the bottom show the density of the posterior distribution of the change-point locations. Gray lines show the average d_S of the inferred blocks. (**C**) Distribution of synonymous divergence values between *S. latifolia* male X and Y gametologs per stratum. (**D**) Fraction of gene losses and pseudogenization on *S. latifolia* sex chromosomes per stratum. Gene losses on Y were inferred using 1:1:1 orthologs among *S. vulgaris*, *S. conica*, and *S. latifolia* X. Pseudogenes were identified as gametologs with premature stop codons. (**E**) Distribution of Y over X gene expression ratio in four *S. latifolia* male flower buds. Box plot represents median, quartiles, and whiskers. (**F**) Sum of repeat lengths around X-Y gene pairs, from 4000 bp upstream to 4000 bp downstream of the gene. (**G**) Mapping of 24–nucleotide (nt) small RNAs (RPM) on X-Y gene pairs for three *S. latifolia* females and males in flower buds and leaves. The red dot represents the mean. Female X alleles are in red, male X alleles are in green, and Y alleles are in blue. (**H**) Plot of X/Y DNA methylation in CHH context. Female X alleles are in red, male X alleles are in green, and Y alleles are in blue. Average proportion of methylated reads at cytosine positions are shown along sliding windows with a 95% confidence interval. Pairwise synteny plots in (A) were generated with RIdeogram or pafR based on Orthofinder's orthologous relationships. Quantitative plots in other panels were prepared with ggplot2.

nonrecombining pericentromeric regions are typically TE rich because recombination helps purge deleterious TE insertions (*24*); this pericentromeric effect on the *S. latifolia* X chromosome is notably large (fig. S2B). Estimates of the ages of complete LTR retrotransposon insertions show that the insertions in the centers in the pericentromeric regions tend to be oldest and those at the borders the youngest (fig. S12), consistent with TEs accumulating at the margins of these pericentromeric regions and expanding them.

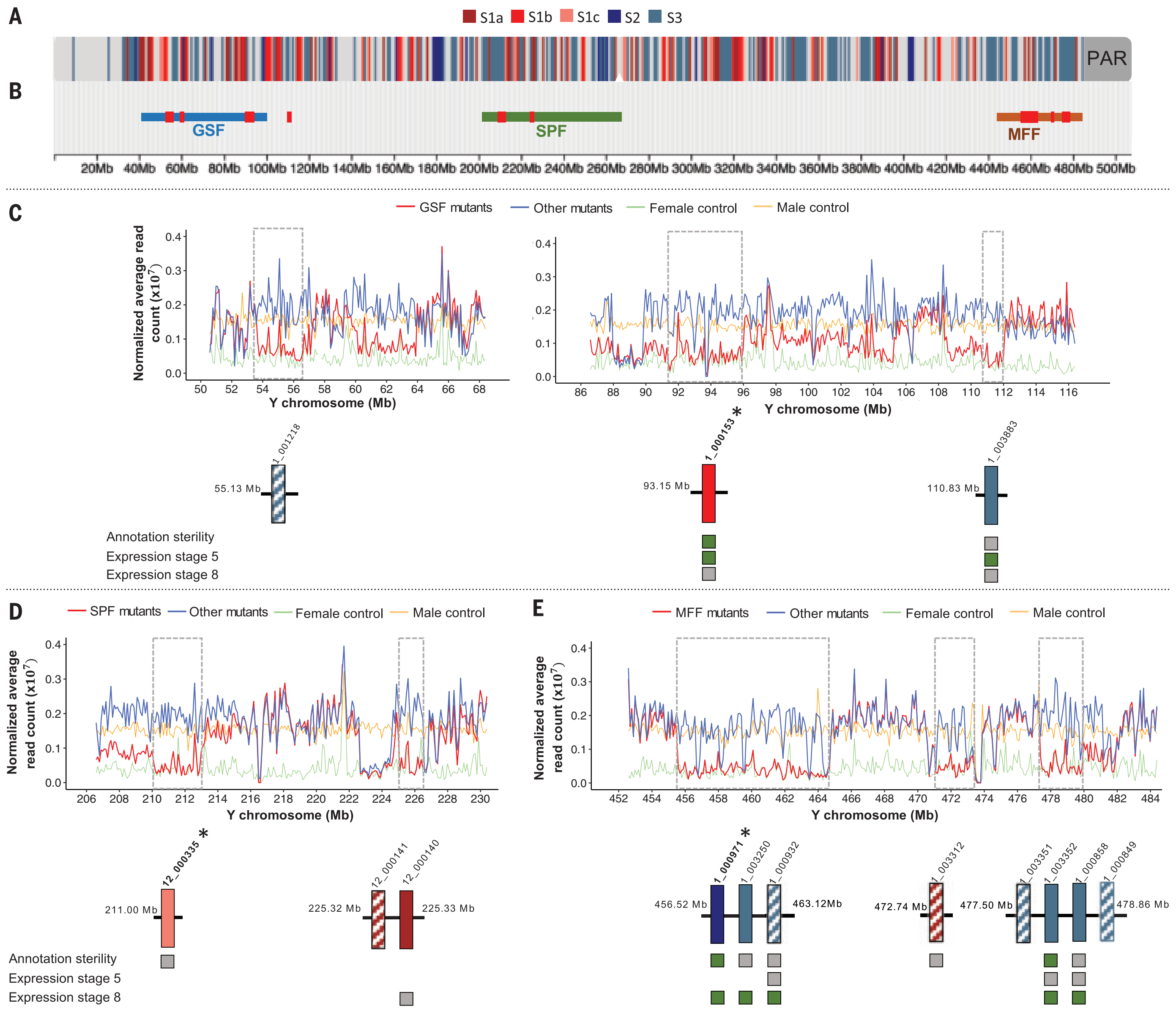

Fig. 3. Identification of deleted genes in the altered sex phenotype mutants. (**A**) The Y chromosome sequence and the evolutionary strata (indicated by 892 Y gametologs). Note that the strata on the Y are mixed up owing to the extensive rearrangements that occurred on this chromosome compared with the X (see text and Fig. 2). The Y is oriented with the PAR on the right side. (**B**) The putative sex-determining regions (MFF, SPF, and GSF) with estimated locations from Bergero *et al*. (*16*). (**C**) Zoom-in on the GSF deletions. Only deletions containing a gene are detailed. Each coverage plot shows the mean normalized read count for GSF mutants, other mutants, control male, and control female. GSF deletions (rectangles) are inferred when the GSF mutant coverage is similar to or lower than that of the control female while the other mutants' coverage was similar to that of the male control. Three genes deleted in all GSF mutants are shown with Y position, stratum assignment [as in (A), hashed fill color indicates that the stratum was inferred from the closest genes due to absence of an X gametolog], and a summary of female sterility annotation and RNA-seq–based expression at stage 5 and 8 in normal male flowers [green, expectations for GSF candidate met (i.e., expressed at stage 5); gray, expectations not met; no square, no data available]. (**D**) Zoom-in on the SPF deletions. Same legend as (C), except for annotation (information on male sterility is indicated). (**E**) Zoom-in on the MFF deletions. Same legend as (D), except for expression (expression for a MFF candidate is expected to be stage 8). The best-supported candidates for sex-determining genes (discussed in the text) are pinpointed by asterisks.

The Y chromosome exhibits signs of considerable degeneration. We found 1541 1:1:1 orthologs in *S. latifolia*, *S. conica*, and *S. vulgaris* on the X chromosome, of which 963 (62%) have no detectable ortholog on the Y chromosome. We also mapped all 3520 genes in our X assembly onto our Y assembly and found homologous genes of about the same size for 1654 (47%), whereas the other 1866 genes (53%) were missing from the Y. A model-based phylogenetic analysis of gene gains and losses also indicated that about 1519 genes (56%) were lost from the Y out of 2694 genes originally present (fig. S13A). Thus, 53 to 62% of the genes appear to have been lost since the Y stopped recombining with the X ~11 Ma, which is higher than previous estimates (*25*). Complete loss of genes is more prominent in older strata, whereas pseudogenes show the opposite trend, consistent with the conclusion that recombination was suppressed more recently in strata S2 and S3, resulting in more recent losses of function (Fig. 2D). We detected a similar proportion of genes with premature stop codons on both sex chromosomes

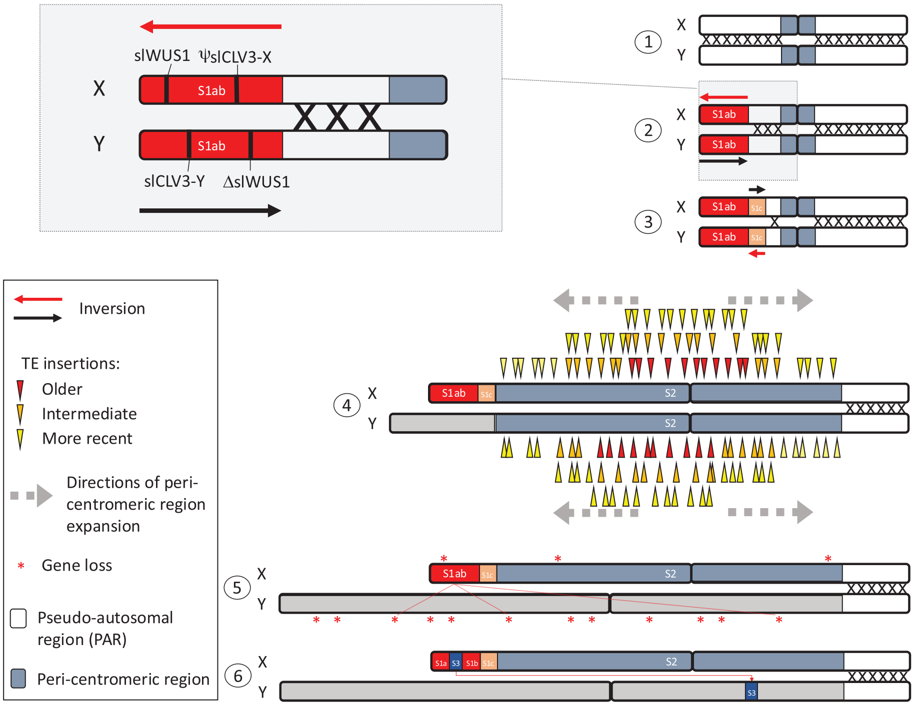

Fig. 4. Scenario for the evolution of sex chromosomes in *S. latifolia*. (1) Pair of autosomes, ancestors of the sex chromosomes; (2) ~11 Ma: inversion on the X generating the stratum S1ab, indicated by a red arrow; (3) ~11 Ma: inversion on the Y generating the stratum S1c, indicated by a red arrow [the inset at the top left represents a zoom-in on the S1 stratum, showing the candidate sex-determining genes *Clavata3* (GSF) and *Wuschel1*. *slCLV3* (GSF); and *slWUS1* is in stratum S1ab defined by the inversion on the X]; (4) ~5 Ma: pericentromeric region extension by TE accumulation forming stratum S2, TE insertions being depicted by arrowheads [MFF candidates were found in this stratum (not shown)]; (5) gene losses on the Y chromosome, those from future stratum S3 (located in S1) are highlighted by red dashed lines connecting X and Y genes; and (6) ~4.5 Ma: duplication and translocation of a fragment from the X to the Y, possibly for compensating gene losses from (5), formation of S3, X-Y d_S values become 0 in the X translocated region.

(fig. S13B), which suggests that the X is also losing genes, as expected given its lack of recombination in stratum S2 (*26*). Among the gametologs with apparently functional X and Y copies, 77% of those with significantly different rates of nonsynonymous versus synonymous substitutions (d_N versus d_S) in the X and Y lineages had higher values in Y lineages, indicating less effective selection (fig. S13C). Restriction site–associated DNA sequencing (RAD-seq) estimates within two populations showed that the Y chromosome has considerably lower nucleotide diversity than the X or the autosomes (fig. S14), as predicted for a chromosome with lower effective population size and undergoing genetic hitchhiking processes (*1*, *27*). Degenerated Y-linked genes have lower expression compared with their X counterparts (Fig. 2E), as already reported in *S. latifolia* (*28*–*30*). This may be explained by epigenetic modifications because Y genes tend to have more TEs nearby than other genes (Fig. 2F) and show two hallmarks of silencing—a higher number of mapped 24-nucleotide small RNAs (Fig. 2G) and higher DNA methylation levels, especially at proximal promoters [200 base pairs (bp) upstream of the transcription start site (TSS)] and gene bodies in the CHH context (where H is any base except G, see Fig. 2H; other methylation contexts are shown in fig. S15).

The sex-determining genes on the Y chromosome

Y chromosome deletions display three sex phenotype categories (*15*, *16*, *31*, *32*): hermaphrodite mutants, asexual mutants in which anther development stops early or at intermediate stages in flower development, and males with pollen defects (late effects). Genetic markers roughly located these deletions in three Y chromosome sex-determining regions (*15*, *16*): a single female-suppressing region [carrying a gynoecium-suppressing factor (GSF)] and two male-promoting regions [one carrying a stamen-promoting factor (SPF) and the other a male fertility factor (MFF) affecting pollen production]. The SPF and MFF mutants are phenotypically quite diverse, and these regions could include several genes affecting those phenotypes (*16*, *33*).

We identified candidate sex-determining genes by low-coverage sequencing of 18 well-characterized sex phenotype mutants with Y deletions (table S5). We mapped the mutants' reads onto our reference Y chromosome along with reads from a phenotypically normal control individual of each sex from the same U17 population as our reference (fig. S16). Although female coverage on the Y is generally low, it is not always zero because X reads may mis-map to the Y chromosome. We therefore classified a region as deleted in a mutant if its coverage was similar to the control female value or less. Coverage similar to the control male indicates absence of Y deletions. Although the data are noisy, they clearly identify deletions specific to each mutant category: four for the GSF mutant category, two for SPF, and three for MFF (Fig. 3B), almost all in the three sex-determining regions previously defined (*16*) (fig. S3).

Figure 3 shows the genes located within the deletions, those with functional annotations of sterility terms, and their expression during early (stage 5) or late (stage 8) flower development (table S6). The GSF deletions include the Y *Clavata3* gene (*slCLV3-Y* with gene ID scaffold1_000153), confirming this recently proposed GSF candidate (*17*, *18*). The functional role of *slCLV3* in male and female organ development is not well understood, but differences in the balance of gene expression in the Clavata-Wuschel pathway between males and females were proposed to explain carpel formation versus inhibition in female and male flowers in *S. latifolia*, respectively (*17*, *18*). Indeed, *Clavata3*, known as a carpel inhibitor in *Arabidopsis thaliana* and other plants, has a functional copy on the Y and a gametolog pseudogene on the X [*ψslCLV3-X* (*17*, *18*)]. *Wuschel1*, known as a carpel promoter in *A. thaliana* and other plants, is present on the X (*slWUS1-X*) and deleted from the Y [*ΔslWUS1-Y* (*18*, *34*)]. Our results independently confirm the role of this gene pair in determining female fertility or sterility in *S. latifolia* (Fig. 3).

We found several MFF candidate genes, including *slCyp704B1-Y* (gene ID scaffold1_000971), which is homologous to the *A. thaliana Cyp704B1* gene, encoding a cytochrome P450 protein crucial for pollen maturation. *slCyp704B1-Y* is expressed in the tapetum and is involved in the synthesis of sporopollenin (a pollen cell wall component). Its inactivation causes male sterility in *A. thaliana*. *slCyp704B1-Y* is expressed during late development (stage 8) of *S. latifolia* male flowers only based on RNA sequencing (RNA-seq) and quantitative polymerase chain reaction (qPCR) (fig. S17), consistent with an MFF function. Another MFF candidate is *slTHI1-Y* (gene ID scaffold1_003352), which is homologous to the *A. thaliana THI1* gene, encoding a papain-like cysteine protease that is also expressed in the tapetum, is important for pollen maturation (through involvement in proteolysis and tapetal cell degeneration), and is also annotated as a male fertility gene.

We identified one SPF candidate based on deletion mutants (gene ID scaffold12_000335, homolog to the *A. thaliana Scarecrow-like 4* and *7* transcription factors *SCL4/7*). The *slSCL4-Y* gene is pseudogenized by a premature stop codon but is expressed in flower buds at developmental stage 5, when sex is determined (fig. S19). Because deletion of this pseudogene leads to the loss of the male function in *S. latifolia* flowers, we hypothesize that its expression as a long noncoding RNA (lncRNA) is important for sex determination. However, the mechanism through which it may regulate sex determination remains unclear (supplementary text, section S2) (*19*).

Based on the location of these genes on the X chromosome, both *slWUS1* and *slCLV3* are in stratum S1 (in S1a and S1b, respectively). The *slCyp704B1-Y* MFF candidate has no X gametolog, but its orthologs are located in the *S. conica* chromosome 1 and *S. vulgaris* scaffold 1 in syntenic blocks homologous to the middle of the *S. latifolia* X chromosome stratum S2 (around positions 140 to 150 Mb). *slTHI1* is in stratum S3. Therefore, both MFF candidates appear to be a late addition to the nonrecombining region of the Y chromosome. An inversion on the X coincides with S1ab, and an inversion on the Y coincides with S1c, which suggests that these inversions suppressed recombination between the sex chromosomes, thereby forming strata S1ab and S1c (Fig. 4, stratum S1 panel). GSF potential sex-determining genes are thus concentrated in the small, oldest stratum S1. This is consistent with models for the evolution of dioecy in plants, with a yet-unknown initial male-sterility mutation and subsequent partially female-suppressing mutations creating selection for suppressed recombination (*35*). This model predicts that multiple linked mutations will create complete maleness. The candidate GSF genes that we detect in *S. latifolia*, together with the paracentric inversions forming S1ab, are consistent with this model. The MFF region, on the other hand, evolved well after dioecy was established and is associated with stratum S2. MFF genes may simply be male-function genes lost from the X because there is no selection to keep them on that chromosome (*26*), or they may have sexually antagonistic effects that led to polymorphisms favoring stratum S2 formation (*1*).

Conclusions

Our high-quality *S. latifolia* sex chromosome assemblies provide insights about their structure, function, and evolution (Fig. 4). These sex chromosomes originated ~11 Ma with the differentiation of a small region carrying the GSF sex-determining genes. A first stratum was probably formed by one paracentric inversion on each of the X and the Y. More recently, another stratum, S2, encompassing the centromere and including MFF, formed ~5 Ma, probably in the context of a general expansion of the pericentromeric regions in the *S. latifolia* genome, whose cause remains unclear. This generated a very large, nonrecombining, and TE-rich region on the Y. This is similar to what was observed in *Rumex hastatulus*, in which the Y chromosome is massively rearranged and repeat rich despite its recent origin (<10 Ma) (*36*). The absence of recombination also led to genetic degeneration, with half of the ancestral genes being lost from the Y, despite the expression of Y-linked genes in the haploid stages in plants (*37*, *38*). The X chromosome's pericentromeric region is also extremely large, perhaps because of increased TE accumulation under a reduced effective population size and absence of recombination of this stratum S2 on the X chromosome relative to autosomes (*39*, *40*).

REFERENCES AND NOTES

1. D. Charlesworth, B. Charlesworth, G. Marais, *Heredity* **95**, 118–128 (2005).
2. D. Bachtrog *et al.*, *PLOS Biol.* **12**, e1001899 (2014).
3. R. Ming, A. Bendahmane, S. S. Renner, *Annu. Rev. Plant Biol.* **62**, 485–514 (2011).
4. L. A. M. Rosolen, M. R. Vicari, M. C. Almeida, *Cytogenet. Genome Res.* **156**, 215–222 (2018).
5. A. Muyle, R. Shearn, G. A. Marais, *Genome Biol. Evol.* **9**, 627–645 (2017).
6. S. S. Renner, N. A. Müller, *Nat. Plants* **7**, 392–402 (2021).
7. G. Bernasconi *et al.*, *Heredity* **103**, 5–14 (2009).
8. K. B. Blackburn, *Nature* **112**, 687–688 (1923).
9. S. Matsunaga, M. Hizume, S. Kawano, T. Kuroiwa, *Cytologia* **59**, 135–141 (1994).
10. S. Qiu *et al.*, *Mol. Ecol.* **25**, 414–430 (2016).
11. M. Nicolas *et al.*, *PLOS Biol.* **3**, e4 (2004).
12. D. A. Filatov, *Genetics* **170**, 975–979 (2005).
13. J. Yue *et al.*, *Curr. Biol.* **33**, 2504–2514.e3 (2023).
14. R. Hobza *et al.*, *Genes* **8**, 302 (2017).
15. M. Westergaard, *Adv. Genet.* **9**, 217–281 (1958).
16. R. Bergero, D. Charlesworth, D. A. Filatov, R. C. Moore, *Genetics* **178**, 2045–2053 (2008).
17. Y. Kazama *et al.*, *Mol. Biol. Evol.* **39**, msac195 (2022).
18. Y. Kazama, T. Kobayashi, D. A. Filatov, *BioEssays* **45**, 2300111 (2023).
19. See the supplementary materials.
20. A. Muyle *et al.*, *Genome Biol. Evol.* **8**, 2530–2543 (2016).
21. A. Muyle *et al.*, *Nat. Plants* **4**, 677–680 (2018).
22. V. Bačovský, R. Čegan, D. Šimoníková, E. Hřibová, R. Hobza, *Front. Plant Sci.* **11**, 205 (2020).
23. M. Krasovec, M. Chester, K. Ridout, D. A. Filatov, *Curr. Biol.* **28**, 1832–1838.e4 (2018).
24. B. Charlesworth, P. Sniegowski, W. Stephan, *Nature* **371**, 215–220 (1994).
25. A. S. Papadopulos, M. Chester, K. Ridout, D. A. Filatov, *Proc. Natl. Acad. Sci. U.S.A.* **112**, 13021–13026 (2015).
26. A. Mrnjavac, K. A. Khudiakova, N. H. Barton, B. Vicoso, *Evol. Lett.* **7**, 4–12 (2023).
27. I. Gordo, B. Charlesworth, *Curr. Biol.* **11**, R684–R686 (2001).
28. M. V. Chibalina, D. A. Filatov, *Curr. Biol.* **21**, 1475–1479 (2011).
29. R. Bergero, D. Charlesworth, *Curr. Biol.* **21**, 1470–1474 (2011).
30. A. Muyle *et al.*, *PLOS Biol.* **10**, e1001308 (2012).
31. A. Lardon, S. Georgiev, A. Aghmir, G. Le Merrer, I. Negrutiu, *Genetics* **151**, 1173–1185 (1999).
32. I. Farbos *et al.*, *Genetics* **151**, 1187–1196 (1999).
33. J. Zluvova *et al.*, *Genetics* **177**, 375–386 (2007).
34. Y. Kazama *et al.*, *G3* **2**, 1269–1278 (2012).
35. B. Charlesworth, D. Charlesworth, *Am. Nat.* **112**, 975–997 (1978).
36. B. Sacchi *et al.*, *Mol. Biol. Evol.* **41**, msae074 (2024).
37. G. Sandler, F. E. G. Beaudry, S. C. H. Barrett, S. I. Wright, *Evol. Lett.* **2**, 368–377 (2018).
38. J. E. Mank, *Phil. Trans. R. Soc. B* **377**, 20210218 (2022).
39. J. Wang *et al.*, *Proc. Natl. Acad. Sci. U.S.A.* **109**, 13710–13715 (2012).
40. D. W. Bellott *et al.*, *Nature* **466**, 612–616 (2010).
41. C. Moraga, A. Di Genova, Silene-genome/genome-paper: V1.0, version 1.0, Zenodo (2024); https://doi.org/10.5281/zenodo.14434538.

ACKNOWLEDGMENTS

We thank E. Lacroix, technician at Université Claude Bernard Lyon 1 glasshouse, for her help for growing the *S. latifolia* U17 plants; C. Scutt for discussion about floral development; and three anonymous referees for suggestions and comments that improved this manuscript. All the computationally demanding bioinformatics were performed using the computing facilities of the CC LBBE/PRABI of Université Claude Bernard Lyon 1; the supercomputing infrastructure of the High-Performance Computing UOH laboratory (FIC 40059065-0) of Universidad de O'Higgins, Rancagua; the supercomputing infrastructure of the NLHPC (CCSS210001), by the e-INFRA CZ project (ID: 90254), supported by the Ministry of Education, Youth and Sports of the Czech Republic; and by the National Academic Infrastructure for Supercomputing in Sweden (NAISS, projects 2023/23-315 and 2023/22-242), funded by the Swedish Research Council through grant agreement no. 2022-06725. **Funding:** This study received support from Agence Nationale de la Recherche (ANR) grants ANR-20-CE20-0015-01 (G.A.B.M. and A.Be.), ANR-20-CE02-0015 (G.A.B.M.), and ANR-22-CE02-0024 (A.M.); the Fédération de Recherche "Biodiversité, Eau, Environnement, Ville & Santé" (FR BIOEENVIS) of University of Lyon 1 grant (G.A.B.M. and J.B.); the Czech Science Foundation grants 21-00580S and 22-00364S (P.J.); the European Research Council (ERC) EvolSexChrom (832352) grant (T.G.); the ERC NectarGland (101095736) grant (A.Be.); the CNRS Biology starting grant (A.M.); the ANID Chile, Grants Fondecyt Regular 1221029, and SIA grant SA77210017 (A.D.G.); the US National Science Foundation grant MCB-2048407 (D.B.S.); the US National Institutes of Health grant R35GM148134 (D.B.S.); and the US National Science Foundation grant DEB-1353970 (L.F.D.). **Author contributions:** Conceptualization: G.A.B.M., R.H., M.-A.M., A.D.G., A.Be., T.G., D.C., A.M.; Formal analysis: C.M., C.Br., Q.R., P.V., P.J., A.M., M.H., R.C.R.d.l.V., E.T., X.L., E.M.-G., C.L., P.D.F., C.Be., R.Ce., G.A., A.E.F., V.M., A.V., S.K., A.D.G., M.-A.M.; Methodology: C.M., C.Br., R.L., A.D.G., G.A.B.M.; Investigation: C.M., C.Br., Q.R., P.V., P.J., A.M., M.H., R.C.R.d.l.V., E.T., X.L., E.M.-G., C.L., P.D.F., C.C., K.L., C.Be., J.B., S.S., R.Ce., R.L., G.A., A.Bo., R.T., D.B.S., S.K., L.F.D., D.C., T.G., A.Be., A.D.G., M.-A.M., R.H., G.A.B.M.; Resources: R.H., A.D.G., L.F.D., D.B.S., M.S.O., D.R.T., O.A.J.A., M.K., H.Št., H.Ši., P.C., Z.T., H.T., L.W., S.D., B.S., D.P., A.M.; Software: C.M., C.Br., E.T., R.L., R.C.R.d.l.V., A.V., A.D.G.; Validation: A.C., R.Co., C.F.; Visualization: C.M., C.Br., Q.R., P.V., A.M., R.C.R.d.l.V., E.T., R.L., D.P., S.K., M.-A.M.; Funding acquisition: G.A.B.M., A.Be., J.B., P.J., T.G., A.M., A.D.G., D.B.S., L.F.D.; Project administration: G.A.B.M.; Supervision: G.A.B.M., R.H., M.-A.M., A.D.G., A.Be., T.G., L.F.D., S.K., D.B.S., R.Co., R.T., A.Bo., R.C.R.d.l.V., R.L., A.M.; Writing – original draft: G.A.B.M., M.-A.M., A.Be., S.K., D.B.S., S.S., J.B., P.D.F., X.L., E.T., A.M., Q.R., C.Br., C.M.; Writing – review & editing: G.A.B.M., T.G., D.C., L.F.D., S.K., R.C.R.d.l.V., C.Br., E.M.-G., A.Bo., A.M., P.V., C.M., Q.R., P.J., R.Ce., R.H., and all authors. **Competing interests:** The authors declare that they have no competing interests. **Data and materials availability:** Sequencing data (long reads, short reads, and Omni-C datasets), genome assembly, and annotation are available under the project PRJNA1132743 on the National Center for Biotechnology Information (NCBI). All analyses and pipelines to generate figures are available on GitHub (https://github.com/Silene-genome/genome-paper) and Zenodo (*41*).

SUPPLEMENTARY MATERIALS

science.org/doi/10.1126/science.adj7430
Materials and Methods
Supplementary Text
Figs. S1 to S20
Tables S1 to S7
References (*42*–*132*)
MDAR Reproducibility Checklist

Submitted 18 September 2023; resubmitted 22 April 2024
Accepted 18 December 2024
10.1126/science.adj7430

EVOLUTION

Rapid and dynamic evolution of a giant Y chromosome in *Silene latifolia*

Takashi Akagi[1,2,3]†*, Naoko Fujita[1,4]†, Kenta Shirasawa[5], Hiroyuki Tanaka[6], Kiyotaka Nagaki[7], Kanae Masuda[1], Ayano Horiuchi[1], Eriko Kuwada[1], Kanta Kawai[1], Riko Kunou[1], Koki Nakamura[7], Yoko Ikeda[7], Atsushi Toyoda[8,9], Takehiko Itoh[6], Koichiro Ushijima[1], Deborah Charlesworth[10]

Some plants have massive sex-linked regions. To test hypotheses about their evolution, we sequenced the genome of *Silene latifolia*, in which giant heteromorphic sex chromosomes were first discovered in 1923. It has long been known that the Y chromosome consists mainly of a male-specific region that does not recombine with the X chromosome and carries the sex-determining genes and genes with other male functions. However, only with a whole Y chromosome assembly can candidate genes be validated experimentally and their locations determined and related to the suppression of recombination. We describe the genomic changes as the ancestral chromosome evolved into the current XY pair, testing ideas about the evolution of large nonrecombining regions and the mechanisms that created the present recombination pattern.

Chromosomal sex determination is common not only in animals, but also in a diversity of plant species. Most extant flowering plants are functional hermaphrodites, the sex chromosomes of which evolved much more recently than those of many animals and independently in different lineages [reviewed in (*1*)]. They are therefore interesting for studying sex chromosome establishment when separate sexes evolved from ancestral hermaphroditism. Close linkage between male and female-determining genes may be involved (*2*), and subsequent selection for sexual dimorphism involving traits that benefit only one sex (sexually antagonistic, or SA, traits) can lead to the establishment of polymorphisms closely linked to the sex-determining factor(s), favoring further recombination suppression (*3*). These ideas can explain the extensive male-specific regions of Y chromosomes (MSYs), that do not recombine with and become differentiated from the X chromosome. However, physically extensive MSYs may not require sexually antagonistic selection. For example, sex-determining factors may evolve within a genome region that was already recombinationally inactive (*4*). One alternative suggestion is that inversions carrying no SA factors may be more likely to persist on sex chromosomes than on autosomes (*5*, *6*). Moreover, sexual dimorphisms can be caused by the pleiotropic effects of the sex-determining factors themselves and do not require separate genetic factors with SA effects (*7*). The plant *Silene latifolia* is well suited for testing such ideas.

The first observation of sex chromosomes in a flowering plant was in *S. latifolia*, the karyotype of which is $2n = 22A + XY$ (*8*). Its "giant" Y chromosome (now known to be ~500 Mb; Fig. 1A) has been a model for studying heteromorphic sex chromosomes with large MSYs. After decades of cytogenetic and theoretical studies, empirical studies using limited numbers of molecular markers (*9*, *10*) revealed a pattern resembling the "evolutionary strata"

---

[1]Graduate School of Environmental and Life Science, Okayama University, Okayama, Japan. [2]Japan Science and Technology Agency (JST), PRESTO, Kawaguchi-shi, Saitama, Japan. [3]Kihara Institute for Biological Research, Yokohama City University, Yokohama, Kanagawa, Japan. [4]National Museum of Nature and Science, Tsukuba-shi, Ibaraki, Japan. [5]Kazusa DNA Research Institute, Kazusa-Kamatari, Kisarazu, Chiba, Japan. [6]School of Life Science and Technology, Tokyo Institute of Technology, Meguro-ku, Tokyo, Japan. [7]Institute of Plant Science and Resources, Okayama University, Kurashiki, Okayama, Japan. [8]Comparative Genomics Laboratory, National Institute of Genetics, Mishima, Shizuoka, Japan. [9]Advanced Genomics Center, National Institute of Genetics, Mishima, Shizuoka, Japan. [10]Institute of Ecology and Evolution, University of Edinburgh, Edinburgh, UK.
***Corresponding author. Email: takashia@okayama-u.ac.jp or claclatakashi@gmail.com**
†These authors contributed equally to this work.

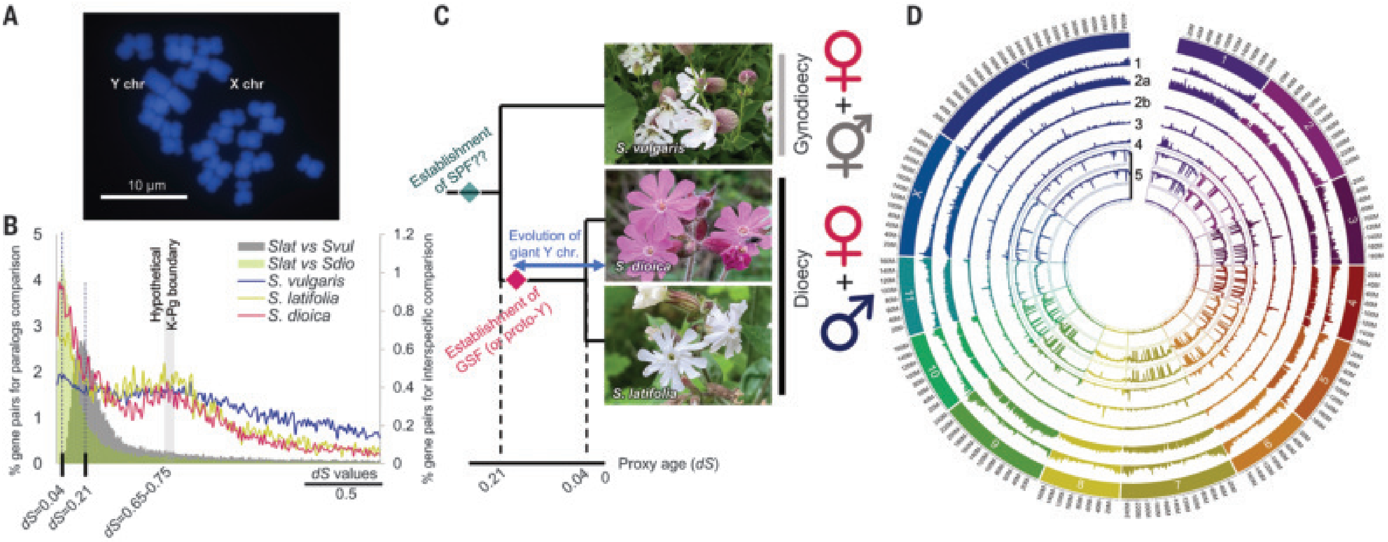

Fig. 1. Overview of the sex chromosomes and genome characteristics in *S. latifolia* and the two related species, *S. dioica* and *S. vulgaris*. (**A**) Cytogenetic observations of the giant Y and X chromosomes with 4′,6-diamidino-2-phenylindole (DAPI) staining. (**B**) Histogram of the pairwise dS values between paralogous genes within each genome and between orthologous genes in two species (*Slat* versus *Sdio* and *Slat* versus *Svul*). The interspecific dS values exhibited a peak at dS = 0.04 and 0.21, which corresponds the proxy age for divergence of *S. latifolia* and *S. dioica* and *S. latifolia* and *S. vulgaris*, respectively. (**C**) Estimated evolutionary context of the two sex-determining factors, SPF and GSF, in dioecious species (*S. latifolia* and *S. dioica*). (**D**) Bird's-eye views of the genomes of *S. latifolia*. Circle layer 1, gene density; layer 2, TE density (2a, LTR-type TEs; 2b, non-LTR); layer 3, standardized CENH3/H3 estimates; layer 4, standardized H3K9me2/H3 estimates; and layer 5, weighted DNA methylation rate (CG, CHG, and CHH, respectively, from the outer to the inner ring).

first discovered in humans (*11*), with Y-X sequence divergence lowest for genes closest to the pseudo-autosomal region that still recombines. Such divergence differences indicate that Y chromosome recombination suppression occurred at different times. However, important gaps in our understanding remain, including why the Y-linked region is so large and to what extent its lack of recombination has led to genetic degeneration, such as mammalian Y chromosomes (*12*). Recent advances in genome sequencing have yielded data suggesting that partial degeneration (*13*, *14*) and possibly dosage compensation (*15*–*18*) have evolved, but degeneration cannot be accurately quantified without an assembled Y chromosome.

Observations of Y chromosome deletions revealed that the *S. latifolia* Y chromosome carries two sex-determining factors, a stamen-promoting factor (SPF) and a gynoecium-suppressing factor (GSF) (*19*). This plant's Y therefore fits the "two-mutation model" (*20*), in which a loss-of-function mutation in an SPF in an ancestral hermaphrodite species creates females, and males arise by a dominant femaleness-suppressing mutation, GSF, in a closely linked gene. Consistent with this model, two genes have been found within physically small sex-determining genome regions in several dioecious plants (*21*–*24*). The very different situation in the *S. latifolia* Y chromosome suggests that, as the model proposes, selection favored closer linkage between initially recombining genes, with loss of Y-X recombination triggering repetitive sequence accumulation (*25*, *26*) and creating the giant Y chromosome.

Genome sequences of *Silene* species

The *S. latifolia* sex chromosomes, which are shared with its close dioecious relative, *S. dioica* in the subgenus Behenantha, evolved after divergence from *S. vulgaris*, a gynodioecious species (with female and hermaphrodite individuals, and $2n = 24A$ chromosomes) (Fig. 1, B and C). We assembled chromosome-scale sequences of *S. latifolia* and *S. dioica* males and a *S. vulgaris* hermaphrodite using PacBio HiFi reads and Bionano optical mapping or Hi-C contact mapping, cytogenetic anchoring with molecular markers, and genetic maps (Fig. 1D and fig. S1). BUSCO (*27*) analysis found 93.1%, 99.7%, and 97.7% of universal single-copy orthologous eudicotyledonous plant genes in our *S. latifolia*, *S. dioica*, and *S. vulgaris*, genome sequences, respectively (table S1). Synonymous site divergence (dS) between *S. latifolia* and *S. dioica* and *S. latifolia* and

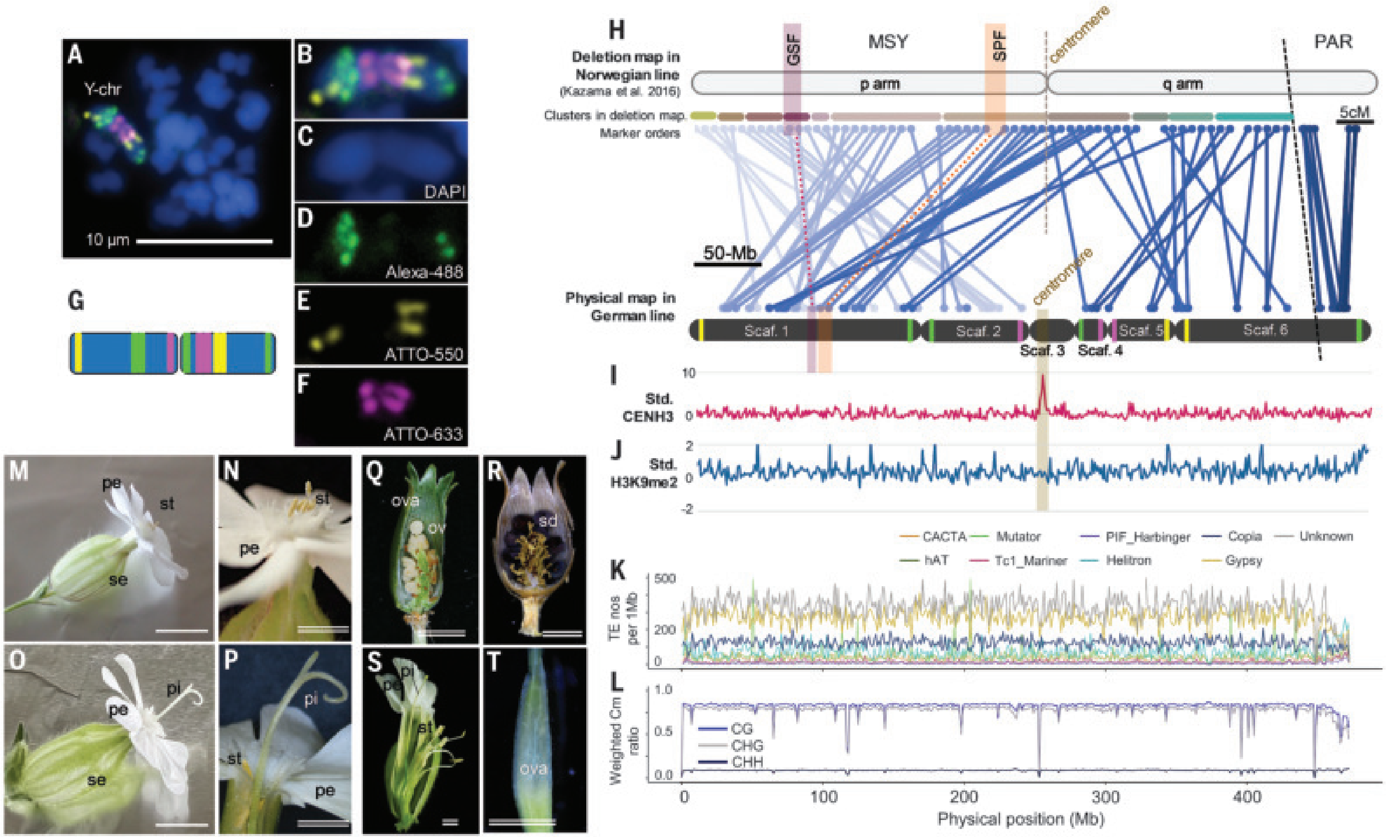

Fig. 2. Genomic context of the *S. latifolia* Y chromosome. (**A** to **G**) FISH anchoring of the genomic contigs. (A) Detection of the Y chromosome by myTag probes. (B) Enlarged image of the Y chromosome in (A) merging the signals with DAPI. (C to F) Staining for three probes, Alexa Fluor-488 (D), ATTO-550 (E), and ATTO-633 (F). (G) Ideogram of the Y chromosome based on the signals. (**H** to **L**) Genomic context of the Y chromosome. (H) Comparative analysis of the deletion map in a Norwegian line (*30*) (with only marker orders given because no assembly was available) and our genome sequence of a German line. The regions including the two sex-determining genes are highlighted. In the recombinationally active PAR, the genetic map positions from Bergero *et al*. (*10*) correlate with the physical positions in our genome sequences. (I and J) CENH3 content (standardized by H3 amounts) (I) exhibits a clear single peak, whereas the standardized H3K9me2 levels (J) fluctuate but show no major pattern along the chromosome. (K) TE distribution in 1-Mb windows. LTR-TEs, especially *Gypsy* and *unknown* classes, show high densities in the MSY compared with the PAR. (L) CG and CHG DNA methylation levels show a similar pattern. (**M** and **N**) VIGS of *Y-SlCLV3* resulted in the production of hermaphrodite flowers in a genetically male *S. latifolia*. Control male flowers [(M) and (N)] exhibited functional stamens (st) but no elongated pistils. (**O** to **R**) ALSV-induced gene silencing resulted in elongation of functional pistils (pi) with normal stamens in male plants [(O) and (P)], producing ovules (ov) (Q) to be viable seeds (sd) (R). (**S** and **T**) ALSV-infected male lines often induced imperfect sterile pistils. pe, petal; se, sepal; ova, ovary. Scale bars, 1 cm (single line) and 5 mm (double line).

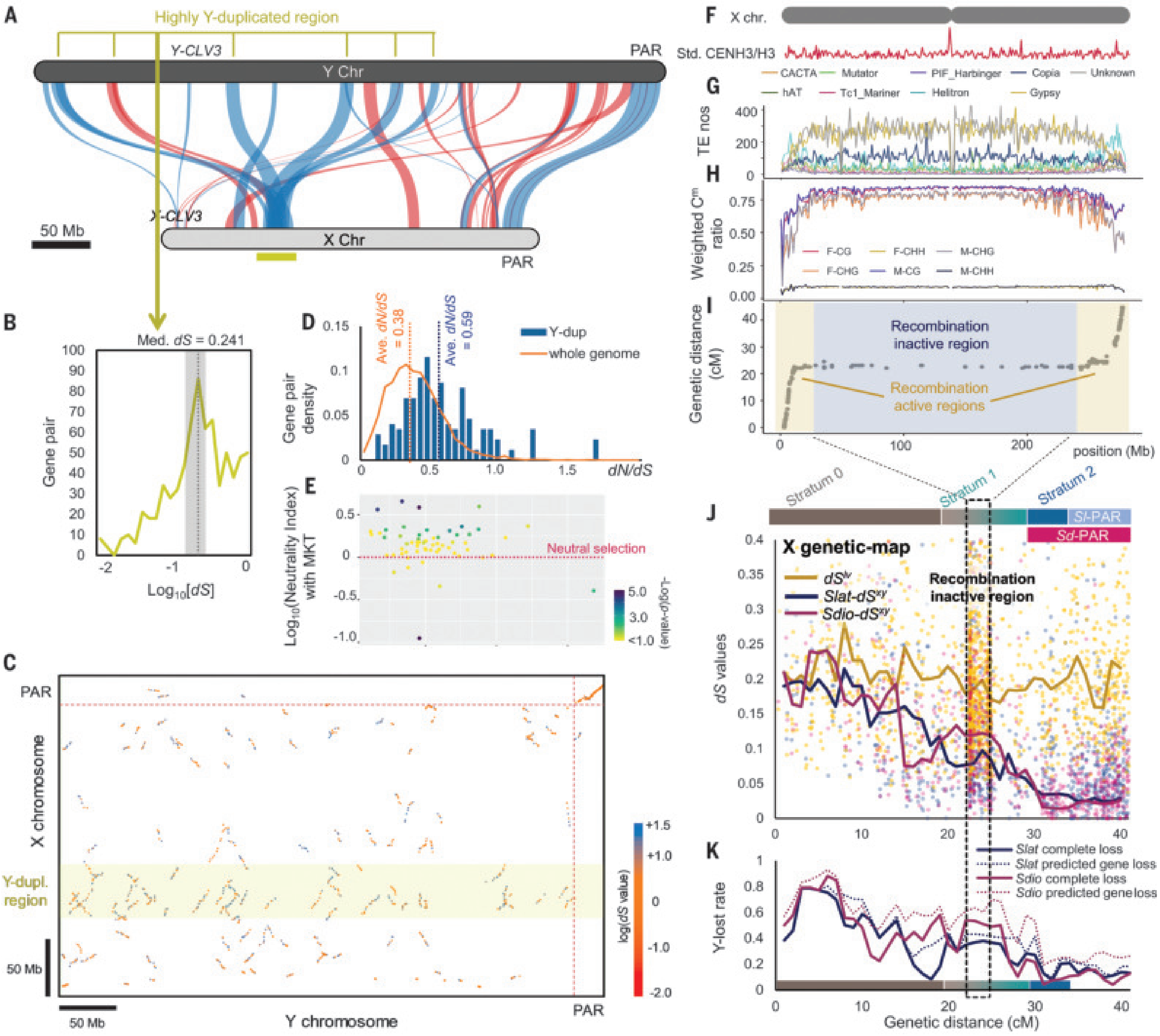

Fig. 3. Comparative analysis of Y and X chromosomes in *S. latifolia*. (**A**) Gene order–based synteny analysis between the X and Y chromosomes. Blue and red bands indicate synteny with forwarded and inverted directions, respectively. The X-linked region marked with a gold horizontal band includes sequences that are highly duplicated in the Y chromosome. (**B**) Pairwise dS values of genes in the Y-duplicated regions. The peak with dS values of 0.158 to 0.316 is highlighted in gray. (**C**) Locations of syntenic blocks in the X and Y chromosomes, with colors indicating the mean dS values between the X- and Y-linked sequences (see the key). (**D**) Values of dN/dS in the paralogous gene pairs with dS in the interval between 0.158 and 0.316; pairs are shown separately for the Y-duplicated region and the whole genome. (**E**) Distribution of the neutrality index in McDonald-Kreitman tests [the *x*-axis values are the dN/dS values given in (D)]. (**F** to **I**) Characteristics of the X chromosome. (F) Standardized CENH3 amount (corrected by H3 amount). (G) TE distribution with 1-Mb windows. (H) Weighted DNA methylation levels. (I) Genetic recombination map estimated using an F1 population of 228 individuals, showing that the regions with highly elevated LTR-TEs, especially the *Gypsy* and *unknown* classes, and CG and CHG DNA methylation levels corresponding with the recombination arrested region. (**J** and **K**) Evolutionary strata in terms of Y-X dS and of genetic degeneration in *S. latifolia* and *S. dioica*. For *S. dioica*, the genetic distances were defined with the orthologous genes in *S. latifolia*. The *x* axis shows positions in the X chromosome genetic map (fig. S15 shows the same data with positions in the X assembly). (J) dS values between X- and Y-linked alleles (*Slat*-dS^{XY} and *Sdio*-dS^{XY} in *S. latifolia* and *S. dioica*, respectively) and between *S. latifolia* X-linked alleles and their orthologs in *S. vulgaris* (dS^{lv}). The lines indicate median dS values in 1-cM bins. Based on Pettitt's change-point test using the estimated *Slat*-dS^{XY} values, we defined three strata, 0 (dS^{XY} > ~0.10), 1 (0.05 to 0.10), and 2 (0.01 to 0.05). (K) Proportion of genes ancestrally present (defined in the text) that have been lost from the *S. latifolia* and *S. dioica* Y chromosome. Complete loss means that the genome region corresponding to the gene is completely absent from the Y chromosome. Predicted gene loss means that the putative gene is not predicted in the Y sequence by our annotation or it is disrupted.

S. vulgaris average 0.04 and 0.21, respectively. Most sequences in these species are diploid despite an ancient genome duplication event at the K-Pg boundary (with dS = 0.65 to 0.75; Fig. 1B and fig. S1), which is consistent with other plant polyploidization events (*28*, *29*).

The *S. latifolia* Y chromosome sequence forms six super-contigs totaling ~480 Mb. Genetic mapping of markers in male meiosis revealed a large nonrecombining male-specific region of the Y chromosome (MSY) and a pseudoautosomal region (PAR) at one chromosome end

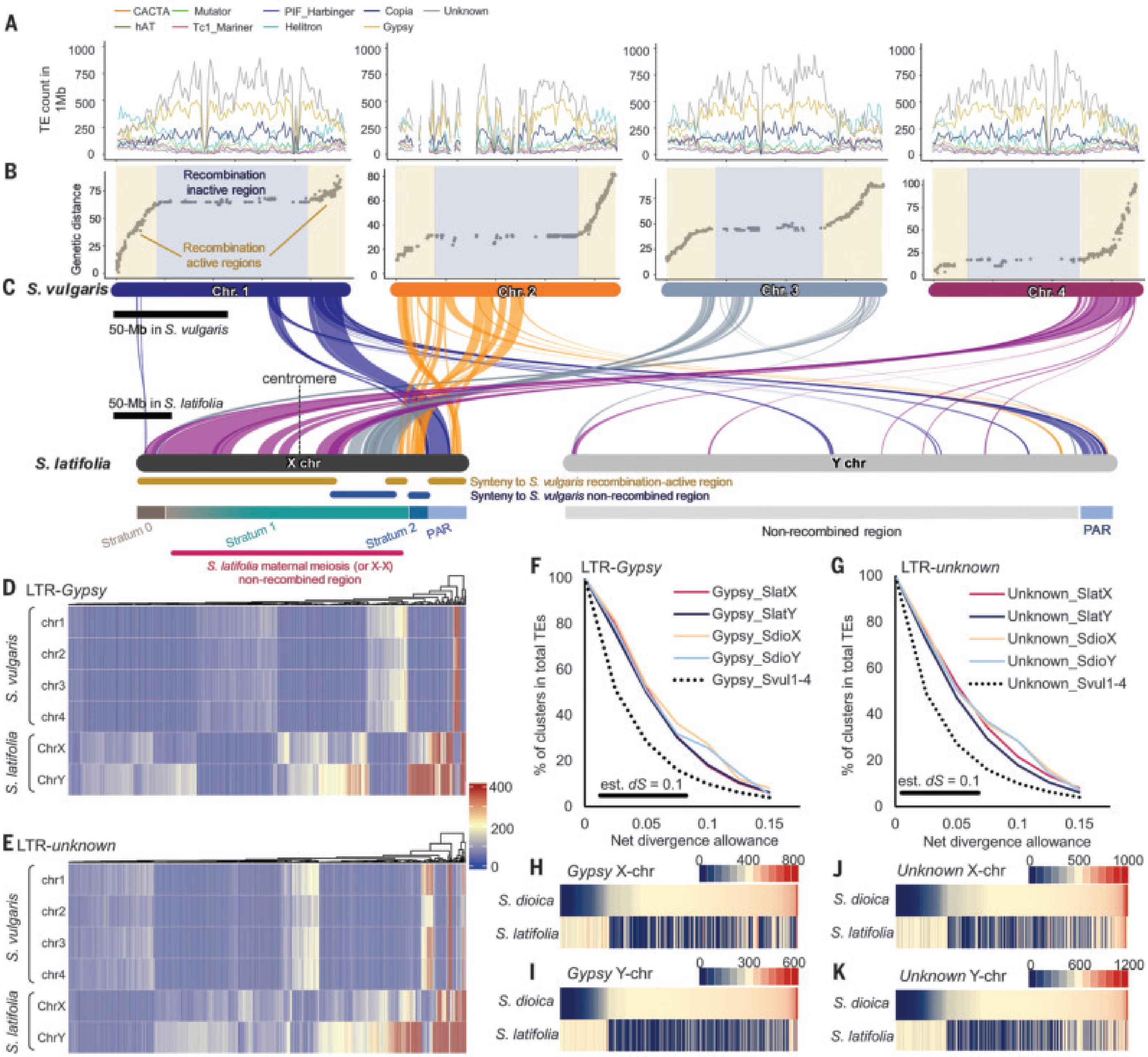

Fig. 4. Comparative genomic analysis between *S. latifolia* and *S. vulgaris*. (**A** to **C**) Genomic contexts of chromosomes 1 to 4 of *S. vulgaris* and their detailed relationship with the X and Y chromosomes of *S. latifolia*. (A) TE distribution. (B) Genetic recombination map showing wide, recombinationally inactive regions with accumulation of *Gypsy* and *unknown* LTR-TE classes (fig. S17). (C) Half of the X chromosome (and potentially also the ancestral Y chromosome) shows synteny with recombinationally active regions of *S. vulgaris* chromosome 4. The other half may be derived from fusions involving *S. vulgaris* chromosomes 1 to 3 regions, some of which are currently nonrecombining. (**D** and **E**) Sequence homology–based clustering of the *Gypsy* (D) and *unknown* LTR-TE classes (E) extracted from X/Y chromosomes in *S. latifolia* and chromosomes 1 to 4 in *S. vulgaris*. Many are specific to the X or Y chromosome or are lineage specific. (**F** and **G**) Numbers of *Gypsy* (F) and *unknown* type (G) TE clusters (defined as sequences with the divergence values indicated on the *x* axis) as proportions of the total numbers of each TE type in *S. latifolia* and *S. dioica*. The *x* axis shows clusters defined using threshold values of up to 15%, which approximately quantify the divergence of extant insertions from their ancestral sequences and therefore reflect the insertions' ages. The figure shows that the X and Y chromosomes of both species are rich in TE bursts that are older than bursts on the *S. vulgaris* chromosome 4. (**H** to **K**) Sequence homology–based clustering of the recent (>95% identity) *Gypsy* [(H) for X and (I) for Y] and *unknown* classes of LTR [(J) for X and (K) for Y] TEs extracted in *S. latifolia* and *S. dioica*. Most clusters indicate lineage-specific bursts.

(*10*, *15*). We anchored MSY contigs cytogenetically by fluorescence in situ hybridization (FISH) using dense probes specific to each contig end (see Fig. 2, A to H; fig. S2; and the materials and methods for details). All chromosomes are metacentric, but the Y arrangements differ within *S. latifolia*, as the arrangement in our family (using parent plants from Germany) differs from that in a Norwegian family (named K-line) used to determine marker orders by deletion mapping (*30*) (Fig. 2H and fig. S3). CENH3 antibody peaks and dense tandem repeats indicate the autosome centromere locations (figs. S4 and S5). No mature repeats were found in the Y centromeric region (Fig. 2I and fig. S5B), supporting rearrangements changing the relative Y chromosome centromere location. Consistent with this, the densities of H3K9me2 (a common heterochromatin epimark) and DNA methylation in young leaves (mainly in the CG and CHG contexts) are highly distributed throughout the MSY (Fig. 2, J to L). Long terminal repeats (LTRs) of the *Gypsy* and *Unknown* classes are enriched across the MSY and in autosomal pericentromeric low-recombination regions (Fig. 2K, figs. S6 and S7, and table S2), as discussed below.

Identification of the sex-determining gene candidates

Deletion mapping confirmed Westergaard's finding of MSY regions affecting male and female flower organs (*31*, *32*). We identified regions in our assembly syntenic with two previously identified; the GSF and SPF regions (figs. S8 and S9), both in the current Y*p* arm (*30*), which include 31 and 62 candidates, respectively (tables S3 and S4). Some candidate genes are absent from the *S. dioica* Y chromosome and were excluded from further consideration. Expression analysis in early flower primordia supported the previous GSF candidate (*33*), a *CLAVATA3*-like gene (*SlCLV3*) that may affect flower meristem size and gynoecium development. Its X and Y copies are highly diverged ($dS^{XY} = 0.179$), and in male flower bud primordia, we detected only *Y-SlCLV3* expression, consistent with the previous study. Experimental virus–induced gene silencing (VIGS) of *Y-SlCLV3* in male *S. latifolia* with apple-latent spherical virus (ALSV) (*34*) resulted in the formation of functional hermaphrodite flowers (Fig. 2, M to S; fig. S10; and table S6), validating this conclusion for the first time. One candidate within the SPF region is an ortholog of the immunophilin-like *FKBP42/TWISTED DWARF1* (*TWD1*) gene, which is required for androecium development in angiosperms (*35*, *36*). This gene is Y specific in *S. latifolia* and *S. dioica* and exhibits high expression in male flower primordia (table S4); the effects of silencing *TWD1* have not yet been tested.

Differentiation of X and Y chromosomes in *Silene*

The *S. latifolia* and *S. dioica* MSYs show little homology with their X counterparts (fig. S11). Gene-based syntenic block analyses detected many Y-specific duplications (Fig. 3, A to C, and

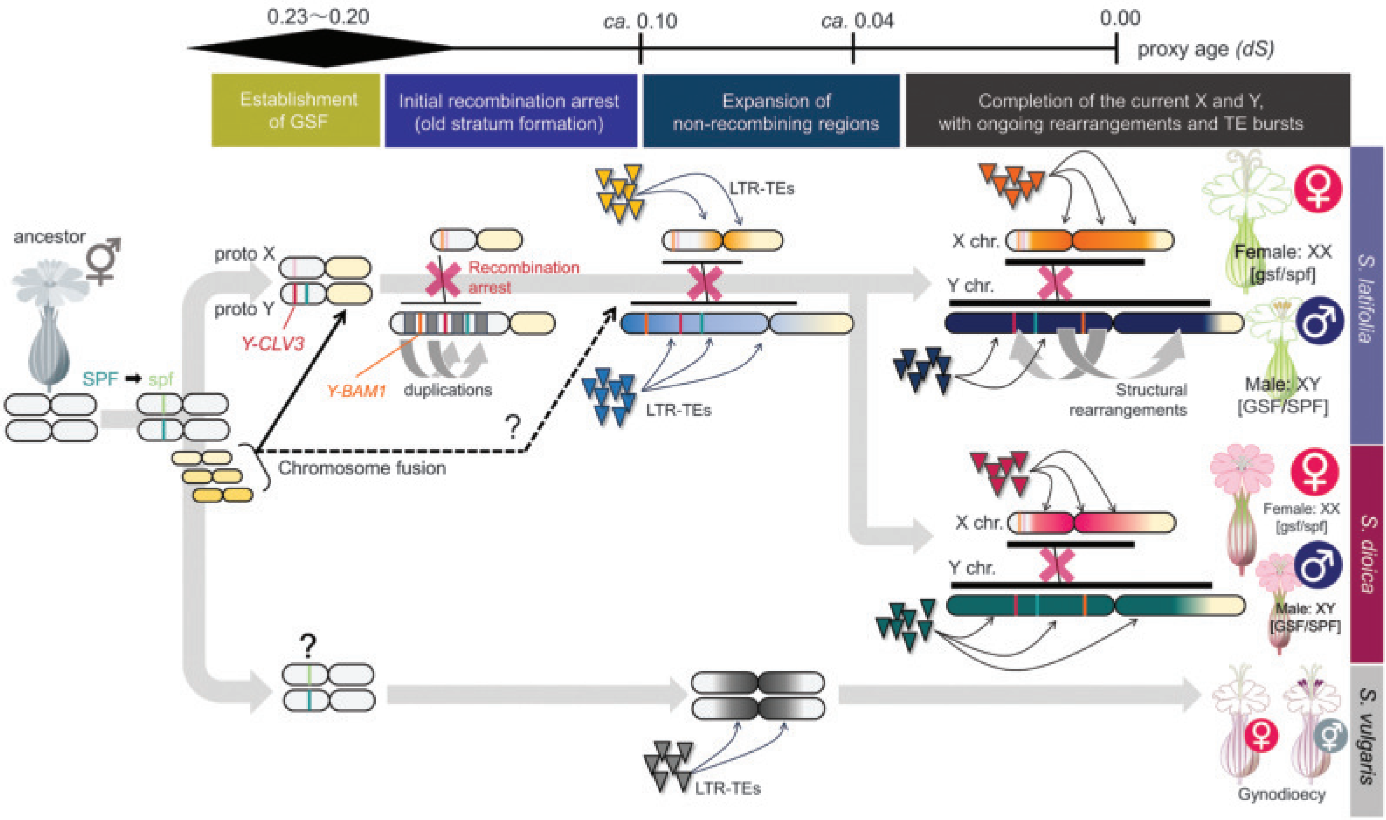

Fig. 5. Model for the rapid and dynamic sex chromosome evolution in *S. latifolia* and *S. dioica*. Under the two-mutation model for the evolution of separate males and females from a hermaphroditic plant, the SPF loss-of-function mutation occurred first, before the oldest nonrecombining stratum evolved. The SPF gene has not yet been identified. The second mutation (gain of a dominant gynoecium-suppressing function on the Y chromosome, the *Y-SlCLV3* allele), produces males. This gene has an X-linked allele, allowing its location to be identified as being within the oldest stratum, 0, consistent with its high Y-X divergence. Assuming that the SPF, *Y-SlCLV3*, and a possible sexually antagonistic gene, *SlBAM1*, were within the left ancestrally recombining region, selection would have favored suppressed recombination, explaining the evolution of stratum 0. After recombination stopped, the duplicated regions evolved on the Y chromosome left arm, also before the split of *S. latifolia* and *S. dioica*. Recombination subsequently stopped across the pericentromeric region in which it was previously infrequent. Each time recombination became suppressed, TEs and rearrangements accumulated, including accumulating to even higher than previous levels in the pericentromeric regions.

figs. S12 and S13), especially in *S. dioica*. One highly duplicated region (highlighted in gold in Fig. 3C and fig. S13) is shared by both species. In *S. latifolia*, these paralogs show high dS, peaking at 0.241 ± 0.022 (Fig. 3B), similar to the value of 0.213 for *S. latifolia*–*S. vulgaris* divergence and for the oldest recombination suppression event (Fig. 3J). Duplications therefore started accumulating immediately after XY recombination stopped, which was almost contemporaneous with the split of *S. latifolia* and *S. dioica* from the *S. vulgaris* lineage. These duplicates have much higher nonsynonymous site divergence (dN) than for genome-wide paralog pairs with similar dS values (0.158 to 0.316); the respective mean dN/dS values are 0.59 versus 0.38 ($P = 4.6 \times 10^{-26}$, Wilcoxon's test) (Fig. 2D). McDonald-Kreitman tests (*37*) indicated that a few of the *S. latifolia* duplicates may be positively selected ($P < 0.1$; Fig. 3E), possibly increasing their expression from the degenerating Y chromosome, but most are selected against or evolving nearly neutrally (neutrality index = 0.8~1.5, $P > 0.1$, G tests), consistent with the expected weaker purifying selection after duplication (*38*).

Recombination in *S. latifolia* female meiosis is also infrequent across much of the X chromosome (Fig. 3I) (*39*, *40*). Recombinationally inactive regions occupy most of the middle region of all chromosomes, including in *S. vulgaris*, supporting previous results suggesting the presence of physically large pericentromeric regions (*10*, *15*). Consistent with rare recombination, LTR retrotransposons (LTR-TEs) and DNA methylation densities in these regions are almost as high as in the MSY (Fig. 3, F to I, and figs. S6 and S7).

To test whether recombination suppression has occurred, and when, we estimated dS between complete X chromosome coding sequences and their MSY alleles. In both *S. latifolia* and *S. dioica*, genes distant from the PAR have the highest values (*Slat-dS*^{XY} and *Sdio-dS*^{XY}, respectively, in Fig. 3J). Within this oldest stratum, 0, median *Slat-dS*^{XY} values in 1-cM bins range from 0.10 to 0.23, close to the *S. latifolia* and *S. vulgaris* divergence (*dS*^{lv}) estimates. Using either X genetic or physical map positions, *dS*^{XY} declines toward the PAR, which recombines in both sexes (Fig. 3J), confirming results using X genetic map positions without an X assembly (*15*, *40*, *41*). Change-point tests (*42*) detected two changes in *Slat-dS*^{XY} values (with $P = 2.6 \times 10^{-11}$ and $P = 2.7 \times 10^{-3}$), indicating two recombination suppression events (Fig. 3J).

The availability of Y chromosome assemblies allows us to relate Y chromosome degeneration to strata ages. Following the approach developed for humans (*12*), we first defined ancestral genes that are present on the *S. latifolia* or *S. dioica* X chromosome and found in similar proportions across all homologous *S. vulgaris* regions (fig. S14). We used two degeneration criteria: (i) loss of the gene's complete sequence from the Y chromosome and (ii) genes not predicted on the Y chromosome (including disrupted genes). In many stratum 0 windows (corresponding to part of the X chromosome–recombining region to the left of the central rarely recombining region), >70% of *S. latifolia* and *S. dioica* genes are X specific (Fig. 3K), much greater degeneration than was previously estimated without a Y assembly (*43*). Degeneration is less in stratum 1, which includes parts of both recombining X regions plus the >200-Mb pericentromeric rarely recombining region (Fig. 3, I and J; the dotted box includes genes within this small genetic map interval). Ancestral gene losses are even rarer in the small stratum 2 near the PAR (Fig. 3K), which includes partially sex-linked genes in *S. dioica* that stopped recombining in *S. latifolia* since the species split (*41*, *44*, *45*) and shows slightly, but significantly, higher Y-X divergence (fig. S15).

Processes to establish recombinationally inactive regions in sex chromosomes

Chromosome-wide synteny analysis with *S. vulgaris* found that most of the *S. latifolia* and *S. dioica* X chromosomes correspond to a single *S. vulgaris* chromosome, chromosome 4, but portions correspond to three other *S. vulgaris* chromosomes (Fig. 4, A to C, and fig S16), indicating either fusions with other *S. vulgaris* chromosomes before the *S. latifolia* and *S. dioica* split or rearrangements in the *S. vulgaris* lineage. Stratum 0 and part of stratum 1 overlapping the X pericentromeric region correspond with a recombinationally active part of *S. vulgaris* chromosome 4 (Fig. 4C), confirming that the *S. latifolia* and *S. dioica* MSYs newly evolved suppressed recombination. Their homologous strata 0 and 1 regions are arranged differently, and therefore rearrangements must have independently evolved in their MSYs after recombination became suppressed.

In both *S. latifolia* and *S. vulgaris*, recombinationally inactive regions are highly enriched with LTR-*Gypsy* and LTR-*unknown* class TEs (Fig. 4, A and B, $r = -0.68$ to -0.6; figs. S6 and S7 and S17 and S18). To examine the potential involvement of TEs in sex chromosome expansion, we extracted *Gypsy* and *unknown*-class TEs from the *S. latifolia* X- and Y-chromosome sequences and the four syntenic *S. vulgaris* chromosome regions. Using a 20% net divergence threshold, most sequences are specific to one species or to the *S. latifolia* X or Y chromosome (Fig. 4, D and E, and table S6). In clusters shared by the *S. latifolia* X and Y chromosomes, or by both species, recently generated subclusters (bursts defined by $dS < 0.1$) tended to be more chromosome specific than older ones, as expected (fig. S19 and table S6). Divergence estimates of LTR coding sequences (Fig. 4, F and G) suggest that most insertions occurred recently, consistent with generally being deleterious (*25*). Insertions in the *S. latifolia* X and Y chromosomes tend to be older than those in *S. vulgaris*. Nevertheless, most bursts occurred after the oldest stratum 0 formed ($dS > 0.1$, see above), and were therefore not the cause of recombination arrest, but rather probably contributed to MSY expansion after recombination stopped. Furthermore, LTR-TE accumulation in the X and Y chromosomes occurred independently in *S. latifolia* and *S. dioica* (based on clusters having net divergence < 0.05; Fig. 4, H to K). Synteny analysis also detected rearrangements between the large *S. latifolia* and *S. dioica* X chromosome pericentromeric regions (fig. S20A), and even within *S. latifolia* (*39*) (figs. S20B and S21), suggesting ongoing rearrangements of these rarely recombining regions, perhaps involving TE activities.

What might have caused suppressed MSY recombination in regions that recombine between the X chromosomes in females? Under the two-gene hypothesis described above, both primary sex-determining genes should be in the region that first evolved suppressed recombination. The GSF, *Y-SlCLV3,* is indeed within stratum 0 (the terminal location of its X-linked copy probably reflects its ancestral position; it is between 84 and 86 Mb of our Y assembly, reflecting MSY rearrangements; Fig. 3A and fig. S8). However, because of the SPF candidate's Y specificity in *S. latifolia* and *S. dioica* and Y rearrangements, its X position cannot be assigned. We found a possible sexually antagonistic gene, *SlBAM1*, near the left end of stratum 0 (fig. S22, A to C) that potentially contributes to *S. latifolia*'s secondary sexual trait dimorphism(s). *BARELY ANY MERISTEM 1/2* (*BAM1/2*)–like receptor-like kinases often function in reproductive processes and flower morphological development through *CLV1/3*-related pathways (*46*–*48*). *SlBAM1* has male-specific *Y-BAM1* sequences in our *S. latifolia* and *S. dioica* individuals, and the gene is also present in the hermaphrodite *S. conica* (fig. S22B). Ectopic expression of *Y-BAM1* in *Nicotiana tabacum* under the regulation of its native promoter substantially increased flower numbers per inflorescence ($P = 0.39 \times 10^{-4}$) and reduced flower size ($P = 0.00015$), as in *S. latifolia* males (fig. S23 and table S7) (*49*). Thus, selection for closer linkage between the primary sex-determining factors and *SlBAM1* might have contributed to stratum 0 evolution.

It is unclear how or why the other strata evolved. Assuming that the ancestral state resembled the present X chromosome, stratum 1 formation involved cessation of recombination between stratum 0 and regions corresponding to parts of *S. vulgaris* chromosomes 2 and 3, including regions that are pericentromeric and recombinationally inactive in females and in *S. vulgaris* (Fig. 4D). Sexually antagonistic polymorphisms in this region that were undetected in Y deletion experiments could have favored recombination suppression. However, alternatives are possible. It was recently proposed (*5*, *6*) that successive "lucky" inversions (or other changes) might become fixed among Y chromosomes by chance, extending the nonrecombining region without being favored through involvement of SA polymorphisms. In one model, re-evolution of recombination is prevented by evolution of low expression of Y-linked alleles, accompanied by higher expression of their X counterparts, a form of dosage compensation (*5*). We tested this by quantifying gene expression in young leaves of male and female *S. latifolia*. For genes in both stratum 0 and the probably still degenerating stratum 1, mean male values (normalized to equalize autosomal values in both sexes) are above half those in females (fig. S24 and table S8), confirming the previously reported partial compensation (*16*–*18*). However, in the younger, much less degenerated stratum 2, expression is similar in both sexes (fig. S24), whereas the Lenormand and Roze (*5*) model requires early repression of Y-linked alleles and up-regulation of their X alleles. The expression estimates also do not reflect DNA methylation patterns (fig. S25), as proposed previously (*50*).

A model for evolution of the *Silene* sex chromosomes

Figure 5 summarizes a model for the evolution of the *Silene* Y and X chromosomes based on our results supporting suppressed recombination between factors in X chromosome regions that formerly recombined. Under the two-mutation evolutionary scenario (*20*), the establishment of the (as yet unidentified) SPF mutation creating females was probably followed by the GSF (*SlCLV3*) mutation in a closely linked genome region. Selection favored suppressed XY recombination, creating stratum 0. This was possibly followed by further selection due to the Y-linked *SlBAM1* gene that we found to control a major sexual dimorphism in the species, strongly suggesting that its alleles are sexually antagonistic. Once recombination became rare, TE insertions and rearrangements accumulated in the MSY region, including Y-specific duplications (Fig. 3A and fig. S12A), further hindering recombination within stratum 0 and perhaps also with the pericentromeric region, enlarging the Y-linked region.

It is unknown how or why stratum 1 evolved. Fusions or Y duplications could have expanded the rarely recombining pericentromeric region by shifting crossovers toward the PAR, creating stratum 1. Y deletion maps suggest a pericentric inversion, which could have linked the initial stratum 0 MSY with segregating SA polymorphisms in the pericentromeric region or nearer the current PAR on the Y*q* arm. Our genome sequences thus help to explain the evolution of a giant Y chromoson and why the X chromosome is also large. The fewer X than Y structural rearrangements suggest that its large pericentromeric region does not completely lack recombination but occasionally recombines. TE insertions, including recent female-specific proliferation of some active retrotransposon types (*51*), can nevertheless enlarge this rarely recombining region, and our results show that the *S. latifolia* and *S. dioica* X chromosome pericentromeric regions are independently expanding through TE activities. However, rare recombination will prevent gene loss, and degeneration therefore mainly affects the Y chromosome. The Y chromosome is still actively rearranging, because we detected Y structural differences. It is also still degenerating, although stable heterochromatic epimarks, including DNA methylation, are present throughout the MSY. Many X-linked genes are already hemizygous in males, and dosage compensation has started to evolve in strata 0 and 1, but Y degeneration and X-linked allele up-regulation do not account for the youngest stratum, stratum 2.

REFERENCES AND NOTES

1. R. Ming, A. Bendahmane, S. S. Renner, *Annu. Rev. Plant Biol.* **62**, 485–514 (2011).
2. B. Charlesworth, *Proc. Natl. Acad. Sci. U.S.A.* **75**, 5618–5622 (1978).
3. D. Charlesworth, *Philos. Trans. R. Soc. Lond. B Biol. Sci.* **372**, 20160456 (2017).
4. D. Charlesworth, *New Phytol.* **224**, 1095–1107 (2019).
5. T. Lenormand, D. Roze, *Science* **375**, 663–666 (2022).
6. P. Jay, E. Tezenas, A. Véber, T. Giraud, *PLOS Biol.* **20**, e3001698 (2022).
7. T. Akagi *et al*., *Nat. Plants* **9**, 393–402 (2023).
8. K. B. Blackburn, *Nature* **112**, 687–688 (1923).
9. D. A. Filatov, F. Monéger, I. Negrutiu, D. Charlesworth, *Nature* **404**, 388–390 (2000).
10. R. Bergero, S. Qiu, A. Forrest, H. Borthwick, D. Charlesworth, *Genetics* **194**, 673–686 (2013).
11. B. T. Lahn, D. C. Page, *Science* **286**, 964–967 (1999).
12. M. A. Wilson Sayres, K. D. Makova, *Mol. Biol. Evol.* **30**, 781–787 (2013).
13. M. V. Chibalina, D. A. Filatov, *Curr. Biol.* **21**, 1475–1479 (2011).
14. R. Bergero, D. Charlesworth, *Curr. Biol.* **21**, 1470–1474 (2011).
15. A. S. Papadopulos, M. Chester, K. Ridout, D. A. Filatov, *Proc. Natl. Acad. Sci. U.S.A.* **112**, 13021–13026 (2015).
16. A. Muyle *et al*., *PLOS Biol.* **10**, e1001308 (2012).
17. A. Muyle *et al*., *Nat. Plants* **4**, 677–680 (2018).
18. M. Krasovec, Y. Kazama, K. Ishii, T. Abe, D. A. Filatov, *Curr. Biol.* **29**, 2214–2221.e4 (2019).
19. M. Westergaard, *Naturwissenschaften* **40**, 253–260 (1953).
20. B. Charlesworth, D. Charlesworth, *Am. Nat.* **112**, 975–997 (1978).
21. A. Harkess *et al*., *Nat. Commun.* **8**, 1279 (2017).
22. T. Akagi *et al*., *Plant Cell* **30**, 780–795 (2018).
23. T. Akagi *et al*., *Nat. Plants* **5**, 801–809 (2019).
24. M. Massonnet *et al*., *Nat. Commun.* **11**, 2902 (2020).
25. B. Charlesworth, P. Sniegowski, W. Stephan, *Nature* **371**, 215–220 (1994).
26. T. V. Kent, J. Uzunović, S. I. Wright, *Philos. Trans. R. Soc. Lond. B Biol. Sci.* **372**, 20160458 (2017).
27. F. A. Simão, R. M. Waterhouse, P. Ioannidis, E. V. Kriventseva, E. M. Zdobnov, *Bioinformatics* **31**, 3210–3212 (2015).
28. Tomato Genome Consortium, *Nature* **485**, 635–641 (2012).
29. Y. Van de Peer, E. Mizrachi, K. Marchal, *Nat. Rev. Genet.* **18**, 411–424 (2017).
30. Y. Kazama *et al*., *Sci. Rep.* **6**, 18917 (2016).
31. I. S. Donnison, J. Siroky, B. Vyskot, H. Saedler, S. R. Grant, *Genetics* **144**, 1893–1901 (1996).
32. R. Bergero, D. Charlesworth, D. A. Filatov, R. C. Moore, *Genetics* **178**, 2045–2053 (2008).
33. Y. Kazama *et al*., *Mol. Biol. Evol.* **39**, msac195 (2022).
34. N. Fujita *et al*., *Int. J. Mol. Sci.* **20**, 1031 (2019).
35. I. Kurek *et al*., *Plant Mol. Biol.* **48**, 369–381 (2002).
36. J. Liu, R. Ghelli, M. Cardarelli, M. Geisler, *J. Exp. Bot.* **73**, 4818–4831 (2022).
37. J. H. McDonald, M. Kreitman, *Nature* **351**, 652–654 (1991).
38. J. B. Walsh, *Genetics* **139**, 421–428 (1995).
39. J. Yue *et al*., *Curr. Biol.* **33**, 2504–2514.e3 (2023).
40. R. Bergero, A. Forrest, E. Kamau, D. Charlesworth, *Genetics* **175**, 1945–1954 (2007).
41. D. A. Filatov, *J. Evol. Biol.* **35**, 1696–1708 (2022).
42. A. N. Pettitt, *Appl. Stat.* **28**, 126–135 (1979).
43. G. A. Marais *et al*., *Curr. Biol.* **18**, 545–549 (2008).
44. J. L. Campos, S. Qiu, S. Guirao-Rico, R. Bergero, D. Charlesworth, *Heredity* **118**, 395–403 (2017).
45. S. Qiu *et al*., *Mol. Ecol.* **25**, 414–430 (2016).
46. B. J. DeYoung *et al*., *Plant J.* **45**, 1–16 (2006).
47. C. L. H. Hord, C. Chen, B. J. Deyoung, S. E. Clark, H. Ma, *Plant Cell* **18**, 1667–1680 (2006).
48. Z. L. Nimchuk, Y. Zhou, P. T. Tarr, B. A. Peterson, E. M. Meyerowitz, *Development* **142**, 1043–1049 (2015).
49. L. F. Delph, C. R. Herlihy, *Evolution* **66**, 1154–1166 (2012).
50. V. Bačovský, A. Houben, K. Kumke, R. Hobza, *Planta* **250**, 487–494 (2019).
51. J. Puterova *et al*., *BMC Genomics* **19**, 153 (2018).

ACKNOWLEDGMENTS

We thank I. M. Henry and L. Comai (Department of Plant Biology and Genome Center, University of California, Davis) for discussion and comments on this study. **Funding:** This work was supported by PRESTO from the Japan Science and Technology Agency (JST grant JPMJPR20D1) and the Japan Society for the Promotion of Science Grants-in-Aid for Transformative Research Areas (A) (grants 22H05172 and 22H05173 to T.A. and grant 22H05181 to K.S.; Grant-in-Aid for JSPS Fellow JSPS grant JP23KJ1615 to N.F., JSPS KAKENHI grant JP23K05226 to N.F.; grant 23H04747 to Y.I.; and grant 22H02598 to T.I.). **Author contributions:** Conceptualization: T.A., D.C.; Funding acquisition: T.A., N.F., K.S., Y.I.; Investigation: T.A., N.F., K.S., K.N., K.M., A.H., E.K., K.K., R.K., K.N., K.U.; Methodology: T.A., N.F., K.S., H.T., Y.I., A.T., T.I., K.U., D.C.; Project administration: T.A., D.C.; Supervision: T.A., K.U., D.C.; Visualization: T.A., N.F., H.T., K.N., K.M., A.H., K.U.; Writing – original draft: T.A., D.C.; Writing – review & editing: T.A., N.F., K.U., D.C. **Competing interests:** The authors declare no competing interests. **Data and materials availability:** All of the genome sequences and the annotated data were deposited to Plant GARDEN (https://plantgarden.jp/en/index) (*S. latifolia*: https://plantgarden.jp/en/list/t37657, *S. vulgaris*: https://plantgarden.jp/en/list/t42043, *S. dioica*: https://plantgarden.jp/en/list/t39879). The raw sequencing data have been deposited in the DDBJ database: Sequence Read Archives database (BioProject ID PRJDB16402, Run ID DRR496111-DRR496477 and DRR540087-DRR540088 for genome sequencing, Hi-C sequencing, DNA methylome and ChIP-seq data, and BioProject ID PRJDB16382, Run ID SAMD00635100-00635106 and SAMD00636369-00636376 for RNA-seq data in flower buds.

SUPPLEMENTARY MATERIALS

science.org/doi/10.1126/science.adk9074
Materials and Methods
Figs. S1 to S25
Tables S1 to S11
References (*52*–*98*)
MDAR Reproducibility Checklist

Submitted 18 September 2023; resubmitted 8 April 2024
Accepted 13 August 2024
10.1126/science.adk9074

TOPOLOGICAL OPTICS

Four-dimensional conserved topological charge vectors in plasmonic quasicrystals

Shai Tsesses[1,2], Pascal Dreher[3], David Janoschka[3], Alexander Neuhaus[3], Kobi Cohen[1], Tim C. Meiler[4,5], Tomer Bucher[1], Shay Sapir[1,6], Bettina Frank[4], Timothy J. Davis[3,4,7], Frank Meyer zu Heringdorf[3], Harald Giessen[4], Guy Bartal[1]*

According to Noether's theorem, symmetries in a physical system are intertwined with conserved quantities. These symmetries often determine the system topology, which is made ever more complex with increased dimensionality. Quasicrystals have neither translational nor global rotational symmetry, yet they intrinsically inhabit a higher-dimensional space in which symmetry resurfaces. Here, we discovered topological charge vectors in four dimensions (4D) that govern the real-space topology of 2D quasicrystals and reveal their inherent conservation laws. We demonstrate control over the topology in pentagonal plasmonic quasilattices, mapped by both phase-resolved and time-domain near-field microscopy, showing that their temporal evolution continuously tunes the 2D projections of their distinct 4D topologies. Our work provides a route to experimentally probe the thermodynamic properties of quasicrystals and topological physics in 4D and above.

Topology is the study of geometrical objects and their conserved properties under continuous deformation such as stretching, twisting, and bending. The values of conserved properties, often referred to as topological charges, can have a profound influence on the behavior of the system, from the formation of cosmic objects (*1*) to the dislocations of simple wave interference (*2*). Topological analysis has been especially impactful in the fields of condensed matter physics and optics, revealing robust transport phenomena (*3*, *4*) and exotic phase transitions (*5*, *6*) because of the existence of a topological charge in energy-momentum space known as the Chern number (*7*). Conversely, real-space topological charges can be used to control the way that light interacts with matter (*8*, *9*) or may represent digital information for storage, processing, and transfer (*10*, *11*).

Dimensionality greatly influences the topology and subsequent topological charges of a physical system (*12*–*14*), producing a larger variety of phenomena as it increases (*15*–*17*). The search for more complex topologies in a given physical system led to methods for artificially increasing system dimensionality (*18*–*20*), creating the field of physics in synthetic dimensions (*21*). By contrast, quasicrystalline systems (*22*, *23*) can naturally have higher-dimensional topologies (*24*), resulting in the generation of topological charge vectors, as was previously observed in the band structure of atomic (*25*) and optical (*26*) systems.

Because quasicrystals have additional degrees of freedom compared with ordinary periodic structures, they behave as regular crystals but in a higher-dimensional plane (*27*–*29*). Thus, the topology in this higher-dimensional plane should affect the real-space structure of quasicrystals, making them an ideal platform with which to examine topological physics in higher dimensions. However, because topology is closely linked with the symmetry of the system (*30*), and quasicrystals lack translational or global rotational symmetry in the physical plane, the challenge of identifying and observing their topological charges in real space remains.

High-dimensional dislocations determine the topology of quasicrystals

We start by reviewing the relationship between topological charges and dislocations. The topology of the parameter space associated with a physical system can be determined by mapping the changes in the physical parameters along a closed loop in real space (*31*). For example, a wave exhibiting orbital angular momentum forms a vortex with a phase singularity at its center, which represents a defect also known as a dislocation in the parameter space (i.e., the phase of the wave). By mapping the change in phase along a loop enclosing the singularity, completing the loop accumulates a total phase that is an integer multiple q of 2π. The integer q characterizes the topological charge of the vortex (*32*), denoting the number of times that the phase completes a unit circle along the loop.

The same dislocation can also be described from another perspective: To return to the starting phase, one needs to subtract $b = 2\pi q$, which can be thought of as a one-dimensional (1D) vector. Extending this concept to many dimensions results in dislocation vectors that in turn can give rise to topological charge vectors. This point of view is common in crystallography, where a displacement vector in the crystal, the Burgers vector, defines the existing dislocation and the underlying topology of the crystal (*31*). There is some similarity between the dislocations in a crystal and those in a wave vortex, because summing over the atomic lattice vectors while traversing in a closed loop about the crystal dislocation gives a nontrivial (nonzero) outcome. We will show how dislocations hold the key to understanding the topological charges of quasicrystals, which naturally exhibit higher-dimensional behavior.

Quasicrystals can be represented as a superposition of waves with different phases (*27*–*29*), from which one can deduce the form of the possible dislocations. This work focuses on pentagonal crystals (*33*–*35*), the simplest 2D quasicrystals created by five waves interfering in a plane (Fig. 1C) and represented by the function

$$f(\vec{r}) = \mathrm{Re}\sum_{m=1}^{5}|f_m|e^{i\phi_m}e^{i\vec{k}_m\cdot\vec{r}} \tag{1}$$

where $|f_m|$, ϕ_m, and $\vec{k}_m$ are the amplitude, relative phase, and wave vector of every wave in the interference pattern, respectively, and $\vec{r}$ is an in-plane position vector. This description is valid for any pentagonal system provided that one considers only low-order excitations, wherein the sum of phases $\Gamma = \sum_{m=1}^{5}\phi_m$ is constant up to integers of 2π and $\sum_{m=1}^{5}\vec{k}_m = 0$ (*28*, *36*) (i.e., the wave vectors span a regular pentagon).

Consequently, the form of the dislocation vector associated with defects in the quasicrystal, $\vec{b} = ([b_1, b_2], [b_3, b_4]) = (\vec{b}_{phonon}, \vec{b}_{phason})$, also known as the Burgers vector (*37*), can be constructed solely from the four remaining independent relative phases ϕ_n (*28*, *29*, *36*) as follows:

$$\phi_n = \vec{k}_n\cdot\vec{b}_{phonon} + \frac{\sin(2\pi/5)}{\sin(4\pi/5)}\vec{k}_{\mathrm{mod}(3n,5)}\cdot\vec{b}_{phason} + \frac{\Gamma}{5} \tag{2}$$

where n is an integer with the possible values $n = \{1,\ldots,4\}$. The system of equations in Eq. 2 implies that $\vec{b}_{phonon}$ represents displacements in the physical 2D space known as phonons, and $\vec{b}_{phason}$ represents displacements in two additional degrees of freedom called phasons.

---

[1]Andrew and Erna Viterbi Department of Electrical and Computer Engineering, Technion – Israel Institute of Technology, Haifa, Israel. [2]Department of Physics, MIT-Harvard Center for Ultracold Atoms and Research Laboratory of Electronics, Massachusetts Institute of Technology, Cambridge, MA, USA. [3]Faculty of Physics and Center for Nanointegration, Duisburg-Essen (CENIDE), University of Duisburg-Essen, Duisburg, Germany. [4]4th Physics Institute, Research Center SCoPE, and Integrated Quantum Science and Technology Center, University of Stuttgart, Stuttgart, Germany. [5]Centre for Disruptive Photonic Technologies and School of Physical and Mathematical Sciences, Nanyang Technological University, Singapore, Singapore. [6]Faculty of Mathematics and Computer Science, Weitzmann Institute of Science, Rehovot, Israel. [7]School of Physics, University of Melbourne, Parkville, Victoria, Australia.
***Corresponding author. Email: guy@ee.technion.ac.il**

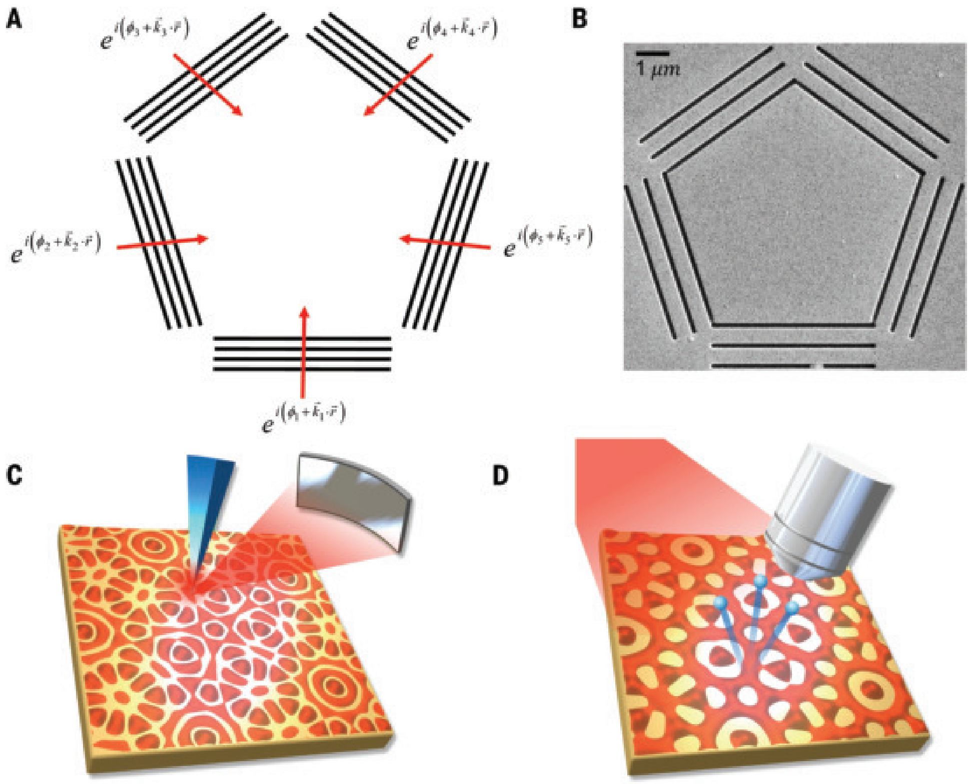

Fig. 1. Studying dislocations in quasicrystals and their resultant topological charges: Concept and implementation. (**A**) Close to their ground state, quasicrystals in pentagonal symmetry can be described by the interference of five waves, oriented at angles that are integer multiples of 2π/5. (**B**) Implementation of the concept in (A) using a pentagonal coupling slit carved in a gold layer, launching electromagnetic surface waves (SPPs) from each of its edges. (**C** and **D**) The amplitude, phase, and vector properties of the interference pattern are measured in two complementary ways: scattering scanning near-field optical microscopy (s-SNOM), which is time-averaged (C), and two-photon photoemission electron microscopy (2PPE-PEEM), which is time dependent (D). In s-SNOM, light is collected by scattering the near field with a sharp metallic tip, and in 2PPE-PEEM, electrons are emitted from the sample and used to image the near field through a short laser pulse arriving after the initial excitation. [See (*36*) for further explanations about the measurement methods.]

This representation is consistent with a periodic 4D space with elementary reciprocal vectors $\vec{g}_n = \left(\left[\vec{k}_n\right], \left[\frac{\sin(2\pi/5)}{\sin(4\pi/5)}\vec{k}_{\mathrm{mod}(3n,5)}\right]\right)$ defining the higher-dimensional space (*28*, *36*). Equation 2 illustrates the inherent higher dimensionality of quasicrystals and identifies the two ways to influence their topology: (i) by individually engineering the relative phases of waves comprising the crystal or (ii) by tuning their sum.

Identifying topological charge vectors in quasicrystals

From Eq. 2, it is clear that every configuration of relative phases φ_n will result in some dislocation vector in the 4D space, affecting the 2D projection of the quasicrystal (*38*, *39*). For the specific choice $\phi_n = \frac{2\pi n Q}{5}, Q \in \{0, \pm 1, \pm 2\}$ we found, unexpectedly, that the resulting vectors $\vec{b}$ represent multidimensional topological charges, or topological charge vectors. Specifically, they adhere to a vector topological charge conservation law similar to that of other scalar systems (*7*, *40*), which takes the form

$$\vec{b}_{Q_1} - \vec{b}_{Q_2} = \vec{b}_{Q_1-Q_2} \tag{3}$$

where $\vec{b}_{Q_1}, \vec{b}_{Q_2}, \vec{b}_{Q_2-Q_1}$ are different topological charge vectors, found by assuming $\phi_n = \frac{2\pi n Q_1}{5}$, $\frac{2\pi n Q_2}{5}$, and $\frac{2\pi n(Q_1-Q_2-5\lfloor(Q_1-Q_2)/3\rfloor)}{5}$, respectively, in Eq. 2. Equation 3 is strictly fulfilled up to an elementary lattice vector in the emergent periodic 4D space and has a cyclic dependence because of the finite number of solutions (*40*). See (*36*) for the full list of vectors fulfilling Eq. 3 and verification that it indeed persists. The vector $\vec{b}_{Q=0}$ is the trivial vector because there are only four nontrivial topological charge vectors according to Eq. 2, yet it is added for completeness of the point group symmetry of the system.

A similar requirement on the relative phases in a periodic or circular 2D system results in the existence of scalar topological charges, which are identified as phase singularities in the time-averaged wave interference pattern (*40*). These phase singularities have little meaning in the real-valued function of the crystal (Eq. 1), which is often used to define a charge distribution (*27*–*29*), but are immensely important in the analysis of waves (*31*). As we show experimentally below, such phase singularities are incapable of identifying the topology of the system for a quasicrystal, thus requiring the existence of topological charge vectors in the higher-dimensional space.

Although the topological charge vectors are 4D, they have only two nonzero components: one related to $\vec{b}_{phonon}$ and the physical 2D space topology and another related to $\vec{b}_{phason}$ and the topology in the two additional dimensions of the quasicrystal. This property, which stems from the two incommensurate length scales in our system (*28*, *29*), greatly resembles the extension of the Chern number to a two-component vector in the 4D quantum Hall effect with quasicrystals (*25*, *26*).

4D topology of pentagonal plasmonic quasilattices

We explore the 4D topology described above by creating a pentagonal quasilattice of surface plasmon polaritons (SPPs) (*41*), electromagnetic surface waves existing at the interface between metallic and dielectric materials. For this, we used gold surfaces with pentagonal coupling slits nanofabricated through focused ion beam milling (Fig. 1D). Such a system exhibits the spin-orbit interaction of light (*40*), and similar designs were recently used to investigate a variety of nanophotonic topological charges (*42*, *43*). The spin-orbit interaction of light determines the topological charge vector in the plasmonic quasilattice through a conservation law similar to Eq. 3 (*36*), where Q_1,Q_2 and $Q_2 - Q_1$ are replaced by physical constants related to the angular momentum of light, as in systems with the same SPP excitation mechanism (*40*, *44*).

To fully characterize the topology, we used two complementary techniques: phase-resolved scattering scanning near-field optical microscopy (SNOM; Fig. 1E) (*40*, *42*, *45*) and time-resolved two-photon photoemission electron microscopy (2PPE-PEEM; Fig. 1F) (*43*, *46*). 2PPE-PEEM is capable of recording the deep subcycle temporal evolution of the SPP quasilattice, which has a cycle time of a few femtoseconds,

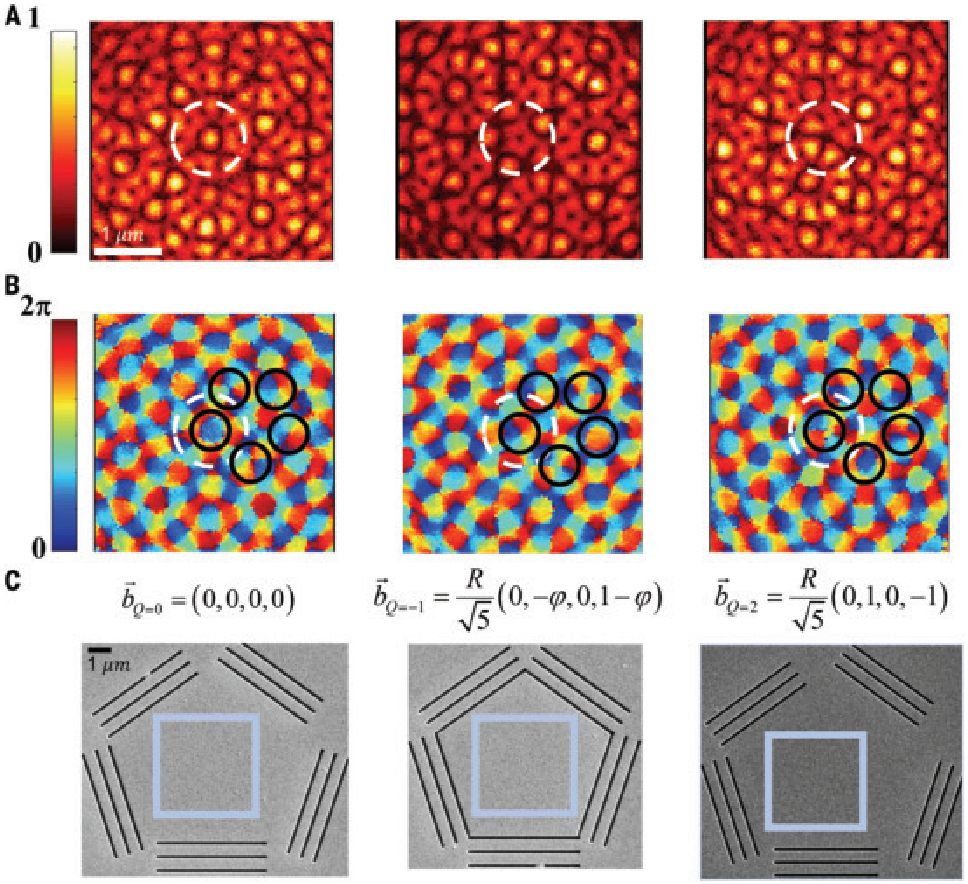

Fig. 2. Phase-resolved near-field microscopy of pentagonal plasmonic quasilattices. We showed that different pentagonal plasmonic quasilattices are not topologically distinct in 2D by examining their phase singularities. (**A** to **C**) Amplitude (A) and phase (B) of the out-of-plane field E_z of three different interference patterns of SPPs generated by impinging three different coupling slits with light carrying the same circular polarization (C). The positions of the edges making up the coupling slits were shifted to produce the required relative phases $\phi_n = \frac{2\pi n Q}{5}$ in Eq. 2, which generate the distinct topological charge vectors $\vec{b}_Q$ written above each panel in (C) [R is a characteristic length in the 4D space of the quasilattices, $\varphi = (1+\sqrt{5})/2$ is the golden ratio] (*40*). In each pattern, the central interference area, marked by a dashed circle in (A) and (B), shows the expected phase singularity from the relative phases, which should characterize the entire mode. By contrast, the solid circles in (B) show that all five possible phase singularities in 5-fold symmetry ($-2 \le q \le 2$) appear in each of the modes, albeit at different locations. One phase singularity is insufficient for characterizing the modes in their 2D representation, making them topologically indistinguishable in 2D. The imaged area is marked by a light square in each panel of (C), the location of which varies in accordance with the shifted position of the SPP interference pattern.

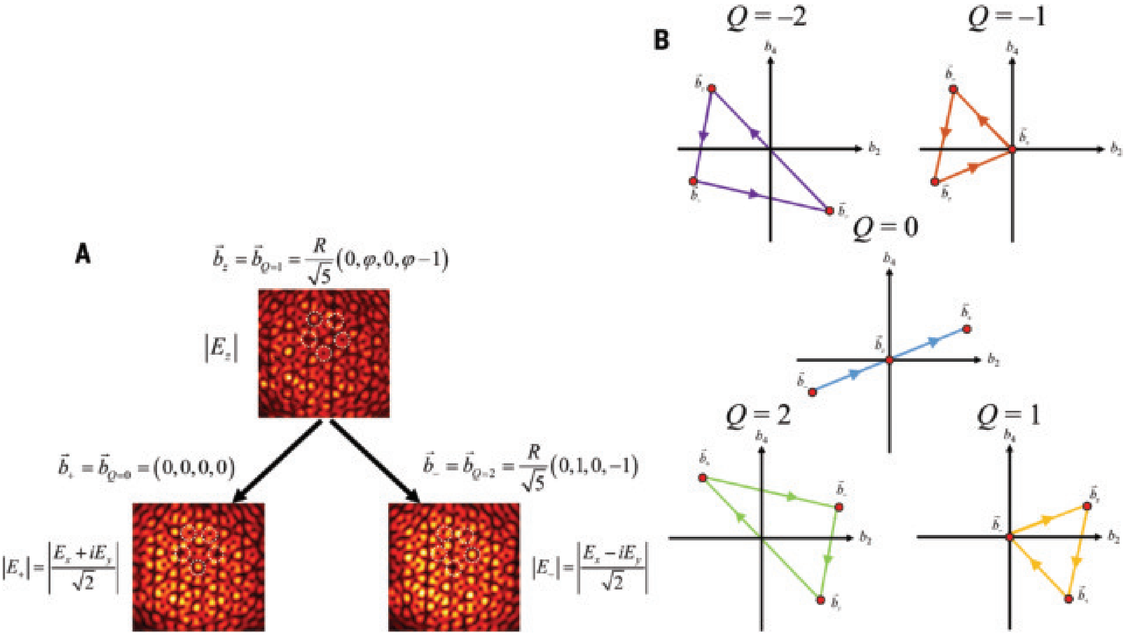

Fig. 3. Topological charge conservation in pentagonal plasmonic quasilattices. (**A**) Measured amplitude of the out-of-plane electric field E_z, for a coupling slit with shifted edges such that $\phi_n = \frac{2\pi n}{N}$ ($Q = 1$). Because both amplitude and phase are extracted in the measurement, it is possible to reconstruct the two in-plane field components in the circular basis (E_+ and E_-) through Maxwell's equations (*42*). Whereas the out-of-plane field has a topological charge vector $\vec{b}_z$, the two in-plane field components have different topological charge vectors, $\vec{b}_+$ and $\vec{b}_-$, respectively. In the physical 2D plane, this manifests as a constant difference between the winding of every phase singularity for each field component (examples are marked in every panel by a dotted circle). (**B**) By choosing a different value of $\varphi_n = \frac{2\pi n Q}{N}$ through incident polarization or coupling slit design, a different set of topological charge vectors is generated. Conveniently, all topological charge vectors can be represented in the same plane, because for $\vec{b} = ([b_1, b_2], [b_3, b_4])$, only their b_2 and b_4 values are nonzero. Thus, the topological charge vectors of each mode form a triangle with a certain area. By performing a line integral through Stokes' law, keeping the direction of integration constant, and normalizing by the area of the projected 4D unit cell, the area of each triangle becomes exactly Q. Thus, topological charge conservation for vector pentagonal quasilattices is identical to an area law conservation.

whereas SNOM provides time-averaged mapping of its amplitude and phase. Both methods have a sufficient deep-subwavelength spatial resolution.

The symmetry of the measured SPP field in both methods is different (as illustrated in Fig. 1, E and F): SNOM captures the time-averaged, complex field, exhibiting strictly pentagonal symmetry, whereas 2PPE-PEEM extracts the time-dependent, real part of the field, resulting in decagonal symmetry. Furthermore, SNOM captures the out-of-plane field component E_z, whereas in a pump-probe experiment involving SPPs, 2PPE-PEEM predominantly measures the in-plane field components E_x and E_y (*47*). Both methods, nevertheless, are capable of extracting the full vector field independently (*42*, *43*). For more information about our various sample preparation and measurement protocols, see (*36*).

The time-averaged out-of-plane field measurements of pentagonal SPP quasilattices (Fig. 2, A and B) revealed that each lattice contains all possible phase singularities (i.e., $q = -2,-1,0,1,2$), albeit at different locations. Furthermore, as suggested in (*29*) and further investigated in (*36*), the lattices are locally isomorphic, meaning that a field pattern in one lattice can always be found in the others. Thus, the lattices appear to be topologically indistinguishable in 2D despite being distinguishable in 4D and having different topological charge vectors (displayed above each image in Fig. 2C).

In contrast to the purely scalar fields considered thus far, SPPs are composed of a 3D electric field (*42*, *43*). Thus, each of the three field components is associated with a different topological charge vector determined by a conservation law articulated in (*36*). This conservation law is a direct result of Maxwell's equations, and relates the topology of the in-plane rotating fields (i.e., left-circular or right-circular) to the topology of the out-of-plane component. Therefore, 2D phase singularities around the same point appear with different windings in different field components, as demonstrated through time-averaged measurements and in accordance with the relation between their respective values of Q (Fig. 3A). Combined with topological indistinguishability in 2D, this unique vectorial trait changes the field orientation at any given position with time, effectively causing vector field features to disappear at one location and reappear in another (as demonstrated in movies S1 and S2).

Indistinct as it may be in 2D, the behavior of SPP quasilattices can be clearly understood in the 4D higher-dimensional space of quasicrystals, where the topological charge vectors of all field components form a triangle (Fig. 3B). A line integral surrounding the area of the triangle (i.e., using Stokes' law) gives exactly the value Q (*36*). Therefore, the vector nature of SPPs transforms the topological charge conservation in Eq. 3 into an area conservation law, holding true for any divergence-free vector field fulfilling similar relations to Maxwell's equations (*48*, *49*).

Controlling the 2D projection of plasmonic quasilattices with temporal phase

After exploring how the relative phases of the waves affect the topology of a quasicrystsal, we then investigated the influence of their sum. In doing so, we return to Eq. 1, noticing that it has the same functional form as the time-dependent solutions of the wave equation. Thus, one can write the relative phases ϕ_m of any monochromatic system satisfying the wave equation, e.g., electromagnetic, acoustic, etc., in the form $\phi_m = \alpha_m - \omega t$. Here, ω is the temporal frequency of the waves, t is the time coordinate, and α_m is the set of parameters tuning

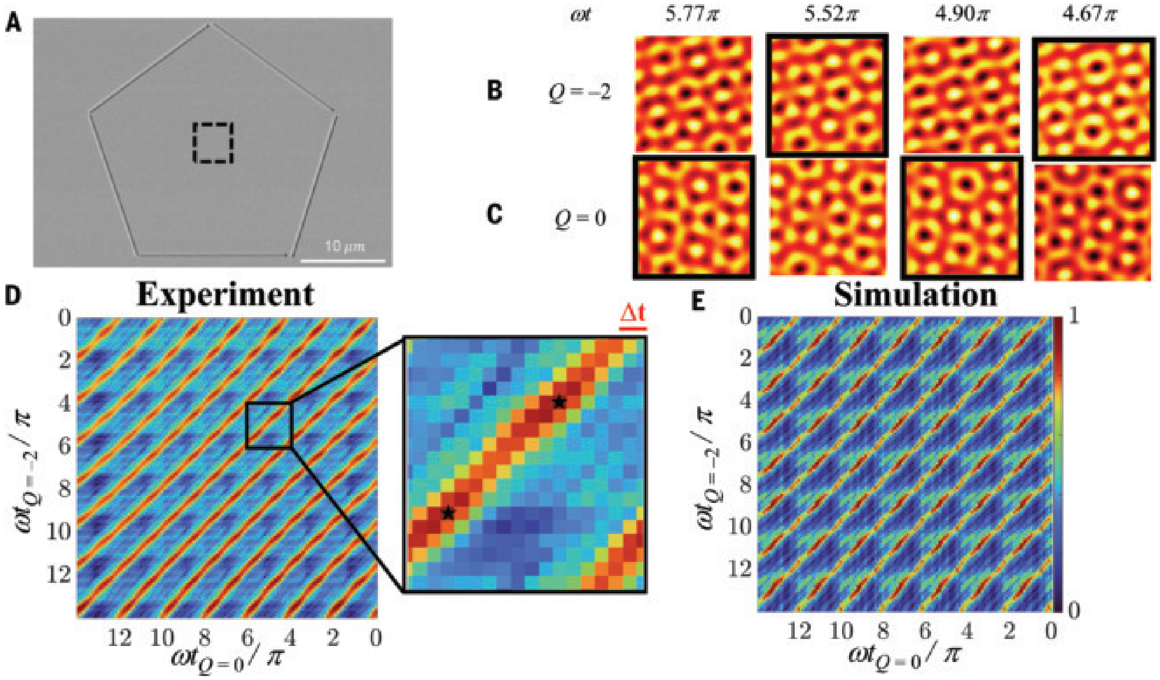

Fig. 4. Controlling the 2D projection of topologically distinct quasilattices with the temporal phase. We verified that two plasmonic quasilattices are topologically distinct by measuring their temporal evolution, which exhibits similar patterns at different times. To this end, we examined two lattices generated by the same coupling slit. (**A**) SEM micrograph of the coupling slit used for the time-resolved measurement supporting two plasmonic quasilattices with relative phases $\phi_n = \frac{2\pi n Q}{5}$, $Q = 0,-2$, determined by changing the handedness of incident illumination. (**B**) Real out-of-plane electric field of a quasilattice with $Q = -2$, extracted from a time-resolved PEEM experiment (*51*). The different accumulated temporal phase appears above every panel in (B). The dashed square in (A) marks the field area shown. (**C**) Same as (B) but with $Q = 0$. Similar field distributions are marked by bold frames and appear at different times for different quasilattices, as predicted. (**D** and **E**) Measured (D) and simulated (E) correlation between the two topologically distinct quasilattices as a function of their respective accumulated temporal phases. The vertical and horizontal axes represent the accumulated temporal phase of the field presented in (B) and (C), respectively. Inset in (D) shows a magnified region of the measurement times presented in (B) and (C), where the stars mark the coincidents of similar distributions indicated by the bold frames. The temporal distance between the similar distribution remains the same up to the temporal resolution of the measurement (manifesting in a phase error of ~0.125π) and is marked by Δ*t* in the inset of (D). Color bar for both (D) and (E) is shown in the inset of (E) and represents the value of correlation between images of the two lattices at various times. The experimental correlation map in (D) greatly depends on the available field of view and the temporal resolution of the measurement. However, (E) shows that both effects can be accounted for by the simulation. Correlation without any such restrictions is given in fig. S2. The dynamics of the full vector field in (B) and (C) is given in movies S1 and S2, respectively.

the independent relative phases. For the choice of $\alpha_m = \frac{2\pi m Q}{5}$, Eq. 2 remains the same, but the sum of all relative phases Γ becomes exactly $-5\omega t$ (*36*). In this case, the topological charge vector does not change with Γ, which relates directly to the global time-dependent phase accumulation of the interference pattern. Instead, a constant phase factor is added to the interference, changing the 2D projection of the quasicrystal in time. Thus, whereas the time-averaged measurements of SPP quasilattices could not distinguish between lattices with a different topology, a time-dependent measurement can obtain the necessary information to do so.

A corresponding observation of this principle is presented in Fig. 4. We measured two topologically distinct SPP lattices at different times (examples are shown in Fig. 4, B and C) and correlated the time-resolved measurements as a function of the time difference (Fig. 4, D and E). We found that topologically distinct quasicrystals exhibited a similar real-space shape at different times [see (*36*) and fig. S2], and this time difference remained constant throughout their temporal evolution [see explanation in (*36*)]. Therefore, measuring the quasilattice at certain times allows one to select specific 2D projections and reveals the relationship between topological charge vectors of different quasilattices. Finally, understanding the topology of a quasicrystal made of interfering waves can only be complete once it is examined both in a time-averaged and a time-resolved manner.

Outlook

Our results prove the existence of topological charge vectors in the higher-dimensional space of 2D quasicrystals. The quasicrystal field distribution is a projection from higher-dimensional space and contains information about the higher-dimensional topology, which we monitored and controlled in a model experimental system: the interference of electromagnetic surface waves on gold. In principle, many of our results could be reproduced in other wave systems. Therefore, we conclude that quasicrystalline wave interference patterns are a simple and straightforward path to examine the topology of physical systems in higher dimensions.

Because of the pentagonal symmetry that we investigated, our topological charge vectors manifest in 4D. However, a higher prime-number symmetry provides more degrees of freedom and more nondegenerate topological charge vectors, scaling up the dimension of the examined topology. Additionally, it is possible that 3D topological defects such as skyrmions (*42*, *43*) exist in our 2D quasicrystalline wave interference. Although skyrmion-like features appear (see movies S1 and S2), the boundary of a skyrmion is ill defined in our system, and thus they do not exist. Nevertheless, 4D spatiotemporal skyrmions were recently found to exist in time-modulated 3D quasicrystalline wave interference (*50*).

Figures 2 and 3 illustrate that the information contained within a quasicrystalline interference pattern is not local; that is, the correct characterization of its topological charge requires measuring the field in several locations. This property could benefit security protocols for the transport of both classical and quantum information (*51*) while making the information more resilient to noise and other interferences (*52*). Conversely, topological protection of the information could be achieved by producing quasicrystalline interference inside a nonlinear medium, creating nonlinear quasilattices (*38*, *39*).

Although the model that we presented in Eqs. 1 to 3 is not system specific, it is heavily based on the model of interfering charge-density waves that has been used previously to explain the mechanical and thermodynamic properties of quasicrystalline materials (*27*–*29*). The correspondence between these models (*36*) suggests that the time-dependent phase accumulation of wave interference can be directly related to the variation of ground-state free energy in a given quasicrystalline material. Thus, our results shown in Fig. 4 provide a simulator exemplifying the way that free energy compensates for the presence of dislocations in a material. Further experiments can use this trait to examine the thermodynamics of quasicrystals under an adiabatic change in free energy, which is a very difficult task to perform by other means.

REFERENCES AND NOTES

1. T. W. B. Kibble, *J. Phys. Math. Gen.* **9**, 1387–1398 (1976).
2. J. F. Nye, M. V. Berry, *Proc. R. Soc. A Math. Phys. Eng. Sci.* **336**, 165–190 (1974).
3. M. König *et al.*, *Science* **318**, 766–770 (2007).
4. Z. Wang, Y. Chong, J. D. Joannopoulos, M. Soljacić, *Nature* **461**, 772–775 (2009).
5. J. M. Kosterlitz, D. J. Thouless, *J. Phys. C Solid State Phys.* **6**, 1181–1203 (1973).
6. H. N. S. Krishnamoorthy, Z. Jacob, E. Narimanov, I. Kretzschmar, V. M. Menon, *Science* **336**, 205–209 (2012).
7. D. J. Thouless, M. Kohmoto, M. P. Nightingale, M. Den Nijs, *Phys. Rev. Lett.* **49**, 405–408 (1982).
8. N. B. Simpson, K. Dholakia, L. Allen, M. J. Padgett, *Opt. Lett.* **22**, 52–54 (1997).
9. C. Wu *et al.*, *Sci. Adv.* **8**, eabk3075 (2022).
10. C. Nayak, S. H. Simon, A. Stern, M. Freedman, S. Das Sarma, *Rev. Mod. Phys.* **80**, 1083–1159 (2008).
11. G. Gibson *et al.*, *Opt. Express* **12**, 5448–5456 (2004).
12. S.-C. Zhang, J. Hu, *Science* **294**, 823–828 (2001).
13. W. A. Benalcazar, B. A. Bernevig, T. L. Hughes, *Science* **357**, 61–66 (2017).
14. J. B. Tai, I. I. Smalyukh, *Science* **365**, 1449–1453 (2019).
15. T. Bauer *et al.*, *Science* **347**, 964–966 (2015).
16. C. W. Peterson, W. A. Benalcazar, T. L. Hughes, G. Bahl, *Nature* **555**, 346–350 (2018).
17. M. Serra-Garcia *et al.*, *Nature* **555**, 342–345 (2018).
18. O. Boada, A. Celi, J. I. Latorre, M. Lewenstein, *Phys. Rev. Lett.* **108**, 133001 (2012).
19. K. Fang, Z. Yu, S. Fan, *Nat. Photonics* **6**, 782–787 (2012).
20. E. Lustig *et al.*, *Nature* **567**, 356–360 (2019).
21. L. Yuan, Q. Lin, M. Xiao, S. Fan, *Optica* **5**, 1396–1405 (2018).
22. D. Shechtman, I. Blech, D. Gratias, J. W. Cahn, *Phys. Rev. Lett.* **53**, 1951–1953 (1984).
23. D. Levine, P. J. Steinhardt, *Phys. Rev. Lett.* **53**, 2477–2480 (1984).
24. Y. E. Kraus, Y. Lahini, Z. Ringel, M. Verbin, O. Zilberberg, *Phys. Rev. Lett.* **109**, 106402 (2012).
25. M. Lohse, C. Schweizer, H. M. Price, O. Zilberberg, I. Bloch, *Nature* **553**, 55–58 (2018).
26. O. Zilberberg *et al.*, *Nature* **553**, 59–62 (2018).
27. P. Bak, *Phys. Rev. Lett.* **54**, 1517–1519 (1985).
28. D. Levine *et al.*, *Phys. Rev. Lett.* **54**, 1520–1523 (1985).
29. J. E. S. Socolar, T. C. Lubensky, P. J. Steinhardt, *Phys. Rev. B Condens. Matter* **34**, 3345–3360 (1986).
30. C.-K. Chiu, J. C. Y. Teo, A. P. Schnyder, S. Ryu, *Rev. Mod. Phys.* **88**, 035005 (2016).
31. N. D. Mermin, *Rev. Mod. Phys.* **51**, 591–648 (1979).
32. M. R. Dennis, K. O'Holleran, M. J. Padgett, *Prog. Opt.* **53**, 293–363 (2009).
33. F. M. Huang, Y. Chen, F. J. Garcia de Abajo, N. I. Zheludev, *J. Opt. A, Pure Appl. Opt.* **9**, S285–S288 (2007).
34. C. Rockstuhl, F. Lederer, T. Zentgraf, H. Giessen, *Appl. Phys. Lett.* **91**, 151109 (2007).
35. D. Pacifici, H. J. Lezec, L. A. Sweatlock, R. J. Walters, H. A. Atwater, *Opt. Express* **16**, 9222–9238 (2008).
36. See the supplementary materials for additional information.
37. J. M. Burgers, in *Selected Papers of J. M. Burgers* (Springer, 1995), pp. 335–389.
38. B. Freedman *et al.*, *Nature* **440**, 1166–1169 (2006).
39. B. Freedman, R. Lifshitz, J. W. Fleischer, M. Segev, *Nat. Mater.* **6**, 776–781 (2007).
40. S. Tsesses, K. Cohen, E. Ostrovsky, B. Gjonaj, G. Bartal, *Nano Lett.* **19**, 4010–4016 (2019).
41. S. A. Maier, *Plasmonics: Fundamentals and applications* (Springer, 2007).
42. S. Tsesses *et al.*, *Science* **361**, 993–996 (2018).
43. T. J. Davis *et al.*, *Science* **368**, eaba6415 (2020).
44. Y. Gorodetski, A. Niv, V. Kleiner, E. Hasman, *Phys. Rev. Lett.* **101**, 043903 (2008).
45. N. Ocelic, A. Huber, R. Hillenbrand, *Appl. Phys. Lett.* **89**, 101124 (2006).
46. G. Spektor *et al.*, *Science* **355**, 1187–1191 (2017).
47. D. Podbiel *et al.*, *Nano Lett.* **17**, 6569–6574 (2017).
48. H. Ge *et al.*, *Phys. Rev. Lett.* **127**, 144502 (2021).
49. K. Y. Bliokh, H. Punzmann, H. Xia, F. Nori, M. Shats, *Sci. Adv.* **8**, eabm1295 (2022).
50. D. Marco, M. A. Alonso, arXiv:2212.01366 (2022).
51. A. Sit *et al.*, *Optica* **4**, 1006–1010 (2017).
52. R. Zhang *et al.*, *Nat. Photonics* **15**, 743–750 (2021).

ACKNOWLEDGMENTS

Funding: The authors acknowledge support from the ERC (Complexplas, 3DPrintedoptics); DFG (GRK2642, SPP1391 Ultrafast Nanooptics, CRC 1242 "Non-Equilibrium Dynamics of Condensed Matter in the Time Domain" project no. 278162697-SFB 1242); BMBF (Printoptics); BW Stiftung (Spitzenforschung, Opterial); Car-Zeiss Stiftung; the Russel Berrie Nanotechnology institute (RBNI); the Helen Diller Quantum Center (HDQC); and the Micro-Nano Fabrication Unit (MNFU) at the Technion. S.T. acknowledges support from the Adams fellowship program of the Israel Academy of Science and Humanities, the Rothschild fellowship of the Yad Hanadiv foundation, the VATAT-Quantum fellowship of the Israel Council for Higher Education, the Helen Diller Quantum Center postdoctoral fellowship the Viterbi fellowship of the Technion – Israel Institute of Technology. T.J.D. acknowledges support from the MPI Guest Professorship Program and from the DFG (GRK2642) Photonic Quantum Engineers for a Mercator Fellowship. **Author contributions:** All authors contributed to the theoretical description, sample fabrication, data acquisition, data analysis, and the writing of the manuscript. **Competing interests:** The authors declare no competing interests. **Data and materials availability:** All relevant data are available in the main manuscript or the supplementary materials. **License information:**

SUPPLEMENTARY MATERIALS

science.org/doi/10.1126/science.adt2495
Materials and Methods
Supplementary Text
Figs. S1 to S3
Table S1
References (*53*–*57*)
Movies S1 and S2

Submitted 18 September 2024; accepted 7 January 2025
10.1126/science.adt2495

ANIMAL COMMUNICATION

Whale song shows language-like statistical structure

Inbal Arnon[1]*, Simon Kirby[2]*, Jenny A. Allen[3,4], Claire Garrigue[5,6], Emma L. Carroll[7], Ellen C. Garland[8,9]*

Humpback whale song is a culturally transmitted behavior. Human language, which is also culturally transmitted, has statistically coherent parts whose frequency distribution follows a power law. These properties facilitate learning and may therefore arise because of their contribution to the faithful transmission of language over multiple cultural generations. If so, we would expect to find them in other culturally transmitted systems. In this study, we applied methods based on infant speech segmentation to 8 years of humpback recordings, uncovering in whale song the same statistical structure that is a hallmark of human language. This commonality, in two evolutionarily distant species, points to the role of learning and cultural transmission in the emergence of properties thought to be unique to human language.

Human language has properties that make it unique among the communicative behaviors of our nearest relatives. Every human language consists of statistically coherent parts, such as words, where elements within those parts are relatively predictable. Across languages, few of these parts are highly frequent, many are infrequent, and there is a power law relation between frequency and rank [called a Zipfian distribution (*1*, *2*)]. The presence of such a distribution in nonhuman communication is debated, with few studies showing a fit similar to human language (*3*) and most only achieving a fit to a more convex distribution [known as Zipf-Mandelbrot (*4*–*9*)]. Having statistically coherent parts and having them follow a Zipfian distribution facilitates various aspects of human language learning (*10*–*15*). Much work has demonstrated that language characteristics that aid learning can arise through cultural transmission, as language is a sequential behavior that is repeatedly learned and used by multiple generations (*16*–*18*). Indeed, a recent experimental study demonstrated that cultural transmission can promote both properties (statistically coherent parts and their Zipfian distribution) in humans (*19*). This raises the possibility that the statistical structure that is a hallmark of human language may exist in other species whose communication systems are culturally transmitted and involve complex sequential behavior. Humpback whale song has these properties (*20*–*23*): It is among the most complex acoustic displays in the animal kingdom and is culturally transmitted, making it an excellent model to test the impact of culture on foundational properties of human language.

Humpback whale song is long, repetitive, complex, and structured in a nested hierarchy (*24*, *25*). Individual "sound elements" are sung in a stereotyped "phrase," which is repeated multiple times to create a "theme" (*24*). Several themes are sung in a stereotyped sequence to form a "song," with multiple songs making up a "song session" (*24*). Only males sing (*26*), and there is strong cultural conformity to the current song arrangement by most males within a population (*27*). However, the song also constantly changes within a season, progressively leading to a different song after a few years through theme turnover (*22*). In contrast to this slow change, song revolutions also occur when the entire song arrangement is rapidly and completely replaced by a song introduced from a neighboring population (*20*, *21*). This wholesale change is notable; multiple song revolutions have been documented spreading eastwards across the South Pacific (*21*, *28*, *29*).

Understanding how humpback whales learn their song is extremely challenging given the inability to conduct laboratory experiments on these wild, free-ranging animals. However, recent work on hybrid songs, where a whale was recorded in the process of changing his song during a song revolution, has provided invaluable data on how songs are learned (*30*). Sequence analyses (*31*) revealed that songs are learned as segments (complete themes), akin to birdsong and human language learning. Revolutionary themes were spliced into the song at the position of highest structural similarity ("switch when similar" rule), allowing songs to be combined in predictable ways (*30*). Such studies indicate that songs are learned, and they suggest that whale song exhibits sequential structure and that this structure is relied on during cultural transmission.

If the emergence of the statistical structure found in human language is driven by it being learned and culturally transmitted, we may expect to find similar structure in whale song. We predicted that (i) statistically coherent subsequences will be present in whale song and (ii) the distribution of these subsequences will follow a language-like power-law distribution. We tested these predictions by applying an infant-inspired segmentation method (*19*) to analyze 8 years of humpback whale song from a single population. Our method detects dips in transitional probability between the basic acoustic building blocks in humpback whale song (sound elements), uses them to segment the song into subsequences, and looks at the distribution of those subsequences. These are

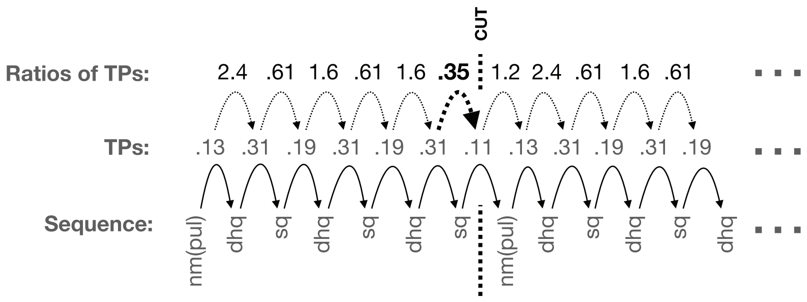

Fig. 1. An example of our infant-inspired segmentation method applied to whale song data. This is the start of one recording taken in 2017. For each year, we created a long sequence of sound elements (bottom row). We then used all the recordings from a particular year to estimate the transitional probabilities (TPs) between all pairs of sound elements (middle row). Next, we computed the ratios between subsequent TPs (top row) to find ones that merit segmentation. One ratio, shown in bold, is below 0.5, indicating a big dip in TP—in other words, the next sound element is unexpected in context. We used these dips as cues to "cut" the sequence, leading to the addition of a subsequence (i.e., sequence of elements) to the set of units we infer for that year. In the example above, we would add the subsequence nm(pul)-dhq-sq-dhq-sq-dhq-sq to the units inferred for 2017 [nm(pul) is a pulsed n-shaped moan, dhq is a descending high squeak, and sq is a squeak; see table S3].

---

[1]Psychology Department, Hebrew University, Jerusalem, Israel. [2]Centre for Language Evolution, University of Edinburgh, Edinburgh, UK. [3]Bio-Telemetry and Behavioral Ecology Laboratory, Institute of Marine Science, Long Marine Laboratory, University of California, Santa Cruz, Santa Cruz, USA. [4]Southern Ocean Persistent Organic Pollutants Programs (SOPOPP), Griffith University, Nathan, QLD, Australia. [5]IRD, UMR ENTROPIE (IRD, Université de La Réunion, Université de la Nouvelle-Calédonie, CNRS, Ifremer), Nouméa, New Caledonia. [6]Opération Cétacés, Nouméa, New Caledonia. [7]School of Biological Sciences, University of Auckland–Waipapa Taumata Rau, Auckland, Aotearoa New Zealand. [8]Sea Mammal Research Unit (SMRU), Scottish Oceans Institute, School of Biology, University of St Andrews, St Andrews, UK. [9]Centre for Social Learning and Cognitive Evolution, School of Biology, University of St Andrews, St Andrews, UK.
***Corresponding author. Email: inbal.arnon@mail.huji.ac.il (I.A.); simon.kirby@ed.ac.uk (S.K.); ecg5@st-andrews.ac.uk (E.C.G.)**

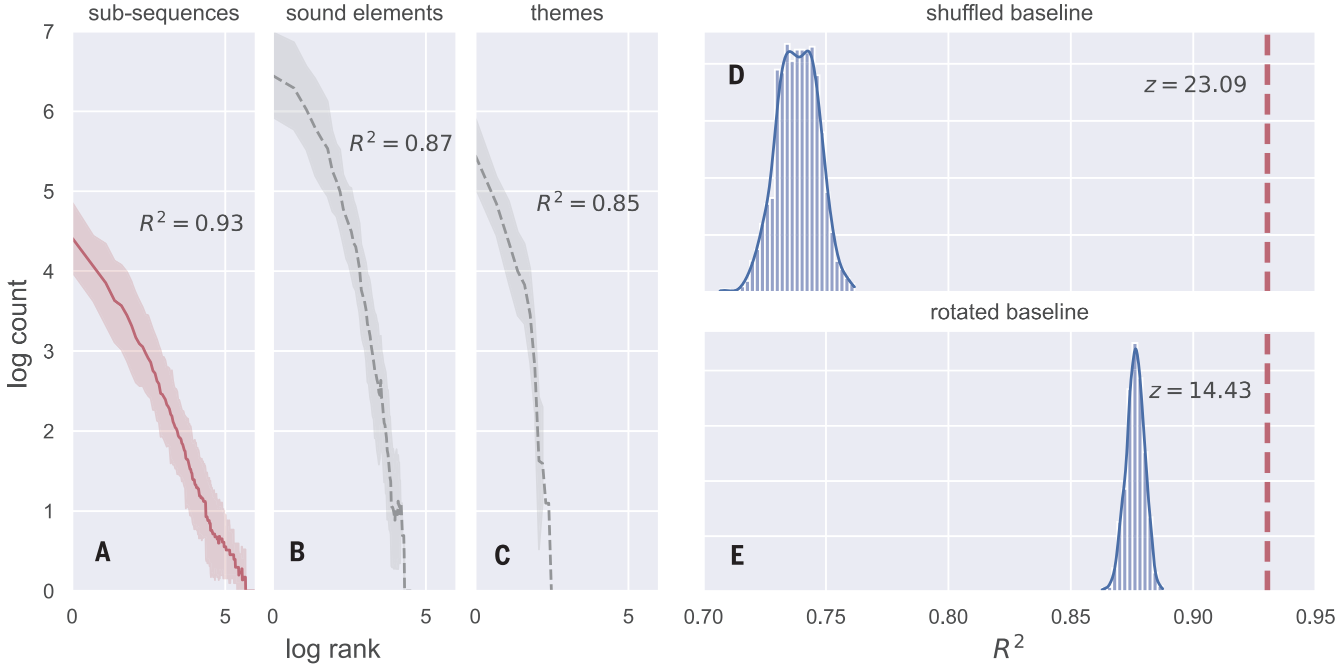

Fig. 2. Subsequences detected by our infant-inspired segmentation method in humpback whale song follow a Zipfian frequency distribution. (**A**) The frequency of each subsequence ordered by rank, plotted on a log scale for both axes. There is a small number of highly frequent subsequences and a long tail of low-frequency ones. We calculated the frequency of the subsequences independently for each year and then aggregated the frequency by rank over the eight different years (we show the mean and 95% bootstrapped confidence intervals around the mean). The straight line is diagnostic of a power law distribution that is typical of word frequency distributions in human languages. (**B**) The same plot, but based on the distribution of the individual sound elements (the basic acoustic building blocks of whale song). The distribution is skewed but shows less of a fit to a power law than the distribution of subsequences in (A). (**C**) The distribution of the human categorized "themes" (*55*) in the dataset. For each distribution in (A) to (C), the mean R^2 value is shown. This indicates how well the distribution fits a power law. The best fit for a Zipfian distribution is found for units detected using our infant-inspired method. (**D** and **E**) Comparison of the Zipfian fit of our detected subsequences to two baselines. The dashed lines indicate the R^2 for the real data. The histogram in (D) shows the distribution of R^2 values derived by running our full segmentation pipeline on 1000 randomly shuffled datasets. The histogram in (E) shows the distribution of R^2 values for 1000 randomly rotated datasets. The *z*-scores demonstrate that the real data are a far better fit to a Zipfian distribution than any of the baseline datasets.

the same cues used by human infants to segment speech (*32*, *33*): Because words are statistically coherent, transitional probabilities within words are higher (on average) than those between words. Our method does not assume learners are looking to build a lexicon, an assumption that cannot be reasonably applied to whales.

Subsequences found in whale song follow a Zipfian distribution

If whale song, like human language, contains statistically coherent parts, we should detect local dips in transitional probability. To identify such dips, we estimated the transitional probability between each two consecutive sound elements in a given year. For example, if the song contained the sequence "grunt," "grunt," "ascending moan," we estimated the probability of "grunt" coming after "grunt" in the entire song. Segmentation boundaries were inferred, following previous work, on the basis of the ratio between consecutive transitional probabilities (*19*). We inferred a segmentation boundary when that ratio was "unusually low." We used the ratios and not the transitional probabilities per se to capture relative dips: A transitional probability of 0.45 may not be very low; however, a drop from 0.95 to 0.45 would indicate a meaningful drop. There is no a priori reason for setting the threshold at a particular point: given that whale song is hierarchically structured (*24*), different settings of the cutting parameter may discover different types of units (themes, phrases).

Previous work (*19*) applying a similar segmentation method to data from human participants used a threshold of 0.425 to detect a boundary. This threshold was derived from a random baseline that was similar to the structured output participants produced. However, we could not derive such a random baseline for whale song data. Instead, we chose a 0.5 threshold, similar to that used with human experimental data. That is, we cut whenever the current transition was half that of the prior one, suggesting that the next sound element was unexpected in context. Figure 1 illustrates our segmentation method for a 2017 song sequence. Notably, we repeated the analyses with two additional thresholds of 0.25 and 0.75 and show that the results are robust to changes in cutting sensitivity (see figs. S1 to S4). In other words, despite differences in how many units are detected, we find the same statistical structure at different unit sizes, as expected if changing the threshold leads to detecting a larger subset of the existing units.

We ran this segmentation pipeline for each year separately (as song content differs across years). Each year's data included multiple separate recordings (table S1). Sound elements from each recording were concatenated after removing (human-assigned) theme and song-cycle boundaries. Our method detected subsequences within the song: We performed an average of 1562 cuts on the data from each year. For each year, we calculated the frequency of each of the segmented subsequences (table S2). Figure 2A plots the frequency distribution of the segmented units, collapsed across the years. The distribution shows an excellent fit to a power law (mean $R^2 = 0.93$, Pearson product moment correlation). That is, applying a segmentation method based on infant language learning to whale song resulted in the detection of subsequences that follow a Zipfian distribution.

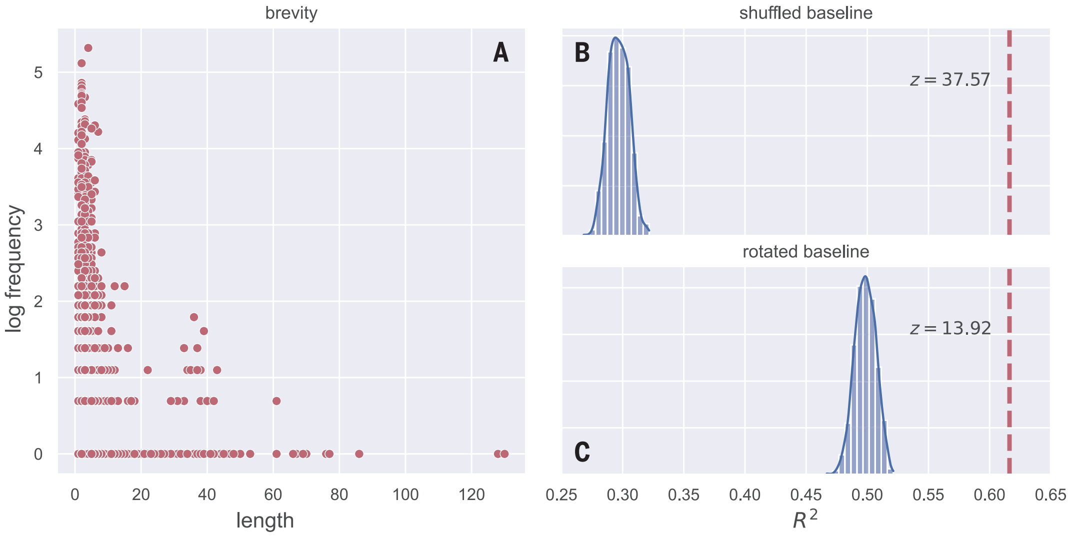

Fig. 3. Subsequences detected by our segmentation method follow Zipf's law of brevity. Each point in (**A**) is one subsequence (see table S2 for examples of the most frequent ones). The figure shows the frequency distribution of all subsequences discovered by our segmentation method across the entire dataset plotted by length (number of sound elements). More frequent subsequences are shorter than less frequent ones, indicating that the detected subsequences not only follow a Zipfian distribution (as shown in Fig. 2) but also follow Zipf's second law, the law of brevity, that is typical of human language and other animal communication systems. (**B** and **C**) Comparison of the R^2 of the real data (0.62, shown with a dashed line) to two random baselines. The histogram in (B) shows the distribution of R^2 values for the relation between frequency and length derived by running our full segmentation method on 1000 randomly shuffled datasets. The histogram in (C) shows the distribution of R^2 values for 1000 randomly rotated datasets. The *z*-scores demonstrate that the real data are a far better fit to Zipf's law of brevity than any of the baseline datasets.

To ensure that the Zipfian distribution is not dependent on our particular segmentation method, we implemented two additional segmentation pipelines, both of which rely on cues used by infants and do not assume a lexicon. One expands the sequential context (using the transitional probabilities based on the two previous sound elements), and the second uses backward transitional probability (the probability of each sound element given the one that follows). This last pipeline is a particularly good validation because infants also use backward transitional probabilities in segmenting speech (*34*). The resulting distribution of subsequences using these additional infant-inspired methods also showed an excellent fit to a Zipfian distribution [$R^2 = 0.93$ (fig. S5) and $R^2 = 0.94$ (fig. S6), respectively].

Zipfian distribution reflects sequential structure in whale song

We performed several validation tests to ensure that the Zipfian distribution was not an artifact of the distribution of sound elements. First, we examined the distribution of sound elements, themes, and our detected subsequences. While all three had a skewed distribution, our detected subsequences showed the best fit to a power law (Fig. 2, A to C). This alone does not rule out the possibility that the skewed distribution of sound elements by itself will lead to a Zipfian distribution of segmented subsequences. To address this, we created 1000 pseudodatasets by shuffling the sound elements within each song. This preserves the distribution of individual sound elements but destroys any sequential structure. We then reran our segmentation pipeline with each of these 1000 shuffled datasets and calculated the R^2 to capture the fit to a power law. If the statistical structure observed in whale song reflects sequential structure, the shuffled pseudodatasets should not produce the same results. Figure 2D shows that the R^2 line of 0.93 derived from the real data is substantially higher than any derived from the shuffled datasets ($z = 23.09$, $P < 0.00001$). We also ran this baseline analysis for the two additional segmentation pipelines mentioned above with similar results [expanded-context pipeline, $z = 26$, $P < 0.00001$ (fig. S7); backward-transitional-probabilities pipeline, $z = 24.67$, $P < 0.00001$ (fig. S8)].

To further ensure that the distribution we found was related to the specific cue we used to segment the song, we performed an additional, more stringent, validation that preserved the ordering of the sound elements and the length distribution of the segmented units, but where the cuts no longer corresponded to dips in transitional probabilities. To do this, we generated 1000 "rotated" datasets by taking the cutting points from the original dataset for each year and shifting them by a random number of steps (e.g., if the random number was 5 for a particular dataset, a cut at position 10 of the sequence would now be placed in position 15). We calculated the frequency distribution of the segmented units for each "rotated" dataset. The fit to the Zipfian distribution in the real data was again significantly higher than in the rotated datasets ($z = 14.43$, $P < 0.00001$; Fig. 2E). We also ran this conservative baseline for the additional segmentation pipelines and found similar results [expanded-context pipeline, $z = 17.55$, $P < 0.00001$ (fig. S9); backward-transitional-probabilities pipeline, $z = 17.32$, $P < 0.00001$ (fig. S10)].

Subsequences found in whale song follow Zipf's law of brevity

Zipf also demonstrated that frequent words tend to be shorter than infrequent words, a concept known as Zipf's law of brevity (*2*). This relationship between length and frequency is demonstrated in a range of species (*35*–*37*), is taken as evidence for compression (*35*), and is seen as a result of adaptation for communicative efficiency (*38*). If our method for discovering subsequences is capturing units that are relevant for whales, we might expect the subsequences we find to have lengths that reflect Zipf's law of brevity. Indeed, Fig. 3A shows a strong relationship between length and log frequency ($R^2 = 0.62$). As above, we ran the shuffled and rotated baselines to ensure that the pattern we found was not an artifact. The fit to Zipf's law of brevity in the real data was vastly better than the fit of the two baseline sets [1000 shuffled datasets: $z = 37.57$, $P < 0.00001$ (Fig. 3B); 1000 rotated datasets: $z = 13.92$, $P < 0.00001$ (Fig. 3C)]. We also ran the same baseline analyses for the other two segmentation pipelines, with similar results (figs. S11 and S14) [expanded-context pipeline, shuffled baseline, $z = 53.09$, $P < 0.00001$ (fig. S12); rotated baseline, $z = 18.61$, $P < 0.00001$ (fig. S13); backward-transitional-probabilities pipeline, shuffled baseline, $z = 45.46$, $P < 0.00001$ (fig. S15); rotated baseline, $z = 19.32$, $P < 0.00001$ (fig. S16)]. These analyses clearly show that Zipf's law of brevity is a feature of whale song that holds for subsequences detected using several infant-inspired segmentation methods.

Discussion

Uncovering precisely how whales learn their songs is a challenging, potentially intractable, problem. Laboratory experiments such as those done with human infants are clearly impossible in this species. However, we can apply infant-inspired techniques to the songs of humpback whales. Doing so reveals hitherto hidden structure in whale song. We detected statistically coherent subsequences: a characteristic design feature shared with human language. The frequency of these subsequences closely follows a Zipfian distribution—this, too, is a property found in all human languages. Finally, the length of the detected subsequences follows Zipf's second law, the law of brevity. Frequent units tend to be shorter than less frequent ones. Once again, this property is found in all human languages. This work reveals a deep commonality between two unrelated species united by the fact that their communication systems are culturally transmitted.

One concern might be that the Zipfian distribution of the detected subsequences is an inevitable artifact of the distribution of the basic sound elements, or of our segmentation procedure, and that such a distribution will be found whenever cuts are made. However, two baseline analyses show this to be unlikely. Neither our shuffled dataset nor our rotated dataset had a fit close to the one found in the real whale data (Fig. 2, D and E). Equally, the fit to a Zipfian distribution is not as strong when using human-annotated units (sound elements, themes; Fig. 2, B and C). The subsequences extracted with our method also follow Zipf's law of brevity, another linguistic universal (*39*–*41*), suggesting that we are detecting units relevant to the whales (Fig. 3). Zipf's law of brevity is found in a range of species (*35*, *37*), including humans (*42*), and likely arises from optimizing efficient coding (*2*, *38*, *40*). The fact that using transitional probabilities led us to detect units that follow this law suggests that humpback whales, like human infants, may learn their song by tracking transitional probabilities between elements, and using dips in those probabilities as a cue for unit boundary (*32*).

Our infant-inspired method relies on transitional probabilities as a cue to segmentation. This cue is not expected to provide the most accurate segmentation for natural language, as language has multiple probabilistic cues to segmentation. Instead, we wanted to simulate early learning, relying on cues actually used by infants without making additional assumptions about the learner. Indeed, transitional probabilities have been used to extract word candidates from child-directed speech (*43*, *44*) and are used by infants early on (*32*, *33*), before the use of other cues such as stress (*45*). To ensure that the results were not dependent on this particular method, we implemented two additional infant-inspired segmentation methods, both of which resulted in the detection of subsequences whose frequency showed a very good fit to the Zipfian distribution (figs. S5 to S10). These converging findings present evidence that Zipfian distributions are found in whale song when using infant-inspired methods to detect units.

Of course, there are many differences between whale song and human language. Above all, expressions in language have semantic content. The meaning of sentences is composed of the meanings of the parts and how they are put together. We make no such claim for whale song. We have little understanding of the "meaning" of the songs, let alone the different units, for humpback whales. Furthermore, having similar statistical structure does not entail similar expressive function. In fact, similar statistical structure is also found in music—a culturally transmitted behavior where individual units do not have explicit expressive meaning but nevertheless show a good fit to a Zipfian distribution (*46*). While there are multiple explanations for the presence of Zipfian distributions in human language [see (*1*) for a review], only a subset of them seem relevant for the analysis of whale song. Existing accounts (for human language) can be broadly divided into ones pertaining to the coding of meaning (*36*, *41*, *47*, *48*), to communicative efficiency (*38*, *49*), and to learnability (*11*, *50*). As discussed above, it is unlikely that explanations pertaining to meaning are relevant for whale song (*5*, *23*, *51*), leaving efficiency and learnability explanations as the most relevant.

Our work is by no means the first to look for linguistic laws in nonhuman communication (*52*, *53*). Indeed, much work has specifically focused on Zipfian distributions. However, as noted above, the vast majority of studies have only found a fit to Zipf-Mandelbrot's extension, which has an additional parameter, and will necessarily fit a wider range of data. These findings could be, and sometimes are, interpreted to reflect a meaningful difference between human language and nonhuman communication (*5*). Alternatively, they could arise from the choice of "units" being counted, as we have seen here; counting individual sound elements in whale song leads to a Zipf-Mandelbrot distribution (Fig. 2B) (*5*), whereas counting subsequences detected using our segmentation method reveals a pure Zipfian distribution. This leads to a strong prediction that applying our infant-inspired segmentation method will lead to a similar shift from Zipf-Mandelbrot to Zipf in species with learned sequential signals. Songbirds provide a particularly promising model to explore this prediction, as multiple passerine species have culturally transmitted songs and several show a good fit to the Zipf-Mandelbrot distribution [e.g., (*6*–*8*)]. Some, including house finches (*Haemorhous mexicanus*) and zebra finches (*Taeniopygia guttata*), are also sensitive to transitional probabilities in learning (*8*, *54*).

We have revealed a deep commonality between two unrelated, evolutionarily distant species, humans and humpback whales, united by the cultural transmission of their communication systems. This points to the crucial role of learning and transmission in the emergence of structure within such systems. Whether the units detected by our infant-inspired segmentation method are salient to the whales themselves remains an open question. These findings also raise the intriguing possibility that similar statistical structure will be found wherever complex sequential behavior is transmitted culturally, and they suggest that our understanding of the evolution of language can benefit from looking not only at our closest primate relatives but also at cases of convergent evolution elsewhere in nature. We can do this by looking beyond the proximate functions of language, for example, as a system conveying semantic information, and instead consider how language is learned and transmitted culturally over multiple generations. Once thought of as the hallmark of human uniqueness, it may transpire that foundational aspects of human language are shared across species.

REFERENCES AND NOTES

1. S. T. Piantadosi, *Psychon. Bull. Rev.* **21**, 1112–1130 (2014).
2. G. Zipf, *Human Behavior and the Principle of Least Effort: An Introduction to Human Ecology* (Addison-Wesley Press, 1949).
3. B. McCowan, S. F. Hanser, L. R. Doyle, *Anim. Behav.* **57**, 409–419 (1999).
4. B. Mandelbrot, *Commun. Theory* **84**, 486–502 (1953).
5. J. A. Allen, E. C. Garland, R. A. Dunlop, M. J. Noad, *Proc. Biol. Sci.* **286**, 20192014 (2019).
6. E. Briefer, T. S. Osiejuk, F. Rybak, T. Aubin, *J. Theor. Biol.* **262**, 151–164 (2010).
7. M. L. Cody, E. Stabler, H. M. Sánchez Castellanos, C. E. Taylor, *Bioacoustics* **25**, 41–54 (2016).
8. M. Youngblood, *Proc. Biol. Sci.* **291**, 20240250 (2024).
9. J. P. Hailman, M. S. Ficken, R. W. Ficken, *Semiotica* **56**, 191–224 (1985).
10. C. Kurumada, S. C. Meylan, M. C. Frank, *Cognition* **127**, 439–453 (2013).
11. O. Lavi-Rotbain, I. Arnon, *Cognition* **223**, 105038 (2022).
12. A. T. Hendrickson, A. Perfors, *Cognition* **189**, 11–22 (2019).
13. J. K. Boyd, A. E. Goldberg, *Mod. Lang. J.* **93**, 418–429 (2009).
14. O. Lavi-Rotbain, I. Arnon, *Cognition* **206**, 104492 (2021).
15. K. D. Schuler, P. A. Reeder, E. L. Newport, R. N. Aslin, *Lang. Learn. Dev.* **13**, 357–374 (2017).
16. S. Kirby, *Psychon. Bull. Rev.* **24**, 118–137 (2017).
17. S. Kirby, H. Cornish, K. Smith, *Proc. Natl. Acad. Sci. U.S.A.* **105**, 10681–10686 (2008).
18. S. Kirby, M. Dowman, T. L. Griffiths, *Proc. Natl. Acad. Sci. U.S.A.* **104**, 5241–5245 (2007).
19. I. Arnon, S. Kirby, *Sci. Rep.* **14**, 5255 (2024).
20. M. J. Noad, D. H. Cato, M. M. Bryden, M.-N. Jenner, K. C. S. Jenner, *Nature* **408**, 537–537 (2000).
21. E. C. Garland *et al*., *Curr. Biol.* **21**, 687–691 (2011).
22. K. Payne, R. S. Payne, *Z. Tierpsychol.* **68**, 89–114 (1985).
23. E. C. Garland, C. Garrigue, M. J. Noad, *Philos. Trans. R. Soc. Lond. Ser. B* **377**, 20200313 (2022).
24. R. S. Payne, S. McVay, *Science* **173**, 585–597 (1971).
25. L. M. Herman, W. N. Tavolga, in *Cetacean Behaviour: Mechanisms and Functions*, L. M. Herman, Ed. (Wiley 1980), pp. 149–209.
26. D. A. Glockner, in *Communication and Behavior of Whales*, R. Payne, Ed. (Westview Press Inc., 1983), pp. 447–464.

27. K. Payne, P. Tyack, R. Payne, in *Communication and Behavior of Whales*, R. Payne, Ed. (Westview Press Inc., 1983), pp. 9–57.
28. C. Owen *et al.*, *R. Soc. Open Sci.* **6**, 190337 (2019).
29. J. N. Schulze, J. Denkinger, J. Oña, M. M. Poole, E. C. Garland, *R. Soc. Open Sci.* **9**, 220158 (2022).
30. E. C. Garland, L. Rendell, L. Lamoni, M. M. Poole, M. J. Noad, *Proc. Natl. Acad. Sci. U.S.A.* **114**, 7822–7829 (2017).
31. E. C. Garland *et al.*, *J. Acoust. Soc. Am.* **142**, 460–472 (2017).
32. J. R. Saffran, R. N. Aslin, E. L. Newport, *Science* **274**, 1926–1928 (1996).
33. T. Teinonen, V. Fellman, R. Näätänen, P. Alku, M. Huotilainen, *BMC Neurosci.* **10**, 21 (2009).
34. B. Pelucchi, J. F. Hay, J. R. Saffran, *Cognition* **113**, 244–247 (2009).
35. S. Semple, M. J. Hsu, G. Agoramoorthy, *Biol. Lett.* **6**, 469–471 (2010).
36. L. Favaro *et al.*, *Biol. Lett.* **16**, 20190589 (2020).
37. M. Huang, H. Ma, C. Ma, P. A. Garber, P. Fan, *Anim. Behav.* **160**, 145–155 (2020).
38. J. Kanwal, K. Smith, J. Culbertson, S. Kirby, *Cognition* **165**, 45–52 (2017).
39. S. T. Piantadosi, H. Tily, E. Gibson, *Proc. Natl. Acad. Sci. U.S.A.* **108**, 3526–3529 (2011).
40. R. Ferrer-i-Cancho *et al.*, *Cogn. Sci.* **37**, 1565–1578 (2013).
41. R. Ferrer-i-Cancho, C. Bentz, C. Seguin, *J. Quant. Linguist.* **29**, 165–194 (2022).
42. C. Bentz, R. Ferrer-i-Cancho, in *Proceedings of the Leiden Workshop on Capturing Phylogenetic Algorithms for Linguistics*, C. Bentz, G. Jäger, I. Yanovich, Eds. (Univ. of Tubingen, 2016).
43. K. Stärk, E. Kidd, R. L. A. Frost, *Lang. Speech* **65**, 3–27 (2022).
44. A. Cristia, E. Dupoux, N. B. Ratner, M. Soderstrom, *Open Mind* **3**, 13–22 (2019).
45. E. D. Thiessen, J. R. Saffran, *Dev. Psychol.* **39**, 706–716 (2003).
46. B. Manaris *et al.*, *Comput. Music J.* **29**, 55–69 (2005).
47. R. Ferrer-i-Cancho, *Complexity* **21**, 409–411 (2016).
48. D. Y. Manin, *Cogn. Sci.* **32**, 1075–1098 (2008).
49. R. Ferrer i Cancho, R. V. Solé, *Proc. Natl. Acad. Sci. U.S.A.* **100**, 788–791 (2003).
50. C. Bentz, D. Alikaniotis, M. Cysouw, R. Ferrer-i-Cancho, *Entropy* **19**, 275 (2017).
51. L. M. Herman, *Biol. Rev. Camb. Philos. Soc.* **92**, 1795–1818 (2017).
52. S. Semple, R. Ferrer-I-Cancho, M. L. Gustison, *Trends Ecol. Evol.* **37**, 53–66 (2022).
53. P. Sharma *et al.*, *Nat. Commun.* **15**, 3617 (2024).
54. J. Chen, C. Ten Cate, *Behav. Processes* **117**, 29–34 (2015).
55. J. A. Allen, E. C. Garland, C. Garrigue, R. A. Dunlop, M. J. Noad, *Sci. Rep.* **12**, 8999 (2022).

ACKNOWLEDGMENTS

We thank S. Derville for providing comments on a previous version of this manuscript and two anonymous reviewers for their suggestions, including additional models to test. We thank and acknowledge the numerous volunteers, students, and researchers at Opération Cétacés and elsewhere who contributed to this dataset through data collection, in particular S. Derville, D. Boillon, C. Bonneville, M. Chambellant, R. Dodemont, J. Greaves, and V. Pérard. Thanks also to L. Wolters, N. Claidiere, L. Carmel, S. Fisher, T. Fitch, S. Goldin-Meadow, K. Okanoya, and L. Raviv for stimulating and insightful discussions and for always having their quills ready for us. **Funding:** Surveys of humpback whales in New Caledonia were made possible by contributions from Fondation d'Entreprise Total and Total Pacifique; the Provinces Sud, North, and Isles; and the Ministère de la Transition Ecologique et Solidaire. This work was funded by the following grants to E.C.G: Royal Society University Research Fellowship (UF160081 and URF\R\221020), Royal Society Research Fellows Enhancement Award (RGF\EA\180213), Royal Society Research Grants for Research Fellows 2018 (RGF\R1\181014), National Geographic Grant (NGS-50654R-18), Carnegie Trust Research Incentive Grant (RIG007772), British Ecological Society Small Research Grant (SR18/1288), and School of Biology Research Committee funding. E.L.C. was supported by a Rutherford Discovery Fellowship from the Royal Society of New Zealand Te Aparangi. J.A.A. was supported by a National Science Foundation Office of Polar Programs Postdoctoral Fellowship (2218949) and a grant from the Winifred Violet Scott Trust. I.A. was supported by an Israeli Science Foundation Grant (ISF 445/20). I.A. and S.K. were supported by a fellowship from the Israel Institute for Advanced Studies. **Author contributions:** I.A., S.K., and E.C.G. conceived of and designed the study. C.G., E.C.G., and J.A.A. collected and curated the data. J.A.A. and E.C.G. transcribed and analyzed the whale song data. I.A. and S.K. designed the human infant–inspired segmentation pipeline and adapted it to whale song, with input from E.C.G. S.K. conducted the statistical analyses. E.C.G., C.G., and E.L.C. secured funding. I.A., S.K., and E.C.G. wrote the first drafts of the manuscript, with assistance from J.A.A., and all authors contributed to the final draft. **Competing interests:** The authors declare that they have no competing interests. **Data and materials availability:** All data and code that support the findings of this study are available in the supplementary materials. Data used in the analysis are available for the purposes of reproducing or extending the Zipfian analysis.

SUPPLEMENTARY MATERIALS

science.org/doi/10.1126/science.adq7055
Materials and Methods
Figs. S1 to S18
Tables S1 to S3
References (*56*–*62*)
MDAR Reproducibility Checklist
Code S1
Data S1 to S3

Submitted 29 May 2024; resubmitted 30 August 2024
Accepted 4 December 2024
10.1126/science.adq7055

SPECTROSCOPY

Squeezed dual-comb spectroscopy

Daniel I. Herman[1]*, Mathieu Walsh[2], Molly Kate Kreider[1,3], Noah Lordi[3], Eugene J. Tsao[1], Alexander J. Lind[1], Matthew Heyrich[1,3], Joshua Combes[1], Jérôme Genest[2]*, Scott A. Diddams[1,3]*

Optical frequency combs have enabled distinct advantages in broadband, high-resolution spectroscopy and precision interferometry. However, quantum mechanics ultimately limits the metrological precision achievable with laser frequency combs. Quantum squeezing has led to substantial measurement improvements with continuous wave lasers, but experiments demonstrating metrological advantage with squeezed combs are less developed. Using the Kerr effect in nonlinear optical fiber, a 1-gigahertz frequency comb centered at 1560 nanometers is amplitude-squeezed by >3 decibels (dB) over a 2.5-terahertz bandwidth. Dual-comb interferometry yields mode-resolved spectroscopy of hydrogen sulfide gas with a signal-to-noise ratio nearly 3 dB beyond the shot-noise limit. The quantum noise reduction leads to a twofold quantum speedup in the determination of gas concentration, with implications for high-speed measurements of multiple species in dynamic chemical environments.

Measurements of physical quantities including time, frequency, and distance have been reshaped by a quarter century of optical frequency comb (OFC) developments (*1*). Traceable, phase-coherent, and broadband OFCs are widely used for atomic and molecular spectroscopy. As an active light source from the terahertz to the ultraviolet, OFCs extend the technological frontier for both fundamental and applied spectroscopy (*2*, *3*), including biological and chemical sensing (*4*) and high-resolution measurements of quantum systems (*5*). The rising importance of comb-based applications motivates the need to understand and reduce the fundamental quantum noise limitations with these distinct measurement tools.

Recently, OFC metrology has reached the quantum shot-noise limit (SNL) imposed by a coherent state (Fig. 1, A and B) (*6*–*8*). To extend spectroscopic sensitivity beyond this limit, one can incorporate squeezed states, as has been achieved previously for continuous wave lasers (*9*). Several proposals exist for using squeezed OFCs as spectroscopic tools (*10*, *11*), in which attainable levels of squeezing (~10 dB) may yield considerable quantum advantage with useful power levels (microwatts to milliwatts). In parallel, there has been substantial progress in quantum OFC generation using optical parametric oscillators, microresonator OFCs, and other platforms (*12*–*14*). These advances have accompanied research in which quantum OFCs are used as a quantum resource for quantum computation (*15*) and timing measurements (*16*). However, metrological advantage with squeezed OFCs has not been demonstrated for spectroscopy, which is one of the most impactful OFC applications.

In this paper, we describe a simple scheme for the generation of a bright amplitude-squeezed 1-GHz OFC and its application for mode-resolved dual-comb spectroscopy (DCS) of molecular samples. Existing quantum-enhanced OFC spectroscopy proposals utilize optical nonlinearities to squeeze a few comb modes (*10*, *11*). Although it is possible to apply $\chi^{(2)}$ nonlinearities over wide optical bandwidths (*17*), we instead utilize the more accessible $\chi^{(3)}$ nonlinearity to suppress quantum noise in the amplitude measurement of >2500 comb modes over a ~2.5-THz wide optical bandwidth. Our setup builds upon well-established soliton squeezing techniques

---

[1]Department of Electrical, Computer and Energy Engineering, University of Colorado Boulder, Boulder, CO, USA. [2]Centre d'Optique, Photonique et Laser, Université Laval, Québec, QC, Canada. [3]Department of Physics, University of Colorado Boulder, Boulder, CO, USA.
***Corresponding author. Email: daniel.i.herman@colorado.edu (D.I.H.); jgenest@gel.ulaval.ca (J.G.); scott.diddams@colorado.edu (S.A.D.)**

(*18–20*) including recent interferometric phase measurements (*21*). We show that bright-amplitude squeezing provides a metrological advantage for broadband colinear DCS even when only one of the two OFCs is squeezed. Overlapping the OFCs prior to sample interrogation provides a baseline-calibrated transmission measurement that fully benefits from quantum squeezing. Our technique enables the development of real-world use cases for quantum-enhanced DCS.

Quantum noise in DCS

The DCS technique enables traceable spectroscopy across terahertz optical bandwidths with comb mode resolution, but without mechanical delay lines or diffractive optical elements (*3*). In DCS, two combs with different mode spacing are interfered to down-convert the optical comb spectrum and absorption information to the radio frequency (RF) domain where the signal is recorded and calibrated against an absolute frequency scale (Fig. 1B). In the frequency domain, dual-comb interference appears as a multiheterodyne RF comb whereas the time domain waveform is a periodic interferogram. The molecular absorption is encoded as dips in the RF comb spectrum and as free induction decay (FID) signals trailing the interferogram. DCS pushes the state of the art for broad bandwidth, high-resolution, traceable sensing across the electromagnetic spectrum with applications that include open-path environmental sensing (*22*), chemical reaction monitoring (*4*), chemical imaging (*23*), and generation of accurate archival spectra for widely distributed databases (*24*). By reducing technical noise sources, such as the comb relative intensity noise, detector noise, and thermal noise, the fundamental quantum shot noise of a coherent state is the dominant uncertainty in the measurement of the comb mode amplitudes (Fig. 1B) (*25, 26*). Assuming time-stationary noise processes, the shot-noise–limited photocurrent fluctuations in a 1-Hz bandwidth are expressed as $\sigma_{SNL} = \sqrt{2ei_{avg}}$, where e is elementary charge and i_{avg} is average photocurrent (*27*). We refer to this limit as the time-stationary SNL. In some cases, it is possible to surpass this SNL in comb measurements by utilizing the cyclo-stationary pulsed properties of the photocurrent noise (*28, 29*) or by including the higher frequency "copies" of the dual-comb interferogram (*6*). By contrast, our work shows that quantum states of light can be utilized to overcome the time-stationary SNL in DCS. Quantum-enhanced techniques should also surpass the cyclo-stationary limits.

Our quantum-enhanced method addresses properties of dual-comb measurements that previous theoretical approaches do not fully capture. In the time domain, the interferogram can be decomposed into two regions: zero optical path difference (centerburst) and large

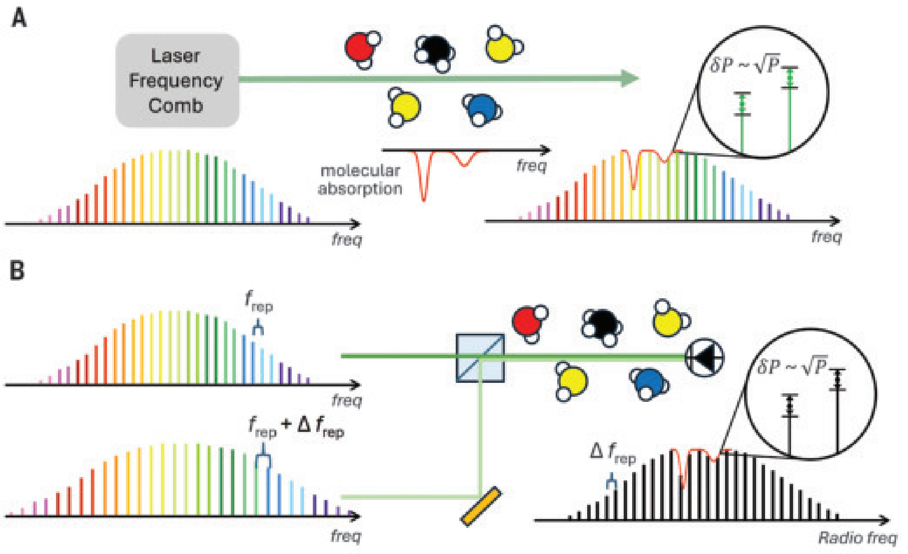

Fig. 1. Frequency comb spectroscopy and quantum noise. (**A**) Schematic of direct OFC spectroscopy. Molecular absorption is imprinted on the OFC and the ultimate quantum sensitivity limit is set by amplitude shot noise on the individual comb modes. (**B**) The interference of two OFCs with a difference in repetition rates (Δf_{rep}) maps optical frequencies to radio frequencies in a one-to-one manner. The Fourier transform of the photodetector output generates a radio frequency comb signal. Here, the ultimate sensitivity limit is set by shot noise on the radio frequency comb modes.

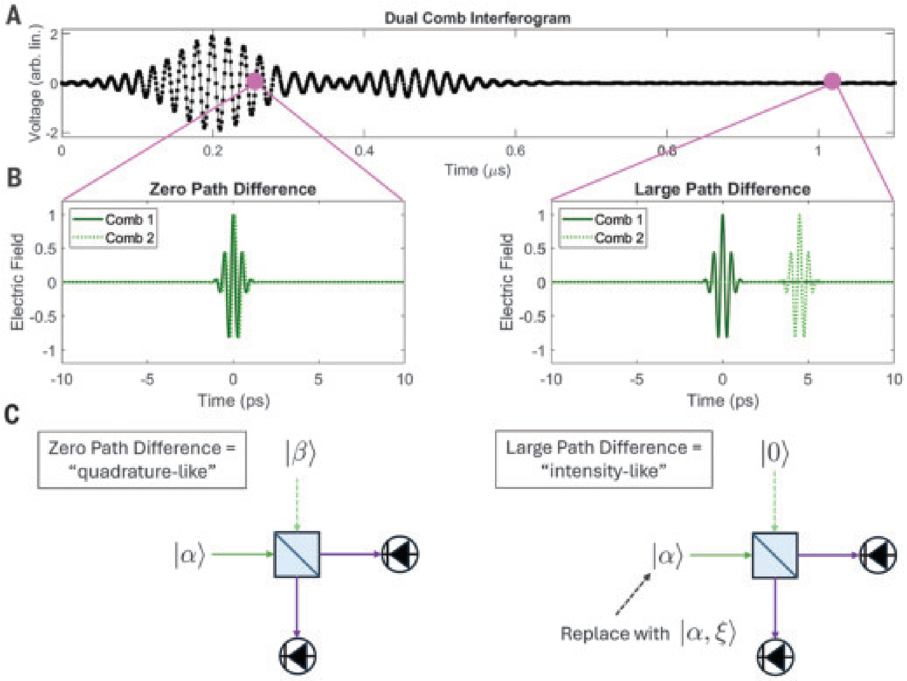

Fig. 2. Time-domain quantum measurement picture of dual-comb interferometry. (**A**) A digitized interferogram where the *x*-axis is lab time. Each interferogram point arises from the integrated interferometric overlap of two subsequent pulses from the dual combs. This concept is illustrated further in (**B**) where we show a simplified model of electric fields generating the interferogram from zero path difference (left) and large path difference (right) cases. Here, the *x*-axis is effective optical path separation time. (**C**) Simplified single-mode picture of quantum measurement in two extreme cases. For zero path difference, the measurement obtains a quadrature-like character that one would receive from interfering two coherent states of intensityand on a beamsplitter. For large path difference, the measurement has an intensity-like character which amounts to interfering a coherent state with a vacuum state (from the perspective of either OFC). The quantum noise of a dual-comb measurement is reduced by replacing the coherent state with an amplitude-squeezed state of intensity and squeezing factor ξ (*38*).

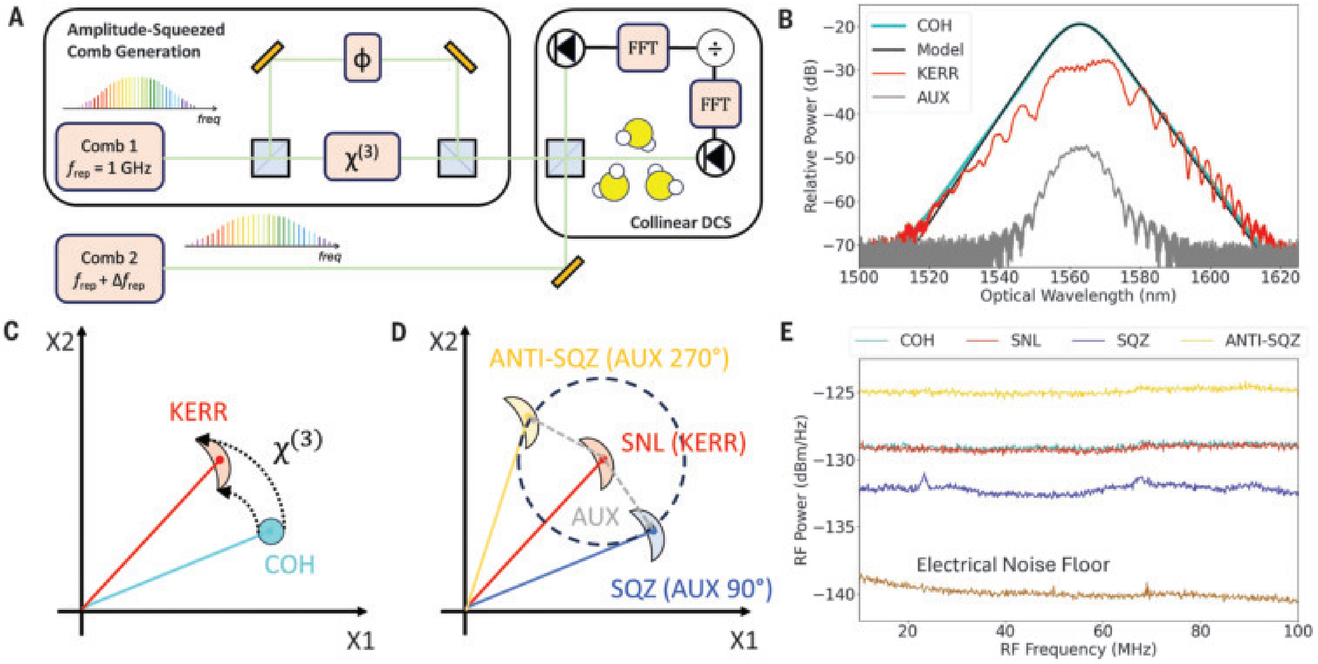

Fig. 3. DCS schematic and single-comb squeezing concept with results. (**A**) Simplified schematic of quantum-enhanced DCS setup. A nonlinear Mach-Zehnder interferometer generates an amplitude-squeezed frequency comb, which is then combined with a coherent state frequency comb. Molecules are placed in one of the dual-comb beams, each of which is detected, digitized and then fast Fourier-transformed (FFT). The outputs are then divided to generate a quantum-enhanced normalized transmission spectrum. (**B**) Optical spectrum of the unsqueezed coherent state OFC (COH, light blue, with soliton model spectrum in black), strong squeezed pulse (KERR, red) after propagation through PM-HNLF, and the weak auxiliary pulse (AUX, gray) after propagation on the orthogonal axis of the PM-HNLF. (**C**) Phase space diagram for generation of Kerr squeezed states. An amplitude-dependent phase shift generates a tilted crescent-shaped distribution (KERR) from a coherent state (COH). X1 and X2 represent the bosonic quadrature operators, analogous to position and momentum. (**D**) Phase space diagram of auxiliary pulse displacement. By displacing the KERR state (SNL) with the appropriate magnitude and phase, we produce an amplitude-anti-squeezed (ANTI-SQZ) or amplitude-squeezed state (SQZ). (**E**) Electrical spectrum of photocurrent noise of coherent, Kerr, auxiliary-displaced squeezed, and auxiliary-displaced anti-squeezed states, with the electrical noise floor in brown (*33*).

path difference. In the centerburst, the optical pulses from each OFC are overlapped in time and the measurement is mode-matched (Fig. 2, A and B). The centerburst contains information about the spectral envelope of the two OFCs, whereas absorption by a molecular or atomic gas is observed as a FID signal that is mostly separated in time from the centerburst (*3*). From the quantum optical perspective (Fig. 2C), classical centerbursts are generated by a beamsplitter interaction between a coherent state from the first OFC and a mode-matched coherent state from the second OFC, resulting in a "quadrature-like" measurement (*30*). Here, the phase and amplitude noise quadratures of the comb fields are accessed by means of homodyne or heterodyne comparisons, which provide a pure quadrature measurement in the strong local oscillator comb limit (*31*). For large optical path differences, the two pulse trains are temporally separated. This region is modeled by a beamsplitter interaction between coherent states from either OFC and a vacuum state which results in an "intensity-like" measurement (*30*). Thus, for large path differences, the noise is derived from the shot noise of the independent OFCs for any comb power ratio. Because the duty cycle (ratio of the pulse length to the pulse repetition period) of the 1-GHz OFC used in the experiment is about 0.025%, the quantum noise of DCS is dominated by intensity-like measurement noise.

For the FID, the noise remains dominated by shot noise from an intensity-like measurement provided that the absorption depth and the corresponding FID ringing is small. Equivalently, the mode mismatch between the long-duration, narrow-bandwidth FID pulse and the short-duration, broadband sampling comb pulse allows the FID to be approximately treated as vacuum. This interpretation is consistent with analyses of traditional Fourier transform spectroscopy (FTS). When compared with tunable laser spectroscopy, FTS techniques (including DCS) suffer a noise penalty due to shot noise from photons that do not interact with the absorbing medium (*32*). We gain an advantage in DCS by using a bright-amplitude–squeezed OFC to reduce the shot noise in the large path difference region assuming small absorption depths and loss, consistent with previous analyses (*10*). Although amplitude squeezing adds phase noise to the detected FID signal, colinear detection is sensitive to the FID magnitude and thus the absorption measurement should not be biased by this added noise. A full quantum treatment of the centerburst region will enable extensions of quantum-enhanced dual-comb interferometry for other applications, such as ranging and time transfer.

Single-comb squeezing

A simplified schematic of the squeezed dual-comb spectrometer is shown in Fig. 3A [details in (*33*)]. The OFCs are generated using two femtosecond lasers with 1-GHz repetition rates (*4*) emitting soliton pulses centered at 1563 nm (Fig. 3B). The OFCs are phase-locked to a common optical reference to ensure mutual coherence. One OFC is compressed to 260 fs and split into a strong pulse (24 mW average power) and a weak auxiliary pulse at a 10:1 power ratio. These pulses are coupled onto the orthogonal polarization axes of a $\chi^{(3)}$ nonlinear fiber, where the strong pulse experiences an intensity-dependent phase shift as a result of the Kerr effect. In phase space, this transforms the uncertainty of the coherent state to a crescent-like squeezed noise distribution (Fig. 3C). Because the Kerr effect is photon-number–conserving, the squeezing angle is aligned such that an intensity noise measurement of the

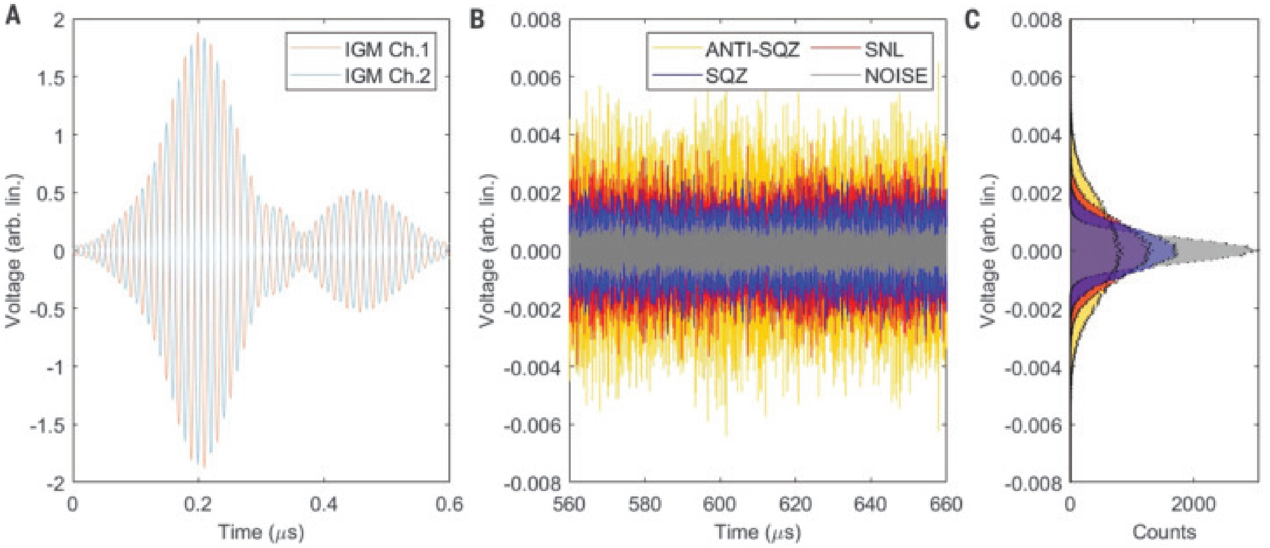

Fig. 4. Dual-comb time-domain data. (**A**) Nearly identical interferograms generated on each side of the combining beamsplitter. Note the 180° phase shift between the two interferograms. The interferograms have been digitally filtered (center frequency 50 MHz; bandwidth 20 MHz). (**B**) Interferogram signal at large path difference after digital addition of two detector signals under four experimental conditions. The SNL is the undisplaced Kerr state. The displaced SQZ and ANTI-SQZ states are shown along with the electrical detection chain noise floor (gray). A QNR of 2.6 dB is estimated between SNL and SQZ. (**C**) Histogram of voltage noise from (B) clearly showing QNR and quantum noise amplification of SQZ and ANTI-SQZ states.

undisplaced Kerr state yields the same value as the input coherent state (i.e., the time-stationary SNL) (*20*). By slightly displacing the Kerr state, the squeezing angle is shifted such that quantum noise reduction (QNR) or quantum noise amplification is observable on an intensity measurement. This small displacement is implemented by recombining the strong squeezed state pulses and the weak auxiliary coherent state pulses (with an adjustable phase shift applied) on a variable beamsplitter at a 100 to 1 power ratio. For relative phases of approximately 90° or 270°, the displaced state has the same mean field amplitude as the original Kerr state but with observable squeezing or anti-squeezing of the amplitude quadrature variance (Fig. 3D).

We use a single high quantum efficiency (η = 93%) photodetector to characterize the squeezing of the Kerr state (fig. S1). A calibration curve is recorded at varying optical power levels to demonstrate the shot-noise-limited nature of the OFC (fig. S2). With the auxiliary pulse, we measure up to 3.8 dB of squeezing and 4.0 dB of anti-squeezing near 45 MHz and >3-dB squeezing in a broader window from 10 MHz to 100 MHz (Fig. 3E). The most squeezing is measured when 14.7 mW of the Kerr state is recombined with ~150 μW of the auxiliary pulse (after coupling losses), which is comparable to previous measurements (*20*). Without the auxiliary pulse, the measured intensity noise matches that of a coherent state OFC of equivalent power, as expected. Another high-speed detector with η = 70% is used to measure squeezing from 20 MHz to 500 MHz at the ~2 dB level (fig. S3). Generally, quantum sensing applications have utilized either broadband low-frequency squeezing [e.g., Laser Interferometer Gravitational-Wave Observatory (LIGO)] or narrowband, high-frequency squeezing (*34, 35*). While broadband high-frequency squeezing is used for quantum information processing (*36*), our results demonstrate that DCS is another compelling application for bright broadband squeezing. For example, with a 5-kHz repetition rate difference, the 500-MHz electrical bandwidth supports >90 THz of quantum-enhanced DCS.

Colinear quantum-enhanced DCS

The time-domain picture of DCS shows that bright squeezed states can be used for quantum enhancement. However, we must consider which dual-comb geometries are compatible with the use of bright amplitude-squeezed states. Recently, a quantum-enhanced DCS scheme proposed two-mode squeezing between a comb mode and its sidebands with the absorber in the path of one OFC before the combining beamsplitter (i.e., asymmetric DCS) (*3, 10*). However, this two-mode squeezing proposal is not trivial to implement using off-the-shelf components. Alternatively, we employ one OFC in a bright single-mode amplitude-squeezed state, which is produced with the established and simple technique described above (*20*). After mixing the squeezed OFC with a coherent state OFC on a beamsplitter, the output interferograms will have opposite signs and the quantum noise will be partly anticorrelated. The optimal measurement strategy for asymmetric DCS is balanced photodetection, but this photocurrent subtraction would both maximize the DCS signal and destroy the squeezing advantage.

Instead, we send the combined OFCs through the absorber (i.e., colinear DCS) (fig. S4). In this case, the absorption signal is imprinted on one interferogram while the other interferogram acts as a spectral baseline reference. Fourier transformation of the two interferograms yields complex spectra which can be divided to produce an enhanced estimate of molecular transmittance (see supplementary materials for derivation). Importantly, the time-domain correlations generated by squeezing persist in the spectral domain as a result of the linearity of Fourier transformation. Furthermore, in the limits of high SNR and low absorbance, spectral division treats anticorrelated noise similarly to time-domain addition of the photocurrents, which is the standard method for characterizing amplitude-squeezed states (*37, 38*). We digitally post-process two interferograms separately for easy comparison of time-domain addition and spectral division. Adding the two photocurrents cancels the opposite sign interferograms, in a manner similar to that of optical techniques used for background suppression in DCS (*39*). Here, the noise is also anticorrelated and is thus also partially cancelled by the photocurrent addition.

Experimentally, we generated interferograms between the amplitude-squeezed OFC (~15 mW) and a weak (~10 μW) coherent state OFC. Even with this imbalance, the DCS data has a quality factor comparable to the state-of-the-art (>10^7 Hz$^{-1/2}$) (*3*). We set the optical lock frequencies to center the interferogram at 50 MHz. With a repetition rate difference of 5.6 kHz, the dual-comb spectrum covers a RF bandwidth of ~25 MHz. The two centerbursts are matched

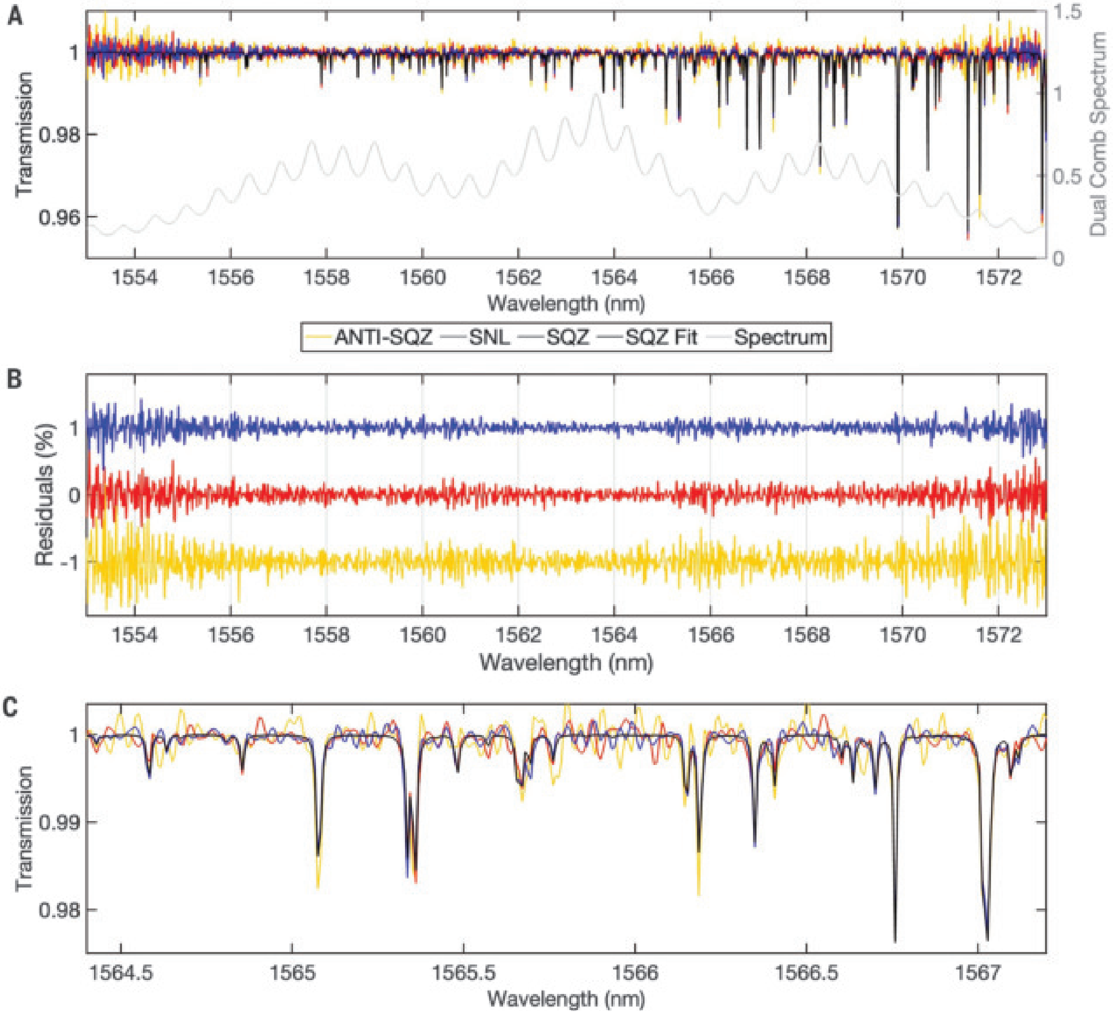

Fig. 5. Dual-comb transmission spectrum and fits. (**A**) Averaged dual-comb transmission spectrum generated from the ratio of the Fourier transform of each individual channel. These data are obtained from the averaging of 1112 interferograms or ~198 ms of data acquisition. The narrow H_2S absorption features are most clearly visible in the black curve, which is a fit to the SQZ dataset. In gray, a dual-comb spectrum from one of the channels is shown for reference. (**B**) Residuals (transmission minus fit) are shown for three cases: SNL (red), SQZ (blue), and ANTI-SQZ (yellow). For this averaging condition, the QNR was ~2.6 dB. The variation in the noise of the residuals results from the uneven power in the dual-comb spectrum that is shown above. (**C**) Zoom-in on several H_2S absorption lines showing the high-quality nature of the data and fitting routine.

except for a 180° phase shift (Fig. 4A). In initial analysis, the raw interferograms are temporally aligned using a cross correlation and summed (Fig. 4, B and C). The quantum noise away from the centerburst is then analyzed for the no auxiliary pulse (SNL), squeezed (SQZ) and anti-squeezed (ANTI-SQZ) cases. The raw time-domain QNR is 55% (2.6 dB). When we account for the electrical noise floor of the high-speed digitizer, the squeezing level is 3.5 dB. Similar QNR is obtained if the SNL is derived by either adding the photocurrents with no auxiliary pulse or by subtracting the squeezed photocurrents. These results confirm the single-comb squeezing measurements and show that the squeezing translates to a dual-comb context.

Frequency-domain DCS results

Measuring comb-mode–resolved spectra with our quantum-enhanced dual-comb system requires interferogram phase correction (fig. S5) to remove comb phase and timing fluctuations (*40, 41*). The mode-resolved spectrum of each individual channel's phase-corrected interferogram train shows signatures of squeezing (fig. S6). Next, the phase-corrected interferograms are co-added to generate one high SNR interferogram per channel. The full QNR is revealed after the interferograms from each channel are phase-aligned using a cross-correlation, Fourier-transformed (FFT), and divided to yield a transmission spectrum. Remaining spectral baseline variations are corrected using cepstral domain filtering, which simultaneously removes etalons and noise at extremely large path length differences (*42*). We fit the transmittance to a HITRAN2020 model (*24*) using a nonlinear least squares regression to extract number density with pressure, temperature, and path length as input parameters. The fit covers a 20-nm bandwidth centered at 1563 nm and includes 67 rovibrational transitions of H_2S with spectral line intensity above 10^{-23} cm^{-1}/ (molecule × cm^{-2}) (Fig. 5, A and B). The cell's low pressure (100 Torr) produces linewidths of ~1 GHz and thus only a few comb modes sample any given absorption feature (Fig. 5C). Nonetheless, our data closely matches the model with residuals in the subpercent regime in <10 ms of averaging, validating the performance of our processing algorithm.

Further analysis of the fit residuals shows that they average as in all three conditions (SNL, SQZ, and ANTI-SQZ), where N_i is the number of averaged interferograms (fig. S7). A power law is fit to each of the three conditions to reveal the reduction in noise as function of number of averages. The squeezing or anti-squeezing acts to change the constant prefactors on this power law (*9*). The ratio of the constant prefactors between the SQZ and SNL cases is 0.51, representing a 2.9-dB improvement in power SNR (equivalently a 2× quantum speed up), nearly the same result seen in the raw time-domain data.

A similar QNR is seen in the spectral domain as the residuals vary with the dual-comb power (fig. S8). We also note that the squeezing did not bias the fit result which also showed improved precision matching the QNR in the time and frequency domains. Specifically, the fitted number density in ANTI-SQZ, SNL, and SQZ cases are respectively 5.197 ± 0.150 mol/m^3, 5.427 ± 0.098 mol/m^3, and 5.382 ± 0.072 mol/m^3, demonstrating that squeezing reduces the uncertainty in the determination of the concentration. All fit values are statistically consistent with the cell manufacturer's stated number density of 5.454 mol/m^3 (corresponding to 100 Torr at 294 K). With the current dataset, we were not able to conclude whether squeezing was degraded at points of higher molecular absorption (fig. S9).

Finally, we note that the resolution limit of the demonstrated colinear DCS technique is ~50 MHz. This limit is set by the optical mode frequency separation rather than the comb mode linewidth as is assumed for asymmetric DCS and could be improved by modeling the effects of spectral sampling at two sets of frequencies. This resolution is sufficient for a large array of applications, including atmospheric spectroscopy (*22*).

Discussion and outlook

We have incorporated advances from quantum optical sensing into frequency comb metrology which allows us to realize quantum-enhanced mode-resolved DCS over an unprecedented 2.5-THz optical bandwidth with 2.9 dB QNR below the SNL. Our simple implementation employs bright Kerr squeezing and colinear spectroscopy to realize a significant metrological advantage that was not predicted in recent theoretical proposals. Consequently, this work will stimulate research to test the limits of quantum-enhanced OFC metrology and spectroscopy. For example, other DCS geometries can be evaluated over a range of comb powers and combined with larger amounts of squeezing using different platforms. Although it is known that Raman effects in fibers limit the achievable squeezing (*43*), these effects may be less deleterious to nanophotonic squeezing platforms [e.g., silicon nitride (*44*)].

Furthermore, our work provides a foundation for investigating even greater increases in the SNR achievable with quantum-enhanced DCS. To maximize the SNR, the two OFCs should be power-matched. However, this poses a challenge for digital processing as a single analog-to-digital converter (ADC) cannot simultaneously record the centerburst and the quantum-limited electrical noise floor. One path to overcome this limitation would involve combining multiple ADCs to yield a wider dynamic range (*45*). Related techniques are already being explored to boost the dynamic range of cross-comb spectroscopy (*46*). With an improved ADC dynamic range and power-balanced OFCs, the largest possible SNR in a colinear DCS experiment results from squeezing both OFCs, as we outline in the supplementary materials. Two power-matched squeezed OFCs in a colinear experiment could achieve a QNR of ~7 dB, which is the greatest reported level of Kerr fiber squeezing (*43*). Efforts to maximize SNR should also investigate whether quantum-enhanced DCS techniques are compatible with multicopy (*6*) and/or frequency-multiplexed DCS techniques (*25*).

Squeezed DCS will have a number of immediate use cases including improved characterization of fast reaction kinetics (*4*), reduced power levels for spectro-imaging of biological samples (*23*), and improved SNR to overcome limitations arising from detector nonlinearities (*3*). Quantum-enhanced DCS with small sample absorption and high SNR will be critical for trace gas analysis at atmospheric pressures (*22*). Additionally, quantum-enhanced DCS techniques will reduce the amount of time required to obtain high SNR background spectra for time-resolved experiments (*4*). The present measurements extend over 2.5 THz but many applications will benefit from still broader optical bandwidth of squeezed states, as has been recently demonstrated with nanophotonic technology (*17*). As an FTS variation with improved speed, sensitivity, and frequency axis traceability, DCS presents numerous opportunities for trace gas sensing, spectro-imaging and industrial analysis. Although FTS has begun to harness single photon states (*47*), no FTS technique has yet taken advantage of bright squeezed states of light. Our insights into the quantum noise of DCS have pushed the state-of-the-art for quantum FTS as a whole. Finally, this work will inform quantum-enhanced versions of OFC heterodyne and homodyne techniques for applications in distance metrology, optical clock comparison, and optical time transfer.

REFERENCES AND NOTES

1. S. A. Diddams, K. Vahala, T. Udem, *Science* **369**, eaay3676 (2020).
2. N. Picqué, T. W. Hänsch, *Nat. Photonics* **13**, 146–157 (2019).
3. I. Coddington, N. Newbury, W. Swann, *Optica* **3**, 414–426 (2016).
4. N. Hoghooghi *et al.*, *Optica* **11**, 876–882 (2024).
5. C. Zhang *et al.*, *Nature* **633**, 63–70 (2024).
6. M. Walsh, P. Guay, J. Genest, *APL Photonics* **8**, 071302 (2023).
7. B. Xu, Z. Chen, T. W. Hänsch, N. Picqué, *Nature* **627**, 289–294 (2024).
8. E. D. Caldwell *et al.*, *Nature* **618**, 721–726 (2023).
9. E. S. Polzik, J. Carri, H. J. Kimble, *Phys. Rev. Lett.* **68**, 3020–3023 (1992).
10. H. Shi *et al.*, *NPJ Quantum Inf.* **9**, 1–12 (2023).
11. A. Belsley, *Phys. Rev. Lett.* **130**, 133602 (2023).
12. O. Pinel *et al.*, *Phys. Rev. Lett.* **108**, 083601 (2012).
13. C. Riek *et al.*, *Nature* **541**, 376–379 (2017).
14. M. A. Guidry, D. M. Lukin, K. Y. Yang, R. Trivedi, J. Vučković, *Nat. Photonics* **16**, 52–58 (2022).
15. N. C. Menicucci, S. T. Flammia, O. Pfister, *Phys. Rev. Lett.* **101**, 130501 (2008).
16. S. Wang *et al.*, *Phys. Rev. A* **98**, 053821 (2018).
17. R. Nehra *et al.*, *Science* **377**, 1333–1337 (2022).
18. M. Rosenbluh, R. M. Shelby, *Phys. Rev. Lett.* **66**, 153–156 (1991).
19. C. X. Yu, H. A. Haus, E. P. Ippen, *Opt. Lett.* **26**, 669–671 (2001).
20. M. Fiorentino, J. E. Sharping, P. Kumar, D. Levandovsky, M. Vasilyev, *Phys. Rev. A* **64**, 031801 (2001).
21. N. Kalinin *et al.*, *Nanophotonics* **12**, 2945–2952 (2023).
22. F. R. Giorgetta *et al.*, *Laser Photonics Rev.* **15**, 2000583 (2021).
23. T. Ideguchi *et al.*, *Nature* **502**, 355–358 (2013).
24. I. E. Gordon *et al.*, *J. Quant. Spectrosc. Radiat. Transf.* **277**, 107949 (2022).
25. N. R. Newbury, I. Coddington, W. Swann, *Opt. Express* **18**, 7929–7945 (2010).
26. M. Walsh *et al.*, in *Optica Sensing Congress 2023 (AIS, FTS, HISE, Sensors, ES)* (Optica Publishing Group, 2023), p. JTh1A.1.
27. P. J. Winzer, *J. Opt. Soc. Am. B* **14**, 2424–2429 (1997).
28. F. Quinlan *et al.*, *Nat. Photonics* **7**, 290–293 (2013).
29. J.-D. Deschênes, J. Genest, *Phys. Rev. A* **87**, 023802 (2013).
30. N. Lordi, E. J. Tsao, A. J. Lind, S. A. Diddams, J. Combes, *Phys. Rev. A* **109**, 033722 (2024).
31. H. A. Haus, *Electromagnetic Noise and Quantum Optical Measurements* (Springer, 2000).
32. D. T. D. Childs *et al.*, *Appl. Spectrosc. Rev.* **50**, 822–839 (2015).
33. Materials and methods are available as supplementary materials.
34. W. Jia *et al.*, *Science* **385**, 1318–1321 (2024).
35. J. Junker, D. Wilken, E. Huntington, M. Heurs, *Opt. Express* **29**, 6053–6068 (2021).
36. V. D. Vaidya *et al.*, *Sci. Adv.* **6**, eaba9186 (2020).
37. S. F. Pereira, M. Xiao, H. J. Kimble, J. L. Hall, *Phys. Rev. A.* **38**, 4931–4934 (1988).
38. H.-A. Bachor, T. C. Ralph, *A Guide to Experiments in Quantum Optics* (Wiley, 2019).
39. T. Tomberg, A. Muraviev, Q. Ru, K. L. Vodopyanov, *Optica* **6**, 147–151 (2019).
40. J. Roy, J.-D. Deschênes, S. Potvin, J. Genest, *Opt. Express* **20**, 21932–21939 (2012).
41. N. B. Hébert *et al.*, *Opt. Express* **25**, 8168–8179 (2017).
42. R. K. Cole, A. S. Makowiecki, N. Hoghooghi, G. B. Rieker, *Opt. Express* **27**, 37920–37939 (2019).
43. R. Dong *et al.*, *Opt. Lett.* **33**, 116–118 (2008).
44. F. Gyger *et al.*, *Phys. Rev. Lett.* **124**, 013902 (2020).
45. P. F. Bernath, *J. Quant. Spectrosc. Radiat. Transf.* **186**, 3–16 (2017).
46. C. P. Bauer *et al.*, *Nat. Commun.* **15**, 7211 (2024).
47. Y. Mukai, R. Okamoto, S. Takeuchi, *Opt. Express* **30**, 22624–22636 (2022).
48. D. I. Herman *et al.*, Squeezed dual-comb spectroscopy, Dryad (2024); https://doi.org/10.5061/dryad.4qrfj6qkc.

ACKNOWLEDGMENTS

We thank J.-D. Deschênes, C. Rau, S. Geller and A. Kyle for helpful discussions. We thank J. Ye and N. Newbury for valuable comments on the manuscript. We also thank K. Cossel, I. Coddington, and T.-H. Wu for loaning technical equipment. **Funding:** The authors acknowledge funding from the NSF QLCI Award OMA-2016244 and ONR N000142212438. E.J.T. acknowledges support from the NDSEG Fellowship. M.K.K. and M.H. acknowledge support from the NSF Graduate Research Fellowship Program. M.W. and J.G. acknowledge support from NSERC and Photonique Quantique Québec (PQ2). **Author contributions:** Conceptualization: D.I.H., M.W., M.K.K., N.L., E.J.T., J.C., J.G., and S.A.D. Methodology: D.I.H., M.W., M.K.K., A.J.L., M.H., J.G., and S.A.D. Software: D.I.H., M.W., M.K.K., and J.G. Formal analysis: D.I.H., M.W., M.K.K., N.L., J.C., J.G., and S.A.D. Investigation: D.I.H., M.K.K., M.W., J.G., and S.A.D. Resources: J.G. and S.A.D. Writing – original draft preparation: D.I.H., M.K.K., J.G., and S.A.D. Writing – review and editing: All authors. Visualization: D.I.H., M.K.K., M.W., J.G., and S.A.D. Supervision: J.C., J.G., and S.A.D. Project administration: S.A.D. Funding acquisition: J.C. and S.A.D. **Competing interests:** The authors declare no competing interests. **Data and materials availability:** All data needed to evaluate the conclusions in the paper are present in the figures of the paper and/or the supplementary materials. The data can also be accessed at Dryad (*48*).

SUPPLEMENTARY MATERIALS

science.org/doi/10.1126/science.ads6292
Materials and Methods
Supplementary Text
Figs. S1 to S9
References (*49*–*50*)

Submitted 28 August 2024; accepted 30 December 2024
Published online 16 January 2025
10.1126/science.ads6292

BIOMATERIALS

Does the mantis shrimp pack a phononic shield?

N. A. Alderete[1], S. Sandeep[2], S. Raetz[2], M. Asgari[1]†, M. Abi Ghanem[3]*, H. D. Espinosa[1]*

The powerful strikes generated by the smasher mantis shrimp require it to possess a robust protection mechanism to withstand the resultant forces. Although recent studies have suggested that phononic bandgaps complement the mantis shrimp's defensive suite, direct experimental evidence for this mechanism has remained elusive. In this work, we explored the phononic properties of the mantis shrimp's dactyl club using laser ultrasonic techniques and numerical simulations. Our results demonstrate that the dactyl club's periodic region functions as a dispersive, high-quality graded system, exhibiting Bloch harmonics, flat dispersion branches, ultraslow wave modes, and wide Bragg bandgaps in the lower megahertz range. These features effectively shield the shrimp from harmful high-frequency stress waves generated by cavitation bubble collapse events during impact.

Among the various notable evolutionary adaptations displayed by the animal kingdom (*1*–*6*) lies the ability to withstand high peak forces delivered over short periods of time (*7*). Perhaps the most formidable species that exhibits this capability is the renowned peacock mantis shrimp (*Odontodactylus scyllarus*), a smasher stomatopod native to the Indo-Pacific seabed (Fig. 1A). Despite its relatively small size (ranging from 3 to 18 cm), this mantis shrimp is known to execute a well-orchestrated strike sequence that spans over seven orders of magnitude in time (from hundreds of milliseconds to nanoseconds) (*8*) and reaches peak forces in the vicinity of ~1500 N (i.e., exceeding 1000 times its body weight) (*9*). At the center of this distinctive attack system is the mantis shrimp's dactyl club (Fig. 1B), a hammer-shaped appendage that impacts the target in less than 50 μs (*9*) and generates cavitation bubbles that, upon collapse (*8*, *10*), trigger ultrashort nanosecond shock waves with frequency contents that can reach hundreds of MHz (*11*, *12*). As such, each strike delivers a dual blow capable of breaking hard exoskeletons. Unlike other natural attack systems, which are used only once (*13*), the dactyl club can strike multiple times in between molting cycles without sustaining macroscopic fracture.

A major contributing element to the dactyl club's strike power is its hierarchical design, made from a limited but exquisitely tuned arrangement of mineral and organic materials (*14*). Three distinct layers make up the club from the exterior to the interior: the impact surface, the impact region, and the periodic region (Fig. 1C). The impact surface is a hard (~60 GPa), thin (~70 μm) hydroxyapatite coating that prevents catastrophic failure by exhibiting viscoplasticity and localized damage (*15*). Next, the impact region (~500 μm) consists of mineralized chitin fibers in a herringbone architecture, which enable damage dissipation through diffuse cracking, crack arrest, and crack deflection (*14*, *16*). Last, the periodic region features a spatially graded Bouligand arrangement of chitin fiber bundles [~80- to 10-μm pitch (p), 2° to 6° interlayer rotation angle (ψ)] (*17*), which modulates stress wave propagation during impact, akin to a backing layer. Together, these region-specific mechanisms form a synergistic protection system that withstands repeated high-intensity impacts without substantial damage.

It has been proposed that the Bouligand structure also endows the dactyl club with shear wave–filtering capabilities in the form of ultrasonic phononic bandgaps (i.e., select frequency ranges at which the propagation of elastic energy is forbidden or strongly attenuated) (*18*). Although phononic bandgaps have been put forward as an optimized engineering strategy for prey-predator interactions (*19*), experimental evidence of phononic behavior in nature remains rare, particularly when compared with the more extensively documented biophotonic phenomena (*20*). Notably, experiments have shown that the scales covering the wings of certain moth species have evolved to absorb sound waves, through local resonance in the 20- to 160-kHz range, and provide acoustic camouflage against the echolocating sonar of predatory bats (*21*).

Motivated by the limited understanding of the phononics of the dactyl club, we investigated the dispersion characteristics of the impact and periodic regions across various acoustic scales by using two optoacoustic setups and finite element analysis (FEA). Specifically, we analyzed surface acoustic wave (SAW) propagation in the MHz range within these regions using nanosecond and picosecond pump-probe laser ultrasonics (NLU and PLU, respectively) setups. Laser ultrasonics techniques were chosen for their ability to generate nondestructive ultrasonic and hypersonic waves and for their capacity to spatially interrogate the sample. The use of SAWs, which combine longitudinally and transversely polarized waves (with a predominant detection of the latter due to the technique's sensitivity to out-of-plane motion), was particularly suited for this study. This approach was grounded on the established notion that helicoidal fiber arrangements primarily influence shear wave propagation while leaving longitudinal waves mostly unaffected (*22*). Additionally, studying wave propagation on the surface of the dactyl club provided access to distinct local regions, offering a spatially targeted view of wave phenomena on the club. Selection of the temporal regime responds to the characteristic length scales of the periodic region and to the fact that shrimp impacts contain frequencies in the ultrasonic range (*9*), which has led to shrimp-inspired solutions that point to ultrasonic filtering as a key attenuation mechanism (*23*). Furthermore, combined access to nanosecond and picosecond scales provides insight into the hierarchy of the periodic region, from the effective medium scale down to the individual layers that make up the Bouligand structure. As such, and in line with the hypothesis of the dactyl club's phononic capabilities, our experimental measurements and computational analyses unveiled a complex phononic landscape, with dispersion effects stemming from a variety of mechanisms elicited by the multiscale, hierarchical nature of the dactyl club.

Results

NLU experiments

The phononic spectra of the dactyl club's impact and periodic regions were first investigated using a time-resolved pump-probe NLU method called transient grating spectroscopy (TGS; Fig. 1D). In TGS, two subnanosecond laser pump pulses are crossed at an angle at the aluminum-coated surface of the sample, forming an optical interference pattern (*24*). The elicited rapid thermoelastic expansion in the metal generates counterpropagating SAWs with an acoustic wavelength (λ_{ac}) equal to the spacing of the optical interference fringes. In the experiment, SAWs were monitored in the time domain by measuring the diffraction of a quasi–continuous wave probe beam caused by the transient vertical displacement of the surface (see materials and methods section S3). SAW-modes propagating in the xz plane (i.e., across or along the Bouligand layers) result in high-frequency oscillations in the signal. By varying the acoustic wavelength (Fig. 1D) and analyzing the spectrum of each measured signal, the frequency–acoustic wave number (f-k) relationship can be established, enabling characterization of the material's phononic dispersion.

---

[1]Department of Mechanical Engineering, Northwestern University, Evanston, IL, USA. [2]Laboratoire d'Acoustique de l'Université du Mans (LAUM), UMR 6613, Institut d'Acoustique–Graduate School (IA–GS), CNRS, Le Mans Université, Le Mans, France. [3]Universite Claude Bernard Lyon 1, CNRS, Institut Lumière Matière, Villeurbanne, France.
***Corresponding author. Email: maroun.abi-ghanem@univ-lyon1.fr (M.A.G.); espinosa@northwestern.edu (H.D.E.)**
†Present address: Department of Medical Engineering, University of South Florida, Tampa, FL, USA.

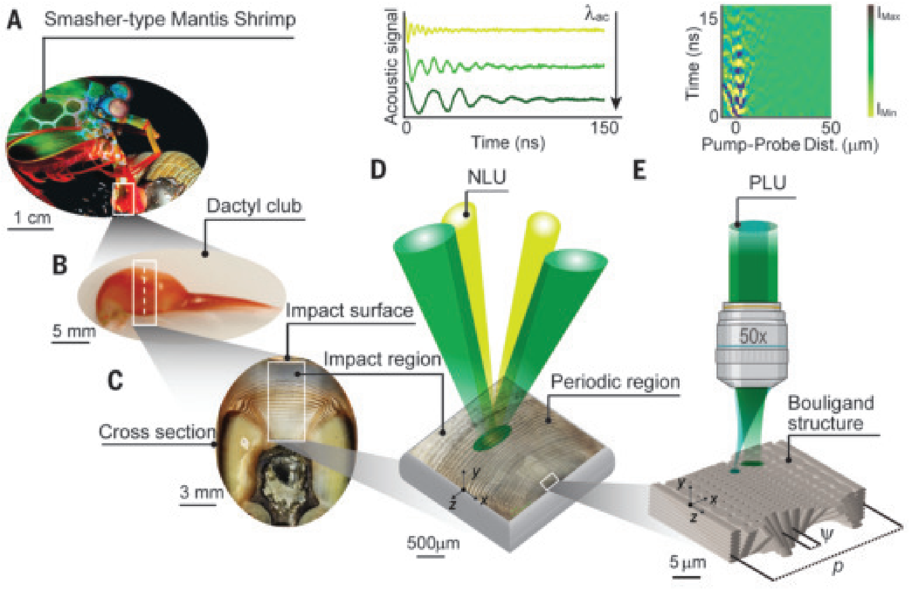

Fig. 1. Mantis shrimp club and our approach to characterize its phononic behavior. (**A**) Smasher mantis shrimp using its dactyl club against a seashell. [Photo credit: R. Caldwell] (**B**) Dissected dactyl club (whole, side view). (**C**) Transverse cross section of the club with distinct layers highlighted. (**D** and **E**) Schematic and characteristic signals of (D) NLU characterization of the impact and periodic regions by TGS and (E) PLU characterization by ASOPS, as well as a schematic of the Bouligand arrangement of the fibers with a relative angle between plies (ψ) and pitch (*p*).

The TGS technique provides access to surface acoustic phonons with wavelengths ranging from 6 to 31 μm.

To gain insight into the mechanical properties of the club, we measured the frequency variation of SAWs along the *z* direction at a fixed acoustic wavelength (λ_{ac} = 30 μm). We examined four different spots: one in the impact region (~200 μm from the impact–periodic region interface; blue spot in Fig. 2B) and three within the periodic region with characteristic pitches of *p* = 45, 40, and 35 μm (green, blue, and orange spots in Fig. 2B). We note that the pitch within the periodic region varies continuously in a gradient fashion and that the reported pitch values represent an average periodicity measured over the probed spot size. From measured frequencies, the variation in phase velocity of the SAWs was obtained from $v_{\text{SAW}}^{\text{LW}} = f_{\text{SAW}}\lambda_{\text{ac}}$, where LW is long wavelength, as shown in Fig. 2A. A clear change in phase velocity was identified from faster to slower speeds. These results are consistent with previously reported elastic modulus measurements of 30 to 60 GPa in the impact region and a lower modulus, ranging from ~10 to 20 GPa, in the periodic region (*14*).

Next, we performed TGS experiments to obtain dispersion curves for acoustic waves propagating along the *x* direction of the sample (Fig. 2C). The impact region exhibited a dispersionless curve with a single SAW mode at a phase velocity of 2380 m s^{-1}. By contrast, the periodic region displayed a more complex behavior, featuring two primary propagating SAW modes with average phase velocities of 3450 and 1540 m s^{-1}, corresponding to surface skimming longitudinal (SSL) and Rayleigh (R) waves, respectively. These velocities align well with longitudinal and transverse wave speeds estimated from composite properties by static indentation tests (*14*, *18*). The invariance of R- and SSL-wave velocities with respect to pitch is consistent with the presence of a composite made of transverse isotropic laminas with similar mechanical properties and stacking characteristics. Additionally, for pitches of *p* = 45 and 40 μm, another propagating mode with a phase velocity of 2030 m s^{-1} (SAW-2) branches from the R-wave mode around k = 0.3 μm^{-1}.

In addition to the aforementioned modes, we observe a mode parallel to the R-mode that was characterized by a similar group velocity ($v_g = d\omega/dk$, where ω is the angular frequency) but shifted by a spacing (Δ*k*). This shift is evident in all three dispersion diagrams of the periodic region (green, purple, and orange diagrams) but absent in the impact region (blue diagram) (Fig. 2C). Notably, this spacing, indicated by double-headed arrows in the diagrams, increases as the pitch decreases. Between the identified modes (dotted lines), several additional frequency peaks are detected, which appear to correspond to small segments of other acoustic modes (see, for example, the black and orange arrows in Figs. 2C and 3B, respectively, and spectrograms in supplementary text section S1). Additionally, low-frequency oscillatory signals (<50 MHz, mode A along dashed lines) are present in all dispersion diagrams, consistent with acoustic oscillations in air (*25*).

To interpret TGS experimental observations, we used finite element modeling (FEM) to simulate SAW propagation through idealized periodic microstructures with geometric pitches matching those in the experiments. Because the wavelengths probed by TGS are much larger than the fiber diameter and interfiber distance, we modeled the Bouligand microstructure as a composite laminate of transversely isotropic laminas. For the composite's physical and mechanical properties, we adopted values reported by Guarín-Zapata *et al.* (*18*), that is, ρ = 1400 kg m^{-3}, E_{T} = 30 GPa, E_{P} = 15 GPa, G_{TP} = 1.65 GPa, and $v_{\text{P}} = v_{\text{TP}}$ = 0.25, where ρ, *E*, and *G* are the density, elastic modulus, and shear modulus, respectively, and subscripts T and P refer to transverse and plane properties, respectively. The components of the stiffness matrix (C_{ij}), as a function of the ply rotation angle, are shown in the polar plots of Fig. 3A. We assumed an interply rotation angle of ψ = 5°, which resulted in ply thicknesses ($t = p\psi/180°$) on the order of ~1 μm, consistent with previous reports (*17*).

Figure 3B presents the FEM-obtained dispersion diagrams for *p* = 45, 40, and 35 μm alongside the experimental data. The computational results reveal a complex dispersion landscape with several key features. First, a repetitive pattern emerges, marked by parallel propagative lines above 25 MHz and characteristic branch folding (peaks and valleys) below 25 MHz. This pattern results from considering wave numbers that span multiple Brillouin zones (BZs), where the BZ length is BZ$\left[-\frac{\pi}{p}, \frac{\pi}{p}\right]$. As the pitch decreases, the number of repeated patterns decreases within the same wave number range. This periodic repetition of the pattern at exact integer multiples of the BZ gives rise to Bloch harmonic modes, highlighted for the SSL- and R-modes by white dashed lines. For instance, at *p* = 45 μm, ~6 Bloch harmonics fit within the wave number range 0 to 1 μm^{-1}, whereas at *p* = 35 μm, ~5 Bloch harmonics fit within the same range. These Bloch harmonic lines appear parallel because they share the same group velocity and correspond to the same acoustic mode. As the pitch decreases, the spacing between these Bloch harmonics (Δ*k*) increases. To focus on the most relevant features, we examined the first two BZs for *p* = 45 μm, as shown in the expanded view of Fig. 3B. The diagram reveals the nondispersive nature of the SSL-mode and the opening of a bandgap (indicated by dotted lines and BG) for the R-wave mode around 25 MHz, with a width of ~2 MHz. The different dispersion characteristics of these modes can be attributed to the modulation of the relevant elastic constants along the pitch: The SSL-mode, with its main displacement along the x axis, experiences no elastic modulation, whereas the R-wave, with its displacement along the y axis, is modulated elastically. The R-wave bandgap, predicted for all pitches (p = 45, 40, and 35 μm), widens as the pitch decreases.

By comparing the numerically obtained dispersion diagrams with the experimental data, we identified three key findings. First, the model-predicted phase velocities align well with the experimentally measured phase velocities of the R-wave and SSL-waves, validating both the model and the used mechanical properties. Second, consistent with simulations, R-wave

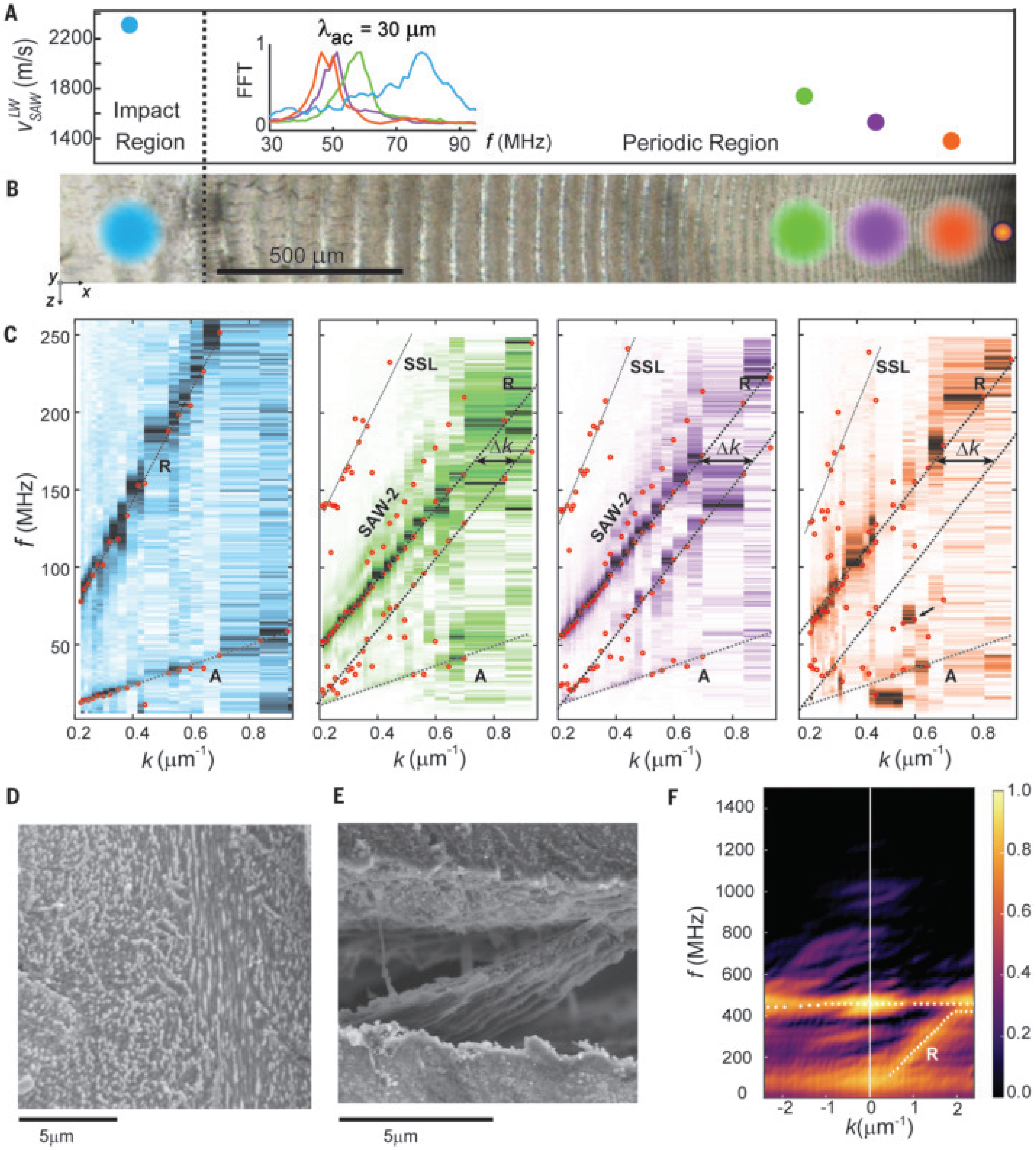

Fig. 2. Ultrasonic phononic dispersion of the mantis shrimp's dactyl club. (**A**) Frequency (f) spectrogram obtained by fast Fourier transform (FFT) and phase speed variation in the impact and periodic regions obtained by TGS at an acoustic wavelength (λ_{ac} = 30 μm). (**B**) Enlarged view of the cross section of the dactyl club with regions probed by TGS (large spot sizes) and PLU (small spot size); the colored regions illustrate the position and sizes of the probed regions. (**C**) Phononic dispersion curves obtained from TGS at locations highlighted in (B). (**D** and **E**) SEM images of the region probed by PLU showing (D) the chitinous-organic composite and (E) fiber bundles made of individual chitin fibrils. (**F**) Phononic dispersion curves obtained from PLU. Red and white dots in (C) and (F), respectively, represent pixels with maximum intensity in the pseudocolor plots.

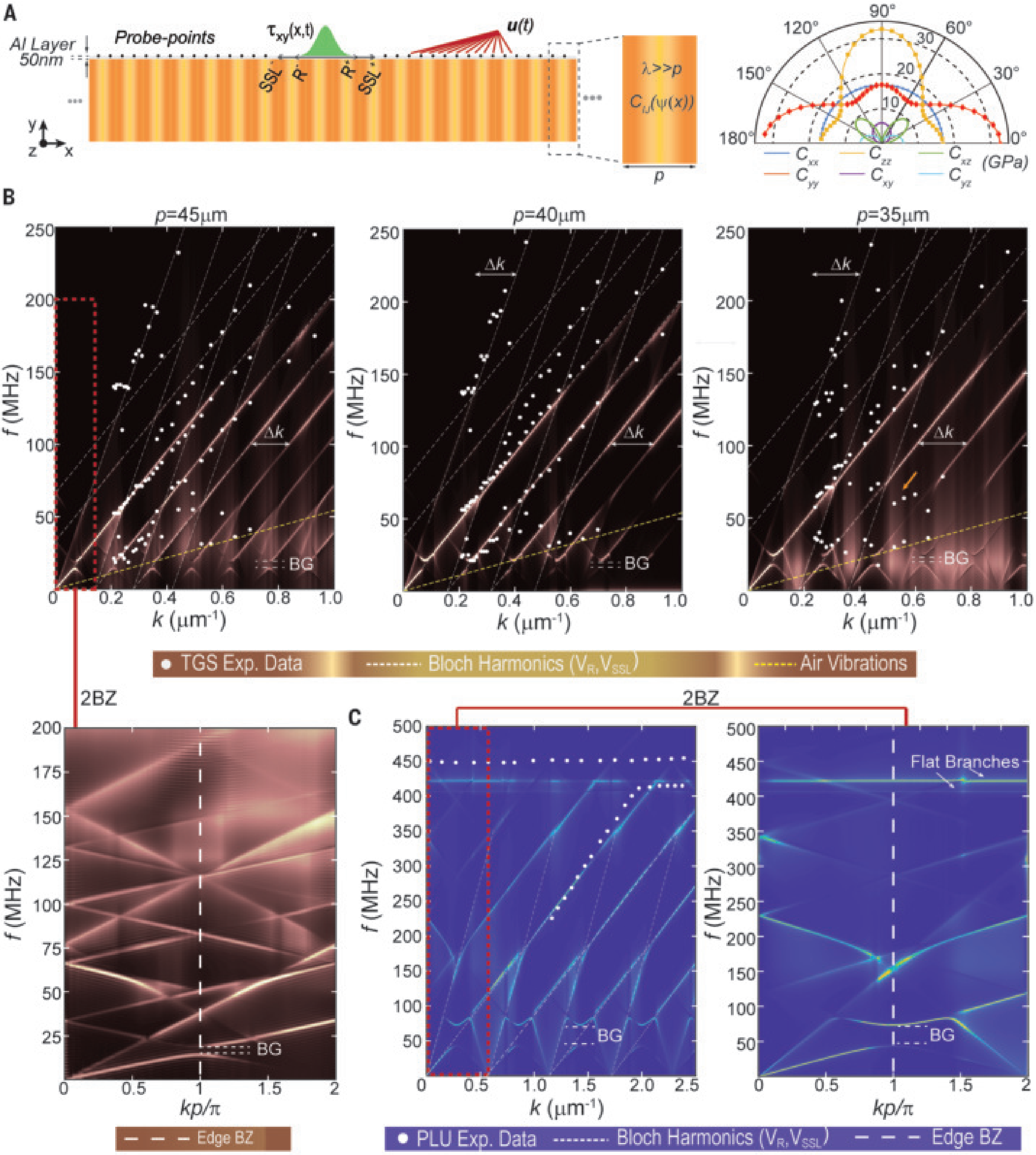

Fig. 3. Finite element simulations of phononic dispersion. (**A**) Schematic of simulation domain for surface wave propagation in the Bouligand microstructure. Applied surface traction τ_{xy} (x, t), displacement field $u(t)$ collection points (where u is displacement), and angular variation of the stiffness matrix components are shown. (**B**) FEM-obtained surface wave dispersion diagrams (k-f) for three pitches. Experimental points obtained with TGS are superimposed. For the case p = 45 μm, a detailed view of the first two BZs is shown (the edge of the first BZ is shown as a dashed line). In all cases, the bandgap for R-waves is highlighted. (**C**) FEM-obtained surface wave dispersion diagrams (k-f), with experimental points superimposed for the region probed by PLU. A zoomed-in view within the first two BZs is also depicted.

Bloch harmonic modes (parallel modes shifted by Δ*k* in Fig. 2C) are detected experimentally, whereas SSL-wave Bloch harmonics are less pronounced, likely because of the technique's sensitivity to *y*-axis displacement. Some peaks labeled as SAW-2 in Fig. 2C may correspond to SSL-wave Bloch harmonics crossing R-wave Bloch harmonics, or they could indicate a second pseudosurface acoustic mode, which is commonly seen in waves propagating on anisotropic surfaces (*26*). This second mode warrants further investigation beyond the scope of this study (see additional details in supplementary text section S3). Third, the observed increase in Δ*k* with decreasing pitch confirms

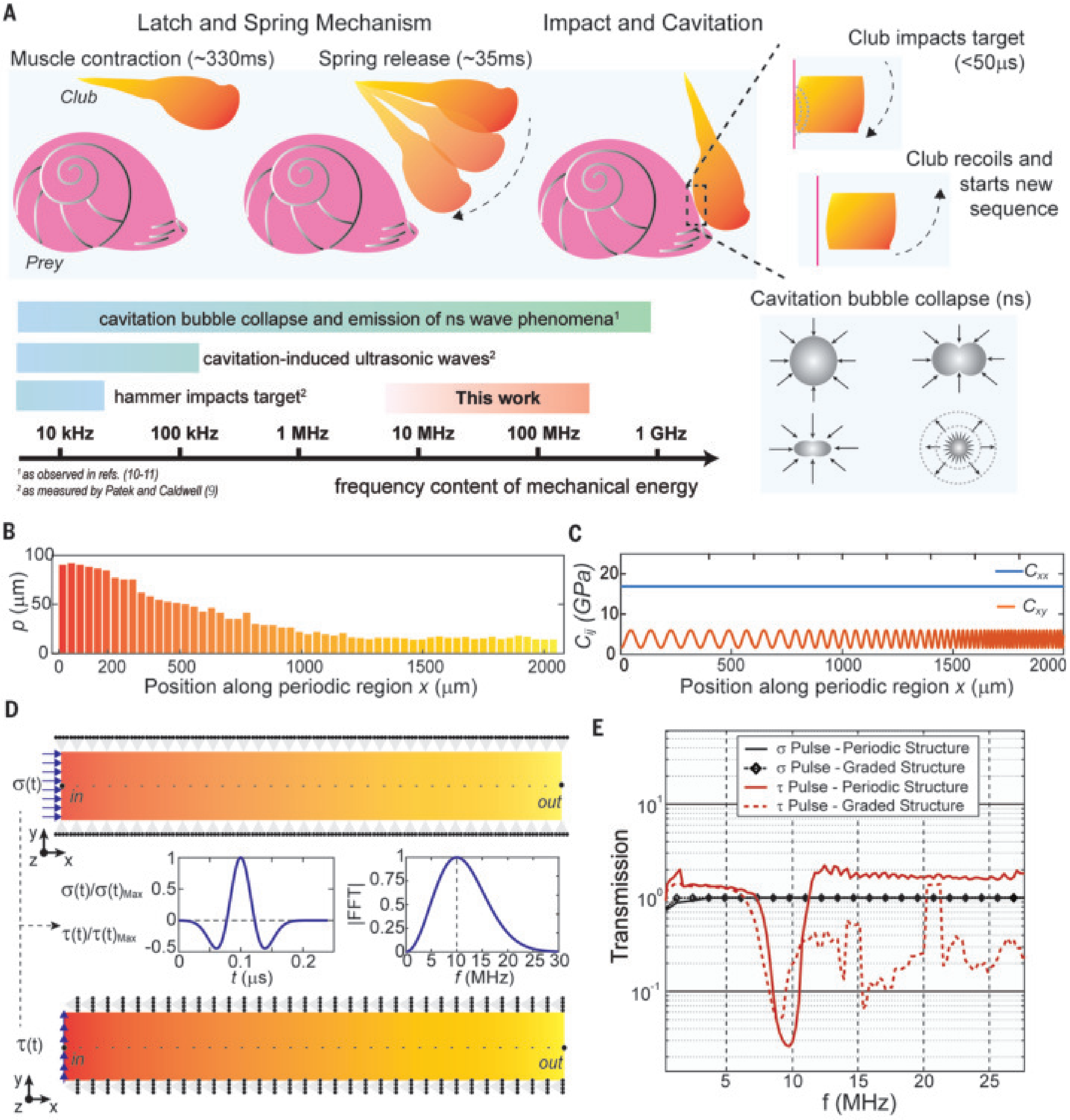

Fig. 4. Role of the mantis shrimp's graded microstructure in impact attenuation. (**A**) Key events in the strike sequence of the smasher mantis shrimp together with relevant timescales and frequency content. (**B**) Spatial modulation of the geometric pitch of the Bouligand microstructure as measured along the median axis of the club. (**C**) Modulation of elastic constants for spatially modulated microstructures with pitch following (B). (**D**) Schematics of FEA models for plane longitudinal and shear wave propagation in response to a Ricker-type pulse (pulse and spectrum are shown in the insets). (**E**) Transmission spectra of single-pitch periodic microstructure and graded microstructure under the applied pulses.

the parallel mode as a Bloch harmonic of the R-wave. The experimental detection of these modes highlights the high-quality periodicity of the structure, akin to a phononic crystal. Additionally, R-wave folding above the bandgap is observed but partially masked by air oscillations. Interestingly, when a simplified model consisting of laminates with isotropic plies exhibiting an oscillating elastic modulus is used, the model also captures the emergence of SSL-wave and R-wave Bloch harmonics [see supplementary text section S4 and (*27*)].

PLU experiments

Thus far, TGS experiments provided insight into the first-order hierarchical features within the periodic region of the mantis shrimp's dactyl club, revealing characteristics associated with the helicoidal laminate structure. At a finer hierarchical level (i.e., at smaller wavelengths), individual elements of the helicoidal laminate, such as chitin fiber bundles embedded in a soft matrix with an interfiber distance of ~1 μm (*17*), become discernible.

Scanning electron microscopy (SEM) images taken from a cracked portion of the club (Fig. 2, D and E) show these details. To explore this finer hierarchy, we used the ultrafast PLU technique, which involves femtosecond pump pulses focused normal to the sample surface, creating a circular spot (~1.25 μm in diameter). The pump pulses generated thermoelastic expansion in the Al layer, launching a broadband SAW pulse that propagated in the x-z plane of the sample. Time-domain detection was achieved through asynchronous optical sampling (ASOPS) between the pump and probe pulses (see materials and methods section S4) (*28*). The spatial information of the traveling waves is obtained by scanning the pump relative to the probe in a one-dimensional (1D) fashion (Fig. 1E), allowing the generation of space-time diagrams. From these diagrams, SAW dispersion curves are extracted by 2D Fourier transformation. This ASOPS-based PLU setup enables the resolution of wavelengths down to 2.5 μm, with the ability to probe surface modes up to several GHz (*29*). Thus, the technique extends the experimental window to wavelengths approaching the composite-layer characteristic length (e.g., fiber bundle diameter and interfiber distance) and, owing to the point-source geometry, also allows exploration of potential 3D effects that arise from material anisotropy and structure.

Figure 2F presents the dispersion diagram obtained with the PLU technique, highlighting two key observations. First, a primary SAW mode is observed with a phase velocity of 1350 m s^{-1}, closely matching the R-wave identified in TGS experiments (~6% difference). We identified this mode as the R-wave. Unlike the R-wave in TGS, this mode is dispersive, as evidenced by the folding near the end of the accessible wave number range (k ~ 2.1 μm^{-1}). Additionally, a flat branch is observed around ~450 MHz, extending across the entire probed wave number range. A small bandgap (~20 MHz) is identified between the R-wave mode and the flat mode. Notably, the R-wave mode was not detected for wave numbers $k < 1$ μm^{-1}. This can be attributed to two factors: the influence of the pump-related thermal background (low-frequency) near the pump and probe laser beams and the 3D effects inherent to the PLU technique due to point-source generation, which lead to wave attenuation at the observation point. This feature is important not only for interpreting the PLU results but also for gaining insights into the biomechanical function of the club, as discussed in the next section.

We conducted FEM simulations for a microstructure with a pitch of ~11 μm to interpret the PLU results, capturing acoustic wavelengths down to ~2.5 μm. The predicted R-wave mode matches experimental data, with a flat branch near ~425 MHz, though its intensity is overshadowed by the stronger R-wave mode. Zooming into the first two BZs reveals the nondispersive SSL-wave and the dispersive R-wave, which exhibit a broader bandgap (50 to 75 MHz) due to folding. At higher frequencies, two flat branches are predicted: one at 405 MHz and another at 425 MHz. The first flat branch corresponds to the flattening of the R-wave mode observed in experiments, whereas the second flat branch shows qualitative agreement with the experimental flat mode that spans the entire range of probed wave numbers. Although there are slight discrepancies in frequency (likely due to assumed material properties and model geometrical assumptions), the gap between these branches (~20 MHz) is in close agreement with the experimental observations. To further investigate the mode shapes related to these branches, we performed 3D simulations with Bloch-Floquet periodic boundary conditions [see supplementary text section S5 and (*30*)]. These simulations revealed that the flat branch (fig. S6) is predominantly a surface mode, with both horizontal (z) and vertical (y) displacement components, indicative of a zero-group velocity ($\partial\omega/\partial\kappa \approx 0$) mode, where the energy is localized within the structure (no propagation). The detection of these experimental features confirms the phononic characteristics of the mantis shrimp's periodic region and highlights the influence of 3D effects arising from the complex material anisotropy and club structure in this region.

Elastic wave filtering as strategy for impact mitigation

In the preceding sections, we presented an experimental evaluation of the phononic behavior of the mantis shrimp's dactyl club, at the local level within its periodic region, and its interpretation through modeling. We now shift focus to exploring the integrated wave-filtering capabilities of the club's periodic region in the context of the dactyl club's strike. Specifically, we address two key questions: What is the role of the graded Bouligand structure from a phononics perspective and what are the implications of selective filtering of MHz shear waves?

The mantis shrimp's strike involves a series of energy release mechanisms, starting with muscle contraction and energy storage, followed by a latch-like release, and culminating in the club's high-speed impact on the target, accompanied by the generation and collapse of cavitation bubbles (Fig. 4A). Although the impact phase represents less than 0.1% of the total strike sequence duration (*8*), its temporal characteristics are crucial for understanding the role of the discovered phononic mechanisms. The initial contact with the target lasts under 50 μs (*14*) and resembles a pyrotechnic shock, characterized by high-frequency, short-duration, and high-magnitude stress waves consistent with kHz-range vibrations (*23*, *31*). Following this, the collapse of cavitation bubbles violently releases energy over tens of nanoseconds, generating shockwaves in the MHz range (*8*, *32*, *33*), potentially reaching frequencies up to 1 GHz (~ns^{-1}) (*11*). Although both the contact blow and cavitation blow are used by the mantis shrimp to strike its prey, the cavitation blow has only about half the peak force of the initial contact blow but exhibits a much higher frequency spectrum (*9*). Moreover, the hierarchical multilayer structure of the dactyl club, as predicted by FEA, concentrates the highest principal stresses near the impact surface, allowing lower-amplitude, high-frequency stress waves to propagate through the periodic region (*14*). These observations emphasize the importance of high-frequency waves in the shrimp's impact dynamics.

Owing to the rapid dynamics of the strike, experimental measurements of the impact's frequency spectrum have so far been limited to vibrations up to 170 kHz (*9*). However, this upper limit reflects the limitations of the sensing devices rather than the absence of higher-frequency energy transport. In this context, our observations of phononic dispersion, including Bragg bandgaps in the tens of MHz range within the periodic region, align with other shrimp-inspired phononic studies (*34*). These findings suggest that the mantis shrimp uses phononic mechanisms to shield itself from high-frequency transients associated with cavitation-induced shocks during impact (Fig. 4A). Furthermore, they underscore the importance of reevaluating the dynamics of the shrimp's powerful strike using more advanced instrumentation.

To advance this understanding, we evaluated the effectiveness of the mantis shrimp's functionally graded microstructure in mitigating impact under representative conditions. We used a 2D, linear elastic finite element plane-wave model (Fig. 4, B to D) to independently simulate longitudinal and transverse bulk wave propagation across Bouligand microstructures that mimic those of the mantis shrimp. This simplified model was used to isolate the effects of microstructure on bulk wave propagation, which avoided the complexities that arise during a dactyl club strike event, such as underwater fluid-structure interaction, 3D effects, wave propagation across multiple regions, and the curvature of the club's surface. In our simplified 2D strip model, we replicated the geometrically graded structure of the periodic region by incorporating the variation in pitch length observed in dactyl club cross sections (Fig. 4, B and C). Alongside the geometric grading, we accounted for spatially modulated anisotropic elastic properties, varying the components of the stiffness tensor as a function of position, as illustrated in Fig. 4B. To benchmark the graded microstructure, we compared it against a simpler single-pitch microstructure corresponding to the largest pitch measured in our dactyl club samples (80 μm). This control design not only reflected the location of larger pitches closer to the impact surface but also accounted for their tendency to generate Bragg gaps at lower frequencies. To excite longitudinal and transverse waves, we applied a spatially uniform pulse centered at 10 MHz (Fig. 4D) modeled as a normal pressure [$\sigma(t)$] and a tangential traction [$\tau(t)$], respectively (where t is time). Although detailed modeling of the underwater dynamics of the mantis shrimp's strike is beyond the scope of this study, the effects of the cavitation blow are approximated through the applied stress pulse and material properties validated by surface wave experiments. (For an evaluation of MHz phononic behavior under hydrated conditions, refer to supplementary text section S7). We quantified wave attenuation by comparing the frequency spectrum at the end of the domain (node "out" in Fig. 4D) with that of the applied pulse (node "in" in Fig. 4D). Further details of the modeling approach are provided in the materials and methods.

The frequency spectra of transmitted normal and shear stress components, for both single-pitch and graded models, are displayed in Fig. 4E. For longitudinal stress waves, the input and output stress spectrograms overlap, indicating no notable filtering. This is expected, because the variation of the material stiffness in the x direction is invariant of position, that is, the medium is uniform for longitudinal waves propagating in the x direction. By contrast, for shear waves, the spectrograms reveal a pronounced influence of the microstructural arrangement. In the single-pitch microstructure, a frequency dip centered around 8 MHz aligns with the bandgap predicted from the dispersion diagrams (see supplementary text section S6). For the graded microstructure, a much broader gap emerges, spanning most of the frequency range of the applied pulse. This highlights the structural gradient's ability to affect a wider frequency range. Signal energy calculations show that 100% of the incoming pressure pulse is transmitted, whereas only 66 and 43% of the shear pulse energy is transmitted through the single-pitch periodic and graded-pitch structures, respectively.

Beyond the linear plane wave model, which emphasizes the interaction between microstructure and high-frequency waves in shielding against nanosecond-scale shockwaves, we note that real-world impacts may act as point sources. In such cases, bulk elastic waves could diffract in three dimensions, further broadening the frequency range of filtering. Furthermore, if bulk waves are not plane waves propagating strictly along the periodic region, even longitudinal waves could become sensitive to the periodic variation in elastic properties. Consequently, most wave energy and frequency content would be filtered, with only a fraction propagating through (primarily polarized and traveling along the x-direction).

Selective filtering of shear waves, by Bouligand-like spatially modulated structures, hints at the potentially detrimental effects of these waves to the dactyl club's functionality. Extensive experimental and computational studies on behind-armor blunt trauma (nonpenetrating impacts) have demonstrated that gross motions induced by shear waves are critical contributors to damage in organs and tissues, leading to lacerations, contusions, interfacial disruptions, and fractures (*35*–*37*). Shear waves are also linked to traumatic brain injuries, such as diffuse axonal injury, through mechanisms such as shear wave focusing and shear shockwave generation with high-frequency harmonic components (*38*, *39*). Given the precise neural control required for the mantis shrimp's striking motion (*40*), protecting nerve fibers is essential, because it ensures the structural integrity of the club's tissue and the organic membranes within, particularly during high-strain-rate events and successive molting cycles (*41*, *42*). Similarly, in synthetic materials, transverse (shear) waves have been shown to cause delamination and interlayer cracking in impact-resistant composites, compromising their structural integrity and dynamic load resistance (*43*, *44*). The mantis shrimp's design, which selectively shields against the highest frequencies rather than the entire spectrum, reflects an advanced strategy that recognizes that strain rate can be as damaging as, or more damaging than, load magnitude, a phenomenon observed in studies on the effects of ultrasound (*35*, *42*). This selective filtering also relates to the overall size limitation of the periodic region within the dactyl club, given that filtering lower frequencies would require larger pitches. Furthermore, the periodic region provides additional advantages, including enhanced toughness attributed to the Bouligand architecture (*45*, *46*). This architectural motif offers dual benefits: high-frequency phononic filtering and mechanical toughening. Interestingly, these phenomena may not be independent but rather interdependent, with phononic mechanisms potentially enhancing extrinsic toughening by facilitating stable crack growth and mitigating catastrophic failure (*47*, *48*).

Discussion and conclusions

The mantis shrimp has long been regarded as a paragon of biological engineering owing to its notable impact-related properties. More recently, numerical analyses have suggested that the helicoidal fiber arrangement in the periodic region of the dactyl club gives rise to phononic shear wave bandgaps, complementing the suite of defensive mechanisms of the mantis shrimp.

By combining nanosecond and picosecond laser ultrasonic techniques with modeling, we have presented experimental evidence of phononic behavior facilitated by the Bouligand microstructure of the mantis shrimp. The phononic nature of the periodic region of the dactyl club was revealed through the observation of Bloch harmonics, dispersive surface modes, flat modes, and phononic bandgaps. These observations arise from the interactions of waves with the hierarchical architecture of the dactyl club, as shown by transient wave propagation simulations. Using dynamic finite element models, we assessed the role of the graded Bouligand arrangement in impact mitigation through wave-filtering mechanisms and compared it with simpler microstructural configurations.

We conclude that the graded Bouligand arrangement in the mantis shrimp selectively filters shear waves generated by nanosecond-scale cavitation bubble collapse over an extended range in the lower MHz regime. This characteristic, which stems from the distinctive material and geometric properties of the periodic region, suggests an evolutionary advantage in shielding soft tissues from harmful high-frequency shear waves, which are particularly detrimental to soft tissues and neural synapses.

In the broader context of natural phononic structures, our measurements and analyses extend the known range of functional phononic behavior into the MHz regime, providing evidence of phononic Bragg scattering mechanisms (akin to those seen in phononic crystals), rather than local resonance, as a biological functionality. Additionally, this work highlights nature's ability to engineer a high-quality ultrasonic chirped phononic crystal, exhibiting Bloch harmonics, with a level of sophistication that would typically require advanced micro- and nanomanufacturing techniques. Furthermore, the discovery of flat bands extending into the hundreds of MHz suggests the potential for spatial energy localization, which can be dissipated locally with minimal damping, offering further insights into how these natural structures may mitigate high-frequency energy.

REFERENCES AND NOTES

1. P.-Y. Chen, J. McKittrick, M. A. Meyers, *Prog. Mater. Sci.* **57**, 1492–1704 (2012).
2. F. Barthelat, H. Tang, P. D. Zavattieri, C.-M. Li, H. D. Espinosa, *J. Mech. Phys. Solids* **55**, 306–337 (2007).
3. H. D. Espinosa *et al.*, *Nat. Commun.* **2**, 173 (2011).
4. H. D. Espinosa *et al.*, *Matter* **1**, 1246–1261 (2019).
5. M. Asgari, N. A. Alderete, Z. Lin, R. Benavides, H. D. Espinosa, *Acta Biomater.* **122**, 236–248 (2020).
6. M. J. Chon *et al.*, *J. Mech. Behav. Biomed. Mater.* **76**, 30–37 (2017).
7. A. Sakes *et al.*, *PLOS ONE* **11**, e0158277 (2016).
8. S. N. Patek, *Integr. Comp. Biol.* **59**, 1573–1585 (2019).

9. S. N. Patek, R. L. Caldwell, *J. Exp. Biol.* **208**, 3655–3664 (2005).
10. D. Lohse, B. Schmitz, M. Versluis, *Nature* **413**, 477–478 (2001).
11. J. Holzfuss, M. Rüggeberg, A. Billo, *Phys. Rev. Lett.* **81**, 5434–5437 (1998).
12. R. Pecha, B. Gompf, *Phys. Rev. Lett.* **84**, 1328–1330 (2000).
13. J. R. Shorter, O. Rueppell, *Insectes Soc.* **59**, 1–10 (2012).
14. J. C. Weaver *et al.*, *Science* **336**, 1275–1280 (2012).
15. W. Huang *et al.*, *Nat. Mater.* **19**, 1236–1243 (2020).
16. N. A. Yaraghi *et al.*, *Adv. Mater.* **28**, 6835–6844 (2016).
17. L. K. Grunenfelder *et al.*, *Acta Biomater.* **10**, 3997–4008 (2014).
18. N. Guarín-Zapata, J. Gomez, N. Yaraghi, D. Kisailus, P. D. Zavattieri, *Acta Biomater.* **23**, 11–20 (2015).
19. F. Bosia *et al.*, *Matter* **5**, 3311–3340 (2022).
20. P. Vukusic, J. R. Sambles, *Nature* **424**, 852–855 (2003).
21. T. R. Neil, Z. Shen, D. Robert, B. W. Drinkwater, M. W. Holderied, *Proc. Natl. Acad. Sci. U.S.A.* **117**, 31134–31141 (2020).
22. S. K. Yang, V. V. Varadan, A. Lakhtakia, V. K. Varadan, *J. Phys. D Appl. Phys.* **24**, 1601–1608 (1991).
23. H. Le Ferrand, *Compos. Struct.* **224**, 111105 (2019).
24. J. A. Rogers, A. A. Maznev, M. J. Banet, K. A. Nelson, *Annu. Rev. Mater. Sci.* **30**, 117–157 (2000).
25. A. A. Maznev, K. A. Nelson, J. A. Rogers, *Opt. Lett.* **23**, 1319–1321 (1998).
26. W. P. Mason, R. N. Thurston, *Physical Acoustics: Principles and Methods* (Academic Press, 1972).
27. T. C. Lim, P. Cheang, F. Scarpa, *Phys. Status Solidi, B Basic Res.* **251**, 388–396 (2014).
28. A. Abbas *et al.*, *Opt. Express* **22**, 7831–7843 (2014).
29. Q. Xie *et al.*, *Nat. Commun.* **10**, 2228 (2019).
30. R. S. Westafer, thesis, Georgia Institute of Technology (2011).
31. J. R. Lee, C. C. Chia, C. W. Kong, *Measurement* **45**, 631–642 (2012).
32. C. E. Brennen, *Cavitation and Bubble Dynamics*, Oxford Engineering Science Series (Oxford Univ. Press, 1995).
33. Y. Tomita, A. Shima, *J. Fluid Mech.* **169**, 535–564 (1986).
34. R. P. Behera, H. Le Ferrand, *Matter* **4**, 2831–2849 (2021).
35. L. Cannon, *J. R. Army Med. Corps* **147**, 87–96 (2001).
36. Institute of Medicine, *Long-term Effects of Blast Exposures*, vol. 9 of *Gulf War and Health* (National Academies Press, 2014).
37. G. J. Cooper, D. E. Taylor, *J. R. Army Med. Corps* **135**, 58–67 (1989).
38. S. Chandrasekaran *et al.*, *J. Biomech.* **166**, 112021 (2024).
39. B. Giammarinaro, D. Espíndola, F. Coulouvrat, G. Pinton, *Phys. Rev. Appl.* **9**, 014011 (2018).
40. M. Burrows, *J. Comp. Physiol. A Neuroethol. Sens. Neural Behav. Physiol.* **62**, 361–381 (1969).
41. S. Amini *et al.*, *Proc. Natl. Acad. Sci. U.S.A.* **116**, 8685–8692 (2019).
42. Z. Izadifar, P. Babyn, D. Chapman, *Ultrasound Med. Biol.* **43**, 1085–1104 (2017).
43. H. D. Espinosa, S. Dwivedi, H. C. Lu, *Comput. Methods Appl. Math.* **183**, 259–290 (2000).
44. Y. B. Gao, L. T. Shi, T. Lu, W. B. Xie, X. M. Cai, *Eng. Fract. Mech.* **295**, 109797 (2024).
45. N. Suksangpanya, N. A. Yaraghi, D. Kisailus, P. Zavattieri, *J. Mech. Behav. Biomed. Mater.* **76**, 38–57 (2017).
46. A. Zaheri *et al.*, *Adv. Funct. Mater.* **28**, 1803073 (2018).
47. F. Atrash, A. Hashibon, P. Gumbsch, D. Sherman, *Phys. Rev. Lett.* **106**, 085502 (2011).
48. B. Davies *et al.*, *Sci. Rep.* **4**, 7538 (2014).

ACKNOWLEDGMENTS

We thank R. Fulcrand for assistance with SEM image acquisition. **Funding:** H.D.E. acknowledges financial support from the Air Force Office of Scientific Research (AFOSR) through award no. FA9550-20-1-0258, the Office of Naval Research (award no. N000142212133), and the National Science Foundation (award no. CMMI-1953806). M.A.G. acknowledges financial support from the Institut Lumière Matière (ILM) and Fédération de Recherche André-Marie Ampère (FRAMA) through start-up funds. **Author contributions:** Conceptualization: N.A.A., M.A.G., H.D.E.; Methodology: N.A.A., S.R., M.A.G., H.D.E.; Resources: M.A., H.D.E.; Investigation: N.A.A., S.S., S.R., M.A.G., H.D.E.; Visualization: N.A.A., M.A.G., H.D.E.; Funding acquisition: M.A.G., H.D.E.; Project administration: H.D.E.; Supervision: H.D.E.; Writing – original draft: N.A.A., M.A.G., H.D.E.; Writing – review & editing: S.R., H.D.E. **Competing interests:** The authors declare that they have no competing interests. **Data and materials availability:** All data are available in the main text or the supplementary materials. **License information:**

SUPPLEMENTARY MATERIALS

science.org/doi/10.1126/science.adq7100
Materials and Methods
Supplementary Text
Figs. S1 to S10
Table S1
References

Submitted 27 May 2024; accepted 9 December 2024
10.1126/science.adq7100

PLANT SCIENCE

Moisture-responsive root-branching pathways identified in diverse maize breeding germplasm

Johannes D. Scharwies[1]*, Taylor Clarke[1], Zihao Zheng[2]†, Andrea Dinneny[1], Siri Birkeland[3]‡, Margaretha A. Veltman[4,5]§, Craig J. Sturrock[6], Jason Banda[6], Héctor H. Torres-Martínez[1], Willian G. Viana[1], Ria Khare[7], Joseph Kieber[7], Bipin K. Pandey[6], Malcolm Bennett[6], Patrick S. Schnable[2], José R. Dinneny[1,8]*

Plants grow complex root systems to extract unevenly distributed resources from soils. Spatial differences in soil moisture are perceived by root tips, leading to the patterning of new root branches toward available water in a process called hydropatterning. Little is known about hydropatterning behavior and its genetic basis in crop plants. Here, we developed an assay to measure hydropatterning in maize and revealed substantial differences between tropical/subtropical and temperate maize breeding germplasm that likely resulted from divergent selection. Genetic analysis of hydropatterning confirmed the regulatory role of auxin and revealed that the gaseous hormone ethylene locally inhibits root branching from air-exposed tissues. Our results demonstrate how distinct signaling pathways translate spatial patterns of water availability to developmental programs that determine root architecture.

Climate change is predicted to increase the duration and severity of droughts (*1*). This will threaten crop production, which depends heavily on water. Plant water uptake is facilitated by an intricate network of roots. Breeding plants with improved root access to water is a potential method to make crops resilient to climate change (*2*). Root networks are established by branching of the primary root axis. The development of lateral root branches is highly responsive to the spatiotemporal distribution of resources such as water and nutrients in soils (*3*, *4*). Plants sense micrometer-scale heterogeneity in water availability at their root tips, with spatial differences along the root tip circumference determining the patterning of lateral roots through hydropatterning (*5*, *6*) (Fig. 1A). This response may allow plants to capture water more efficiently while minimizing the metabolic cost of root growth in dry soil (*7*). Understanding the extent of phenotypic variation for this trait within breeding populations and determining its genetic basis may facilitate crop improvement. Furthermore, understanding the mechanistic basis of hydropatterning will illuminate how heterogeneity in moisture is sensed by organisms to enact an adaptive response.

Hydropatterning in domesticated maize

Here, we investigated hydropatterning in the cereal crop species maize (*Zea mays*), which constitutes a major source of calories worldwide. To capture the phenotypic diversity of hydropatterning, we developed an assay using germination paper to create a controlled gradient of water availability across the circumference of the growing primary root (Fig. 1B and fig. S1). Simultaneous characterization of a diverse set of 250 maize inbred lines (data S1) from the Goodman-Buckler association panel allowed us to cover most of the genetic diversity present in current public sector breeding programs (*8*).

For all tested maize inbred lines, we observed that primary roots preferentially formed lateral roots on the side touching the water-saturated germination paper (the contact side), which is

---

[1]Department of Biology, Stanford University, Stanford, CA, USA. [2]Department of Agronomy, Iowa State University, Ames, IA, USA. [3]Faculty of Chemistry, Biotechnology and Food Science, Norwegian University of Life Sciences, Ås, Norway. [4]Natural History Museum, University of Oslo, Oslo, Norway. [5]Naturalis Biodiversity Center, CR Leiden, Netherlands. [6]Plant and Crop Sciences, School of Biosciences, University of Nottingham, Sutton Bonington, UK. [7]Department of Biology, University of North Carolina, Chapel Hill, NC, USA. [8]Howard Hughes Medical Institute, Stanford University, Stanford, CA, USA.
***Corresponding author. Email: joscha@stanford.edu (J.D.S.); dinneny@stanford.edu (J.R.D.)**
†Present address: Vegetable & Flower Seeds Development, Syngenta Crop Protection LLC, Greensboro, NC, USA.
‡Present address: Natural History Museum, University of Oslo, Oslo, Norway.
§Present address: Institut de Recherche pour le Développement, Montpellier, France.

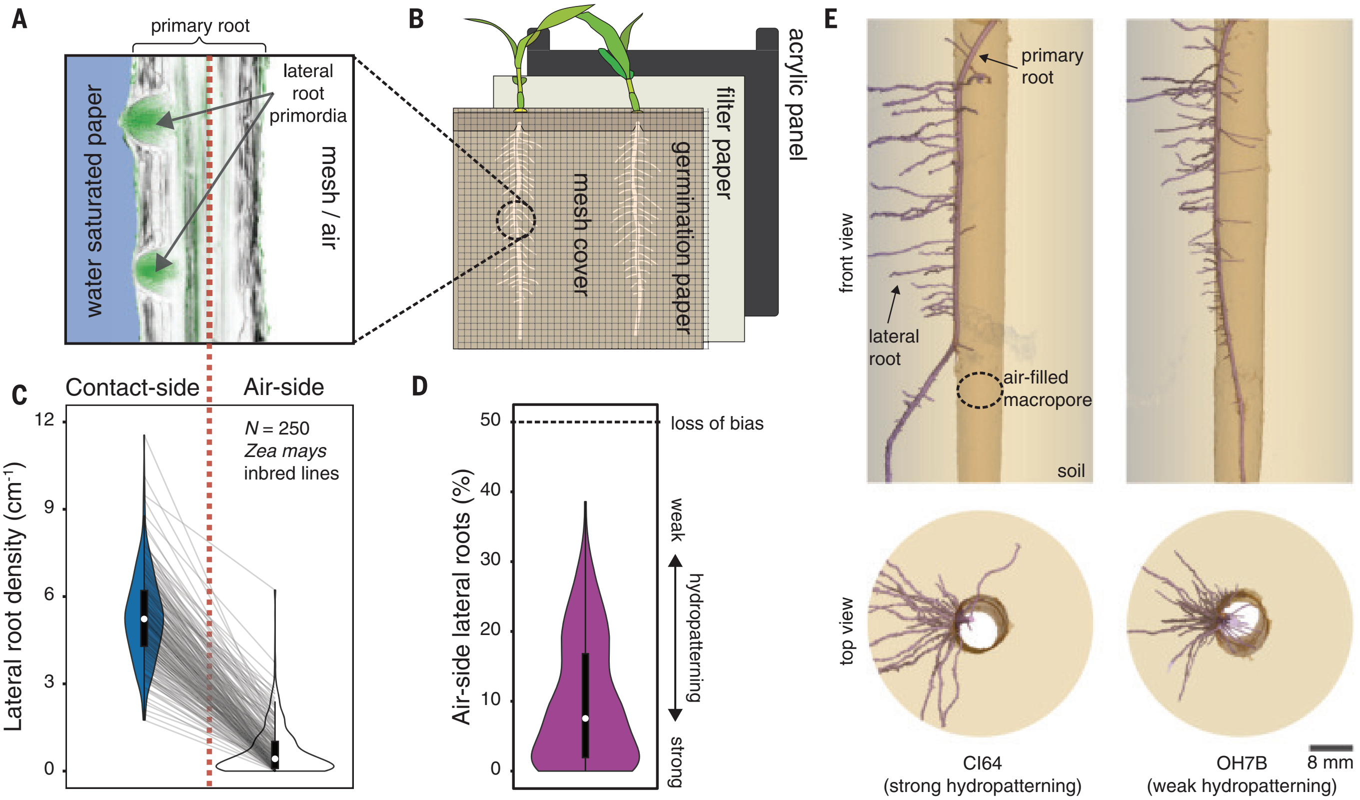

Fig. 1. Hydropatterning responses revealed in public sector breeding lines of maize. (**A** and **B**) Schematic of the hydropatterning response (A) in our custom-built hydropatterning assay (B). Primary roots of maize seedlings were grown in a vertical position along moist paper while being prevented from growing off the paper by a mesh cover. Lateral root primordia were preferentially induced toward the water-saturated paper (contact side) and suppressed on the air-exposed side (air side). Shown is a longitudinal cross section of maize root (B73 inbred) stained with calcofluor white (gray) and SYBR green (green) which stain cell walls and cell nuclei, respectively. The contact and air sides are separated by a dashed red line. (**C** and **D**) Distribution of contact-side (blue) and air-side (white) lateral root densities from 250 maize inbred lines characterized using the hydropatterning assay (C) and calculated percentage of air-side lateral roots (purple) (D). Each inbred line is represented by its median value (n = 1 to 3 seedlings per inbred line) (data S2). Gray lines connect corresponding inbred lines. Population median is shown as white circles. (**E**) Three-dimensionally rendered x-ray computed tomography images, viewed from the front and the top, showing lateral root patterning on primary roots of strong (CI64) and weak (OH7B) hydropatterning inbred lines grown through an air-filled macropore in soil.

consistent with the inductive effect of water availability previously observed in the maize reference inbred B73 and in other species (*5*) (Fig. 1C and data S2). Nevertheless, a substantial proportion of all surveyed maize inbred lines developed air-side lateral roots as well, resulting in an observed phenotypic range of 0 to 39% air-side lateral roots across all 250 inbred lines (Fig. 1D). This suggests that a larger portion of maize inbred lines exhibit weakened hydropatterning (i.e., more air-side lateral roots) than previously indicated (*9*). Additionally, in a set of 20 maize inbred lines with diverse hydropatterning responses, we observed that hydropatterning in primary roots was significantly correlated to hydropatterning in crown roots, which make up the bulk of mature maize root systems (fig. S2, A to C, and data S3). Our results highlight the substantial variation of hydropatterning across maize root types, allowing this trait to be used for understanding how quantitative genetic variation contributes to overall root architecture.

In the B73 maize inbred line, lateral root founder cells initiate primordium development ~12 mm from the root tip (*10*). Prior research using B73 found that moisture availability cues, which determine the patterning of lateral roots, are perceived closer to the root tip, specifically within the first 5 to 6 mm (*9*). This suggests that moisture cues act on lateral root development at the founder cell patterning stage rather than at later developmental stages. Comparing lateral root patterning in several strong (<5% air-side lateral roots) and weak (>20% air-side lateral roots) hydropatterning inbred lines, we found that pre-emerged lateral root primordia and post-emergence lateral roots exhibited the same bias in distribution between the contact sides and the air sides, corresponding to the hydropatterning strength of each inbred line (fig. S2, D and E). Our observations provide further evidence that hydropatterning primarily acts at the lateral root founder cell patterning stage.

We next investigated how the observed variation in hydropatterning correlates with root architecture in soil conditions. In nature, large air spaces in the soil matrix called macropores are commonly created by prior root growth or burrowing invertebrate activity, such as by earthworms. We tested how lateral roots were patterned when primary roots were grown through artificial macropores. Strong hydropatterning inbred lines initiated their lateral roots preferentially toward the side of the root in contact with soil, as observed by microscale x-ray computed tomography (Fig. 1E). By contrast, weak hydropatterning inbred lines displayed a reduced bias, with more lateral roots growing into the air-filled macropore. Quantification across multiple strong and weak hydropatterning inbred lines found that they made similar percentages of air-side lateral roots in the soil macropore and our hydropatterning assay (fig. S2, F to H). These results demonstrate that our hydropatterning assay generates reproducible phenotypes that translate to soil conditions.

To explore how variation in hydropatterning relates to other phenotypic traits of field-grown

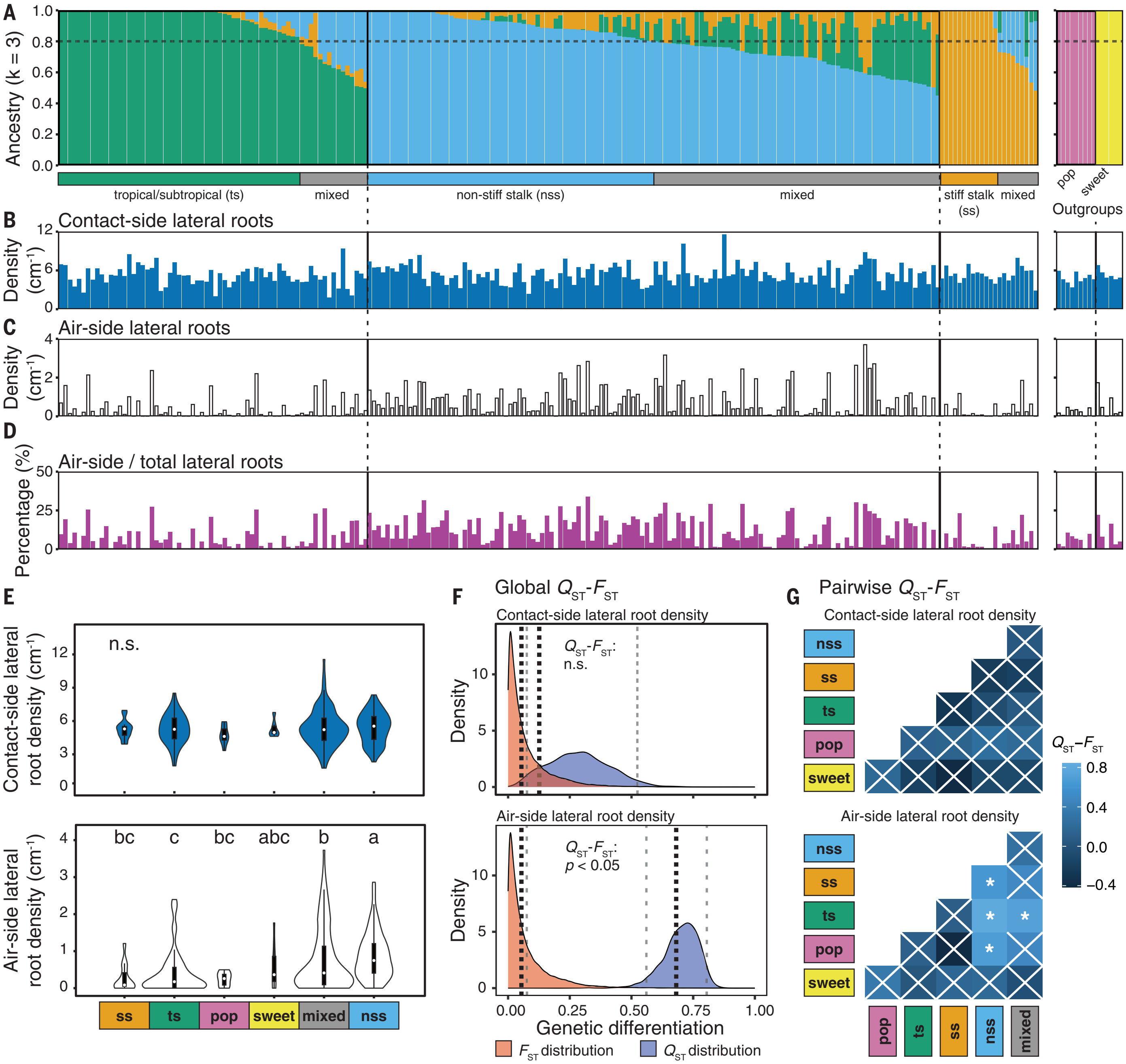

Fig. 2. Differences in hydropatterning across breeding subpopulations may have been caused by divergent selection. (**A** to **D**) Population structure and hydropatterning traits of 231 maize inbred lines (19 inbred lines from original population of $N = 250$ were excluded due to missing genotypic data). (A) Ancestry components and subpopulation assignments. Inbred lines <80% group identity (dashed line) is "mixed." Popcorn (pop) and sweet corn (sweet) groups were defined a priori. (B to D) Phenotypic data of contact-side (B) and air-side (C) lateral root density and percentage air-side lateral roots (D) are shown as the median value for each inbred line ($n = 1$ to 3 seedlings per inbred line) (data S2). (**E**) Subpopulation comparisons of contact-side (top) and air-side (bottom) lateral root density. Violin plot area was adjusted for the number of inbred lines/subpopulation. Letters denote significant differences between subpopulations ($P \leq 0.05$, Kruskal-Wallis and Dunn's post hoc tests); n.s., no significant differences. (**F**) Population-wide comparison of F_{ST} (fixation index) and Q_{ST} (genetic differentiation regarding a quantitative trait) distributions for contact-side (top) and air-side (bottom) lateral root density. Black dotted lines indicate means; gray dashed lines indicate 95% confidence intervals. (**G**) Subpopulation pairwise $Q_{ST} - F_{ST}$ comparisons. Asterisks denote significant differences between Q_{ST} and F_{ST} ($^*P \leq 0.05$, Benjamini and Hochberg adjusted). White crosses, not significant. Number of inbred lines in each subpopulation across all panels: $n_{ts} = 53$, $n_{nss} = 63$, $n_{ss} = 14$, $n_{mixed} = 88$, $n_{pop} = 9$, and $n_{sweet} = 6$.

maize plants, we performed a correlation analysis with 64 compiled trait sets measured from field-grown plants (*11*). We found that both air-side lateral root density and the percentage of air-side lateral roots correlated significantly with root crown depth and the number of nodes with brace roots (fig. S3, A to C, and data S4). Weaker hydropatterning inbred lines generally exhibited more shallow root systems with fewer brace roots according to data collected in two studies from Iowa (fig. S3, D to F) (*12*, *13*). This suggests that more efficient placement of root branches toward water may improve the ability of root systems to attain greater depths, possibly due to the metabolic

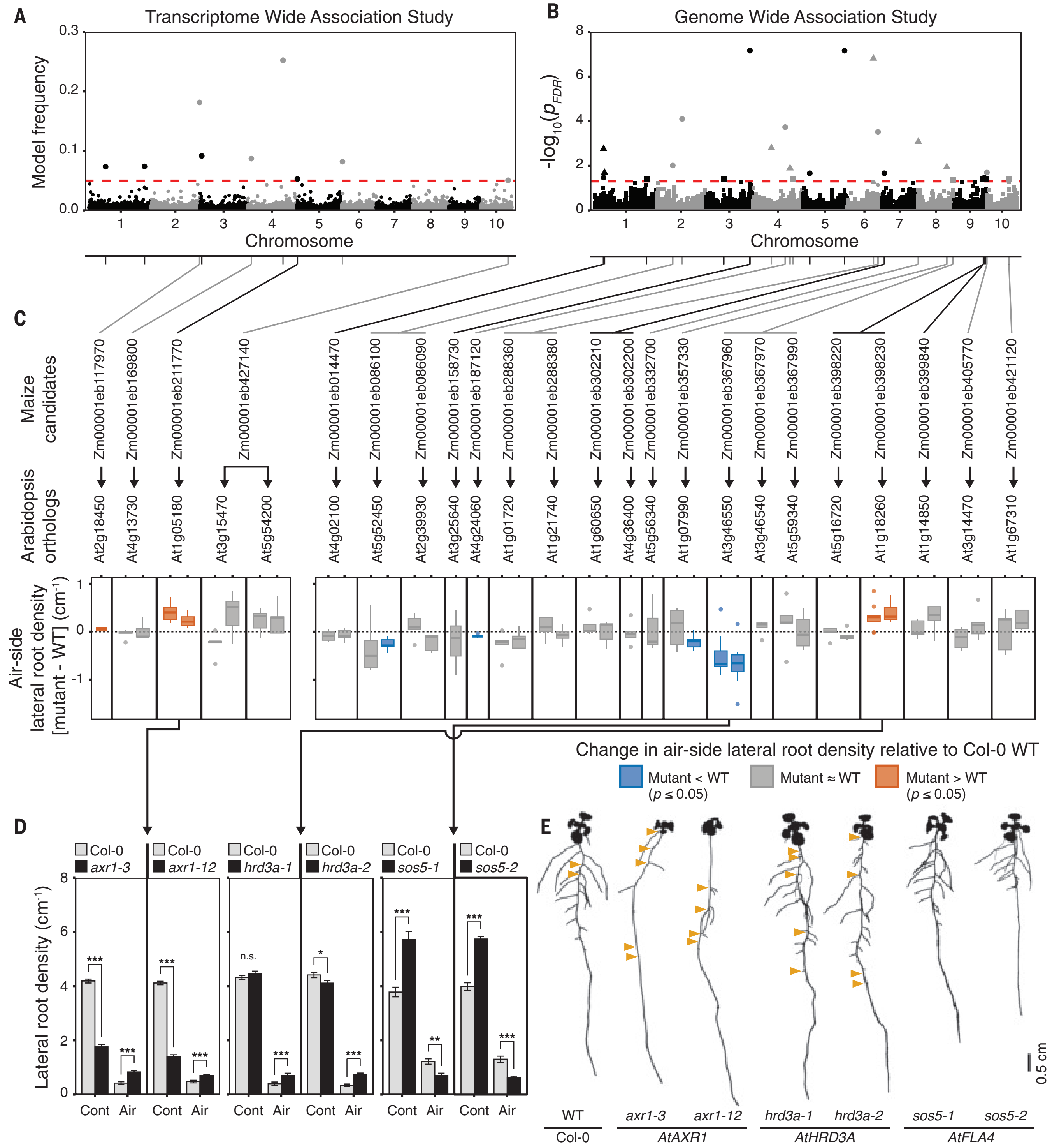

Fig. 3. Genetic control for hydropatterning revealed in maize and validated in *Arabidopsis*. (**A** and **B**) Manhattan plots of TWASs and GWASs for air-side lateral root density in maize. (A) TWAS used gene expression data from maize root tips (*19*). Significance threshold: model frequency = 0.05 (red dashed line). (B) GWAS shows smallest value for each SNP across three minor allele frequency cutoffs: ≥0.4% (solid circles), ≥2.2% (solid triangles), and ≥4.4% (solid squares). *P* = 0.05, FDR-adjusted significance threshold (red dashed line). Gray and black lines connect SNPs and associated candidate genes corresponding to the chromosome coloration. (**C**) Validation of maize candidate genes using mutants of corresponding gene orthologs in *Arabidopsis*. Air-side lateral root densities of mutants are shown relative to Col-0 WT. Fill color denotes significant differences ($P \leq 0.05$, paired Student's *t* test): mutants > WT are shown in orange, mutants < WT in blue, and not significant in gray; *n* = 5 to 10 plates per mutant (five WT and five mutant seedlings per plate). (**D**) Comparisons of contact-side (Cont) and air-side (Air) lateral root densities between Col-0 WT (gray) and mutants for *AtAXR1*, *AtHRD3A*, and *AtFLA4* (all mutants black). *n* = 10 plates per mutant (five WT and five mutant seedlings per plate). Asterisks denote significant differences (*$P \leq 0.05$, **$P \leq 0.01$, ***$P \leq 0.001$, paired Student's *t* test). Bar graphs indicate the mean ± SEM. (**E**) Binary images of 11-d-old seedlings. Orange triangles mark air-side lateral roots. Scale bar, 0.5 cm. Dilation was used on images to improve visibility.

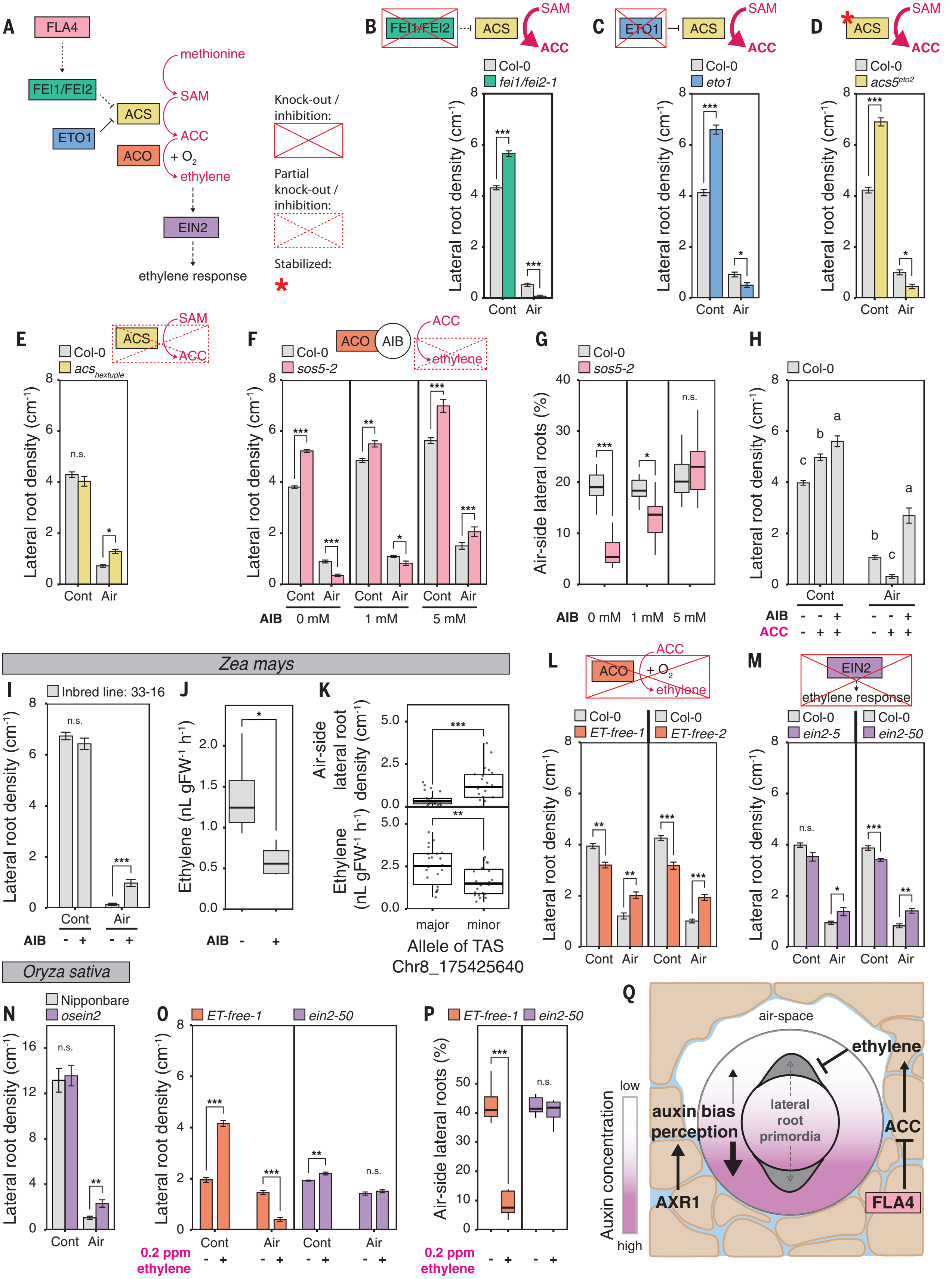

Fig. 4. Ethylene inhibits the formation of air-side lateral roots in *Arabidopsis*, maize, and rice. (**A**) FLA4 and the ethylene pathway in *Arabidopsis* (27). (**B** to **E**) Contact-side (Cont) and air-side (Air) lateral root densities in *Arabidopsis* mutants *eto1* (blue, *n* = 5 plates) (C), *acs5^{eto2}* (yellow,

n = 5 plates) (D), and *acs2-1/4-1/5-2/6-1/7-1/9-1* hextuple mutant (yellow, n = 5 plates) relative to Col-0 (gray) (E). (**F** and **G**) Effect of AIB on *Arabidopsis* mutant *sos5-2* relative to Col-0 (pink, n = 10 plates per treatment). (**H**) *Arabidopsis* Col-0 response to ACC, AIB, and combination: – indicates mock control and + indicates plus 0.05 mM ACC or 5 mM AIB; n = 10 plates per treatment. Letters denote significant differences between treatments (ANOVA, post-hoc Tukey HSD test). (**I** and **J**) Response of maize inbred 33-16 to (+) 10 mM AIB relative to (–) mock control (n = 20 plants per treatment), and related ethylene production (n = 4 samples of five roots per treatment). (**K**) Air-side lateral root density and root ethylene production for maize inbred lines (n = 22/allele) with the major (G) or minor (T) allele at TAS Chr8_175425640. (**L** to **N**) Contact- and air-side lateral root densities in *Arabidopsis* mutants *ET-free-1* and *ET-free-2* (orange, n = 8 to 9 plates) (L) and *ein2-5* and *ein2-50* (purple, n = 10 plates) relative to Col-0 (M), and in rice mutant *osein2* (purple, n = 11 seedlings) relative to Nipponbare WT (gray, n = 16 seedlings) (N). (**O** and **P**) Effect of exogenous ethylene treatment on *Arabidopsis* mutants *ET-free-1* (n = 8 plates per treatment) and *ein2-50* (n = 8 plates per treatment). (**Q**) Working model of hydropatterning controlled by auxin and ethylene. Asterisks denote significant differences ($*P \leq 0.05$, $**P \leq 0.01$, $***P \leq 0.001$, Student's t test), n.s., not significant. Bar graphs indicate mean ± SEM.

savings achieved by limiting branching in dry soil (*14*). No significant correlations were observed with contact-side lateral root density, suggesting that this trait has less relevance to the in-field root architecture traits measured.

Variation and selection of hydropatterning across maize breeding subpopulations

We reassessed population structure and assigned subpopulations for all phenotyped inbred lines that had matching whole-genome sequencing data available (n = 231). Inbred lines with <80% subpopulation identity were assigned to a mixed group (*8*) (Fig. 2A and data S5). Although variation in contact-side lateral root density was uniform across all subpopulations, inbred lines with higher air-side lateral root density and a higher percentage of air-side lateral roots were predominantly associated with the non–stiff-stalk mixed groups (Fig. 2, B to D). This led to significantly weaker hydropatterning for the large temperate non–stiff-stalk group compared with the large tropical/subtropical group or the smaller temperate–stiff-stalk group (Fig. 2E and fig. S4A).

To test whether this divergence in hydropatterning was best explained by neutral evolution or selection, we compared quantitative genetic differentiation with regard to contact-side or air-side lateral root density (Q_{ST}) to the population genetic differentiation due to genetic structure (F_{ST}). We found that Q_{ST} and F_{ST} distributions overlapped for contact-side lateral root density, which suggests that genetic differentiation for this trait occurred through neutral evolution. Conversely, Q_{ST} was significantly in excess of F_{ST} for air-side lateral root density, as well as the percentage of air-side lateral roots, indicating divergence through differential selection for these hydropatterning traits (Fig. 2F, fig. S4B, and data S6). Pairwise comparisons between subpopulations showed the largest $Q_{ST} - F_{ST}$ differences between the non–stiff-stalk and tropical/subtropical groups, suggesting that divergence in selective pressures for hydropatterning occurred predominantly after the split between tropical/subtropical and temperate germplasm (Fig. 2G, fig. S4C, and data S6). Stronger hydropatterning in the tropical/subtropical subpopulations may have resulted from selection for drought tolerance, among other abiotic stress factors, during breeding (*15*, *16*). By contrast, weakened hydropatterning in the temperate non–stiff-stalk subpopulation could be the result of relaxation in selection pressures on efficient water uptake in temperate environments. However, linkage between hydropatterning and other traits could have contributed to differences in hydropatterning between subpopulations. Pronounced $Q_{ST} > F_{ST}$ differences for air-side lateral root density and contrasting observations for contact-side lateral root density support our hypothesis, but inbreeding may inflate Q_{ST} estimates (*17*).

Genetic architecture of hydropatterning in domesticated maize

Previous work in *Arabidopsis* (*Arabidopsis thaliana*) has shown that the auxin-signaling pathway promotes branching on the contact side of roots during hydropatterning. Mutants that disrupt auxin biosynthesis and polar transport are known to weaken hydropatterning (*5*). Similar to *Arabidopsis*, we found in maize that auxin accumulates preferentially on the contact side of hydropatterning roots, which creates a bias for lateral root induction (fig. S5). Furthermore, it has been shown that the auxin-response transcription factor AUXIN RESPONSE FACTOR 7 (ARF7) is sumoylated in cells on the air side of roots, promoting binding to the repressor protein INDOLE-3-ACETIC ACID INDUCIBLE 3 (IAA3), which blocks the initiation of lateral root founder cells (*18*). To identify new loci and associated genes for hydropatterning with relevance to maize, we conducted genome-wide (GWAS) and transcriptome-wide (TWAS) association studies, which associate single-nucleotide polymorphisms (SNPs) or variations in gene expression among the study population with variation in a trait of interest.

TWAS (*13*) identified nine genes with expression in germinating seedling roots (*19*) that was significantly associated with differences in air-side lateral root density (Fig. 3A and data S7). Among these TWAS genes, we found *Zm00001eb211770*, a maize ortholog of *AUXIN RESISTANT 1* (*ZmAXR1*). In *Arabidopsis*, AXR1 together with E1 C-terminal related 1 (ECR1) act as ubiquitin-activating enzymes that facilitate the RUB modification of CULLIN 1 (CUL1), which is part of the $\mathrm{SCF}^{\mathrm{TIR/AFB}}$ complex at the center of auxin perception. RUB modification is necessary to allow auxin signal transduction for lateral root induction (*20*). TWAS in maize found that higher gene expression of *ZmAXR1* is associated with increased air-side lateral root densities (fig. S6A and data S7), which may be due to an increased sensitivity for auxin perception, leading to more frequent induction of lateral roots on the air side. To analyze the origin of the variation in *ZmAXR1* gene expression, we mapped the associated expression quantitative trait loci. This analysis revealed several significant expression-associated SNPs (e-SNPs) (fig. S6B and data S8 and S9). The most significant e-SNP, Chr5_2705946, colocalized with *ZmAXR1* itself, indicating that cis-acting regulatory variation may explain the variation in *ZmAXR1* gene expression associated with air-side lateral root density. Input data for the TWAS suggested expression of *ZmAXR1* in root tips of most inbred lines (fig. S6A). This was confirmed through in situ detection of *ZmAXR1* transcripts in root tips of the maize inbred line B73 by hybridization chain reaction (fig. S7, A to C). These results indicate that auxin regulation and related processes play a role in hydropatterning for maize roots, as previously demonstrated in *Arabidopsis* (*5*, *18*).

In parallel, GWAS (*21*, *22*) identified 30 unique trait-associated SNPs (TASs) for air-side lateral root density (Fig. 3B; fig. S6, C and D; and data S10), suggesting that variation in hydropatterning is controlled by numerous loci in maize. In almost all cases, higher air-side lateral root density was associated with the less-frequent allele (minor allele) of the TAS within our population, except for TAS Chr8_143668219, as shown by the effect estimate (data S10). This supports our hypothesis that weakening of hydropatterning may have been caused by relaxation of selection, because selection typically constrains the occurrence of genetic variants (*23*). We identified a total of 40 genes within 20-kb windows centered on the TASs. In cases where no gene was located within these windows, the next closest gene was included (data S11). These were considered candidates for genes that may control air-side lateral root density in maize.

Validation of maize candidate genes using *Arabidopsis* orthologs

We identified maize candidate gene orthologs in *Arabidopsis* and screened available mutant lines for hydropatterning defects (fig. S8A and data S12 and S13). Screening revealed seven genes for which at least one mutant allele showed a significant change in air-side lateral root density and percentage of air-side lateral roots (Fig. 3C and fig. S8B). For three of these genes, two independent mutant alleles both showed significant, matching changes in air-side lateral root density, confirming their association with hydropatterning (Fig. 3, D and E)

The auxin-signaling pathway mutants *axr1-3* and *axr1-12* of *AtAXR1* showed significant increases in air-side lateral root density and percentage of air-side lateral roots compared with the wild type (WT), whereas contact-side lateral root density decreased significantly (Fig. 3, D and E). This defect is similar to the phenotype of other auxin-pathway mutants in *Arabidopsis* (*5*, *18*), and it confirms that the auxin hormone pathway plays an important role in promoting the bias in lateral root development toward the moisture-contacting side of the root both in *Arabidopsis* and maize.

Similarly, we observed significant increases in air-side lateral root density and percentage of air-side lateral roots in *Arabidopsis* mutants of HMG-CoA REDUCTASE DEGRADATION 3A (*AtHRD3A*), *hrd3a-1* and *hrd3a-2* (Fig. 3, D and E). *AtHRD3A*, an ortholog of GWAS candidate *Zm00001eb398230* (*ZmHRD3A*), recruits misfolded proteins for endoplasmic reticulum–associated protein degradation to the HRD1/HRD3 complex (*24*). Targets include misfolded receptor-like kinases and glycosylated proteins (*25*), suggesting that hydropatterning may rely upon proteins acting at the plasma membrane that are also targets of endoplasmic reticulum–associated protein degradation. In contrast to mutants of *AtAXR1*, *hrd3a-1* and *hrd3a-2* showed either no changes or a relatively small change in contact-side lateral root densities, respectively. This suggests that HRD3A may primarily function in the suppression of air-side lateral root development. In maize, *ZmHRD3A* was discovered as one of three candidate genes associated with TAS Chr9_147576641 (data S11). Mutants of *At5g16720*, an ortholog of *Zm00001eb398220* associated with the same TAS, did not affect hydropatterning (fig. S8B). *ZmHRD3A* is expressed at the root tip in the same region where moisture signals control the patterning of lateral roots (fig. S7, A and D).

In contrast to *axr1* and *hrd3a*, *Arabidopsis* mutants of *FASCICLIN-LIKE ARABINOGALACTAN-PROTEIN 4* (*AtFLA4*), named *salt overly sensitive5* (*sos5-1* and *sos5-2*), showed significant strengthening of hydropatterning with decreases in air-side lateral root density and percentage of air-side lateral roots compared with WT (Fig. 3D). The mutant *sos5-1* was identified for its defects in growth on saline media (*26*). Although the primary root phenotype under salinity and ionic stress has been studied extensively (*27*), no reports have described a lateral root phenotype. *AtFLA4* belongs to a group of 21 fasciclin-like arabinogalactan proteins and carries two fasciclin 1 domains that allow it to interact with the extracellular cell wall matrix (*28*, *29*), which may allow it to sense extracellular cues originating from the environment. The decrease in air-side lateral root density in the *sos5* mutants was accompanied by a significant increase in contact-side lateral root density and a significant reduction in primary root length (Fig. 3, D and E, and fig. S9A). Taking this reduction of primary root length into account, *sos5-1* and *sos5-2* both showed a significant decrease in the total number of emerged air-side lateral roots per seedling, but only a small or no increase in total contact-side lateral roots per seedling (fig. S9B). Thus, these data indicate that *sos5* primarily suppresses air-side lateral roots, whereas changes in contact-side lateral root density may result from pleiotropic effects on root length. *AtFLA4* is an ortholog of GWAS candidate *Zm00001eb367960* (*ZmFLA4*), which was discovered as one of four candidate genes associated with TAS Chr8_175425640 (data S11). Similar to *AtFLA4*, *ZmFLA4* contains two fasciclin 1 domains (*30*). Orthologous *Arabidopsis* mutants of two other candidate genes associated with the same TAS, *Zm00001eb367970* and *Zm00001eb367990*, showed no defect in hydropatterning (fig. S8B). This provides evidence that variation associated with *ZmFLA4* may be the primary determinant of the observed variation in hydropatterning at TAS Chr8_175425640. In maize, *ZmFLA4* is expressed at the root tip (fig. S8, A and E).

Ethylene as an air-side signal mediating hydropatterning

Ethylene is a gaseous plant hormone that regulates development in response to several abiotic stresses (*31*). Accumulation of root-produced ethylene in compacted soils serves as a signal leading to root growth inhibition (*32*). In *Arabidopsis*, *AtFLA4* may act in a genetic pathway regulating the synthesis of ethylene precursor 1-aminocyclopropane-1-carboxylate (ACC) from S-adenosylmethionine (SAM) (Fig. 4A) (*27*). In this pathway, AtFLA4 acts upstream of two leucine-rich repeat receptor-like kinases, AtFEI1 and AtFEI2 (*33*). These kinases interact with 1-AMINOCYCLOPROPANE-1-CARBOXYLATE SYNTHASE (ACS) 5 and 9, which are involved in the synthesis of ACC. Associated with this pathway, ETHYLENE OVERPRODUCER 1 (AtETO1) functions as a negative regulator of type-2 ACS enzymes, including ACS5 and ACS9 (*34*).

We found that double mutants of *AtFEI1* and *AtFEI2* (*fei1*/*fei2-1*), as well as single mutants of *AtETO1* (*eto1*) and *AtACS5* (*acs5*^{eto2}, which carries a C-terminal mutation in ACS5 that increases protein stability), all showed similar reductions in air-side lateral root density as observed in the *AtFLA4* mutants *sos5-1* and *sos5-2*. Concomitantly, all mutants showed an increase in contact-side lateral root density and a reduction in primary root length (Fig. 4, B to D, and fig. S9, C to E). Screening of the single mutants *fei1* and *fei2-1* revealed no significant effects on air-side lateral root density (fig. S9F), corroborating a suggestion that both genes may act in a redundant fashion (*33*). Although both *eto1* and *acs5*^{eto2} increase ACC synthesis, a reduction of ACC synthesis in the *AtACS* hextuple mutant (*acs2-1*, *acs4-1*, *acs5-2*, *acs6-1*, *acs7-1*, and *acs9-1*) led to a significant increase in air-side lateral root density (Fig. 4E). We also tested the single mutant *acs5-1*, but observed no difference compared with WT (fig. S9G). This result is likely due to the high level of redundancy between *ACS* genes in *Arabidopsis*, which has eight functional ACS homologs (*35*). Our results suggest that genetic modulation of ACC synthesis affects hydropatterning in a way that resembles the phenotypes of *sos5-1* and *sos5-2*.

Next, we investigated whether ACC itself or ethylene, which is synthesized from ACC by ACC-oxidases (ACOs), causes the observed repression in air-side lateral root development. We found that treatment with 2-aminoisobutyric acid (AIB), a competitive inhibitor of ACOs, caused an increase in air-side lateral root density and rescued the *sos5-2* mutant phenotype (Fig. 4, F and G). Likewise, treatment of Col-0 WT with ACC alone reduced air-side lateral root density, likely due to the increased production of ethylene, because this effect was reversed by cotreatment with AIB (Fig. 4H). Both ACC and ACC + AIB treatments showed significant increases in contact-side lateral root density compared with mock-treated Col-0 WT. These increases could be due to a concomitant reduction in primary root length with both treatments (fig. S9H) and/or to the effects of ACC itself on lateral root induction (*36*). Taken together, these observations suggest a central role for ethylene in the suppression of air-side lateral root development that does not require localized ACC synthesis, because exogenous ACC application on the contact side was able to induce the same effect.

In maize, AIB treatment of a strong hydropatterning inbred line 33-16 increased air-side lateral root density and significantly reduced ethylene production (Fig. 4, I and J). This indicates that ethylene suppresses air-side lateral root development in maize as well. Measurements of ethylene production from root tips of maize inbred lines that either carry the major or minor allele for TAS Chr8_175425640, localized ~2 kb upstream of *ZmFLA4*, showed that the minor allele was associated with lower ethylene production and higher air-side lateral root densities (Fig. 4K). This may suggest that TAS Chr8_175425640 is linked to genetic variation that affects *ZmFLA4* function, leading to the observed differences in ethylene production.

Complete disruption of ethylene synthesis in two *AtACO* quintuple mutants (*ET-free-1* and *ET-free-2*), in which all five *AtACO* genes were mutated by CRISPR/Cas9 (*37*), showed a significant increase in air-side lateral root density (Fig. 4L). Similarly, the ethylene perception mutants *ein2-5* and *ein2-50* showed a significant increase in air-side lateral root density (Fig. 4M). These observations confirm that ethylene suppresses air-side lateral root development. Concomitantly, we observed a decrease in contact-side lateral root density for *ET-free-1*, *ET-free-2*, *ein2-5*, and *ein2-50* that mirrored the increase in air-side lateral root density leading to no change in total lateral root density (fig. S9, I and J). Because lateral root induction can only occur at one of the two xylem poles in *Arabidopsis* (*38*), it is possible that a derepression of air-side lateral root development in these mutants leads to lateral root redistribution from the contact side. Although mutants for *EIN2* have not been described in maize, a mutant allele of *OsEIN2* in rice was available and showed a similar defect in hydropatterning as the *Arabidopsis* mutant alleles (Fig. 4N), providing further evidence that ethylene-dependent regulation of hydropatterning is conserved between *Arabidopsis* and grasses. A double mutant of ETHYLENE-INSENSITIVE3 (EIN3) and ETHYLENE-INSENSITIVE3-LIKE 1 (EIL1), *ein3/eil1*, two major transcriptional regulators of ethylene signaling that act downstream of EIN2, showed no difference in air-side lateral root density compared with Col-0 WT (fig. S9K). This might be due to redundancy in transcriptional regulation or to an alternative pathway (*39*) that leads to air-side suppression of lateral root development by ethylene. Exogenous treatment of *ET-free-1* and *ein2-50* with 0.2 ppm ethylene was sufficient to suppress air-side lateral root development in *ET-free-1*, whereas *ein2-50* showed no response (Fig. 4, O and P). Our results suggest that localized ethylene synthesis is not necessary, and additional mechanisms must exist that control air-side specific suppression of lateral roots by ethylene.

Because auxin is necessary for lateral root induction and ethylene has been shown to induce local auxin biosynthesis (*40*), we generated a double mutant of *sos5-2* and *axr1-3* to study their epistatic interactions. Although the disruption of auxin signaling led to an increase in air-side lateral roots, the double mutant *sos5-2*/*axr1-3* showed a significant decrease in air-side lateral root density (fig. S9L). Our results indicate an additive interaction between auxin and ethylene responses. Further work will be necessary to elucidate how air-side lateral root suppression by ethylene is connected to auxin-controlled lateral root induction on the contact side.

Conclusions

Our results reveal that hydropatterning is a crop-relevant response of roots to heterogeneity in soil moisture. The development of modern breeding germplasm in maize led to the weakening of hydropatterning in temperate regions, likely through relaxation of selection. This divergence in hydropatterning may relate to the different selection pressures experienced by each subpopulation. Using genetic analyses, we detected associations between hydropatterning and the auxin- and ethylene-signaling pathways. Investigation of these pathways in maize, rice, and *Arabidopsis* demonstrated that auxin signaling promotes a bias in lateral root development toward moisture-contacting surfaces of the root, whereas ethylene suppresses branching on air-exposed surfaces (Fig. 4Q and fig. S9M). FLA4, acting at the top of a signaling pathway that restricts ethylene biosynthesis, may perceive an as-yet-unknown environmental cue to tune the degree to which root architecture is responsive to local soil structure and water availability. Further genetic work in maize is needed to validate our findings in *Arabidopsis*. A deeper understanding of these pathways may allow for the control of moisture-responsive root growth to improve drought resilience in maize.

REFERENCES AND NOTES

1. Y. Satoh *et al*., *Nat. Commun.* **13**, 3287 (2022).
2. J. P. Lynch, *Plant J.* **109**, 415–431 (2022).
3. M. C. Drew, *New Phytol.* **75**, 479–490 (1975).
4. P. Voothuluru, Y. Wu, R. E. Sharp, *Plant Cell* **36**, 1377–1409 (2024).
5. Y. Bao *et al*., *Proc. Natl. Acad. Sci. USA.* **111**, 9319–9324 (2014).
6. J. D. Scharwies, J. R. Dinneny, *J. Plant Res.* **132**, 311–324 (2019).
7. J. R. Dinneny, *Annu. Rev. Cell Dev. Biol.* **35**, 239–257 (2019).
8. S. A. Flint-Garcia *et al*., *Plant J.* **44**, 1054–1064 (2005).
9. N. E. Robbins II, J. R. Dinneny, *Proc. Natl. Acad. Sci. USA.* **115**, E822–E831 (2018).
10. L. Jansen, I. Roberts, R. De Rycke, T. Beeckman, *Philos. Trans. R. Soc. Lond. B Biol. Sci.* **367**, 1525–1533 (2012).
11. R. V. Mural *et al*., *Gigascience* **11**, giac080 (2022).
12. Z. Zheng *et al*., *Plant Physiol.* **182**, 977–991 (2020).
13. H.-Y. Lin *et al*., *Genome Biol.* **18**, 192 (2017).
14. A. Zhan, H. Schneider, J. P. Lynch, *Plant Physiol.* **168**, 1603–1615 (2015).
15. Y. Wu *et al*., *Theor. Appl. Genet.* **129**, 753–765 (2016).
16. S. K. Vasal, S. Mclean, *The Lowland Tropical Maize Subprogram* (CIMMYT, 1994).
17. A. W. Santure, J. Wang, *Genetics* **181**, 259–276 (2009).
18. B. Orosa-Puente *et al*., *Science* **362**, 1407–1410 (2018).
19. K. A. G. Kremling *et al*., *Nature* **555**, 520–523 (2018).
20. J. C. del Pozo *et al*., *Plant Cell* **14**, 421–433 (2002).
21. X. Liu, M. Huang, B. Fan, E. S. Buckler, Z. Zhang, *PLOS Genet.* **12**, e1005767 (2016).
22. A. Kusmec, P. S. Schnable, *Plant Direct* **2**, e00053 (2018).
23. M. Lynch *et al*., *Nat. Rev. Genet.* **17**, 704–714 (2016).
24. W. Su, Y. Liu, Y. Xia, Z. Hong, J. Li, *Proc. Natl. Acad. Sci. USA.* **108**, 870–875 (2011).
25. S. Hüttner, R. Strasser, *Front. Plant Sci.* **3**, 67 (2012).
26. H. Shi, Y. Kim, Y. Guo, B. Stevenson, J.-K. Zhu, *Plant Cell* **15**, 19–32 (2003).
27. G. J. Seifert, *Genes* **12**, 145 (2021).
28. K. L. Johnson, B. J. Jones, A. Bacic, C. J. Schultz, *Plant Physiol.* **133**, 1911–1925 (2003).
29. H. Xue *et al*., *Plant J.* **91**, 613–630 (2017).
30. C. J. A. Sigrist *et al*., *Brief. Bioinform.* **3**, 265–274 (2002).
31. H. Chen, D. A. Bullock Jr., J. M. Alonso, A. N. Stepanova, *Plants* **11**, 33 (2021).
32. B. K. Pandey *et al*., *Science* **371**, 276–280 (2021).
33. S.-L. Xu, A. Rahman, T. I. Baskin, J. J. Kieber, *Plant Cell* **20**, 3065–3079 (2008).
34. H. Yoshida, M. Nagata, K. Saito, K. L. C. Wang, J. R. Ecker, *BMC Plant Biol.* **5**, 14 (2005).
35. A. Tsuchisaka *et al*., *Genetics* **183**, 979–1003 (2009).
36. J. K. Polko, J. J. Kieber, *Front. Plant Sci.* **10**, 1602 (2019).
37. W. Li *et al*., *Mol. Plant* **15**, 354–362 (2022).
38. B. Parizot *et al*., *Plant Physiol.* **146**, 140–148 (2008).
39. B. M. Binder, L. A. Mortimore, A. N. Stepanova, J. R. Ecker, A. B. Bleecker, *Plant Physiol.* **136**, 2921–2927 (2004).
40. A. N. Stepanova *et al*., *Cell* **133**, 177–191 (2008).
41. J. D. Scharwies *et al*., Data for: Moisture-responsive root-branching pathways identified in diverse maize breeding germplasm, Zenodo (2024); https://doi.org/10.5281/zenodo.13347148.
42. J. D. Scharwies *et al*., Data for: Moisture-responsive root-branching pathways identified in diverse maize breeding germplasm, Dryad (2024); https://doi.org/10.5061/dryad.3ffbg79sv.

ACKNOWLEDGMENTS

We gratefully acknowledge the many thoughtful discussions with V. Walbot (Stanford University) regarding experiments in maize. We also thank the USDA-ARS US National Plant Germplasm System for providing the maize seeds from the Goodman-Buckler association panel; S. Leiboff (Oregon State University) and C. Rasmussen (University of California–Riverside) for providing the maize DII-VENUS-NLS reporter lines; C. Schultz (University of Adelaide) and G. Seifert (BOKU Vienna) for discussions regarding the function and role of FLA4; staff at Stanford University and the Carnegie Institution for Science for their support; and all members of the Dinneny laboratory for their help with revisions of the draft manuscript. **Funding:** This work was supported by a Faculty Scholars Grant from the Simons Foundation and Howard Hughes Medical Institute (grant 55108515 to J.R.D.); the Advanced Research Projects Agency-Energy (ARPA-E), US Department of Energy (DE-AR grant 1565-1555 to J.R.D. and DE-AR grant 0000826 to P.S.S.); the Biological and Environmental Research (BER) Program, US Department of Energy (grant DE-SC0023160 to J.R.D.); a Howard Hughes Medical Institute Investigator award (J.R.D.); the National Science Foundation (grant MCB-2427432 to J.K.); UKRI Frontiers Research ERC StG (grant EP/Y036697/1 to B.K.P.); the Biotechnology and Biological Sciences Research Council (BBSRC) (grant BB/V003534/1 to C.J.S., J.B., and M.B. and grants BB/T001437/1, BB/W008874/1, and BB/W015080/1 to M.B.); the European Research Council (grant HYDROSENSING 101118769 to M.B.); HORIZON EUROPE (Marie Sklodowska-Curie Actions grant 765000 to M.A.V.); and EVOTREE (grant RCN 287465 to S.B.). **Author contributions:** Conceptualization: J.D.S., J.R.D.; Data acquisition: J.D.S., T.C., A.D., C.J.S., J.B., H.H.T.-M., W.G.V.; Data analysis: J.D.S., Z.Z., S.B., M.A.V.; Funding acquisition: J.R.D., J.K., B.K.P., P.S.S., C.J.S., J.B., M.B., M.A.V., S.B.; Project administration: J.D.S.; Resources: R.K., J.K., B.K.P., M.B., P.S.S.; Supervision: J.D.S., J.R.D.; Visualization: J.D.S., C.J.S., S.B., M.A.V.; Writing – original draft: J.D.S., J.R.D.; Writing – review & editing: all authors. **Competing interests:** P.S.S. is a cofounder and CEO of Dryland Genetics, Inc.; a cofounder and managing partner of Data2Bio, LLC; a member of the scientific advisory boards of Kemin Industries and Centro de Tecnologia Canavieira; and the recipient of research funding from Iowa Corn and Bayer Crop Science. The remaining authors declare no competing interests. **Data and materials availability:** Data and summary statistics are available in the supplementary materials. Software, raw data, and code for image processing to generate data, statistics, and figures are available on Dryad and Zenodo (*41*, *42*).

SUPPLEMENTARY MATERIALS

science.org/doi/10.1126/science.ads5999
Materials and Methods
Figs. S1 to S9
References (*43*–*72*)
Data S1 to S16
MDAR Reproducibility Checklist

Submitted 21 August 2024; accepted 6 January 2025
10.1126/science.ads5999

METABOLISM

Endothelial insulin resistance induced by adrenomedullin mediates obesity-associated diabetes

Haaglim Cho[1], Chien-Cheng Lai[1], Rémy Bonnavion[1], Mohamad Wessam Alnouri[1], ShengPeng Wang[2], Kenneth Anthony Roquid[1], Haruya Kawase[1], Diana Campos[3], Min Chen[4], Lee S. Weinstein[4], Alfredo Martínez[5], Mario Looso[6,7], Miloslav Sanda[3], Stefan Offermanns[1,2,7,8,9]*

Insulin resistance is a hallmark of obesity-associated type 2 diabetes. Insulin's actions go beyond metabolic cells and also involve blood vessels, where insulin increases capillary blood flow and delivery of insulin and nutrients. We show that adrenomedullin, whose plasma levels are increased in obese humans and mice, inhibited insulin signaling in human endothelial cells through protein-tyrosine phosphatase 1B–mediated dephosphorylation of the insulin receptor. In obese mice lacking the endothelial adrenomedullin receptor, insulin-induced endothelial nitric oxide–synthase activation and skeletal muscle perfusion were increased. Treating mice with adrenomedullin mimicked the effect of obesity and induced endothelial and systemic insulin resistance. Endothelial loss or blockade of the adrenomedullin receptor improved obesity-induced insulin resistance. These findings identify a mechanism underlying obesity-induced systemic insulin resistance and suggest approaches to treat obesity-associated type 2 diabetes.

Diabetes is a major cause of morbidity, mortality, and high health care costs worldwide (*1*, *2*). The majority of diabetic patients suffer from obesity-induced insulin resistance and type 2 diabetes mellitus (*3*). Insulin resistance in type 2 diabetes has primarily been linked to major metabolic target cells such as skeletal muscle cells, adipocytes, and hepatocytes (*4*–*6*). To exert its effects on these cells, insulin has to reach them through the circulation and needs to pass the endothelial barrier. Evidence has been provided that these processes represent rate-limiting steps in the in vivo action of insulin (*7*–*9*). The insulin receptor is highly expressed on the luminal side of endothelial cells (*10*, *11*) and can mediate insulin's metabolic effects in different ways. Activation of endothelial insulin receptors leads to phosphorylation and activation of endothelial nitric oxide (NO)–synthase (eNOS), which results in NO-mediated vasodilation (*12*) and thereby promotes perfusion of insulin target organs such as the skeletal muscle (*13*, *14*). This increased perfusion leads to an increase in transendothelial transport of insulin and glucose as well as increased insulin action (*15*–*18*). Insulin via its receptor can also promote its own transendothelial transport (*9*, *19*–*21*). In mice with endothelium-specific loss of the insulin receptor or insulin receptor substrate 2, systemic insulin sensitivity is reduced owing to diminished insulin effects on skeletal muscle and adipose tissue but not on the liver (*16*, *22*). Because vascular insulin effects have been shown to be impaired in obesity-induced type 2 diabetes (*16*, *23*–*25*), we explored mechanisms of endothelial insulin resistance.

Adrenomedullin inhibits endothelial insulin signaling through G_s and PKA in vitro

When studying the endothelial role of the heterotrimeric GTP-binding protein (G protein) G_s in human umbilical venous endothelial cells (HUVECs) (*26*), we observed that small interfering RNA (siRNA)–mediated knockdown of $G\alpha_s$, which is encoded by the *GNAS* gene, increased insulin-induced eNOS phosphorylation and phosphorylation of AKT (Fig. 1A) as well as insulin-induced formation of NO (Fig. 1B). Knockdown of $G\alpha_s$ enhanced insulin receptor autophosphorylation at tyrosine residues 1162 and 1163 as well as its downstream signaling, including phosphorylation of phosphoinositide 3-kinase and AKT (Fig. 1C), suggesting that the presence of G_s normally inhibits insulin receptor autophosphorylation and downstream signaling in endothelial cells. Consistent with this, activation of G_s-coupled β-adrenergic receptors with isoproterenol inhibited insulin receptor autophosphorylation as well as downstream signaling (fig. S1A). Inhibition of protein kinase A (PKA)—a major downstream target of G_s-mediated signaling—with the specific myristoylated PKA inhibitor peptide PKI had a similar effect as knockdown of $G\alpha_s$, resulting in increased insulin receptor autophosphorylation and downstream signaling (fig. S1B).

To identify a putative G protein–coupled receptor (GPCR) operating upstream of G_s in endothelial cells to inhibit insulin signaling, we chose 16 receptors from GPCRs expressed in HUVECs, which showed high expression and which are either G_s-coupled or orphan receptors (*26*), and performed an siRNA-mediated knockdown of these receptors. Knockdown of the calcitonin receptor–like receptor (CALCRL) increased insulin-induced insulin receptor phosphorylation to a similar degree as knockdown of $G\alpha_s$ (Fig. 1D). CALCRL is a G_s-coupled receptor that in endothelial cells, together with receptor activity-modifying proteins 2 (RAMP2), functions as a receptor for adrenomedullin (*26*, *27*) (fig. S1C). An alternative siRNA directed against *CALCRL*—as well as treatment of cells with the adrenomedullin receptor antagonist peptide ADM(22-52)—also increased insulin-induced insulin receptor phosphorylation (fig. S1D and S2A), and adrenomedullin inhibited insulin receptor phosphorylation and downstream signaling, an effect blocked by the PKA inhibitor PKI (Fig. 1E and fig. S2, B and C). Adrenomedullin is highly expressed in endothelial cells (*26*, *28*), and its knockdown also increased insulin receptor phosphorylation and downstream signaling (fig. S2D). Adrenomedullin can induce eNOS activation in endothelial cells through PKA-mediated phosphorylation of serine residue 633 (*26*). However, the comparably strong insulin-induced phosphorylation of eNOS at serine residues 633 and 1177 was inhibited by adrenomedullin in HUVECs and microvascular cells (fig. S2, E to H). Thus, although adrenomedullin can induce some phosphorylation of eNOS in the absence of insulin, in the presence of insulin, which is a much stronger stimulator of eNOS phosphorylation, adrenomedullin inhibits insulin receptor phosphorylation and downstream signaling, including eNOS phosphorylation, through activation of PKA.

Adrenomedullin-induced dephosphorylation of the endothelial insulin receptor is mediated by PTP1B

Because PKA signaling can increase the activity of protein-tyrosine phosphatase 1B (PTP1B) (*29*, *30*), a phosphotyrosine phosphatase known to dephosphorylate the insulin receptor at tyrosine residues 1162 and 1163 (*31*, *32*), we determined the effect of adrenomedullin on PTP1B activity in the absence and presence of insulin. As expected, insulin induced inhibition of PTP1B activity (Fig. 1F and fig. S3). However, basal PTP1B activity was increased by adrenomedullin, and adrenomedullin prevented insulin-induced PTP1B inhibition, an effect which depended on PKA, because it was blocked by the PKA inhibitor peptide PKI (Fig. 1F and fig. S3). These data suggested that adrenomedullin inhibits insulin-induced insulin receptor phosphorylation by increasing PTP1B activity. Purified PTP1B alone

---

[1]Max Planck Institute for Heart and Lung Research, Department of Pharmacology, Bad Nauheim, Germany. [2]Department of Cardiovascular Medicine, the First Affiliated Hospital of Xi'an Jiaotong University, Xi'an, Shaanxi, China. [3]Max Planck Institute for Heart and Lung Research, Biomolecular Mass Spectrometry, Bad Nauheim, Germany. [4]Metabolic Disease Branch, National Institute of Diabetes and Digestive and Kidney Diseases, National Institutes of Health, Bethesda, MD, USA. [5]Oncology Area, Center for Biomedical Research of La Rioja (CIBIR), Logroño, Spain. [6]Max Planck Institute for Heart and Lung Research, Bioinformatics, Bad Nauheim, Germany. [7]Cardiopulmonary Institute (CPI), Bad Nauheim, Germany. [8]Center for Molecular Medicine, Goethe University Frankfurt, Frankfurt, Germany. [9]German Center for Cardiovascular Research (DZHK), partner site Frankfurt/Rhine-Main, Bad Nauheim, Germany.
***Corresponding author. Email: stefan.offermanns@mpi-bn.mpg.de**

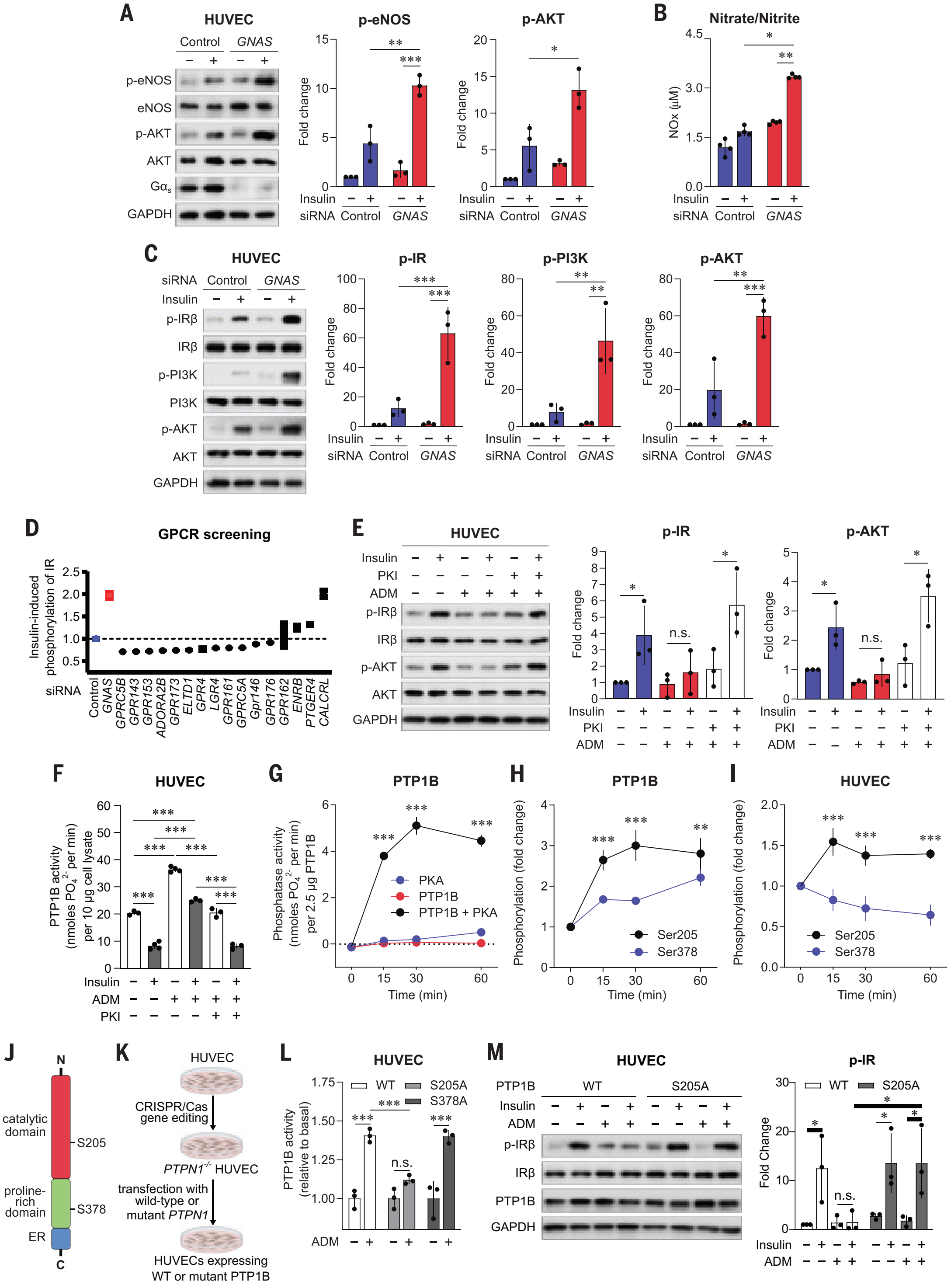

Fig. 1. Adrenomedullin inhibits endothelial insulin signaling. (**A**) Knockdown of Gα$_s$ (*GNAS*) in HUVECs increases phosphorylation of eNOS (S1177) and AKT (S473) induced by 100 nM insulin. GAPDH, glyceraldehyde-3-phosphate dehydrogenase; p-ERK, phosphorylated extracellular signal-related kinase. (**B**) Effect of Gα$_s$ knockdown on insulin-induced nitrate and nitrite (NOx) formation in HUVECs. (**C**) Knockdown of Gα$_s$ promotes insulin-induced phosphorylation of insulin receptor β-subunit [IRβ, Y1162/1163 (where Y is tyrosine)], phosphoinositide 3-kinase p85 subunit (PI3K, Y458), and AKT (S473) in HUVECs. (**D**) Effect of knockdown of the 16 indicated GPCRs on insulin-induced insulin receptor (IR) phosphorylation determined by phospho-insulin receptor enzyme-linked immunosorbent assay (ELISA) in HUVECs. The plot represents the ranked average ratios of three experiments. (**E**) Adrenomedullin (ADM; 100 nM) inhibits insulin-induced phosphorylation of insulin receptor β-subunit (IRβ, Y1162/1163) and of AKT (S473) in HUVECs, and pretreatment with 3 μM of the PKA inhibitor PKI for 30 min inhibits this effect. Bar graphs show densitometric analyses of blots (*n* = 3 independent experiments). (**F**) HUVECs were preincubated in the absence or presence of 100 nM adrenomedullin without or with 3 μM PKA inhibitor PKI for 30 min followed by 15 min of treatment with 100 nM insulin. Thereafter, PTP1B activity was determined (*n* = 3 independent experiments). (**G** and **H**) Amounts of 2.5 μg of purified full-length PTP1B and 1 μg of PKA were incubated alone (G) or together [(G) and (H)] at 30°C for the indicated time periods, and PTP1B activity was determined (G) or samples were analyzed for changes in protein phosphorylation by phosphoproteomic analysis (H) (*n* = 3). In (H), the sites of PTP1B found to be phosphorylated are shown, and their phosphorylation over time is presented as fold change compared with time point 0. (**I**) HUVECs were incubated for the indicated time periods with 100 nM adrenomedullin, and cellular proteins were analyzed by phosphoproteomics (*n* = 3). Shown is the phosphorylation of PTP1B at S205 and S378 over time as fold change compared with time point 0. (**J** and **K**) Schematic representation of the domain structure of PTP1B (ER, endoplasmic reticulum targeting domain) (J) and of the experimental design (K). WT, wild type. (**L**) Effect of 100 nM adrenomedullin on PTP1B activity in HUVECs expressing WT PTP1B or the phospho-site mutants PTP1B(S205A) or PTP1B(S378A). (**M**) Adrenomedullin (100 nM) inhibits insulin receptor phosphorylation induced by 100 nM insulin in HUVECs expressing WT PTP1B but not cells expressing the S205A mutant of PTP1B (*n* = 3). Data are presented as mean ± SD. *$P \leq 0.05$; **$P \leq 0.01$; ***$P \leq 0.001$; n.s., not significant. Mann-Whitney test for (A) to (C), (E), (F), (L), and (M); two-way analysis of variance (ANOVA) (Tukey's multiple comparison test) for (G) to (I).

showed hardly any phosphatase activity; however, phosphatase activity strongly increased when PTP1B was incubated together with the catalytic subunit of PKA, which itself had no activity (Fig. 1G). Phosphoproteomic analysis revealed that serine residues 205 and 378 of PTP1B showed increased phosphorylation in the presence of PKA (Fig. 1H). However, only serine 205 phosphorylation occurred with a similar time course as PKA-dependent increases in phosphatase activity (Fig. 1G and H), and serine 205 was also found to be phosphorylated in adrenomedullin-treated HUVECs (Fig. 1I). We then expressed phosphosite mutants of PTP1B in HUVECs after knockout of endogenous PTP1B (Fig. 1, J and K) and determined adrenomedullin effects on PTP1B activity. Wild-type PTP1B and the S378A mutant (S378→A, where S is serine, and A is alanine) showed adrenomedullin-induced activation of PTP1B. However, the S205A mutant failed to respond with increased activity to adrenomedullin treatment (Fig. 1L), although it was expressed at the same level as wild-type PTP1B (Fig. 1M). In HUVECs expressing the S205A mutant, adrenomedullin lost the ability to inhibit insulin-induced insulin receptor phosphorylation compared with cells expressing wild-type PTP1B (Fig. 1M).

Endothelial loss of G_s and adrenomedullin receptor improves insulin resistance in obese mice

In Tek-CreER^{T2};*Gnas*$^{fl/fl}$ mice (herein referred to as EC-$G\alpha_s$-KO mice) with inducible endothelium-specific $G\alpha_s$ deficiency, body weight and glucose tolerance were unchanged when animals were kept under a normal chow diet (fig. S4, A and B). EC-$G\alpha_s$-KO mice fed a high-fat diet (HFD) also showed normal weight gain (Fig. 2A and fig. S4C). However, obese HFD-fed EC-$G\alpha_s$-KO mice had an improved glucose tolerance compared with wild-type controls (Fig. 2B and fig. S4D) and after 16 weeks of HFD showed improved insulin sensitivity compared with controls (Fig. 2C and fig. S4E). By contrast, glucose-stimulated insulin secretion was indistinguishable between wild-type and EC-$G\alpha_s$-KO animals (fig. S4F). To analyze insulin sensitivity in insulin target organs, we injected insulin into HFD-fed mice (Fig. 2D). As shown in Fig. 2E, insulin-induced phosphorylation of the insulin receptor, of AKT, and of extracellular signal–regulated kinases 1 and 2 (ERK1/2) in skeletal muscle—as well as in the visceral white adipose tissue (vWAT)—were increased in tissues of EC-$G\alpha_s$-KO mice compared with control animals.

Similarly to EC-$G\alpha_s$-KO mice, inducible endothelium-specific CALCRL-deficient mice (Tek-CreER^{T2};*Calcrl*$^{fl/fl}$; hereafter referred to as EC-Calcrl-KO) had normal glucose tolerance when fed normal chow (fig. S5, A and B) and when fed a HFD showed normal weight gain but also an improved glucose tolerance (Fig. 2, F and G, and fig. S5, C and D), which was accompanied by increased systemic insulin sensitivity (Fig. 2H and fig. S5E) and by increased insulin-induced insulin receptor phosphorylation and downstream signaling in skeletal muscle and vWAT (fig. S5F). Thus, loss of endothelial adrenomedullin receptor and G_S signaling in vitro and in vivo increases insulin-induced insulin receptor activation and improves insulin sensitivity in obese type 2 diabetic mice.

Increased insulin-induced vascular effects in obese mice lacking endothelial CALCRL or G_s

Insulin-induced eNOS phosphorylation and activation were increased not only after knockdown of endothelial $G\alpha_s$ in vitro (Fig. 1, A and B), but also under in vivo conditions in the skeletal muscle and vWAT of HFD-fed EC-$G\alpha_s$-KO and EC-Calcrl-KO mice (Fig. 3, A and B), and their nitrate and nitrite plasma levels were elevated compared with control animals (Fig. 3C). However, in normal chow-fed mice treated with insulin, phosphorylation of eNOS in tissues and nitrate and nitrite plasma levels were unchanged (fig. S6, A to C). We then determined the effect of insulin on skeletal muscle perfusion in obese mice by laser speckle contrast imaging directly on the medial muscles of the upper thigh. Insulin induced some increase in skeletal muscle perfusion in HFD-fed control mice, but this effect was strongly increased in EC-$G\alpha_s$-KO and EC-Calcrl-KO mice (Fig. 3, D and E). Thus, insulin-induced endothelial eNOS activation and skeletal muscle perfusion are reduced in HFD-fed obese mice owing to activation of the G_s-coupled adrenomedullin receptor. Because of the strong adrenomedullin receptor–mediated effect on tissue perfusion, we could not determine potential effects on endothelial transcytosis of insulin in vivo. However, in vitro, we found that adrenomedullin inhibited insulin uptake and insulin-induced insulin receptor internalization, as well as insulin transcytosis, in human microvascular cells (Fig. 3F and fig. S6, D and E), a factor that may contribute to the adrenomedullin effects on insulin activity in skeletal muscle and adipose tissue.

Plasma levels of adrenomedullin and of adrenomedullin binding protein (CFH) are increased in obese mice and humans

Adrenomedullin plasma levels are increased severalfold in obese diabetic patients (*33–36*). We found that plasma levels of adrenomedullin were also increased in *ob*/*ob* mice as well as in HFD-fed mice compared with normal lean animals (Fig. 4, A and B, and fig. S7, A and B), whereas levels of adrenomedullin 2 were decreased (fig. S7C). Most of the increase in plasma adrenomedullin levels under in vivo conditions was due to adrenomedullin produced by adipocytes, because plasma levels of adipocyte-specific adrenomedullin-deficient mice (Adipoq-CreER^{T2};*Adm*$^{fl/fl}$; AC-Adm-KO) did not increase in contrast to control animals or mice lacking adrenomedullin in endothelial cells (Tek-CreER^{T2};*Adm*$^{fl/fl}$; EC-Adm-KO) (Fig. 4C and fig. S7D). Consistent with this, adrenomedullin expression was increased in adipocytes from obese mice compared with lean control animals (fig. S7E), and mice lacking adrenomedullin specifically in adipocytes but not in endothelial cells showed improved glucose tolerance and insulin sensitivity when fed a HFD to induce obesity but not after normal chow feeding (fig. S7, F to K). Adrenomedullin binds to complement factor H (CFH), also known as adrenomedullin binding protein 1 (*37*, *38*), and CFH promotes activation of the adrenomedullin receptor by adrenomedullin (*39*), an effect we also observed in HUVECs (Fig. 4D). CFH plasma levels also increase in patients with obesity and type 2 diabetes (*40*), and plasma CFH concentrations were also increased in HFD-fed obese mice (Fig. 4E and fig. S7L). This suggests that increased plasma adrenomedullin and CFH levels cooperatively lead to increased endothelial adrenomedullin receptor activation in obese mice, resulting in endothelial insulin resistance and reduced glucose tolerance. Also in human adipocytes, adrenomedullin expression increases during obesity (fig. S7, M and N), and we could confirm elevated plasma levels of adrenomedullin and of CFH and decreased levels of adrenomedullin 2 in obese type 2 diabetic patients compared with a metabolically healthy control group. Adrenomedullin levels correlated within both groups with the body mass index (BMI) (Fig. 4, F and G; fig. S7O; and table S1).

The endothelial adrenomedullin receptor mediates systemic insulin sensitivity

When normal chow-fed mice were treated with adrenomedullin through an osmotic pump to reach plasma levels similar to those found in obese humans and mice (Fig. 4, H and I), a decrease in both glucose tolerance (Fig. 4J)—which in individual animals correlated with the plasma adrenomedullin concentration (Fig. 4J)—and insulin sensitivity (Fig. 4K) was observed. However, in EC-Calcrl-KO mice, the same adrenomedullin treatment had no effect (Fig. 4, L to N). This finding further supports the critical role of endothelial adrenomedullin receptor signaling in promoting endothelial and systemic insulin resistance in type 2 diabetes.

Loss of endothelial adrenomedullin signaling improves glucose tolerance in obese type 2 diabetic mice

To test whether inhibition of the endothelial adrenomedullin receptor system and its downstream signaling can serve as a therapeutic approach to increase insulin sensitivity in obese type 2 diabetic mice, we fed mice for 7 weeks with a HFD and then treated them for 5 days with tamoxifen to induce endothelium-specific $G\alpha_s$ or adrenomedullin receptor deficiency while continuing the HFD feeding. Both EC-$G\alpha_s$-KO and EC-Calcrl-KO mice showed a comparable

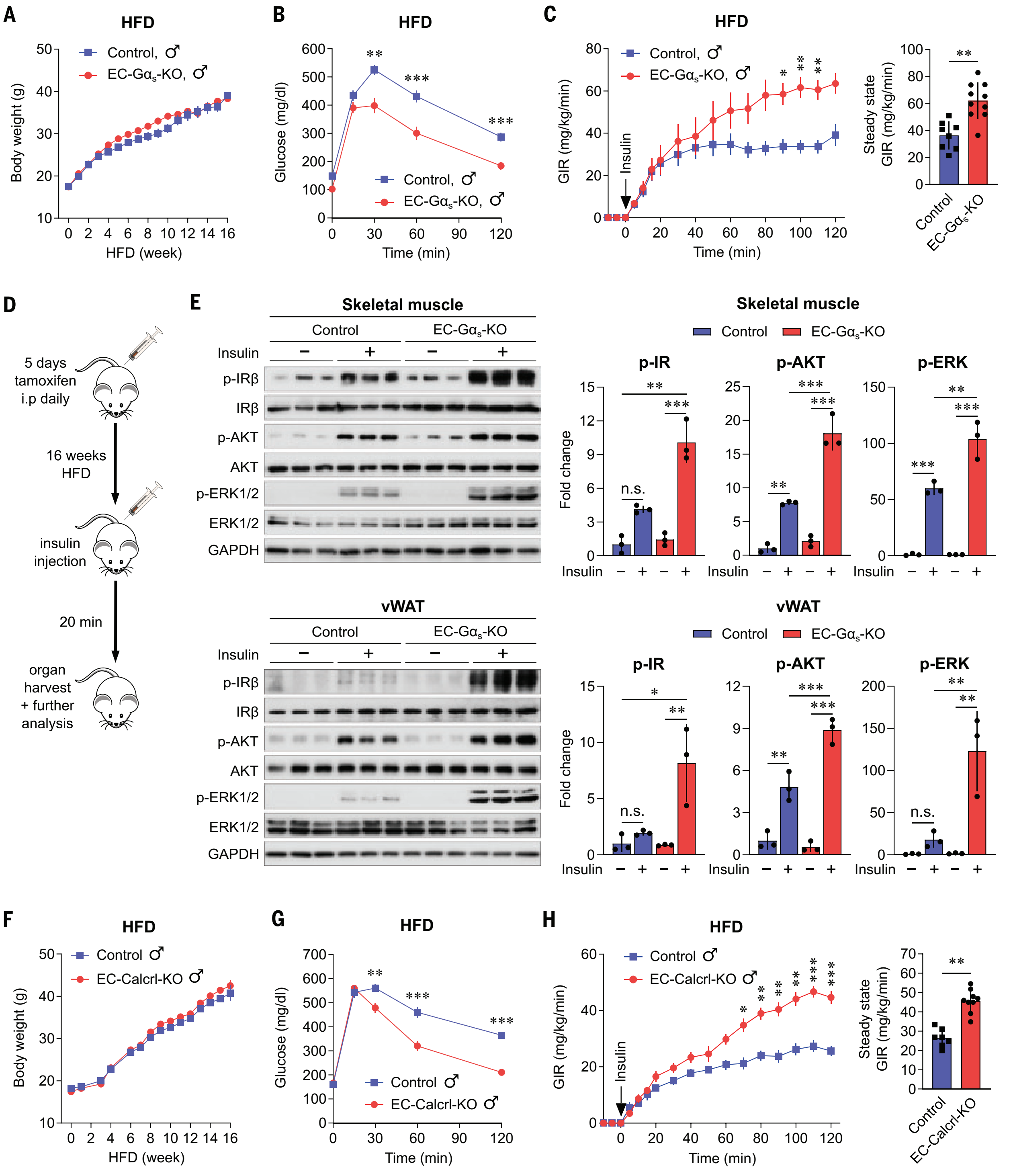

Fig. 2. Increased insulin sensitivity in type 2 diabetic mice with endothelial loss of G_s or the adrenomedullin receptor. (**A**) Body weight of male control and EC-Gα_s-KO mice during 16 weeks of high-fat diet (HFD) feeding (*n* = 10 mice). (**B** and **C**) Glucose tolerance (B) and glucose infusion rate (GIR) during glucose clamp experiment (C) of male control and EC-Gα_s-KO mice after 16 weeks of HFD feeding (*n* = 10 mice). (**D**) Schematic representation of experimental design. i.p., intraperitoneal. (**E**) Control or EC-Gα_s-KO animals fed a HFD for 16 weeks were injected with insulin (100 IU/kg body weight) and were euthanized after 20 min to determine insulin receptor phosphorylation and downstream signaling in skeletal muscle and visceral white adipose tissue (vWAT). Total and phosphorylated levels of the indicated proteins in tissue lysates were determined by Western blotting. The bar graphs in the right panels show the densitometry analyses of the blots (*n* = 3 animals per group). (**F**) Body weight of male control and EC-Calcrl-KO mice during 16 weeks of HFD feeding. (**G** and **H**) Glucose tolerance (G) and GIR during glucose clamp experiments (H) after 16 weeks of HFD feeding in male control animals (*n* = 6 mice) and EC-Calcrl-KO mice (*n* = 10 mice). Data are presented as mean ± SEM in (A), (B), and (C) (left panel), (F), (G), and (H) (left panel), or as SD in (C) (right panel), (E), and (H) (right panel). $^*P \le 0.05$; $^{**}P \le 0.01$; $^{***}P \le 0.001$; n.s., not significant. Two-way ANOVA with Bonferroni's multiple comparisons for (A), (B), and (C) (left panel), (F), (G), and (H) (left panel); Mann-Whitney test for (C) (right panel), (E), and (H) (right panel).

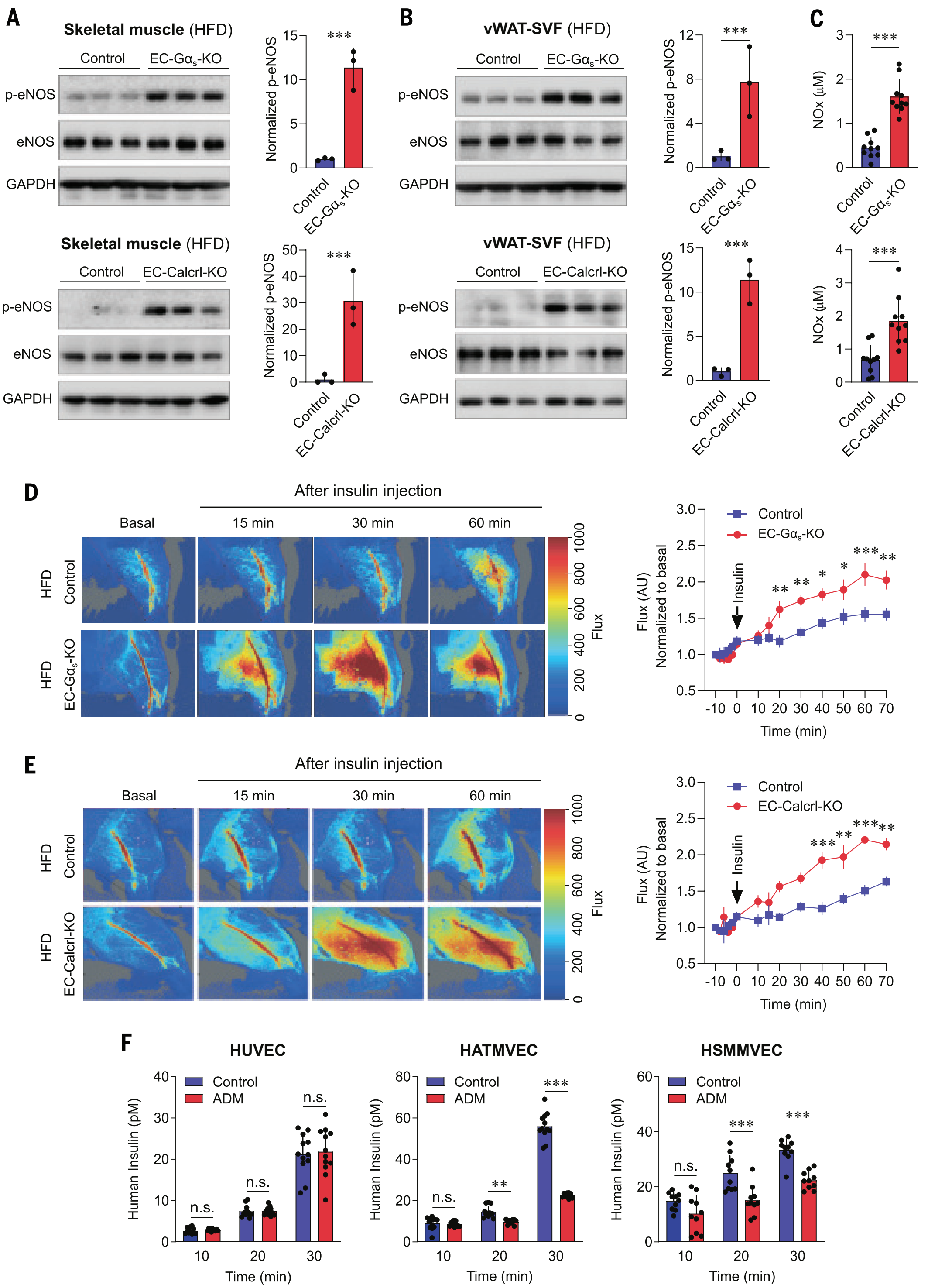

Fig. 3. Increased insulin-induced vascular effects in obese mice lacking endothelial CALCRL or G_s. (**A** to **C**) Control [(A) to (C)], EC-$G\alpha_s$-KO [(A) and (C)], and EC-Calcrl-KO animals [(B) and (C)] were fed a HFD for 16 weeks. After 6 hours of fasting, mice were intravenously injected with insulin (100 IU/kg body weight). Mice were euthanized 20 min later, and phosphorylation of murine eNOS (S1176) in skeletal muscle (A) or vWAT-derived stroma vascular fraction (vWAT-SVF) (B) or NOx concentration in the plasma (C) was determined [*n* = 3 mice for (A) and (B); *n* = 10 mice for (C)]. (**D** and **E**) Control and EC-$G\alpha_s$-KO (D) or EC-Calcrl-KO animals (E) were fed a HFD for 16 weeks. Anesthetized mice were injected intravenously with 100 IU/kg insulin, and insulin-dependent changes of skeletal muscle perfusion were determined through laser speckle contrast imaging directly on the upper thigh muscle for the indicated time periods [*n* = 8 mice per group (D) or 4 mice per group (E)]. AU, arbitrary units. (**F**) HUVECs as well as human adipose tissue and skeletal muscle microvascular endothelial cells (HATMVECs and HSMMVECs, respectively) were seeded on transwell dishes, and transcytosis of recombinant insulin was analyzed in the absence or presence of 100 nM adrenomedullin for the indicated time periods [*n* = 12 (HUVECs and HATMVECs) and *n* = 10 (HSMMVECs) independent experiments]. Data are presented as mean ± SD in (A) to (C) and (F), or as SEM in (D) and (E). $^*P \leq 0.05$; $^{**}P \leq 0.01$; $^{***}P \leq 0.001$; n.s., not significant. Mann-Whitney test for (A) to (C) and (F); two-way ANOVA test with Bonferroni's multiple comparisons test for (D) and (E).

weight gain compared with control animals (fig. S8, A and B). After 6 weeks of HFD and before induction of EC-$G\alpha_s$-KO or EC-Calcrl-KO mice, their glucose tolerance was indistinguishable from that of control animals (Fig. 5, A and B). However, only 2 weeks after induction of endothelial $G\alpha_s$ or adrenomedullin receptor deficiency, glucose tolerance had already improved (Fig. 5, A and B). Under continuous HFD feeding for 12 and 16 weeks, glucose tolerance in control animals further decreased, but glucose tolerance of EC-$G\alpha_s$-KO and EC-Calcrl-KO mice remained unchanged (Fig. 5, A and B) and insulin sensitivity was increased in both knockout models (fig. S8, C and D).

Lastly, treatment of obese type 2 diabetic mice—which had been fed a HFD for 15 weeks—with the adrenomedullin receptor antagonist peptide ADM(24-50) (*41*) (Fig. 5C and fig. S8E) led to an increase in glucose tolerance and insulin sensitivity compared with vehicle-treated animals (Fig. 5, D and E).

Discussion

Pioneering experiments in the 1990s had suggested that delivery of insulin through the vascular system and across the endothelial cell layer

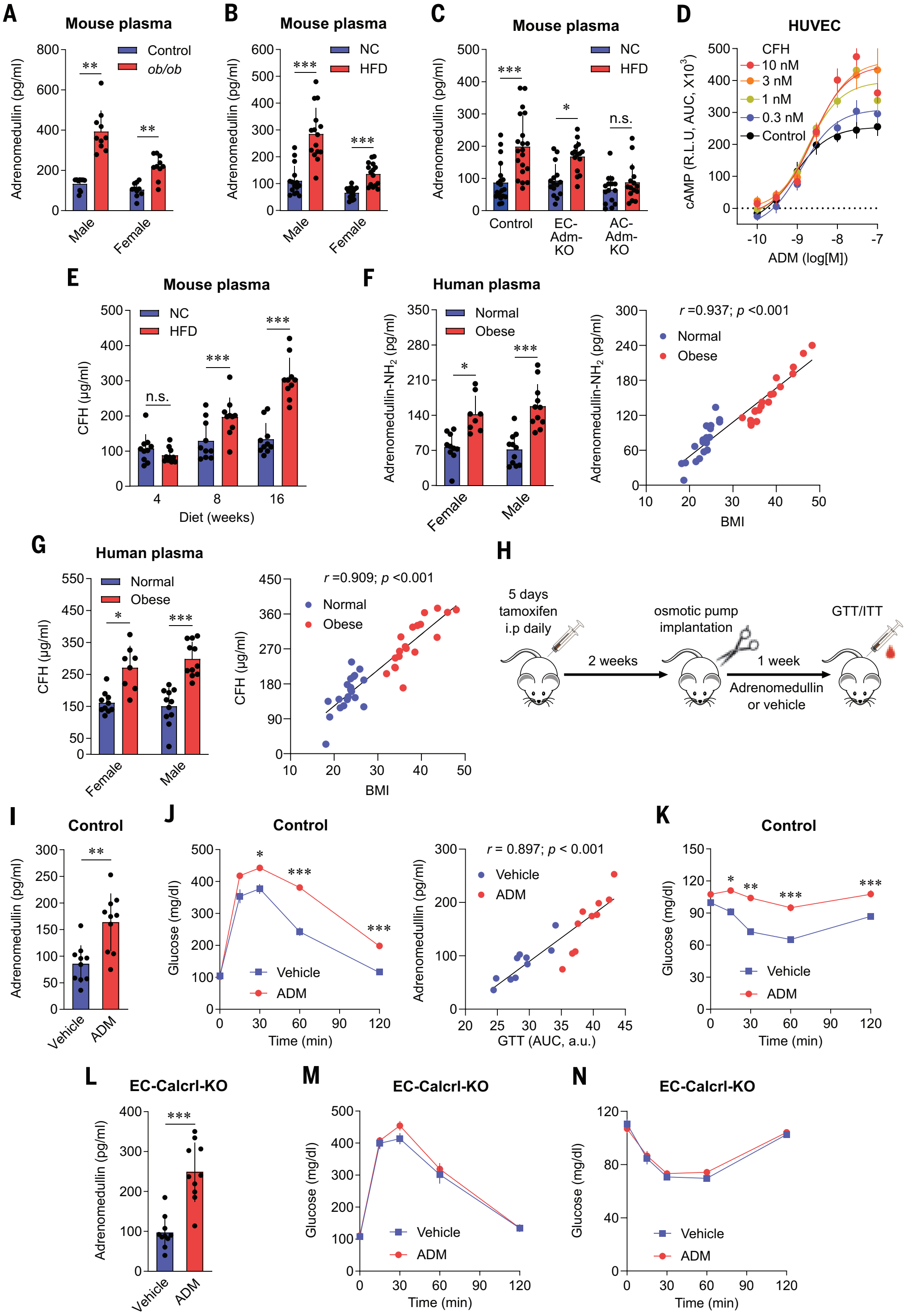

Fig. 4. Adrenomedullin and CFH plasma levels and adrenomedullin effects on glucose tolerance. (**A** to **C**) Adrenomedullin plasma levels in control mice [(A) to (C)], leptin-deficient *ob/ob* mice (A), or in endothelium-specific or adipocyte-specific adrenomedullin-deficient mice (EC-Adm-KO and AC-Adm-KO, respectively) (C) fed either normal chow (NC) diet [(A) to (C)] or HFD [(B) and (C)] [*n* = 10 mice for (A); *n* = 15 mice for (B) and for (C) KOs; *n* = 20 mice for (C) controls]. (**D**) Effect of increasing concentrations of complement factor H (CFH) on adrenomedullin-induced increases in cAMP concentration in HUVECs. Shown is a representative of two independently performed experiments; *n* = 6. RLU, relative luminescence units; AUC, area under the curve. (**E**) Plasma CFH levels determined by mass spectrometry in mice kept for the indicated time periods on NC diet or HFD (*n* = 10 mice per group). (**F** and **G**) Plasma adrenomedullin (F) and CFH (G) levels in obese patients (obese) and in metabolically healthy control subjects (control) [*n* = 8 (obese females); *n* = 10 (healthy females); *n* = 11 (obese and healthy males]. Graphs on the right show the correlation between body mass index (BMI) and plasma adrenomedullin and CFH levels in individual subjects. (**H**) Schematic representation of the experimental design. (**I** to **N**) Control mice [(I) to (K)] or EC-Calcrl-KO animals [(L) to (N)] received 150 µg/day ADM or vehicle through an osmotic pump over 1 week. Thereafter, plasma adrenomedullin levels [(I) and (L)], glucose tolerance [(J) and (M)], and insulin sensitivity (K) and (N) were determined (*n* = 10 mice per group). The right-hand graph in (J) shows the correlation between glucose tolerance and the plasma adrenomedullin concentration in individual animals. Shown are mean values ± SD in (A) to (D), (E) to (G), (I), and (L), or SEM in (J), (K), (M), and (N). *$P \leq 0.05$; **$P \leq 0.01$; ***$P \leq 0.001$; n.s., not significant. Mann-Whitney test for (A) to (C), (E) to (G), (I), and (L); two-way ANOVA test with Bonferroni's multiple comparisons test for (J), (K), (M), and (N). A significant correlation ($P < 0.001$) is indicated by Pearson's correlation coefficient test in (F), (G), and (J), right-hand panels.

is a rate-limiting step in the in vivo action of insulin (*7*, *42*, *43*) and that insulin-induced increase in capillary-flow velocity—which is mediated by eNOS activation—and transendothelial insulin transport may be impaired in patients with type 2 diabetes (*13*, *24*, *44*, *45*). Subsequent studies in humans and in animal models provided additional evidence for a link between systemic insulin resistance and reduced endothelial insulin sensitivity leading to reduced insulin-induced perfusion of metabolic target organs and thereby impaired insulin actions at metabolic target cells (*23*, *25*). Endothelial insulin resistance in type 2 diabetes has been proposed to be due to inflammatory or metabolic processes (*46*, *47*). However, the underlying cellular mechanisms have remained elusive, and the potential role of endothelial insulin resistance in type 2 diabetes could not be proven directly. In this study, we have shown that obesity-associated endothelial insulin resistance is caused by increased adrenomedullin-mediated endothelial activation of G_s/PKA signaling, resulting in activation of PTP1B and dephosphorylation of the

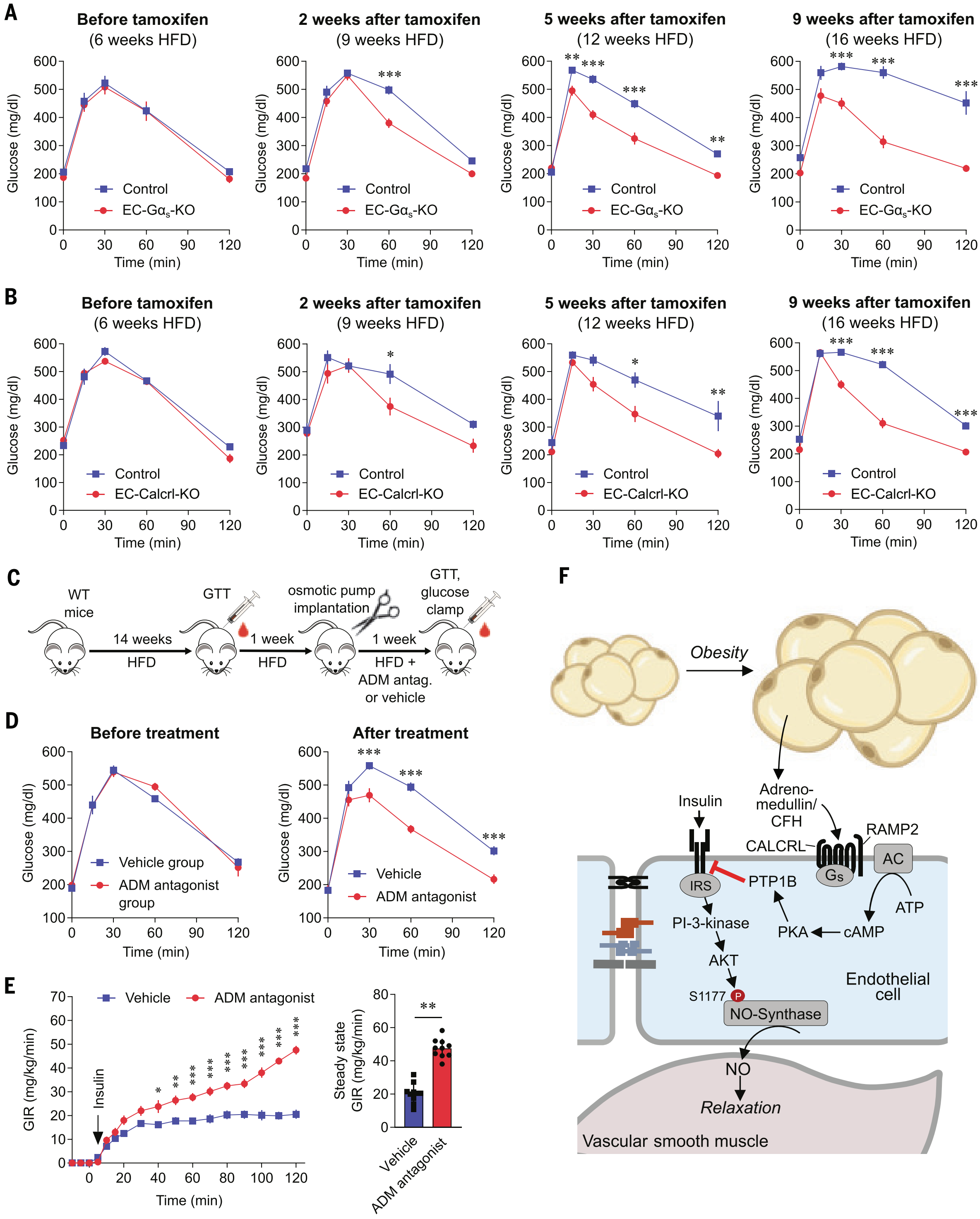

Fig. 5. Loss of endothelial adrenomedullin signaling improves glucose tolerance in obese type 2 diabetic mice. (**A** and **B**) Glucose tolerance of control and EC-$G\alpha_s$-KO (A) or EC-Calcrl-KO mice (B) was determined 1 week before induction of the endothelium-specific knockout by tamoxifen injection (after 6 weeks of HFD feeding) as well as 2, 5, and 9 weeks after the beginning of the tamoxifen treatment (after 9, 12, and 16 weeks of HFD feeding, respectively) [*n* = 8 (control and EC-$G\alpha_s$-KO mice); *n* = 6 and 7 (control and EC-Calcrl-KO mice, respectively)]. (**C**) Schematic representation of experimental design. GTT, glucose tolerance test. (**D** and **E**) Glucose tolerance (D) and insulin sensitivity (E) of wild-type mice fed a HFD for 14 weeks before treatment with the adrenomedullin receptor antagonist ADM(24-50) (D) and after 16 weeks of HFD feeding and a 1-week treatment with 150 μg/day of ADM(24-50) or vehicle [(D) and (E) (*n* = 10 mice per group). (**F**) Schematic representation of the mechanism underlying the adrenomedullin-induced endothelial insulin resistance in obesity-associated type 2 diabetes. AC, adenylyl cyclase. Data are presented as mean ± SEM in (A), (B), (D), and (E) (left panel), or as SD in (E) (right panel). $^*P \leq 0.05$; $^{**}P \leq 0.01$; $^{***}P \leq 0.001$. Two-way ANOVA with Bonferroni's multiple comparisons for (A), (B), (D), and (E) (left panel); Mann-Whitney test for (E) (right panel).

endothelial insulin receptor, which thereby inhibits insulin receptor–mediated vasorelaxation and transendothelial insulin transport (Figs. 3 and 5F).

We have also shown that systemic insulin resistance in obese mice can be effectively treated by loss or blockade of the endothelial adrenomedullin receptor and downstream signaling events (Fig. 5), indicating that endothelial insulin resistance substantially contributes to systemic insulin resistance in obesity. Loss of endothelial adrenomedullin signaling had no effect on the glucose tolerance of lean, nondiabetic animals. This finding suggests that endothelial adrenomedullin signaling is increased in obese mice because of elevated plasma adrenomedullin levels as compared with lean mice and that this mechanism is responsible for decreased endothelial insulin sensitivity, resulting in systemic insulin resistance. A similar increase in plasma adrenomedullin has been reported by multiple studies in humans with type 2 or gestational diabetes (*33*–*36*), and we were able to confirm this result in a group of obese type 2 diabetic patients in whom plasma levels of adrenomedullin strongly correlated with their BMI (Fig. 4F). We found that the obesity-induced increase in plasma adrenomedullin levels was mainly due to adrenomedullin produced by adipocytes and that adipocytes from both obese mice and humans showed increased expression of adrenomedullin.

CFH, which serves as an adrenomedullin binding protein, enhances adrenomedullin-induced cellular effects (*37*, *39*) (Fig. 4D) through incompletely understood mechanisms. CFH plasma levels are increased in obese type 2 diabetic patients (*48*–*51*) and mice (Fig. 4, E and G), and elevated CFH plasma levels in obese type 2 diabetic patients correlated with their BMI (Fig. 4G). Our data indicate that the increase in plasma adrenomedullin levels during obesity leads to increased endothelial adrenomedullin receptor activation and insulin receptor dephosphorylation and that this effect is potentiated by the parallel increase in plasma levels of the adrenomedullin-binding protein CFH.

PTP1B, which we identified as a critical mediator of adrenomedullin-induced endothelial insulin signaling, plays an important role in insulin receptor dephosphorylation (*52*) and is regarded as a key regulator of insulin sensitivity (*53*). It has been shown that PKA can increase the activity of PTP1B and thereby inhibit insulin signaling (*29*, *30*). Through a combination of phosphoproteomic analysis and site-directed mutagenesis, we identified serine residue 205 of PTP1B as a substrate of PKA. Replacement of serine 205 of PTP1B by an alanine residue prevented stimulation of PTP1B activity through PKA and blocked adrenomedullin-induced inhibition of insulin-induced insulin receptor phosphorylation in endothelial cells. Serine 205 is located in the S-loop (residues 201 to 209) of the N-terminal catalytic domain of PTP1B (*54*). The S-loop has been proposed to be crucial for the conformational motions of the WPD-loop (residues 177 to 188) (*55*), which is essential for the catalytic mechanism of PTP1B (*55*, *56*). Thus, PTP1B serine 205 phosphorylation by PKA is a critical mechanism of the regulation of insulin sensitivity and may be involved in the regulation of insulin signaling by cyclic adenosine monophosphate (cAMP) in other insulin target organs (*57*–*60*).

Insulin resistance is the key pathophysiological process underlying the development of type 2 diabetes, which occurs very early during disease manifestation, when plasma glucose levels are still normal owing to a compensatory increase in insulin release by pancreatic β cells. In addition to its central role in type 2 diabetes, insulin resistance has also been implicated as a risk factor for various other diseases, including cardiovascular diseases, nonalcoholic steatohepatitis, cancer, and neurodegenerative disorders (*61*–*64*). Studies to explore the mechanisms underlying insulin resistance have focused on primary metabolic target cells of insulin, such as skeletal muscle cells, adipocytes, and hepatocytes. To induce anabolic effects in these cell types, insulin must reach these organs via the circulation by increasing organ perfusion and must pass the endothelial layer through transendothelial transport; these processes are mediated by the insulin receptor expressed on endothelial cells. Our data identify endothelial cells as a critical site of insulin resistance in type 2 diabetes, and we have provided evidence for a central mechanism of endothelial insulin resistance induced by elevated plasma levels of adrenomedullin and CFH in obesity and type 2 diabetes. Adrenomedullin-induced, G_s/PKA–mediated endothelial inhibition of insulin receptor phosphorylation may serve as a target for approaches to prevent and treat insulin resistance.

REFERENCES AND NOTES

1. X. Lin *et al.*, *Sci. Rep.* **10**, 14790 (2020).
2. D. Tomic, J. E. Shaw, D. J. Magliano, *Nat. Rev. Endocrinol.* **18**, 525–539 (2022).
3. S. Klein, A. Gastaldelli, H. Yki-Järvinen, P. E. Scherer, *Cell Metab.* **34**, 11–20 (2022).
4. M. C. Petersen, G. I. Shulman, *Physiol. Rev.* **98**, 2133–2223 (2018).
5. D. E. James, J. Stöckli, M. J. Birnbaum, *Nat. Rev. Mol. Cell Biol.* **22**, 751–771 (2021).
6. T. M. Batista, N. Haider, C. R. Kahn, *Diabetologia* **64**, 994–1006 (2021).
7. Y. J. Yang, I. D. Hope, M. Ader, R. N. Bergman, *J. Clin. Invest.* **84**, 1620–1628 (1989).
8. P. D. Miles *et al.*, *Diabetes* **44**, 947–953 (1995).
9. W. L. Lee, A. Klip, *Physiology* **31**, 336–345 (2016).
10. R. S. Bar, J. C. Hoak, M. L. Peacock, *J. Clin. Endocrinol. Metab.* **47**, 699–702 (1978).
11. M. van Houten, B. I. Posner, *Nature* **282**, 623–625 (1979).
12. I. Fleming, *Pflugers Arch.* **459**, 793–806 (2010).
13. H. O. Steinberg, G. Brechtel, A. Johnson, N. Fineberg, A. D. Baron, *J. Clin. Invest.* **94**, 1172–1179 (1994).
14. U. Scherrer, D. Randin, P. Vollenweider, L. Vollenweider, P. Nicod, *J. Clin. Invest.* **94**, 2511–2515 (1994).
15. M. A. Vincent *et al.*, *Diabetes* **53**, 1418–1423 (2004).
16. T. Kubota *et al.*, *Cell Metab.* **13**, 294–307 (2011).
17. P. M. McClatchey *et al.*, *Am. J. Physiol. Endocrinol. Metab.* **317**, E1022–E1036 (2019).
18. T. Akerstrom *et al.*, *Microcirculation* **27**, e12593 (2020).
19. G. L. King, S. M. Johnson, *Science* **227**, 1583–1586 (1985).
20. I. M. Williams, D. H. Wasserman, *Endocrinology* **163**, bqab252 (2022).
21. S. Yazdani, J. R. Jaldin-Fincati, R. V. S. Pereira, A. Klip, *Traffic* **20**, 390–403 (2019).
22. M. Konishi *et al.*, *Proc. Natl. Acad. Sci. U.S.A.* **114**, E8478–E8487 (2017).
23. E. J. Barrett, Z. Liu, *Rev. Endocr. Metab. Disord.* **14**, 21–27 (2013).
24. M. Laakso, S. V. Edelman, G. Brechtel, A. D. Baron, *J. Clin. Invest.* **85**, 1844–1852 (1990).
25. C. Rask-Madsen, G. L. King, *Nat. Clin. Pract. Endocrinol. Metab.* **3**, 46–56 (2007).
26. A. Iring *et al.*, *J. Clin. Invest.* **129**, 2775–2791 (2019).
27. D. R. Poyner *et al.*, *Pharmacol. Rev.* **54**, 233–246 (2002).
28. T. Koyama *et al.*, *J. Atheroscler. Thromb.* **22**, 647–653 (2015).
29. L. Wang *et al.*, *Nat. Commun.* **11**, 2995 (2020).
30. J. Tao, C. C. Malbon, H. Y. Wang, *J. Biol. Chem.* **276**, 29520–29525 (2001).
31. J. Bakke, F. G. Haj, *Semin. Cell Dev. Biol.* **37**, 58–65 (2015).
32. S. C. Yip, S. Saha, J. Chernoff, *Trends Biochem. Sci.* **35**, 442–449 (2010).
33. Y. Dong *et al.*, *J. Clin. Endocrinol. Metab.* **104**, 697–706 (2019).
34. M. Hayashi *et al.*, *Lancet* **350**, 1449–1450 (1997).
35. A. Katsuki *et al.*, *Eur. J. Endocrinol.* **147**, 71–75 (2002).
36. A. Martínez *et al.*, *Peptides* **20**, 1471–1478 (1999).
37. R. B. Sim *et al.*, *Mol. Immunol.* **68**, 45–48 (2015).
38. T. H. Elsasser *et al.*, *Endocrinology* **140**, 4908–4911 (1999).
39. R. Pío *et al.*, *J. Biol. Chem.* **276**, 12292–12300 (2001).
40. J. M. Moreno-Navarrete, J. M. Fernández-Real, *Semin. Cell Dev. Biol.* **85**, 164–172 (2019).
41. S. D. Robinson, J. F. Aitken, R. J. Bailey, D. R. Poyner, D. L. Hay, *J. Pharmacol. Exp. Ther.* **331**, 513–521 (2009).
42. G. R. Freidenberg *et al.*, *Diabetes* **43**, 118–126 (1994).
43. P. A. Jansson, J. P. Fowelin, H. P. von Schenck, U. P. Smith, P. N. Lönnroth, *Diabetes* **42**, 1469–1473 (1993).
44. A. D. Baron *et al.*, *J. Clin. Invest.* **96**, 786–792 (1995).
45. P. D. Miles *et al.*, *J. Clin. Invest.* **101**, 202–211 (1998).
46. J. A. Kim, M. Montagnani, K. K. Koh, M. J. Quon, *Circulation* **113**, 1888–1904 (2006).
47. L. Zhao *et al.*, *Clin. Sci. (Lond.)* **129**, 1025–1036 (2015).
48. C. Pomeroy *et al.*, *Clin. Exp. Immunol.* **108**, 507–515 (1997).
49. J. M. Moreno-Navarrete *et al.*, *Diabetes* **59**, 200–209 (2010).
50. A. E. Butler, A. S. M. Moin, T. Sathyapalan, S. L. Atkin, *Cells* **12**, 2002 (2023).
51. Z. Z. Chen *et al.*, *Diabetes* **72**, 532–543 (2023).
52. L. V. Ravichandran, H. Chen, Y. Li, M. J. Quon, *Mol. Endocrinol.* **15**, 1768–1780 (2001).
53. M. Delibegović, S. Dall'Angelo, R. Dekeryte, *Nat. Rev. Endocrinol.* **20**, 366–378 (2024).
54. R. Liu *et al.*, *Int. J. Mol. Sci.* **23**, 7027 (2022).
55. J. F. Wang, K. Gong, D. Q. Wei, Y. X. Li, *Interdiscip. Sci.* **1**, 214–219 (2009).
56. S. C. Kamerlin, R. Rucker, S. Boresch, *Biochem. Biophys. Res. Commun.* **356**, 1011–1016 (2007).
57. S. Mangmool *et al.*, *Mol. Endocrinol.* **30**, 118–132 (2016).
58. A. Guilherme, L. A. Rowland, H. Wang, M. P. Czech, *Trends Cell Biol.* **33**, 340–354 (2023).
59. P. Jost *et al.*, *Am. J. Physiol. Endocrinol. Metab.* **283**, E146–E153 (2002).
60. S. R. Richmond, C. D. Touchberry, P. M. Gallagher, *Appl. Physiol. Nutr. Metab.* **34**, 916–925 (2009).
61. T. M. Barber, I. Kyrou, H. S. Randeva, M. O. Weickert, *Int. J. Mol. Sci.* **22**, 546 (2021).
62. E. J. Gallagher, D. LeRoith, *Nat. Rev. Cancer* **20**, 629–644 (2020).
63. A. Di Pino, R. A. DeFronzo, *Endocr. Rev.* **40**, 1447–1467 (2019).
64. R. C. R. Meex, M. J. Watt, *Nat. Rev. Endocrinol.* **13**, 509–520 (2017).

ACKNOWLEDGMENTS

We thank C. Kopp, U. Krüger, D. Magalei, Y.-J. Sa, and M. Winkels for technical support; C. Vitzthum for organizational support; and

S. Hümmer for secretarial help. **Funding:** This work was supported by the Max Planck Society and by the German Research Foundation [Collaborative Research Center 1531 (project-ID 456687919)] (S.O.). **Author contributions:** H.C. performed most experiments, analyzed and discussed data, and contributed to writing the manuscript. C.-C.L. helped with in vitro and in vivo experiments. R.B., M.W.A., and K.A.R. helped with in vitro experiments. S.P.W. and H.K. performed in vivo experiments. M.C., L.S.W., and A.M. provided experimental tools and discussed data. M.L. analyzed and discussed data. D.C. and M.S. did the proteomic and phosphoproteomic analyses and discussed data. S.O. initiated and supervised the study, discussed the data, and wrote the manuscript. All authors commented on the manuscript. **Competing interests:** The authors declare that they have no competing interests. **Data and materials availability:** All data are available in the manuscript or the supplementary materials. **License information:**

SUPPLEMENTARY MATERIALS

science.org/doi/10.1126/science.adr4731
Materials and Methods
Figs. S1 to S8
Tables S1 to S5
References (*65*–*76*)
MDAR Reproducibility Checklist

Submitted 4 July 2024; accepted 17 December 2024
10.1126/science.adr4731

NEUROSCIENCE

Overwriting an instinct: Visual cortex instructs learning to suppress fear responses

Sara Mederos[1]*, Patty Blakely[1], Nicole Vissers[1], Claudia Clopath[1,2], Sonja B. Hofer[1]*

Fast instinctive responses to environmental stimuli can be crucial for survival but are not always optimal. Animals can adapt their behavior and suppress instinctive reactions, but the neural pathways mediating such ethologically relevant forms of learning remain unclear. We found that posterolateral higher visual areas (plHVAs) are crucial for learning to suppress escapes from innate visual threats through a top-down pathway to the ventrolateral geniculate nucleus (vLGN). plHVAs are no longer necessary after learning; instead, the learned behavior relies on plasticity within vLGN populations that exert inhibitory control over escape responses. vLGN neurons receiving input from plHVAs enhance their responses to visual threat stimuli during learning through endocannabinoid-mediated long-term suppression of their inhibitory inputs. We thus reveal the detailed circuit, cellular, and synaptic mechanisms underlying experience-dependent suppression of fear responses.

Instinctive behaviors are automatic responses to specific environmental challenges that have evolved to furnish animals with a repertoire of behaviors vital for survival and reproductive success. These behaviors allow animals to quickly detect and respond to potential dangers or opportunities in their environment without the need for prior learning or experience (*1*, *2*) and are usually implemented by brainstem pathways independent of neural processes in the forebrain (*3*–*5*). However, to ensure continuing success in changing environments, it is also important to be able to suppress instinctive reactions if they are no longer appropriate or advantageous (*6*–*9*). Many animals can modify instinctive behaviors based on experience or changing circumstances (*5*, *7*, *10*–*14*). This behavioral flexibility allows them to fine-tune responses to their specific environment to conserve resources, avoid unnecessary risks, or capitalize on new opportunities. The neural basis of this ethologically highly relevant form of learning, the overwriting of instinctive reactions, is still unclear.

Fear responses to visual threats, such as escape from an approaching aerial predator, are examples of instinctive reactions particularly crucial for survival (*1*, *3*, *4*, *15*, *16*). Escapes from overhead looming stimuli mimicking aerial predators are mediated by neural circuits involving the medial superior colliculus and the periaqueductal gray (*3*, *17*–*19*). This visuo-motor pathway in the brainstem autonomously drives escape responses independently of the forebrain (*3*, *20*). However, animals can suppress these fear responses as they learn that a perceived visual threat proves harmless (*5*, *7*, *10*, *11*, *14*, *21*), and this form of adaptive behavior may involve neocortical circuits. Sensory circuits in the neocortex can modulate different forms of instinctive or reflexive reactions to sensory stimuli (*12*, *22*–*24*). Higher visual areas (HVAs) in rodents integrate both visual and diverse behavioral and task-related variables and have been linked to numerous functions that go beyond basic visual processing (*25*–*29*). HVAs posterolateral to the primary visual cortex (V1) contribute to learning and execution of various learned visually guided behaviors. These areas, including the postrhinal, lateromedial, posteriomedial, and laterointermediate cortices, which we will collectively refer to as posterolateral HVAs (plHVAs), are also important for encoding visual and spatial context, are modified by prior experience, and have been shown to adaptively modulate innate behaviors (*22*, *25*, *26*, *30*–*33*). plHVAs thus may provide suitable candidate regions for implementing experience-dependent control over visually driven instincts through their extensive cortico-fugal projections. One pathway that provides visual cortical areas with a route to exert strong inhibitory control over brainstem processing and, thus, over behavioral output, is the dense projection to the ventrolateral geniculate nucleus (vLGN) in the prethalamus (*11*, *34*–*36*). Prethalamic areas, including the vLGN and the adjacent zona incerta, are part of the diencephalon, consist mainly of GABAergic neurons, and act as inhibitory control hubs of diverse instinctive behaviors (*35*, *37*). The vLGN, in particular, receives visual input from the retina and has powerful control over fear responses to visual threat (*11*, *35*, *36*).

Higher visual cortex is crucial for learning to suppress instinctive fear responses

Escape behavior evoked by a looming (i.e., dark overhead expanding) stimulus is a well-established protocol for assessing instinctive fear responses (*3*, *15*). When naïve mice are presented with this visual stimulus, they consistently escape to a shelter provided at the other end of an elongated arena (Movie 1). However, mice can adapt their behavior and suppress

Movie 1. Escape behavior in response to looming stimulus presentation in a naive example mouse.

Movie 2. Looming stimulus presentation in an example mouse during the learning protocol with the barrier.

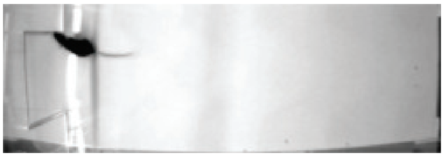

Movie 3. Lack of escape to looming stimulus presentation in an example mouse after the learning protocol.

---

[1] Sainsbury Wellcome Centre, University College London, London, UK. [2] Bioengineering Department, Imperial College London, London, UK.
***Corresponding author. Email: smederos.cr@gmail.com (S.M.); s.hofer@ucl.ac.uk (S.B.H.)**

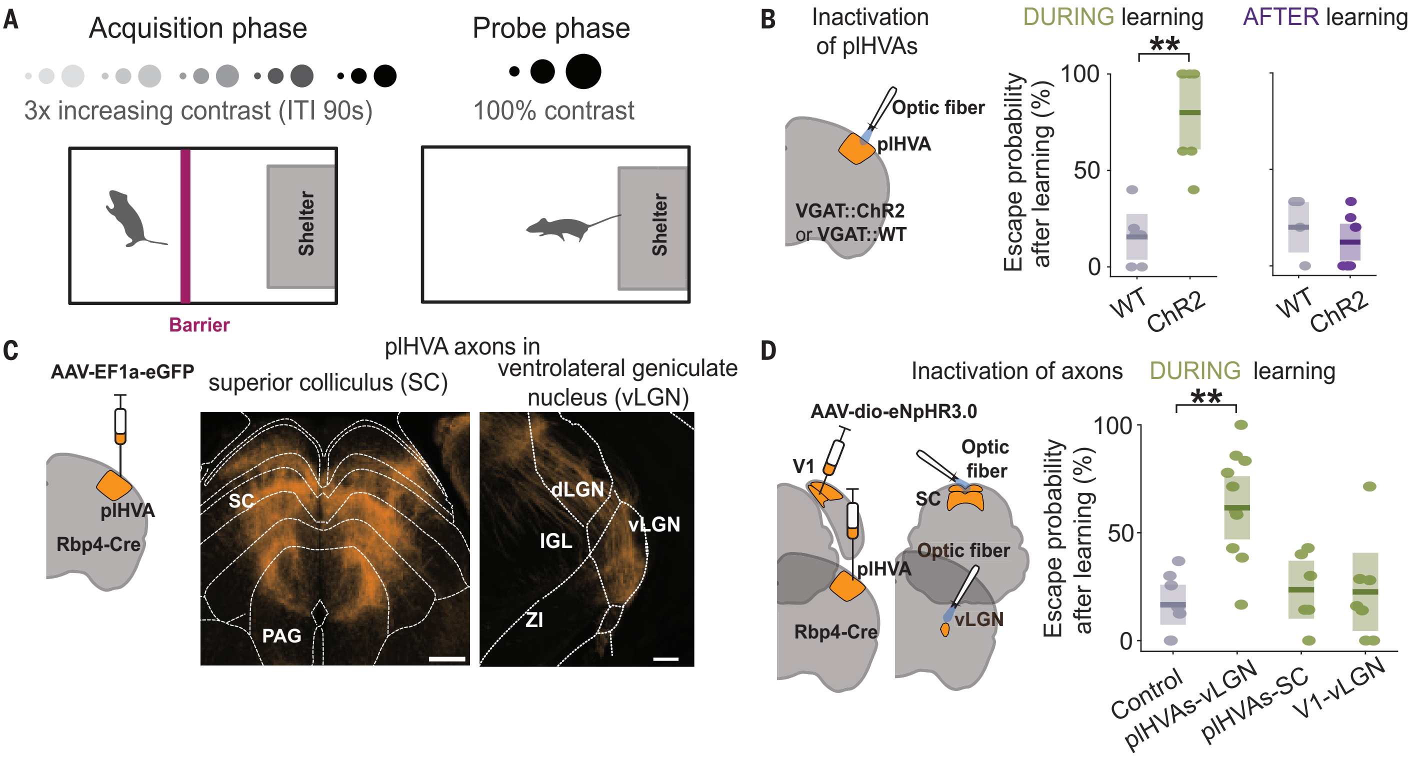

Fig. 1. plHVAs instruct learning through corticofugal projections to the vLGN. (**A**) Schematic of the task and stimulus protocols. Acquisition phase: A barrier is used to prevent escape to a shelter while looming stimuli with increasing contrast are shown sequentially. Probe phase: The barrier is removed and 6 to 10 100%-contrast looming stimuli are shown. ITI, intertrial interval. (**B**) (Left) Experimental approach. (Middle) Boxplot (showing median and interquartile range) of escape probability after learning with (green) and without (gray) silencing of plHVAs during learning. Dots show individual animals. $P = 0.003$, Kruskal-Wallis test; $n = 6$ [wildtype (WT) control] and 7 mice (ChR2, green). (Right) Same as middle, but plHVAs are silenced only after learning. $P = 0.222$, Kruskal-Wallis test; $n = 6$ (WT control) and 8 mice (ChR2, purple). (**C**) (Left) Schematic of tracer injection in plHVAs. (Right) Labeled plHVA axons in different target areas. Scale bars, 500 (left) and 250 μm (right). PAG, periaqueductal gray; SC, superior colliculus; IGL, intergeniculate leaflet; dLGN, dorsal geniculate nucleus; ZI, zona incerta; eGFP, enhanced green fluorescent protein. (**D**) (Left) Experimental design. (Right) Boxplots of escape probabilities after learning in control animals and when plHVA axons in vLGN (plHVA-vLGN) or SC (plHVA-SC) are silenced, or when V1 axons in vLGN are silenced during learning (V1-vLGN). Dots represent individual animals. plHVA-vLGN versus control, $P = 0.003$; plHVA-SC versus control, $P = 0.856$; V1-vLGN versus control, $P = 0.973$; Kruskal-Wallis test; $n = 8$, 11, 6, and 7 mice, respectively. $^{**}P < 0.01$.

this fear response if they learn that the potential threat stimulus does not result in negative consequences (*10*, *11*). But, if animals are given the opportunity to seek shelter, then they often keep escaping to high-contrast looming stimuli for many stimulus repetitions and several behavioral sessions (fig. S1, A and B). We therefore adapted a protocol developed by Lenzi and colleagues (*10*) in which we prevented access to the shelter with a dividing barrier and presented looming stimuli with increasing contrast (acquisition phase, Fig. 1A and Movie 2). We then removed the barrier and assessed the likelihood of mice to escape from high-contrast looming stimuli (probe phase, Fig. 1A). Control mice showed strongly decreased fear responses after this learning protocol, and only rarely escaped from the looming stimulus (Fig. 1B; Movie 3; and fig. S2A).

To test whether neural activity in plHVAs is important for this learned suppression of escape responses, we used transgenic mice expressing channelrhodopsin-2 (ChR2) in GABAergic neurons and implanted optical fibers to silence neural activity bilaterally in plHVAs with blue light (*38*). Silencing plHVAs while presenting looming stimuli in naïve mice had no effect on the animals' probability to escape or other behavioral measures (fig. S2C), consistent with previous results showing that visual cortex has little influence on the instinctive escape response to visual threats (*3*). However, when plHVAs were silenced during the learning protocol (during all stimulus presentations in the acquisition phase), mice failed to learn and still showed high escape probabilities to looming stimuli in the probe phase (Fig. 1B, center). We repeated these experiments with a long learning protocol with access to the shelter, in which mice eventually ceased to escape after presentation of high-contrast looming stimuli over several days (fig. S1). Silencing plHVAs with muscimol had little effect on instinctive escape behavior in naïve mice but, when applied throughout the learning protocol, prevented mice from learning to suppress escape responses (fig. S1, A to C), corroborating that plHVAs are necessary for learning to suppress escape responses independent of the experimental protocol. By contrast, optogenetic silencing of plHVAs only after mice had learnt had no effect on the learnt behavior, as mice still suppressed escape responses when plHVAs were silenced (Fig. 1B, right, and fig. S2B).

plHVA input to vLGN mediates learning to suppress fear responses

We next aimed to identify the specific pathways through which plHVAs mediate learnt suppression of fear responses. Anterograde axon labeling from layer 5 (L5) neurons in plHVAs using Rbp4-Cre mice showed dense projections in several subcortical regions, including the medial and deep layers of the superior colliculus (SC), previously shown to be crucial for generating escape responses to looming stimuli (*3*, *17*). Another clear target of plHVA projections was the vLGN (Fig. 1C), an inhibitory prethalamic area that has strong control over fear behavior and that, when activated, can fully block escape responses by inhibiting SC activity (*11*, *35*, *36*). To test the relevance of these two plHVA pathways for learning, we optogenetically silenced plHVA axonal projections selectively in either SC or

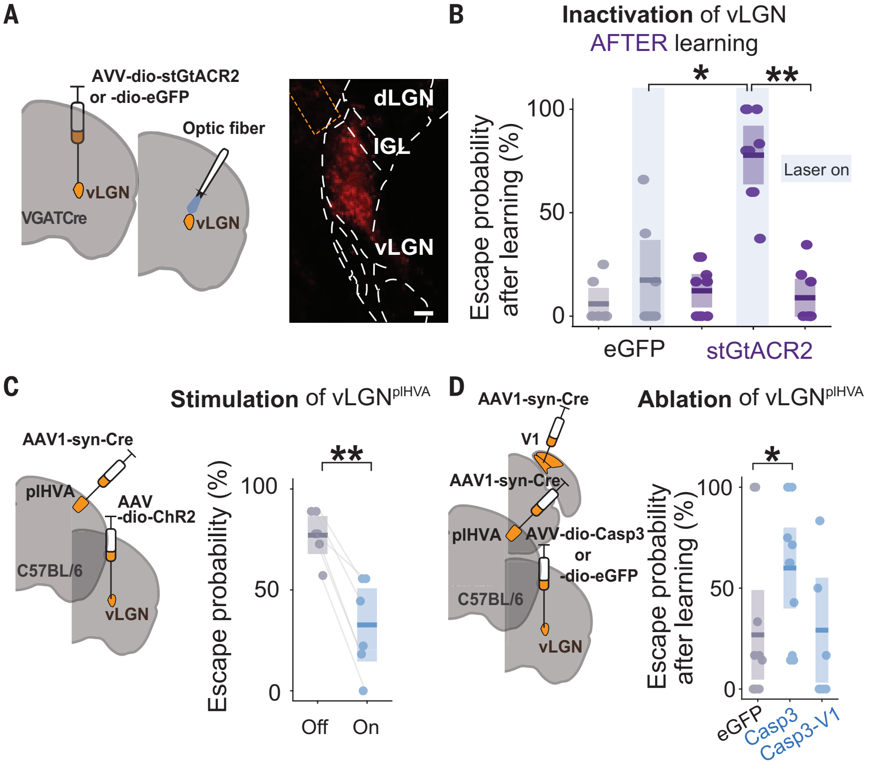

Fig. 2. vLGN cells receiving plHVA input are necessary for learning. (**A**) (Left) Experimental approach for acute inhibition of vLGN. (Right) Example image of vLGN neurons expressing stGtACR2. Scale bar, $150\ \mu\text{m}$. (**B**) Boxplot (showing median and interquartile range) comparing postlearning escape probabilities to 6 to 10 high-contrast looming stimuli for control mice expressing eGFP in vLGN with and without laser (gray, $n = 7$ mice, $P = 0.954$, Kruskal-Wallis test) and mice with stGtACR2 expression in GABAergic vLGN neurons without laser, with laser, and, subsequently, without laser again [purple, $n = 9$ mice, without before versus with laser: $P = 0.0057$ repeated-measures analysis of variance (ANOVA); with laser versus without laser after: $P = 0.0020$, repeated-measures ANOVA; laser eGFP versus laser stGtACR2: $P = 0.005$, Kruskal-Wallis test]. (**C**) (Left) Experimental approach for activating vLGN cells receiving input from plHVAs (vLGN$^{\text{plHVA}}$ neurons). (Right) Boxplot of escape probabilities to 100%-contrast looming stimuli of naive mice without (off, gray) or with activation of plHVA-innervated vLGN neurons expressing ChR2 (on, blue; $P = 0.004$, paired t test, $n = 6$ mice). (**D**) (Left) Experimental approach for specifically lesioning plHVA- or V1-innervated vLGN cells. (Right) Boxplot of postlearning escape probabilities of control mice (gray, $n = 7$ mice) and mice with plHVA-innervated vLGN cells ablated before learning (blue, $n = 11$ mice, $P = 0.039$, Wilcoxon rank sum test) or V1-innervated vLGN cells ablated before learning (blue, $n = 7$ mice, $P = 0.886$, Wilcoxon rank sum test). Dots represent individual animals. $^*P < 0.05$; $^{**}P < 0.01$.

vLGN by optical stimulation of halorhodopsin eNpHR3.0–expressing plHVA axons during the acquisition phase of the learning protocol (Fig. 1, A and D). Silencing plHVA projections to vLGN prevented learning, as mice continued to escape to the looming stimulus afterwards (Fig. 1D). By contrast, silencing plHVA projections to SC had no effect on learning (Fig. 1D). Moreover, silencing projections from V1 to vLGN also did not affect learning, showing that it is specifically projections from plHVAs to vLGN that are necessary for mice to learn to suppress escape responses (Fig. 1D and fig. S3, A to D). We corroborated the necessity of the plHVA-to-vLGN pathway for learning with a chemogenetic approach by which we targeted the inhibitory designer receptor hM4Di selectively to plHVA L5 neurons in Rbp4-cre mice and applied the agonist Clozapine *N*-oxide locally in vLGN or SC (fig. S3, E and F). Chemogenetic silencing of projections from plHVA to vLGN but not to SC also impeded learning.

plHVA-innervated vLGN cells are necessary and sufficient for suppression of escape responses

The experience of looming stimuli during the learning protocol likely induces lasting changes in neural circuits, i.e., a memory of this prior experience, leading to the adapted behavioral response to the visual threat stimulus. Our data show that, although plHVAs are required for learning to suppress fear responses, they are no longer necessary after learning. This indicates that the learning-induced memory is stored in neural circuits downstream of plHVAs. Because activation of vLGN by plHVA projections is necessary for learning, vLGN is one potential substrate for memory formation. We therefore set out to test this hypothesis. First, we examined if activity in vLGN is required for the adapted behavioral response, i.e., the suppression of escape to looming stimuli after learning. We expressed Cre-dependent stGtACR2 in vLGN of VGAT-Cre mice through AAV injections to optogenetically silence inhibitory cells, which constitute the large majority of vLGN neurons (*11*, *34*, *35*). When we silenced vLGN during stimulus presentation after learning (in the probe phase), mice resumed escaping from looming stimuli (Fig. 2A, B). This suggests that, unlike plHVAs, vLGN is necessary for the learned behavioral response. Mice immediately reverted to the learned behavior of suppressing escape responses when optogenetic manipulation was switched off, indicating that transient inhibition of vLGN neurons did not cause a sustained increase in a fear- or anxiety-related state (Fig. 2B).

However, silencing of vLGN could generally lower the threshold for threat-evoked escape responses independently of the plHVA-dependent learning process (*11*, *36*). To test the role of the plHVA-vLGN pathway in learned suppression of escape responses more specifically, we selectively targeted vLGN neurons receiving input from plHVAs by combining anterograde transfer of Cre recombinase from plHVAs to vLGN and Cre-dependent gene expression in vLGN (see materials and methods; fig. S4). vLGN neurons receiving input from plHVAs were GABAergic cells projecting to SC and other target areas (fig. S4). Expressing ChR2 specifically in these plHVA-innervated vLGN neurons and activating them during looming stimulus presentation suppressed mice's escape responses (Fig. 2C and movies S1 and S2), showing that increased activity in these neurons is sufficient to produce the learned behavior without prior experience of looming stimuli. Moreover, when we ablated plHVA-innervated vLGN neurons using Cre-dependent caspase expression (Fig. 2D, left), mice showed impaired learning with a higher likelihood to escape from looming stimuli than control mice after the learning protocol (Fig. 2D, right). By contrast, ablating V1-innervated vLGN cells had no effect on learning, even though these neurons constitute a larger fraction of vLGN cells (Fig. 2D and fig. S4, G and H).

plHVA-innervated vLGN neurons increase their looming responses over learning

To determine how neural activity in vLGN changes during learning, we performed electrophysiological single-unit recordings during presentation of high-contrast looming stimuli. We recorded over many stimulus presentations until animals learned not to escape (long learning protocol; see also fig. S1) and tracked responses of the same neurons over learning by using chronically implanted silicon probes in vLGN (Fig. 3A, fig. S5, and materials and methods). We selected cells responsive to the looming stimulus within 0 to 300 ms after stimulus onset (before learning, after learning, or both). Restricting the analysis

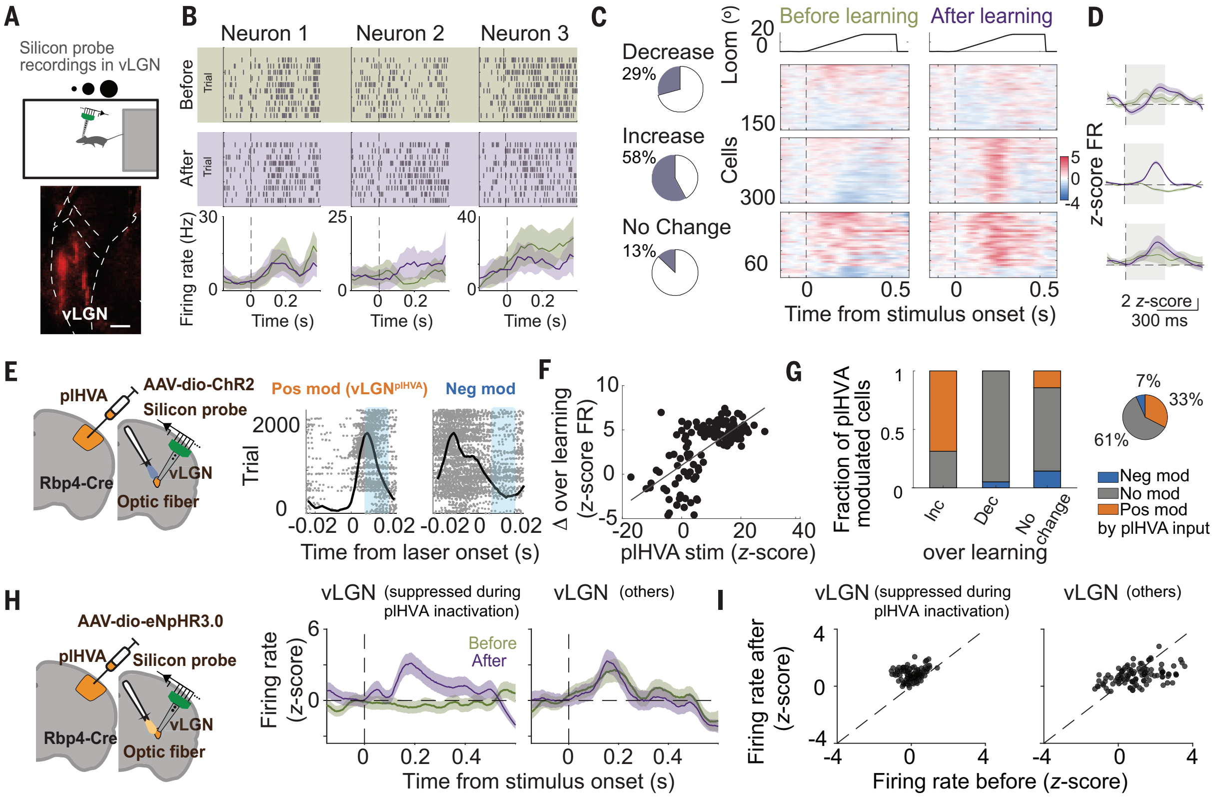

Fig. 3. plHVA-innervated vLGN neurons increase responses to looming stimuli during learning. (**A**) (Top) Experimental approach: Chronic electrophysiological recordings in vLGN while freely-moving animals are exposed to high-contrast looming stimuli until they learn to suppress escape responses. (Bottom) Example image with probe shank locations. Scale bar, 200 μm. (**B**) Looming stimulus responses of three vLGN example cells before and after learning. (**C**) (Left) Pie charts of fraction of vLGN neurons with increased and decreased responses or no change in response strength over learning in a time window of 0 to 300 ms after stimulus onset. (Right) *Z*-scored spike rate responses aligned to looming stimulus onset of all isolated units classified as looming-stimulus responsive neurons (from $n = 9$ mice) before or after learning, allocated according to their response change over learning. (**D**) Mean peristimulus histograms (PSTHs) of looming responses before and after learning of the three groups of vLGN neurons in (C). The dashed lines show stimulus onset, and the shaded areas denotes time window used for analysis [$n = 152$, 301, and 67 cells (top to bottom) from 9 mice]. (**E**) (Left) Experimental design. (Right) Spike responses to optogenetic stimulation of plHVA axons and PSTHs for example vLGN neurons. (**F**) Change (Δ) in looming stimulus response magnitude over learning of individual vLGN neurons as a function of their response magnitude to plHVA stimulation (correlation coefficient $r = 0.680$, $P < 0.0001$, Pearson correlation; $n = 131$ cells from 5 mice). FR, firing rate. (**G**) (Left) Fraction of negatively modulated (neg mod), positively modulated (pos mod), and nonmodulated neurons (no mod) during stimulation of plHVAs for vLGN neurons that increase, decrease, or show no change in response to looming stimuli over learning. (Right) Pie chart shows the fraction of units exhibiting modulation by plHVA activation out of all recorded neurons ($n = 175$, 302, and 36 cells from 5 mice). (**H**) (Left) Experimental design. (Right) Mean PSTHs in response to looming stimuli for neurons suppressed during plHVA silencing (left) and other vLGN neurons (right). [$n = 108$ (left) and 281 cells (right) from 4 mice]. Green, before learning; purple, after learning. (**I**) Scatterplots of looming stimulus response strength before and after learning (0 to 300 ms after stimulus onset) for individual vLGN neurons divided as in (H) (suppressed during plHVA silencing, $P < 0.0001$; other vLGN neurons, $P = 0.0521$; Wilcoxon signed-rank tests).

to this early time window allowed us to isolate visual signals and minimize the influence of motor-related activity because the average escape latency of mice was 1.73 ± 0.08 s (mean ± SD), and we excluded the few trials in which mice initiated an escape earlier than 300 ms after stimulus onset (fig. S6, D and E). Moreover, mice exhibited freezing before escapes in a subset of trials, and neural activity was not different in escape versus freezing trials, indicating that these early stimulus responses in vLGN were not affected by the animals' behavior (fig. S6, A to C). vLGN neurons exhibited diverse responses to looming stimuli, and many neurons changed their activity during learning. To capture such changes, we divided neurons depending on whether they significantly increased their firing rate, decreased their firing rate, or showed no change in looming stimulus response over learning (Fig. 3, B to D).

In a subset of animals, we expressed ChR2 in L5 neurons of plHVAs in Rbp4-Cre mice to combine electrophysiological recordings of vLGN cells with optogenetic activation of plHVA axons in vLGN. This allowed us to identify vLGN neurons excited by plHVAs (positively modulated), inhibited (negatively modulated), or not affected by plHVA axon activation, and these groups of neurons showed differences in their electrophysiological properties and in how their looming stimulus responses changed over learning (Fig. 3, E to G, and fig. S7). The large majority of vLGN neurons excited by plHVAs increased their responses to looming stimuli during learning (Fig. 3, E to G), indicating a crucial role for plHVA inputs in shaping vLGN responses to looming stimuli over learning. To corroborate these findings and test whether plHVA inputs contribute to looming responses of vLGN neurons, we performed another set of experiments in which we optogenetically inactivated plHVAs inputs to vLGN using eNpHR3.0 during a subset of interleaved looming stimuli trials while recording from vLGN neurons. We identified vLGN neurons receiving excitatory input from plHVAs as those that were significantly suppressed during plHVA inactivation (fig. S8, A to C). These vLGN neurons again showed on

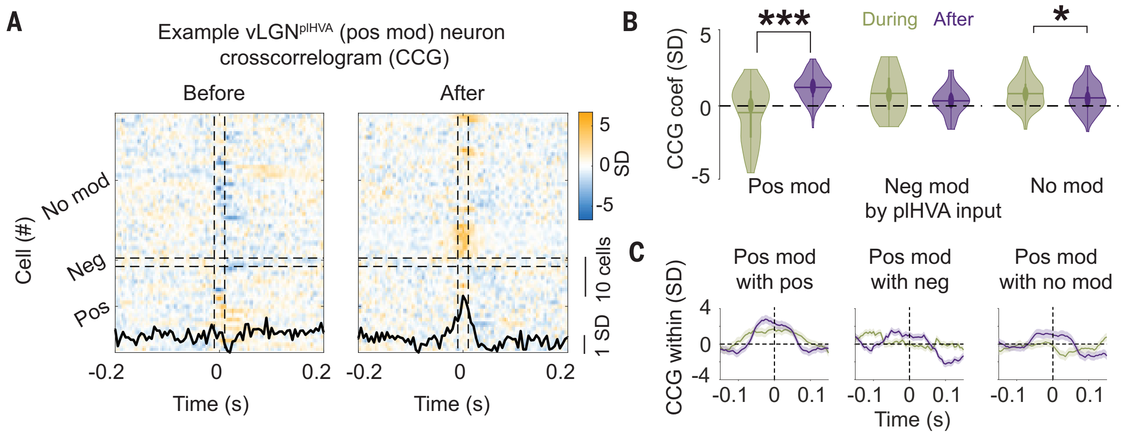

Fig. 4. Inhibitory influence on plHVA-innervated vLGN neurons may be decreased during learning. (**A**) Cross-correlograms (CCGs) of temporal spiking relationships (excluding periods of looming stimulus presentation) before and after learning between an example vLGN neuron positively modulated by plHVA activation (vLGN$^{\text{plHVA}}$) and all other simultaneously recorded units (each row in the heatmap shows a CCG of one neuron with one other unit: the spiking variation of the example neuron conditioned on the spiking of one other neuron at time 0). The black line represents the average of all CCGs in the plot. (**B**) Average CCG spiking variation around lag 0 (–1 to +4 ms) and distribution for all vLGN neurons positively, negatively, or not modulated during plHVA optogenetic activation with the rest of the vLGN population before (green) and after (purple) learning [before versus after learning: pos mod, $P < 0.001$; neg mod, $P = 0.785$; no mod, $P = 0.011$; Kruskal-Wallis test; $n = 121$, 29, and 249 cells (from left to right) from 5 mice]. Coef, coefficient. (**C**) Average spike CCG for all vLGN neurons positively modulated by plHVA stimulation with other neurons from the three groups before (green) and after (purple) learning. $^{*}P < 0.05$; $^{***}P < 0.001$.

average a clear increase in looming stimulus responses over learning (Fig. 3, H and I), even when plHVA input was removed (fig. S8). By contrast, the remaining vLGN population showed on average no response change over learning (Fig. 3, H and I). The time course of looming response increase in vLGN neurons was tightly correlated with the time course of behavioral changes over the session: mice that showed earlier increases in vLGN looming responses also learned faster (fig. S7F). Both plHVA activation and inactivation experiments show that it is predominantly those vLGN neurons receiving excitatory input from plHVAs that increase their firing responses to looming stimuli over learning. Notably, as demonstrated above, these vLGN neurons are necessary for learning to suppress escape responses, and increases in their neural looming response cause suppression of escape (Fig. 2, C and D).

Decreased inhibition onto plHVA-innervated vLGN neurons through endocannabinoid-mediated plasticity

Next, we set out to explore the potential cellular and synaptic mechanisms of this learning-induced change in vLGN activity. To determine whether functional interactions between different groups of vLGN neurons change during learning, we calculated pairwise cross-correlation functions of the spike trains of all simultaneously recorded vLGN neurons. Neurons that were positively modulated by plHVA activation again stood out in that many of them had negative spike time correlations with the rest of the vLGN network, especially with the neurons not affected by plHVA activation (Fig. 4, A to C, and fig. S9, A and B). For many of these cell pairs, the troughs in the cross correlogram were biased toward positive time lags (fig. S9C), suggesting that neurons that receive plHVA input may be inhibited by the local vLGN network before learning. This is consistent with the observation that these vLGN neurons are inhibited by looming stimuli before learning, particularly when excitatory plHVA input is removed (fig. S8D). Spike timing relationships, specifically between vLGN neurons positively modulated by plHVA activation and the rest of the network, changed with learning, such that these neurons showed positive correlations with the remaining vLGN neurons after learning, suggesting a release from inhibition over learning (Fig. 4, A to C, and fig. S8).

A potentially related form of synaptic plasticity, long-term depression of inhibition (iLTD), has been described in multiple brain areas in vitro and is dependent on endocannabinoid (eCB) signaling (*39*–*43*). Heterosynaptic iLTD can be triggered by activation of group I metabotropic glutamate receptors (mGluR1 or mGluR5) in postsynaptic neurons (*41*, *42*, *44*). This causes release of eCBs, which act as retrograde messengers, activating eCB receptors (CB1R) on nearby presynaptic inhibitory terminals, which can induce a long-lasting reduction of presynaptic GABA release probability (*39*–*43*). The eCB receptor, CB1R, and mGluR5 are present in vLGN (fig. S10, A and B) (*45*, *46*), and the majority of plHVA-innervated vLGN neurons highly express the mGluR5 receptor (fig. S10, C to E). We therefore investigated whether eCB-dependent iLTD in vLGN could mediate learned suppression of escape.

We first tested whether learning to suppress fear responses was dependent on activation of mGluR5 by infusing mGluR5 antagonist, MPEP, in vLGN (Fig. 5A). Blocking mGluR5 receptors specifically in vLGN compromised learning: mice showed higher escape probabilities to looming stimuli after the learning protocol compared with vehicle-injected littermates (Fig. 5B). Blocking mGluR5 receptors in the hippocampus (dorsal of vLGN) instead had no effect on learning (fig. S10G). Next, we examined if learning was mediated by eCB signaling. We infused a cocktail of eCBs synthesis inhibitors, LEI401+DO34, in vLGN (Fig. 5A). This intervention prevented animals from learning, as they still showed a high probability to escape from looming stimuli after the learning protocol (Fig. 5B). The same effect could be achieved by infusing a CB1 receptor antagonist (rimonabant) in vLGN (Fig. 5B). Inversely, infusion of an CB1 receptor agonist in vLGN caused long-term cessation of escapes to looming stimulus without the learning protocol, demonstrating that eCB signaling in vLGN can drive the suppression of instinctive fear response (fig. S10H). Notably, infusion of the eCB synthesis antagonist into vLGN did not affect escape probabilities to looming stimuli of varying threat levels (using different contrast levels) before learning, showing that blocking of eCB signaling in vLGN does not affect instinctive escape responses or general fear levels (fig. S10I).

Although our results so far indicate that eCB-dependent plasticity in vLGN underlies the learning process, it still remains open whether and how synaptic connectivity in vLGN is altered by learning. We thus performed whole-cell recordings in vLGN, specifically from vLGN neurons receiving input from plHVAs (Fig. 5, C to G). Bath application of eCBs decreased the frequency, but not the amplitude of spontaneous inhibitory postsynaptic currents (sIPSCs) recorded from plHVA-innervated vLGN neurons of naïve mice (Fig. 5D), demonstrating eCB-induced suppression of inhibitory input onto these neurons. To identify learning-induced changes in vLGN circuits, we next performed whole-cell recordings in mice that had undergone our learning protocol and learned to suppress escapes. We found that the frequency but not the amplitude of sIPSCs in plHVA-innervated vLGN neurons was significantly decreased after learning (Fig. 5, E to G), and their excitability was increased (fig. S11C). By contrast, vLGN neurons that did not receive input from plHVAs showed no changes over learning (fig. S11). These data indicate that release probability of GABA from presynaptic inhibitory terminals specifically onto vLGN$^{\text{plHVA}}$ neurons is decreased during learning through eCB-dependent iLTD (*44*, *47*) (Fig. 5H).

To formalize these findings, we built a simple computational model recapitulating our experimental results by simulating mean-field activity of two inhibitory neuronal populations both receiving sensory input from the retina, with only one population additionally excited by plHVAs and inhibited by the second population with plastic inhibitory weights (fig. S12).

Discussion

In this study, we uncovered a subcortical synaptic plasticity mechanism for learning to suppress instinctive defensive behavior instructed by visual cortical areas. Our findings highlight the critical role of the neocortex, specifically plHVAs, in modulating instinctive fear responses based on experience. This is consistent with previous work showing that top-down projections from sensory cortex can influence instinctive behaviors and reflexes (*12*, *13*, *22*, *23*) and suggests that one evolutionary advantageous role of neocortical circuits could be to enable more flexible and adaptive behavior through the regulation of brainstem-driven instincts (*6*–*9*).

We found that higher-order visual cortex was essential for learning to suppress instinctive defensive reactions to visual threats. Notably, visual cortex did not prove necessary for executing and sustaining the adaptive behavior once it was learned. This challenges traditional models that attribute learning and behavioral flexibility mainly to plasticity in telencephalic brain regions. Although visual cortex activity may also change over learning, our results show that plasticity in these cortical circuits does not underlie the behavioral changes after learning. Instead, visual cortex activity crucially contributes to inducing experience-dependent plasticity downstream, namely in the vLGN. vLGN neurons driven by plHVAs increase their responses to the visual threat stimulus over learning, and such increased activity in vLGN circuits abolishes fear responses through their inhibitory influence on downstream areas that mediate escapes from visual threat, such as the superior colliculus (*11*, *35*, *36*). The vLGN, and perhaps caudal prethalamic areas more generally (*35*, *37*), can thus link cognitive, neocortical processes with “hard-wired” brainstem-mediated behaviors, providing a plastic inhibitory control pathway for experience-dependent adaptive behavior.

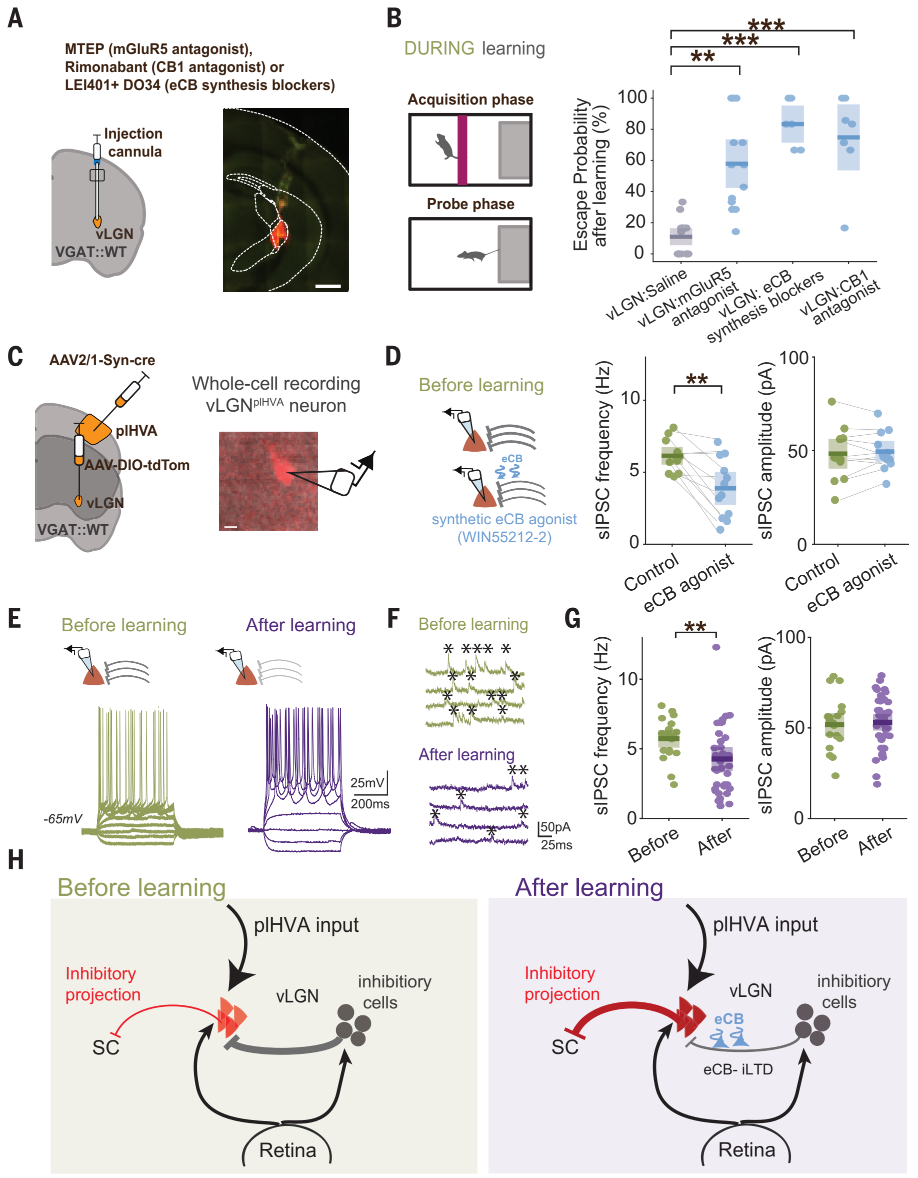

Fig. 5. eCB-mediated long-lasting disinhibition as a mechanism for learning to suppress fear responses. (**A**) (Left) Experimental approach. (Right) Coronal section with an example injection. Scale bar, 1 mm. (**B**) (Left) Schematic of the task design. (Right) Boxplot (with median and interquartile range) of postlearning escape probabilities to 100%-contrast looming stimuli for different reagents injected before the learning protocol; vLGN injection of saline ($n = 13$ mice), mGluR5 antagonist MTEP ($P = 0.001$, $n = 15$ mice), eCB synthesis blockers LEI401 and DO34 ($P = 0.0004$, $n = 6$ mice), and CB1 receptor antagonist Rimonabant ($P = 0.0008$, $n = 7$ mice). Kruskal-Wallis test followed by Tukey post hoc test was performed for all conditions. Dots indicate individual animals. (**C**) (Left) Experimental approach to visualize vLGN neurons receiving input from plHVAs (vLGN$^{\text{plHVA}}$). (Right) Example image of a recorded vLGN$^{\text{plHVA}}$ neuron. Scale bar, 30 μm. (**D**) (Left) Schematic of experiment. (Right) Boxplots of frequency and amplitude of spontaneous inhibitory postsynaptic currents (sIPSCs) in vLGN$^{\text{plHVA}}$ neurons recorded with and without bath application of the eCB agonist WIN5521-2 (frequency, $P = 0.003$; amplitude, $P = 0.603$; paired t test; $n = 12$ cells from 4 mice). Dots indicate individual neurons. (**E**) Membrane potential traces of two example vLGN$^{\text{plHVA}}$ neurons in response to current injections of different amplitudes before and after learning to suppress escape responses. (**F**) Example traces of sIPSCs under voltage clamp in vLGN$^{\text{plHVA}}$ neurons before (green) or after learning (purple). (**G**) Boxplots of frequency and amplitude of sIPSCs recorded from mice before and after learning [frequency, $P = 0.002$; amplitude, $P = 0.827$; Kruskal-Wallis test; $n = 20$ cells from 4 mice (before learning) and 39 cells from 5 mice (after learning)]. Dots indicate individual neurons. (**H**) Schematic of the mechanism underlying learnt suppression of escape responses: eCB-mediated iLTD of presynaptic inhibition onto vLGN$^{\text{plHVA}}$ neurons, likely induced through depolarization induced by direct visual looming stimulus input from the retina combined with input from plHVAs. $^{**}P < 0.001$; $^{***}P < 0.001$.

Learning to suppress fear responses relied on an eCB-mediated form of inhibitory long-term synaptic plasticity, known as iLTD. This mechanism acts on inhibitory synapses onto vLGN neurons activated by plHVAs, decreasing presynaptic release probability. eCB-dependent iLTD has been demonstrated in multiple brain areas as an heterosynaptic in vitro plasticity mechanism induced through activation of glutamatergic mGluR5 receptors through repeated electrical stimulation in brain slices (*40–43*). We found that learning to suppress fear responses in vivo depended on eCB release and eCB receptor CB1 activation specifically in vLGN. mGluR5 receptor activation in vLGN was important for learning, but additional pathways could contribute to triggering eCB release in vLGN (*39–43*). Moreover, vLGN neurons receiving input from plHVAs were susceptible to eCB-dependent suppression of inhibition and showed decreased inhibitory input after animals had learned to suppress escape responses. Our study thus provides direct evidence of this plasticity mechanism, eCB-mediated decrease of inhibitory input, occurring in vivo to mediate learning. Although the source of the plastic inhibitory input onto plHVA-driven vLGN neurons remains to be identified, it likely stems at least partly from local inhibitory interneurons: our cross-correlogram analysis suggests that plHVA-driven vLGN neurons are inhibited by other vLGN neurons before learning but not after learning. Their neural responses to looming stimuli, likely driven by both plHVAs and direct projections from the retina (*34*), thus become released from inhibition during learning and the increased activity of these GABAergic neurons in turn inhibits down-stream target areas to suppress threat-evoked escape reactions (*11*, *35*).

eCBs have long been implicated in the regulation of fear and anxiety and are necessary for extinction of fear conditioning (*48*, *49*). The suppression of instinctive fear responses studied in this work and the extinction of learnt fear share similarities in that both involve active learning to attenuate defensive behaviors in response to a stimulus that no longer predicts danger (*50*). However, these two forms of learning likely engage distinct neural circuits and may differ in their specificity and time course (*49*, *51*). The plasticity mechanism described in this study is likely part of a larger network for regulating defensive behavior, including processes in downstream areas, superior colliculus and periaqueductal gray, as well as complementary top-down pathways through the basal ganglia, hypothalamus, and amygdala (*21*, *51–56*).

The ability to suppress instinctive fear responses when threat expectations are violated is an ethologically crucial form of behavioral adaptation, the absence of which could lead to inappropriate or excessive fear responses (*56*). Such maladaptive fear processing is a hallmark of fear and anxiety disorders and posttraumatic stress disorder (*52*, *57*). Dysfunction of pathways through vLGN [also called pregeniculate nucleus in primates (*58*)] or impairments in eCB-dependent plasticity could thus contribute to these disorders. Conversely, targeting these pathways, for example, by using deep brain stimulation, or enhancing eCB-dependent plasticity within these circuits may facilitate suppression of maladaptive fear responses, suggesting new therapeutic strategies for fear-related disorders.

REFERENCES AND NOTES

1. N. Tinbergen, *The Study of Instinct* (Oxford Univ. Press, 1951).
2. D. Mobbs, P. C. Trimmer, D. T. Blumstein, P. Dayan, *Nat. Rev. Neurosci.* **19**, 419–427 (2018).
3. D. A. Evans *et al*., *Nature* **558**, 590–594 (2018).
4. T. Branco, P. Redgrave, *Annu. Rev. Neurosci.* **43**, 417–439 (2020).
5. D. Rossier, V. La Franca, T. Salemi, S. Natale, C. T. Gross, *Proc. Natl. Acad. Sci. U.S.A.* **118**, e2013411118 (2021).
6. W. H. R. Rivers, *Instinct and the unconscious: A contribution to a biological theory of the psycho-neuroses* (Cambridge Univ. Press, ed. 2, 2006), pp. 66–70.
7. D. A. Evans, A. V. Stempel, R. Vale, T. Branco, *Trends Cogn. Sci.* **23**, 334–348 (2019).
8. S. Sangha, M. M. Diehl, H. C. Bergstrom, M. R. Drew, *Neurosci. Biobehav. Rev.* **108**, 218–230 (2020).
9. C. H. Rankin *et al*., *Neurobiol. Learn. Mem.* **92**, 135–138 (2009).
10. S. C. Lenzi *et al*., *Curr. Biol.* **32**, 2972–2979.e3 (2022).
11. A. Fratzl *et al*., *Neuron* **109**, 3810–3822.e9 (2021).
12. S. Natale, M. Esteban Masferrer, S. Deivasigamani, C. T. Gross, *Eur. J. Neurosci.* **54**, 6044–6059 (2021).
13. T. B. Franklin *et al*., *Nat. Neurosci.* **20**, 260–270 (2017).
14. A. Tafreshiha, S. A. van der Burg, K. Smits, L. A. Blömer, J. A. Heimel, *J. Exp. Biol.* **224**, jeb230433 (2021).
15. M. Yilmaz, M. Meister, *Curr. Biol.* **23**, 2011–2015 (2013).
16. G. De Franceschi, T. Vivattanasarn, A. B. Saleem, S. G. Solomon, *Curr. Biol.* **26**, 2150–2154 (2016).
17. C. Shang *et al*., *Nat. Commun.* **9**, 1232 (2018).
18. A. S. Bittencourt, E. M. Nakamura-Palacios, H. Mauad, S. Tufik, L. C. Schenberg, *Neuroscience* **133**, 873–892 (2005).
19. J. T. DesJardin *et al*., *J. Neurosci.* **33**, 150–155 (2013).
20. P. Tovote *et al*., *Nature* **534**, 206–212 (2016).
21. K. Wu *et al*., *Neuron* **111**, 3650–3667.e6 (2023).
22. B. H. Liu, A. D. Huberman, M. Scanziani, *Nature* **538**, 383–387 (2016).
23. X. R. Xiong *et al*., *Nat. Commun.* **6**, 7224 (2015).
24. J. Liu, Y. He, A. Lavoie, G. Bouvier, B.-H. Liu, *Nat. Commun.* **14**, 8467 (2023).
25. L. L. Glickfeld, S. R. Olsen, *Annu. Rev. Vis. Sci.* **3**, 251–273 (2017).
26. M. Jin, L. L. Glickfeld, *Curr. Biol.* **30**, 4682–4692.e7 (2020).
27. M. L. Andermann, A. M. Kerlin, D. K. Roumis, L. L. Glickfeld, R. C. Reid, *Neuron* **72**, 1025–1039 (2011).
28. C. Stringer, M. Michaelos, D. Tsyboulski, S. E. Lindo, M. Pachitariu, *Cell* **184**, 2767–2778.e15 (2021).
29. P. M. Goltstein, S. Reinert, T. Bonhoeffer, M. Hübener, *Nat. Neurosci.* **24**, 1441–1451 (2021).
30. S. Ruediger, M. Scanziani, *eLife* **9**, 1–24 (2020).
31. L. Tang, M. J. Higley, *Neuron* **105**, 346–354.e5 (2020).
32. N. D. Nguyen *et al*., *Nature* **625**, 110–118 (2024).
33. V. J. Estela-Pro, R. D. Burwell, *Behav. Neurosci.* **136**, 101–113 (2022).
34. U. Sabbagh *et al*., *J. Neurochem.* **159**, 479–497 (2021).
35. A. Fratzl, S. B. Hofer, *Neuron* **110**, 2728–2742 (2022).
36. L. D. Salay, A. D. Huberman, *Cell Rep.* **37**, 109792 (2021).
37. X. Wang, *Trends Neurosci.* **43**, 82–87 (2020).
38. Z. V. Guo *et al*., *Neuron* **81**, 179–194 (2014).
39. G. L. Gerdeman, J. Ronesi, D. M. Lovinger, *Nat. Neurosci.* **5**, 446–451 (2002).
40. V. Chevaleyre, P. E. Castillo, *Neuron* **38**, 461–472 (2003).
41. B. D. Heifets, P. E. Castillo, *Annu. Rev. Physiol.* **71**, 283–306 (2009).
42. A. Bilbao *et al*., *iScience* **23**, 100951 (2020).
43. Y. W. Wu *et al*., *Cell Rep.* **10**, 75–87 (2015).
44. J. Xu, Y. Zhu, A. Contractor, S. F. Heinemann, *J. Neurosci.* **29**, 3676–3684 (2009).
45. S. M. Sunkin *et al*., *Nucleic Acids Res.* **41** (D1), D996–D1008 (2013).
46. G. Govindaiah, C. L. Cox, *J. Neurophysiol.* **101**, 1761–1773 (2009).
47. C. Lüscher, K. M. Huber, *Neuron* **65**, 445–459 (2010).
48. B. Lutz, G. Marsicano, R. Maldonado, C. J. Hillard, *Nat. Rev. Neurosci.* **16**, 705–718 (2015).
49. G. Marsicano *et al*., *Nature* **418**, 530–534 (2002).
50. K. M. Myers, M. Davis, *Mol. Psychiatry* **12**, 120–150 (2007).
51. B. A. Silva, C. T. Gross, J. Gräff, *Learn. Mem.* **23**, 544–555 (2016).
52. P. Tovote, J. P. Fadok, A. Lüthi, *Nat. Rev. Neurosci.* **16**, 317–331 (2015).
53. A. V. Stempel *et al*., *Curr. Biol.* **34**, 3031–3039.e7 (2024).
54. J. P. Fadok *et al*., *Nature* **542**, 96–100 (2017).
55. W. Menegas, K. Akiti, R. Amo, N. Uchida, M. Watabe-Uchida, *Nat. Neurosci.* **21**, 1421–1430 (2018).
56. C. T. Gross, N. S. Canteras, *Nat. Rev. Neurosci.* **13**, 651–658 (2012).
57. J. E. Sherin, C. B. Nemeroff, *Dialogues Clin. Neurosci.* **13**, 263–278 (2011).
58. K. Niimi, T. Kanaseki, T. Takimoto, *J. Comp. Neurol.* **121**, 313–323 (1963).
59. S. Medoros, Overwriting an instinct: visual cortex instructs learning to suppress fear responses, Zenodo (2024); https://zenodo.org/uploads/14249472.

ACKNOWLEDGMENTS

We thank M. Lohse, A. Fratzl, and M. Valero for their feedback on the manuscript; Mrsic-Flogel and Hofer Lab members for helpful discussions; and A. Fratzl for initial discussions, conceptualization, and help with experimental setups and analysis. We thank S. C. Lenzi and T. W. Margrie for help with the behavioral paradigm. We thank M. Li for animal husbandry and genotyping; Neurogears (A. Almeida, J. J. Frazão, and G. Lopes) for help building the behavioral setup; A. M. Koltchev and L. Daveau for help with animal handling; R. Campbell for help with serial two-photon imaging; J. Broni-Trabi for help with RNAscope; and P. Nowak from the Sainsbury Wellcome Centre viral core for providing viruses. We thank SWC FabLabs for technical support and A. Covelo for advice on endocannabinoid experiments. **Funding:** This work was supported by the Sainsbury Wellcome Centre core grant from the Gatsby Charitable Foundation and the Wellcome Foundation (090843/F/09/Z), a Wellcome Investigator Award (S.B.H., 219561/Z/19/Z), an EMBO postdoctoral fellowship (S.M., EMBO ALTF 327-2021), and a Wellcome Early Career Award (S.M., 225708/Z/22/Z). **Author contributions:** Conceptualization: S.M. and S.B.H.; Methodology: S.M., S.B.H., and N.V.; Investigation: S.M., P.B., and N.V.; Experimental setup: S.M. and P.B.; Computational model conceptualization: C.C., S.M., and S.B.H.; Computational model investigation: C.C.; Funding acquisition: S.M. and S.B.H.; Writing – original draft: S.M. and S.B.H.; Writing – review & editing: S.M., S.B.H., P.B., N.V., and C.C. **Competing interests:** The authors declare that they have no competing interests. **Data and materials availability:** Data have been made available and deposited in Zenodo (*59*).

SUPPLEMENTARY MATERIALS

science.org/doi/10.1126/science.adr2247
Materials and Methods
Figs. S1 to S12
References (*60–74*)
MDAR Reproducibility Checklist

Submitted 17 July 2024; accepted 6 January 2025
10.1126/science.adr2247

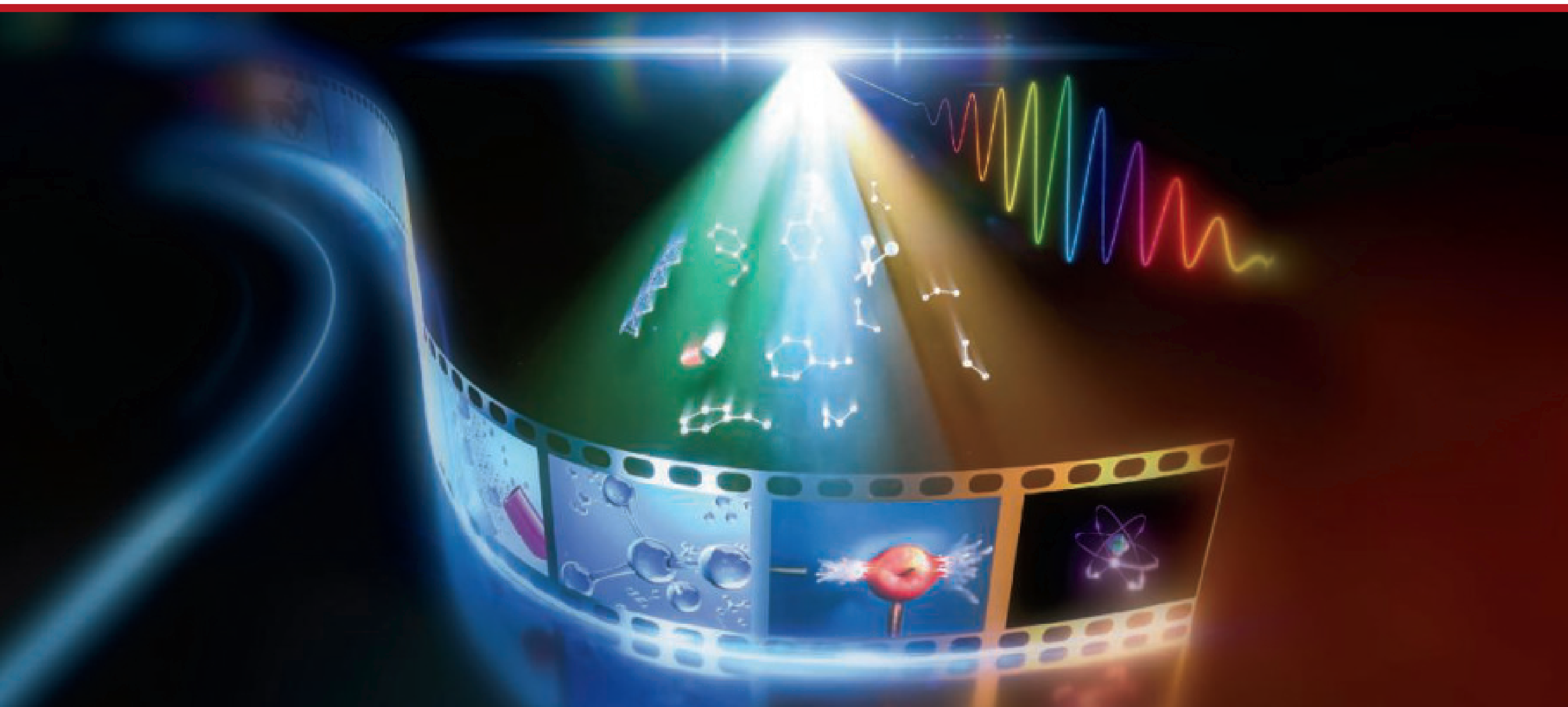

CALL FOR PAPERS

SPJ
SCIENCE PARTNER JOURNALS

Ultrafast Science

OPEN ACCESS

Ultrafast Science is an online-only, Open Access journal published in affiliation with **Xi'an Institute of Optics and Precision Mechanics (XIOPM)** of CAS and distributed by the **American Association for the Advancement of Science (AAAS)**. The mission of the journal is to build a platform for ultrafast scientific research; present new theories, concepts, ideas, technologies and progress in this field; publish the latest research representing the forefront of the discipline and that of international concern; and promote academic exchange and development worldwide. *Ultrafast Science* publishs high-quality original research articles, comprehensive reviews, editorials, and perspectives which feature high novelty, significance and technical quality in cutting-edge and emerging topics in ultrafast science with broad interest from scientific communities.

Submit your research to *Ultrafast Science* today!
Learn more at **spj.science.org/ultrafastscience**

The Science Partner Journal (SPJ) program was established by the American Association for the Advancement of Science (AAAS), the nonprofit publisher of the *Science* family of journals. The SPJ program features high-quality, online-only, Open-Access publications produced in collaboration with international research institutions, foundations, funders and societies. Through these collaborations, AAAS furthers its mission to communicate science broadly and for the benefit of all people by providing top-tier international research organizations with the technology, visibility, and publishing expertise that AAAS is uniquely positioned to offer as the world's largest general science membership society.

Visit us at **spj.science.org**

@UltrafastSci **@SPJournals** **@SPJournals**

ARTICLE PROCESSING CHARGES WAIVED UNTIL JANUARY 2026

HPLC Pump Qualification Pack
TESTA Analytical has launched the HPLC Pump Qualification Pack - an efficient, fast, and reliable tool for regulated laboratories looking to qualify the operation and performance of their HPLC systems. Flow rate is one of the most important parameters in any liquid chromatography system, it determines retention time or volume and therefore has a major influence on reproducibility. The TESTA Analytical LC flowmeter is a trusted device for continuous non-invasive measurement of flow rate in HPLC and UHPLC systems. Comprising a calibrated LC flowmeter, data validation tool and tablet-computer with pre-installed software – the pack automatically performs all necessary flow data calculations plus operational and performance qualification checks. Using the HPLC Pump Qualification Pack considerably reduces the time required for HPLC pump qualification, while improving traceability of results.By focusing on data traceability and simplifying the qualification process, this new all-in-one pack is an affordable solution for laboratories seeking to maintain compliance and optimize their HPLC systems quickly and effectively.
Testa Analytical Solutions
For Info: +49-30-864-24076
www.testa-analytical.com

Synthetic Nanodiscs
AMSBIO announce a new range of Synthetic Nanodiscs that enable preparation of multi-pass transmembrane proteins in their active form, revolutionizing the future of membrane protein research and drug development. Membrane Proteins account for more than 60% of all FDA-approved drug targets and 90% of antibody-based drug targets. Many traditional sample preparation methods struggle with challenges in obtaining water-soluble and bioactive forms of multi-pass transmembrane proteins. Commonly, detergent has been widely used to produce multi-pass transmembrane proteins. However, a major downside of this technique is that the detergent cannot be completely removed. This can be problematic for downstream applications, as the presence of detergent may interfere with experiments or affect the protein structure. An alternative technique to obtain proteins with good solubility and correct folding is to use peptides derived from the N-terminus or extracellular loops. Unfortunately, transmembrane proteins prepared by this method may not retain the structural features and conformation of the original extracellular loops of the transmembrane protein in the native membrane. Another method is to use membrane fractions, whole cells or VLPs to maintain the natural structure of transmembrane proteins, but immunization with these products has been shown to result in high levels of non-specific antibody background. Based upon an innovative polymer-based platform, Synthetic Nanodiscs offer a more advanced solution compared with these traditional solutions. Synthetic Nanodiscs have been shown, in multiple applications, to produce full-length membrane proteins with high purity and excellent solubility in aqueous solutions. Beneficially the proteins incorporated into Synthetic Nanodiscs are in a native membrane environment, ensuring they remain biologically active. There is no detergent in these products, making them suitable to use in cell- based assays and other experiments. Overall Synthetic Nanodiscs eliminate the need for membrane scaffold proteins, creating a streamlined cleaner system with reduced interference in downstream assays. In this way, our Synthetic Nanodiscs enable the functional characterization of multi-pass transmembrane proteins in their active form, revolutionizing the membrane protein research and drug development.
AMS Biotechnology
For Info: +44-1235-828200
www.amsbio.com

Dual-cap Sample Collection Tube
Azenta Life Sciences has launched Cap2TM - a new 0.2ml PCR microcentrifuge tube featuring a novel dual-cap design with both hinged lid and screw cap to preserve the integrity of samples used in genetic testing workflows. Acting as both a collection and processing tube, sample transfer can be minimized making for greater efficiency and less wastage. Designed to ensure sample traceability in wide ranging genetic testing workflows, including pre-implantation genetic testing (PGT) – each Cap2 tube has a unique 2D datamatrix code as well as a numerical human readable identifier to prevent sample tracking errors. All Azenta tubes, including the new Cap2, are developed with broad compatibility in mind, performing without compromise in conjunction with automated code reading, capping and sample management systems from Azenta and all other industry-recognized manufacturers. Manufactured from high quality virgin polypropylene, in a class 8 clean room environment, each batch of tubes is tested to certify them endotoxin and DNase/RNase free as well as containing no detectable leachables or extractables. Vital considerations for sample collection tubes used in genetic testing workflows.
AZENTA Life Sciences
For Info: +44 -161-777-2098
www.azenta.com

Foresight Pro 45
Expanding on Bio-Rad's portfolio of Foresight Pro columns with inner diameters ranging from 5 to 33 cm, the new, larger 45 cm ID Foresight Pro Column offers biopharma manufacturers an easily integrated solution for downstream purification of biomolecules, including vaccines, antibodies, and recombinant proteins. Foresight Pro Columns are manufactured and packed in a controlled ISO Class 7 cleanroom, providing good manufacturing practice (GMP) ready columns. The standardized design and format, in a range of diameters and bed heights, offer a convenient and reliable solution, packed with either CHT™ Ceramic Hydroxyapatite Media Type I, Type II, or XT. Bio-Rad's CHT Media is a rigid mixed-mode support media for biomolecule purification. CHT's unique composition, Ca10(PO4)6OH2, allows biomolecules to interact with the media by means of metal affinity interactions via calcium atoms and/or cation exchange interactions via phosphate groups.
Bio-Rad Laboratories, Inc.
For Info: +1 510-356-7909
www.bio-rad.com

Electronically submit your new product description or product literature information! Go to www.science.org/about/new-products-section for more information.

Newly offered instrumentation, apparatus, and laboratory materials of interest to researchers in all disciplines in academic, industrial, and governmental organizations are featured in this space. Emphasis is given to purpose, chief characteristics, and availability of products and materials. Endorsement by *Science* or AAAS of any products or materials mentioned is not implied. Additional information may be obtained from the manufacturer or supplier.

Post-Docs in the Virgil Percec Lab at the University of Pennsylvania Department of Chemistry

Penn
University of Pennsylvania

Employer: University of Pennsylvania

Location: Philadelphie, Pennsylvania

Salary: Commensurate with Education and Experience

Opening: Immediately

Post-docs in the Virgil Percec Lab at the University of Pennsylvania (Penn), Department of Chemistry in the design, synthesis and structural analysis combined with in vivo activity for one-component delivery systems for mRNA.

Virgil Percec Lab together with Drew Weissman Lab from the Perelman School of Medicine at Penn discovered and developed a one-component multifunctional sequence-defined ionizable amphiphilic Janus dendrimer (IAJD) delivery system for mRNA (JACS 2021, 143, 12315). IAJDs co-assemble with mRNA into dendrimersome nanoparticles (DNPs) which eliminate some of the disadvantages and complement the four-component lipid nanoparticles (LNPs) elaborated and employed in the delivery of mRNA from Covid 19 vaccines. These postdoc positions are immediately available and require excellent background in organic synthesis, supramolecular chemistry and characterization by NMR, HPLC, MALDI-TOF combined with in vivo experiments performed in collaboration with Weissman Laboratory. The goal of these positions is to develop a Nanoperiodic Table correlating the primary structure of IAJDs with in vivo mRNA delivery. This work is expected to impact the new field of nanomedicine by creating new, less expensive and more activer vaccines and therapeutics based on mRNA.

To apply, please email your CV to: percec@sas.upenn.edu

JOHNS HOPKINS POSTDOCTORAL
FELLOWSHIP RECRUITMENT
MOLECULAR AND DEVELOPMENTAL NEUROBIOLOGY
AND VASCULAR AND CARDIAC IMMUNOLOGY

Johns Hopkins
School of Medicine

Employer: Johns Hopkins University School of Medicine
PI: Roger A. Johns MD, PhD
Location: Laboratory is located on the medical campus of Johns Hopkins University
Discipline: Neuroscience
Position Type: Full Time
Position Type: Full Time
Salary: Open
Job Type: Postdoctoral Fellow

POSTDOCTORAL POSITION available to study the role of postsynaptic scaffolding proteins (MAGUKs) and inflammation in developmental neurotoxicity, long-term cognitive dysfunction and chronic pain. Focus is on the role of the PSD-95 family of MAGUK proteins and their downstream pathways in regulating the NLRP3 inflammasome, synaptic development and function, neurotoxicity, and chronic pain. Critical skills include a strong technical expertise in biochemistry, imaging, rodent behavior, cellular and molecular biology. Helpful to have knowledge of MAGUK scaffolding protein function and experience in neurophysiology, fret imaging, protein-protein interaction, and dendritic spine analysis.
Highly motivated PhDs with a strong publication record are encouraged to apply.

Send application letter, CV and contact information for three references to:
Dr. Roger Johns c/o hhammon3@jh.edu

Discipline: Vascular Biology/Immunology
Position Type: Full Time
Position Type: Full Time
Salary: Open
Job Type: Postdoctoral Fellow

POSTDOCTORAL POSITION available to study the immunology of vascular and cardiac remodeling and inflammation. The group focuses on the immunoregulation and immunotherapy of cardiovascular and pulmonary diseases and other lung inflammation-related pathology with a special interest in pulmonary hypertension, vascular and cardiac remodeling. The role of the resistin family of protein cytokines, the NLRP3 inflammasome and their downstream pathways are actively being pursued at multiple levels including cell and molecular biology, pathophysiology, biomarker and development of therapeutics. Critical skills include a strong technical expertise in biochemistry and molecular biology, imaging, in the context of vascular and immunobiology.
Highly motivated PhDs with a strong publication record are encouraged to apply.

Send application letter, CV and contact information for three references to:
Dr. Roger Johns c/o hhammon3@jh.edu


HO
OH
C
O

WORKING LIFE

By **Anas Bedraoui**

The impostor club

Standing on the stage at my first overseas conference, I remember feeling dazzled. The marble hall glistened under the soft light. Experts from around the globe exchanged thoughts in low, confident tones. And I had been invited here to give a talk about my own research. It should have been a major boost to my confidence. But as I fumbled with my notes, I heard a familiar whisper: *What if they find out you don't really belong here?*

I'd been experiencing impostor syndrome since long before the conference. It first crept up on me after I failed my final year of high school. I didn't value learning then, and being surrounded by classmates who had already given up—and teachers who didn't seem to care—only reinforced my apathy. Changing schools and then starting university gave me a fresh chance, but I was worried I would be exposed as someone who didn't belong.

Even after I hit my stride as an undergraduate in Morocco, I often felt far removed from the global scientific community. In Morocco, at public universities, science is taught in French, and I found this a barrier to connecting with the wider, predominantly English-speaking field. The limited funding and scarce opportunities for international collaboration or career development only deepened this feeling.

"Maybe impostor syndrome wasn't a sign of failure, but a sign of growth."

My Ph.D. work made me feel like even more of an impostor. I set out to use artificial intelligence to better understand the proteins in snake venom. My background was in mechanical design and bionics, yet suddenly I was plunged into the world of neural networks, biomolecules, and data sets, struggling to connect the dots. As I tried to catch up by teaching myself the basics, I was once again terrified that someone would call me out.

However, something changed in me at that conference. Despite my fears, my presentation went well, and the encouragement I received from senior researchers gave me a much-needed spark of validation. But the real boost came later in the meeting, after I attended a session for early-career researchers that featured talks by established scientists.

I had expected the session to be filled with advice and strategies for those starting out. Instead, I got raw honesty. A highly accomplished scientist from Germany—someone whose papers I had cited—leaned forward and said, "I still feel like an impostor sometimes." You could feel the collective sigh of relief ripple through the room. We were all thinking the same thing: Wait, you feel it, too?

One after another, the speakers shared stories of doubt. Researchers with decades of experience, prestigious awards, and countless publications all admitted to moments when they felt they didn't measure up, that they weren't really qualified, that they'd somehow tricked the world into believing they were experts. I couldn't believe it. These were people I admired, people whose work defined fields. And yet, they, too, wrestled with the same ghost that haunted me.

That moment reframed everything for me. Maybe impostor syndrome wasn't a sign of failure, but a sign of growth. These people were deeply knowledgeable—but that also meant they could see the vastness of what's still unknown, and were all the more humble for it. If that's what made them feel like impostors, then I was happy to be a part of that club.

Now, when I'm writing an article or giving a talk, I still sometimes hear that voice asking me what I'm doing here. But thanks to the supportive community I found at that conference, I know I'm in good company.

Still, academia needs to do more to ensure that early-career researchers feel they belong in the scientific community—particularly those from the Global South, who often don't have access to the same networks and resources as those in more affluent countries. More international societies could provide discounted membership rates, for instance, and increase support for travel and visa applications; conference organizers should also consider holding more events in the Global South.

This kind of support opens doors, makes us feel invited and welcome, and tells us: *You are needed here*. And maybe that's how we finally silence the whisper for good. ■

Anas Bedraoui is a Ph.D. student at Mohammed VI Polytechnic University.

ILLUSTRATION: ROBERT NEUBECKER

Cold Spring Harbor Laboratory 2025 Meetings & Courses

Meetings

meeting dates / abstracts due

Probabilistic Modeling in Genomics March 5 - 8

Network Biology March 11 - 15

Nucleic Acid Therapies March 19 - 22

Cancer Genetics: History & Consequences
March 26 - 29

Ubiquitins, Autophagy & Disease April 1 - 5

Brain Barriers April 8 - 12

Systems Immunology April 22 - 26

Telomeres & Telomerase April 29 - May 3 / February 7

Biology of Genomes May 6 - 10 / February 14

Mechanisms of Metabolic Signaling
May 13 - 17 / February 21

Retroviruses May 19 - 24 / February 28

89th Symposium: Senescence & Aging
May 28 - June 1 / March 7

Genomic Data Science and Beyond with *Galaxy & Bioconductor* June 23 - 26 / April 4

Advances in Brain Tumor Research & Therapy
July 17 - 20 / April 25

Genome Engineering: CRISPR Frontiers
August 12 - 16 / May 23

Eukaryotic mRNA Processing August 19 - 23 / May 30

Mechanisms of Eukaryotic Transcription
August 26 - 30 / June 6

Eukaryotic DNA Replication & Genome Maintenance
September 2 - 6 / June 13

Microbial Pathogenesis & Host Response
September 8 - 12 / June 20

Biology of Cancer: Microenvironment & Metastasis
September 16 - 20 / June 27

Cell Fate Conversions September 24 - 27 / July 7

Bioengineered Tissue Systems & Models
September 28 - October 1 / July 11

Neurobiology of *Drosophila* October 7 - 11 / July 21

Immune Engineering & Cellular Immunotherapy
October 28 - 31 / August 15

Genome Informatics November 5 - 8 / August 22

Single Cell Analyses November 12 - 15 / August 29

Zebrafish Neurobiology November 19 - 22 / September 5

Plant Genomes, Systems Biology & Engineering
December 3 - 6 / September 12

Assembloids & Complex Cell-Cell Interactions Across Tissues & Organs
December 8 - 11 / September 19

Courses

course dates / applications due

Tutorials in Genomics & Bioinformatics: RNA-Seq Analysis May 11 - 13 / no application, rolling admission

Advanced Bacterial Genetics June 2 - 22 / March 1

Ion Channels in Synaptic & Neural Circuit Physiology
June 2 - 22 / March 1

Mouse Development, Stem Cells & Cancer
June 2 - 22 / March 1

Pancreatic Cancer June 3 - 10 / March 1

Statistical Analysis of Genome Scale Data
June 6 - 20 / March 1

Metabolomics June 6 - 22 / March 1

Vision: A Platform for Linking Circuits, Behavior & Perception June 12 - 28 / March 1

Advanced Techniques in Molecular Neuroscience
June 26 - July 12 / March 15

Single Cell & Spatial Transcriptomics Analysis
June 26 - July 14 / March 15

***Drosophila* Neurobiology: Genes, Circuits & Behavior**
June 26 - July 17 / March 15

Frontiers & Techniques in Plant Science
June 26 - July 17 / March 15

Neural Data Science July 7 - 21 / March 15

Autism Spectrum Disorders July 22 - 29 / March 31

Synthetic Biology July 22 - August 5 / March 31

Chromatin, Epigenetics & Gene Expression
July 22 - August 10 / March 31

Imaging Structure & Function in the Nervous System July 22 - August 12 / March 31

Yeast Genetics & Genomics
July 22 - August 12 / March 31

Neuroscience of Addiction
July 29 - August 5 / March 31

Bench to Biotech August 5 - 12 / March 31

Proteomics August 5 - 19 / March 31

Macromolecular Crystallography
October 12 - 28 / July 15

Programming for Biology
October 12 - 28 / July 15

Antibody Engineering & Display Technologies
October 14 - 28 / July 15

High Throughput Neuroanatomy
October 16 - 28 / July 15

Tutorials in Genomics & Bioinformatics
November 9 - 11 / no application, rolling admission

Advanced Sequencing Technologies & Bioinformatics Analysis November 9 - 22 / August 15

Scientific Writing Retreat November 10 - 15 / August 15

Computational Genomics December 2 - 10 / August 15

Photo: The 2024 Chromatin, Epigenetics & Gene Expression Course taking a break on the Christeen off the Cold Spring Harbor Beach

meetings.cshl.edu

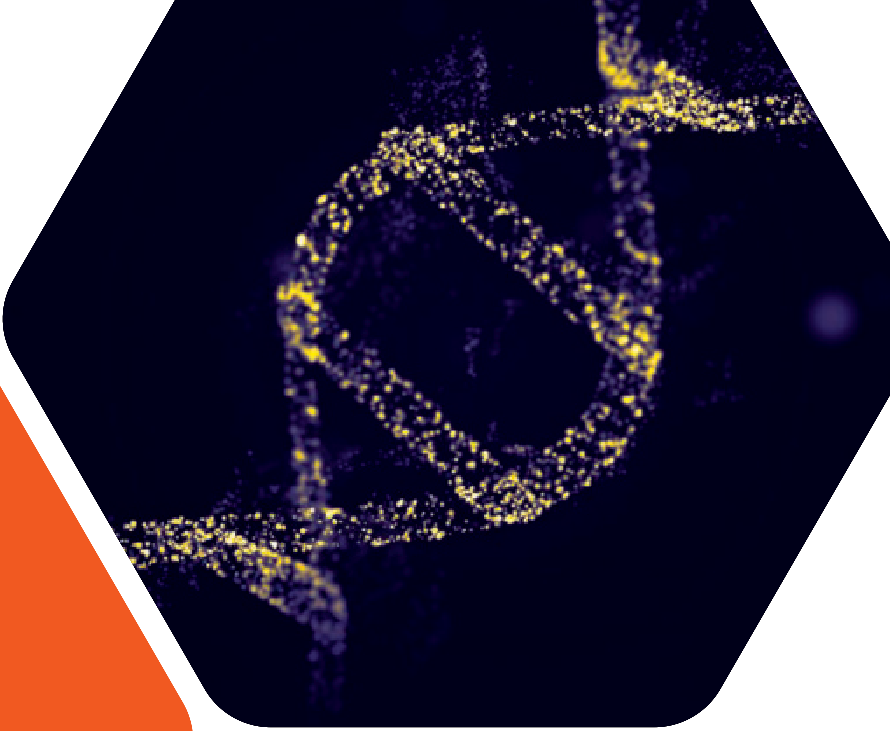

NOSTER

Connecting life & gut microbiome

Utilizing NOSTER's
original lipid metabolite database

Postbiotics Scan Metabolome
Analysis Service

By conducting a thorough analysis of lipid metabolites produced by gut bacteria, you can gain valuable insights into the metabolic mechanisms of the microorganisms, discover novel biomarkers and therapeutic targets, and uncover new functional properties of food products.

16S rRNA Gene Analysis

Analysis Service
Gut Microbiota

By employing cutting-edge next-generation sequencing technology, we are able to conduct a comprehensive assessment of the diversity and distribution of microorganisms within samples. Moreover, by merging NOSTER's advanced cultivation techniques with real-time PCR analysis, we have developed the capability to quantitatively analyze gut bacteria that were previously challenging to culture and evaluate.

Application areas

Wide range of areas related to lipids and microorganisms such as gut bacteria as described below.

Food sector

Development of supplements and exploration of new functions of fats and oils and fermented foods.

Basic research

Analysis of metabolic mechanisms of gut bacteria.

Medical fields

Elucidation of pathological mechanisms / Search and development of diagnostic markers / Evaluation of therapeutic effects

Others

Studies related to gut microbiota and disease.

Noster Inc., Kyoto, Japan
https://www.noster.inc/
Email : contact@noster.inc